

**AEDC-TR-09-T-19**

**40 Years of AEDC Development, Evolution  
and Application of Numerical Simulations for  
Integrated Test and Evaluation of Turbine  
Engine Turbomachinery Operability Issues**

**Milt W. Davis, Jr., Alan A. Hale, and Jason Klepper  
Aerospace Testing Alliance**

**March 2010**

**Final Report for Period September 2009**

**Statement A: Approved for public release; distribution is unlimited.**

**ARNOLD ENGINEERING DEVELOPMENT CENTER  
ARNOLD AIR FORCE BASE, TENNESSEE  
AIR FORCE MATERIEL COMMAND  
UNITED STATES AIR FORCE**



## NOTICES

When U. S. Government drawings, specifications, or other data are used for any purpose other than a definitely related Government procurement operation, the Government thereby incurs no responsibility nor any obligation whatsoever, and the fact that the Government may have formulated, furnished, or in any way supplied the said drawings, specifications, or other data, is not to be regarded by implication or otherwise, as in any manner licensing the holder or any other person or corporation, or conveying any rights or permission to manufacture, use, or sell any patented invention that may in any way be related thereto.

Qualified users may obtain copies of this report from the Defense Technical Information Center.

References to named commercial products in this report are not to be considered in any sense as an endorsement of the product by the United States Air Force or the Government.

## DESTRUCTION NOTICE

For unclassified, limited documents, destroy by any method that will prevent disclosure or reconstruction of the document.

## APPROVAL STATEMENT

### Prepared by:



MILT W. DAVIS, JR.  
Aerospace Testing Alliance

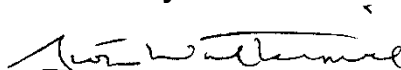


ALAN A. HALE  
Aerospace Testing Alliance



JASON KLEPPER  
Aerospace Testing Alliance

### Reviewed by:



SCOTT W. WALTERMIRE  
Air Force Project Manager  
649th Test Squadron

### Approved by:



CHARLES R. VINING, PhD  
Technical Director  
717<sup>th</sup> Test Squadron

REPORT DOCUMENTATION PAGE				Form Approved OMB No. 0704-0188	
<p>The public reporting burden for this collection of information is estimated to average 1 hour per response, including the time for reviewing instructions, searching existing data sources, gathering and maintaining the data needed, and completing and reviewing the collection of information. Send comments regarding this burden estimate or any other aspect of this collection of information, including suggestions for reducing the burden, to Department of Defense, Washington Headquarters Services, Directorate for Information Operations and Reports (0704-0188), 1215 Jefferson Davis Highway, Suite 1204, Arlington, VA 22202-4302. Respondents should be aware that notwithstanding any other provision of law, no person shall be subject to any penalty for failing to comply with a collection of information if it does not display a currently valid OMB control number.</p> <p><b>PLEASE DO NOT RETURN YOUR FORM TO THE ABOVE ADDRESS</b></p>					
1. REPORT DATE (DD-MM-YYYY) xx-03-2010		2. REPORT TYPE Final Report		3. DATES COVERED (From – To) September 2009	
4. TITLE AND SUBTITLE 40 Years of AEDC Development, Evolution and Application of Numerical Simulations for Integrated Test and Evaluation of Turbine Engine Turbomachinery Operability Issues			5a. CONTRACT NUMBER		
			5b. GRANT NUMBER		
			5c. PROGRAM ELEMENT NUMBER		
6. AUTHOR(S) Davis, Jr., Milt W., Hale, Alan A. and Klepper, Jason Aerospace Testing Alliance			5d. PROJECT NUMBER 11808		
			5e. TASK NUMBER		
			5f. WORK UNIT NUMBER		
7. PERFORMING ORGANIZATION NAME(S) AND ADDRESS(ES) Aerospace Testing Alliance (ATA) Computational Simulation, Modeling & Analysis Technology and Analysis Branch 1099 Avenue C, MS9013 Arnold Air Force Base, TN 37389-9013				8. PERFORMING ORGANIZATION REPORT NO.  AEDC-TR-09-T-19	
9. SPONSORING/MONITORING AGENCY NAME(S) AND ADDRESS(ES) 649 Test System Squadron Arnold AFB, TN 37388				10. SPONSOR/MONITOR'S ACRONYM(S)	
				11. SPONSOR/MONITOR'S REPORT NUMBER(S)	
12. DISTRIBUTION/AVAILABILITY STATEMENT <b>Statement A:</b> Approved for public release; distribution is unlimited.					
13. SUPPLEMENTARY NOTES Available in the Defense Technical Information Center (DTIC).					
14. ABSTRACT AEDC has invested in the full spectrum of compression system analysis simulations. The main emphasis of this report is to provide an overview and specific examples of the compression system codes developed over the last 40 years at AEDC and how they may benefit the test and evaluation capability. A historical perspective of the code development and applications are presented to provide the reader with a sense of continuity between the development process and the application process. Code applications are presented to provide the reader with a sense of what can be done with each of the codes and when to use them and at what fidelity. Finally, the technical approach is presented to provide the reader with a detailed explanation of how each code works and the basic assumptions.					
15. Subject Terms Compression System Operability Analysis, Numerical Simulations, Computer Modeling, Compressor Surge, Rotating Stall, Inlet Distortion Effects, Dynamic Simulation, Parallel Compressor Model, 3D Euler Code, DYNTECC, TEACC, TEACCSTALL					
16. SECURITY CLASSIFICATION OF:			17. LIMITATION OF ABSTRACT	18. NUMBER OF PAGES	19A. NAME OF RESPONSIBLE PERSON
A. REPORT	B. ABSTRACT	C. THIS PAGE			Milt W. Davis, Jr.
Unclassified	Unclassified	Unclassified	Same as Report	466	19B. TELEPHONE NUMBER (Include area code) 931-454-5370

This page is intentionally left blank.



## PREFACE

This Technical Report serves as a reference to those who wish to be introduced to the modeling and simulation capabilities for the analysis of compression system operability issues developed at AEDC over the last 40 years. This document has been compiled from technical papers presented over that same timeframe to bring the knowledge of operability modeling and simulation into one place so that new users and ultimately new developers can see what has been done in the past and how best to use what is available or what needs to be invented.

Many AEDC employees have been involved in the development of the M&S codes and respective analysis. They are listed below to acknowledge their contributions and provide the reader with a sense of what has been accomplished and the importance that AEDC placed on this development process. Major contributors were:

Bill Kimzey (ret.)	Ted Garretson (ret.)	Milt Davis	Claude Chamblee (ret.)
Grant Patterson (ret.)	Virgil Smith(ret.)	Alan Hale	Brian Feather
Jason Klepper	Jackie Chalk	Karl Kniele (ret.)	Doug Garrard
Peter Montgomery	Sherri Smith	Sarah Asbury	Sam Snyder
Kimble Shahrohki,	Jim Sirbaugh	Anthony Watts*	



## CONTENTS

1	INTRODUCTION.....	21
1.1	Document Organization .....	21
1.2	The Integrated Test and Evaluation (IT&E) Methodology .....	23
1.3	References .....	24
2	HISTORICAL BACKGROUND .....	25
2.1	The Beginning.....	26
2.2	Kimzey's Codes .....	26
2.3	DYNMOD, THREED and DYNTECC .....	27
2.4	Parallel Compressor Theory Code .....	28
2.5	The Dynamic Turbine Engine Code, ATEC .....	29
2.6	The JDAPS Alliance.....	29
2.7	The 3D Turbine Engine Analysis Compressor Code, TEACC .....	29
2.8	The 2D Streamline Curvature Code, SLCC, and the 1D Meanline Code.....	31
2.9	Turbomachinery CFD.....	33
2.10	Fly The Mission Vision .....	34
2.11	Funding and Joint Efforts .....	34
2.12	AEDC Generated Specific Technical References.....	34
3	APPLICATIONS .....	40
3.1	Surge, Rotating Stall and Compression System Recovery .....	42
3.1.1	Compression System Component Loading for Single-Spool Systems ....	44
3.1.2	Compression System Component Loading for Dual-Spool Systems.....	47
3.1.3	Compressor Post-stall Analysis and Behavior .....	51
3.1.4	Hardware Modifications – Flow Area & Inter-Stage Bleed .....	57
3.1.5	Effect of Heat Transfer on Post-Stall Behavior (Nine-Stage Model) .....	66
3.1.6	The Effect of Casing Treatment on System Operability .....	70
3.1.7	The Effect of Camber or Variable Vane Re-Positioning on System Operability.....	81
3.1.8	Compression System Component Behavior During Oscillating Flow .....	85
3.1.9	Compression System Behavior During Hot Gas Ingestion.....	90
3.1.10	Axi-Centrifugal Compression System Post-Stall Behavior .....	96
3.1.11	Dynamic Engine Simulation of Post-Stall Behavior and Engine Starting .....	104
3.2	Inlet Distortion.....	109
3.2.1	Inlet Total Pressure Distortion – Parallel Compressor Theory.....	112

3.2.2	Inlet Total Pressure Distortion – TEACC–Validation of a High-Fidelity Technique .....	121
3.2.3	Inlet Total Pressure Distortion – TEACCSTALL, Higher Fidelity Simulation .....	137
3.2.4	Inlet Total Temperature Distortion Analysis – Parallel Compressor Theory.....	151
3.2.5	Combined Pressure and Temperature Distortion Analysis.....	157
3.2.6	Inlet Swirl Distortion Analysis.....	172
3.3	Airframe-Propulsion Integration via Numerical Simulations .....	188
3.3.1	Aircraft-Propulsion Integration – One-Dimensional Analysis .....	194
3.3.2	Airframe-Propulsion Integration 3D Analysis .....	205
3.3.3	Aero-Structural for System Interaction Analysis.....	222
3.4	Propulsion Facility Issues Addressed By Numerical Simulations For Operability .....	227
3.4.1	Facility Duct Length Analysis for Test Article Post-Stall Behavior .....	229
3.4.2	Facility Overpressure Analysis for Test Article Post-Stall Behavior.....	233
3.4.3	E311 Distortion Analysis.....	236
3.4.4	16T Wind Tunnel Dynamic Simulation.....	242
3.5	Steam And Water Ingestion Issues .....	247
3.5.1	Steam Ingestion for a Generic HPC.....	248
3.5.2	Water Ingestion Analysis for the FT8.....	258
3.5.3	Steam Ingestion Predictions for a Modern Military Compression System .....	267
4	NUMERICAL SIMULATIONS – TECHNICAL DETAILS.....	273
4.1	An Overview of Codes and Technical Approaches.....	274
4.2	Meanline Code (MLC) Technical Approach.....	283
4.3	Streamline Curvature Code, SLCC, Technical Approach .....	286
4.4	1D Dynamic Compression System Technical Approach,.....	304
4.4.1	Single Spool DYNMOD & DYNTTECC .....	305
4.4.2	Dual Spool DYNMOD & DYNTTECC.....	318
4.5	1D Dynamic Engine Code, ATEC, Technical Approach .....	321
4.6	Parallel Compression System Code.....	345
4.7	3D Euler Code, TEACC & TEACCSTALL Technical Approach .....	351
4.8	ALE3D Technical Approach .....	366
4.9	Turbomachinery CFD Codes,Turbo & Overflow, Technical Approach .....	369
4.10	Water/Steam Ingestion Technical Approach .....	376

	4.11	Integration of ML & DYNTTECC, Technical Approach .....	383
5		LESSONS LEARNED.....	384
6		LIST OF REFERENCES.....	386
	6.1	Chapter 2 References.....	386
	6.2	Chapter 3 References.....	390
	6.3	Chapter 4 References.....	405

## APPENDICES

APPENDIX A	JOINT DYNAMIC AIRBREATHING PROPULSION SIMULATIONS (JDAPS) .....		414
	A.1	Vision, Mission and Goals of JDAPS.....	415
	A.2	JDAPS Organizational Structure .....	416
	A.3	Development of Production Simulations.....	417
	A.4	Research and Development Activities.....	420
	A.5	References: .....	422
APPENDIX B	FLIGHT SIMULATION VISION FOR AEROPROPULSION GROUND TEST FACILITIES .....		424
	B.1	The Plant Flight Simulation Vision.....	426
	B.2	Technical Approach – Non-Distorted Inlet Flow .....	427
	B.3	Non-Distorted Inlet Airflow Simulation Demo.....	431
	B.4	Technical Approach – Distorted Inlet Flow .....	434
	B.5	Putting the Pieces Together.....	436
	B.6	References: .....	438
APPENDIX C	STREAMLINE CURVATURE CODE (SLCC) HTSC RESULTS.....		439
	C.1	REPLICAS Calibration Procedure.....	439
	C.2	Overall 1-D Maps .....	440
	C.3	Transition of SLCC Solution to TEACCSTALL .....	445
	C.4	Specific Data Analysis Tools .....	446
APPENDIX D	ONE-DIMENSIONAL COMPRESSOR STAGE CHARACTERISTICS .....		448
	D.1	Unstalled Forward Flow .....	449
	D.2	Stalled Forward Flow Modeling Technique.....	450
	D.3	Reversed Flow Modeling Technique .....	452
	D.4	Empirical Observations and Additions.....	453
	D.4.1	Criteria Used For Stall Inception.....	453
	D.4.2	Stalled-Flow Jet Exit Angle .....	454

D.4.3	Recovery Hysteresis .....	454
D.4.4	Reversed-Flow Pressure Prediction .....	455
D.5	Assembly into a Wide Range Prediction Model .....	455
D.5.1	Application to a Low-Speed Compressor .....	456
D.5.2	Application to a High-Speed Compressor .....	457
D.6	Stage Model Summary .....	461
D.7	Additional References .....	461
NOMENCLATURE .....		463

## FIGURES

Figure 1.1	Computational Techniques Complexity as a Function of Approximate Computational Time .....	021
Figure 1.2	Integrated Test and Evaluation Concept .....	23
Figure 2.1	Timeline of Major Code Developments and Specific Applications .....	25
Figure 3.1	Path Taken During Transient Events .....	40
Figure 3.2	Compression System Instability Anatomy .....	42
Figure 3.3	Surge Cycle Representation .....	43
Figure 3.4	Rotating Stall Representation .....	43
Figure 3.5	Schematic of the Single-Spool, Ten-Stage Compression System Modeled .....	44
Figure 3.6	Ten-Stage Single-Spool HPC Model Comparison to Experimental Results .....	45
Figure 3.7	Ten-Stage HPC Loading Comparison to Experimental Results .....	46
Figure 3.8	Stage Static Signature Indicating Seventh Stage As Critical Stage .....	46
Figure 3.9	Schematic of the Mixed Flow Turbofan Compression System Modeled .....	47
Figure 3.10	HPC Loading Comparison to Experimental Results .....	48
Figure 3.11	Static Pressure Signature Indicating Stage Instability .....	49
Figure 3.12	Fan Loading Comparison to Experimental Results .....	50
Figure 3.13	Stage Characteristics for a 3-Stage, Low-Speed Compressor .....	52
Figure 3.14	Post-Stall Behavior of Compressor Rig, $B = 0.65$ .....	54
Figure 3.15	Three-Stage Model Overall System Post-Stall Behavior, Rotating Stall, $B = 0.65$ .....	54
Figure 3.16	Post-Stall Behavior of Compressor Rig, $B = 1.0$ .....	55
Figure 3.17	Three-Stage Model Overall System Post-Stall Behavior, Rotating Stall, $B = 1.0$ ...	55
Figure 3.19	Three-Stage Model Overall System Post-Stall Behavior, Rotating Stall, $B = 1.0$ ...	56

Figure 3.18 Post-Stall Behavior of Compressor Rig, $B = 1.58$ .....	56
Figure 3.20 Ten-Stage Compressor Stage Definition .....	57
Figure 3.21 Ten-Stage Compressor Rig Setup & Model Control Volume Definition.....	57
Figure 3.22 Model Simulation of Rotating Stall/Surge Boundary .....	58
Figure 3.23 Model Simulation of Overall Rotating Stall Performance and Comparison with Data.....	59
Figure 3.24 Model Simulation of Interstage Rotating Stall Performance and Comparison with Data.....	59
Figure 3.25 Model Simulation of Experimentally Determined Compressor Recovery Hysteresis .....	60
Figure 3.26 Effect of Enlarge Rear Stage Flowpath on Stage Performance .....	61
Figure 3.27 Overall Compressor Map Showing Predicted Improved Recovery Behavior Due to Enlarged Rear Stage Flowpath.....	61
Figure 3.28 Stall-Related Prediction Resulting from Stage 5 Bleed Outflow .....	62
Figure 3.29 Predicted Compressor Recovery Resulting from Stage 10 Bleed Outflow .....	62
Figure 3.30 Effect of Bleed Flow Location on Stage 9 Dynamic Behavior .....	63
Figure 3.31 Schematic of the Single-Spool, Nine-Stage Compression System Modeled.....	66
Figure 3.32 Predicted Stage Temperature Distribution Max and Idle Power and Corresponding Blade Store Thermal Energy .....	67
Figure 3.34 Typical Stage Heat-Transfer Rate Based Upon Experimental Results .....	68
Figure 3.33 Typical Stage Heat-Transfer Rate Based Upon Experimental Results .....	68
Figure 3.35 Typical Stage Heat-Transfer Rate Based Upon Experimental Results .....	69
Figure 3.36 Possible Tip Treatment Modification and the Effect on Stage Characteristic .....	71
Figure 3.37 Three-Stage Overall Compression System Post-Stall Behavior, Rotating Stall, $B = 0.65$ .....	72
Figure 3.38 Postulated Stage Pressure Characteristic Modification as a Result of Tip Treatment .....	72
Figure 3.39 Model prediction of the Effect of 1 <sup>st</sup> Stage Tip Treatment on Post-Stall Behavior, $B=0.66$ .....	73
Figure 3.40 Schematic of ADLARF Fan .....	74
Figure 3.41 Typical ADLARF Stage Characteristics, 98% .....	75
Figure 3.42 Comparison of Model Compression System Overall Pressure Rise and Efficiency to Experimental Results .....	76

Figure 3.43 Static Pressure Signature at Compression System Instability – Stage 2 as Critical Stalling Stage .....	76
Figure 3.44 Stage 2 Modification for Casing Treatment of 5%.....	77
Figure 3.45 Effect on Overall System Operability of a Stage 1 Modification for Casing Treatment of 20% .....	78
Figure 3.46 Comparison of ADLARF Compression System Operability Characteristics with Tip Casing Treatment of 20% on the 1 <sup>st</sup> stage and 13% on the 2 <sup>nd</sup> Stage to Baseline.....	78
Figure 3.47 Effect of Camber on Stage Performance .....	82
Figure 3.48 Postulated Stage Pressure Characteristic Modification as a Result of Increasing Blade Camber.....	82
Figure 3.49 Model Prediction of the Effect of Increasing Blade Camber on Post-Stall Behavior, $B = 0.66$ .....	82
Figure 3.50 Schematic of ADLARF Fan .....	83
Figure 3.51 Stage 2 Modification for Variable Vane Re-Positioning.....	83
Figure 3.52 Effects of Variable Vane Re-Positioning on ADLARF Overall Compression System Performance.....	83
Figure 3.53 Schematic of the Single-Spool, Ten-Stage Compression System Modeled .....	85
Figure 3.54 Schematic of the Mixed Flow Turbofan Compression System Modeled .....	86
Figure 3.55 Model Predicted with Full-Face Oscillatory Inlet Total Pressure, Speed = 98% .....	86
Figure 3.56 Typical Model Predicted Oscillatory Inflow Effects on Compression System Operation .....	87
Figure 3.57 Model Predicted Stability Limits for Planar Oscillating Inflow .....	88
Figure 3.58 Prediction of Compression System Stability Limit Trends for Planar Oscillating Inflow .....	89
Figure 3.59 Schematic of the Single-Spool, Ten-Stage Compression System Modeled .....	90
Figure 3.60 Schematic of the Mixed Flow Turbofan Compression System Modeled .....	91
Figure 3.61 Model Predicted with Full-Face Inlet Temperature Ramp – Initial Speed = 98%....	91
Figure 3.62 Temperature Ramp Convected Downstream with Velocity Field .....	92
Figure 3.63 Model Prediction with 180° Segment Temperature Ramp – Initial Speed = 98% ...	92
Figure 3.64 Model Predicted Stability Limits for Inlet Temperature Ramps.....	93
Figure 3.65 Model Predicted Effects of Rapid Inlet Temperature Ramps on Compression System Behavior .....	93
Figure 3.66 Schematic of TF30 Compression System Modeled .....	94
Figure 3.67 Schematic of TF30 Compression System Modeled .....	95



Figure 3.68 T55-L-712 Turboshift Engine.....	96
Figure 3.69 T55 Model Geometry.....	97
Figure 3.70 Final Stage Characteristic at 80% .....	98
Figure 3.71 Axial String of Transducers .....	99
Figure 3.72 Experimental Static Pressure Signature at Time of System Instability 80% Speed .....	100
Figure 3.73 Model Predicted Static Pressure Signature at Time of System Instability at 80% Speed .....	100
Figure 3.74 System Response to a Throttle Closure at 80% Speed -- Deep Surge.....	101
Figure 3.75 Static Pressure Signature During Surge Cycles at 80% Speed .....	101
Figure 3.76 Cousins Reading of the Experimental Results.....	103
Figure 3.77 Comparison of Component Level and ATEC Model and Simulation Technology for Gas Turbine Engine Modeling .....	104
Figure 3.78 Relative Compressor Pressure Ratio as a Function of Time.....	105
Figure 3.79 Relative Total Pressure as a Function of Axial Distance and Time .....	106
Figure 3.80 Relative Mass Flow Rate at Time of Surge Cycles .....	106
Figure 3.81 Relative Total Temperature at Time of Surge Cycles .....	106
Figure 3.82 Combustor Equivalence Ratio during Engine Transient.....	107
Figure 3.83 Relative Rotor Speed .....	107
Figure 3.84 Compressor Pressure Ratio as a Function of Time for the Engine Starting Process.....	107
Figure 3.85 Gas Generator Rotor Speed as a Function of Time for the Engine Starting Process.....	108
Figure 3.86 Compressor Pressure Ratio as a Function of Compressor Inlet Mass Flow Rate for the Engine Starting Process .....	108
Figure 3.87 Subscale Model Wind Tunnel Test.....	109
Figure 3.88 Direct Connect Test Cell Schematic.....	109
Figure 3.89 Direct Connect with Distortion Screens .....	110
Figure 3.90 SAE Airframe-Propulsion Integration Methodology.....	110
Figure 3.91 Simulation of Time-Variant Distortion with Steady-State Patterns .....	112
Figure 3.92 Parallel Compressor Concept.....	113
Figure 3.93 Simulation of Time-Variant Distortion with Steady-State Patterns .....	114
Figure 3.94 Static Pressure Signature at Time of Compression System Instability.....	114
Figure 3.95 Model Predicts Overall Distorted Stability Limit Within 3% .....	115

Figure 3.96 Model Prediction with 180-deg Total Pressure Distortion .....	115
Figure 3.97 Static Pressure Signature Indicating Stalling Stage for 180-deg Circumferential Distortion .....	116
Figure 3.98 Reproduction of the J85-GE-13 Experimental Data for Clean Inlet [Figure 3 of Ref. 3.73] .....	117
Figure 3.99 Parallel Compressor Model Results at the Same Corrected Speeds as Experimental Data for Clean Inlet.....	117
Figure 3.100 Parallel Compressor Model Results Compared to 180-deg Circumferential Total Pressure Distortion Implemented by a Distortion Screen.....	118
Figure 3.101 Comparisons of the DYNTECC Parallel Compressor Model Loss in Stall Pressure Ratio to Those Observed Experimentally [3.75] .....	118
Figure 3.102 Overall TEACC Approach.....	122
Figure 3.103 Clean Inlet Overall Pressure Ratio Compared with Experimental Data.....	122
Figure 3.104 Clean Inlet Efficiency Compared to Experimental Data .....	123
Figure 3.105 Clean Inlet Radial Comparisons .....	124
Figure 3.106 Screen Location and Labeling .....	125
Figure 3.107 Distorted inlet, Overall Performance Map with Total Pressure Ratio at 100% Corrected Speed.....	125
Figure 3.108 Distorted Inlet Overall Performance Map with Efficiency at 100% Corrected Speed.....	126
Figure 3.109 Distorted Inlet, Exit Total Pressure on 100% Speedline.....	126
Figure 3.110 Distorted Inlet, Exit Total Temperature on 100% Speedline.....	127
Figure 3.111 Grid and Distortion Screen Modeling for Rotor 1B.....	128
Figure 3.112 Overall Performance Maps for Rotor 1B with Radial Inlet Total Pressure Distortion.....	129
Figure 3.113 Radial Comparisons of TEACC with Experimental Results for Rotor 1B with Radial Inlet Distortion at 100% Corrected Speed .....	130
Figure 3.114 Grid and Overall Performance for Stage 35.....	131
Figure 3.115 Radial Comparisons of TEACC Results and Data for Stage 35 at 70% Corrected Speed.....	132
Figure 3.116 Grid and Performance for Three-Stage Fan at 80% Corrected Speed.....	133
Figure 3.117 Total and Static Pressure for Three-Stage Fan at 80% Corrected Speed.....	133
Figure 3.118 Mach Number Associated Streamlines for the Three-Stage Fan at 80% Speed .....	134

Figure 3.119 Grid and Performance for Nine-Stage High Pressure Compressor at 90% Corrected Speed.....	135
Figure 3.120 Mach Number Associated Streamlines for the Nine-Stage High-Pressure Compressor at 90% Speed .....	136
Figure 3.121 Total and Static Pressure Profiles for a Nine-Stage High-Pressure Compressor at 90% Corrected Speed.....	136
Figure 3.122 TEACCSTALL Technical Approach.....	137
Figure 3.123 HTSC Two-Stage Fan Schematic.....	138
Figure 3.124 HTSC First Rotor.....	139
Figure 3.125 Radial View of Rotor 1 Showing Hub Section and Precompression Tip Profile.....	140
Figure 3.126 CRF Inlet Station 10 Instrumentation.....	140
Figure 3.127 CRF Distortion Measurement Station 15 Instrumentation .....	140
Figure 3.128 Stator 1 Leading-Edge Instrumentation .....	141
Figure 3.129 Fan Discharge Instrumentation .....	141
Figure 3.130 HTSC Clean and Distorted Data Points for 68.0% Speed.....	142
Figure 3.131 HTSC Rotor 1 Non-Dimensional OSPAN File Data .....	142
Figure 3.132 Axisymmetric HTSC TEACCSTALL Grid.....	143
Figure 3.133 Axisymmetric Overall 1-D Characteristic of HTSC – Clean.....	143
Figure 3.134 TEACCSTALL Solution at Stall .....	144
Figure 3.135 TEACCSTALL Clean Steady Results around WOD: $W_c = 93.01 \text{ lb}_m/\text{sec}$ .....	145
Figure 3.136 Inlet Distortion Pattern.....	145
Figure 3.137 Overall 1-D Characteristics of the HTSC – Distortion .....	146
Figure 3.138 TEACCSTALL Distorted Solution at Stall .....	146
Figure 3.139 TEACCSTALL Distorted Steady Results around WOD: $W_c=92.04 \text{ lb}_m/\text{sec}$ .....	147
Figure 3.140 180-deg Distortion Results. ....	148
Figure 3.141 CX3 Distortion Results. ....	149
Figure 3.142 Aircraft with Gun Gas Ingestion.....	151
Figure 3.143 Aircraft in Hover Re-ingesting Exhaust Gas .....	151
Figure 3.144 Parallel Compressor Concept.....	153
Figure 3.145 Aircraft in Hover Re-ingesting Exhaust Gas .....	153
Figure 3.146 Comparison of a Typical Experimental Temperature Profile to That Used with the Parallel Compressor Model.....	154

Figure 3.147 Reproduced Figure [3.96] Indicating the Effect of Temperature Distortion on the Stability Limit.....	155
Figure 3.148 Parallel Compressor Model Results of the Effects of Temperature Distortion on Compressor Operability for Minimum Level of 5%.....	155
Figure 3.149 Comparison of DYNTECC Parallel Compressor Results for Total Temperature Distortion to Those Observed Experimentally .....	156
Figure 3.150 Model Prediction with 180° Opposing Pressure and Temperature Distortion – Initial Speed = 98% .....	157
Figure 3.151 Model Prediction with 180° Opposing Pressure and Temperature Distortion – Initial Speed = 98% .....	158
Figure 3.152 Model Prediction with 180° Opposing Pressure and Temperature Ramp – Initial Speed = 98% .....	158
Figure 3.153 Model Prediction with 180° Concurrent Pressure and Temperature Ramp – Initial Speed = 98% .....	159
Figure 3.154 The Northrop Grumman T-38, Talon, Trainer .....	159
Figure 3.155 The J85-GE-5 Afterburning Turbojet Engine .....	160
Figure 3.156 New PMP Ejector Nozzles to Reduce Drag Associated with Overexpansion [3.108].....	160
Figure 3.157 New PMP Inlet Nozzle to Increase Takeoff Thrust [3.108].....	160
Figure 3.158 Engine Bay Cooling and the Potential for Flow Re-Ingestion.....	161
Figure 3.159 Reproduced Experimental Results [3.116] for Combined Pressure and Temperature Distortion – Opposed .....	162
Figure 3.160 Reproduced Experimental Results [3.116] for Combined Pressure and Temperature Distortion – Concurrent .....	163
Figure 3.161 Parallel Compressor Model Results of Temperature and Pressure Distortion – Opposed .....	163
Figure 3.162 Parallel Compressor Model Results of Temperature and Pressure Distortion – Concurrent .....	164
Figure 3.163 T-38 Inlet Interface Hardware to the J85 Engine .....	165
Figure 3.164 Representative Steady State CFD AIP Pressure and Temperature Distortion Patterns at a Typical Cruise Flight Condition.....	165
Figure 3.165 Simplified Pressure and Temperature Distortion Patterns for Use Within the Parallel Compressor Model .....	166

Figure 3.166 Parallel Compressor Model Prediction of the Loss in Stability Limit for Pressure and Temperature Distortion Separately and in Combination for the Altitude Condition.....	166
Figure 3.167 Representative Steady State CFD AIP Pressure and Temperature Distortion Patterns at SLS.....	167
Figure 3.168 Parallel Compressor Model Prediction of the Loss in Stability Limit for Pressure and Temperature Distortion Separately and in Combination at SLS.....	167
Figure 3.169 Comparison of the Parallel Compressor Results to that Predicted by the NASA Algorithm Based Upon Experimental Results .....	168
Figure 3.170 Measured Temperature Distortion Near the Tip of the Compressor and a Representation of the Simplification Necessary for the Parallel Compressor Model.....	169
Figure 3.171 Parallel Compressor Model Prediction of the Effect on System Operability Due to Various Levels of Pressure Distortion and the Measured Temperature Distortion.....	169
Figure 3.172 Projected Velocity Vectors Produced with Paired Swirl [3.124].....	172
Figure 3.173 Projected Velocity Vectors Produced with Bulk Swirl [3.124] .....	172
Figure 3.174 Single-Stage Rotor 1B.....	174
Figure 3.175 Two-Stage HTSC as Tested at the Compressor Research Facility [3.125].....	174
Figure 3.176 Results of R1B Meanline Calibration Process at 100% Speed .....	175
Figure 3.177 Effect of Swirl on Rotor 1B Loss and Diffusion Factor .....	175
Figure 3.178 The Effect of +/- 5 deg of Swirl on HTSC Overall Performance .....	176
Figure 3.179 The Effect of +/- 5 deg of Swirl on HTSC First Rotor Performance .....	177
Figure 3.180 Effect of +/- 5 deg of Swirl on HTSC First Rotor Loss and Diffusion Factor .....	177
Figure 3.181 Effect of +/- 5 deg of Swirl on HTSC Second Rotor Performance .....	178
Figure 3.182 Effect of +/- 5 deg of Swirl on HTSC Second Rotor Loss and Diffusion Factor .....	178
Figure 3.183 The Effects of Co- and Counter Bulk Swirl on Rotor 1B Performance and Operability.....	179
Figure 3.184 The Effects of Twin Bulk Swirl on Rotor 1B Performance and Operability .....	180
Figure 3.185 The Effects of Twin Bulk Swirl on Rotor 1B Performance and Operability .....	180
Figure 3.186 The Effects of Twin Bulk Swirl in Combination with Total Pressure Distortion on Rotor 1B Performance and Operability .....	181
Figure 3.187 The Effects of Co- and Counter Bulk Swirl on HTSC Performance and Operability.....	181

Figure 3.188 The Effects of Co- and Counter Bulk Swirl on HTSC Rotor 1 Performance and Operability.....	182
Figure 3.189 The Effects of Co- and Counter Bulk Swirl on HTSC Rotor 2 Performance and Operability.....	182
Figure 3.190 The Effects of Twin Bulk Swirl in Combination with Total Pressure Distortion on HTSC Performance and Operability .....	182
Figure 3.191 Predictions of the Effect of Swirl on F109 Fan Performance.....	183
Figure 3.192 Determination of Stall Point Using Diffusion Factor and Loss .....	184
Figure 3.193 The Effects of Bulk Swirl on F109 Fan Performance and Operability.....	184
Figure 3.194 The Effects of Twin Paired Swirl on F109 Fan Performance and Operability .....	185
Figure 3.195 The Effects of Twin Bulk Swirl on F109 Performance and Operability .....	185
Figure 3.196 The Effects of Differing Amounts of Twin Swirl on F109 Performance and Operability.....	186
Figure 3.197 Predictions of the Effect of Bulk Swirl Using a 3-D Euler Compression System Simulation .....	187
Figure 3.198 The Society of Automotive Engineers S-16 Committee for Turbine Engine Inlet Flow Distortion .....	188
Figure 3.199 Aircraft-Propulsion Integration Issues.....	189
Figure 3.200 Current Weapons System Integration Process.....	191
Figure 3.201 Improved Test and Evaluation Process Through Numerical Simulations .....	193
Figure 3.202 Schematic of the Coupled Inlet-Engine Codes .....	195
Figure 3.203 A 4060 Inlet and J85-13 Turbojet Installed in the LeRC 10x10 Supersonic Wind Tunnel [3.140].....	195
Figure 3.204 Cross-Sectional View of the 4060 Inlet and J85-13 Turbojet Installation [3.140].....	196
Figure 3.205 Bleed Bypass Doors Percent Open as a Function of Time .....	196
Figure 3.206 Centerbody Extension (Values Normalized by Cowl Lip Radius) .....	197
Figure 3.207 Test Data: Ratio of Compressor Inlet Total Pressure to Freestream Total Pressure [3.141].....	198
Figure 3.208 Test Data: Ratio of Compressor Exit Total Pressure to Freestream Total Pressure [3.141].....	198
Figure 3.209 Test Data: Engine Shaft Rotational Speed [3.141, with reference to 3.142].....	199
Figure 3.210 Model Predictions: Ratio of Compressor Face Total Pressure to Freestream Total Pressure .....	199

Figure 3.211 Model Predictions: Ratio of Compressor Exit Total Pressure to Freestream Total Pressure.....	200
Figure 3.212 Model Predictions: Engine Rotational Speed.....	200
Figure 3.213 Inlet Shock Location Normalized by Cowl Lip Radius .....	201
Figure 3.214 Relative Total Pressure in the Inlet at Three Different Times.....	201
Figure 3.215 Mach Number in the Inlet at Three Different Times .....	202
Figure 3.216 Relative Total Pressure in the J85-13 Turbojet at Three Different Times.....	202
Figure 3.218 Compressor Pressure Ratio as a Function of Compressor Inlet Corrected Mass Flow Rate .....	203
Figure 3.217 Compressor Pressure Ratio .....	203
Figure 3.219 CFD Flow-Field and Inlet Computations of an Advanced Inlet.....	206
Figure 3.220 Computational Techniques Complexity as a Function of Approximate Computational Time.....	206
Figure 3.221 Complex Flow-Field Calculation using RANS CFD for Turbomachinery .....	207
Figure 3.222 Technical Approach for 3D Euler Turbomachinery Code for the Analysis of Inlet Distortion.....	208
Figure 3.223 Solution of the Integrated Aircraft – Propulsion System.....	209
Figure 3.224 Prediction of Fan Stall at a Typical Flight Condition.....	209
Figure 3.225 Doghouse Plot.....	211
Figure 3.226 Wind Tunnel Installation and Total Pressure Probes at AIP.....	211
Figure 3.227 Calculated Loss in Stability Pressure Ratio for a 4-sec Transient. ....	212
Figure 3.228 ARP-1420 Estimated Loss in Stability Pressure Ratio for Selected Wind Tunnel-Produced Inlet Distortion Patterns.....	213
Figure 3.229 Methods for Determining Loss in Stability Pressure Ratio. ....	214
Figure 3.230 Inlet Total Pressure Recovery for the 17 Chosen Data Points. ....	215
Figure 3.231 Comparison of Steady-State CFD Generated Inlet Distortion Intensities to Wind Tunnel Data for the Airframe/Inlet on a Doghouse Plot. ....	216
Figure 3.232 Total Pressure Distortion Intensity Comparison for Chosen Data Point 6. ....	216
Figure 3.233 Total Pressure Distortion Intensity Comparison for Chosen Data Point 3. ....	217
Figure 3.234 Comparison of the CFD Stability Pressure Ratio Loss Using the ARP-1420 Methodology to Steady State Inlet WT Data.....	218
Figure 3.235 Nosecone Differences Between WT Model and CFD Calculations.....	218
Figure 3.236 TEACCSTALL Technical Approach.....	219
Figure 3.237 Integration of OVERFLOW and TEACCSTALL Using DiRTlib.....	220

Figure 3.238 Comparison of Predicted Surge Frequency and Pressure Ratio to Experimental Results .....	223
Figure 3.239 Model Predicted Compressor Inlet Total Pressure During Surge Event.....	224
Figure 3.240 Pressure Contours at Equilibrium with Imbedded Normal Shock During Steady Operation .....	224
Figure 3.241 Surge Pressure Boundary Condition for Mock HSCT Inlet.....	225
Figure 3.242 Inlet Unstart Due to Engine Surge Cycle .....	226
Figure 3.243 Effect of Inlet Unstart on Aircraft Wing Assembly .....	226
Figure 3.244 An Aerial View of the Arnold Engineering Development Center.....	227
Figure 3.245 An Aerial View of the Aeropropulsion System Test Facility, ASTF .....	228
Figure 3.246 Typical Test Cell Installation in the ETF.....	229
Figure 3.247 Simulation Geometry and Initial Total Pressure Distribution for Configuration 1.....	230
Figure 3.248 Fan Total Pressure Ratio as a Function of Time for Configuration 1 .....	230
Figure 3.249 Fan Pressure Ratio as a Function of Percent Design Corrected Airflow Rate for Configuration 1 .....	230
Figure 3.250 Simulation Geometry and Initial Total Pressure Distribution for Configuration 2.....	231
Figure 3.251 Fan Pressure Ratio as a Function of Time for Configuration 2 .....	231
Figure 3.252 Fan Pressure Ratio as a Function of Percent Design Corrected Airflow Rate for Configuration 2.....	231
Figure 3.253 Simulation Geometry and Initial Total Pressure Distribution for Configuration 3 .....	232
Figure 3.254 Fan Pressure Ratio as a Function of Percent Design Corrected Airflow Rate for Configuration 3.....	232
Figure 3.255 Fan Pressure Ratio as a Function of Percent Design Corrected Airflow Rate for Configuration 3.....	232
Figure 3.256 Typical Test Cell Installation in the ETF.....	233
Figure 3.257 Simulation Geometry with Flex Duct.....	233
Figure 3.258 DYNTECC Predicted Results for Surge Cycle Behavior of a Typical Military HPC System.....	234
Figure 3.259 Flex Duct Overpressure Force Analysis for Surge Cycle Behavior of a Typical Military HPC System .....	235
Figure 3.260 ASTF Exhaust System .....	236



Figure 3.261 Schematic of the E311 Inlet Flow Environment .....	236
Figure 3.262 Exhauster Compressor Volume Flow .....	238
Figure 3.263 Potential Effect of Inlet Pressure Distortion on the E311 Exhaust Compressor .....	239
Figure 3.264 DYNTECC Calculated Results vs. Westinghouse Calculated Performance.....	239
Figure 3.265 The Potential Effect of Inlet Pressure Distortion on the E311 Exhaust Compressor .....	240
Figure 3.266 The Potential Effect of Temperature Distortion and Combined Effects of Temperature and Pressure Distortion on the E311 Compressor .....	240
Figure 3.267 16T Wind Tunnel Circuit.....	242
Figure 3.268 16T Wind Tunnel Circuit.....	243
Figure 3.269 AFAST 16T Wind Tunnel Total Pressure.....	244
Figure 3.270 Comparison of AFAST and SS Model Results for Total Pressure.....	245
Figure 3.271 Comparison of AFAST and SS Model Results for Total Temperature .....	245
Figure 3.272 Comparison of AFAST and SS Model Results for Mach Number .....	246
Figure 3.273 Carrier Launched Aircraft with Steam Ingestion [3.178].....	247
Figure 3.274 Parametric Study Results – Changes in Fluid Properties as a Function of Percentage of Steam and Axial Distance with Constant Quality of 50%.....	250
Figure 3.275 Parametric Study: Effect of Amount of Steam at 50-Percent Quality on Compressor Stage Performance.....	251
Figure 3.276 Parametric Study: Effect of Amount of Steam at 50% Quality on Overall Compressor Performance.....	252
Figure 3.277 Parametric Study Results: Changes in Fluid Properties as a Function of Steam Quality and Axial Distance for Constant Amount of Steam of 1%.....	254
Figure 3.278 Parametric Study: Effect of Quality of Steam for an Amount of 1% on Compressor Stage Performance.....	255
Figure 3.279 Parametric Study: Effect of Quality of Steam for an Amount of 1% on Compressor Performance.....	256
Figure 3.280 FT8-2 Gas Turbine Engine for Power Production .....	258
Figure 3.281 Test Cell and FT8 as Modeled .....	259
Figure 3.282 Reduction in Total Temperature Due to Fogging Water Evaporation in Plenum Chamber.....	260
Figure 3.283 Temperature of the Gas Mixture and Liquid Water Droplets .....	262

Figure 3.284 Evaporative Energy Transfer from Liquid Droplets to Gas Mixture and Convective Heat Transfer from Gas Mixture to Liquid Water Droplets.....	263
Figure 3.285 Corrected Map Relating Percent Differences in Fogging Results About the Mean Fogging Point for Speed and Flow .....	264
Figure 3.286 Normalized Static Pressure for FT8 Validation with Fogging Water.....	265
Figure 3.287 Normalized Total Pressure Ratio for FT8 Validation with Fogging Water.....	265
Figure 3.288 Normalized Total Temperature Ratio for FT8 Validation with Fogging Water.....	266
Figure 3.289 Predicted Fan Pressure Ratio vs. Corrected Gas Mass Flow for Various Liquid Water Loading Factors.....	268
Figure 3.290 Predicted Fan Temperature Ratio vs. Corrected Gas Mass Flow for Various Liquid Water Loading Factors .....	268
Figure 3.291 Mass Fraction of Water Vapor vs. Axial Distance .....	269
Figure 3.292 Liquid Water Loading Factor vs. Axial Distance.....	270
Figure 3.293 Change in Blade Incidence Angle from Dry vs. Blade Row.....	270
Figure 3.294 Per Blade Row Pressure Ratio Percent Difference from Dry vs. Axial Distance .....	271
Figure 3.295 Per Blade Row Temperature Ratio Percent Difference from Dry vs. Axial Distance .....	271
Figure 4.1 Meanline Theory In Terms of Velocity Diagrams .....	274
Figure 4.2 Streamline Curvature Code Computational Grid.....	275
Figure 4.3 Control Volume Technique.....	276
Figure 4.4 Parallel Compressor Theory Concept.....	277
Figure 4.5 3D Euler Technical Approach.....	278
Figure 4.6 Typical CFD Grid and Results with Inlet Distortion Taken from Ref. 4.29 .....	279
Figure 4.7 Axial Flow Compressor Cascade Geometry and Velocity Triangles .....	283
Figure 4.8 Axial Flow Compressor Blade Geometry .....	284
Figure 4.9 Schematic of SLCC Inputs .....	286
Figure 4.10 Geometry of Computing Station [4.41] .....	286
Figure 4.11 Velocity Triangle Nomenclature Used in SLCC .....	287
Figure 4.12 Representative Loss Bucket.....	294
Figure 4.13 Schematic of Lewis, Miller, Hartman Shock Model .....	294
Figure 4.14 P Factor for Minimum Loss Calculation [4.46] .....	295
Figure 4.15 Schematic of Boyer Shock Model [4.33].....	298
Figure 4.16 Schematic of Deviation.....	297

Figure 4.17 Schematic of Streamtube Geometry Change Due to Axial Velocity Variation .....	299
Figure 4.18 Deviation Angle Slope Versus Solidity [4.46] .....	300
Figure 4.19 DYNTECC Control Volume Technique .....	305
Figure 4.20 Schematic of Variable Time-Step Routine .....	309
Figure 4.21 Typical Stage Characteristics .....	311
Figure 4.22 Time-Dependent Compressor Model Solution procedure, McCormick Formulation .....	318
Figure 4.23 Schematic of the 13-Stage, Dual-Spool Compression System Model .....	319
Figure 4.24 Schematic Bypass Flow Calculation Procedure .....	319
Figure 4.25 ATEC Control Volume Technique .....	321
Figure 4.26 Typical Compressor Pressure and Temperature Stage Characteristics .....	322
Figure 4.27 Application of Time Constants During Post-Stall Operation .....	323
Figure 4.28 Flammability Data as Given By Herbert [4.68] .....	324
Figure 4.29 Combustion Efficiency Correlation as Given by Lefebvre [4.69] .....	324
Figure 4.30 Combustor Total Pressure Ratio as a Function of Inlet Mach Number and Pressure Loss Coefficient .....	326
Figure 4.31 Typical Turbine Performance Specification Curves .....	327
Figure 4.32 Axial Compressor Heat Transfer Model .....	329
Figure 4.33 Schematic of the Explicit Split Flux Differencing Scheme Used in ATEC .....	330
Figure 4.34 Time Derivative Split to Adjacent nodes by Implicit Characteristic Based Split Flux Difference Scheme Used in ATEC .....	331
Figure 4.35 Schematic of Variable Time-Step Routine .....	333
Figure 4.36 Typical Stage Characteristics .....	336
Figure 4.37 Classical Parallel Compressor Theory Concept .....	345
Figure 4.38 Illustration of the Circumferential Mass Redistribution Model .....	346
Figure 4.39 Illustration of the Radial Mass Redistribution Model .....	347
Figure 4.40 Unsteady Lift Coefficient Magnitude Ratio .....	348
Figure 4.41 Unsteady Blade Response to Circumferentially Nonuniform Flow .....	349
Figure 4.42 Illustration of Work Redistribution Concept with Radial Variation of Pressure Ratios .....	350
Figure 4.43 TEACC Source Term Methodology .....	351
Figure 4.44 Modifications to SLCC for Calculating Source Terms .....	353
Figure 4.45 Turbomachinery Blade Force Calculations .....	354
Figure 4.46 Interpolation of Radial Distribution of Source Terms .....	354

Figure 4.47	Circumferential Distribution of Source Terms .....	355
Figure 4.48	Boundary Condition TEACC Overall Approach to Solution.....	356
Figure 4.49	Detailed Technique to Advance a Solution to Convergence .....	358
Figure 4.50	Representation of TEACCSTALL .....	359
Figure 4.51	Turning Forces Generated by the Rotor .....	363
Figure 4.52	Turning Forces Generated by the Stator .....	364
Figure 4.53	Streamline Angles and Velocity Components .....	365
Figure 4.54	Grid Remapping Feature of ALE3D.....	367
Figure 4.55	Single Fan Stage Structural Analysis Using DYNA3D .....	367
Figure 4.56	Example Two-Dimensional Grid .....	371
Figure 4.57	Sample Mean Surface.....	372
Figure 4.58	Sample Passage Grid .....	373
Figure 4.59	Blade Passage Geometry .....	378
Figure 4.60	Heat and Work Process Involved Within a Region Defined in a Relative Coordinate System .....	379
Figure 4.61	Conceptual Picture for Defining the Two Constant Mass Flow Control Volumes Used for MLC/MPC Heat-Transfer Calculations .....	380
Figure A.1	JDAPS Logo .....	415
Figure A.2	DYNTECC General Modeling Technique .....	418
Figure A.3	TEACC Overall Technical Approach .....	419
Figure A.4	ATEC Technical Approach.....	420
Figure B.1	Typical Ground Test Facility/Engine Configuration.....	425
Figure B.2	Typical Test Cell Configuration .....	425
Figure B.3	Non-Distorted Inlet Flow Plant Flight Simulation Vision.....	426
Figure B.4	Numerical Simulation of the Non-Distorted Inlet Airflow Plant Simulation Vision ...	427
Figure B.5	Diagram for the J-Turbine Engine Test Facility as it Currently Exists .....	428
Figure B.6	Proposed Future Modification to the J-Cells Facility to Allow Additional Cooling ...	429
Figure B.7	The Aircraft Simulator, GENESIS .....	430
Figure B.8	AIRFOX's FlightLab Simulator .....	430
Figure B.9	Component-Level Engine Model Representation .....	431
Figure B.10	Altitude and Mach Number Conditions for Zoom-Climb from 25,000 to 40,000 ft at Mach Number of 0.8 – Conditions Obtained with GENESIS Flight Simulator .....	431
Figure B.11	Facility Conditions for Zoom Climb from 25,000 to 40,000 ft Altitude with Current Facility Configuration.....	432

Figure B.12 Inlet Temperature Conditions for Zoom-Climb Using the Future Facility Configuration .....	433
Figure B.13 Altitude and Mach Number Conditions for Mach Dash from 0.8 to 1.2 at 25,000 ft Altitude – Conditions Obtained with GENESIS Flight Simulator .....	433
Figure B.14 Facility Conditions for Mach Dash from 0.8 to 1.2 at 25,000 ft Altitude with Current Facility Configuration .....	434
Figure B.15 Inlet Temperature Conditions for Mach Dash Using the Future Facility Configuration .....	434
Figure B.16 Distorted Inlet Flow Plant Flight Simulation Vision .....	435
Figure B.17 Transient Distortion Generator Concept – An Array of Blockage Elements Distributed Over .....	435
Figure B.18 Inlet Data Obtained from Tests and CFD .....	436
Figure B.19 Distortion Simulator Database Concept .....	436
Figure B.20 Plant Flight Simulation Vision – Distorted Inlet Flow – Numerical Simulation .....	437
Figure B.21 TEACC Zooming to Accomplish Modifications in Compression System Maps Due to Distortion .....	437
Figure C.1 REPLICAS Calibration Procedure .....	440
Figure C.2 Overall 1-D Characteristics of the HTSC .....	441
Figure C.3 Radial Calibration – WOD $W_c=92.97 \text{ lb}_m/\text{sec}$ .....	441
Figure C.4 Radial Calibration – OL1 $W_c=92.65 \text{ lb}_m/\text{sec}$ .....	442
Figure C.5 Radial Calibration – OL2 $W_c=92.26 \text{ lb}_m/\text{sec}$ .....	443
Figure C.6 Radial Calibration – OL3 $W_c=87.23 \text{ lb}_m/\text{sec}$ .....	444
Figure C.7 Radial Calibration – PE $W_c=90.70 \text{ lb}_m/\text{sec}$ .....	445
Figure C.8 Radial Calibration – NS $W_c=82.58 \text{ lb}_m/\text{sec}$ .....	446
Figure D.1 Mean Radius Section of a Compressor Stage in Forward-Flow Operations .....	449
Figure D.2 Compressor Cascade Geometry and Nomenclature for Stalled Operation .....	451
Figure D.3 Mean Radius Section of a Compressor Stage in Reversed-Flow Operation .....	452
Figure D.4 Corrected Pressure Losses in a Reversed-Flow Compressor Cascade .....	453
Figure D.5 Three Stage Test Compressor Pressure Characteristics .....	456
Figure D.6 Ten-Stage Compressor First-Stage Characteristics .....	458
Figure D.7 Ten-Stage Compressor Third-Stage Characteristics .....	458
Figure D.8 Ten-Stage Compressor Fifth-Stage Characteristics .....	459
Figure D.9 Ten-Stage Compressor Tenth-Stage Characteristics .....	459

## TABLES

Table 3.1 Stalling Stages at Compressor Instability & Comparison to Experimental Results ....	45
Table 3.3 ADLARF Design Performance Parameters.....	74
Table 3.4 Tabulated Parametric Results Using DYNTECC .....	79
Table 3.5 Design Parameters of the First-Stage Rotor .....	139
Table D.1 FULRANGE Model Input Parameters. ....	455

# 40 Years of AEDC Development, Evolution and Application of Numerical Simulations for Integrated Test and Evaluation of Turbine Engine Turbomachinery Operability Issues

## 1 INTRODUCTION

Through the last 40 years, computer models for the prediction of gas turbine compression system operability issues have evolved both in complexity and into a very wide range of applications. This document has been written to aid test and analysis personnel analyze compression system operability issues using fundamental concepts with fast and accurate numerical simulations. These simulations can help one to understand compression system performance behavior, analyze system operability issues, in a fast and a user-friendly manner. They have also become very useful for operability analysis, preliminary design studies of compression systems, and changes to system performance and operability due to potential hardware modifications.

### 1.1 DOCUMENT ORGANIZATION

AEDC has invested in the full spectrum of compression system analysis simulations as shown in [Figure 1.1](#). This technical report summarizes these techniques (with the exception of cycle codes) and provides examples where they have been used. CFD techniques for aircraft-inlet simulation are not highlighted in this report but will be examined at an appropriate section to discuss how compression system simulations can interact with the full flowfield calculated by aircraft-inlet CFD codes.

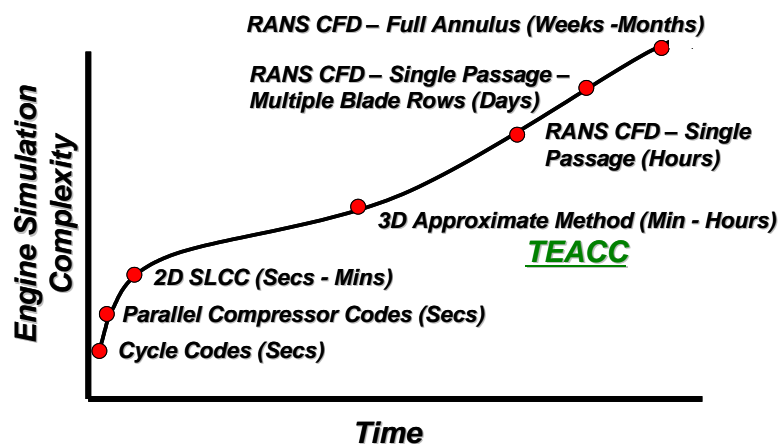


**Figure 1.1 Computational Techniques Complexity as a Function of Approximate Computational Time**

The main emphasis of this report is to provide an overview and specific examples of the compression system codes developed over the last 40 years at AEDC and how they may benefit the test and evaluation capability. A historical perspective of the code development and applications ([Chapter 2](#)) is presented to provide the reader with a sense of continuity between the development process and the application process. Code applications are presented in [Chapter 3](#) and provide the reader with a sense of what can be done with each of the codes and when to use them and at what fidelity. Finally, in [Chapter 4](#) the technical approach is presented to provide the reader with a detailed explanation of how each code works and what are the basic assumptions.

[Chapter 3 \(Applications\)](#) focuses on application of compression system simulations for the following operability issues:

- Surge, Rotating Stall and Compression System Recovery
- Inlet Distortion
- Airframe Propulsion Integration
- AEDC Facility Applications
- Water and Steam Ingestion

**Chapter 4 (Simulations)** introduces all the different types of compression system simulations, their technical approaches and underlying assumptions. The types of codes discussed are:

- 1D dynamic model for analyzing surge, rotating stall, and recovery techniques
- Parallel compressor model for circumferential distortion
- 1D dynamic engine model for both turbojets and turbofan systems
- 3D Euler compression system simulation for complex distortion
- CFD turbomachinery code
- 1D meanline code
- 2D Streamline curvature code

**Chapter 5 (Lessons Learned)** lists a series of lessons learned over the 40 years of development and application of compression system numerical simulations for operability issues.

There are four Appendices that go into detail on the following subjects:

**Appendix A (JDAPS)** describes a past alliance of interested organizations who came together in the 1990's to foster and advocate funding of the development and application of dynamic compression system simulations.

**Appendix B (Flight Simulation Vision for Aeropropulsion Ground Test Facility)** describes a vision for simulating flight maneuvers using the AEDC turbine engine ground test facilities. Typical flight conditions were simulated using an aircraft flight simulator and engine performance was simulated using a cycle code. Facility hardware was simulated by a lump-volume numerical simulation of one of the AEDC direct-connect facilities. In addition to normal turbine engine performance, a vision is presented for inlet distortion testing using wind tunnel or CFD as a mechanism for determining inlet distortion parameters.

**Appendix C (Streamline Curvature Application)** describes an application of the SLCC code to the High Tip Speed Compressor (HTSC). The SLCC in itself is not a code for analyzing compression system operability issues, but may be necessary as a first step in using other operability codes to provide stage or blade row characteristics.

**Appendix D (Development of Post-Stall Stage Characteristics)** describes a method for developing not only pre-stall but post-stall stage characteristics for use within the 1D dynamic codes for surge, rotating stall or recoverability.

As a suggestion of how to read this report, it all depends on the interest of the reader. If the reader is more interested in analysis techniques and specific types of analysis, the reader should consult the Table of Contents in **Chapter 3** and determine which example is best suited for his case. Once the reader is familiar with the specific past analysis, he should explore the technical details of the specific simulation as outlined in **Chapter 4**. If the reader is interested in pursuing the use of one of the highlighted codes, he should contact one of the authors of this report for advice and the code itself.



If the reader is interested in the state-of-the-art (SOA) of compression system simulations, the historical perspective provided in [Chapter 2](#) is a good place to start. This chapter provides a good summary of what others have done to advance the SOA in this area. Then the reader should examine [Chapter 4](#) in detail to understand each of the types of simulations along with their assumptions and potential uses. Examples of each of these simulations can then be found in [Chapter 3](#).

To aid the reader of the electronic version (PDF) of this report, figures, references, and major section references have been hyperlinked. **Figures** callouts are highlighted in **Blue** and by clicking on the callout, the cursor will move to the page where that figure is located (usually on the same page as the callout). To get back to the page where the callout is located, the reader should use the “Previous View” button usually found on the main bar at the top. **References** are highlighted in **Red** and **chapters or sections** are highlighted in **Green**. To get back to where the reader was originally, he should use the “Previous View” button as before.

## 1.2 THE INTEGRATED TEST AND EVALUATION (IT&E) METHODOLOGY

One primary objective of the Arnold Engineering Development Center (AEDC) test and evaluation (T&E) mission is centered on integrating weapon system airframe and propulsion systems. Airframe-propulsion integration encompasses a number of issues ranging from aircraft stability and control to inlet-engine compatibility. Consequently, the integration involves a wide range of technical disciplines with implications to the T&E environment. To address these disciplines, the T&E process requires the application of a variety of test resources as well as analytical and computational tools. Testing for airframe-propulsion integration, and in particular inlet-engine compatibility, generally requires the coupling of component tests conducted in wind tunnels and engine altitude facilities.

A multidimensional conceptual model of the Integrated Test and Evaluation (IT&E) approach is illustrated in [Figure 1.2](#). In the simplest

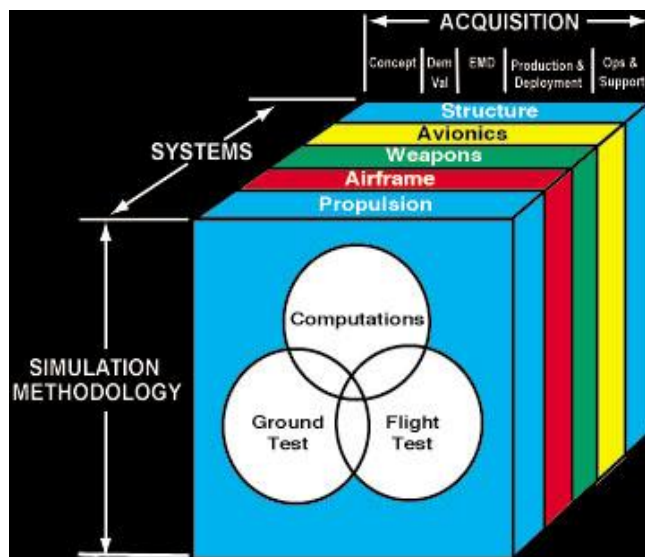


**Figure 1.2 Integrated Test and Evaluation Concept**

sense, IT&E might involve the use of computer modeling tools (such as computational fluid dynamics or engineering methods prediction codes) only to augment or correct data to as tested conditions acquired in a wind tunnel or an engine test cell. The IT&E process relies upon numerical simulations to provide information that may not be obtained during the testing process. For IT&E to become viable in the gas turbine engine business area, rapid multidimensional, interdisciplinary simulations of the full engine are required for analysis ranging from steady-state performance to highly dynamic events that include inlet distortion, gas ingestion, compressor surge/stall, and combustion instability.

However, integrating the modeling and simulation (M&S) tools directly with ground and flight tests enables one to design a better ground-flight test program, validate the ground-flight test

results, extrapolate the results to flight conditions, and assist in decision making for a more efficient or effective ground-flight test program.

The goal is to integrate propulsion system numerical simulations into the Test/Analysis Process is to:

- **Provide** pre-test prediction and post-test assessment of engine test matrix to optimize altitude propulsion testing
- **Provide** pre-test prediction and post-test assessment of flight test matrix to optimize wind tunnel inlet testing
- **Provide** a connectivity between ground test engine/inlet performance/operability test results and actual flight test environment
- **Demonstrate** integrated capabilities in an actual test program

The desired outcome is to reduce the cost of propulsion testing through the use of validated models and simulations, which can also provide confidence in the test results and additional information not obtainable through the testing process.

The information contained within this Technical Report provides examples where modeling and simulation has interacted with the test and evaluation process or had the potential for doing so. This document also serves as a fully documented reference of the efforts of the last 40 years in the area of turbine engine compression system operability and the link to new efforts in the future.

### 1.3 REFERENCES

**1.1** Davis, Milt, Alan Hale, and Dave Beale, "An Argument for Enhancement of the Current Inlet Distortion Ground Test Practice for Aircraft Gas Turbine Engines", *Journal of Turbomachinery*, Vol. 124, Number 2, April 2002, pp. 235-241.

**1.2** Davis, M. W., Jr., W. Baker, G. Power, and D. Beale, "A Proposal for Integration of Wind Tunnel and Engine Test Programs for the Evaluation of Airframe-Propulsion Compatibility Using Numerical Simulations", *Journal of Engineering for Gas Turbines and Power*, Vol. 124, Number 3, July 2002, pp. 447-458.

**1.3** Davis, Milt, Jr., Hale, Alan, Vining, Charles, and Cousins, William, "Application of Numerical Analysis Tools for Airframe-Propulsion Integrated Test and Evaluation", GT2008-50194, Presented at the 2008 ASME International Gas Turbine Institute's Turbo Expo in Berlin, Germany, June 2008.

**1.4** SAE S-16 Committee, ARP 1420, Revision B, "Gas Turbine Inlet Flow Distortion Guidelines," Society of Automotive Engineers, February 2002.

**1.5** SAE Aerospace Information Report AIR-1419, "Inlet Total-Pressure Distortion Considerations for Gas Turbine Engines," May 1983.

## CHAPTER 2 TABLE OF CONTENTS

2	Historical Background .....	25
2.1	The Beginning.....	26
2.2	Kimzey's Codes .....	26
2.3	DYNMOD, THREED and DYNTECC .....	27
2.4	Parallel Compressor Theory Code .....	28
2.5	The Dynamic Turbine Engine Code, ATEC .....	29
2.6	The JDAPS Alliance.....	29
2.7	The 3D Turbine Engine Analysis Compressor Code, TEACC .....	29
2.8	The 2D streamline curvature code, SLCC and the 1D Meanline Code .....	31
2.9	Turbomachinery CFD.....	33
2.10	Fly The Mission Vision .....	34
2.11	Funding and Joint Efforts .....	34
2.12	AEDC Generated Specific Technical References .....	34

## 2 HISTORICAL BACKGROUND

The development and application of compression system modeling and simulation for the analysis of operability issues is a subject that has spanned nearly forty years at AEDC.

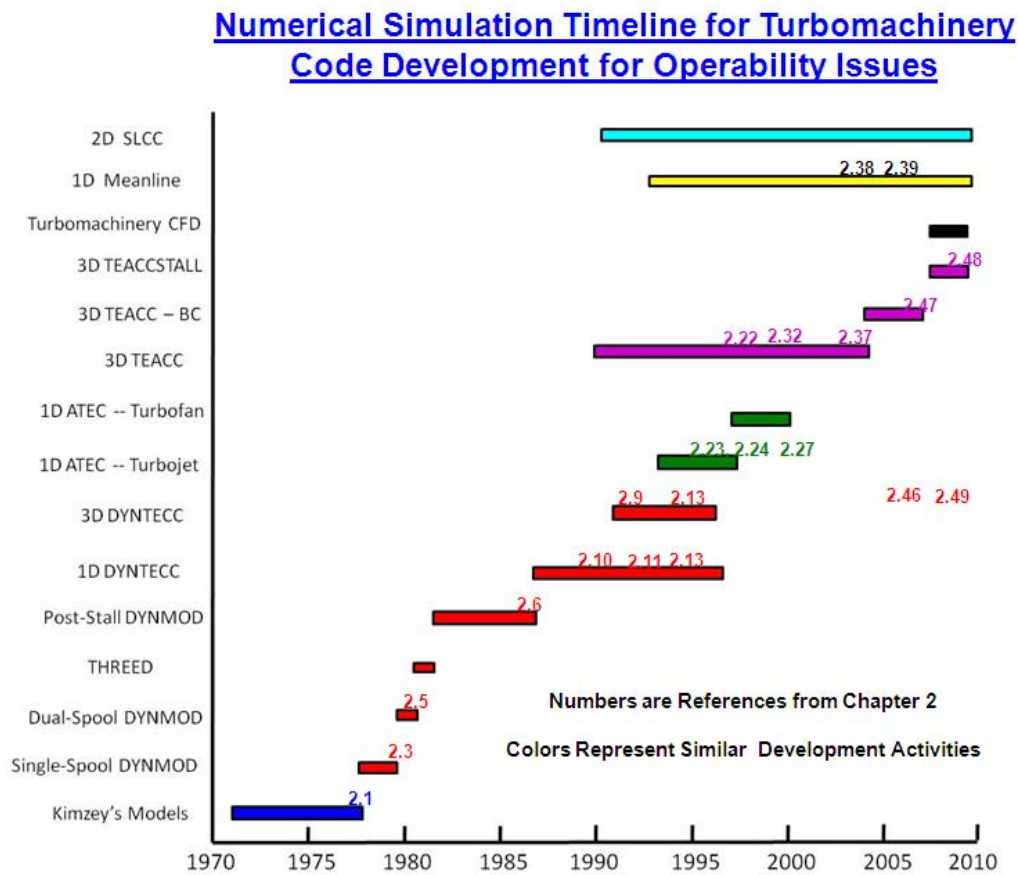


**Figure 2.1 Timeline of Major Code Developments and Specific Applications**

Development of an independent analysis capability in this area has been the objective of AEDC and there have been many people involved. The following historical perspective was written by the primary author whose career encompassed the work efforts over the specific timeline discussed in this Technical Report. This chapter addresses what has been developed, how it is relevant and provides documentation on the actual or potential impact to the AEDC mission. The specific code development efforts both for development and applications are presented in the timeline of [Figure 2.1](#).

Associated with the specific code development timelines are examples of technical papers which are designated by their chapter reference number. In general, the applications came along at the same time as the development of the capability. The major exception is with the **3D DYNTTECC** code which uses parallel compressor theory and has been instrumental in several investigations well after the completion of the code development. Shown at the top of the timeline graph are two specific capabilities that were necessary for the development of other operability capabilities, namely the **Meanline Code(MLC)** and the **stream line curvature codes (SLCC)**. Works on both of these codes were continuous enabling other applications discussed in this report as well.

## 2.1 THE BEGINNING

In the beginning (circa 1970) there was a general desire by the weapon system development community to understand turbine engine compression system operability characteristics (surge and stall) because of the F-111 airframe-propulsion compatibility problem with the TF-30 turbine engine. This issue instigated a series of engine tests and simulation developments that have revolutionized turbine engine analysis techniques.

In 1972, the US Air Force instigated the formation of a national committee to develop a methodology for understanding the airframe-propulsion integration issue such that the problems associated with the development of the F-111 Fighter-Bomber would not happen again. That committee (known as the S-16 committee) under the auspices of the Society of Automotive Engineers, (SAE) developed and published a new test and analysis methodology known as the ARP-1420, Gas Turbine Inlet Flow Distortion Guidelines” and its companion document, the AIR-1419, Inlet Total-Pressure Distortion Considerations for Gas Turbine Engines”. These documents have become standards of the gas turbine industry for understanding, designing, and testing of today’s gas turbine engines for airframe-propulsion compatibility issues. As testing of gas turbine engines is an expensive proposition, ways to predict compression system stall and surge became important especially if it could be proven to be accurate and inexpensive. The development of the digital computer at about this same time, setup a natural mechanism for researchers to development simulations that would not only predict compression system steady state performance but the highly dynamic inception of system stall and or surge and recovery to normal operation.

## 2.2 KIMZEY’S CODES

The first AEDC compression system modeling effort was initiated by Kimzey [\[2.1\]](#) who had been involved with testing of turbine engine operability issues at AEDC in the 1960’s. Kimzey develop a numerical simulation to understand the effects of inlet distortion on compression system operability and how that leads to system breakdown or surge. Kimzey developed both a one-dimensional simulation and a parallel compressor simulation to analyze dynamic behavior up-to system flow breakdown. The initial 1D Kimzey model had some instability issues associated with it. Kimzey’s solution was to dampen out the increasingly unstable nature by

adding large amounts of friction (more than would physically be present) to the inlet and exit ducts of the system. This was similar to today's solution of "artificial dissipation" in many of today's CFD algorithms.

Beside the compression system applications contained within Kimzey's dissertation, the 1D model was applied during this timeframe to the TF-41 by Chamblee [2.2]. In the course of this application, Chamblee also provided another solution to the numerical instability problem associated with the Kimzey model formulation. Chamblee's solution was to average the increasing amplitude of the instability and restart the solution using an average over 5-timesteps.

In 1978, an effort was initiated to improve the parallel compressor model for radial flow distribution when radial distortion was present. Kimzey had developed an algebraic means for flow redistribution when circumferential distortion was present which was derived using an orifice analogy. Over the years, this approximation has shown to be quite useful and accurate but the concept of radial redistribution was not as easily simulated using the same orifice analogy. Kimzey suggested a means for radial flow redistribution which was also an approximation that has to be verified and calibrated with each application. Several new approaches were worked on, but none were able to improve on what had already been programmed within the modified Kimzey parallel compressor model.

## 2.3 DYNMOD, THREED AND DYNTECC

Chamblee's averaging solution worked as an intermediate solution to the 1D model instability problem, but to truly remove the instabilities, a new algorithm would have to be adopted. A study of the existing literature indicated that the McCormick Predictor-Corrector algorithm as the best solution to use at that time. To effectively develop this new algorithm, it was decided not to start with the existing Kimzey FORTRAN code but to develop the new model from scratch. This effort culminated into a new version of the Kimzey formulation known as **DYNMOD**. In addition to reformulation, **DYNMOD** also had been given the capability to analyze dual-spool systems such as the F100 and F110 turbofan engines [2.3, 2.5].

During the later years of the 1970's, the Kimzey's parallel compressor code using the McCormick Predictor-Corrector algorithm was also reformulated which became known as **THREED**. Little if no use was made of **THREED** because by this time, the industry had become interested in the "Nonrecoverable stall" or "stall stagnation" problem and code development at AEDC took a turn to understanding post-stall behavior and recovery techniques from rotating stall.

By 1981 codes able to simulate compression system post-stall behavior were being developed by both the major engine manufacturers, Pratt and Whitney and General Electric. Development of these codes along with testing at AEDC to understand rotating stall and recovery from such events were being funded by an Air Force Research Laboratory (AFRL) project. AEDC was given the opportunity to exercise the newly developed contractor models and analyze them for appropriate behavior. AEDC also wished to have a compression system model for analysis of "Nonrecoverable stall" and initiated an effort to extend **DYNMOD** to post-stall behavior. In late 1982 a full simulation of the F100 High Pressure Compressor, HPC undergoing surge cycles was obtained. In 1987 the extension of **DYNMOD** to the post-stall realm was completed and published by Davis in his dissertation and a companion technical paper [2.6, 2.8].



During 1987, the Compressor Research Facility, CRF, at AFRL decided to become involved with compression system modeling and simulation and a joint effort was initiated between AEDC and AFRL. In 1988, the **DYNMOD** model was applied to an F100 HPC compression system that had been tested in the CRF during 1986-87. For the next eight years, the joint effort was continued with several applications of the AEDC compression system codes to systems being tested at the CRF [2.11].

In 1987 a new solution algorithm based upon Split Characteristics was implemented into a new version of the 1D dynamic model and became known as the **Dynamic Turbine Engine Compressor Code, DYNTTECC** [2.10]. This new code had all the features of the **DYNMOD** code and picked up the capabilities of the **THREED** code as well. To provide ease of use and facilitate the use of **DYNTTECC**, a user friendly input/output was implemented within the **DYNTTECC** code.. Since most analysis would require plots, a new graphical output program designed to provide the most common types of analysis plots was developed. This program became known as **ATDAPT** which was based upon a mainframe plotting package known as **PLOT10** and a follow package known as **DISPLAY**. This add-on or after-the-fact stand alone package served **DYNTTECC** well for the next 5-7 years. Only with the advent of the Personal Computer was a new graphical User Interface (GUI) developed. The GUI is still a part of the **DYNTTECC** package; is quite useful and hasn't been changed since its final version in 1997.

## 2.4 PARALLEL COMPRESSOR THEORY CODE

In addition to adding a GUI to **DYNTTECC**, it was ready to be extended to multi-dimensions for use as a parallel compressor model. The concepts had been proven by Kimzey in his dissertation and the extension of **DYNMOD** to **THREED**. A simple parallel compressor concept was first initiated within **DYNTTECC** and reported in 1991 and 1992 AIAA papers by Davis and Hale, respectively [2.9, 2.10]. The 1991 paper dealt with the combination of pressure and temperature inlet distortion. Of particular interest was whether the temperature distortion and the pressure distortion were in the same area of the annulus area (i.e. were they concurrent or opposed). The paper was written to provide examples of what types of analysis could be done with the parallel compressor model and to point out the complexity associated with combined pressure and temperature distortions.

In 1994, the improvements that Kimzey outlined in his dissertation, mainly circumferential crossflow and dynamic effects near stall were implemented into **DYNTTECC** and were reported in an 1995 AIAA paper and Master's Thesis by Sharokhi [2.15]. Although the circumferential crossflow correlations based upon orifice flows have turned out to be a good approximation of the actual mechanism, a successful radial redistribution algorithm continued to elude the effort. Further improvements to the parallel compressor code were not pursued after the work by Sharokhi.

In recent years, the parallel compressor **DYNTTECC** model was used by Davis to analyze the effects of inlet swirl on system operability [2.47] and the combined effects of pressure and temperature distortion on the J85 turbojet engine as embedded within the T-38 trainer [2.49].

During the early 1990's two parallel efforts began to emerge within the AEDC compression system project. One effort was to extend the **DYNTTECC** dynamic 1D model to a full engine representative for analysis of engine dynamic behavior such as surge, rotating stall, and engine starting, known as **ATEC**. The other effort was to develop a 3D approach to inlet distortion effects that would address radial redistribution, known as **TEACC**.

## 2.5 THE DYNAMIC TURBINE ENGINE CODE, ATEC

The extension of the **1D DYNTTECC** code to a full engine model seemed at first to be a fairly straight forward concept. Just add a combustor, a turbine and a nozzle and one has a simple turbojet dynamic engine model. In 1994, an effort to extend **DYNTTECC** to a simple turbojet version was initiated and became known as the **Aerodynamic Turbine Engine Code, ATEC**. **ATEC** was initially applied to the J-85 turbojet and documented in a dissertation and companion papers by Garrard [2.20, 2.23, and 2.24]. That same year, in a joint effort with the Army Vehicle Propulsion Directorate at NASA Glenn Research Facility, **ATEC** was applied to the General Electric CT7 turboprop engine to study starting options and also reported by Garrard [2.30, 2.31].

In 1997, **ATEC** was applied by Garrard, et. al., for airframe-propulsion compatibility using a 1D inlet simulation known as **LAPIN** [2.27]. Funding for this effort came from NASA Glenn as well as AEDC. After the connection of the J-85 **ATEC** model to the **LAPIN** Inlet model, **ATEC** the 1D dynamic modeling effort was not worked on for nearly 3 years. In 1998, the Australian Defense Agency, requested a version of **DYNTTECC** and **ATEC** to work on modeling some of the engines that the Australian Air Force had in its inventory. In 1999, the Australian Defense Agency provided funding for an initial turbofan **ATEC** capability. In late FY2000; AEDC provided a simple turbofan version based upon generic compressor characteristics and components to the Australian Defense Agency. This version of the **ATEC/DYNTTECC** was used by the Australian Defense Agency for analysis of temperature distortion on a triple spool turbofan engine.

In 2002 a **meanline** code was implemented within **DYNTTECC** by Tibboels [2.34] to augment the stage characteristic method with a time-dependent calculation of instantaneous blade row performance using loss and deviation correlations. This effort was successful by applying the meanline methodology to **DYNTTECC** for a single rotor, R1B. This capability is currently (2009) being reviewed and upgraded for use in analyzing the effects of inlet swirl on the F109 fan.

## 2.6 THE JDAPS ALLIANCE

Beginning in the early 1990's, it rapidly became obvious that for the dynamic modeling and simulation activities at AEDC to continue, other funding sources would have to be obtained beyond what AEDC was willing to support out of its DBA budget. Because of the success in obtaining funding from the Air Force Research Laboratory (AFRL), specifically from the Compressor Research Facility, AEDC along with AFRL started thinking in terms of getting others to join the effort. A joint alliance was initiated known as the **Joint Dynamic Airbreathing Propulsion Simulations (JDAPS)**. A loose alliance with others such as Virginia Tech, Allied Signal, NASA Glenn Research Center, and the Army Research Laboratory was already in place. The **JDAPS** alliance existed for about 5 to 7 years during the 1990's generally obtaining funding from AEDC, AFRL, ARL and NASA GRC. **JDAPS** died in or about 1998 when NPSS (Numerical Propulsion Simulation System) began to flourish and funding dried up from most sources except AEDC. A technical paper by Davis, et. al. [2.17] was written in 1995 at the height of the alliance activities and is presented in [Appendix A](#).

## 2.7 THE 3D TURBINE ENGINE ANALYSIS COMPRESSOR CODE, TEACC

As indicated by the early 1990's, it was decided to follow a parallel approach and develop a new 3D capability to analyze inlet distortion. To obtain a full 3D capability, a new approach was called for that would ultimately lead to the development of the **Turbine Engine Analysis**

**Compressor Code, TEACC.** This code was initiated after reviewing a paper by French researchers, Billet, et. al. which used a streamline curvature code imbedded within a 3D Euler solution technique. The **SLCC** was used to go across the bladed region and provide the turbomachinery aspects of the code, while the 3D Euler portion calculated a transport of fluid between the bladed regions. Because of the limited interest in post-stall behavior once inlet distortion had initiated compression system instability, the new code was designed not to go beyond stall inception. Again due to the desire to be successful and the requirement to show success within a few years, the breadth and depth of this undertaking was not fully comprehended for many years.

The initial development concentrated on using the **ARO1** code developed by AEDC personnel. In the summer of 1994, **TEACC** was applied to a single rotor, R1B for validation purposes which included an inlet distortion case and documented in a dissertation and companion technical paper by Hale [2.22, 2.29]. Within a couple of years after **TEACC** initiation, it was decided to change the numerical integration solver to the **NPARC** code to obtain a more robust Euler solver. The move from the **ARO1** code to the **NPARC** code, documented by Hale, Chalk, et. al., [2.32], was to be the first of many Euler solver choices undertaken during the **TEACC** development process

During the mid 1990's financial support for the 3D **TEACC** code was limited. In 1998, substantial funding by NASA and then AFOSR propelled the **TEACC** code into a full-time activity able to support more than just one investigator. From 1998 through 2002, the **TEACC** code was improved many times to get it to appropriately handle inlet distortion. It was during these years that the code was reformulated with another Euler integrator, the **WIND** code since it was now the CFD code of choice by the NPARC Alliance. This choice of integrator allowed AEDC personnel to get aid in implementing for this application from other experts in the field. All through these years the focus of the effort was on getting the correct performance with inlet pressure distortion because if the performance was not right neither would the stall point be correct.

In the Fall of 2003, funding was obtained from the High Performance Computer and Modernization Program, HPCMP, under the CHSSI program for a full three years. The substantial funding increase allowed the **TEACC** team to explore hooking up the **TEACC** code to a full CFD RANS inlet code to begin to analyze a full system (aircraft and propulsion together). This type of activity also was of interest to Pratt and Whitney who provided additional funding for the next three years to apply **TEACC** to the JSF F135 fan [2.47]. The support from PW not only provided money but the appropriate fan geometry and CFD calculations which were proprietary to PW. This allowed the **TEACC** code to be applied to a relevant and current compression system and brought the development team into weekly contact with turbomachinery and CFD experts that gave advice on what changes to make that would improve the capability of **TEACC**.

During 2006, it became obvious that the **WIND** code was causing some numerical stability problems and it was decided to change the 3D Integrator again, this time to the **OVERFLOW** code. This worked well because at the same time a simplification to the **TEACC** approach was made by only using the **OVERFLOW** code in-between the blade rows and letting the Streamline Curvature Code, **SLCC**, supply the boundaries to the **OVERFLOW** 3D pieces of the code. These changes greatly simplified the process and let solutions be obtained that were becoming elusive. However, this simplification also came with a price tag. **TEACC** would no longer do transient solutions and the stall criteria became, at best, highly dependent upon experimental observation (i.e. **TEACC** was no longer predictive).



In 2007, a stall prediction capability needed to be added to **TEACC**. After investigating what needed to be done to **TEACC** to include this stall capability, it was determined that the latest version of **TEACC** needed to be reformulated to be time accurate and include source terms. To do this more readily, **TEACC** needed to be based on a cylindrical solver. In a survey of the literature to determine an appropriate solver, a cylindrical code developed by Rod Chima at NASA Glenn was discovered. This code, **CSTALL**, was not only a time accurate cylindrical solver, but also included the loss and turning source terms for turbomachinery. It met most of the needs for **TEACC** to meet the goal of predicting stall inception. Chima provided **CSTALL** to AEDC. Although **CSTALL** became the basis for the new formation of **TEACC** with stall prediction capability, previous AEDC knowledge and new developments have been included in the code to meet AEDC's needs. This modified code is now called **TEACCSTALL**. Within a few months, the new **TEACCSTALL** code had been applied to Pratt and Whitney's F135 fan.

In FY08, funding was obtained from a new HPCMP program known as CREATE-AV which is a multi-year program aimed at providing high fidelity software running on high performance computers to aid in the DoD weapons system procurement and acquisition process. One effort within this program dealt with the development and application of high fidelity software to analyze aircraft-propulsion interaction especially in the inlet system. **TEACCSTALL** integrated with aircraft-inlet CFD became a natural first step and reported on by Davis, et. al.[2.48].

During FY08 and portions of FY09, **TEACCSTALL** was applied to two different builds of the F135 fan and began predicting fan stall. As it turned out, both builds of the F135 fan were tested at AEDC and in the case of the second build **TEACCSTALL** was able to provide predictions a priori to the test. From this experience it was learned that in some cases **TEACCSTALL** predicted the stall point in a very acceptable manner, but in other cases, especially when radial distortion was evident, **TEACCSTALL** did not produce a satisfactory prediction. In assessing **TEACCSTALL's** limitation, it was determined that the manner by which radial blade row characteristics were implemented would need to be modified. Instead of implementing those characteristics as a function of blade inlet corrected mass flow, it was determined to use blade loss and turning in terms of incidence angle and relative inlet Mach number. This capability is currently being introduced into **TEACCSTALL**.

Two other development areas are noteworthy since they highly impact the development and use of the other codes mentioned above. One area is the development of steady state compression system codes using loss and deviation correlations: the meanline code and the streamline curvature code. Another area is the development of high fidelity computational fluid dynamic codes as applied to turbomachinery. Both have their individual histories outlined below.

## 2.8 THE 2D STREAMLINE CURVATURE CODE, SLCC AND THE 1D MEANLINE CODE

The streamline curvature code was first introduced to AEDC as **COCODEC**. This code was purchased by the US Government via Oakridge Laboratories and passed down to AEDC as a government owned code. **COCODEC** was a modification of a code known as **HTO300** developed by Richard Hearsay, now retired from Boeing. The original use for **COCODEC** was to calculate blade row performance as applied to AEDC's 16-foot transonic and supersonic wind tunnel compressors. The code worked well for the wind tunnel applications because the loss and deviation correlations built-in were based upon NASA SP-36, a publication with available data from cascade tests for NACA 65 and Double Circular Arc blade shapes. The compressor blades for the 16-foot wind tunnels were NACA 65 series blades making a good match with what was available within **COCODEC**. During the early 80's it became obvious that for **DYNMOD** and its eventual successor, **DYNTECC**, to be viable codes for use at AEDC, a means

to predict stage characteristics would need to be developed. **COCODEC** seemed the logical choice.

**COCODEC** was first used to develop stage characteristics for the nine-stage high pressure compressor for the F101 or F110 GE low by-pass turbofan. **DYNMOD** had just been applied to the F100 high pressure compressor using data taken during a test of the HPC core system during 1975 but had no counterpart for the F101 or F110. Having a dynamic model to analyze “stall-stagnations” of both HPC systems seemed like the right thing to have. Once blade geometry of the F101 HPC had been obtained from GE, **COCODEC** was used to predict stage characteristics for that system. Having only overall system performance obtained during AEDC testing, was somewhat of a disadvantage because one could never really be sure that the stage performance would be correct. There was not a corresponding core test of the F101 or the F110 to obtain stage information for validation. The eventual process involved much calibration (i.e. adding loss or deviation to individual blade row calculations to match overall performance) mainly because the correlations did not handle choke or near stall very well.

During this time, **COCODEC** was used as a “black box” without a real understanding of the physics and code implementation. Hearsay had done a fairly good job of documenting the code through a User’s manual but it would take many years and several investigators before a rudimentary understanding occurred. Once the F101/F110 characteristics were developed (mid to late 1980’s), **COCODEC** was set on the shelf until the next time it was needed to predict stage characteristics

Once the **TEACC** effort got into full swing (circa 1990), an understanding of how **COCODEC** work was an absolute necessity. Over the next several years, the **TEACC** development team learned how **COCODEC** worked since they were in continual interaction with the code. In 1994, Hearsay updated **HTO300** for NASA Ames and AEDC obtained a new version of the streamline curvature code and began to work with a hybrid between the initial version of **COCODEC** and the Ames **HTO300**. The heart of **HTO300** is the loss and deviation correlations. Since these correlations came from NASA SP-36, the AEDC team had to become quite familiar with what was in that document. Hearsay basically lifted the correlations and implemented them into **HTO300**. Each correlation implemented can be traced back to NASA SP-36 through an appropriate figure number.

During the **TEACC** development effort, several times the team contemplated revising or updating these correlations even to considering replacing them with a public domain set published by AGARD. It wasn’t until the late 1990’s that a different look at the correlations by Boyer provided an improved shock loss model within **HTO300** going beyond the original correlation which was based upon a normal terminating shock. Boyer put in a new shock loss model based upon oblique shocks and provided a better prediction of the pressure losses across a transonic blade passage [2.33]

Because of discussions on **TEACC** and **HTO300** with Boeing, AEDC ended up teaming with Boeing and Lawrence Livermore National Laboratories (LLNL) to try to get funding for the development of an airframe-propulsion interaction numerical simulation capability based on part by the **TEACC** code and on part by the LLNL **ALE3D** code. As an outcome of this effort, **ALE3D** was brought in-house to see if it could be utilized as an airframe-propulsion fluid structure code [2.26]. Because **ALE3D** was developed using both a Lagrangian and an Eulerian technique, it could handle both fluid and solid movement at the same time. This seemed like a perfect way to approach turbomachinery aeromechanics. However, the fluid modeling had not been updated as much as the structure modeling and the code wouldn’t

calculate some of the simplest fluid dynamics problems very accurately. After about a year of working with **ALE3D**, the team abandoned the effort and went back to **TEACC** in full force.

A need arose occasionally for a simpler code to use for predicting blade row characteristics. Thus was born the need for a **meanline** code. In 2001 through 2003, AEDC was given an opportunity to develop a **meanline** code through a joint effort with Pratt and Whitney to combine a 1D **multiphase** code with a **meanline** code. This new integrated model would give both PW and AEDC a capability to understand the effects of steam ingestion into the fan of the F135 – a concern for the carrier version of the JSF [2.38, 2.39]. The **meanline** code has since been used to predict stage characteristics for new applications and to use in the analysis of swirl on system operability. Currently, the latest version of **meanline** code is being implemented into the **DYNTECC** code to provide a new tool for the analysis of swirl on the F109 engine being tested at the USAF Academy.

## 2.9 TURBOMACHINERY CFD

As early as the 1990's there was interest in having a turbomachinery CFD capability at AEDC. In the early 1990's, a series of contacts was made with existing experts in the field to discern if there was a code that should be brought to AEDC to initiate a CFD capability. At that time, the **ADPAC** code, developed Allison under a NASA contract seemed to be the best fit for us at AEDC. The **ADPAC** code was acquired by AEDC and the supplied testcases run to verify code operation. In addition, the code was applied to a single rotor system that had been tested in the CARL facility of the Compressor Research Facility. The **ADPAC** effort only lasted a year and the technology was put up on the shelf due to lack of funding.

In 2003, under the HPCMP CHSSI project, another turbomachinery CFD effort was initiated to use the CFD code known as **TURBO** or **MSTURBO** and apply it to the GE High Tip Speed Compressor (HTSC). This effort obtained limited success in that a partially converged solution was obtained. In FY07, an in-house effort was again initiated to explore what other codes that might be appropriate for use by AEDC. The first codes initially pursued were the commercial codes **CFX** and **FLUENT**. After about a year of working with these codes, it was decided that a government owned code was needed so that work on the code could be done to add capability. It was decided to re-exercise the **TURBO** code. At the same time as work began with the **TURBO** code, AEDC modified the **OVERFLOW** code as a turbomachinery code and applied it to the 16T/S wind tunnel compressor.

In FY10, an effort has been initiated using the **TURBO** code as applied to the High Tip Speed Compressor while undergoing inlet pressure distortion. There is plenty of distortion data for this system and General Electric has consented to allowing this application to be used in the government CREATE-AV program.

This is the next big step in numerical simulations for the analysis of inlet distortion effects on system performance and operability. Others in the industry are beginning to calculate with inlet distortion using full-annulus CFD calculations. To be in the forefront of this important weapon system integration issue, AEDC will also need to be developing and applying turbomachinery CFD to a variety of systems gaining insight and understanding how they operate in adverse conditions and what is their performance.

## 2.10 FLY THE MISSION VISION

During the early part of this decade (2000-2004), it was determined that AEDC might have a role in providing turbine test processes that mimicked flight testing. Under the AEDC Long Range Planning Project, studies were instigated that looked at the feasibility of configuring the turbine engine plant system normally configured for direct-connect testing to a system that would mimic flight. Although the studies concentrated on steady state and transient flight maneuvers, it was part of the vision to provide an operability test capability. The studies produced a technical paper by Davis and Montgomery presenting a vision on how such a system might work [2.40]. The study was conducted with modeling and simulation resources and is re-presented in [Appendix B](#).

## 2.11 FUNDING AND JOINT EFFORTS

Throughout the forty years of development and application of the compression system codes, funding has always been an issue. AEDC through its Technology Program provided a certain level of resources for the development of the codes mentioned in this Chapter. Each year, technology activities were ranked, prioritized and funding assigned for those activities which were of high priority. Compression system modeling activities always received a certain level of funding from this AEDC process. This is a testament to the importance that AEDC placed upon this effort. As is the case with almost every research effort, generally more resources were required than those provided by AEDC. Over the last 25 or so years, it became necessary to seek outside funding through joint efforts. AEDC was successful in many joint sponsored endeavors in this area. Some of the major organizations that entered into joint endeavors with AEDC were: the Air Force Research Laboratory, NASA Glenn Research Center, the Army Vehicle Propulsion Directorate, the High Performance Computational and Modernization Program, the Air Force Office of Scientific Research, and Pratt and Whitney Engines. Without these joint efforts, the extent of the research and breath of the applications would not have taken place.

## 2.12 AEDC GENERATED SPECIFIC TECHNICAL REFERENCES

**2.1** Kimzey, W. F., "An Analysis of the Influence of Some External Disturbances on the Aerodynamic Stability for Turbine Engine Axial Flow Fans and Compressors", AEDC-TR-77-80, August, 1977.

**2.2** Chamblee, C. E., M. W. Davis, Jr., and W. F. Kimzey, "A Multi-Stage Axial Flow Compressor Mathematical Modeling Technique with Applications to Two Current Turbofan Compression Systems", AIAA Paper # AIAA-80-0054, Presented at the AIAA 18th Aerospace Sciences Meeting, Pasadena, CA, April, 1980.

**2.3** Davis, Milton W., Jr., "A Stage-by-Stage Compressor Modeling Technique for Single-and Dual-Spool Compression Systems", Unpublished Master's Thesis, University of Tennessee, Knoxville, Tennessee, August 1981.

**2.4** Davis, M. W., Jr., "A Stage-by-Stage Compressor Modeling Technique for Single- and Dual-Spool Compression Systems", AEDC-TR-81-13, March 1982.

**2.5** Davis, M. W., Jr., "A Stage-by-Stage Dual-Spool Compression System Modeling Technique", ASME Paper #82-GT-189, March 1982, Presented at the 1982 IGTI Conference, London, England.

- 2.6** Davis, M. W., Jr., "A Stage-by-Stage Post-Stall Compression System Modeling Technique: Methodology, Validation, and Application", Ph.D. Dissertation, Virginia Polytechnic Institute and State University, December 1986
- 2.7** Davis, M. W., Jr., "A Post-Stall Compression System Modeling Technique", AEDC-TR-86-34, February 1987.
- 2.8** Davis, M. W. , Jr. and W. F. O'Brien, "Stage-by-Stage Poststall Compression System Modeling Technique", **Journal of Propulsion and Power**, Vol. 7, Number 6, November-December 1991, pp. 997-1005.
- 2.9** Davis, M. W., Jr., "Parametric Investigation into the Combined Effects of Pressure and Temperature Distortion on Compression System Stability", AIAA Paper # AIAA-91-1895, Presented at the 27th Joint Propulsion Conference, Sacramento, CA, June 1991.
- 2.10** Hale, A. A. and M. W. Davis, Jr., "DYNAmic Turbine Engine Compressor Code: DYNTECC -- Theory and Capabilities", AIAA Paper # AIAA-92-3190, Presented at the 28th Joint Propulsion Conference and Exhibit, Nashville, TN, July 1992.
- 2.11** Gorrell, S. E. and M. W. Davis, Jr., "Application of a Dynamic Compression System Model to a Low Aspect Ratio Fan: Casing Treatment and Distortion", AIAA Paper # AIAA-93-1871, Presented at the 29th Joint Propulsion Conference and Exhibit, Monterey, CA, June 1993.
- 2.12** Hale, A. A., M. W. Davis, Jr., and K. R. Kneile, "Turbine Engine Analysis Compressor Code: TEACC -- Part I: Technical Approach and Steady Results", AIAA Paper # AIAA-94-0148, Presented at the 32nd Aerospace Sciences Meeting and Exhibit, Reno Nevada, January 1994.
- 2.13** Owen, A. K., and M. W. Davis, Jr., "Modeling the Dynamic Behavior of an Axial-Centrifugal Compression System", AIAA Paper # AIAA-94-2802, Presented at the 30th AIAA Joint Propulsion Conference and Exhibit, Indianapolis, IN. June 1994.
- 2.14** Davis, M. W., Jr. and T. A. Bapty, "Interactive User's Interface for a Dynamic Compression System Simulation," AIAA-95-0244, Presented at the 33rd Aerospace Sciences Meeting, Reno, NV. ,January 1995.
- 2.15** Shahrohi, K. A., "Application of a Modified Dynamic Compression System Model to a Low-Aspect Ratio Fan: Effects of Distortion," Unpublished Master's Thesis, Vanderbilt University, Nashville, Tennessee, May 1995.
- 2.16** Shahrohi, K. A., and M. W. Davis, Jr., "Application of a Modified Dynamic Compression System Model to a Low-Aspect Ratio Fan: Effects of Distortion," AIAA-95-0301, Presented at the 33rd Aerospace Science Meeting, Reno, NV, January 1995.
- 2.17** Davis, M. W., Jr., O'Brien, W. F., Owen, A. K., and W. T. Cousins., "Joint Dynamic Airbreathing Propulsion Simulations Partnership (JDAPS)," ASME Paper # 95-GT-279, Presented at the 40th ASME International Gas Turbine & Aeroengine Congress & Exposition, Houston, Texas, June 1995
- 2.18** Garrard, G. D., M. W. Davis, Jr., and A. A. Hale, "Recent Advances in Gas Turbine Engine Dynamic Models Developed Through JDAPS," ASME Paper # 95-GT-146, Presented at the



40th ASME International Gas Turbine & Aeroengine Congress & Exposition, Houston, Texas, June 1995.

**2.19** Davis, M. W., Jr., A. A. Hale, K. A. Shahrokhi, and G. D. Garrard, "Euler Modeling Techniques for the Investigation of Unsteady Dynamic Compression System Behavior", Presented at the 85th Session of the Propulsion and Energetics Panel of AGARD, Derby, England, May 1995.

**2.20** Garrard, G. D., "ATEC: The Aerodynamic Turbine Engine Code for the Analysis of Transient and Dynamic Turbine Engine System Operations," Ph.D. Dissertation, the University of Tennessee, Knoxville, August, 1995.

**2.21** Chalk, J. C. "Adaptation of a Three-Dimensional Numerical Simulation to Represent Gas Turbine Engine Compression Systems." Master's Thesis, The University of Tennessee, Knoxville, TN, 1996.

**2.22** Hale, A. A., "A Three-Dimensional Turbine Engine Analysis Compressor Code (TEACC) for Steady-State Inlet Distortion." Ph.D Dissertation, Virginia Polytechnic Institute and State University, Blacksburg, VA, 1996.

**2.23** Garrard, Doug, "ATEC, The Aerodynamic Turbine Engine Code for the Analysis of Transient and Dynamic Gas Turbine Engine System Operations, Part 2: Numerical Simulations", ASME Paper # 96-GT-194, June 1996.

**2.24** Garrard, Doug, "ATEC, The Aerodynamic Turbine Engine Code for the Analysis of Transient and Dynamic Gas Turbine Engine System Operations, Part 1: Model Development", ASME Paper # 96-GT-193, June 1996.

**2.25** Garrard, Doug, Davis, Milt, Jr., Hale, Alan, Chalk, Jacqueline, and Savelle, Stephen, "Analysis of Gas Turbine Engine Operability with the Aerodynamic Turbine Engine Code", ISABE 97-7034, Presented at the International Society for Air Breathing Engines Thirteenth International Symposium on Air Breathing Engines, Chattanooga, Tennessee, September 7-12, 1997.

**2.26** Davis, M.W., et. al., "An Approach for the Development of an Aerodynamci-Structural Interaction Simulation for Aeropropulsion Systems", ASME-96-480, June 1996.

**2.27** Garrard, D., Davis, M. W., Wehofer, S. and G. Cole, "A One-Dimensional, Time-Dependent Inlet/Engine Numerical Simulation for Aircraft Propulsion Systems," ASME-97-GT-333, June, 1997

**2.28** Chalk, J. C. H., "Adaptation of a Three-Dimensional Numerical Simulation to Represent Gas Turbine Engine Compression Systems", AEDC TR-97-1, April 1997

**2.29** Hale, A. A., and W. F. O'Brien, "A Three-Dimensional Turbine Engine Analysis Compressor Code (TEACC) for Steady-State Inlet Distortion," Journal of Turbomachinery, Vol. 120, July 1998, pp. 422-430.

**2.30** Garrard, Doug, et. al. "A Parametric Starting Study of an Axial-Centrifugal Gas Turbine Engine Using a One-Dimensional Dynamic Engine Model and Comparisons to Experimental

Results, Part 2: Simulation Calibration and Trade-off Study”, ASME Paper # 98-GT-471, June 1998

**2.31** Garrard, Doug, et. al. “A Parametric Starting Study of an Axial-Centrifugal Gas Turbine Engine Using a One-Dimensional Dynamic Engine Model and Comparisons to Experimental Results, Part 1: Model Development and Facility Description”, ASME Paper # 98-GT-470, June 1998

**2.32** Hale, Alan, Chalk, Jacqueline, Klepper, Jason, and Kneile, Karl, “Turbine Engine Analysis Compressor Code, Part II: Multi-stage Compressors and Inlet Distortion”, AIAA-99-3214, July 1999.

**2.33** Boyer, K.M., “An Improved Streamline Curvature Approach for Off-Design Analysis of Transonic Compression Systems”, Ph.D Dissertation, Virginia Polytechnic Institute and State University, Blacksburg, VA, April 2001.

**2.34** Tibboel, G.A., “Modification of a One-Dimensional Compression System Model to Calculate Stage Characteristics Internally”, Unpublished Master’s Thesis, University of Tennessee Space Institute, November 2002

**2.35** Asbury, Sarah, Roberts, Brandon, and Hale, Alan, “A Graphical Technique for Compressor Analysis to Collocate Velocity Vectors and Mean Camber Lines”, AIAA Paper # 2002-0311, January 2002.

**2.36** Davis, Milt, Alan Hale, and Dave Beale, “An Argument for Enhancement of the Current Inlet Distortion Ground Test Practice for Aircraft Gas Turbine Engines”, **Journal of Turbomachinery**, Vol. 124, Number 2, April 2002, pp. 235-241.

**2.37** Davis, M. W., Jr., W. Baker, G. Power, and D. Beale, “A Proposal for Integration of Wind Tunnel and Engine Test Programs for the Evaluation of Airframe-Propulsion Compatibility Using Numerical Simulations”, **Journal of Engineering for Gas Turbines and Power**, Vol. 124, Number 3, July 2002, pp. 447-458.

**2.38** Klepper, Jason, Hale, Alan, and Davis, Milt, “A Numerical Investigation of Steam Ingestion on Compression System Performance,” ASME Paper #GT2004-54190, 2004 ASME Turbo Expo, June 2004.

**2.39** Hale, Alan, Klepper, Jason, and Hurwitz, Wayne, “A Numerical Capability to Analyze the Effects of Water Ingestion on Compression System Performance and Operability”, ASME Paper # GT2005-68480, June 2005.

**2.40** Davis, Milt and Peter Montgomery, “A Flight Simulation Vision for Aeropropulsion Altitude Ground Test Facilities”, **Journal of Engineering for Gas Turbines and Power**, Vol. 127, January 2005, pp. 8-17.

**2.41** Hale, Alan, Milt Davis, and Jim Sirbaugh, “A Numerical Simulation Capability for Analysis of Aircraft Inlet-Engine Compatibility”, **Journal of Engineering for Gas Turbines and Power**, Vol. 128, July 2006, pp. 473-481.

**2.42** Beale, D., Davis, M., and Sirbaugh, J., "Requirements and Advances in Simulating Aircraft Inlet Total-Pressure Distortion in Turbine Engine Ground Tests," ASME Paper No. GT2006-90038, ASME Turbo Expo 2110, Barcelona, Spain, May 8-11, 2006.

**2.43** Davis, Milt, Beale, Dave, Boyer, Keith, and O'Dowd, Devin, "An Example for Integrated Gas Turbine Engine Testing and Analysis Using Modeling and Simulation", Presented at the 2006 ITEA Modeling and Simulation Conference, Las Cruces, NM, December 2006.

**2.44** Davis, Milt (Tech Editor), "Performance Predictions and Simulation of Gas Turbine Engine Operation for Aircraft, Marine, Vehicular, and Power Generation" RTO-TR-AVT-036, February 2007.

**2.45** Davis, Milt, and Hale, Alan, "A Parametric Study on the Effects of Inlet Swirl on Compression System Performance and Operability Using Numerical Simulations", GT2007-27033, Presented at the 2007 ASME International Gas Turbine Institute's Turbo Expo in Montreal, Canada, May 2007

**2.46** Davis, Milt, Jr., Beale, Dave, and Sheoran, Yogi, "Integrated Test and Evaluation Techniques as Applied to an Inlet Swirl Investigation Using the F109 Gas Turbine Engine", GT2008-50074, Presented at the 2008 ASME International Gas Turbine Institute's Turbo Expo in Berlin, Germany, June 2008.

**2.47** Davis, Milt, Jr., Hale, Alan, Vining, Charles, and Cousins, William, "Application of Numerical Analysis Tools for Airframe-Propulsion Integrated Test and Evaluation", GT2008-50194, Presented at the 2008 ASME International Gas Turbine Institute's Turbo Expo in Berlin, Germany, June 2008.

**2.48** Davis, Milt, et.al., "Demonstration of an Integrated Test and Evaluation (IT&E) Process for Airframe-Propulsion Systems as Applied to a Current Weapon System Program", Presented at the 2010 AIAA Aerospace Sciences Meeting, January 2010.

**2.49** Davis, Milt and Kidman, David, "Prediction and Analysis of Inlet Pressure and Temperature Distortion on Engine Operability from a Recent T-38 Flight Test Program", Presented at the 2010 ASME International Gas Turbine Institute Turbo Expo, June 2010.



## CHAPTER 3 TABLE OF CONTENTS

3	Applications.....	40
3.1	Surge, Rotating Stall and Compression System Recovery .....	42
3.1.1	Compression System Component Loading for Single-Spool Systems .....	44
3.1.2	Compression System Component Loading for Dual-Spool Systems .....	47
3.1.3	Compressor Post-stall Analysis and Behavior.....	51
3.1.4	Hardware Modifications – Flow Area & Inter-Stage Bleed .....	57
3.1.5	Effect of Heat Transfer on Post-Stall Behavior (Nine-Stage Model) .....	66
3.1.6	The Effect of Casing Treatment on System Operability .....	70
3.1.7	The Effect of Camber or Variable Vane Re-Positioning on System Operability ....	81
3.1.8	Compression System Component Behavior During Oscillating Flow.....	85
3.1.9	Compression System Behavior During Hot Gas Ingestion .....	90
3.1.10	Axi-Centrifugal Compression System Post-Stall Behavior.....	96
3.1.11	Dynamic Engine Simulation of Post-Stall Behavior and Engine Starting .....	104
3.2	Inlet Distortion.....	109
3.2.1	Inlet Total Pressure Distortion -- Parallel Compressor Theory.....	112
3.2.2	Inlet Total Pressure Distortion -- TEACC – Validation of a High Fidelity Technique 121	
3.2.3	Inlet Total Pressure Distortion – TEACCSTALL, Higher Fidelity Simulation .....	137
3.2.4	Inlet Total Temperature Distortion Analysis -- Parallel Compressor Theory .....	151
3.2.5	Combined Pressure and Temperature Distortion Analysis .....	157
3.2.6	Inlet Swirl Distortion Analysis .....	172
3.3	Airframe-Propulsion Integration via Numerical Simulations .....	188
3.3.1	Aircraft –Propulsion Integration – One-Dimensional Analysis.....	194
3.3.2	Airframe-Propulsion Integration 3D Analysis .....	205
3.3.3	Aero-Structural for System Interaction Analysis .....	222
3.4	Propulsion Facility Issues Addressed By Numerical Simulations For Operability .....	227
3.4.1	Facility Duct Length Analysis for Test Article Post-Stall Behavior.....	229
3.4.2	Facility Overpressure Analysis for Test Article Post-Stall Behavior .....	233
3.4.3	E311 Distortion Analysis .....	236
3.4.4	16T Wind Tunnel Dynamic Simulation .....	242
3.5	Steam And Water Ingestion Issues .....	247
3.5.1	Steam Ingestion for a Generic HPC .....	248
3.5.2	Water Ingestion Analysis for the FT8 .....	258
3.5.3	Steam Ingestion Predictions for a Modern Military Compression System.....	267

### 3 APPLICATIONS

The gas turbine engine has played a significant role in the advancement of the flight capabilities of modern day aircraft. Because aircraft performance is tied directly and inseparably to the performance of the propulsion device, efforts are continually underway to increase both the thrust generation and fuel efficiency of gas turbine engines. The continuing demands for increased performance, however, have resulted in engine designs which operate near the aerodynamic, thermal, and structural limits of the engine system components. In order for a gas turbine engine to achieve the performance levels and durability for which it was designed, stable operation of the engine must be ensured.

Even during normal operation, a gas turbine engine will be exposed to time variant, or transient, events. A transient event is said to occur when an aerodynamic or mechanical change occurs in the engine that is a function of time without undesirable changes in the engine operating characteristics. An example of a transient event is a change in an engine operating condition due to a fuel flow rate change. If not carefully made, a transient event can potentially force the engine into unstable operation, which can be dynamic in nature. Dynamic engine operation is defined as engine behavior occurring when aerodynamic or mechanical changes in the engine occur very quickly (cyclic frequencies measured in tenths of seconds or less) and are usually undesirable. Dynamic events, which lead to dynamic engine operation, include, but are certainly not limited to, gun gas ingestion and inlet distortion. These transient events and the resulting dynamic operation of the engine could result in loss of thrust, loss of engine control, or possible engine damage due to high heat loads and high cyclic stresses.

The operating characteristics of a given engine during transient and dynamic events must be quantified in order to ensure that the engine will perform as desired over the range of conditions it will experience during normal operation. Because of the open flow paths and mostly subsonic flow throughout the engine, each of the various components in the engine are aerodynamically and, in some cases, mechanically coupled to the other components. It is this coupling that

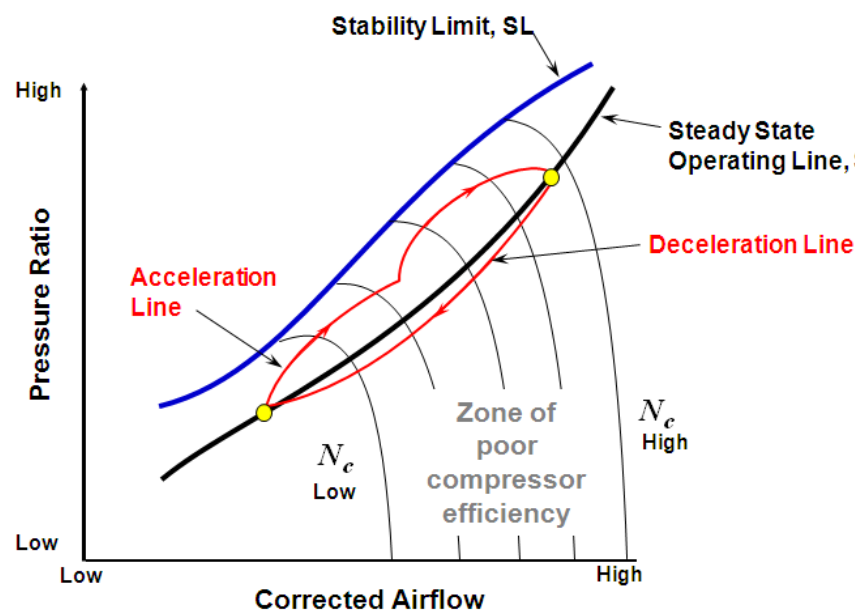


**Figure 3.1 Path Taken During Transient Events**

permits the gas turbine engine to operate as a propulsion device. An insignificant problem in one component, however, can lead to significant problems in other components. For example, a transient increase in fuel flow rate to the combustor can cause the engine compression system to stall. It is important for the engine designer to be able to predict when an engine will encounter a dynamic event such as compressor stall due to transient phenomena, and to understand how the engine will react once a dynamic event occurs.

The path taken by the compressor during the "ideal" transient operation is shown on the map sketched in [Figure 3.1](#) and is called the normal operating line. In reality, the increased fuel flow rate causes all of the events described above, but the rotational moment of inertia of the rotor must be factored in. Even though the turbine extracts excess power, the rotor speed does not immediately increase. The time dependent characteristics of the rotor system are such that the aerodynamic response is much faster, causing the system to follow a different path than if the rotor speed responded immediately. Instead of following the normal operating line to the new operating point, the actual compressor pressure ratio is forced higher due to the increased combustor exit gas temperature. The compressor pressure ratio is increased by the increased combustor exit temperature due to the fact that the higher gas temperature requires a higher pressure in the combustor for the given mass flow rate to pass through the turbine nozzles (assuming they are choked). As the rotor speed gradually increases, the pressure ratio moves to the right, increasing the mass flow rate through the system. Finally, as the entire system reaches equilibrium, the engine returns to the normal operating line at the new operation point. During the initial portion of the transient, the compressor pressure ratio increases along a given speed line. This cannot continue indefinitely. Eventually, a point is reached at which the compressor operation becomes unstable and the boundary layer separates from the compressor blading. The unstable event can occur as one of two phenomena. Surge, which occurs as a fully planar disturbance in which the entire compressor annulus reverses flow, empties the volume downstream of the compressor until the back pressure is relieved and the correct pumping action is reestablished. Rotating stall, another type of compression system instability, occurs when a portion of the blading circumference is locally stalled by some destabilizing event such as a low-pressure region in the engine inlet.

Modeling and simulation technology, coupled with the baseline information provided by the current wind tunnel and test cell test procedures, produce a virtual coupling of the wind tunnel facility with the test cell information. The fusion of computational and experimental data will result in an increased level of information available to the tester for system development risk reduction. AEDC has embarked on a course of action that will provide an engine inlet performance and operability analysis capability by infusing test and computational capabilities.

The numerical simulations utilized in the investigations that follow in this chapter are presented in [Chapter 4](#). Instead of presenting each simulation and a series of examples, an operability issue has been introduced and if more than one simulation can be used to investigate the phenomena, they are presented under that basic issue. The issues that will be covered are:

- Surge, Rotating Stall and Compression System Recovery
- Inlet Distortion
- Airframe Propulsion Integration
- AEDC Facility Applications
- Water and Steam Ingestion

### 3.1 SURGE, ROTATING STALL AND COMPRESSION SYSTEM RECOVERY

An important component of the gas turbine engine is the compression system. The compression system performance strongly influences all the component performance. For most gas turbine engines, the compression system consists of one or more aerodynamically coupled

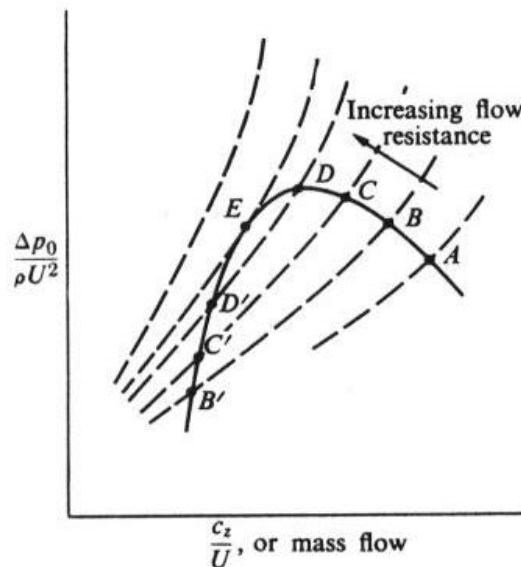


**Figure 3.2 Compression System Instability Anatomy**

axial compressors. These compressors consist of stages with a rotating component (rotor) and a stationary component (stator). The rotor is a series of airfoils which, when rotated, impart kinetic energy to the fluid. The stator diffuses the flow and redirects the flow for the next row of rotors. Thus, it is the function of the compression system to increase the static pressure and density of the fluid. Without stable aerodynamic operation, the compression system cannot deliver the desired increase in static pressure and density

Presented in **Figure 3.2** is a representation of compression system operation. The stage or compressor characteristic is represented by the solid line (A-B-C-D-E-D'-C'-B'). The dotted lines are throttle lines with increasing resistance to the flow shown going to the upper left. As the compressor is throttled by some manner, the airflow decreases and the pressure rises as shown by A through D. At point E the throttle line is just tangent to the characteristic and small departures from this point are either opposed or reinforced. At points D', C', and E', operation is unstable and any shift from these points would be followed by transition either toward B, C, or D or to zero flow. Once airflow delivery is stopped or perhaps even reversed, the pressure in the discharge region drops until the compressor can start again, rapidly refilling the exhaust chamber and repeating the cycle.

During operation of axial-flow multistage compression systems, instability phenomena known as surge and/or rotating stall have been observed. Surge is a violent planar disturbance in which the flow in the compressor reverses direction and empties the compressor volumes as illustrated in **Figure 3.3**. This flow reversal relieves the back pressure on the compression system so that correct pumping action can take place. If, however, the original cause of surge has not been corrected, the compression system will undergo re-pressurization until it reaches the instability limit at which time surge will occur again. Surge typically occurs in a frequency range of 3-to-15 Hz.

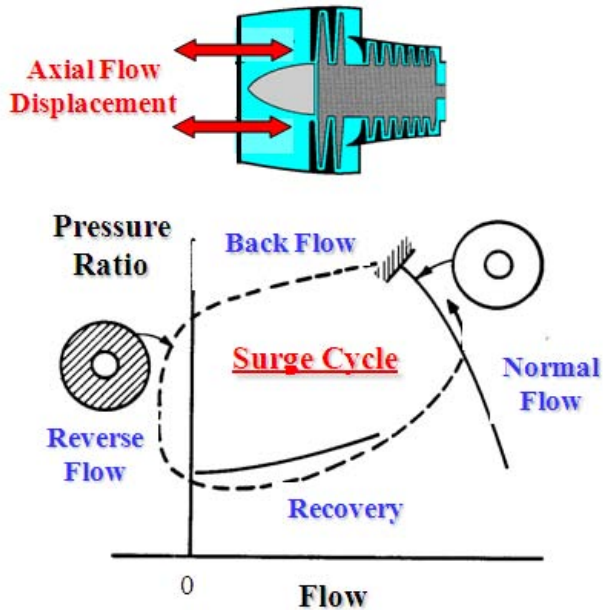
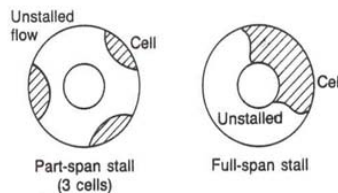


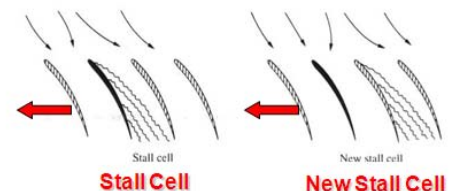
**Figure 3.3 Surge Cycle Representation**

Thus, recovery from rotating stall is usually possible in an engine only by stopping the fuel flow and restarting the engine. With continued engine operation, rotating stall is “non-recoverable”. Rotating stall has been a known phenomenon since the 1950’s. In the late 70’s and 80’s a renewed interest was generated with the “Stagnation Stall” problem associated with the F100 turbofan engine, the propulsion system for both the F-15 and F-16 aircraft. The Stagnation Stall or as it came to be known, “Nonrecoverable Stall” produced the strongest incentive for the understanding of compression system instability.

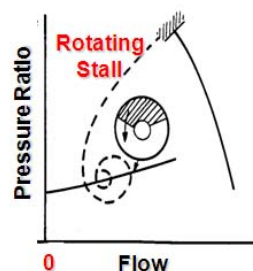
#### Cell Structure



#### Blade-to-Blade



#### Performance Path



#### Signature

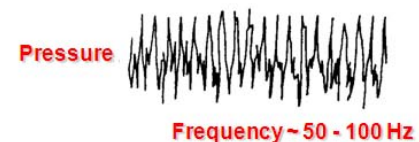


**Figure 3.4 Rotating Stall Representation**

### 3.1.1 Compression System Component Loading for Single-Spool Systems

Stable aerodynamic operation of the compression system of a gas turbine engine is essential for the engine to perform satisfactorily. The aerodynamic stability limit is most commonly defined as a focus of points denoting maximum pressure ratio for stable operation as a function of corrected airflow rate. It is typically determined from experimental results. However, only limited amounts of experimental compressor steady-state, transient and stability limit data can be obtained during a test program because of test hardware and economic constraints. A validated mathematical model, based on limited experimental data, allows performance and stability computations to be made at operating conditions other than tested and with subcomponent hardware configurations different from those actually tested

#### **CITED EXAMPLE(S)**

**3.1** Chamblee, C. E., M. W. Davis, Jr., and W. F. Kimzey, "A Multi-Stage Axial Flow Compressor Mathematical Modeling Technique with Applications to Two Current Turbofan Compression Systems", AIAA Paper # AIAA-80-0054, Presented at the AIAA 18th Aerospace Sciences Meeting, Pasadena, CA, April, 1980

**3.2** Davis, Milton W., Jr., "A Stage-by-Stage Compressor Modeling Technique for Single-and Dual-Spool Compression Systems", Unpublished Master's Thesis -- University of Tennessee, Knoxville, Tennessee, August 1981.

#### **MODELING TECHNIQUE**

The **single-spool one-dimensional dynamic model** ([Section 4.4.1](#)) was configured to a 10-stage high pressure compressor of a current turbofan engine as illustrated in [Figure 3.5](#). To investigate loading of the HPC, the exit static pressure was ramped at a rate (50 Psia/sec) to simulate a combustor hard light. Inlet conditions (total pressure and temperature) as well as corrected speed were held constant since the exit static pressure ramp rate was at a high enough rate so that mechanical speed and inlet temperature would not change in that time frame.

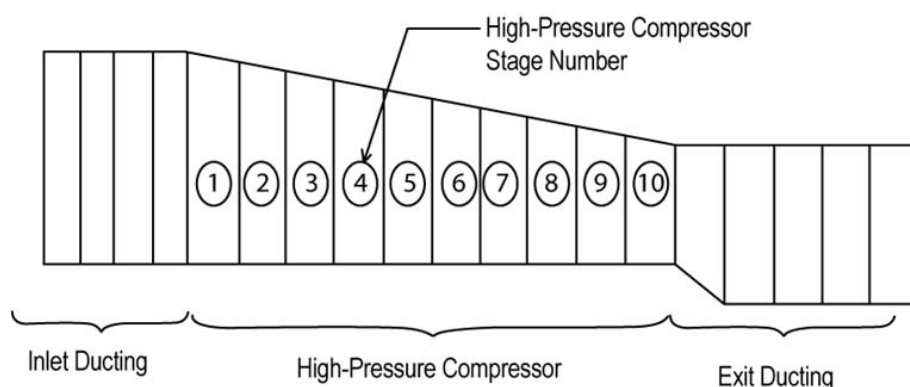


**Figure 3.5 Schematic of the Single-Spool, Ten-Stage Compression System Modeled**



## HIGH-PRESSURE COMPRESSOR LOADING BY COMBUSTOR HARD LIGHT:

Stage characteristics (used for determining stage forces and shaft work) were synthesized using experimental data obtained from the testing of the core machine (compressor, burner, and turbine) of the system of interest. Experimental data available included: (1) compressor inlet and total pressure and temperature providing overall compressor performance, (2) interstage total pressure and temperature measurements providing individual stage performance, and (3) high-response static pressure measurements providing failing stage(s) at time of compressor surge.

Using the 1D compressor model, an iterative procedure was developed for synthesizing stage characteristics

- Each stage characteristic must provide a stage loading distribution consistent with experimental loading distribution for a wide range of compressor speeds.
- The model must predict the overall compressor performance within acceptable tolerances (one percent of that observed experimentally).
- The model must indicate the correct stalling stage(s) as observed experimentally.

The results of this process for five corrected rotor speeds (77, 82, 87, 98, and 102 percent of design) are presented and compared to experimental results in [Figure 3.6](#). The model computes compressor surge pressure ratio and airflow rate within 1 percent, respectively for all corrected rotor speeds investigated. A tabulation of compressor stages that are operating on the stalled side of their characteristic at time of compressor surge as indicated by the model is presented and compared to experimental results in [Table 3.1](#). For most speeds, the model indicates the same stalling stage as was

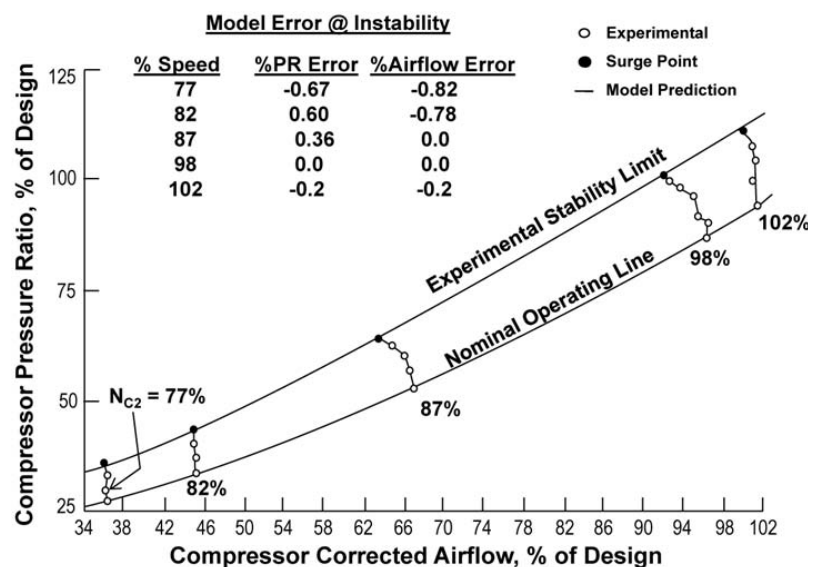


**Figure 3.6 Ten-Stage Single-Spool HPC Model Comparison to Experimental Results**

Rotor Speed %	Critical Stage Experimental	Critical Stage Model
77	7 or 9	5, 7, 8
82	7 or 8	4, 5, 6, 7, 8
87	7 or 8	4, 5, 6, 7, 8
98	7 or 9	8, 9
102	7 or 8	5, 6, 7, 8

**Table 3.1 Stalling Stages at Compressor Instability & Comparison to Experimental Results**

observed during experiment. The model also indicates other stages that are operating on the stalled side of their characteristic that were not observed during the experiment. This indicates that many of the stages in the 10-stage high-pressure compressor are operating at peak performance when the compressor is highly loaded.

The one-dimensional, time-dependent model was developed for analysis of planar, transient, and dynamic disturbances. One type of disturbance is the phenomenon of compressor surge and stage interaction leading to its occurrence. For this example analysis, the compressor model was loaded to compressor surge at a corrected speed of 87 percent of design. The compressor surge event was indicated by the model instability caused by an imbalance of forces across one or more of the stages.

Comparison of the time-dependent solution of the 87 percent corrected rotor speed characteristic steady state experimental result is presented in **Figure 3.7**. The time dependent model computed the stability limit within 0.36 percent in pressure ratio and 1.5 percent in corrected airflow rate to that obtained experimentally.

To identify the critical stage (i.e. stage which initiates complete flow breakdown), static pressure behavior is a good indicator, experimentally as well as theoretically. The critical stage is indicated by a sudden increase in stage entrance static pressure and decrease in exit static pressure. This signature is caused by flow stagnation at the stage entrance and recirculation at stage exit initiated by flow separation on the airfoils. The critical stage static pressure signature is evident across the seventh stage of the model (**Figure 3.8**) and thus indicates that the seventh stage initiates compressor surge at 87-percent corrected speed.

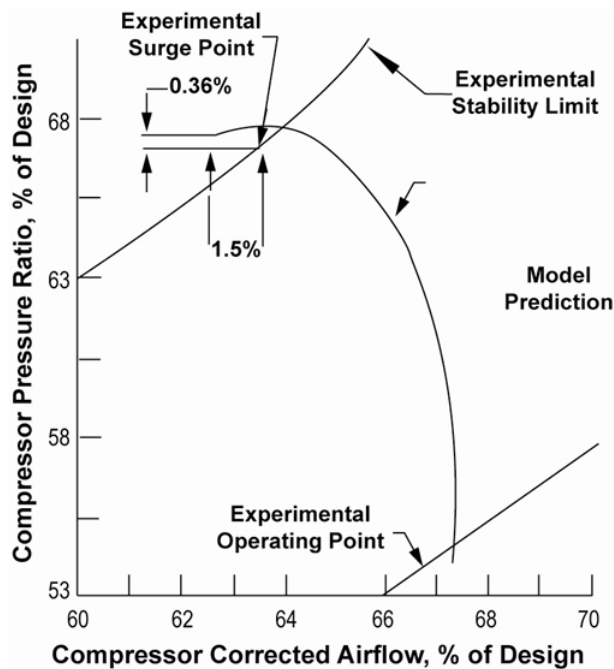


**Figure 3.7 Ten-Stage HPC Loading Comparison to Experimental Results**

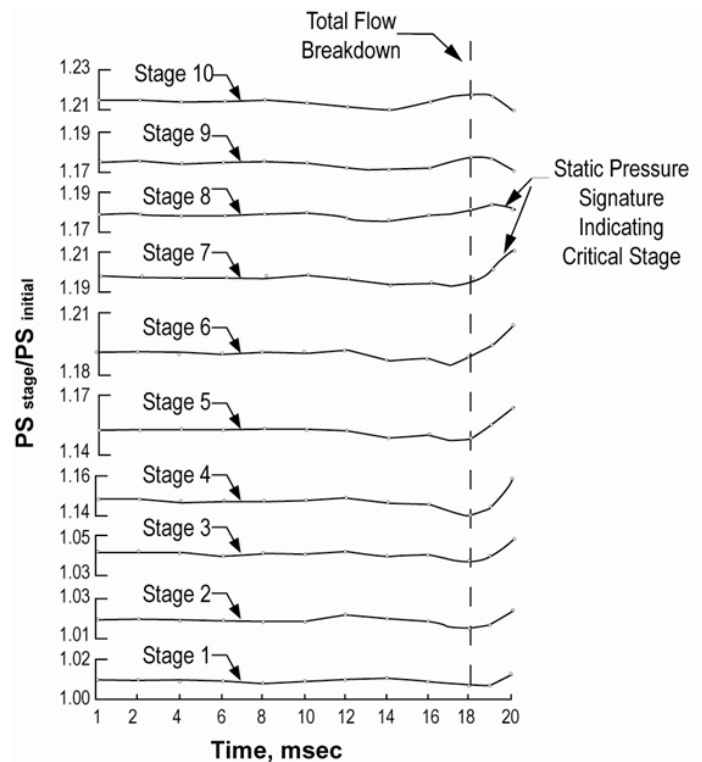


**Figure 3.8 Stage Static Signature Indicating Seventh Stage As Critical Stage**



### 3.1.2 Compression System Component Loading for Dual-Spool Systems

Determining the effects of inlet airflow or combustor/augmenter hard lights on the stability of an aircraft engine is an important part of any aircraft engine development and qualification program. Knowing the response of the engine compression system to these destabilizing influences enables proper matching of the engine with the aircraft.

Spool Interactions refers to the potential for engines with multiple fan/compressors (spools) on different shafts to have stability characteristics that are the result of interactions between the compression system components. One of the fundamental assumptions of the ARP 1420 distortion methodology is that the stability characteristics of an integrated system can be determined from individual component tests. It is known that a fan or compressor has an upstream influence on the entrance flow; therefore closely coupled compressors may influence the stability characteristics of their neighbor requiring additional analysis in the stability assessment process.

Another issue is that performance and stability differences have been documented between the results of compressor component rig tests and fully assembled engine tests. This component to system differences can often be attributed to aero-thermo effects and hardware configuration effects, resulting in the single component rig test not being representative of the engine environment. Thus, a need exists for a simulation technique for component stability analysis when multiple compression systems are embedded together such as in a turbofan engine.

#### CITED EXAMPLE(S)

**3.3** Davis, M. W., Jr., "A Stage-by-Stage Dual-Spool Compression System Modeling Technique", ASME Paper #82-GT-189, March 1982, Presented at the 1982 IGTI Conference, London, England.

#### MODELING TECHNIQUE

The **dual-spool one-dimensional dynamic model** ([Section 4.4.2](#)) was configured to a typical mixed flow turbofan compression system as illustrated in [Figure 3.9](#). To investigate the effect

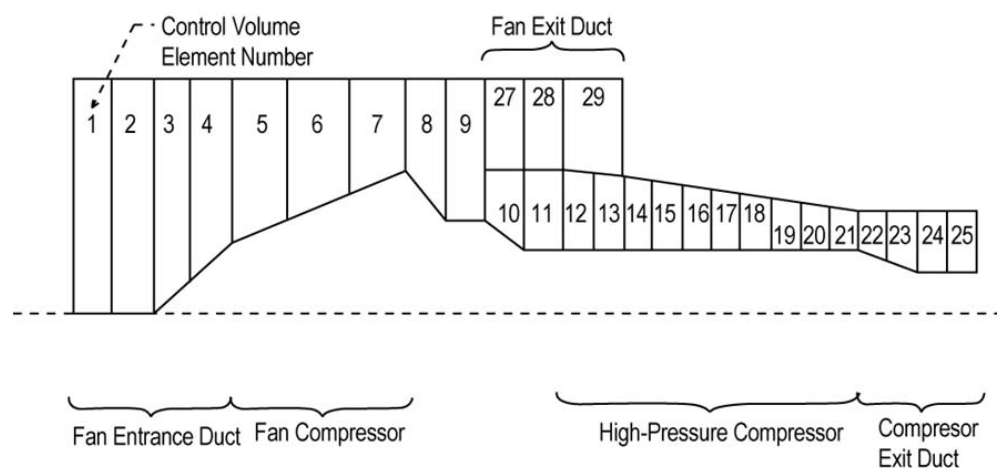


**Figure 3.9 Schematic of the Mixed Flow Turbofan Compression System Modeled**

of combustor or augmenter hard lights, the model was exercised first to load the high pressure

compressor then separately exercised to load the fan component. The high-pressure compressor was loaded to system instability by a rapid increase in compressor exit pressure simulating a main combustor hard light. In addition, the fan component was loaded to surge by rapidly increasing the fan duct bypass pressure simulating a hard augments light.

### **HIGH-PRESSURE COMPRESSOR LOADING BY COMBUSTOR HARD LIGHT:**

To simulate high-pressure compressor loading caused by a rapid pressure ramp in the combustor, the dynamic dual-spool model was initially set at 92 percent fan speed and the HPC at 98% speed, near the nominal operating point of both compression systems. An increase in high-pressure compressor exit static pressure was programmed at a rate of 50 psia/sec, which increased the high-pressure compressor pressure ratio at constant corrected speed until instability occurred. A comparison of model results to those obtained during engine steady-state high-pressure compressor loading by in-bleeding is presented in [Figure 3.10](#).

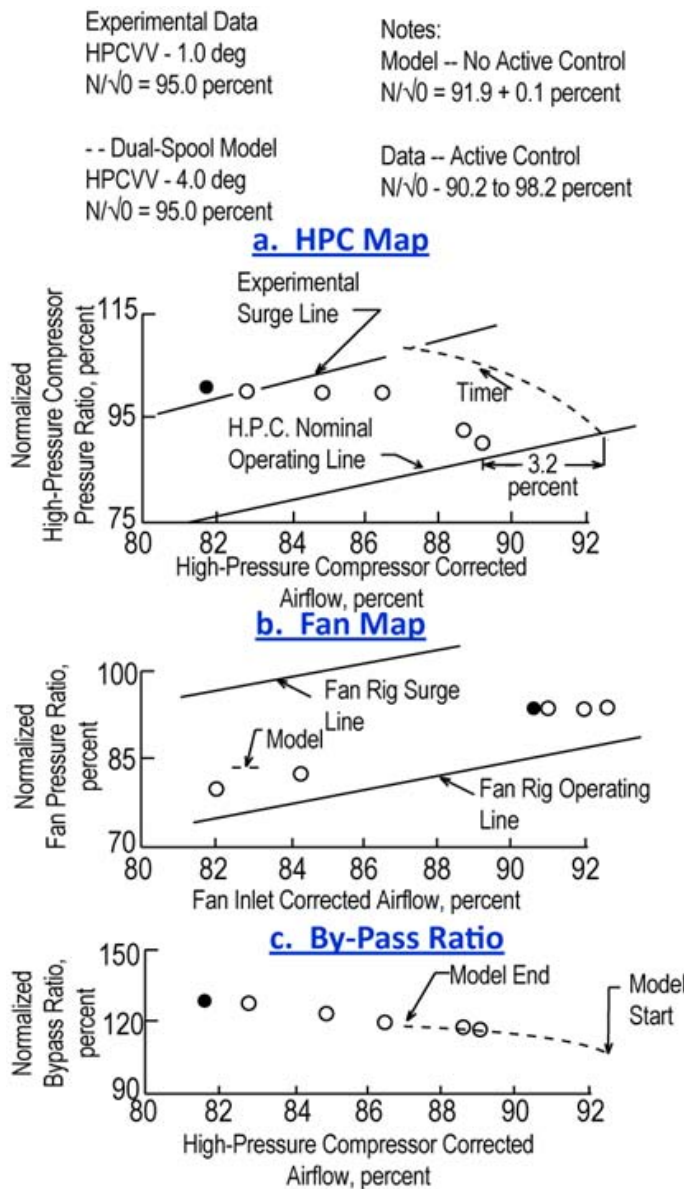


**Figure 3.10 HPC Loading Comparison to Experimental Results**

High-pressure compressor performance during the transient is compared on a compressor map ([Figure 3.10a](#)). An airflow discrepancy between the model and experimental data exists, but can be accounted for by the difference in compressor variable vane (HPCVV) setting. The engine steady-state surge point and model prediction of surge are compared to compressor experimental results from the core engine (compressor-combustor-turbine) of the system modeled. The model predicts surge pressure ratio within 0.5 percent of that obtained from the core engine results. Fan performance is presented on a fan map and compared to the corresponding engine experimental data in [Figure 3.10b](#). Both the model and the experimental data indicate that the fan component operates near its nominal operating line, leaving approximately two thirds of the initial surge margin available. Because the model does not interact with an active control and the experimental data reflect the effects with an active control (mechanical speed varied), the fan performance is only similar in pressure ratio level and not in corrected airflow extent. Compression system bypass ratio behavior is compared to experimental results in [Figure 3.10c](#).

Model bypass ratio behavior was similar in trend to that experienced experimentally but with a different corrected airflow extent because of the difference in HPCVV settings. In addition to overall performance, the model can predict stage performance and indicate which stage initiates compression system surge. To identify the stage which initiates surge, static pressure behavior is a good indicator--experimentally as well as theoretically. A typical trace of model predicted static pressure (obtained during single-spool loading) at time of high-pressure compressor instability is presented and compared to experimental static pressure results at compressor surge in [Figure 3.11](#). At time of compressor surge, the stage that initiates surge will indicate a sudden increase in stage entrance pressure and a sudden decrease in exit pressure. This

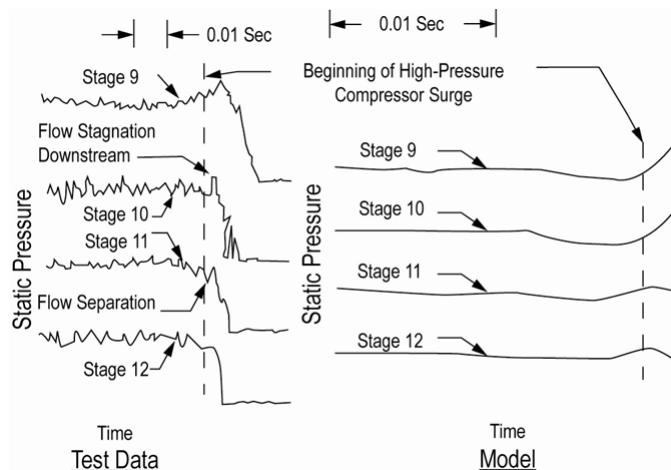


**Figure 3.11 Static Pressure Signature Indicating Stage Instability**

signature is caused by flow stagnation at the stage entrance and recirculation at the stage exit initiated by separation of the airfoils. Using the signature as a means to infer critical stage, the model indicated that the eleventh stage of the compression system (eighth stage of the high pressure compressor) was the stage which initiated compression system instability during dual-spool loading. This is consistent with core engine experimental results which indicate that the seventh or the eighth stage of the high-pressure compressor initiates compressor surge during steady-state in-bleed loading.

#### **FAN LOADING BY AUGMENTOR HARD LIGHT:**

The model was given initial conditions corresponding to 106-percent fan speed near the nominal operating point. Once model stability had been assured, an increase in fan duct exit static pressure was programmed at a rate of 20 psia/sec, which increased the fan pressure ratio at constant corrected speed until instability occurred. A comparison of model results to those obtained during engine steady state fan loading by exit nozzle area closure is presented in [Figure 3.12](#).

Fan performance during the transient is compared on the fan map ([Figure 3.12a](#)). A discrepancy in airflow between the model and data can be accounted for by the difference between experimental and model fan inlet variable vane (FIW) setting. Both the model prediction and the experimental engine data are compared to experimental results from fan rig experimental surge line determination. The model predicted fan surge within 1.0 percent of that observed during rig testing. High-pressure compressor performance is compared to the corresponding experimental engine data on the compressor map ([Figure 3.12b](#)). Both the model and the data indicate that the high-pressure compressor operates near its nominal operating line, thus leaving adequate surge margin. Because the model does not interact with an active control (i.e., mechanical speed was constant) and the experimental data reflect the effects with an active control (mechanical speed increased), the high-pressure compressor performance is only similar in pressure ratio level and not in corrected flow extent. Compression system bypass ratio is compared to experimental results in [Figure 3.12c](#). Again the discrepancy in fan inlet airflow is a result of the different FIVV settings. Using the signature of a rapid

increase in stage entrance pressure and a decrease in stage exit pressure as the criteria for determining the stage initiating compression system surge, it was noted that the model predicted the first stage of the fan as the critical stage. The model's prediction of the stage initiating fan surge cannot be verified because experimental interstage data indicating critical stage at time of fan surge were not available.

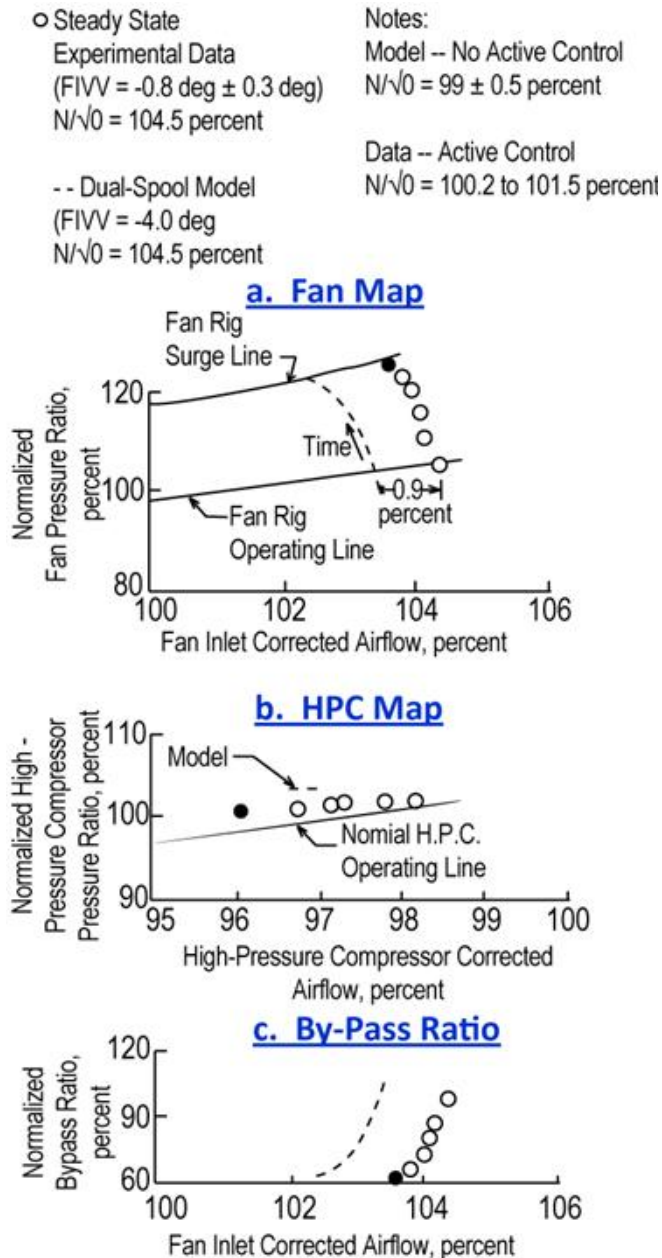


**Figure 3.12 Fan Loading Comparison to Experimental Results**

### 3.1.3 Compressor Post-stall Analysis and Behavior

In most aircraft gas turbine engines, the compression system consists of one or more aerodynamically coupled axial flow compressors. It is the function of the compression system to increase the static pressure and density of the working fluid. Without stable aerodynamic operation, the compression system cannot deliver the desired increase in static pressure and density. During operation of axial-flow multistage compression systems in gas turbine engines and in rigs, undesired system phenomena known as surge and/or rotating stall, have been observed. Of the two types of instabilities, rotating stall is the most detrimental for aircraft gas turbine engines because of the frequently observed inability to recover to normal operation without stopping and restarting the engine. With continued engine operation, rotating stall is "non-recoverable." In experimental cases, results are often limited because of specific test hardware and/or economic constraints. Where more information is desired, validated compression system mathematical models can be used to provide performance and stability information not obtained during experimental testing-

#### **CITED EXAMPLE(S)**

**3.4** Davis, M. W. , Jr. and W. F. O'Brien, "Stage-by-Stage Poststall Compression System Modeling Technique", **Journal of Propulsion and Power**, Vol. 7, Number 6, November-December 1991, pp. 997-1005.

**3.5** Davis, M. W., Jr., "A Stage-by-Stage Post-Stall Compression System Modeling Technique: Methodology, Validation, and Application", Ph.D. Dissertation, Virginia Polytechnic Institute and State University, December 1986

#### **MODELING TECHNIQUE**

Previous (prior to this 1D simulation) post-stall compression system mathematical models have been developed using lumped-volume techniques. A lumped volume approach makes certain assumptions about compressibility within the system. More specifically, the lumped-volume model neglects Mach number effects, uses an isentropic relationship to relate the time-dependent change in density to a time-dependent change in total pressure, and uses a steady-state form of the energy equation. Initially models (whether overall simulations or stage-by-stage) were limited in range to the onset of system instability. During the 1980's post-stall behavior became of more interest, which encouraged the development of numerous models capable of exhibiting aspects of surge or rotating stall. The model presented in this section ([See Section 4.4](#)) removes assumptions inherent in lumped-volume models (i.e., treats compressibility explicitly) and does so on a stage-by-stage basis. The stage-by-stage construction provides a means to study gas path behavior within the compression system and also provides a means to analyze the effects of postulated hardware modifications on system behavior.

In addition, this modeling technique requires a set of stage characteristics that cover not only the prestall operating regime but must cover the post-stall (both rotating stall and reversed flow) as well. An analytical technique was developed by Bloch and O'Brien and is presented in [Appendix D](#).



## POST STALL APPLICATION

To completely validate the 1D modeling technique for these applications requires that the models be exercised and compared to experimental results over the range of intended use. However, only limited experimental data existed for a particular three-stage compressor at the time that the paper upon which this section is taken from was written. The available experimental results from tests of a three-stage, low-speed, compressor research rig of Gamache were utilized [3.7]. Transient inter-stage or overall performance data for surge and rotating stall events were not reported. However, steady-state data were available from which stage characteristics could be synthesized. Overall system performance during surge and rotating stall was available from tests of a similar system, reported by Greitzer [3.6]. Configuring the model to the compression system as reported by Gamache [3.7], but comparing it to measured overall dynamic performance by Eastland [3.8], provided the best available means for qualitative comparisons for "operational verification."

The three-stage, low-speed compressor rig consisted of three non-repeating stages with a constant cross-sectional area annulus. The hub and tip diameters were 53.63 and 60.96 cm, respectively, which produced a hub-to-tip ratio of 0.88. Gamache's major emphasis was the study of the performance of this compressor rig during steady reversed flow. The rig was configured to hold a constant speed while forcing reversed flow through the compressor. By accomplishing this for many flow points, it was possible to obtain overall and stage performance in the reversed flow region. With the previous work of Eastland, [3.8] a complete set of steady-state stage pressure characteristics and corresponding overall steady system performance was available for this rig. A complete temperature rise characteristic was not given for each stage, but energy input to the overall system was given in terms of a torque coefficient. Stage temperature rise characteristics were synthesized as total temperature ratios based upon the overall torque characteristic and two isolated flow points in rotating stall. Temperature characteristics were synthesized which would give the same overall torque as observed experimentally. Lacking any other criteria for stage work division, all stage temperature characteristics were synthesized identically. Measured stage pressure and synthesized temperature rise characteristics for the three-stage, low-speed, research compressor are presented in Figure 3.13. Pressure rise characteristics are based upon reported experimental stage performance measurements which

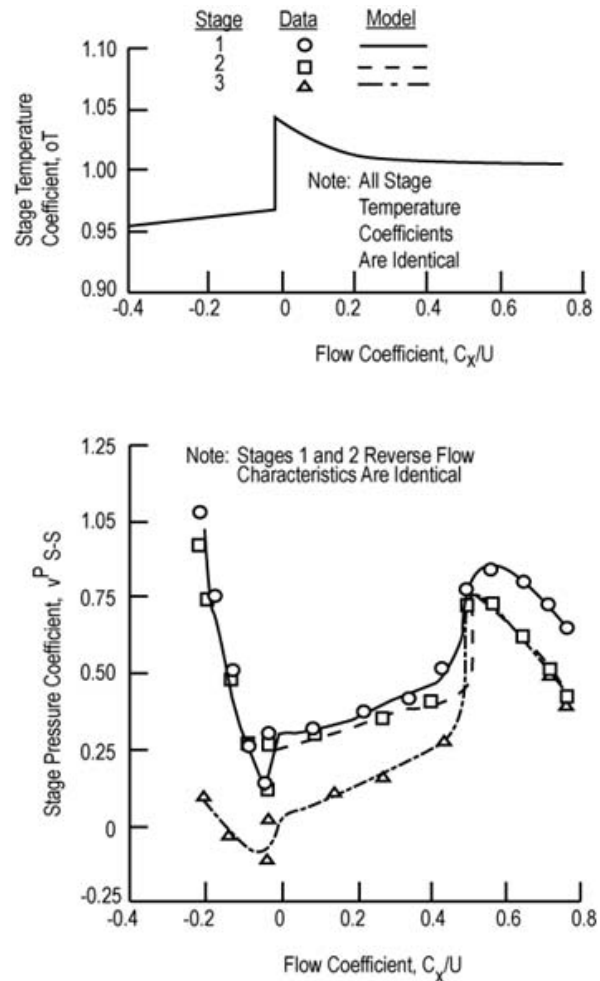


Figure 3.13 Stage Characteristics for a 3-Stage Low-Speed Compressor

described individual stage pressure behavior during un-stalled operation, rotating stall, and reversed flow. Stage temperature rise characteristics have been synthesized as described above.

While the referenced three-stage compression system tests provided excellent stage characteristic data, detailed system behavior during surge and rotating stall was not available from either Refs. 3.7 or 3.8. However, this rig was similar to one used in a previous experimental investigation of surge and rotating stall. Both compression systems consisted of three stages with a constant area annulus. The major differences were in the blading. The rig of Greitzer, [3.6], incorporated three repeating stages, using NACA 400 series airfoils with a hub-to-tip ratio of 0.7, whereas the rig of Gamache, [3.7], (data used to develop stage characteristics) consisted of three non-repeating stages with a hub-to-tip ratio of 0.88. The speed capability of both machines was the same. An extensive experimental investigation to determine system response during post-stall events for a variety of compressor-plenum configurations was performed with this rig. The compression system model was configured to the geometry specified for the compressor-plenum rig of Greitzer, [3.6], but using the stage characteristics developed by Eastland and Gamache as presented in Figure 3.13. For comparison purposes, the "B" parameter was used as a reference variable for both the experimental compressor and the model. The parameter is defined as

$$B = \left( \frac{U}{2a} \right) (Vp/AcLc)^{\frac{1}{2}} \quad \text{Eqn. 3-1}$$

Where

U = Wheel Speed

a = Local Speed of Sound

Vp = Plenum Volume

Ac = Compressor Cross-sectional Area

Lc = Compressor Length

The value of the B parameter has been shown to be an indication of whether rotating stall or surge may be expected to occur in a particular compressor. Three model cases will be compared in this paper to experimental results from Greitzer, [3.6], corresponding to B parameters of 0.65, 1.00, and 1.58. These B parameters produced rotating stall, classical surge and deep surge, respectively, for the system reported by Greitzer, [3.6].

### Rotating Stall

The first experimental transient was conducted at a **B-value** of 0.65. The compressor rig throttle was slowly closed to the point of instability and then held constant. The system became unstable at the uniform flow stall point and then traversed to rotating stall (Figure 3.14). The compressor model was configured in a similar way to a **B-value** of 0.65 at instability initiation. The model "throttle" was closed just enough to cause instability and then held constant. The compressor blade force dynamic lagging constant,  $\tau$ , (a means to obtain dynamic forces using steady-state forces from steady stage characteristics, See Section 4.4 for full explanation) was set at the model boundary between surge and rotating stall such that the overall system

performance traversed immediately to the new operating point indicative of fully developed rotating stall. This modeled post-stall behavior is presented in [Figure 3.15](#). Comparison to the general nature of the experimental results ([Figure 3.14](#)) indicates correctly simulated overall system behavior.

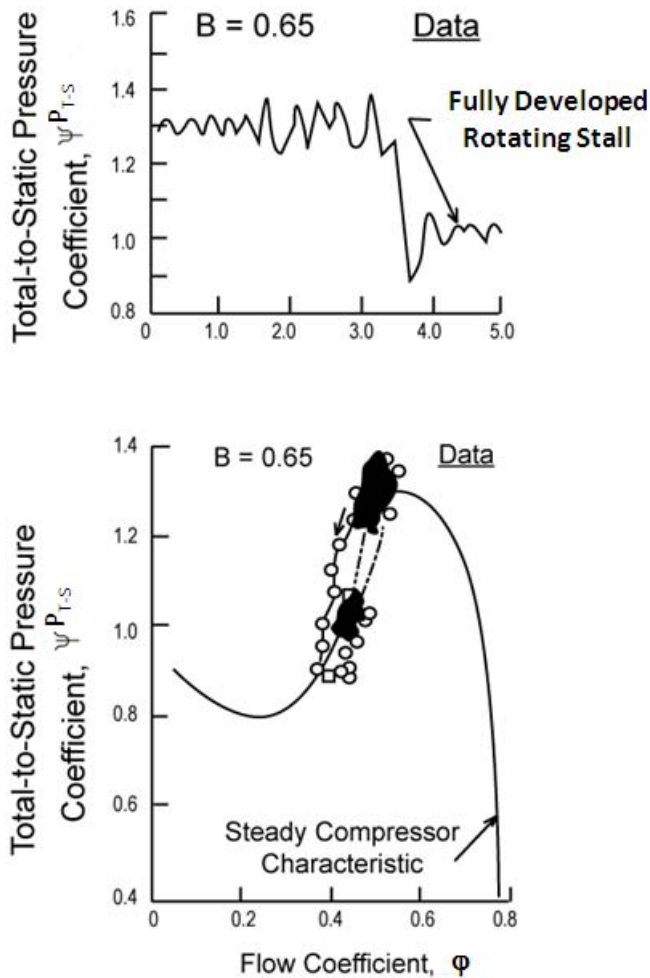


**Figure 3.14 Post-Stall Behavior of Compressor Rig,  $B = 0.65$**

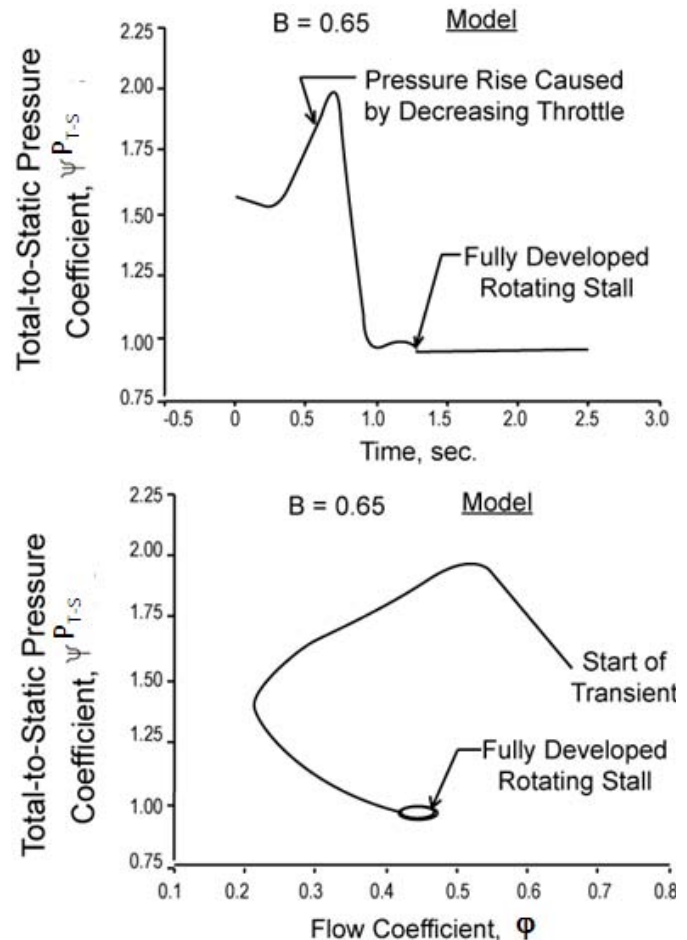


**Figure 3.15 Three-Stage Model Overall System Post-Stall Behavior, Rotating Stall,  $B = 0.65$**

### Classical Surge

In a second test, the compressor rig of Greitzer, [3.6], was reconfigured to operate at a  $B$  value of 1.00. In this condition, the system exhibited classical surge cycles on the order of 1.5 Hz as presented in [Figure 3.16](#). The dynamic model was reconfigured to produce a **B-value** of 1.00 by increasing the exit plenum volume. The blade force time constant,  $\tau$ , was held to the value determined in the previous simulation. Under these conditions, the model also exhibited surge as presented in [Figure 3.17](#). Comparing the time history of the pressure coefficients, one can observe that the change in this parameter is similar in nature and frequency to that observed experimentally ([Figure 3.16](#)). Comparing the model results as depicted on a compressor map,



one can observe that the surge trajectories are circular in nature and are quite similar to those observed experimentally (Figure 3.16).

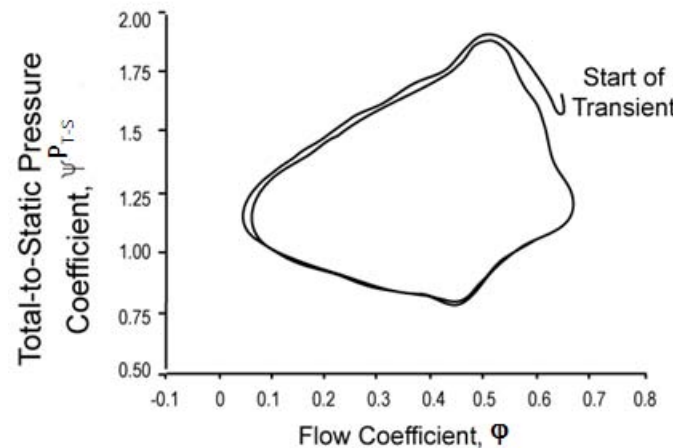
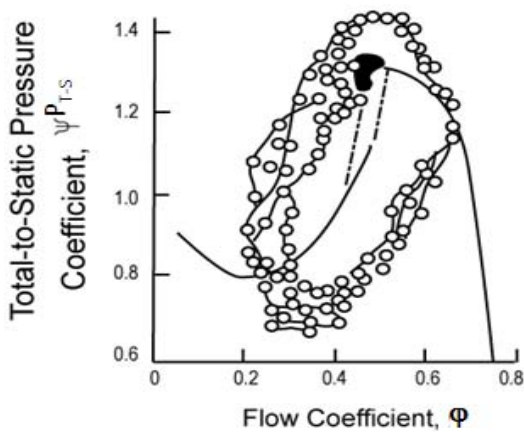
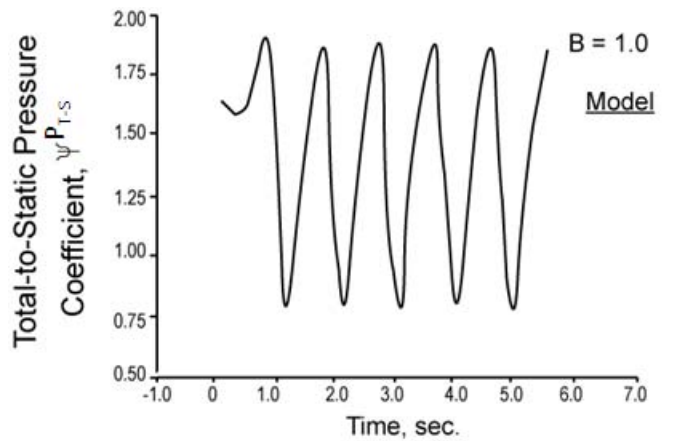
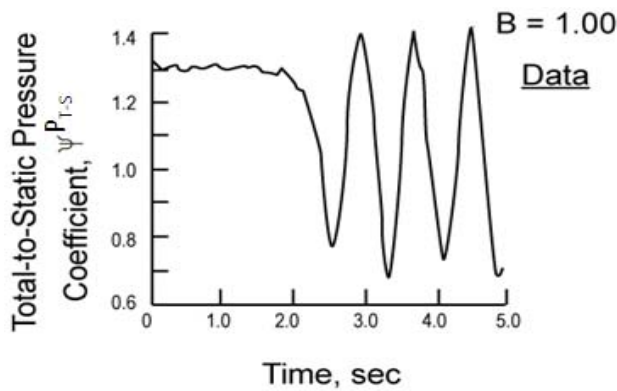
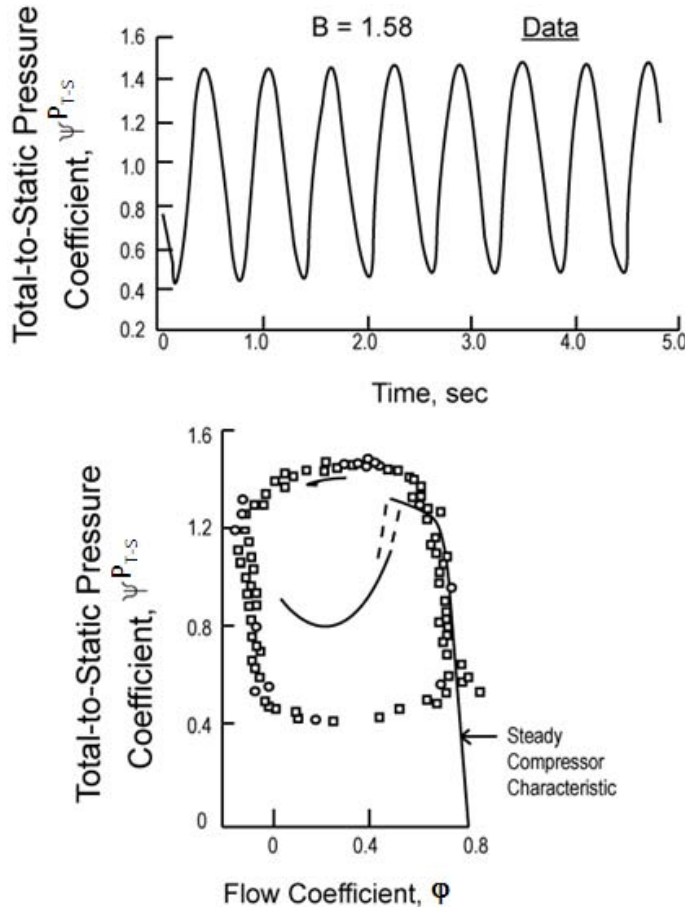


Figure 3.16 Post-Stall Behavior of Compressor Rig,  $B = 1.0$       Figure 3.17 Three-Stage Model Overall System

### Deep Surge

The experimental rig of Greitzer [3.6], was operated with a maximum reported **B-value** of 1.58. For this experimental case, a slightly different system behavior was observed. The surge trajectory became larger with near-zero flow during the surge cycle, but still of the classical type. By decreasing the throttle closure point beyond the initial surge position, it was discovered that the nature of the surge cycles could be affected. Indicated in Figure 3.18 are surge cycles for the same compressor configuration ( $B = 1.58$ ), but at a more restrictive throttle setting. This type of surge cycle has been called a deep surge. The dynamic model was configured for a **B-value** of 1.58 again by increasing the exit plenum volume. Again, the blade force time constant,  $\tau$ , was held at the value associated with a **B-value** of 0.65. The simulated throttle was decreased to a value just small enough to cause compression system instability. Resulting overall system response was indicative of the classical type surge as was expected. Further decreasing the throttle closure to 60% of the minimum value for system instability caused the model to exhibit deep surge, as was observed experimentally. Modeled overall system

response is presented in **Figure 3.19**. Model trajectories are indicative of deep surge post-stall behavior with a frequency of 1 Hz. In summary, the modeling technique described herein was operationally verified by comparison with available experimental results. Comparison of model overall performance during post-surge events to the general nature of the experimental results indicated correct simulated overall system behavior.



**Figure 3.18 Post-Stall Behavior of Compressor Rig,  $B = 1.58$**

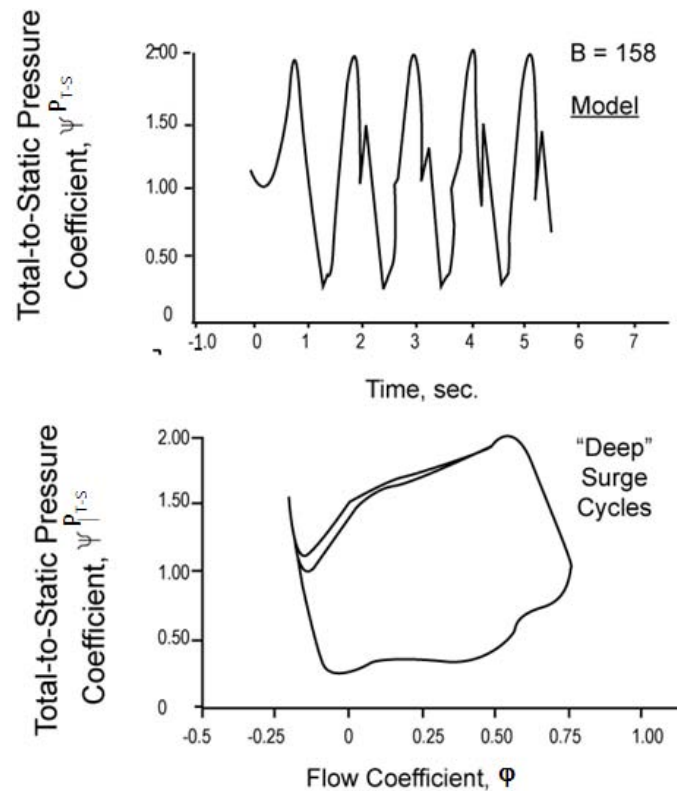


**Figure 3.19 Three-Stage Model Overall System Post-Stall Behavior, Rotating Stall,  $B = 1.58$**

#### ADDITIONAL REFERENCES:

- 3.6** Greitzer, E. M., "Surge and Rotating Stall in Axial Flow Compressors- Part 11: Experimental Results and Comparison with Theory," *ASME Journal of Engineering for Power*, Vol. 98, April 1976, pp. 199-217.
- 3.7** Gamache, R. N., "Axial Compressor Reversed Flow Performance," Ph.D. Dissertation, Massachusetts Inst. of Technology, May 1985.
- 3.8** Eastland, A. H. J., "Investigation of Compressor Performance in Rotating Stall: I-Facility Design and Construction and Initial Steady State Measurements," MIT Gas Turbine and Plasma Dynamics Lab. Rept. 164, June 1982

### 3.1.4 Hardware Modifications – Flow Area & Inter-Stage Bleed

A ten-stage compression system was tested in the Compressor Research Facility (CRF) of Wright-Patterson Air Force Base as reported by Copenhaver, [3.11]. The detailed inter-stage measurements obtained are ideal for comparison with results from the dynamic model. The

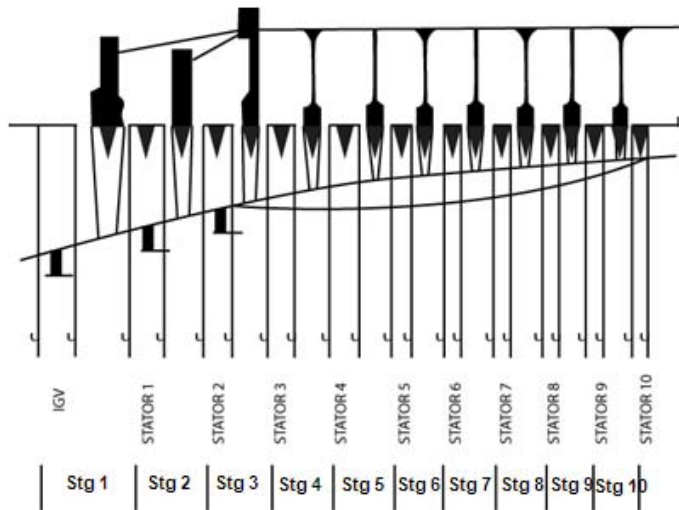


**Figure 3.20 Ten-Stage Compressor Stage Definition**

compressor used in the CRF test program was a high speed, 10-stage, axial-flow compressor assembled from hardware obtained from a modern, high-performance aircraft gas turbine engine. Compressor design parameters include a pressure ratio of 8.3, corrected mass flow of 54.44 lbm/sec, and corrected speed of 10913 rpm. The rig was instrumented to obtain total and static pressures, and total temperatures at various inlet, inter-stage, and exit measurement planes. Compressor measurement plane locations and stage definition are shown in Figure 3.20.

Time-averaged pressure and temperature measurements were used to calculate un-stalled and in-install steady-state stage characteristics required as model input. The in-install mass flow rate was determined from measurements obtained with a venturi located downstream of the compressor exit. Additionally, time-averaged pressure and temperature measurements obtained at the compressor inlet and exit were used to model the boundary conditions. Both time-averaged and close-coupled (transducer close as physically possible to pressure port) pressure measurements were used for comparison with model simulations.

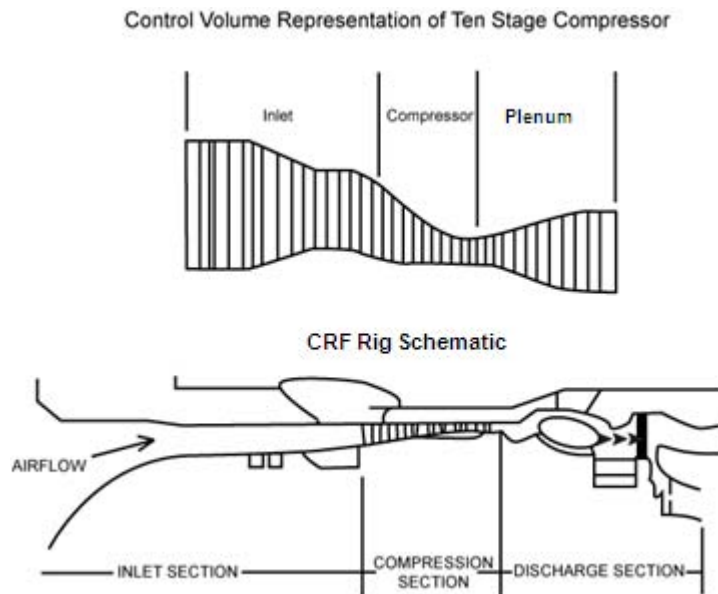


**Figure 3.21 Ten-Stage Compressor Rig Setup & Model Control Volume Definition**

**CITED EXAMPLE(S)**

**3.9** O'Brien, W. F., "Dynamic Simulation of Compressor and Gas Turbine Performance", AGARD Lecture Series, LS-183, May 1992

**3.10** Boyer, K. M., and O'Brien, W. F., "Model Predictions for Improve Recovery of a Multistage Axial-Flow Compressor, AIAA Paper # 89-2687, July 1989.

**Note:** Sections from both cited references have been re-printed with permission of the authors.

**MODELING TECHNIQUE**

For the model study, the one-dimensional modeling technique as described in [Section 4.4.1](#) was utilized. The 10-Stage compressor rig geometry (control volumes) and experimentally-determined stage performance characteristics were used for the development of the necessary stage characteristics. The resulting control volume geometry is shown in [Figure 3.21](#).

Initially, un-stalled performance comparisons were made at numerous speeds to ensure accurate simulation of speedline shape, stall point, etc. Once steady-state performance was verified, the model was exercised to simulate post-stall events (surge or rotating stall). By matching the experimental boundary conditions, model simulations were shown to accurately represent overall and individual stage steady-state, transient, and quasi-steady measured performance. The majority of model simulations were run at or near the compressor's rotating stall/surge boundary speed (78.5% design corrected speed). The post-stall simulations demonstrated the importance of the time lag constant,  $\tau$ , (a means to obtain dynamic forces using steady-state forces from steady stage characteristics, [See Section 4.4](#) for full explanation) in determining which event (stall or surge) would occur.

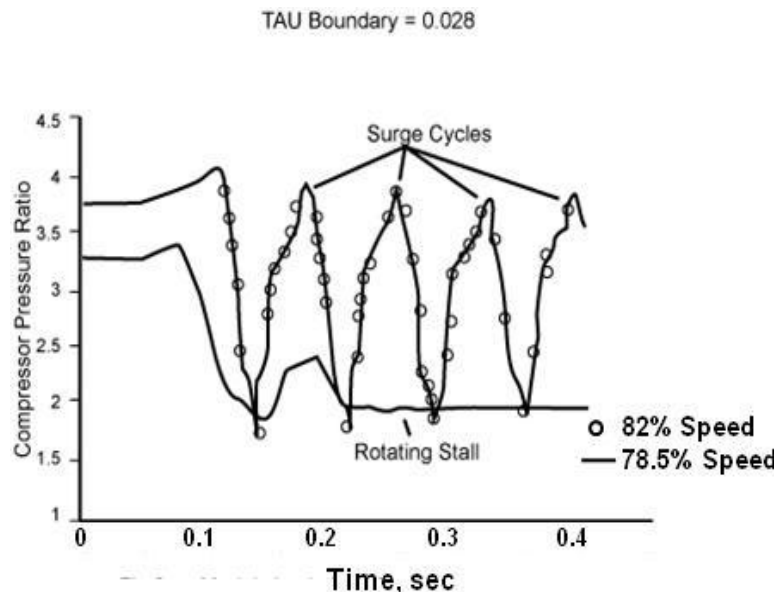


**Figure 3.22 Model Simulation of Rotating Stall/Surge Boundary**

The present requirement to use experimental results to determine correct value of  $\tau$  (or any other model parameter) does not invalidate the usefulness of the model as an analysis aid. Once an initial value for  $\tau$  is determined, it can be left unchanged. As a result, the effect of various design changes or other system parameters on model simulations can be examined. In the present investigation,  $\tau$  was used to calibrate the model at the stall/surge boundary. The model was repeatedly exercised at 78.5% speed until a  $\tau$  boundary of 0.028 seconds was determined. Once determined,  $\tau$  was held constant (along with all other model parameters) and



the model was run at 82.0% speed. **Figure 3.22** displays the results of these runs, and demonstrates the model's ability to simulate the compressor's stall/surge boundary. The value of  $\tau$  was held at a constant value (0.028) throughout all the model simulations.

Model prediction of a rotating stall event is shown in **Figure 3.23** and **Figure 3.24**, along with the experimental performance for the same event. **Figure 3.23** demonstrates overall performance comparison, while **Figure 3.24** shows inter-stage comparisons. Both plots were produced from the results of the same model run, namely, a 78.5% corrected speed simulation. The model was supplied with steady and dynamic boundary conditions that were consistent with the experimental conditions. The model simulation was started away from the stall point because of numerical oscillations associated with the start of a model run.

**Figure 3.23** demonstrates the model's ability to accurately simulate overall compressor stalling features. These features include stall point, transient drop in performance (including the initial surge-like behavior) and final, average in-stall performance.

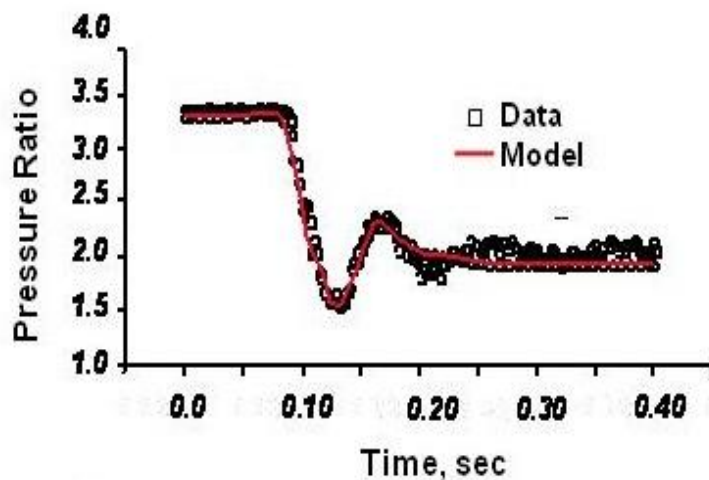


**Figure 3.23 Model Simulation of Overall Rotating Stall Performance and Comparison with Data**

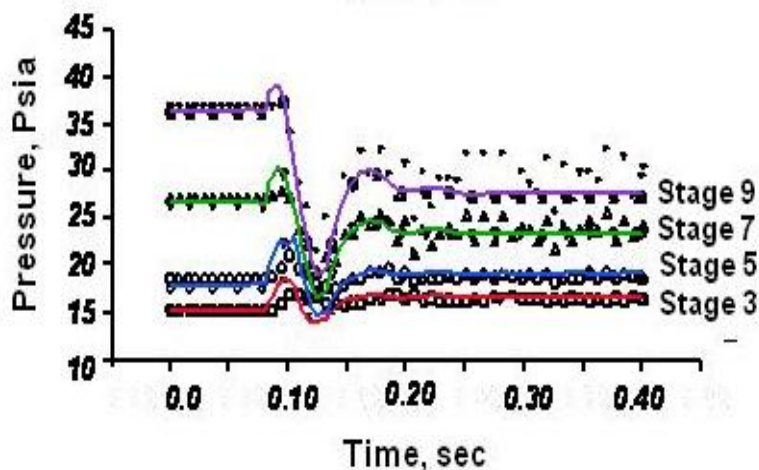


**Figure 3.24 Model Simulation of Interstage Rotating Stall Performance and Comparison with Data**

**Figure 3.24** displays similar agreement on an interstage basis. In a flow-averaged sense, model-predicted overall and interstage steady and transient behavior agrees well with the measured performance.

Of particular interest in **Figure 3.24** is the apparent increase in average performance of the front stages of the compressor once rotating stall developed. The back stages (4-10) exhibited an expected drop in performance associated with a stage operating in rotating stall. The apparent mismatch between stages three and four is the basis for model predictions concerned with improving compressor recoverability. The ability of the model to simulate the extensive hysteresis exhibited by the compressor at the stall/surge boundary speed is of special interest. This ability was made possible through a modification to the model allowing the addition of double-valued stage characteristics (double-valued in terms of flow coefficient). As shown in **Figure 3.25**, the model is able to accurately represent the hysteresis, and

thus the poor recovery behavior exhibited by the compressor rig when operating below its stall/surge boundary speed. The simulation is a result of decreasing the throttling function by 15 percent (as was the case for the simulation described in the preceding paragraphs), holding long enough to establish steady, in-stall performance and then increasing the throttling function 35 percent. This is shown graphically in [Figure 3.25](#). As indicated in the plot, the model does not predict recovery from stall as the "throttle" is opened well beyond its initial stall inception value.

### **MODEL PREDICTIONS FOR IMPROVED RECOVERABILITY – ENLARGED REAR FLOWPATH**

As previously noted, results from the CRF test indicated extensive compressor in-stall hysteresis at 78.5% design corrected speed. Subsequent data analysis yielded important conclusions concerning the influence of stage performance effects on the recovery of the test compressor from rotating stall as reported by Copenhaver, [3.11]. The stage-by-stage model has been shown to accurately represent the compressor transient and quasi-steady, in-stall measured performance ([Figure 3.23](#) and [Figure 3.24](#)) as well as the extensive hysteresis described above ([Figure 3.25](#)). The excellent agreement between model simulations and experimentally-determined performance served to both validate the application of the modeling technique to the CRF compressor rig, and increased the level of confidence placed in model predictions.

Both model and experimental results indicated that at 78.5% design corrected speed the front stages of the compressor may remain un-stalled while the compressor exhibits rotating stall behavior (the first three stages generate a higher time-averaged pressure rise once the compressor is in stall). In addition, the poor recovery behavior (extensive hysteresis) exhibited once the compressor is in stall appeared to be a result of flow blockage of the rear stages. As discussed in detail by Copenhaver [3.11], the prolonged in-stall hysteresis is likely due to

choking in the unblocked portion of the tenth stage rotor. Thus, the hysteresis level can be reduced if the latter stage flow blockage can be reduced or eliminated, improving recoverability. Model investigations for improved compressor recovery behavior involved reducing the in-stall hysteresis by taking actions that reduced or eliminated the rear stage blockage. These actions included enlarging the rear stage flowpath or adding a bleed outflow downstream of the middle stages. Modifications to actual stage geometry are represented as changes in stage characteristics. Enlarging stage flowpath area, both through variable vanes or changes to hub and/or tip geometry, increases the flow capacity of that stage, and results in a shift of its characteristic in the direction of increasing flow. Thus, in order to investigate the effects of an enlarged rear stage flowpath, the tenth stage characteristic was arbitrarily translated by a positive four-hundredths of a flow coefficient. No attempt was made to change the level of the characteristic; the stall and in-stall pressure coefficients of stage ten remained unchanged.

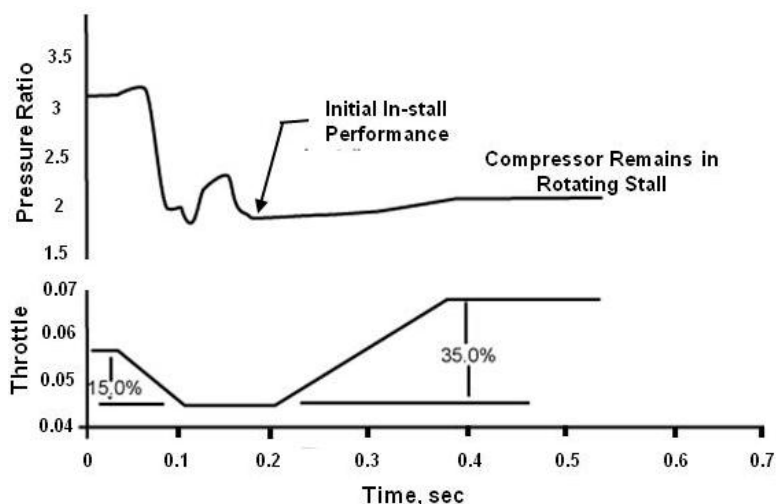


**Figure 3.25 Model Simulation of Experimentally Determined Compressor Recovery Hysteresis**

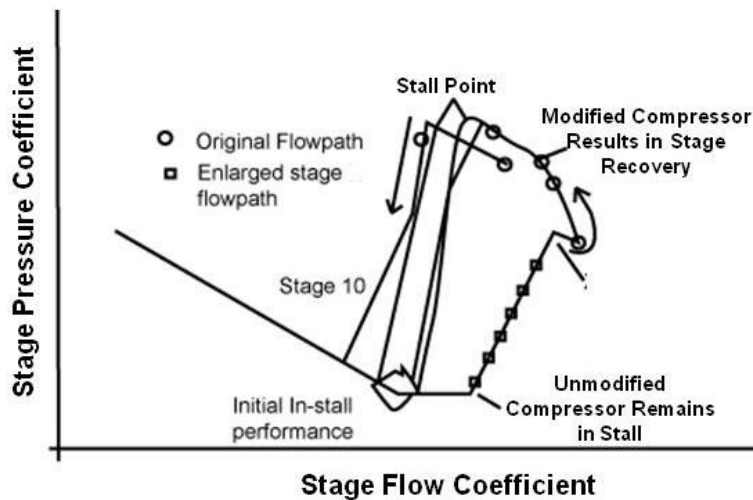


**Figure 3.26 Effect of Enlarge Rear Stage Flowpath on Stage Performance**

reduction resulted in a higher average in-stall mass flow rate for the modified compressor, and thus improved the ability of the compressor to return to un-stalled operation as shown in [Figure 3.26](#).

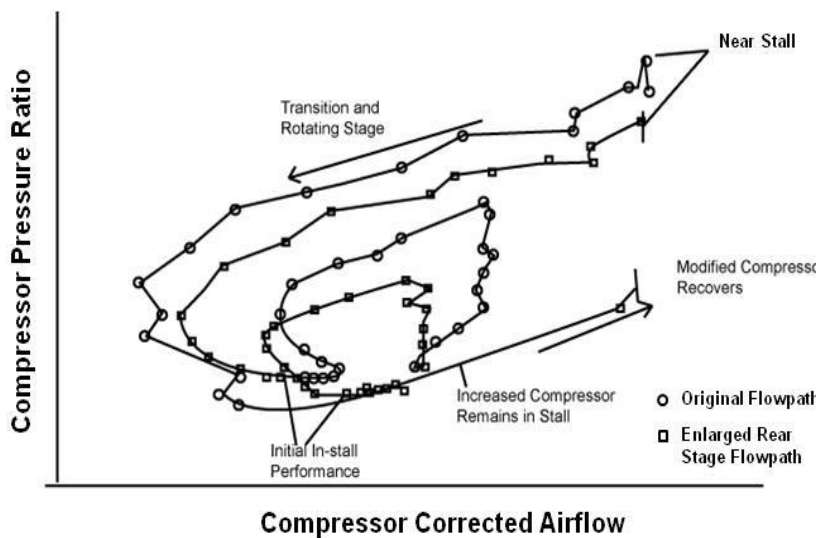


**Figure 3.27 Overall Compressor Map Showing Predicted Improved Recovery Behavior Due to Enlarged Rear Stage Flowpath**

the tenth stage is more highly loaded for a given flow coefficient. By enlarging the rear stage flowpath, the stability limit for stage ten occurs at a higher stage flow coefficient. The resulting change in stage matching produces overall compressor stall at a slightly higher mass flow rate and lower pressure ratio than the original compressor ([Figure 3.26](#)). Further, it appears that the

[Figure 3.26](#) demonstrates the improved compressor recovery behavior predicted by the model as a result of the enlarged tenth stage flow-path simulation. The initiation of and subsequent recovery from rotating stall for the "modified" compressor was achieved via the model throttling function through settings identical to those shown in [Figure 3.25](#). As shown in [Figure 3.26](#), the modified compressor stalls at a slightly higher mass flow rate and lower pressure ratio than does the original compressor. It appears that the increased flowpath resulted in a reduction of the original in-stall aerodynamic blockage extent. The blockage

The improved compressor recovery behavior was not without performance penalties. The approximate five percent reduction in stall pressure ratio indicated in [Figure 3.26](#) also produces a loss in stall margin. Examination of the differences in stage ten performance for the original and modified compressors offers insight into the improved recovery behavior of the enlarged flowpath case.

As shown in [Figure 3.27](#), the shift of the tenth stage characteristic redistributes the stage loading so that during un-stalled operation,

modified stage matching results in decreased levels of dynamic blockage when the compressor is in rotating stall. In doing so, initial in-stall stage average mass flow is increased and stage recovery behavior is improved.

### **MODEL PREDICTIONS FOR IMPROVED RECOVERABILITY – INTER-STAGE BLEED FLOW**

In addition to the enlarged flowpath studies, model recovery investigations were performed to investigate the use of inter-stage bleed flow. The modeling technique here treats bleed flow and its effects as additional source terms in the conservation equations. Results from both the model simulations and data analysis suggest that the effectiveness of inter-stage bleed on compressor recoverability is dependent on bleed location. The results of two model predictions involving inter-stage bleed are presented in [Figure 3.28](#) and [Figure 3.29](#). In both

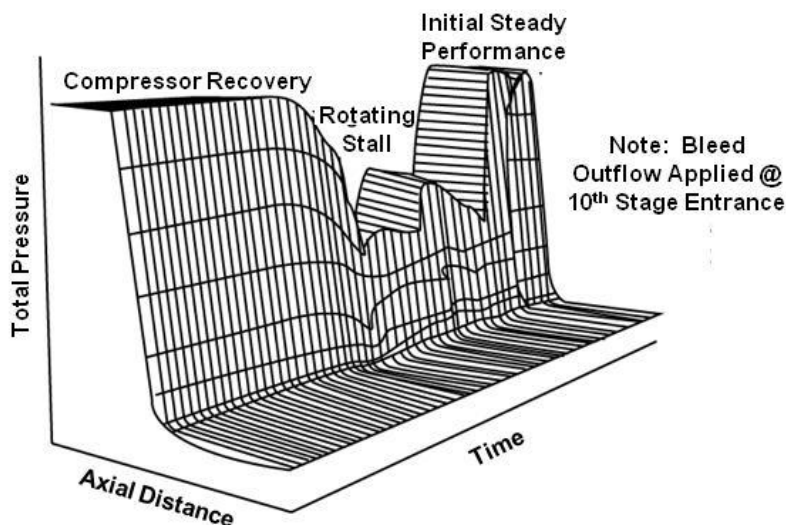


**Figure 3.29 Predicted Compressor Recovery Resulting from Stage 10 Bleed Outflow**

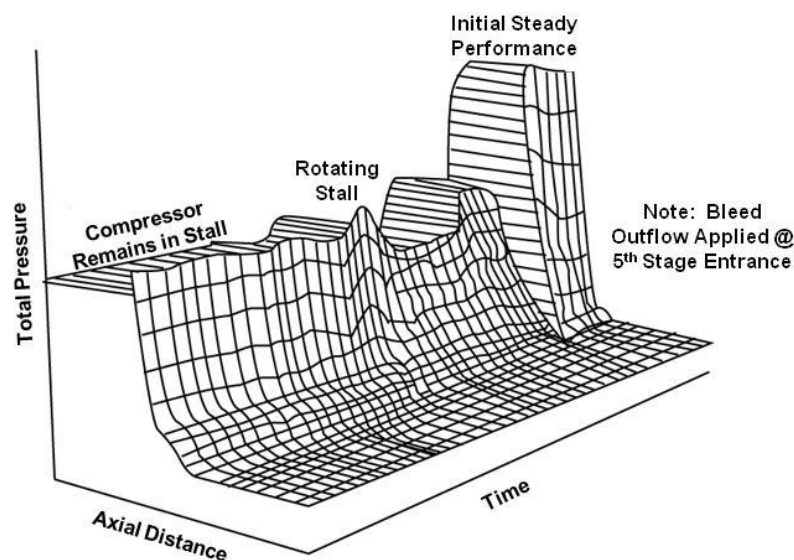


**Figure 3.28 Stall-Related Prediction Resulting from Stage 5 Bleed Outflow**

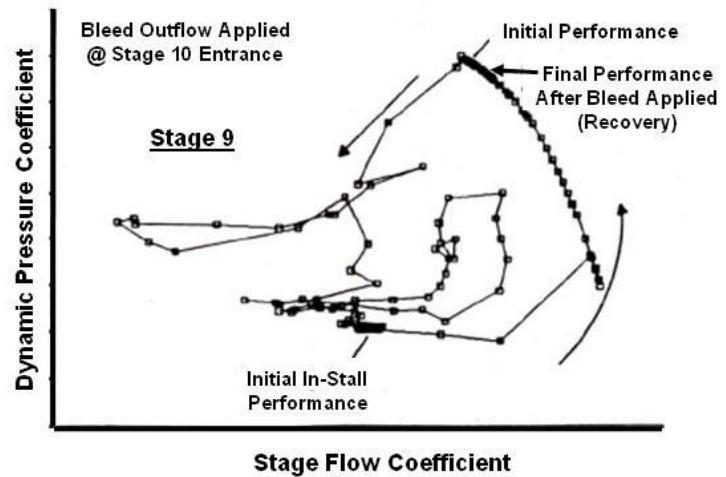
cases, rotating stall was initiated through the use of the model throttling function. To examine bleed effects, the value of the throttling function was left unchanged once rotating stall had developed. Other than bleed location, the model runs were identical. As shown in the two figures, the model predicts that the rear stage blockage *can* be essentially eliminated if a 3.0 lbm/sec bleed outflow (15% of the un-stalled mass flow) is applied at the entrance of the tenth stage. The result is compressor recovery from rotating stall. The same amount of bleed applied upstream of the middle stages ([Figure 3.29](#)) does not

result in recovery; however, the overall compressor in-stall performance is increased. This

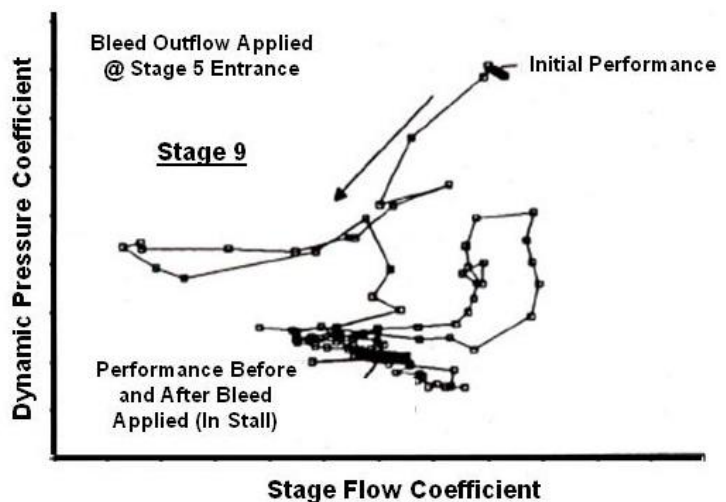


apparent dependence of compressor recoverability on bleed location was also demonstrated through the use of a dynamic component-by-component turbofan engine model as reported by Hopf and Steenken [3.14].

As was done for the increased flowpath study, an examination of stage behavior was performed in an attempt to gain insight into the effects of inter-stage bleed on compressor recoverability. Stage dynamic behavior was examined through the use of a dynamic pressure coefficient, obtained by applying a time lag to the stage steady-state forces. Consistent with the observation that of the front stages of the compressor rig remained unstalled with the compressor operating in rotating stall, the dynamic behavior of the front stages do not significantly deviate from steady performance. When the bleed is applied downstream, the front stages return to higher flow levels indicative of unstalled operation (recovery). Figure 3.30 demonstrates the dependence of stage recovery behavior on bleed location. Bleeding downstream of the stalled middle stages increases the axial velocity, thus reducing the blade angle of attack and unstalling these stages (Figure 3.30a). Applying the same amount of bleed upstream of the middle stages does not result in recovery of the latter stages (Figure 3.30b). Stalled stages, and therefore the compressor, receive little recovery benefit from a bleed outflow applied upstream of the stalled stages.



a. Bleed Applied @ Stage 10 Entrance



b. Bleed Applied @ Stage 5 Entrance

**Figure 3.30 Effect of Bleed Flow Location on Stage 9 Dynamic Behavior**

### Conclusions of Investigation

The following conclusions were based on the combined results of the compressor rig test and model predictions:

1. The improved recovery predictions presented here were made possible by the stage-by-stage compressible model. The following observations are offered:

- a. Analysis of individual stage behavior during transient events such as surge or rotating stall can be performed. This analysis resulted in a more quantitative understanding of post-stall, inter-stage fluid mechanics in multistage axial-flow compressors.
  - b. The effects of design changes to a stage or stages on model-predicted overall and inter-stage performance can be examined.
  - c. The physical features of the modeled compressor were retained. Control volume size is governed by actual stage geometry.
  - d. The usefulness of a stage-by-stage model of this type extends beyond the obvious stall/recovery investigations.
2. The model's ability to provide information that is very difficult or costly to measure is a true asset. For example, in this effort, the dynamic behavior of individual stages was examined in detail and then actions were studied to alter the behavior resulting in a more recoverable compressor. The choice of a stage-by-stage model or a lumped volume representation is dependent on the application. For example, an overall model would be appropriate for a recovery investigation involving overall compressor behavior or studies related to system parameters (discharge volume, compressor length, etc.). However, a detailed investigation involving inter-stage changes would require a stage-by-stage model.
  3. The effect of the actions taken on compressor recoverability was dependent on axial location (i.e. blocking upstream of the middle stages did not result in compressor recovery). As such, the actions point to the importance of stage matching on compressor stalled behavior, and its influence on recoverability. Highly unloaded front stages may result in an extension of the compressor starting problem (front-stage stall, rear-stage choke) into stages downstream. Specifically, the front stages may remain unstalled while the compressor exhibits stalled behavior. If this is the case, actions known to improve compressor starting may improve recovery behavior, but only if they are applied downstream of the stalled stages.

The extension of compressor test results was done in this study, represents one of the primary uses of a model of this type. The following extensions have been identified, and represent only a sample set:

- Study of velocity and/or Mach number profiles within the machine.
- Throttle ramp rate studies, both in and out of stall.
- Stall margin studies, including the graphical representation of the path of each stage toward stall as the flow is reduced.
- Introduction of pressure and/or temperature pulses anywhere in the machine; study of the effect of slow or fast temperature changes.
- Study of the effects of inlet resistance (distortion producing device), combustion, and gas path heat transfer on compression system operation.

#### **ADDITIONAL REFERENCES:**

**3.11** Copenhaver, W. W., "Stage Effects on Stalling and Recovery of a High-speed 10-stage Axial-Flow Compressor," Ph.D. Dissertation, Iowa State University. October 1988.

- 3.12** Copenhaver. W. W., and T. H. Okiishi, "Rotating Stall Performance and Recoverability of a High-speed Ten-Stage Axial-Flow Compressor," AIAA Paper No. 89-2684, July 1989.
- 3.13** Copenhaver. W. W., and C. J. Worland, "Acquisition of Unsteady Pressure Measurements from a High Sped Multi-Stage Compressor." ASME Paper No. 88-GT-189, June 1988.
- 3.14** Hopf, W. R.. and W. G. Steenken, "Stall Recovery Control Strategy Methodology and Results." AIAA Paper No. AIAA-85-1433, July 1985.

### 3.1.5 Effect of Heat Transfer on Post-Stall Behavior (Nine-Stage Model)

Operation of high-speed, high-pressure ratio compressors results in a large temperature rise through the compressor. A portion of the large amount of energy input is stored in the compressor blades, rotors, and disks. Thus, during engine throttle transients as in a bodie maneuver (maximum power to idle then back to maximum power), heat transfer between the compressor metal and the airflow takes place. The release of energy during the transient from maximum power to idle causes a change in density, which produces a shift in the compressor characteristic and lowers the stability limit. This loss in surge margin can result in compression system instability during throttle re-advance to maximum power. Rapid throttle transients from max power to idle then back to max power is known as Bodie maneuver.

#### CITED EXAMPLE(S)

**3.15** Davis, M. W. , Jr. and W. F. O'Brien, "Stage-by-Stage Poststall Compression System Modeling Technique", Journal of Propulsion and Power, Vol. 7, Number 6, November-December 1991, pp. 997-1005.

**3.16** Davis, M. W., Jr., "A Stage-by-Stage Post-Stall Compression System Modeling Technique: Methodology, Validation, and Application", Ph.D. Dissertation, Virginia Polytechnic Institute and State University, December 1986

#### MODELING TECHNIQUE

The **single-spool one-dimensional dynamic model** ([Section 4.4.1](#)) was configured to a 9-stage high pressure compressor of a current turbofan engine as illustrated in [Figure 3.31](#). To investigate loading of the HPC, the exit static pressure was ramped at a rate (50 Psia/sec) to simulate a combustor hard light. Inlet conditions (total pressure and temperature) as well as corrected speed were held constant since the exit static pressure ramp rate was at a high enough rate so that mechanical speed and inlet temperature would not change in that time frame.

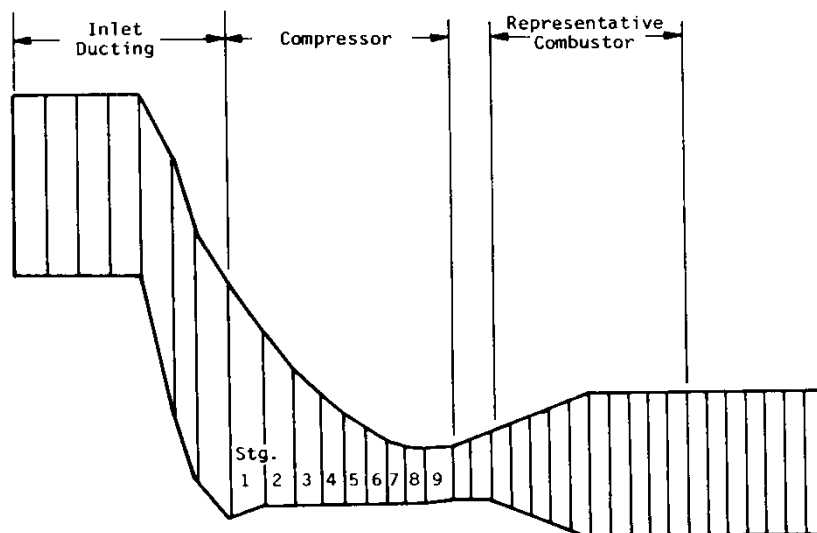


**Figure 3.31 Schematic of the Single-Spool, Nine-Stage Compression System Modeled**

## APPLICATION OF HEAT TRANSFER DURING BODIE MANUEVER

From a modeling study, MacCallum and Pilidis [3.17] concluded that the following thermal effects contribute to the loss in stall margin during reacceleration: non-adiabatic flows causing density changes due to heat transfer; changes in boundary-layer development on the blade airfoils; changes in the boundary layer development near the end walls; changes in tip clearances; and changes in seal clearances. **For this study, only the effect of non-adiabatic flows causing density changes was considered for analysis.** An investigation by Crawford and Burwell [3.18] quantified the magnitude and nature of the heat transfer during turbine engine bodie maneuvers using actual engine test results. A calculation of stage thermal energy was made based upon the following equation:

$$Q = mC(T_{max} - T_{idle})$$

Eqn. 3-2

Where

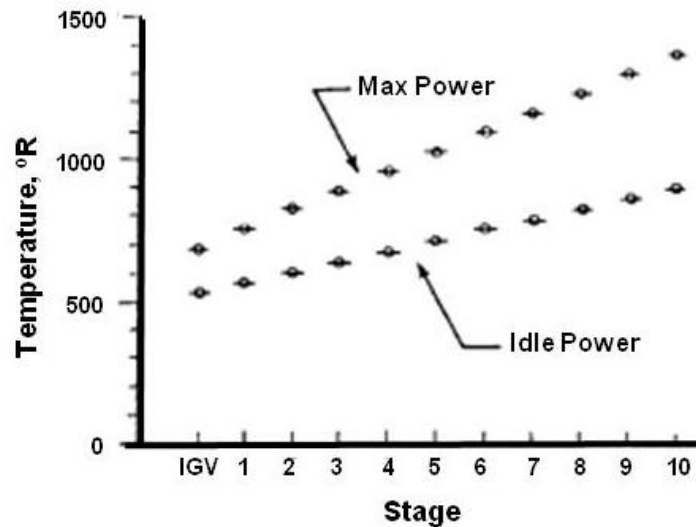
$m$  = mass of the blades, platforms and seals

$C$  = specific heat of the metal

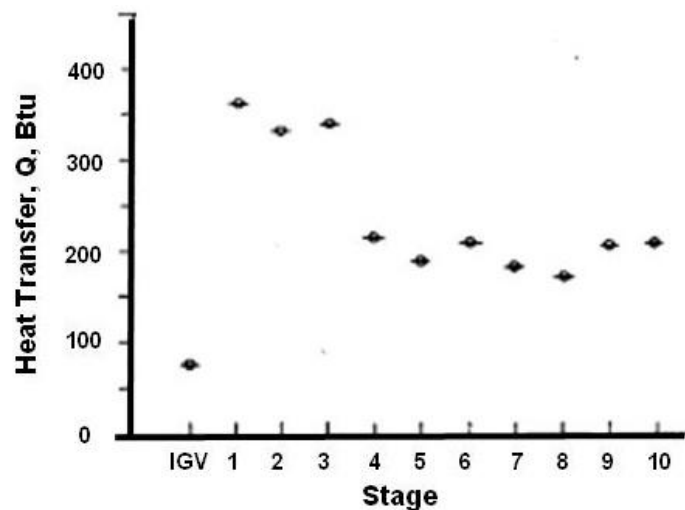
$T_{max}$  = stage total temperature at maximum power

$T_{idle}$  = stage total temperature at idle power

Stage temperature distributions were obtained from a stage stacking model simulating idle and max power operation at the flight conditions tested. Stage temperature distributions for maximum and idle power, along with the corresponding stored thermal energy are presented in Figure 3.32. With a calculation of transient airflow, heat transfer rates (Btu/Sec) were calculated. Typical stage heat-transfer rates calculated from experimental results obtained from current-day high pressure compressors are



a. Core Compressor Temperature Distribution



b. Stored Thermal Energy by Stage

**Figure 3.32 Predicted Stage Temperature Distribution at Max and Idle Power and Corresponding Blade Store Thermal Energy**

presented in [Figure 3.34](#). Using these rates as a guideline, stage heat transfer rates were postulated for a nine-stage compression system which had just completed a bodie transient.

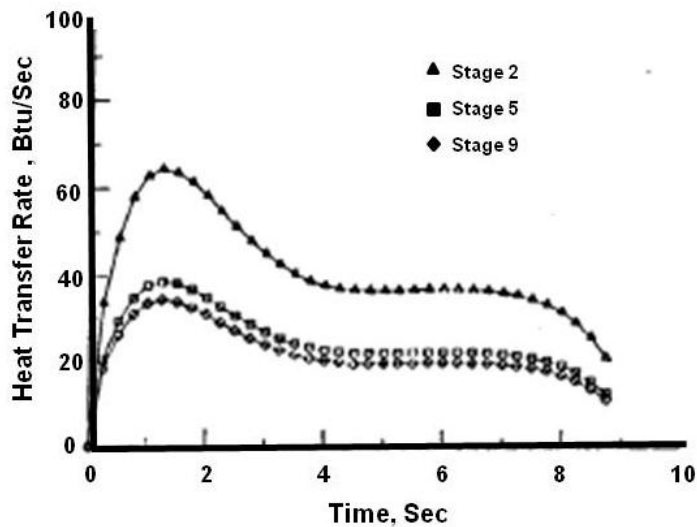


**Figure 3.34 Typical Stage Heat-Transfer Rate Based Upon Experimental Results**

experimentally ([Figure 3.34](#)). The postulated heat-transfer distribution for the nine-stage compressor is illustrated in [Figure 3.33](#). Since the throttle was set such that an instability would occur, the heat-transfer rates are shown to be oscillating during the first second of the dynamic event because the compressor was experiencing surge during this period. However, once the stage heat-transfer rates had reached their maximum values, the compressor moved to the nonrecoverable state as illustrated in [Figure 3.35](#). Once the nonrecoverable state was reached, heat transfer rates reduced because of the reduction in overall airflow. This study assumes that compressor instability will occur during a bodie maneuver and the model was configured to favor this result. Even if such were not the case, the results from the model have indicated that because of the heat transfer generated within the compressor at time of throttle re-advance, the compression system may be more likely to enter the nonrecoverable state (rotating stall) when the system is near the surge/rotating stall boundary.

Thus, the dynamic model was used

The model was operated to simulate operation at 70% speed with the throttle set such that compressor instability would occur. The stage force lagging constant,  $\tau$ , was set at slightly lower value than the model-determined surge/stall boundary to ensure that surge would be the initial post-stall event. (Smaller values of  $\tau$  encourage a surge-like result from the model.) A stage specific heat transfer was chosen for each stage based upon the calculated temperature distribution represented in [Figure 3.32](#). Heat-transfer rates were calculated from the equation given above and were brought to their maximum level exponentially over a time period of approximately one second, as was indicated

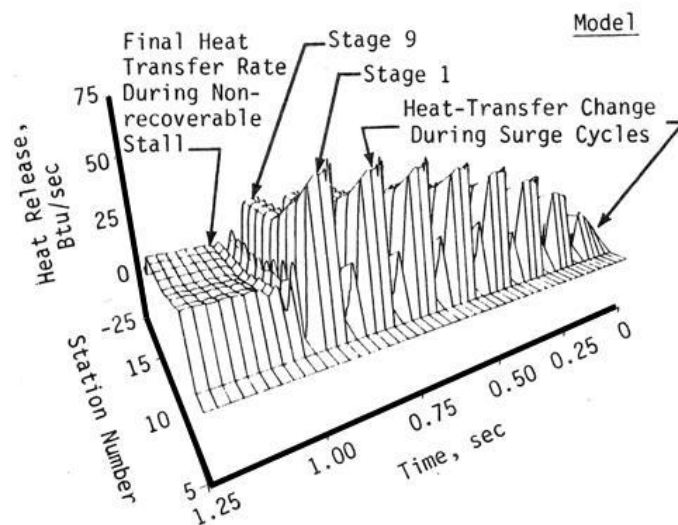


**Figure 3.33 Typical Stage Heat-Transfer Rate Based Upon Experimental Results**



to analyze the effects of heat transfer on system recovery. The system behavior change was due to a decrease in density which leads to an increase in incidence which tripped the system into nonrecoverable stall.

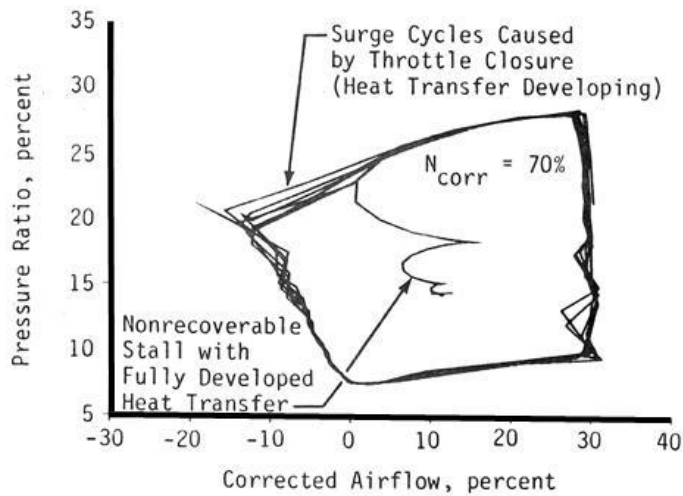


**Figure 3.35 Typical Stage Heat-Transfer Rate Based Upon Experimental Results**

#### **ADDITIONAL REFERENCES:**

**3.17** MacCallum, H. R. L., and Pilidis, P., "The Prediction of Surge Margins During Gas Turbine Transients," ASME Gas Turbine Conference, ASME Paper 85-GT-208, Houston, TX, March 1985.

**3.18** Crawford, R. A., and Burwell, A. E., "Quantitative Evaluation of Transient Heat Transfer on Axial Flow Compressor Stability," AIAA/SAE/ASME/ASEE 21st Joint Propulsion Conference, AIAA Paper 85-1352, Monterey, CA, July 1985

### 3.1.6 The Effect of Casing Treatment on System Operability

The flight envelope of aircraft gas turbine engines is affected by the operating range of the engine's compressor components. A compressor produces an increase in total pressure at a particular corrected airflow and speed. The operating range of a compressor is bounded on the high flow end by blade passage choking and on the low flow end by blade or endwall stalling. At the low flow end, blade stall can lead to system instability such as surge or rotating stall. These events are undesirable and are usually avoided by developing enough stall margin in the compressor design process. Stall margin is the measure of the operating range between the compressor operating point and the onset of system instability. However, there are times when the instability limit will be reached because of some destabilizing influence such as inlet pressure distortion. In these cases, it is possible to increase the available stall margin by some mechanical means such as casing treatment. Casing treatments in axial flow fans and core compressors have been shown by Prince and Wisler [3.22] to effectively lower the mass flow rate at which endwall stall occurs, thus increasing the operating range and the available stall margin.

There are many different types of casing treatments about which many experiments have been carried out to evaluate their effect on compressor performance [3.23, 3.24, 3.25]. These casing treatments include circumferential grooves, axial-skewed slots, blade angle slots, and honeycomb. From these experiments some general observations have been made:

- Casing treatments have similar effects on compressor or stage stall margin for a wide range of Mach numbers ( $M=0.15$  to  $M=1.5$ ); and
- The more a casing treatment improves stall margin the more it may adversely affect the compression system efficiency.

However, this section will be limited to the effect casing treatment has on the stability limit and/or recovery and will not address the efficiency issue.

#### **CITED EXAMPLE(S)**

**3.19** Davis, M. W. , Jr. and W. F. O'Brien, "Stage-by-Stage Post-stall Compression System Modeling Technique", Journal of Propulsion and Power, Vol. 7, Number 6, November-December 1991, pp. 997-1005.

**3.20** Davis, M. W., Jr., "A Stage-by-Stage Post-Stall Compression System Modeling Technique: Methodology, Validation, and Application", Ph.D. Dissertation, Virginia Polytechnic Institute and State University, December 1986

**3.21** Gorrell, S. E. and M. W. Davis, Jr., "Application of a Dynamic Compression System Model to a Low Aspect Ratio Fan: Casing Treatment and Distortion", AIAA Paper # AIAA-93-1871, Presented at the 29th Joint Propulsion Conference and Exhibit, Monterey, CA, June 1993.

#### **MODELING TECHNIQUE**

Since it may not always be feasible to test all configurations because of economic or hardware constraints, validated mathematical models can be used to fill in information not obtained during testing and may even be used to help design the experiment, if enough pre-test information is available. Two studies were performed: one having to do with recoverability and the other with the extension of the stability limit. Both studies were performed with the one-dimensional



single-spool, dynamic simulation. The post-stall investigation was conducted with the earlier version known as **DYNMOD** while the stability limit investigation was conducted with **DYNTECC** [3.27] (Section 4.4).

### **APPLICATION OF CASING TREATMENT – EFFECTS ON RECOVERABILITY**

Once a particular compression system is designed and built, the performance and stability behavior are fixed within certain limits. There are only a limited number of external changes that can be made to improve either performance or stability. If these changes cannot produce the desired result, certain internal or blade changes such as camber, stagger, tip clearance or tip casing treatment can be made which improve performance and stability. A possible change that can be considered is the effect of some type of tip-casing treatment. Takata and Tsukuda [3.24] utilizing a low-speed compressor rig, investigated the effects of certain types of tip-casing treatment on the performance of a single rotor row. Of the several types of treatment investigated, they found that a deep-skewed slot tip treatment most improved the stage characteristics.

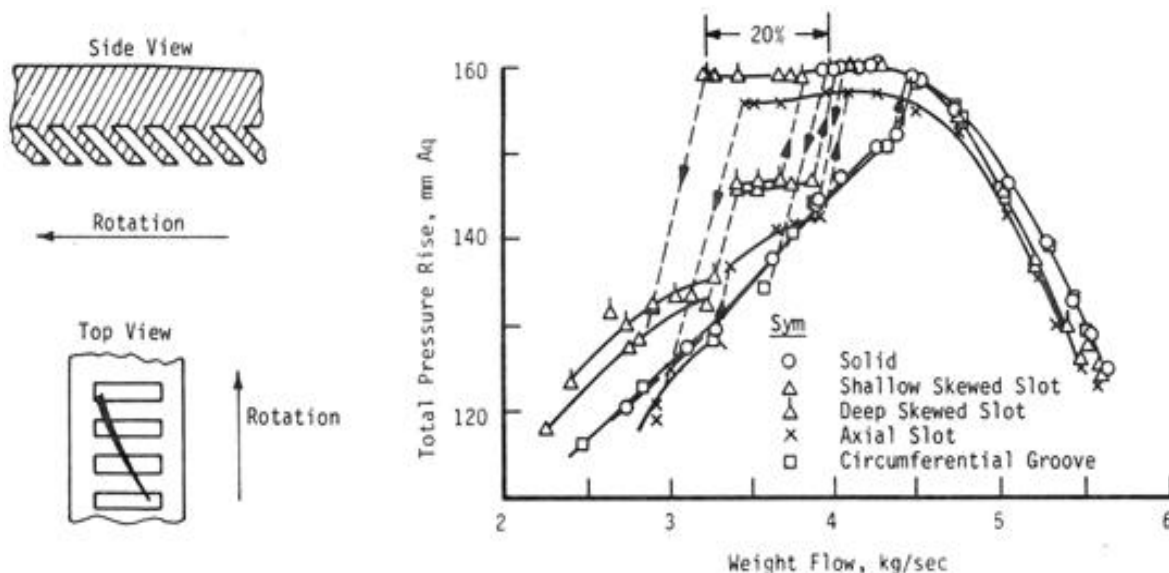


**Figure 3.36 Possible Tip Treatment Modification and the Effect on Stage Characteristic**

Presented in Figure 3.36 is the deep-skewed slot modification and the observed effect on stage performance. Although stage pressure rise is not increased by this technique, the amount of airflow reduction necessary for stall to occur was extended by 20%. This provided more stall margin and reduced the chances for stall occurrence. In addition, a portion of the rotating stall characteristic was presented, which indicated a higher average pressure level during rotating stall. To evaluate the effect of such a modification on compression system post-stall behavior, the three-stage, low-speed model was chosen for study.

A low-speed condition (Figure 3.37) was chosen in which rotating stall was the end result. During these hardware modification studies, all variables (B parameter, force lagging constant,  $\tau$ , speed and plenum configuration) were held constant except for the changes in the quasi-steady characteristics described below. Presented in Figure 3.38 is a postulated first-stage pressure characteristic with stall margin improvement-based upon the results of the deep-

skewed tip-casing treatment. The maximum stall point pressure rise is extended for a 20% reduction in airflow, effectively increasing the stall margin for the first stage. The rotating stall characteristic is assumed to be similar to the original shape, but at a higher pressure, as was indicated experimentally. With this change to the first stage only, the modeled compression system exhibited continuous surge cycles, rather than rotating stall, as illustrated in [Figure 3.39](#). When similar changes were made to the second and third stages individually, the results were nearly identical. However, when changes to all three stages were incorporated collectively, the compression system resisted the stall condition altogether at the throttle setting which had previously caused instability.

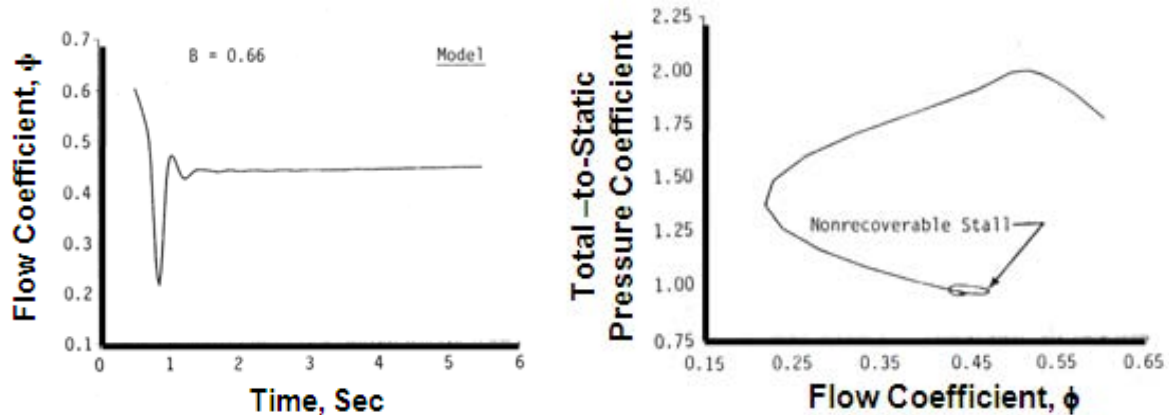


**Figure 3.37 Three-Stage Overall Compression System Post-Stall Behavior, Rotating Stall,  $B = 0.65$**

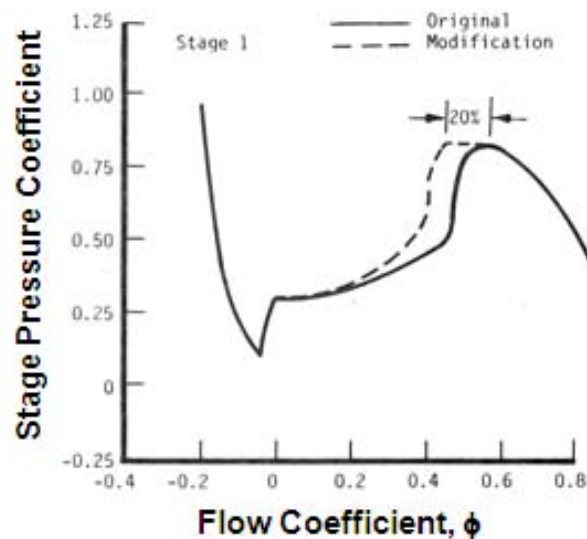


**Figure 3.38 Postulated Stage Pressure Characteristic Modification as a Result of Tip Treatment**

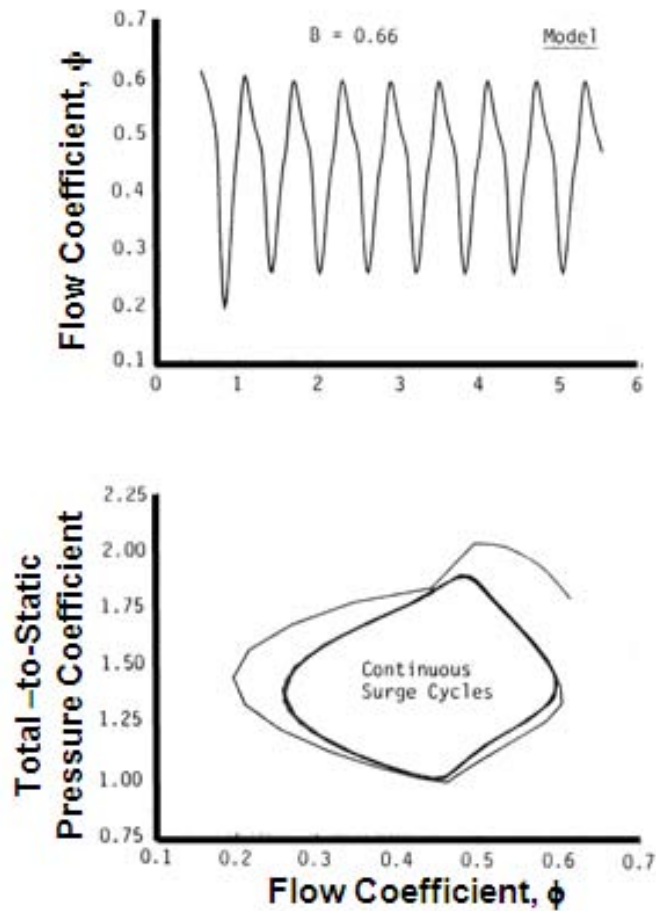


**Figure 3.39 Model prediction of the Effect of 1<sup>st</sup> Stage Tip Treatment on Post-Stall Behavior,  $B = 0.66$**

#### **APPLICATION OF CASING TREATMENT -- EFFECT ON STABILITY LIMIT**

The Compressor Research Facility (CRF) [3.26] at Wright-Patterson Air Force Base conducted a test entitled **Augmented Damping of Low Aspect Ratio Fans (ADLARF)**. One of the phases of the ADLARF test will be to evaluate five different casing treatments over rotor one. This fan was previously tested at the CRF in a baseline configuration which included circumferential grooves over the first rotor tip.

The ADLARF fan (Figure 3.40) is a high speed, two stage, low aspect ratio fan with variable stator one which has been previously tested in the CRF. During this previous test inlet, interstage, and exit steady-state pressure and temperature measurements were acquired to fully document the stage and overall aerodynamic performance of the compressor. Demonstrated design point parameters are listed in Table 3.2.

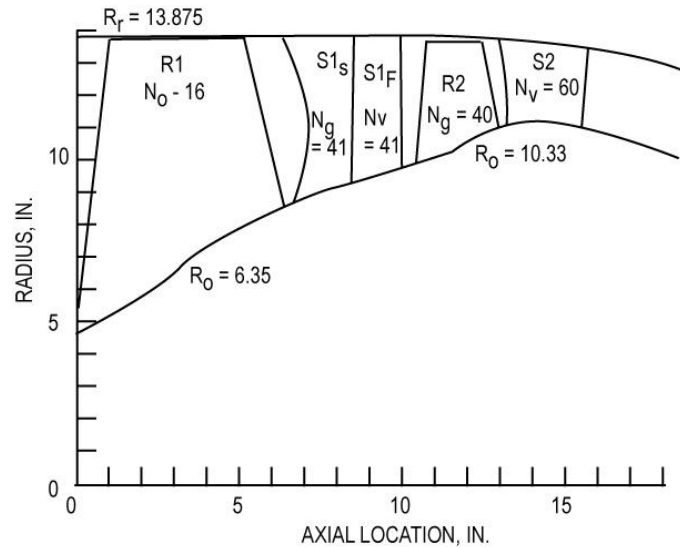


**Figure 3.40 Schematic of ADLARF Fan**

**Table 3.2 ADLARF Design Performance Parameters**

<u>PARAMETER</u>	<u>DEMONSTRATED VALUE</u>
Corrected Speed (%)	98
Total Pressure Ratio	4.30
Corrected Tip Speed (ft/sec)	1577
Corrected Airflow (lbm/sec)	158.3
Flow/Annulus Area (lbm/sec-ft <sup>2</sup> )	0.852
Stall Margin (%)	13

During the initial test of the ADLARF fan, it was determined that the second stage initiated stall for a wide variety of speeds, including the ones of interest for this study. The original ADLARF fan was configured with stage one casing treatment of circumferential grooves. Thus, the baseline for comparison and the calibration was done for the ADLARF fan as tested with circumferential grooves.

On the ADLARF fan, the hardware is such that the casing over rotor one is easily accessible and thus easily changeable. This makes testing several casing treatments possible. However, this also presents a problem if the second stage is the stalling critical stage, as was reported in

the previous test. If various casing treatments are put on the first stage but the second stage is the critical stage, any improvement in performance or operability of the first stage will not be realized. This has led to the conclusion that an operability improvement will have to be made to the second stage as well. Currently, there are plans to incorporate axial grooves over the second stage. In addition, the first stage stator is variable and can be opened to reduce the load on the second stage. Both options will be tried separately and in combination.

### Model Calibration to the ADLARF Compressor

To use **DYNTECC** as a predictive analysis tool for the ADLARF fan, an accurate calibration against experimental results was necessary. Thus, accurate stage characteristics had to be determined from the previous test of the ADLARF fan. The experimental data were reduced to produce a set of stage characteristics based upon the following definitions.

$$\phi = W \frac{\sqrt{T_t/T_{ref}} (N_c)_{des}}{P_t/P_{ref} (N_c)_{act}}$$

Eqn. 3-3

$$\psi^P = (PR - 1) \left[ \frac{(N_c)_{des}}{(N_c)_{act}} \right]^2$$

Eqn. 3-4

$$\psi^T = (TR - 1) \left[ \frac{(N_c)_{des}}{(N_c)_{act}} \right]^2$$

Eqn. 3-5

Stage one was defined as the first rotor only since there was no inlet guide vane and pressure measurements were made on the leading edge of the following stator vanes. Stage two was defined as the variable vane following the first rotor and the second rotor. A duct with appropriate pressure losses was used to represent the exit guide vanes. A total pressure drop was assigned to the duct based upon experimental measurements before and after the exit guide vane position.

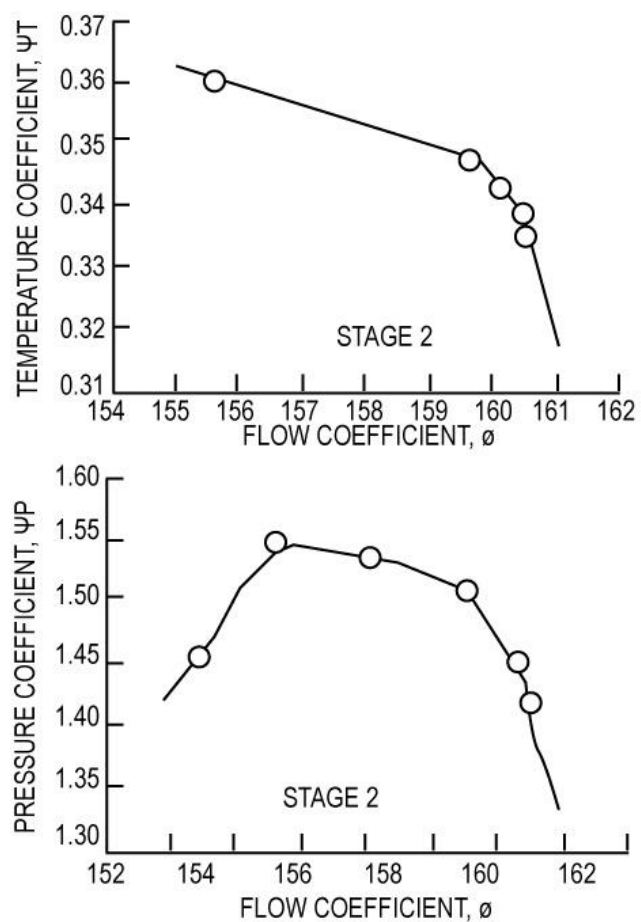
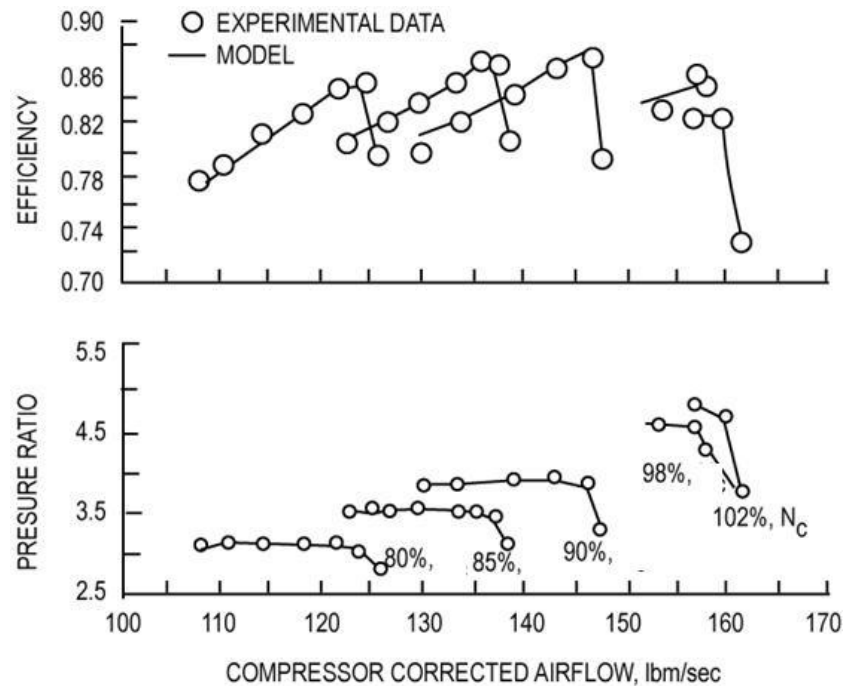
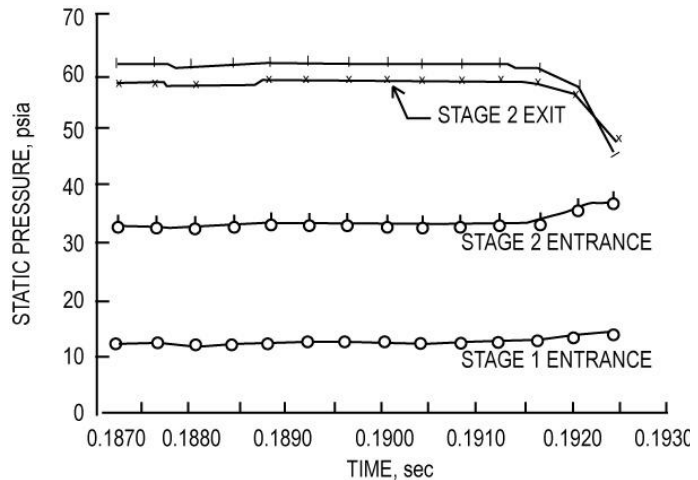


Figure 3.41 Typical ADLARF Stage Characteristics, 98%



**Figure 3.42 Comparison of Model Compression System Overall Pressure Rise and Efficiency to Experimental Results**

Stage characteristics were calibrated for five speeds ranging from 80 to 102 percent of design corrected speed. Typical ADLARF stage pressure and temperature characteristics (Stage one, 98% Speed) are presented in [Figure 3.41](#). The characteristics were implemented into **DYNTECC** and an overall stability limit analysis was conducted at each of the corrected speeds by closing a simulated exit nozzle until system instability was reached. System instability was determined when both stages had reached a predetermined value on each stage characteristic which represented stage stall. Comparison of model compression system overall pressure rise and efficiency to that obtained experimentally is made in [Figure 3.42](#). In general, overall pressure rise was within 1 to 2 percent of that measured experimentally and overall efficiency was within 1 percentage point.



**Figure 3.43 Static Pressure Signature at Compression System Instability – Stage 2 as Critical Stalling Stage**

For a stage-by-stage model to be completely calibrated, it must also indicate the correct stage behavior at the time of system instability. From the previous test of the ADLARF fan, it was determined that the second stage was the critical stalling stage for the speed range of interest. A good parameter to indicate stalling stage is static pressure. Model prediction of



static pressure at time of system stall is presented in [Figure 3.43](#). At the entrance to stage two, there was a rapid increase in static pressure. At the same time, the exit to stage two saw a rapid drop in static pressure. This was caused by blockage within stage two which precipitated flow breakdown.

Because of the plans to incorporate casing treatment on the second stage of the previously tested ADLARF fan, this paper will report the results of a model parametric investigation. The study focuses on the amount the second stage stall margin will have to improve through casing treatment and/or variable vane repositioning before improvements to the first stage operability due to tip its casing treatment can be realized.

### Casing Treatment Model

**DYNTECC** uses stage characteristics based on aerodynamic performance. If casing treatment is incorporated into the stage design, then the aerodynamic performance will be different. To appropriately model this behavior in the stage characteristic, one needs to know how casing

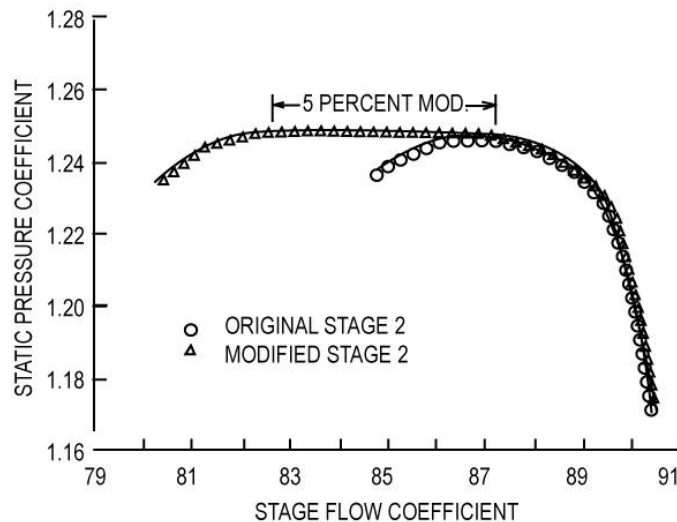


**Figure 3.44 Stage 2 Modification for Casing Treatment of 5%**

treatment model used in this parametric investigation. When casing treatment effects were implemented on a stage characteristic, its peak pressure performance was held over a prescribed airflow range. A typical stage with and without casing treatment effects is presented in [Figure 3.44](#).

treatment will affect stage aerodynamic performance. Several experimental investigations have been performed on a variety of compression systems which have been reported in [Refs. 3.22](#) through [3.25](#). Using the results from Takata and Tsukuda [[3.24](#)] ([Figure 3.36](#)), this investigation indicates that casing treatment has its most profound effect near the stall point. The major improvement seems to be an increase in the amount of airflow reduction capability at the stall limit. Depending upon the type of casing treatment, the increase in airflow reduction can be as much as 20% of that without casing treatment.

These experimental results thus became the basis of the casing

## Parametric Study -- Casing Treatment

Since it was not known what effect a particular casing treatment would have on the performance of the ADLARF fan, a parametric study was conducted to determine the effect of various degrees of stall airflow improvement due to casing treatment on both the first and second stage.

The first case investigated was to decrease the stall airflow capability of the first stage by 20 percent without changing the second stage stall airflow at all. Twenty percent was chosen to be the maximum

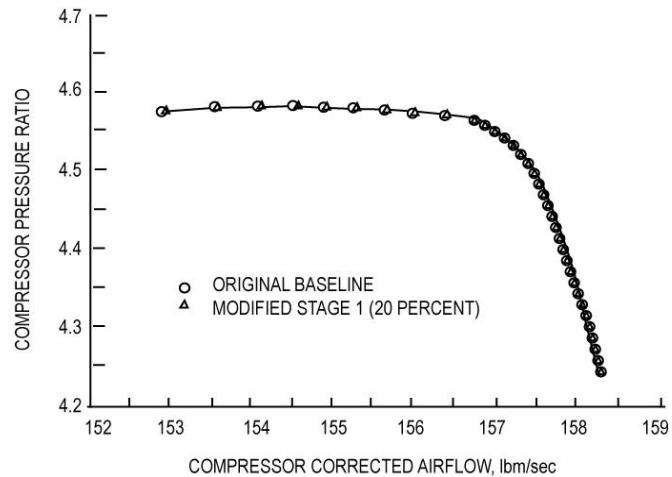


**Figure 3.45 Effect on Overall System Operability of a Stage 1 Modification for Casing Treatment of 20%**

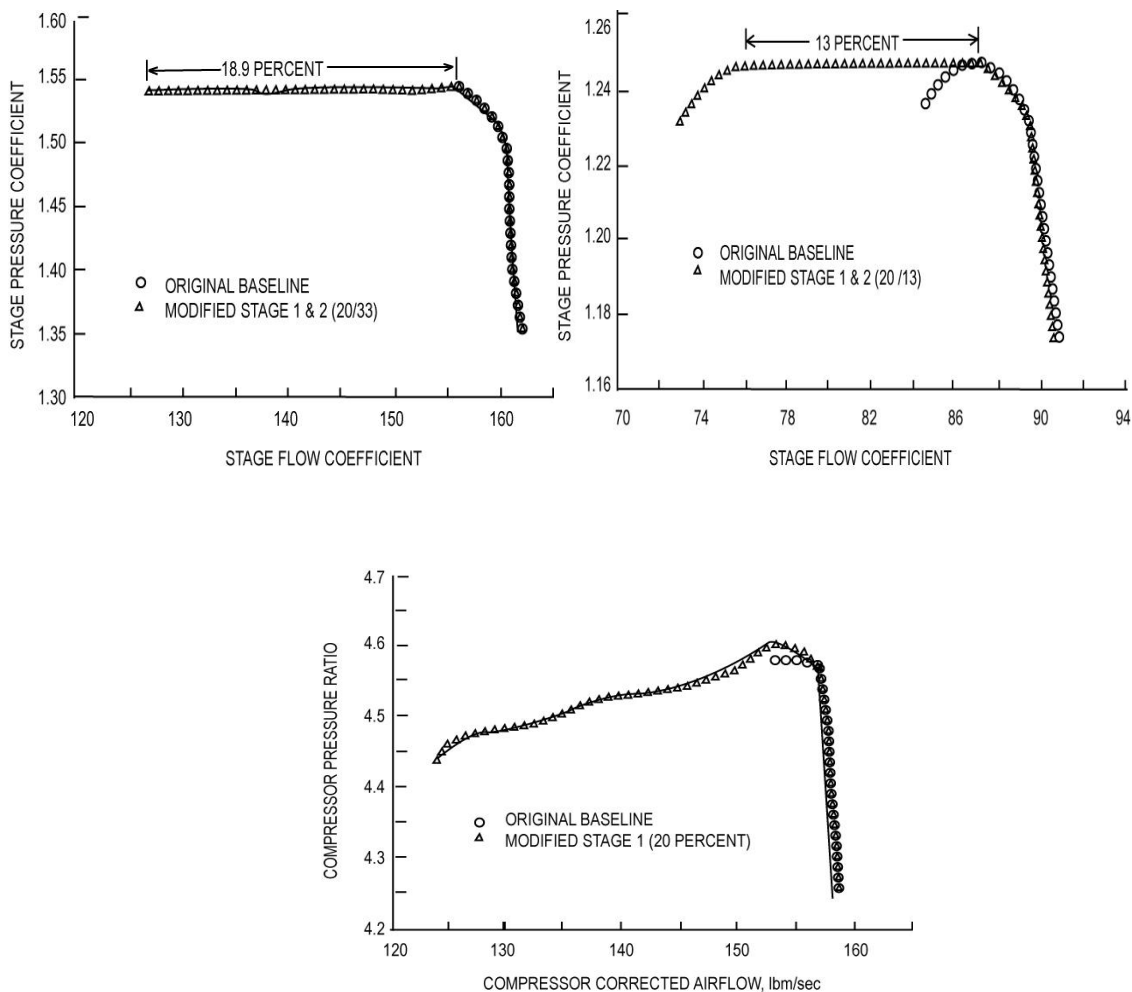


**Figure 3.46 Comparison of ADLARF Compression System Operability Characteristics with Tip Casing Treatment of 20% on the 1<sup>st</sup> Stage and 13% on the 2<sup>nd</sup> Stage to Baseline**



possible improvement based upon experimental results. As indicated in **Figure 3.45**, there was no improvement to overall compression system performance when compared to that without casing treatment. This result was expected since the second stage was the critical stage causing stall.

A series of stall airflow improvements to stage two representing the effect of casing treatment was implemented within **DYNTECC** and parametrically evaluated for overall performance improvement at system stall. Stage two casing treatment improvements ranged from 2 to 20 percent. At approximately 13 to 14 percent stall airflow improvement on stage two, stage one was able to operate to its full stall airflow reduction capability of 20 percent over that of the baseline. Stage performance improvements due to casing treatment and the effects on overall compressor operability are presented in **Figure 3.46** for the 13 percent stage two casing treatment case. A summary of the casing treatment evaluation is presented in **Table 3.3**.

**Table 3.3 Tabulated Parametric Results Using DYNTECC**

CASE	% CHANGE OVERALL SA*	% CHANGE STG 1 SA*	% CHANGE STG 2 SA*	STALL STG
<b>CASING TREATMENTS</b>				
1) Stg 1 20%, Stg 2 0%	0.0	0.0	0.0	2
2) Stg 1 20%, Stg 2 2%	3.1	2.9	2.0	2
3) Stg 1 20%, Stg 2 5%	7.4	7.4	5.0	2
4) Stg 1 20%, Stg 2 10%	14.2	14.4	10.0	2
5) Stg1 20%, Stg 2 13%	18.7	18.9	13.0	2
6) Stg1 20%, Stg 2 15%	20.3	20.0	14.5	1
7) Stg 1 20%, Stg 2 20%	20.3	20.0	14.5	1

\* Note: SA -- Stalling Airflow Change

### **Conclusions – Casing Treatment to ADLARF**

- A properly calibrated dynamic compression system model such as **DYNTECC** can be used as a pre-test predictive analysis tool to guide and prepare for compressor rig tests.
- Casing treatment needs to be implemented over the critical stalling stage to be effective on overall operability.

- For the ADLARF fan, the second stage has been experimentally determined to be the critical stalling stage. Thus, for any casing treatment applied to the first rotor to be effective, the second stage stalling airflow will have to be enhanced by some mechanism such as casing treatment or variable vane repositioning.
- If casing treatment is used on the second stage of the ADLARF fan to enhance its stalling airflow capability, **DYNTECC** predicted that as much as 14% improvement in stall airflow capability will need to be realized to get a 20% increase in stalling airflow capability from stage one.

#### **ADDITIONAL REFERENCES**

**3.22** Prince, Jr, D. C., D. C. Wisler, and D. E. Hilvers. "A Study of Casing Treatment Stall Margin Improvement Phenomena." ASME 75-GT-60.

**3.23** Greitzer, E. M., J. P. Nikkanen, and D. E. Haddad. "A Fundamental Criterion for the Application of Rotor Casing Treatment." **ASME Journal of Fluids Engineering**, 101 (June 1979): 237-244.

**3.24** Takata, H. and Y. Tsukuda. "Stall Margin Improvement by Casing Treatment - its Mechanism and Effectiveness." ASME 75-GT-13.

**3.25** Fujita, H. and H. Takata. "A Study on Configurations of Casing Treatment for Axial Flow Compressors." **Bulletin of JSME**, 27 (August 1984):1675-1681.

**3.26** Ostdiek, F. R., W. W. Copenhaver, and D. C. Rabe. "Compressor Performance Tests in the Compressor Research Facility." AGARD Conference on Unsteady Aerodynamic Phenomena in Turbomachines, Proceedings No. 468, Aug. 1989.

**3.27** Hale, A. A. and M. W. Davis. "DYNamic Turbine Engine Compressor Code DYNTECC - Theory and Capabilities." Presented at the AIAA/ASME/SAE/ASEE Joint Propulsion Conference, AIAA-92-3190, July 1992.

**3.28** Boyer, K. M. and W. F. O'Brien. "Model Predictions for Improved Recoverability of a Multistage Axial-Flow Compressor." Presented at the AIAA/ASME/SAE/ASEE Joint Propulsion Conference, AIAA-89-2687, July 1989.

**3.29** Davis, M. W.. "Parametric Investigation into the Combined Effects of Pressure and Temperature Distortion on Compression System Stability." Presented at the AIAA/ASME/SAE/ASEE Joint Propulsion Conference, AIAA-91-1895, June 1991.

**3.30** Davis, M. W. and W. F. O'Brien. "Stage-by-Stage Post-stall Compression System Modeling Technique." **Journal of Propulsion and Power**, 7 (November-December 1991): 997-1005.

### 3.1.7 The Effect of Camber or Variable Vane Re-Positioning on System Operability

The flight envelope of aircraft gas turbine engines is affected by the operating range of the engine's compressor components. A compressor produces an increase in total pressure at a particular corrected airflow and speed. The operating range of a compressor is bounded on the high flow end by blade passage choking and on the low flow end by blade or endwall stalling. At the low flow end, blade stall can lead to system instability such as surge or rotating stall. These events are undesirable and are usually avoided by developing enough stall margin in the compressor design process. Stall margin is the measure of the operating range between the compressor operating point and the onset of system instability. However, there are times when the instability limit will be reached because of some destabilizing influence such as inlet pressure distortion. In these cases, it is possible to increase the available stall margin by some mechanical means such as variable vane re-scheduling.

#### **CITED EXAMPLE(S)**

**3.31** Davis, M. W., Jr., "A Stage-by-Stage Post-Stall Compression System Modeling Technique: Methodology, Validation, and Application", Ph.D. Dissertation, Virginia Polytechnic Institute and State University, December 1986

**3.32** Gorrell, S. E. and M. W. Davis, Jr., "Application of a Dynamic Compression System Model to a Low Aspect Ratio Fan: Casing Treatment and Distortion", AIAA Paper # AIAA-93-1871, Presented at the 29th Joint Propulsion Conference and Exhibit, Monterey, CA, June 1993.

#### **MODELING TECHNIQUE**

Since it may not always be feasible to test all configurations because of economic or hardware constraints, validated mathematical models can be used to fill in information not obtained during testing and may even be used to help design the experiment, if enough pre-test information is available. Two studies were performed: one having to do with recoverability and the other with the extension of the stability limit. Both studies were performed with the one-dimensional single-spool, dynamic simulation. The post-stall investigation was conducted with the earlier version known as **DYNMOD** while the stability limit investigation was conducted with **DYNTECC** [3.34] (Section 4.4).

#### **APPLICATION OF BLADE CAMBER – EFFECTS ON RECOVERABILITY**

Once a particular compression system is designed and built, the performance and stability behavior are fixed within certain limits. There are only a limited number of external changes that can be made to improve either performance or stability. If these changes cannot produce the desired result, certain internal or blade changes such as camber, stagger, tip clearance or tip casing treatment can be made which improve performance and stability. For this investigation, only the effect of re-setting the stagger or camber will be considered. The effect of camber was measured by Koch [3.38] and is represented in Figure 3.47. For an isolated blade row, more camber increase the peak lift coefficient. This translates to an increase in stage performance as illustrated in Figure 3.47. This change not only increases the pressure coefficient at stall but also increases the pressure characteristics all along the speed line, thus increasing the performance at all pre-stall operating conditions.

To determine the effect of such a change on system recovery, the three-stage compressor characteristics of the MIT/Gamache compressor [3.37] were modified in the following manner. The performance of first stage of the three-stage rig was increased by 25% as illustrated in **Figure 3.48**. Although experimental results indicate this type of change for the pre-stall characteristic only, it will be assumed that a similar effect occurs for the rotating stall region as well. Similar modifications for stage two and three were also made. With changes to the characteristics of less than 25% on only one or two stages, the compression system still exhibited the non-recoverable state during a post-stall event. However, with a 25% increase for all stages, the compression system exhibited continuous surge cycles of the "classic" type as illustrated in **Figure 3.49**.

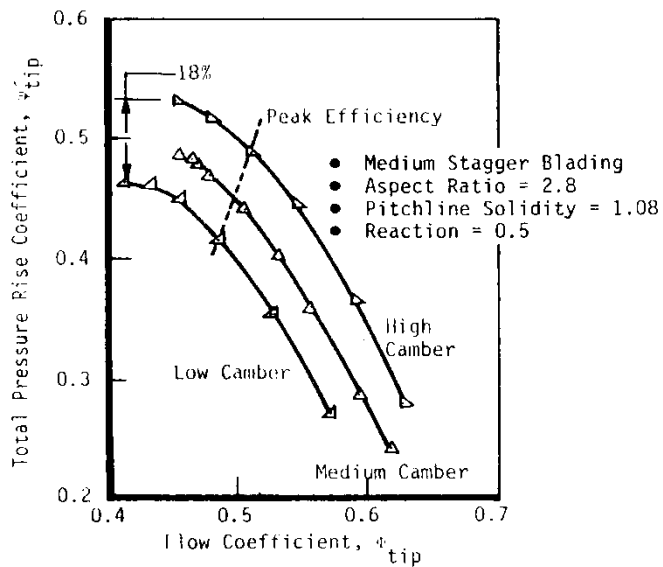


**Figure 3.47 Effect of Camber on Stage Performance**

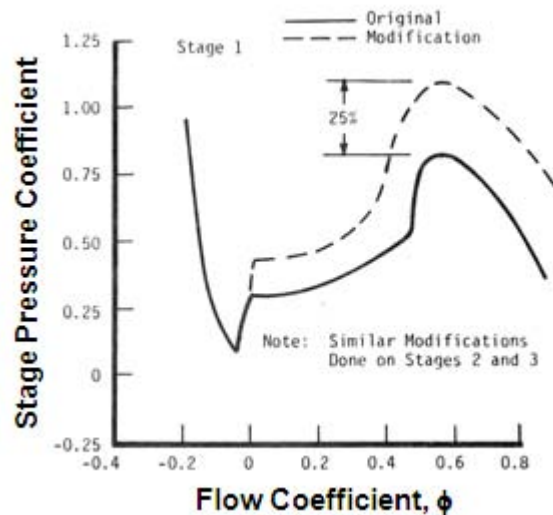


**Figure 3.48 Postulated Stage Pressure Characteristic Modification as a Result of Increasing Blade Camber**

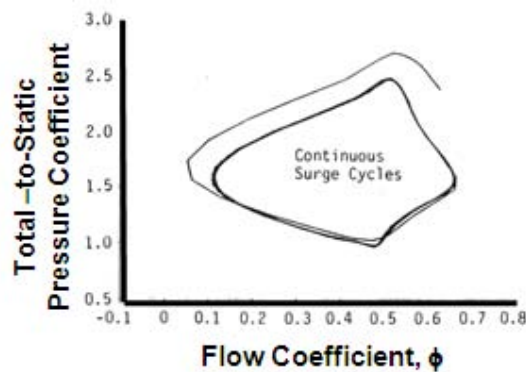
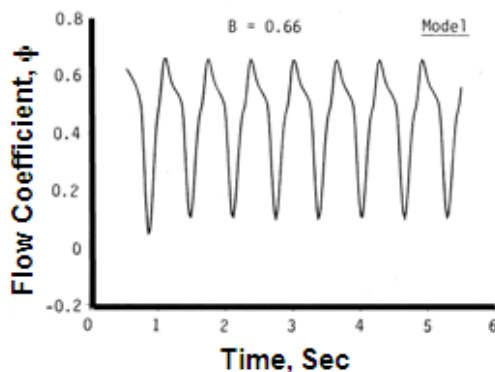


**Figure 3.49 Model Prediction of the Effect of Increasing Blade Camber on Post-Stall Behavior,  $B = 0.66$**

### APPLICATION OF VARIABLE VANE RESET -- EFFECT ON STABILITY LIMIT

The Compressor Research Facility (CRF) [3.33] at Wright-Patterson Air Force Base conducted a test entitled **Augmented Damping of Low Aspect Ratio Fans (ADLARF)**. The ADLARF fan (**Figure 3.50**) is a high speed, two stage, low aspect ratio fan with variable stator one which has been previously tested in the CRF. During this previous test inlet, interstage, and exit steady-state pressure and temperature measurements were acquired to fully document the stage and

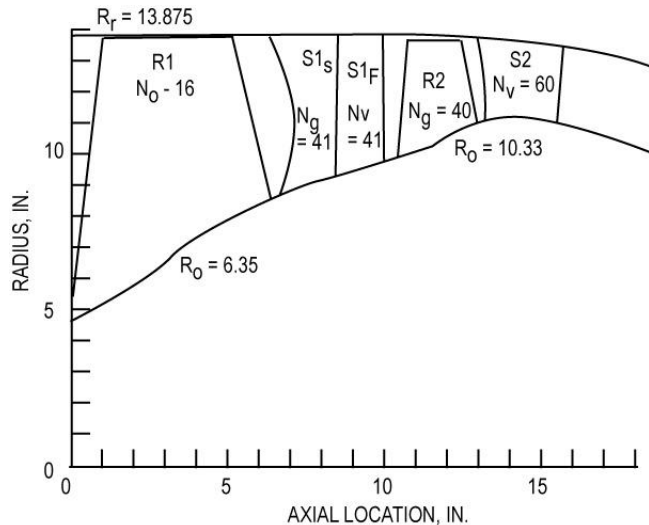


**Figure 3.50 Schematic of ADLARF Fan**

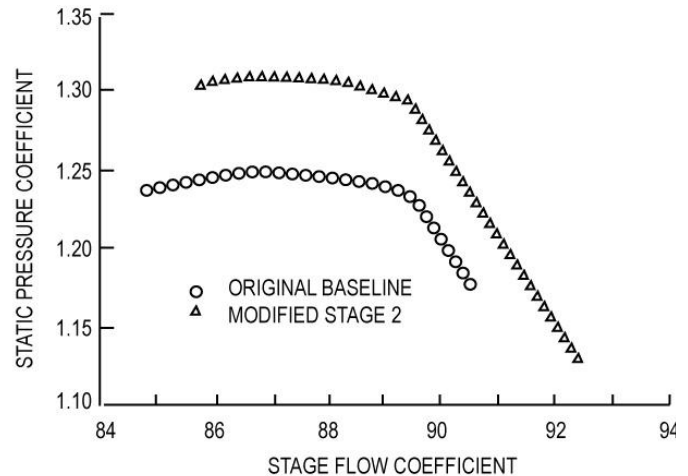


**Figure 3.51 Stage 2 Modification for Variable Vane Re-Positioning**

overall aerodynamic performance of the compressor.

During the initial test of the ADLARF fan, it was determined that the second stage initiated stall for a wide variety of speeds, including the ones of interest for this study. The original ADLARF fan was configured with stage one casing treatment of circumferential grooves. Thus, the baseline for comparison and the calibration was done for the ADLARF fan as tested with circumferential grooves.

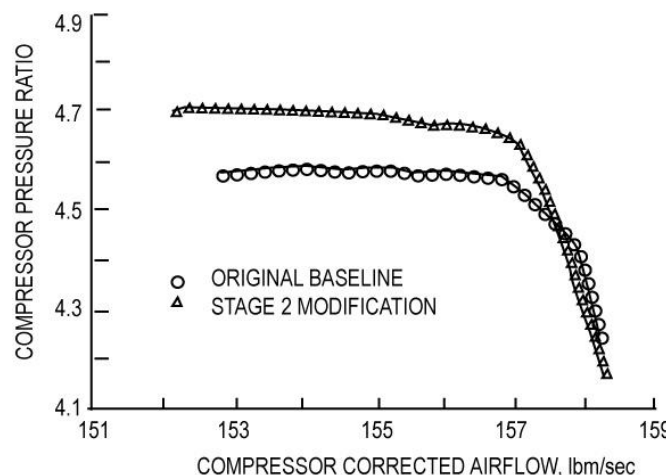


**Figure 3.52 Effects of Variable Vane Re-**

Another available mechanism to improve stage two stall airflow capability would be to unload the stage by changing stage one stator vane position. The ADLARF fan has a variable stage one stator capability and can be cambered more open or more closed. To unload the second stage, the first stage variable vane would need to be more open. Using ADLARF overall compression system performance with a stator vane repositioning of two degrees as a guide, stage two pressure characteristic was modified as presented in **Figure 3.51**. This modification was based on the

effects on stage characteristic as discussed by McCoy and Brown in **Refs. 3.35** and **3.36**, respectively. The effect on overall compression system performance is presented in **Figure 3.52**. The change in overall performance was similar to that observed during the previous test of the ADLARF fan and provides an increase of 0.5% in stall airflow reduction capability.

#### **ADDITIONAL REFERENCES**

**3.33** Ostdiek, F. R., W. W. Copenhaver, and D. C. Rabe. "Compressor Performance Tests in the Compressor Research Facility." AGARD Conference on Unsteady Aerodynamic Phenomena in Turbomachines, Proceedings No. 468, Aug. 1989.

**3.34** Hale, A. A. and M. W. Davis. "DYNamic Turbine Engine Compressor Code DYNTECC - Theory and Capabilities." Presented at the AIAA/ASME/SAE/ASEE Joint Propulsion Conference, AIAA-92-3190, July 1992.

**3.35** McCoy, A. W., and Hooper, A. V., "Blade Adjustment in Axial-Flow Compressor Stages", **Journal of the Aeronautical Sciences**, Vol. 20, 1953, pp. 43-48.

**3.36** Brown, L. E., "The Use of Experimental Interstage Data for Matching the Performance of Axial Compressor Stages Having Variable Setting Angle Blade Rows", ASME Paper No. 76-GT-42, New Orleans, March 1976.

**3.37** Gamache, R. N., "Axial Compressor Reversed Flow Performance." Ph.D. Dissertation, Massachusetts Inst. of Technology, May 1985.

**3.38** Koch, C. C., "Stalling Pressure Rise Capability of Axial Flow Compressor Stages", ASM Paper No. 81-GT-3, Presented at the International Gas Turbine Conference, Houston, Texas, March, 1981.

### 3.1.8 Compression System Component Behavior During Oscillating Flow

Compression system inlets have experienced oscillating pressure excursions or planar waves attributable to both inlet- and externally-generated disturbances included desperation, shock/boundary-layer interaction with adjacent inlet/engines, instability during subsonic flight at low mass flow rate, and supersonic inlet response to control system inputs. Externally generated disturbances include vortex ingestion and ingestion of wakes from nose gear and/or bomb bay doors. These planar waves are one-dimensional in nature and are characterized by oscillating total pressure excursions at the inlet face.

#### CITED EXAMPLE(S)

**3.39** Davis, M. W., Jr., "A Stage-by-Stage Dual-Spool Compression System Modeling Technique", ASME Paper #82-GT-189, March 1982, Presented at the 1982 IGTI Conference, London, England.

**3.40** Davis, Milton W., Jr., "A Stage-by-Stage Compressor Modeling Technique for Single-and Dual-Spool Compression Systems", Master's Thesis, University of Tennessee, Knoxville, Tennessee, August 1981.

**3.41** Davis, M. W., Jr., "Parametric Investigation into the Combined Effects of Pressure and Temperature Distortion on Compression System Stability", AIAA Paper # AIAA-91-1895, Presented at the 27th Joint Propulsion Conference, Sacramento, CA, June 1991.

#### MODELING TECHNIQUE

The **single and dual-spool one-dimensional dynamic models** ([Sections 4.4.1](#) and [4.4.2](#)) were used for this investigation. The single spool system was configured for a 10-stage HPC compressor as shown in [Figure 3.53](#) and the dual-spool was configured to a typical mixed flow turbofan compression system as illustrated in [Figure 3.54](#).

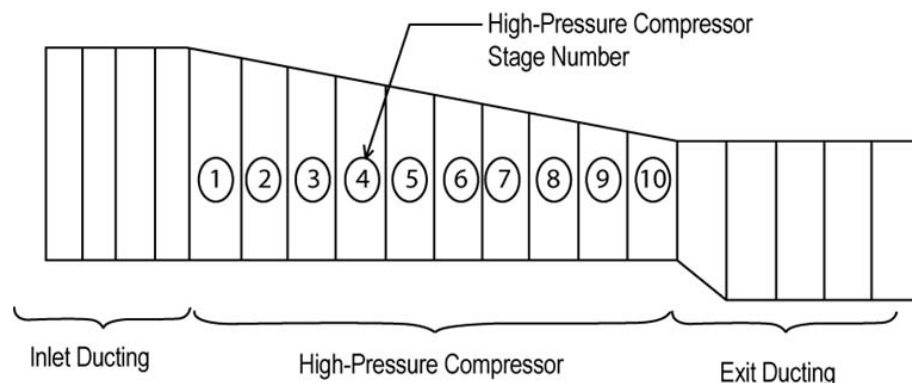


**Figure 3.53 Schematic of the Single-Spool, Ten-Stage Compression System Modeled**

To determine the effects of oscillating inflow on compression system stability, the model was subjected to sinusoidal total pressure variations. The dual-spool model was initially set at 105 percent fan speed near the compression system nominal operating point. For inflow effects, the inlet total pressure was varied sinusoidal with linearly increasing amplitude until system



instability occurred. For outflow effect, the exit static pressure was varied sinusoidal with linearly increasing amplitude until system instability occurred.

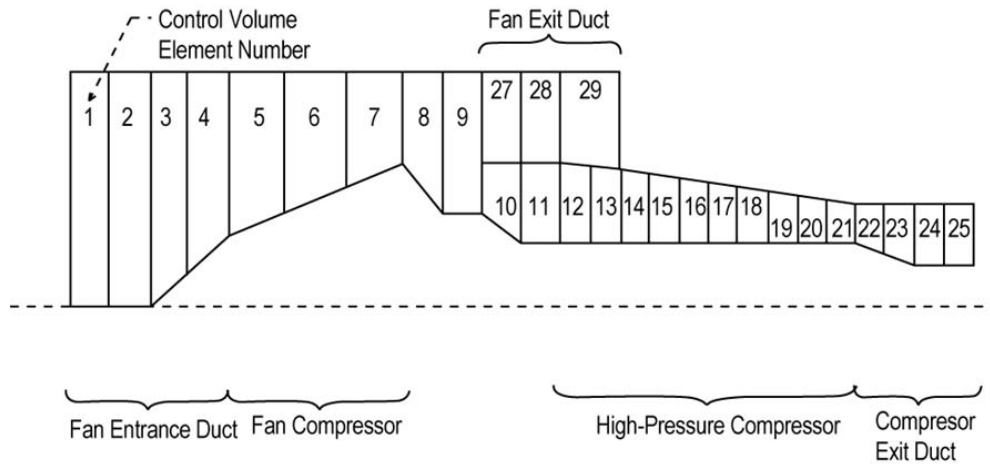


**Figure 3.54 Schematic of the Mixed Flow Turbofan Compression System Modeled**

#### OSCILLATING INFLOW EFFECTS ON SINGLE SPOOL COMPRESSION SYSTEM STABILITY

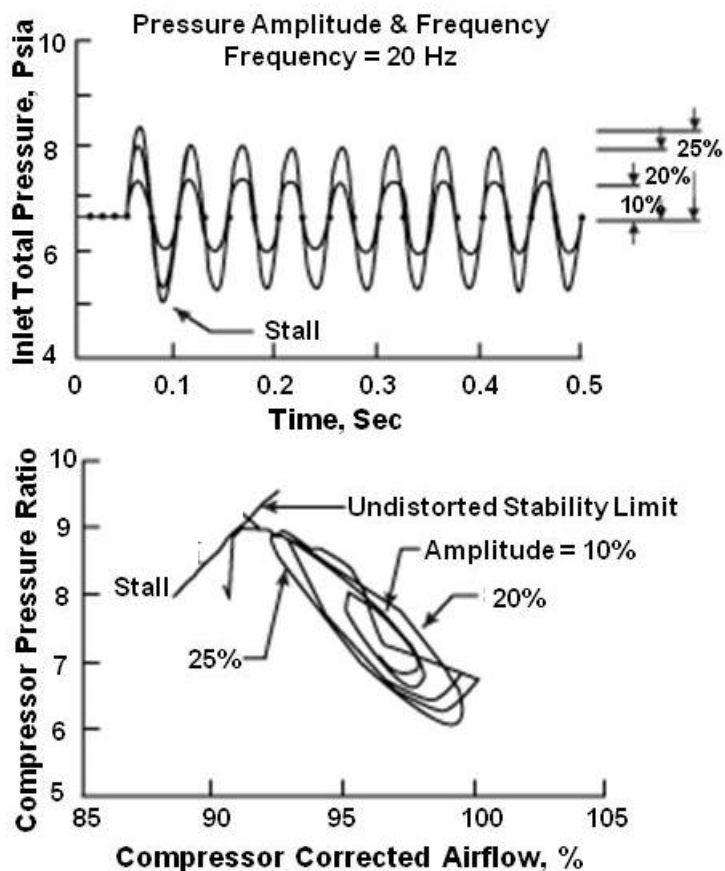


**Figure 3.55 Model Predicted with Full-Face Oscillatory Inlet Total Pressure, Speed = 98%**

Periodic pressure excursions such as sine wave cause the compression system to oscillate about some average operating point. This system behavior is depicted in [Figure 3.55](#). The inlet total pressure was set to oscillate at a frequency of 20 HZ and initial amplitude of 10 percent of the nominal pressure level. At this amplitude, compression system operation was stable but transient. Increasing the amplitude to 20 percent still gave stable operation but a larger orbit of the transient. However, when the amplitude was increased to 25 percent, the system experienced unstable flow. When viewed on the traditional compression system map, the transient appeared to transverse the steady-state stability limit. Analysis of the static pressure signature at time of system instability indicates that the 7<sup>th</sup>



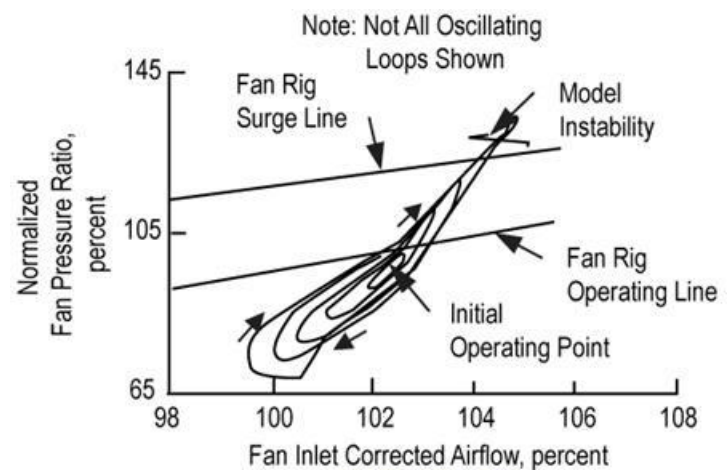
stage was the critical stage triggering the system instability.

This investigation was conducted at only one frequency to illustrate a point. It has been noted by Reynolds that as the frequency increases, the sensitivity to this type of destabilizing event decreases [3.42]. At higher frequencies, the same amount of overshoot of the stability limit as experienced at 20 Hz may not cause a system instability. There seems to be a critical amount of time that the oscillation must be present at a high enough amplitude at the critical stage before a system instability takes place.

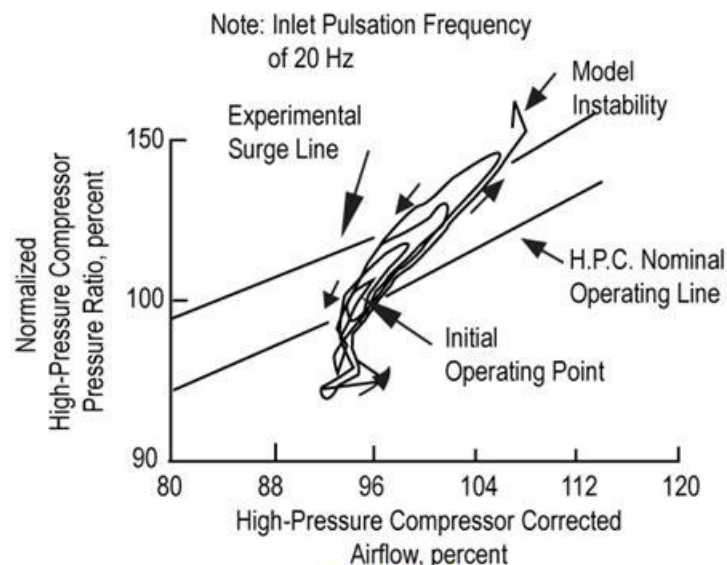
### **OSCILLATING INFLOW EFFECTS ON DUAL SPOOL COMPRESSION SYSTEM STABILITY**

Since with oscillating inflow the system does not operate along constant corrected speedlines, a typical trace of compression system behavior is presented in **Figure 3.56**. With linearly increasing total pressure fluctuations, the fan and the high-pressure compressor loop around the initial operating points. The fan and the high-pressure compressor can traverse their surge lines without surge occurring if the period of time in which they are above those limits are short enough. Once the time above the surge line becomes of a sufficient length, some stage or group of stages within the compression system will be in aerodynamic stall long enough to initiate compression system instability. Model predictions of the thirteen stage compression system stability limits during planar oscillating inflow are presented in **Figure 3.57**.

The amplitude required for instability decreased up to a frequency of 100 Hz, slightly increased to a frequency of 200 Hz, and began to decrease again to a frequency of 300 Hz. At the lower frequencies (20 and 50 Hz), the model predicted that the first stage of the fan component initiated system instability. At a frequency of 100 Hz, the critical stage moved to the third stage of the high-pressure compressor. As the frequency



**a. Fan Map**



**b. HPC Map**

**Figure 3.56 Typical Model Predicted Oscillatory Inflow Effects on Compression System Operation**

increases above 150 Hz, the amplitude attenuation across the forward stages increases and protects the aft stages, allowing a stage further forward to become critical. For comparison purposes other model studies and two experimental investigations were examined for stability trends during planar pulsations. Stability trends from model studies with a 593 analog compressor simulation by Goethert [3.44] and NACA-8 digital simulation by Kimzey [3.43] are presented in Figure 3.58. These studies were obtained with each model initially set at some operating condition on which linearly increasing sinusoidal inlet total pressure fluctuations were imposed (same as the dual-spool procedure). These studies indicate that at low frequencies the compression system can adjust to the fluctuations quickly enough, and thus it takes large amplitudes to produce system instability. As frequency increases, the amplitude required for instability decreases because phase lag and amplitude attenuations across the stages increase, thus increasing some stage or group of stages flow oscillations.

For multistage compression systems a local increase in the required pressure fluctuations for instability may occur because a different stage becomes the critical stage causing system instability. At high frequencies some stage or group of stages may act as a low-pass filter and

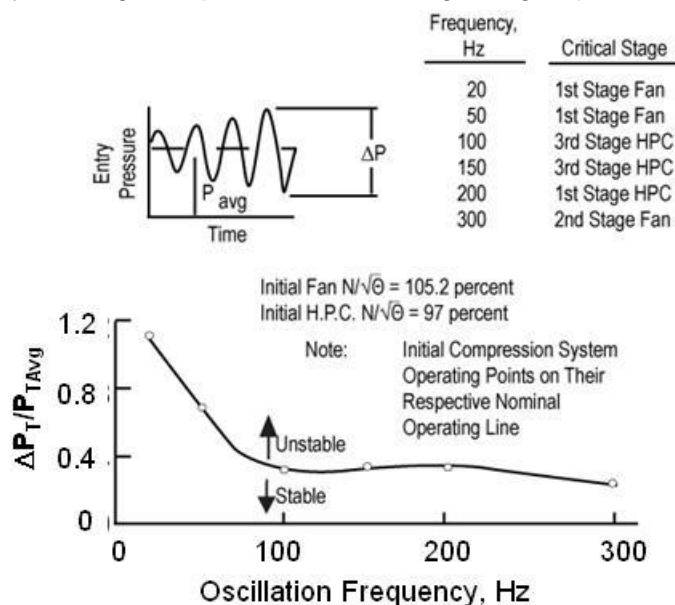


**Figure 3.57 Model Predicted Stability Limits for Planar Oscillating Inflow**

set and nominal pulsation amplitude was applied. If surge did not occur, the pulsation amplitude was increased. The investigation concluded that at low frequencies, the compression system outlet pressure will follow the inlet pressure in both phase and amplitude so that overall pressure ratio remains the same. As frequency increases the outlet pressure lags the inlet pressure in phase and amplitude requiring a smaller pulsation amplitude to cause instability.

For low frequencies the J93, NACA-8, and 13-stage dual-spool model agree in trend with experimental results. Another experimental investigation was conducted by Reynolds [3.45] to determine the sensitivity of a two-stage fan to pressure oscillations. That investigation was conducted differently than the previous investigation and model studies. Using a pulse generator, constant amplitude pulsations at a set frequency were applied to the fan inlet. If surge did not occur, the fan was back-pressured, increasing pressure ratio and decreasing corrected flow while holding corrected speed constant to a new operating point. The same or

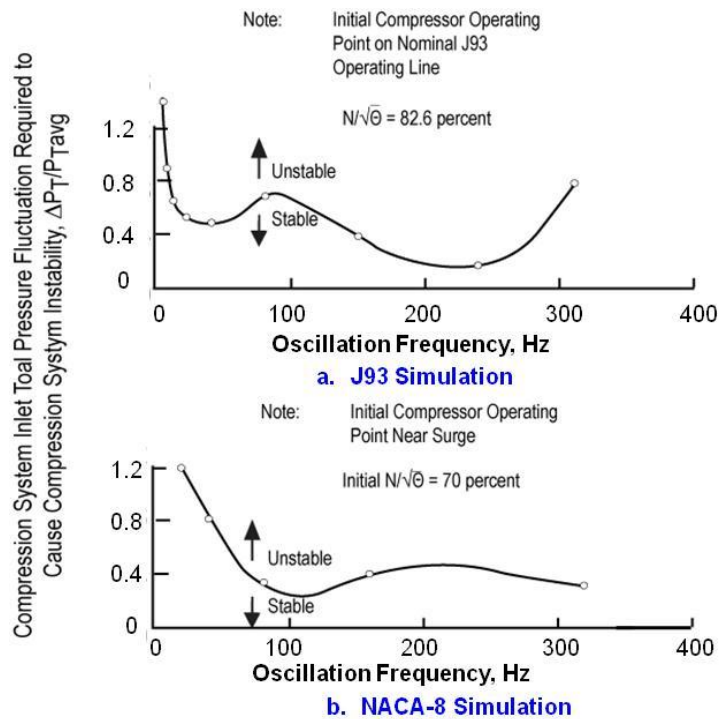


**Figure 3.58 Prediction of Compression System Stability Limit Trends for Planar Oscillating Inflow**

nearly same amplitude pulsations were applied to determine the fan stability limit. This procedure was repeated until the fan surged. Although the procedure differs from the model studies, the experimental results suggest that there is a cutoff frequency beyond which pulsations no longer affects the system stability limit. This is consistent with the J93 model study, which suggests that at high frequencies, the compression system becomes less sensitive to pressure pulsations unless the magnitude of the amplitude is greatly increased. The dual-spool model and the NACA-8 simulation were not run at high frequencies where this phenomenon occurs because of model frequency limitations.

#### **ADDITIONAL REFERENCES**

- 3.42** Reynolds, G. G., W. F. Vier, and T. P. Collins. "An Experimental Evaluation of Unsteady Flow Effects on an Axial Compressor - P3 Generator Program." AFAPL-TR-73-43, July 1973.
- 3.43** Kimzey, W. F. "An Analysis of the Influence of Some External Disturbances on the Aerodynamic Stability of Turbine Engine Axial Flow Fans and Compressors," Arnold Engineering Development Center-TR-77-80 (AD-A043543), Arnold Air Force Station, Tennessee, August 1977.
- 3.44** Goethert, B. H., "Research and Engineering Studies and Analysis of Fan Engine Stall, Dynamic Interaction with Other Subsystems and System Performance," Air Force Aero Propulsion Laboratory TR-70-51, Wright-Patterson AFB, Ohio, July 1970.
- 3.45** Reynolds, G. G., Vier, W. F., and Collins, T. P., "An Experimental Evaluation of Unsteady Flow Effects on an Axial Compressor - P3 Generator Program," Air Force Aero Propulsion Laboratory - TR-73- 43, Wright-Patterson AFR, Ohio, July 1973.

### 3.1.9 Compression System Behavior During Hot Gas Ingestion

Inlet temperature ramps caused by the ingestion of hot gases from weapons firings or steam ingestion during catapult-assisted launches can cause compression system instabilities. Increasing inlet temperature ramps cause the corrected rotor speed to decrease with a corresponding reduction in corrected airflow. If the change occurs slowly, compression system airflow and pressure ratio will shift along the nominal operating line. However, if the change is rapid, system pressure ratio will lag the change in airflow and cause compression system instability. Experimental evidence suggests that ram rates from 2,000 to 10,000 degrees/sec (Rankin or Fahrenheit) are typical during weapons system gas ingestion. If the process is viewed in terms of the compression system map, it appears that the system operating line moves toward the instability limit.

#### **CITED EXAMPLE(S)**

**3.46** Davis, M. W., Jr., "A Stage-by-Stage Dual-Spool Compression System Modeling Technique", ASME Paper #82-GT-189, March 1982, Presented at the 1982 IGTI Conference, London, England.

**3.47** Davis, Milton W., Jr., "A Stage-by-Stage Compressor Modeling Technique for Single-and Dual-Spool Compression Systems", Master's Thesis, University of Tennessee, Knoxville, Tennessee, August 1981.

**3.48** Davis, M. W., Jr., "Parametric Investigation into the Combined Effects of Pressure and Temperature Distortion on Compression System Stability", AIAA Paper # AIAA-91-1895, Presented at the 27th Joint Propulsion Conference, Sacramento, CA, June 1991.

**3.49** Abdel-Fattah, A. M., "Response of a Turbofan Engine Compression System to Disturbed Inlet Conditions" **Journal of Turbomachinery**, Vol. 119, No. 4, October 1997.

#### **MODELING TECHNIQUE**

Investigations were conducted with both the single and the dual-spool one-dimensional system. Both are reproduced here for completeness.

The **single-spool one-dimensional dynamic model** ([Section 4.4.1](#)) was configured to a 10-stage high pressure compressor of a current turbofan engine as illustrated in [Figure 3.59](#). To

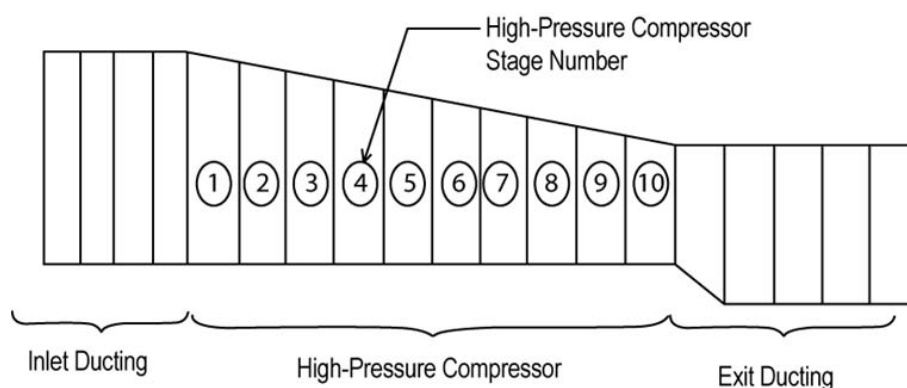


**Figure 3.59 Schematic of the Single-Spool, Ten-Stage Compression System Modeled**

simulate hot gas ingestion, the model was subjected to rapid inlet temperature ramps ranging from 1110 to 5550°K/sec (2,000 to 10,000R/sec), while operating at 98% fan speed near its nominal operating point at sea-level static, standard-day conditions. The system inlet temperature was increased linearly at a particular rate until compression system instability had occurred.

The **dual-spool one-dimensional dynamic model** ([Section 4.4.2](#)) was configured to a typical mixed flow turbofan compression system as illustrated in [Figure 3.60](#). A similar procedure was used but the fan speed was held at 105% speed.

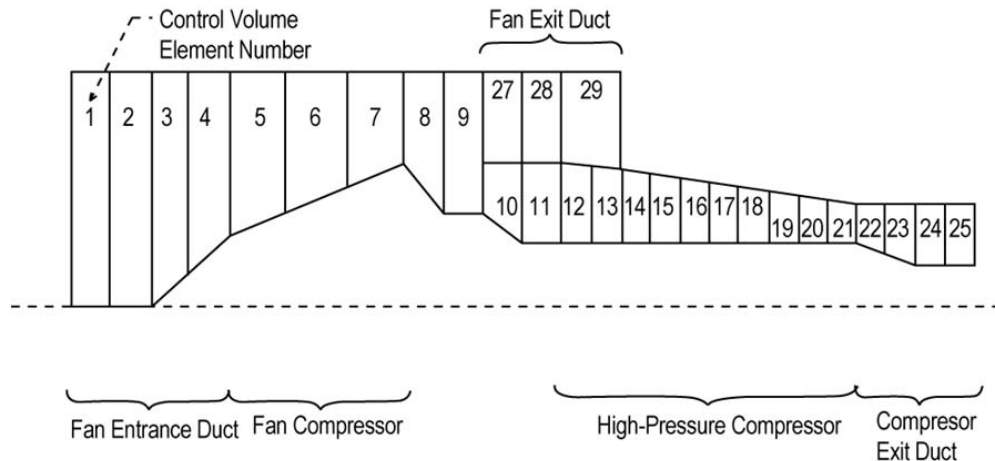


**Figure 3.60 Schematic of the Mixed Flow Turbofan Compression System Modeled**

#### **RAPID TEMPERATURE RAMP RATE EFFECTS ON SINGLE-SPOOL COMPRESSION SYSTEM STABILITY**

The above phenomenon for full face inlet temperature ramps is illustrated in [Figure 3.61](#). The model was initially configured for a speed of 98 percent and airflow on the nominal operating line. A temperature ramp 3,500 degrees/sec was imposed upon the inlet. The temperature ramp was allowed to continue until system instability incurred. Instead of holding the exit static pressure constant, exit Mach Number was held constant, simulating the effect of a choke point in a turbine engine downstream of the compression system. The inlet temperature increase at this ramp rate at the time of instability was 80° R. This magnitude is consistent with experimental result presented in [Ref. 3.50](#).

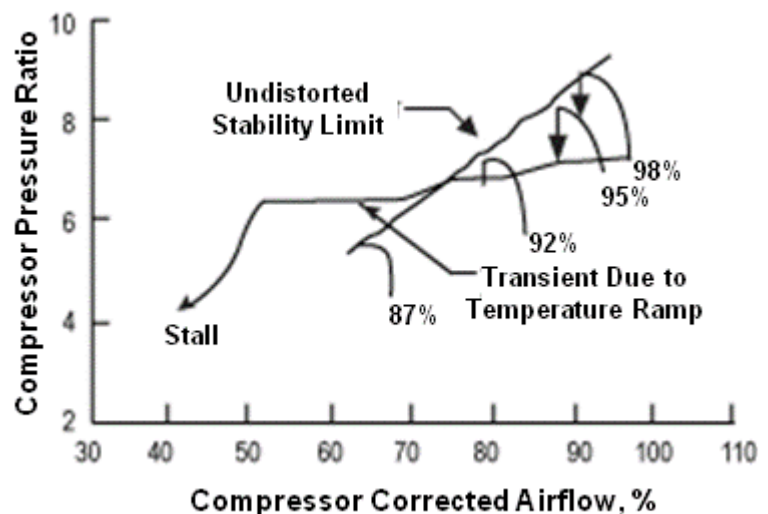


**Figure 3.61 Model Predicted with Full-Face Inlet Temperature Ramp – Initial Speed = 98%**



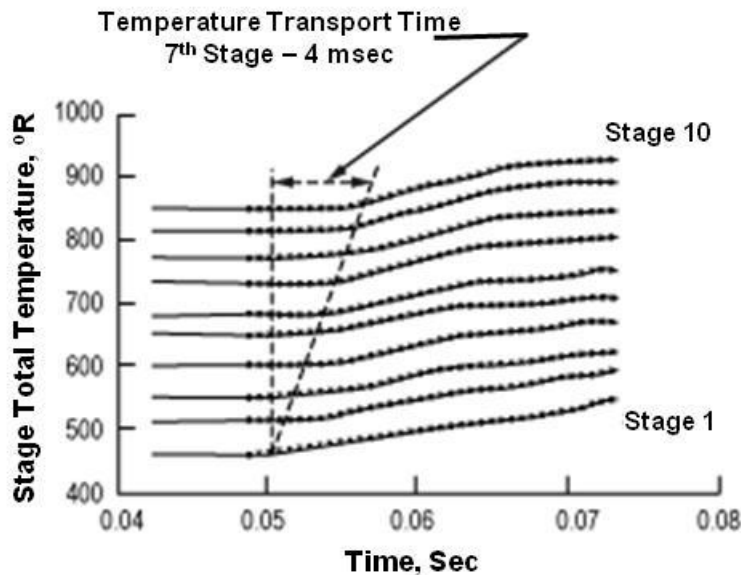


**Figure 3.62 Temperature Ramp Convected Downstream with Velocity Field**

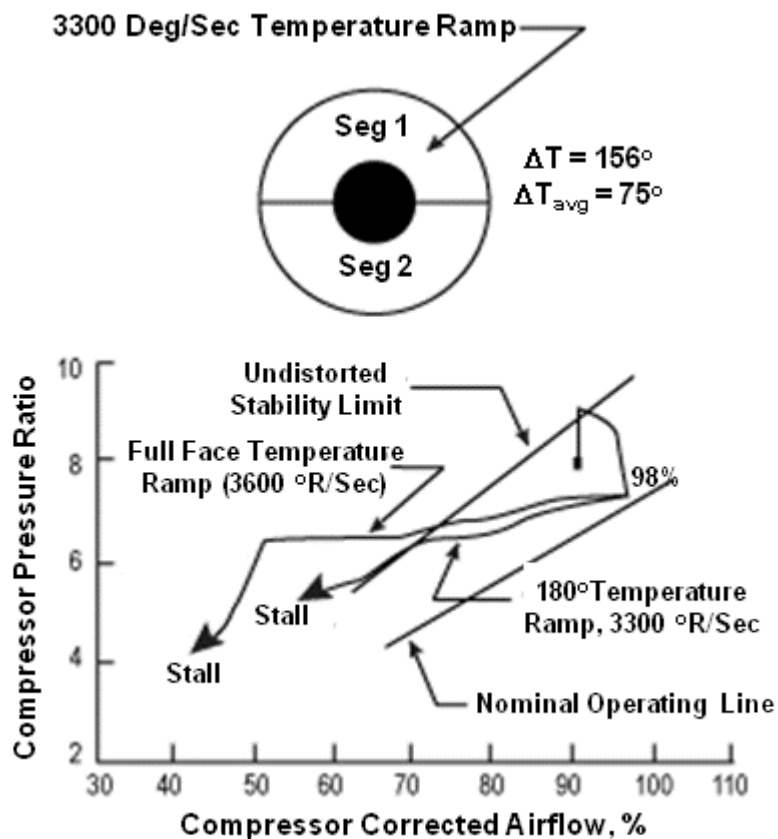


**Figure 3.63 Model Prediction with 180° Segment Temperature Ramp – Initial Speed = 98%**

The explanation that the operating line moves toward or even overshoots the stability limit is a little simplistic. Since the temperature increase is convected downstream by the flowfield, the effect of that increase is not felt instantaneously but lags the inlet by the convection time. This lag is illustrated in [Figure 3.62](#). When the static pressure signature was analyzed, the 7<sup>th</sup> stage was diagnosed to be the state initiating system instability. Higher rates were imposed upon the inlet and produced the expected results (i.e., higher delta temperatures at time of instability for higher rates). A much slower rate allowed the compression system to readjust and decrease in speed along a stable operating line.

Presented in [Figure 3.63](#) is the results of an inlet temperature ram of 3,300 degrees/sec on only one half of the compressor face (i.e., 180-deg segment, Segment 1). When the process is viewed on a compression system map, it has a trajectory similar to the full face temperature ramp. However, the distorted temperature increase was nearly double that observed with the full face ramp. Analysis of the static pressure signature at time of instability indicates that the 7<sup>th</sup> stage of the distorted segment (Segment 1) initiated the instability.

## RAPID TEMPERATURE RAMP RATE EFFECTS ON DUAL-SPOOL COMPRESSION SYSTEM STABILITY

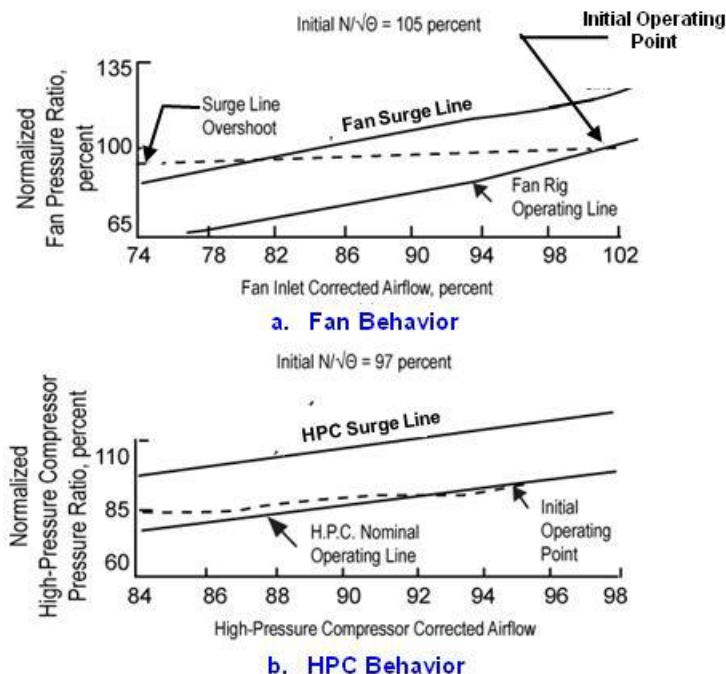


**Figure 3.64 Model Predicted Effects of Rapid Inlet Temperature Ramps on Compression System Behavior**

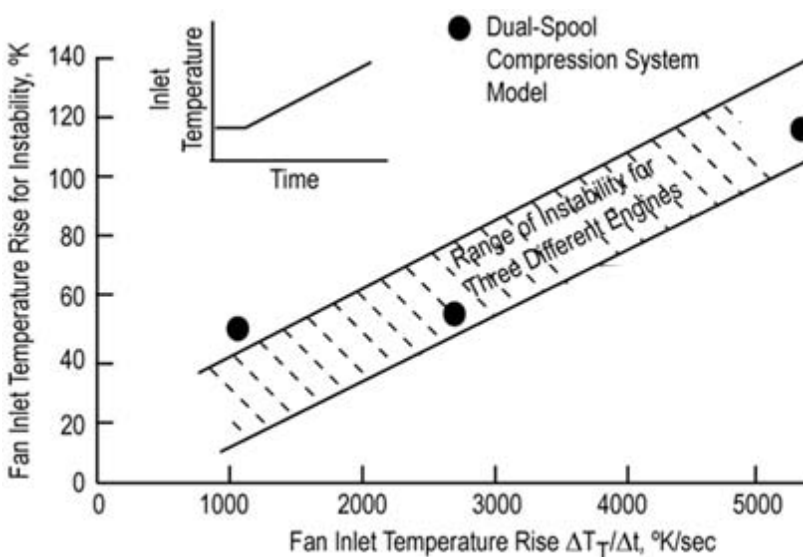


**Figure 3.65 Model Predicted Stability Limits for Inlet Temperature Ramps**

System behavior during a typical temperature transient is indicated in [Figure 3.64](#). Fan corrected airflow and speed decrease because of the increase in inlet temperature. Because of the rapid change in inlet temperature, an engine control would not be able to react, and system transient behavior similar to the model's behavior would be evident. Pressure ratio does not have time to react to the change, but an imbalance in forces among the stages is present. The overshoot of the fan stability limit indicates the front-to-rear airflow mismatch causing system instability. As the front of the fan moves toward the stability limit at a near constant pressure ratio, the high-pressure compressor does not experience as much a temperature change and thus operates at a corrected flow corresponding to stable conditions [Figure 3.64b](#)). Model prediction of the thirteen-stage compression system stability limit (temperature rise for instability) and comparison to experimental results is presented in [Figure 3.65](#). The stability limit established at three temperature ramp rates falls within or above the range of the experimental data, which consists of full face and partial face temperature ramps on three different



compression systems [3.50]. Analysis of the static pressure behavior at time of system instability reveals that the first or second stage of the fan is the stage initiating compression system instability. This is consistent with experimental results which indicate that the front of the compression system can no longer sustain its flow during the transient.

#### RAPID TEMPERATURE RAMP RATE EFFECTS ON THE TF-30 COMPRESSION SYSTEM STABILITY

**DYNTECC** was configured and applied to the geometry of the TF30 compression system as illustrated in [Figure 3.66](#), for an investigation into the effects of temperature ramps on system stability. The TF30 compression system has dual-spool rotors, but with three compressors: fan, low-pressure and high-pressure compressors.

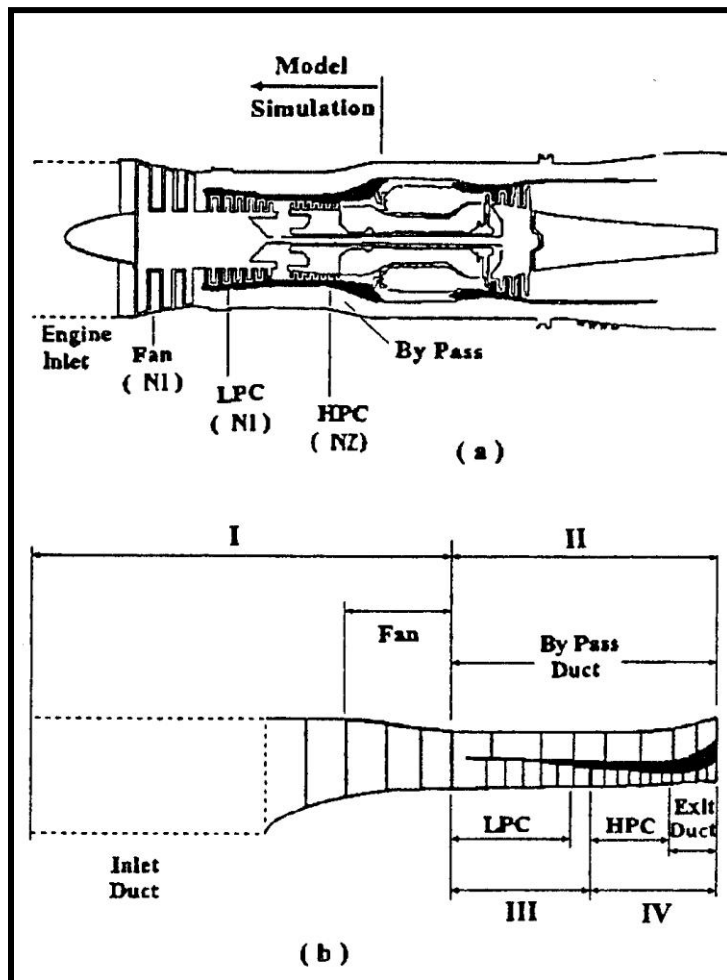
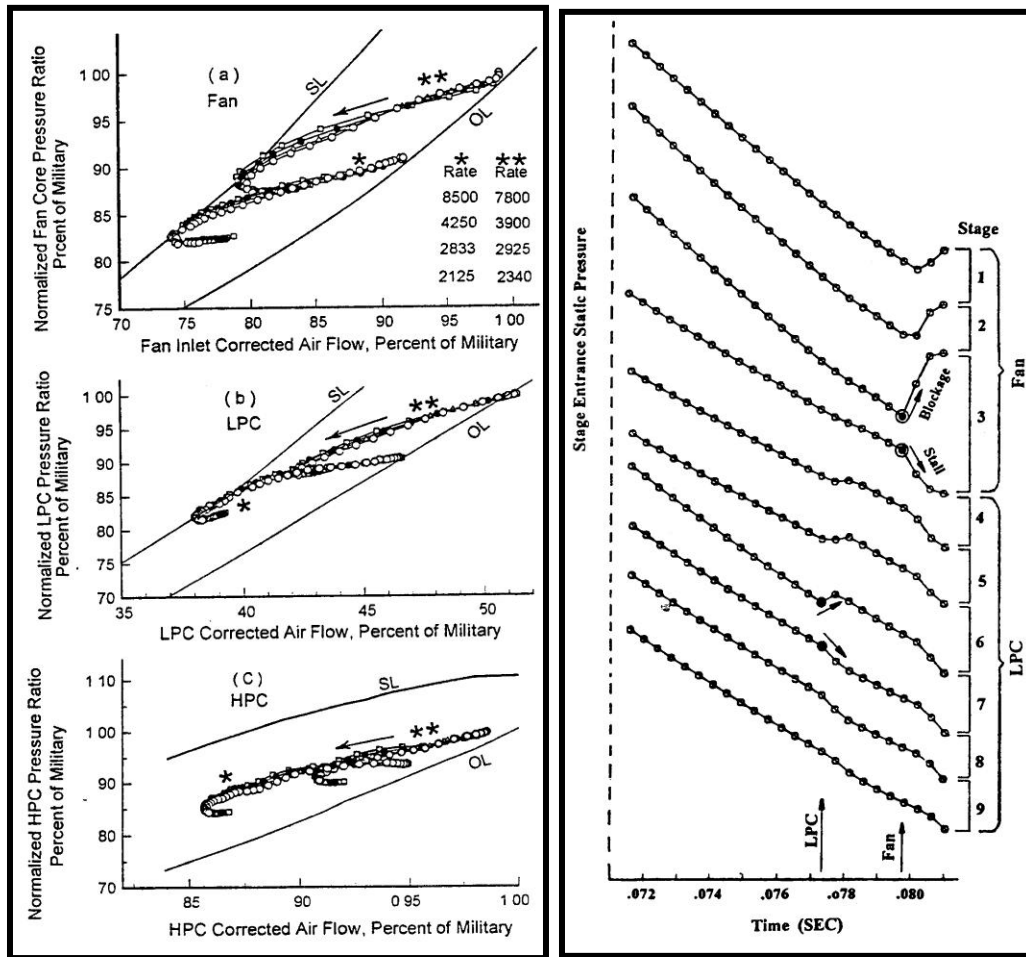


**Figure 3.66 Schematic of TF30 Compression System Modeled**

Using the **DYNTECC** stage-by-stage compression system simulation, the following observations were made with regard to the TF30 gas ingestion investigation:

- The stability limit of the system in response to inlet temperature ramps improved with increasing low rotor speed;
- The stability limit, in terms of temperature rise required to surge the compressor, was found to be independent of the rise rate as illustrated in [Figure 3.67a](#).
- At the time of instability because of inlet temperature ramps, the **DYNTECC** model predicted the possibility of the third stage of the fan as the critical stage responsible for compression system surge initiation as illustrated in [Figure 3.67b](#).



a. Compressor Trajectories

b. Static Pressure Indicating Critical Stage

Figure 3.67 Schematic of TF30 Compression System Modeled

**ADDITIONAL REFERENCES**

**3.50** Distortion Induced Engine Instability, AGARD LS-72-1974.

### 3.1.10 Axi-Centrifugal Compression System Post-Stall Behavior

**Note that at the end of this analysis there is a clarification by Dr. Bill Cousins taken from his Ph.D dissertation. The clarification is on the critical stage which was noted several years after this work was initially published. Dr. Cousins comments are taken directly out of his dissertation with his permission. The authors of the T-55 document concur with Dr. Cousin's analysis**

The development of advanced turbine engine simulations is a critical component of the Army's Non-Recoverable Stall Program (Circa 1993). Extensive rig testing was conducted on a T55-L-712 turboshaft engine compressor at Lycoming acquiring the necessary data for these modeling efforts. Measurements were made which allow for generation of compressor stage characteristics as well as overall performance mapping

Lycoming's T55-L-712 ([Figure 3.68](#)) powers the U.S. Army CH-47 "Chinook" helicopter. This engine installation occasionally displays difficulty completing the start sequence ("hung start"). The U.S. Army Aviation Systems Command asked the Propulsion Directorate (now the Vehicle Propulsion Directorate, VPD, of the Army Research Laboratory) to undertake a program to study these "hung start" events. With the objective in mind to investigate stall phenomena, it was apparent that the extensive instrumentation required for this program provided a much broader test capability for dynamic/transient research than originally planned. The expanded program's goals were to:

- Perform a detailed study of compressor stall events in rig/engine environments,
- Develop advanced dynamic engine and compressor models,
- Validate those models,
- Identify instability precursors in rig and engine environments, and
- Identify methodologies to extend compressor stall margin by active stabilization.

The program's objective was to acquire and analyze this type data outside the laboratory, using production gas turbine hardware, and to address the applicability of this basic research to benefit both industry and government. The program utilizes a cooperative approach between government, industry, and academia to further technological development.

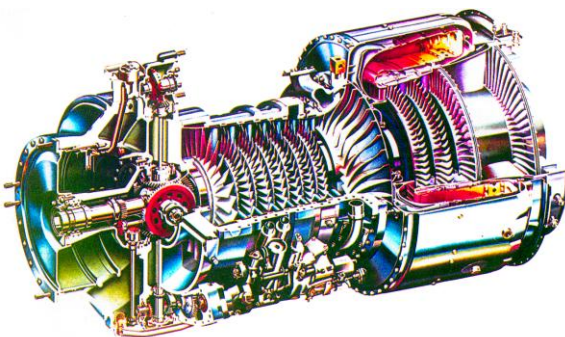


**Figure 3.68 T55-L-712 Turboshaft Engine**

As a part of this program, rig testing of the operational compression system configuration was conducted at Lycoming. Steady and unsteady data were acquired between 20 percent and 100 percent of design speed. These data were utilized in the development of the inputs to the dynamic model used in this preliminary study.

This section addresses the process involved in adapting and validating an existing state-of-the-art axi-centrifugal compression system model and the preliminary results from a study of compression system operation at a typical engine operating condition of 80 percent of design speed.

### CITED EXAMPLE(S)

**3.51** Owen, A. K., and M. W. Davis, Jr., "Modeling the Dynamic Behavior of an Axial-Centrifugal Compression System", AIAA Paper # AIAA-94-2802, Presented at the 30th AIAA Joint Propulsion Conference and Exhibit, Indianapolis, IN. June 1994.

**3.52** Cousins, W. T., "Characteristics of Stall and Surge Behavior in Axi-Centrifugal Compressors", Ph.D Dissertation, Virginia Polytechnic and State University, December 1997.

### MODELING TECHNIQUE

The **single-spool one-dimensional dynamic model** ([Section 4.4.1](#)) was configured to the T-55 axi-centrifugal compression system. The geometry inputs for the **DYNTECC** model were developed with the flowpath shown in [Figure 3.69](#) (a total of 39 control volumes). This geometry extends from the bellmouth to the throttle valve exit. The region upstream of the bellmouth is assumed to be open to atmosphere. The compressor first-stage face is at the inlet

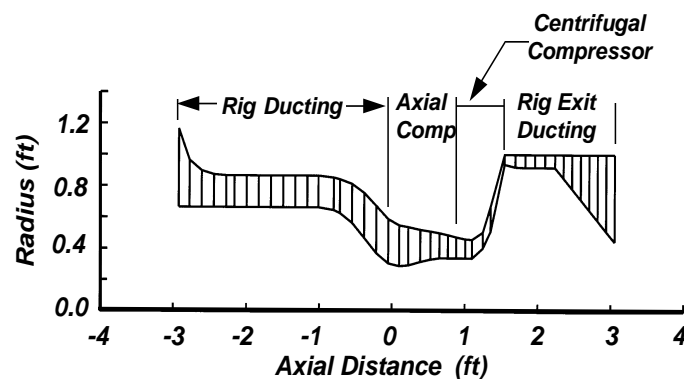


**Figure 3.69 T55 Model Geometry**

of volume 20, and the compressor exit is at volume 32. The control volumes downstream of volume 32 reflect the exhaust plenum area of the rig. Control volumes inside the compression system each contain a stator/rotor combination with the exception of volume 28, which is a duct, and the centrifugal compressor which encompasses control volumes 29 through 32.

Four control volumes were used to describe the centrifugal stage. This minimized the system control

### APPLICATION TO THE T-55 AXI-CENTRIFUGAL COMPRESSION SYSTEM

A set of compressor stage characteristics must be provided for closure of the governing equations within the **DYNTECC** model. Each of these stage characteristics consists of three distinct regions:

- the measured pre-stall characteristic,
- a region between stall onset and reverse flow, and
- a steep negatively sloped pressure coefficient in the reverse flow region.

The Lycoming rig test provided the pre-stall stage characteristics for the speed range tested. To study the post-stall operation of this compression system, the dynamic compression system model requires information on stage characteristic shape beyond the normal stall/surge line. These data, with the exception of speeds below 50 percent of design speed, were not available and were not acquired during the rig test. Therefore, estimates of the post-stall characteristics

were synthesized using insight gained from low-speed rig tests of Gamache [3.53] and recent test data acquired at the Compressor Research Facility on a ten-stage high-pressure/speed compressor rig by Copenhaver and Boyer [3.54, 3.55].

The T55 post-stall stage characteristics were estimated based on observations from other compression systems operating in post-stall conditions. Initially, the region between stall onset and reversed flow for the pressure characteristic was developed with an initial steep drop with a shallow or near flat pressure drop to the cutoff flow. This would not allow surge cycles to develop, which is the correct dynamic behavior at 80 percent speed. The region between stall onset and reversed flow was modified to remove any level or nearly level segment with an initial sharp drop-off at surge initiation followed by a gradual decrease in the pressure characteristic. Post-stall

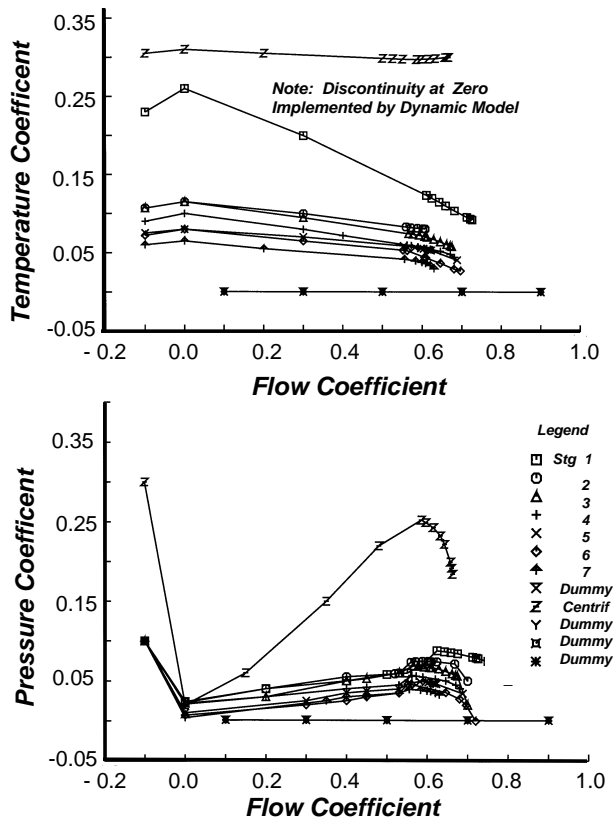


**Figure 3.70 Final Stage Characteristic at 80 Percent**

temperature characteristics were synthesized using the same slope as the pre-stall characteristics. The final characteristics for 80 percent of design speed are shown in **Figure 3.70**.

### **Model Validation**

Model validation involves the comparison of model predictions with those same results from the experimental data. For this investigation, results from **DYNTECC** are validated against the experimental results obtained from the Lycoming rig test. The validation consists of two parts: (1) determination of the critical stage initiating system instability and (2) post-stall operation, namely compression system surge.



## Determination of the Critical Stage

For several reasons, the correct identification of the stage initiating the instability (critical stage) is of great importance to the proper implementation and validation of the model. For example, accurate determination of the critical stage allows the dynamic model to be used for determination of strategies for system instability control (surge/stall control).

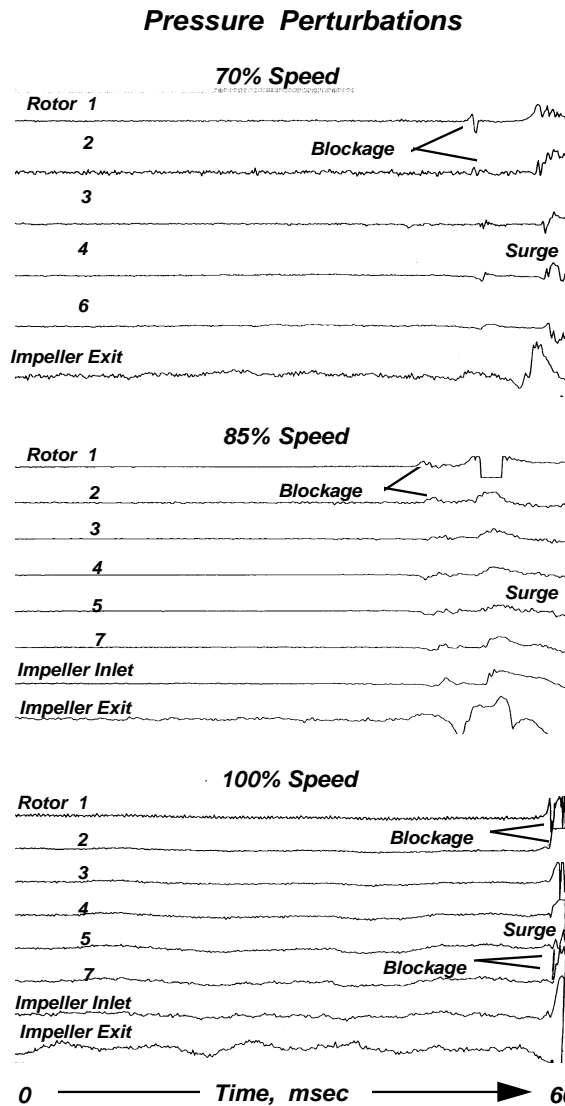


**Figure 3.71 Axial String of Transducers**

As the rotational speed of a multistage compressor increases, critical stage normally moves aft. Many observers believe surge begins as a circumferentially moving blockage in this "critical stage", manifesting itself as a pressure rise forward of the critical stage rotor and a pressure loss aft. Therefore, data from an axial string of pressure transducers ([Figure 3.71](#)) were analyzed to identify the critical stage by searching for this moving blockage at each rotational speed at which data were acquired.

Spatially, all sensors in this axial string were circumferentially within 25 deg. of each other except the impeller exit transducer. For the 70% of design speed case, the transducer was mounted roughly 180° circumferentially away from the other transducers. At other speeds, the transducer was mounted circumferentially 12° in the direction of rotor rotation away from the other transducers.

The surge phenomenon seems to change character as speed increases. At the lower speeds, up to 85 percent of design speed, the critical stage appears to be the first stage. Highlighted in [Figure 3.71](#) is a blockage for 70% and 85% of design speed, as indicated by a classic high/low pressure signature between the first and second stage measuring stations. Little evidence exists in the pressure traces at any location to indicate impending surge other than the blockage noted, which is apparent for at least one rotor revolution prior to surge.

From 90 to 100% speed, the nature of the surge event is less clear. These events show a low-frequency unsteadiness at the impeller exit. It is substantial, exists throughout the digitized data strip prior to surge, does not seem periodic, and is not clearly related to surge. This unsteadiness does appear to effect the upstream stages by causing stage re-matching and disguises the static pressure signature. Regardless of the view that the critical stage moves aft as rotor speed increases, the first indication, a rise in static pressure, of the developing surge at any speed appears to be the first stage. This is also apparent at our chosen speed of interest (80 percent of design) in [Figure 3.72](#).

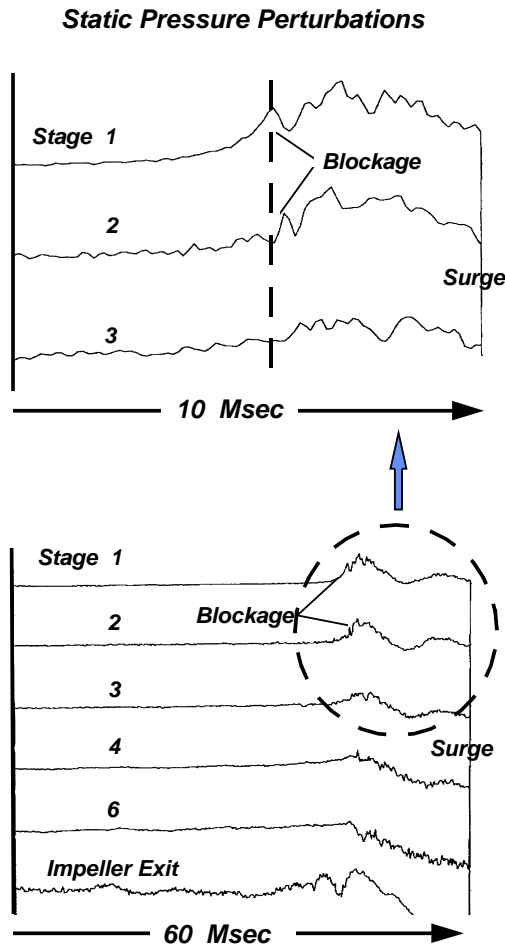


**Figure 3.72 Experimental Static Pressure Signature at Time of System Instability 80% Speed**

In viewing the whole event for many stages, it is difficult at best to determine the critical

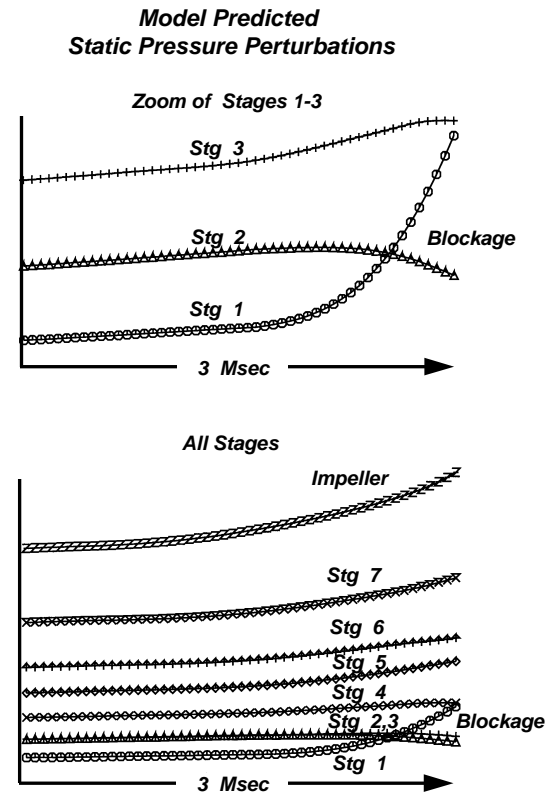


**Figure 3.73 Model Predicted Static Pressure Signature at Time of System Instability at 80% Speed**

stage. However, if one zooms in on a suspected region, the blockage effect of the critical stage is quite evident. Thus, for 80 percent speed, the critical stage is the first stage. Once this signature is established, it is transmitted downstream at acoustic plus fluid velocity.

To determine the critical stage from the **DYNTECC** model, a similar static pressure analysis at time of instability is performed. Results from that analysis are presented in **Figure 3.73**. As was seen experimentally (**Figure 3.72**), the same static pressure signature is present at time of instability, indicating the first stage is the stage initiating surge. As was true with the experimental results, viewing all stages can disguise the event. Zooming in on the suspected region provides a much clearer picture.



## Post-Stall Operation

**Figure 3.74** presents the overall compression system operation in deep surge. Operation is characterized by a relatively slow pressurization as result of throttle closure, followed by a rapid "blowdown" to the reversed flow region. The system then operates in reversed flow for a relatively short period while the pressure rise drops to near zero. The system recovers through a rapid reacceleration to positive flow followed by a relatively slow re-pressurization. The cycle then repeats with final recovery occurring when the throttle is returned to its original position

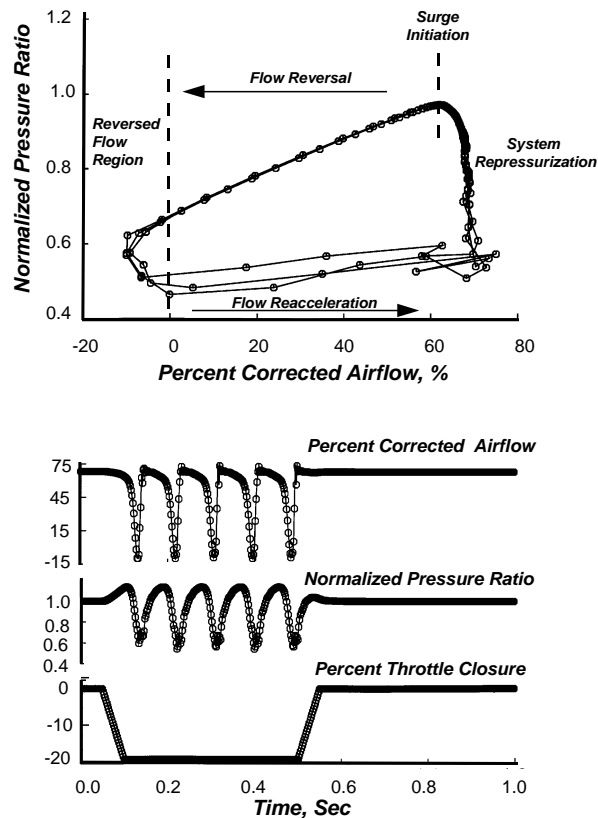


**Figure 3.74 System Response to a Throttle Closure at 80% Speed -- Deep Surge**

approximately 9.5 Hz is very near the measured frequency of about 8.5 Hz. Also apparent is the similarity between the predicted and measured shapes of the curves, for all stages. Clearly, the dynamic predictions closely model the shape of the actual pressure variations in the compressor.

There exists, however, a marked discrepancy in predicted and measured magnitudes of the pressures. Some of the discrepancy can be placed on the accuracy of the measurements. The predicted magnitudes may also be in error due to model limitations during the reverse flow operation of the cycle. Both of these questions need to be resolved.

**Figure 3.75** shows the predicted and measured static pressure traces for several of compressor stages vs time. Several features are apparent from these plots. One is the similarity in predicted and measured surge frequencies. The predicted frequency of

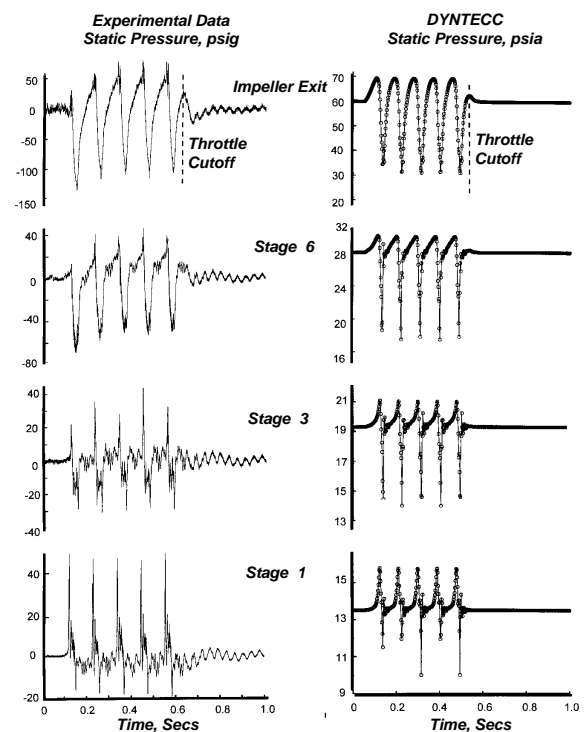


**Figure 3.75 Static Pressure Signature During Surge Cycles at 80% Speed**

## **CONCLUSIONS**

The following conclusions can be drawn from these results:

- The simulation technology developed within the **DYNTECC** code provides a tool for the analysis of axial-centrifugal compression system behavior both pre- and post-stall.
- The modeling of an axial/centrifugal compression system is similar to that for a typical axial compression system.
- Post-stall stage characteristics can be synthesized using observations for other systems with a high degree of confidence as long as there is some level of experimental data available for the system of interest.
- Post-stall stage characteristics must have a significant positive slope over most or all of the post-stall flow range to allow for the re-pressurization required for cyclical surge operation.
- The **DYNTECC** model produces surge cycles that are similar in frequency, static pressure signature to that observed experimentally and can predict the critical stage.

## **ADDITIONAL CLARIFICATION**

**Note that the following is a clarification by Dr. Bill Cousins taken from his Ph.D dissertation. The clarification is on the critical stage which was noted several years after this work was initially published. The authors of the T-55 document concur with Dr. Cousin's analysis**

In other work by Owen and Davis [3.51] the compressor rig for the T55-L-712 axial-centrifugal compressor (hereafter called the T55) was matched with the **DYNTECC** model. In this match, high-response flow data was not available and static pressures were matched with the model. The surge frequency predicted by the model was the same as that observed in the compressor as measured by static pressure transducers in the shroud of the machine. Without high-response flow measurements, whether or not the post-stall flow behavior is correct is not known, since it is probably possible to obtain the correct frequency without the correct flow distribution.

There is a major difference between the T55 compression system and the TFE1042. The T55 has a straight radial impeller (rather than a highly backswept impeller) and the match to the diffuser is significantly different. In the T55, the centrifugal impeller is the surge trigger under standard conditions along the high end of the map. In addition, the rig diffuser was somewhat unstable at high flows (this can be seen in the data presented in the paper). **Figure 3.76** shows a reproduction of Figure 8 from Owen and Davis [3.51]. In the figure, the unsteadiness of the centrifugal stage can be seen. It is the opinion of this author that this unsteadiness is caused by the rig diffuser, just downstream of the centrifugal stage. This diffuser had a half angle that approached 30 degrees. This can also be seen in the geometry input representation of the rig exit ducting in the Owen and Davis paper. In effect, the T55 rig has a compressor not matched as discussed and shown in Cousins dissertation, Figure 4-11 of **Ref. 3.52**.

Matching the centrifugal stage so that it is not the stall trigger at high speed is not possible without a backswept impeller. Having a radial impeller, the centrifugal stage in the T55 is the surge trigger at high speed. In this particular rig, the centrifugal compressor stability is further reduced by the fact that the downstream diffuser is not optimum.

The authors state in the paper that at speeds higher than 80%, it was difficult to fully understand the data due to the centrifugal unsteadiness. The authors also state that in all the results, the first stage appeared to be the stall trigger. In fact, with further investigation, the authors may have realized that what was being observed as a first rotor phenomena was in fact a second order result being triggered by the centrifugal stage causing the axial to mismatch, aggravated by the poor downstream diffuser. If Owen and Davis had the details of the flow provided by high-response flow measurements (a fore-aft probe), they probably would have arrived at a different conclusion.

At the time Owen and Davis obtained this data, much of what has been discussed here was not known. This author has had the benefit of more study of the rig and the overall performance of the T55 compressor than Owen and Davis had at the time their work was performed, due to the acquisition of the Lycoming Company by AlliedSignal Engines, and the availability of more detailed performance models of the compression system.

#### ADDITIONAL REFERENCES

**3.53** Gamache, R. N. "Axial Compressor Reversed Flow Performance," Ph.D. Dissertation, Massachusetts Institute of Technology, May 1985.

**3.54** Boyer, K. and W. F. O'Brien "Model Predictions for Improved Recoverability of a Multistage Axial-Flow Compressor," AIAA Paper 89-2689, Presented at the 25th Joint Propulsion Conference, Monterey, CA, July 1989.

**3.55** Copenhaver, W. W. "Stage Effects on Stalling and Recovery of a High-Speed 10-Stage Axial-Flow Compressor," Ph.D. Dissertation, Iowa State University, Ames, IA, 1988.

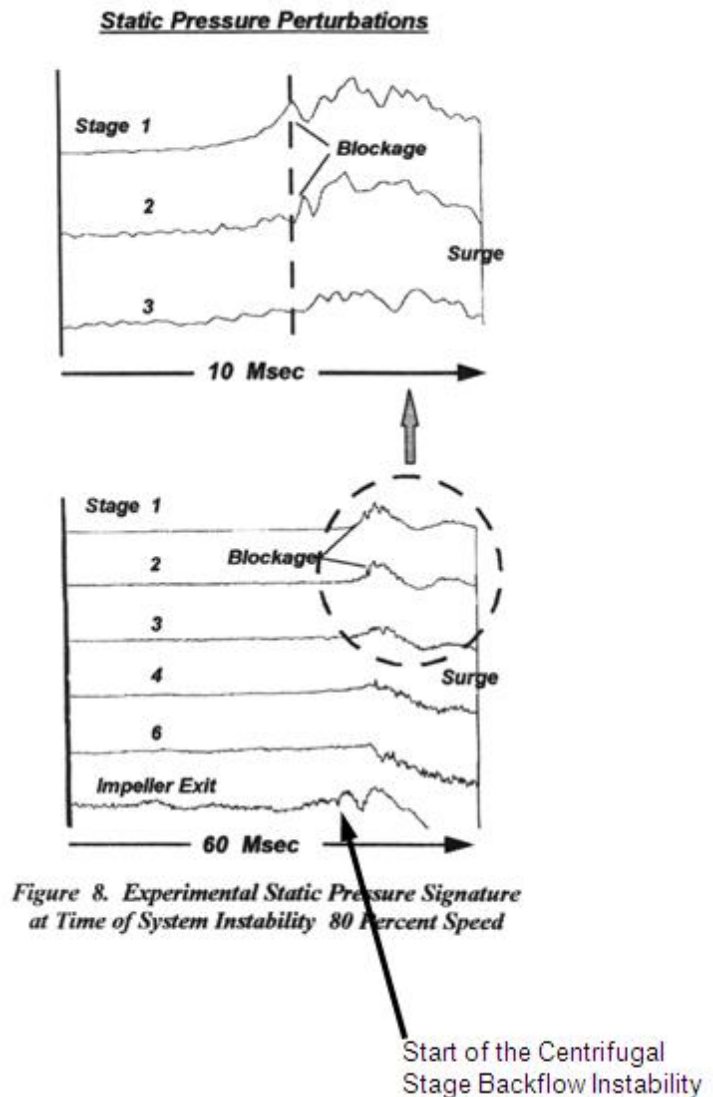


Figure 8. Experimental Static Pressure Signature at Time of System Instability 80 Percent Speed

Figure 3.76 Cousins Reading of the Experimental Results

### 3.1.11 Dynamic Engine Simulation of Post-Stall Behavior and Engine Starting

The gas turbine engine has played a significant role in the advancement of the flight capabilities of modern day aircraft. In order for a gas turbine engine to operate at the performance, operability, and durability level for which it was designed, stable operation of the various engine components must be ensured. Transient and dynamic instabilities, which could push the engine components beyond their operational limits, could result in loss of thrust, loss of engine control, or possible engine damage due to high heat loads and high cyclic stresses. The influence of operating instabilities must be quantified not only from the individual component considerations, but also from the point of view of any interaction between the various components.

#### CITED EXAMPLE(S)

**3.56** Garrard, Doug, “**ATEC**, The Aerodynamic Turbine Engine Code for the Analysis of Transient and Dynamic Gas Turbine Engine System Operations, Part 1: Model Development”, ASME Paper # 96-GT-193, June 1996.

**3.57** Garrard, Doug, “**ATEC**, The Aerodynamic Turbine Engine Code for the Analysis of Transient and Dynamic Gas Turbine Engine System Operations, Part 2: Numerical Simulations”, ASME Paper # 96-GT-194, June 1996.

**3.58** Garrard, G. D., “**ATEC**: The Aerodynamic Turbine Engine Code for the Analysis of Transient and Dynamic Turbine Engine System Operations,” Ph.D. Dissertation, the University of Tennessee, Knoxville, August, 1995.

#### MODELING TECHNIQUE

The applications cited in this section use the Aerodynamic Turbine Engine Code, or **ATEC** ([Section 4.5](#)), a time-dependent turbine engine model and simulation capable of simulating a turbojet engine operating in both transient and dynamic modes. The **ATEC** simulation provides a bridge between the two types of simulations as sketched in [Figure 3.77](#). The **ATEC** simulation provides the computational efficiency that is desired when simulating the gas turbine engine during transient events, but it also provides the appropriate simulation techniques to address overall engine operation during a dynamic event such as compressor surge or combustor blow-out. **ATEC** provides the detailed system resolution needed to analyze a dynamic event (such as a stage-by-stage representation of the compression system), but utilizes the same type of component performance information used in standard transient simulations.

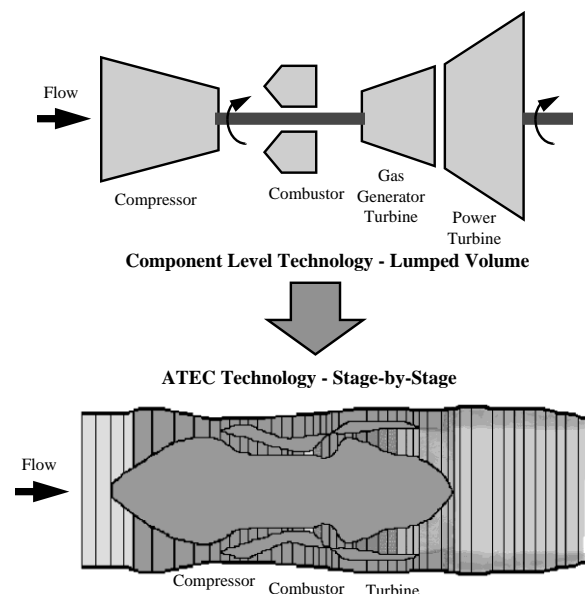


**Figure 3.77 Comparison of Component Level and ATEC Model and Simulation Technology for Gas Turbine Engine Modeling**

## APPLICATION TO THE T-55 TURBOSHAFT ENGINE FOR POST-STALL BEHAVIOR

The test case presented in this section simulates a transient throttle movement using the T55-L-712 ([Figure 3.77](#)) that resulted in the gas generator portion of the engine decelerating from 100 percent speed to approximately 90 percent speed. After a brief pause at the 90 percent speed, the engine was reaccelerated back to the 100 percent speed condition. The change in fuel flow rate during the reacceleration was fast enough to force the compressor into surge cycles. The engine inlet conditions were representative of a standard day, sea-level, static operational environment. Direct comparison of the model results to test data has not been made for this test case due to the lack of an appropriate data set.

The relative compressor pressure ratio as a function of time is shown in [Figure 3.78](#). For all examples shown in the following discussions, relative values represent the particular value of a parameter given by the **ATEC** simulation divided by the maximum value obtained during the simulation for that parameter. Predicted relative total pressure as a function of both time and axial location is shown in [Figure 3.79a](#). The multiple surge cycles cause a significant drop in the total pressure throughout the engine. The predicted relative total pressure during and immediately surrounding the time of the surge cycles is plotted as a function of both time and axial location in the engine in [Figure 3.79b](#).

As with the compressor pressure ratio, the mass flow rate in the engine is reduced by the throttle transient. During the reacceleration process, the mass flow begins returning to its

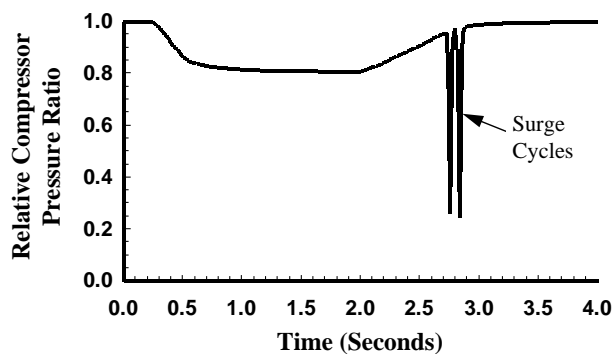
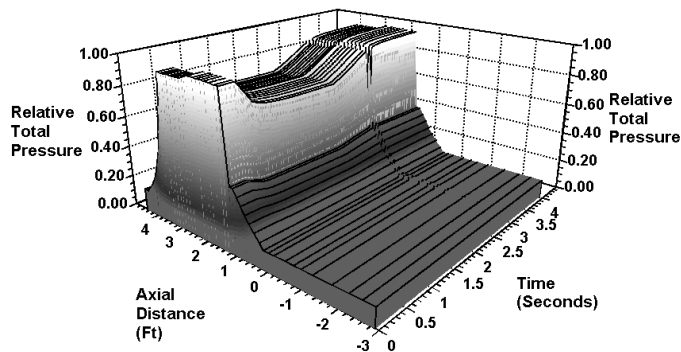


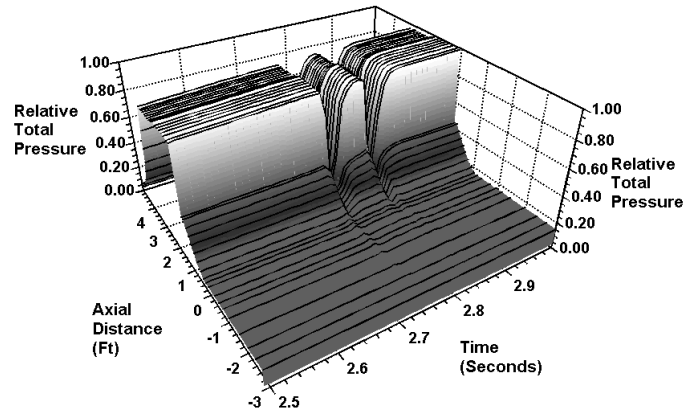
**Figure 3.78 Relative Compressor Pressure Ratio as a Function of Time**

original level. When the compressor enters the surge cycles, however, the depressurization of the volume inside the compressor system forces the mass flow rate to reverse. Once the system recovers from the surge cycles, the mass flow rate quickly returns to the original level. The mass flow rate during and immediately surrounding the time of the surge cycles as a function of both time and axial location in the engine is plotted in [Figure 3.80](#). During the surge cycles, the mass flow rate reverses only in the region of the compressor. While greatly reduced, the mass flow rate downstream of the compressor does not reverse.





a. Full Event  
Exploded View



b.

**Figure 3.79 Relative Total Pressure as a Function of Axial Distance and Time**

The total temperature in the combustor region greatly increases during the surge cycles due to the reduced air mass flow rate. Once the equivalence ratio in the combustor reaches the rich blow out limit, however, the combustion process is extinguished and the temperature falls off. This region of the predicted relative total temperature surface plot is shown in [Figure 3.81](#). The equivalence ratio in the combustor during the time of the surge cycles, along with the rich and lean blow out limits, are shown in [Figure 3.82](#). Once the air flow rate is reestablished, the combustion process is also reestablished and the temperature climbs back to nominal levels.

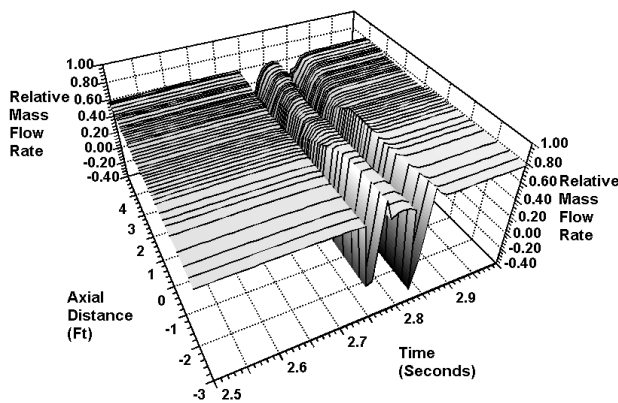


**Figure 3.80 Relative Mass Flow Rate at Time of Surge Cycles**

of time is shown in [Figure 3.83](#). During the surge cycles, there is a reduction in rotor speed. Because of the rotor rotational inertia, however, the reduction is small.

The relative rotor rotational speed as a function

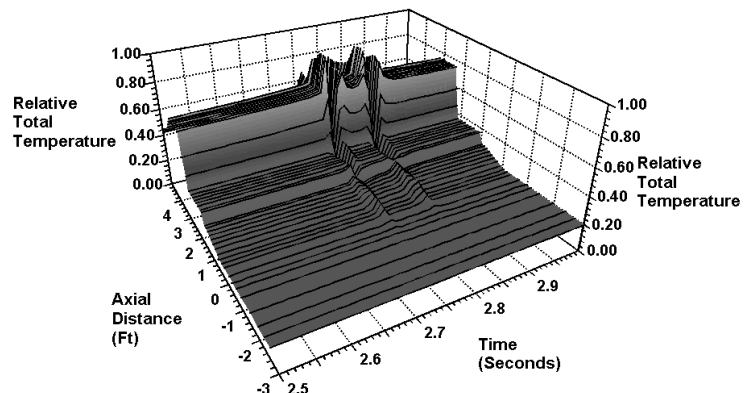


**Figure 3.81 Relative Total Temperature at Time of Surge Cycles**

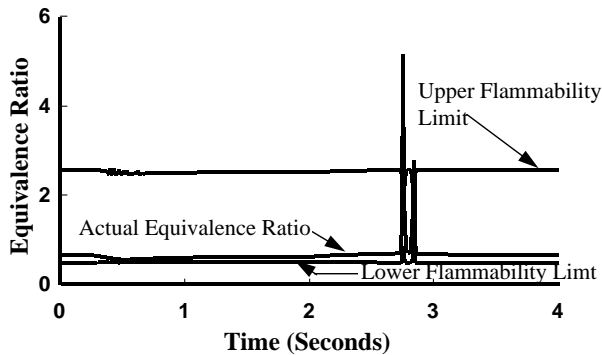


**Figure 3.82 Combustor Equivalence Ratio during Engine Transient**

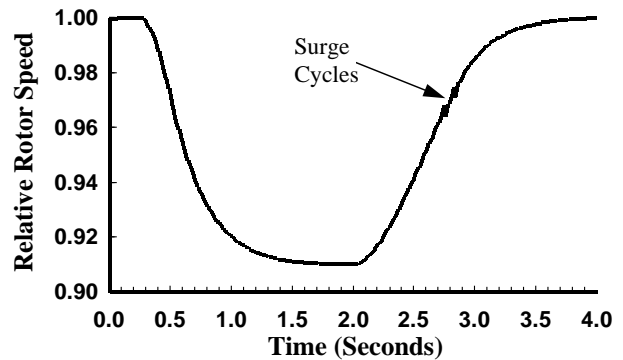


**Figure 3.83 Relative Rotor Speed**

### APPLICATION OF ATEC TO A TURBOSHAFT ENGINE FOR ENGINE STARTING

The final test case to be presented considers the starting process of a turboshaft engine core. The engine under consideration is also a turboshaft engine with a geometry similar to the T55-L-712, but the operating characteristics, such as design pressure ratio and rotor shaft speed, are significantly different. The engine starting process was a “cold” start, in that the engine internal metal temperatures were at ambient temperatures.

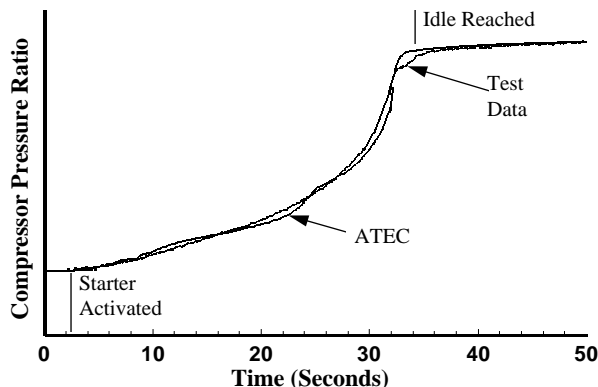


**Figure 3.84 Compressor Pressure Ratio as a Function of Time for the Engine Starting Process**

In addition to the aerodynamic model, a control system model was added to the **ATEC** simulation for this test case. The control system model provided a fuel flow rate to the combustor model. The fuel flow rate was determined as a function of ambient air temperature, the compressor discharge static pressure, and the corrected rotational speed of the gas generator rotor. Minimum and maximum fuel flow rate requirements were also addressed.

The compressor pressure ratio as a function of time as calculated by **ATEC** is compared to test data in **Figure 3.84**. Once the starter was activated, the engine required approximately 31 seconds to reach idle conditions. The **ATEC** results agree closely with the test data, with a difference of less than one second in time for a given pressure ratio during the starting process. When idle conditions are reached, the compressor pressure ratios agree to within one percent. The gas generator rotor speed for both the **ATEC** results and the test data are shown in **Figure 3.85**. As with the compressor pressure ratio, the **ATEC** predicted rotor speed agrees with the test data closely during the start process. At idle, the **ATEC** torque balance in the engine results in the rotor speed being less than three percent lower than the test data. The compressor pressure ratio as a function of compressor inlet mass flow rate is shown in **Figure 3.86** for both data sets.



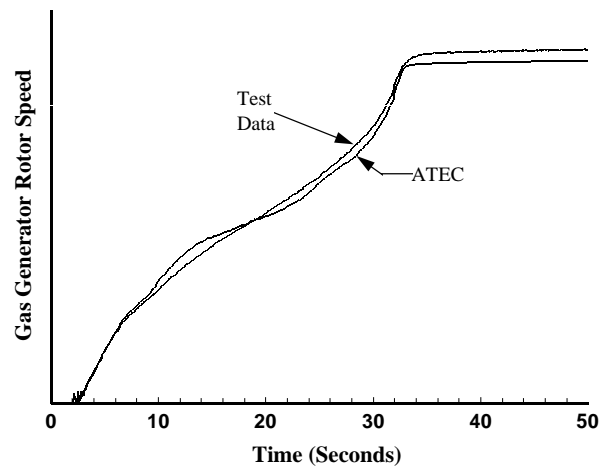


**Figure 3.85 Gas Generator Rotor Speed as a Function of Time for the Engine Starting Process**

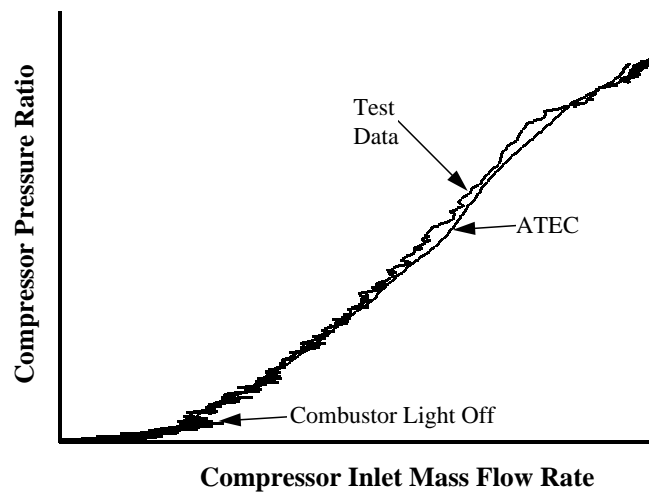


**Figure 3.86 Compressor Pressure Ratio as a Function of Compressor Inlet Mass Flow Rate for the Engine Starting Process**

### 3.2 INLET DISTORTION

Integration of a weapon system airframe and its propulsion system encompasses a number of issues ranging from aircraft stability and control to inlet-engine compatibility. To address these issues, the integrated test and evaluation (IT&E) process requires the application of a variety of test resources as well as a wide range of analytical and computational tools. Testing for airframe-propulsion integration, and in particular inlet-engine compatibility, generally requires the coupling of component tests conducted in both wind tunnels and engine altitude facilities.



**Figure 3.87 Subscale Model Wind Tunnel Test**

The advent of technologies allowing for controlled flight at extremely high angles of attack and sideslip has enabled weapon system developers to consider supermaneuver and post-stall maneuver capabilities as combat tactics. As a result, future fighter aircraft may be required to execute maneuvers containing drastic changes in flight conditions at the high power settings demanded by combat. Such maneuvers bring forth the question of what role the distortion time history might play in the inlet-engine integration task. Large and transient changes in

angle of attack can produce hysteresis and, therefore, deviations from the steady-state condition.

The inlet-engine integration test methodology currently involves two separate processes that are loosely coupled. Subscale inlet tests (**Figure 3.87**) are conducted in a wind tunnel to determine the conditions that must be simulated at the face of a full-scale engine. These conditions, although a function of angle of attack, sideslip, and flight condition, are characterized by a distortion indexing methodology that may lessen the influences of each individual flight variable.

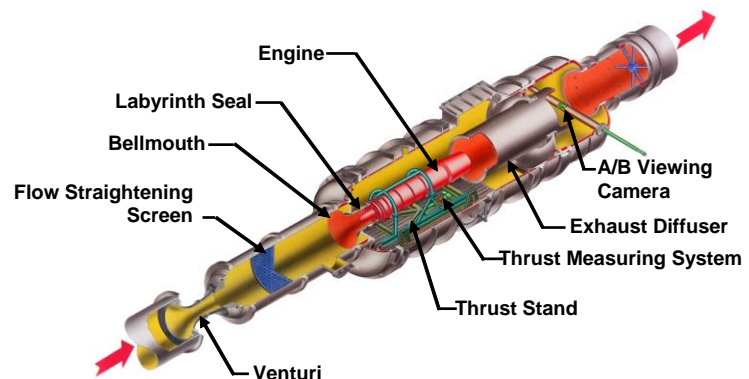


**Figure 3.88 Direct Connect Test Cell Schematic**

In the absence of the inlet and airframe, the direct-connect test methodology (**Figure 3.88**) for propulsion must rely on additional techniques to simulate the distortion produced by the inlet. A number of methods have been applied to simulate steady-state inlet distortion as well as various aspects of time-variant distortion. The two most widely used inlet distortion simulators are the

distortion screen and the air-jet distortion generator. Although efforts are proceeding to improve the inlet simulation devices placed in front of an engine, the current devices neglect time history, flow angularity (swirl), and certain interactions such as the effect of the compressor face on the inlet characteristics.

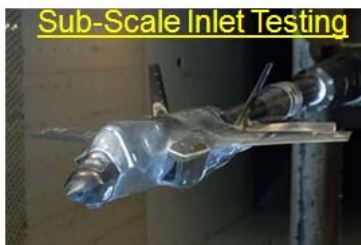
Similarly, the engine test methodology measures the effect of a series of distortion patterns based upon distortion screens on engine operability and performance (**Figure 3.89**). Keeping with one of the fundamental precepts of the recommended practice set forth in the ARP-1420 [3.59] and in its companion document, AIR-1419 [3.60] (namely, that engine stability can be defined by tests using equivalent levels of steady-state distortion), aircraft manufacturers, engine manufacturers, and testing organizations have implemented testing procedures which reflect that premise.



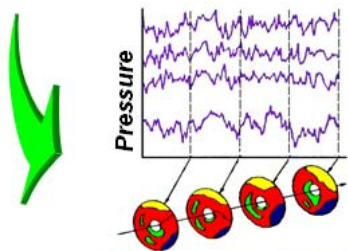
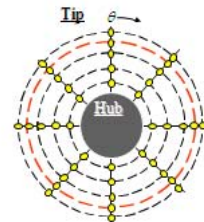
**Figure 3.89 Direct Connect with Distortion Screens**

The inlet-engine integration test methodology as illustrated in **Figure 3.90** is based on engine tests that show that the engine experiences distortion patterns that last for a time of the order of

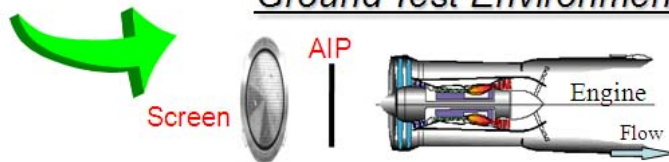
### Inlet Distortion Characteristic from Inlet Test in Wind Tunnel



*Inlet Flow Quality can be Characterized with Numerical Descriptor Derived from an Array of High-Response Total-Pressure Probes*



### Distortion Created in Ground Test Environment



- *Time-variant Distortion Effects Limited to Events Lasting Longer Than Approximately One Revolution of the Machine Represented in test by a Fixed Peak Distortion Pattern Selected From the Distortion Time History*
- *Engine Stability can be Demonstrated by Tests Using Equivalent Levels of Steady-State Distortion*

\* Society of Automotive Engineers, Aerospace Recommended Practice ARP-1420B, 2002

**Figure 3.90 SAE Airframe-Propulsion Integration Methodology**

one engine RPM as if they were steady-state conditions. [Note, that this methodology does not address aerostructural effects on the engine (e.g., high cycle fatigue)]. Thus, subscale inlet tests in a wind tunnel are used to select the conditions that must be simulated at the face of a full-scale engine. These conditions, although a function of angle of attack, sideslip, and flight condition, are characterized by a distortion-indexing methodology. The accuracy of this distortion-indexing methodology is dependent upon the thoroughness of dedicated engine tests with classic distortion patterns and realistic distortion patterns for the particular application.

The current status for airframe-engine integration was best summarized by R. E. Smith, Jr. in the AIAA 1995 Wright Brothers Lectureship in Aeronautics [3.61]:

*“In spite of all the improvements cited in this assessment, significant portions of the current state of the art for the airframe-engine integration process are still dependent on empiricism and scaling rules. Such dependencies always contain exposure to risks that the next configuration and/or next mission requirement will lie outside the bounds of applicability of the empiricism and/or scaling rules. These risks portend the possibility of a major negative surprise. The airframe-engine integration process has produced many such surprises in its history.”*

Clearly the volume of issues facing future integrations of inlet and engine into viable aircraft systems (such as the F/A-22, Joint Strike Fighter, F/A-18, and UAV's) demands improved test techniques coupled with dynamic numerical simulations.

To be able to address inlet distortion from the engine point-of-view, not only viable test techniques must be established but viable numerical simulations must also be available. AEDC has invested into the development of several computational capabilities as described in [Chapter 4](#). Those simulations have been used in investigations into a variety of inlet distortion issues and are gathered in this section. Examples of the use of these codes are listed for the following types of inlet distortion issues:

- Total Pressure Distortion
- Total Temperature Distortion
- Combined Pressure and Temperature Distortion and
- Swirl Distortion

#### **REFERENCES:**

**3.59** SAE Aerospace Information Report, AIR-1419, “Inlet Total-Pressure Distortion Considerations for Gas Turbine Engines”, May 1983.

**3.60** SAE Aerospace Recommended Practice, ARP-1420, “Gas Turbine Engine Inlet Flow Distortion Guidelines”, March

**3.61** Smith, R. E., “Marrying Airframes and Engines in Ground Test Facilities – An Evolutionary Revolution,” AIAA Paper No. 95-0950, 1st AIAA Aircraft Engineering, Technology, and Operations Congress, Los Angeles, CA, September 19- 21, 1995.

### 3.2.1 Inlet Total Pressure Distortion -- Parallel Compressor Theory

Keeping with one of the fundamental precepts of the recommended practice set forth in the ARP-1420, namely, that engine stability can be defined by tests using equivalent levels of steady state distortion, the aircraft manufacturers, engine manufacturers and testing organizations have implemented testing procedures which reflect that premise.

In the absence of the inlet and airframe, the direct-connect approach must rely on additional techniques to simulate the distortion produced by the inlet. A number of methods have been applied to simulate steady-state inlet distortion as well as various aspects of time-variant distortion. The two most widely used inlet distortion simulators are the distortion screen and the air jet distortion generator.

The screen and air jet distortion generator devices provide only steady-state distortion patterns. However, historical wind tunnel test results have shown that the time-variant distortion or swirl can be significantly higher than steady state. To address time-variant distortion, the current methodology applies the following approach. The time-variant distortion measurements obtained in the wind tunnel, the distortion time history, is screened over the time recorded during the particular test point to identify peak levels of distortion. The wind tunnel data acquisition procedure must include a sufficient data record, typically twenty or thirty seconds, to capture peak distortion events.

Experience has shown that turbomachines require a finite time, on the order of one revolution of the compression system, to respond to dynamic distortion events. Therefore, the screening process neglects time-dependent events lasting less than approximately one revolution and does not even begin to address the effects of swirl. The peak level of distortion is then applied in the direct-connect test using the screen or air jet distortion generator. The peak time-variant pattern becomes a steady-state pattern in the engine or compressor test neglecting the effects of time history as illustrated in [Figure 3.91](#).

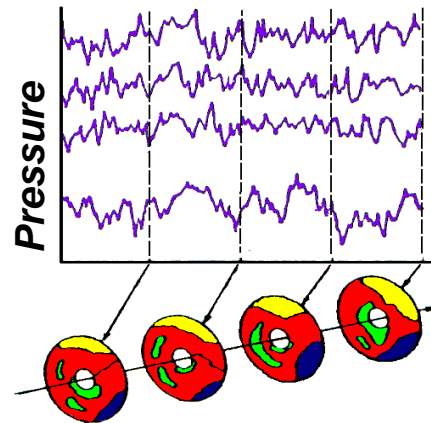


**Figure 3.91 Simulation of Time-Variant Distortion with Steady-State Patterns**

Numerical simulation technology has also taken advantage of the ARP-1420 [\[3.59\]](#) methodology by applying the peak time-variant pattern as a boundary condition to the simulation. Several simulation techniques, introduced in [Chapter 4](#), all use this concept. The first to be discussed is the parallel compressor modeling theory.

#### **CITED EXAMPLE(S)**

**3.62** Davis, M. W., Jr., "Parametric Investigation into the Combined Effects of Pressure and Temperature Distortion on Compression System Stability", AIAA Paper # AIAA-91-1895, Presented at the 27th Joint Propulsion Conference, Sacramento, CA, June 1991.



**3.63** Davis, M. W., Jr., W. Baker, G. Power, and D. Beale, "A Proposal for Integration of Wind Tunnel and Engine Test Programs for the Evaluation of Airframe-Propulsion Compatibility Using Numerical Simulations", **Journal of Engineering for Gas Turbines and Power**, Vol. 124, Number 3, July 2002, pp. 447-458.

**3.64** Davis, Milt, Alan Hale, and Dave Beale, "An Argument for Enhancement of the Current Inlet Distortion Ground Test Practice for Aircraft Gas Turbine Engines", **Journal of Turbomachinery**, Vol. 124, Number 2, April 2002, pp. 235-241.

**3.65** Davis, Milt and Kidman, David, "Prediction and Analysis of Inlet Pressure and Temperature Distortion on Engine Operability from a Recent T-38 Flight Test Program", Presented at the 2010 ASME International Gas Turbine Institute Turbo Expo, June 2010.

### **MODELING TECHNIQUE**

A one-dimensional modeling technique known as **DYNTECC** ([Section 4.4](#)) and as described by Hale and Davis in [Ref. 3.68](#) has been modified by Davis and Sharokhi [[3.69](#), [3.70](#)] for the analysis of distorted inflow using **parallel compressor** theory ([See Section 4.6](#)). As indicated in [Figure 3.92](#), a parallel compressor model uses a multi-segmented circumferential compressor concept. Each circumferential segment is modeled using the one-dimensional technique described by Hale and Davis in [Ref. 3.68](#). Each segment operates independently except at the exit boundary where the specification of either uniform static pressure or uniform Mach number is imposed. This is the only location where the modeling technique transfers information from one segment to another. Different levels of pressure or temperature distortion may be imposed upon the inlet, and each segment will operate to its own limit. In this classical form, when one segment reaches the instability limit the entire compression system is considered to be unstable. Using this approach, the mean operating point at instability is a weighted average of the low flow sector operating at the uniform flow stability boundary, and the high flow sector operating at some other point far from the stability limit as shown in [Figure 3.92](#).

The greatest loss in stability margin occurs with the narrowest distorted sector inlet. This leads to predictions that are inconsistent with experimental observations. For example, the theory would indicate that the whole compression system would be unstable for a 1-degree sector if

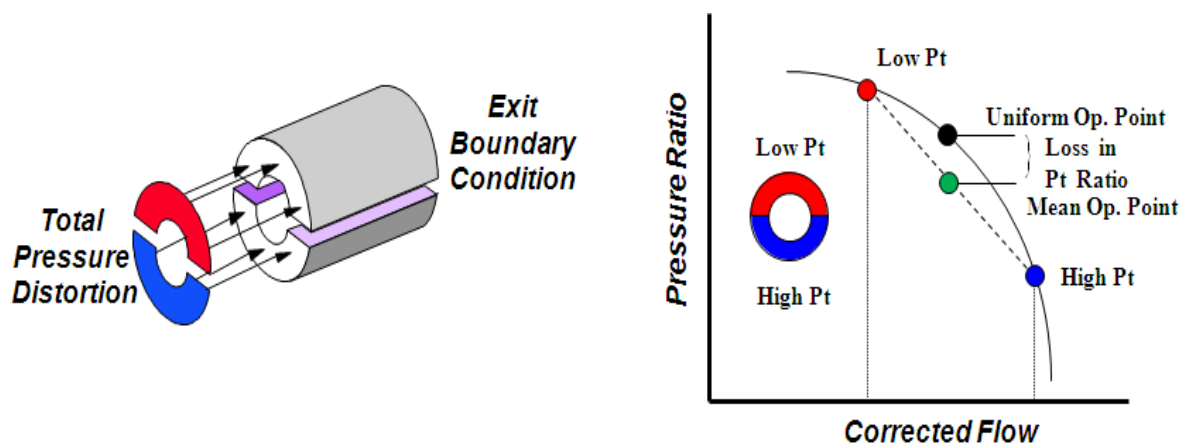


**Figure 3.92 Parallel Compressor Concept**

that sector were stalled.

Evidence indicates that there is a critical angle of extent for this theory to work. Some investigators suggest that 60 degrees or 6 segments is the limit. The implication is that it is possible for a small portion of the compressor annulus to operate beyond the observed stability limit provided that there is enough of the annulus operating on the stable side to maintain overall stability. Modifications to the pure parallel compressor theory to allow for circumferential crossflow between segments have been implemented using an orifice approximation [3.69]. Extensions of the parallel concept for radial distortion require knowledge of the radial distribution of the flow if that redistribution becomes significant.

### APPLICATION TO A 10-STAGE SINGLE-SPOOL COMPRESSOR

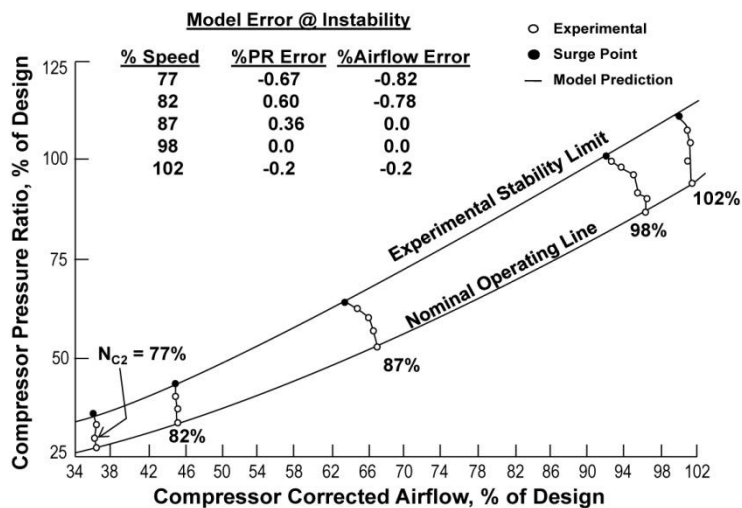


**Figure 3.93 Simulation of Time-Variant Distortion with Steady-State Patterns**

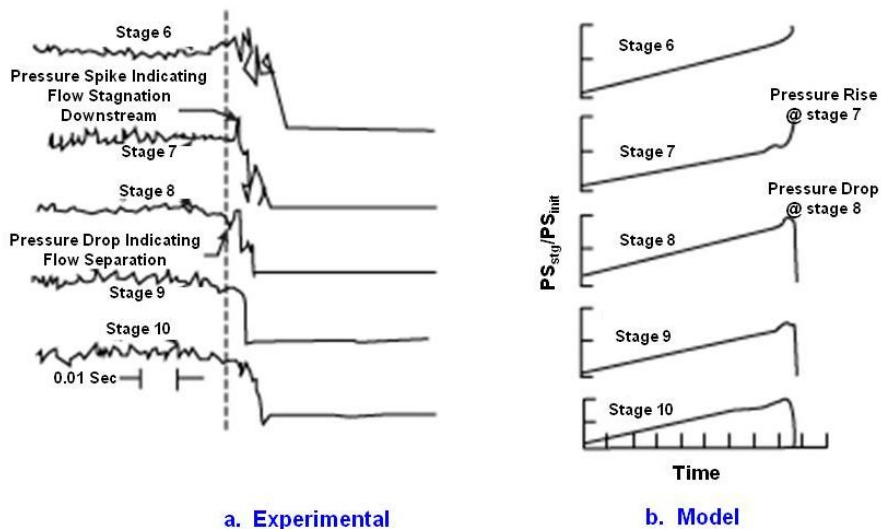


**Figure 3.94 Static Pressure Signature at Time of Compression System Instability**

The parallel compression system model was validated against experimental results for a 10-stage compression system. Initially, the model was validated with a clean inlet, no distortion, and compared to overall compression system performance as indicated in [Figure 3.93](#). For the range of speeds, 87 to 98 percent of design, the model predicted the overall stability limit within 2 percent of that observed experimentally.

For a stage-by-stage model to be completely validated, it must also indicate the correct stage behavior at the time of system instability. Presented in [Figure 3.94a](#) are stage experimental static pressure signatures at time of system instability and comparison to model predictions for the same event. As indicated, for this speed (98%), the entrance to stage 7 indicates a rapid rise in static pressure just prior to the stall event. As indicated, for this



speed (98%), the entrance to state 6 indicates a rapid rise in static pressure just prior to stage 8 (i.e. the exit to stage 7) indicates a rapid drop in static pressure. This is caused by some form of blockage occurring within stage 7 which precipitates flow breakdown. Presented in [Figure 3.94b](#) is the static pressure signature produced by the compression system model. Inspection indicates that the same signature exists within the model results as was observed experimentally.

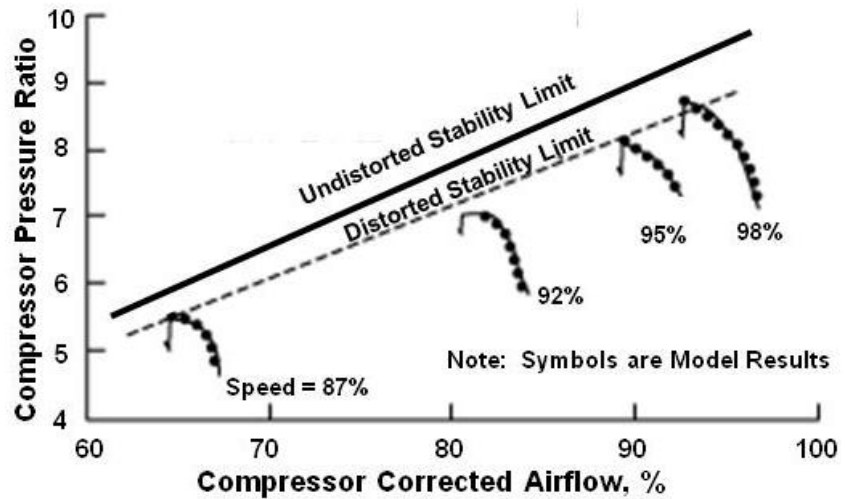


**Figure 3.95 Model Predicts Overall Distorted Stability Limit Within 3%**

In addition to the clean inlet validation, the model was also validated against experimental results with a one-per-rev 180° distortion pattern imposed upon the inlet via a distortion screen. The distortion screen was manufactured with higher density screen porosity in one half of the screen which caused a larger pressure drop in that portion of the inlet. Since the pressure drop across a distortion screen is a function of the airflow, differences in distortion magnitude (as described by the difference in total pressure ratioed to the average) can be observed in the experimental stability limit as a function of speed and thus airflow. Thus, the distortion magnitude at 98 percent (7.5%) was higher than that imposed at 87 percent (1 %).

The model was configured for two circumferentially segmented parallel compressors with the inlet total pressure prescribed by the actual test data. Presented in [Figure 3.95](#) are compression system model overall results compared to the experimental stability limit as observed with distortion. The model predicted the distorted stability limit within 3 percent of the experimental results. This validation occurred without any adjustment to the clean stage characteristics. Stage behavior at time of system instability indicated that the 7<sup>th</sup> stage of the distorted

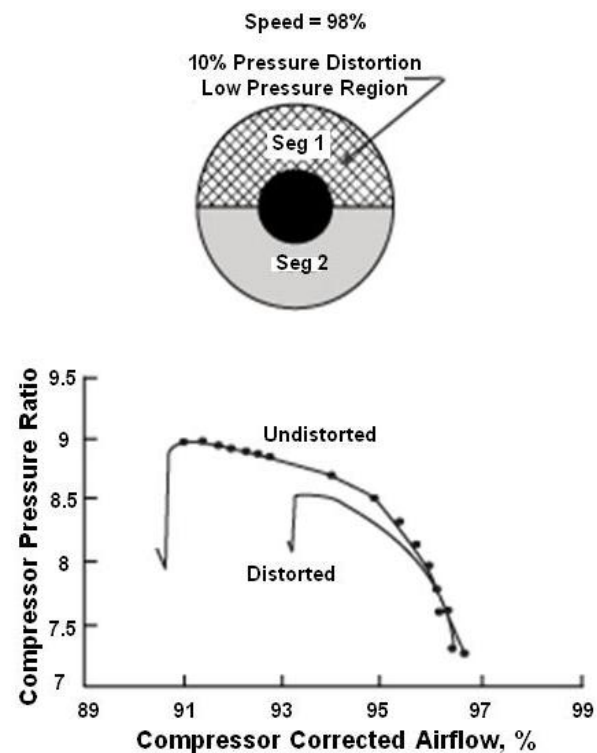


**Figure 3.96 Model Prediction with 180-deg Total Pressure Distortion**

segment initiated the stall. this model result compares with that observed.

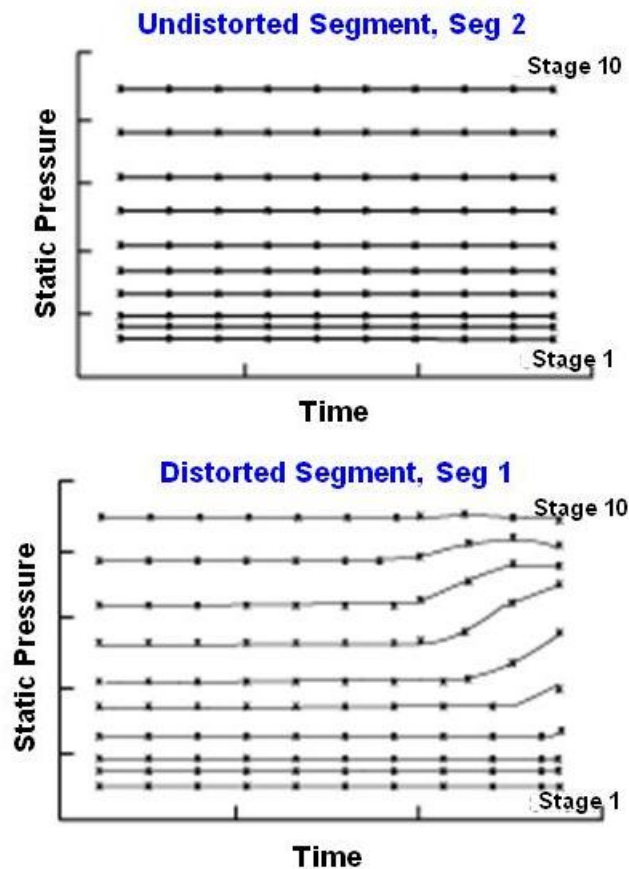


**Figure 3.97 Static Pressure Signature Indicating Stalling Stage for 180-deg Circumferential Distortion**

The predicted results from a 180° circumferential total pressure distortion on system overall performance and stability limit is illustrated in [Figure 3.96](#). A distortion magnitude of 10 percent (10 percent lower pressure in Segment 1 than in Segment 2) was imposed upon the inlet total pressure boundary condition. Once steady operation was verified with the distortion pattern, the exit static pressure was increased at a rate of 50 psia/sec (a rate commensurate with a burner fuel pulse) until system instability was indicated. A drop in the stability limit and thus a decrease in the stability margin was predicted. A good portion of the stability margin is still left and is typical for this level of distortion magnitude.

Presented in [Figure 3.97](#) is the associated stage static pressure signature at time of system instability. As indicated by the rapid increase in the stage inlet pressure and the decrease in the exit pressure, stage 7 of the distorted low pressure region, Segment 1, appears to have caused the flow breakdown.

#### APPLICATION TO THE J85 EIGHT-STAGE SINGLE-SPOOL COMPRESSOR

The first afterburning J85 engine available for the T-38 was the J85-GE-5 engine which has an eight stage compressor and rated at 3600 Lb [\[3.66\]](#). Over the decades since the first production J85-5 was shipped, there have been many modifications. For the PMP program the J85-5R/S is the current designation. Ideally, validation should be conducted on the J85-GE-5R/S version, but there no data published in the open literature on that version. However, there is a tremendous amount of data on the J85-GE-13 engine taken by NASA in the 1970's [\[3.71, 3.72, 3.73, 3.74, & 3.75\]](#),

***“The J85-GE-13, a re-rated version of the J85-GE-5, was selected originally to power the Northrop F-5A supersonic fighter. To modify the -5 engine, turbine inlet temperature was increased to produce 2750 Lb thrust dry and 4080 Lb with afterburner”***[\[3.67\]](#).

Since the only noted difference between the J85-GE-13 and the J85-GE-5 is the re-rated turbine inlet temperature, it can be assumed that the eight stage compression system is identical for both versions. Because of the availability of the data, the parallel compression system model has been validated using the J85-GE-13 version.

### J85-13 Clean Inlet Validation

The first level of validation for the parallel compression system model is to verify that the model produces appropriate clean inlet overall results. Using data taken by Calogeras from **Ref. 3.73**, the model was executed at the same corrected speeds as shown in **Figure 3.98**.

The figure is an exact copy of the hand-drawn figure presented in **Ref. 3.73**. Presented in **Figure 3.99** are the parallel compressor model results at those same corrected speeds.

To obtain a constant corrected speedline with the parallel compressor, the model was set at the desired speed, inlet pressure and temperature while the exit boundary condition was set such that the overall flow rate was near the nominal operating point.

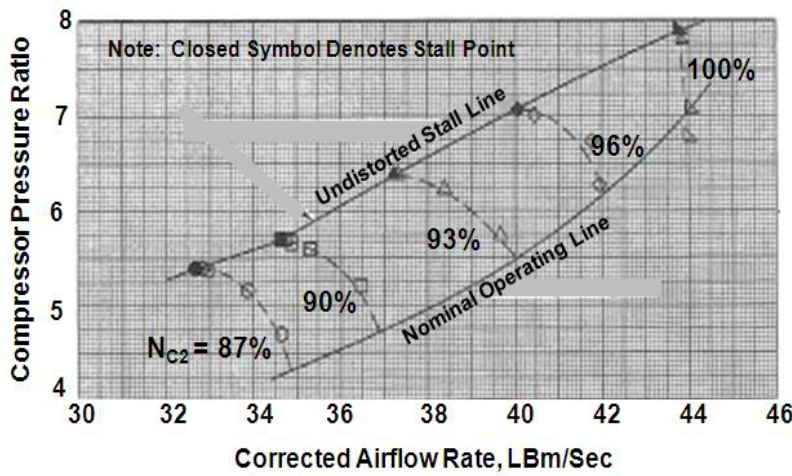


**Figure 3.98 Reproduction of the J85-GE-13 Experimental Data for Clean Inlet [Figure 3 of Ref. 3.73]**

Once steady state operation was obtained, the exit static pressure was ramped at a rate of approximately 50 psia/sec (a rate representing a typical combustor fuel pulse) until overall compressor stall was indicated. Compressor stall was determined within the parallel compressor model when a number of stages had reached their

stall point as indicated by the point of zero slope on the stage pressure ratio versus stage corrected flow input curves. Some latitude was given to the number of stalling stages when comparing to clean inlet, generally 4 or 5. For this eight stage compressor, it was determined that many of the stages are operating near their stall point when the overall system is near stall. This same procedure was followed for inlet distortion with the stalling stage generally found to be in the low pressure region for pressure distortion and in the high temperature region for temperature distortion.

As indicated in **Figure 3.99**, the predicted stability limit at all speeds was within 1-2%

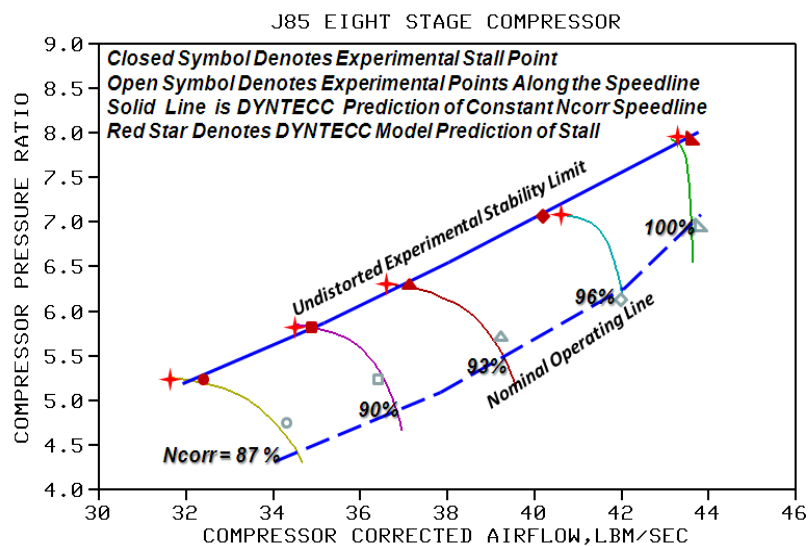


**Figure 3.99 Parallel Compressor Model Results at the Same Corrected Speeds as Experimental Data for Clean Inlet**

of that observed experimentally providing excellent verification of the stage stall criteria used in the parallel compressor model. Note that the undistorted experimental stability limit is indicated on [Figure 3.99](#) and came from the experimental data in [Figure 3.98](#). For the next series of validation cases, the experimental stability limit will be the only portion of the data used for validation instead of the fully available experimental map as has been shown for the clean inlet.

### J85-13 Pressure Distortion Validation

Associated with the data from Calogeras [3.73] are multiple pressure distortion cases to choose from for validation. One of the major cases tested was 180° circumferential total pressure distortion. During the experimental tests conducted in the 1970's, several density 180° distortion screens were used. These screens were identified by their mesh size (7 ½ Mesh and 8 ½ Mesh) with associated pressure drops tabulated as a function of corrected speed (Table 1 of [Ref. 3.73](#)). These pressure drops were modeled within the parallel compressor model as a "square-wave" formation (i.e. the pressure defect was over an 180° portion without any sinusoidal formation).

Presented in [Figure 3.100](#) are the results of the **parallel compressor model** predictions using the 180° circumferential pressure distortion as generated by the 7½ Mesh Screen. The predicted stability limit is within 1-2% of that observed experimentally. Again results are exceptional and provide a good validation for this case. In addition to the 7 ½ mesh screen, other distortion magnitudes using other screens were used in testing as well. Those magnitudes and the subsequent loss in stability pressure ratio are summarized by Braithwaite in [Ref. 3.75](#) and are presented and compared to the parallel compressor model results in [Figure 3.101](#).

#### 180 Degree Circumferential Distortion – 7 ½ Mesh Screen

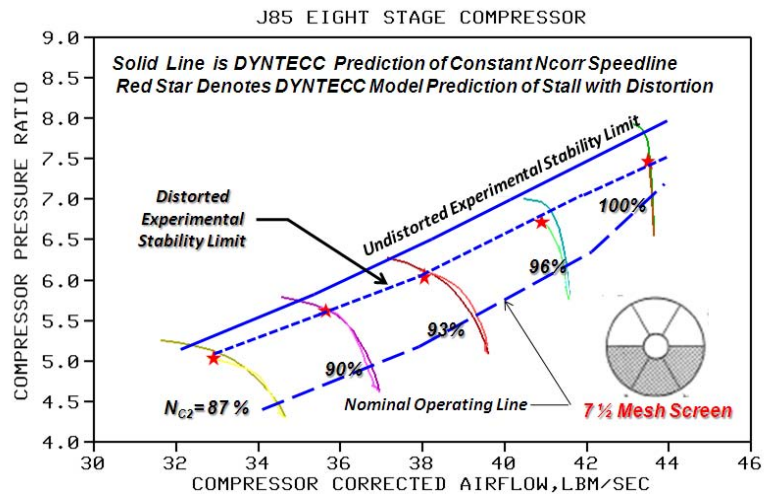


**Figure 3.100 Parallel Compressor Model Results Compared to 180-deg Circumferential Total Pressure Distortion Implemented by a Distortion Screen**

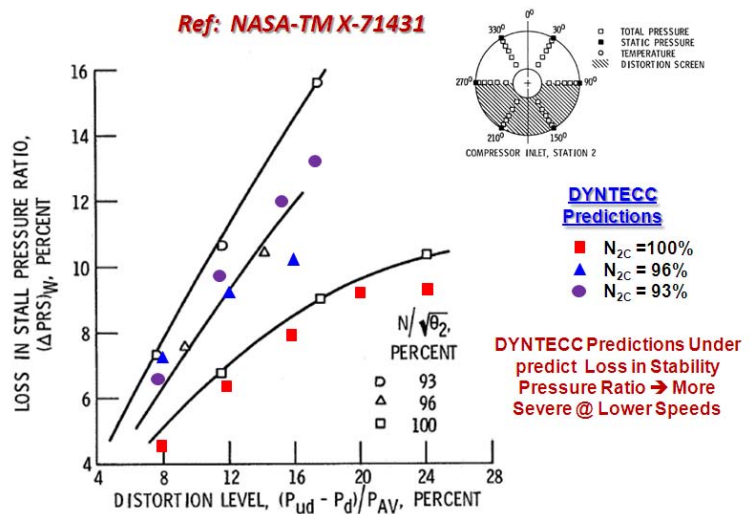


**Figure 3.101 Comparisons of the DYNTECC Parallel Compressor Model Loss in Stall Pressure Ratio to Those Observed Experimentally [3.75]**



In general, the **parallel compressor model** under predicted the effects of the 180° circumferential distortion by as little as 0.5% at 100% speed to as much as 2% at 93% speed in stall pressure ratio loss as indicated in **Figure 3.101**. The trends provided by the **parallel compressor model** were consistent with those observed experimentally and again provides a good validation of the model.

The **parallel compressor model** was also validated for tip radial distortion since that type of distortion has been observed on the J85 during the flight tests. In general, tip radial pressure distortion has little effect on overall compression system stability limit as reported by Calogeras in **Ref. 3.73**. When the **parallel compression system model** was executed with a similar level of tip radial pressure distortion, it too produced little effect on the overall stability limit. It should be noted that there was no attempt to redistribute the flow radially due to radial distortion.

### **ADDITIONAL REFERENCES**

**3.66** Wimer, R. & Hall, A., "Computer Modeling to Solve Problems with the T-38 Propulsion Modernization Program", Paper/Presentation Presented on October 25, 2007 at the NDIA 10<sup>th</sup> Annual System Engineering Conference.

**3.67** Leyes, R. A., The History of North American Small Gas Turbine Aircraft Engines, Chapter 6, General Electric Small Aircraft Engine, "The J85 Turbojet Engine", AIAA Library of Flight Series, 1999, pp. 261-279

**3.68** Hale, A. A. and M. W. Davis, Jr., "DYNamic Turbine Engine Compressor Code: DYNTECC -- Theory and Capabilities", AIAA Paper # AIAA-92-3190, Presented at the 28th Joint Propulsion Conference and Exhibit, Nashville, TN, July 1992.

**3.69** Davis, M. W., Jr., "Parametric Investigation into the Combined Effects of Pressure and Temperature Distortion on Compression System Stability", AIAA Paper # AIAA-91-1895, Presented at the 27th Joint Propulsion Conference, Sacramento, CA, June 1991.

**3.70** Shahrohi, K. A., and M. W. Davis, Jr., "Application of a Modified Dynamic Compression System Model to a Low-Aspect Ratio Fan: Effects of Distortion," AIAA-95-0301, Presented at the 33rd Aerospace Science Meeting, Reno, NV, January 1995.

**3.71** Milner, E. J., "Analytical Prediction of the Performance and Stability of a J85-13 Compressor with distorted Inlet Flow", NASA TM X-3515, May 1977.

**3.72** Tesch, W. A., & Steenken, W. G., "Blade Row Dynamic Digital Compression Program – Volume I: J85 Clean Inlet Flow and Parallel Compressor Models", NASA CR-134978, March 1976.

**3.73** Calogeras, J. E., Mehlic, C. M., & Burstadt, P. L., "Experimental Investigation of the Effect of Screen-Induced Total Pressure Distortion on Turbojet Stall Margin", NASA TM X-2239, March 1971.

**3.74** Mehlic, C. M., & Lottig, R. A., "Stead-State Inlet Temperature Distortion Effects on the Stall Limits of a J85-GE-13 Turbojet Engine", NASA TM X-2990, February 1974.

**3.75** Braithwaite, W. M., Graber, E.J., & Mehlic, C., M., "The effects of Inlet Temperature and Pressure Distortion on TurboJet Performance" NASA TM X-71431, November 1973.

**3.76** SAE S-16 Committee, ARP 1420, Revision B,"Gas Turbine Inlet Flow Distortion Guidelines," Society of Automotive Engineers, February 2002.

**3.77** SAE Aerospace Information Report AIR-1419, "Inlet Total-Pressure Distortion Considerations for Gas Turbine Engines," May 1983.



### 3.2.2 Inlet Total Pressure Distortion--TEACC--Validation of a High Fidelity Technique

Modern high-performance military aircraft are subjected to rapid flight maneuvers which place great operational demands on their air-breathing gas turbine engines. One component of the engine that is particularly sensitive to the fluid dynamic transients that result from rapid aircraft maneuvers is the compressor. The compressor should operate in a stable manner during all aspects of flight. However, rapid flight transients cause the inlet to produce a highly distorted total pressure flow field to the compressor inlet. High distortion levels may cause the compressor to surge at high rotational speeds or slip into rotating stall at lower rotational speeds [3.85]. Since total pressure distortion is one of the primary reasons for reaching the engine stability limit, its effects on system performance and operability need to be understood.

Distortion imposed on a circumferentially swirling flow was shown to have a three-dimensional (3D) nature which is fundamental to the development of both inlets and compressors. Design or analysis engineers are interested in understanding the details of the flow field to determine the effects of inlet total pressure distortion on the compressor. One way to quantify the effects of distortion is to test for that effect in a ground test facility. Currently, the inlet and engine are tested separately. Typically, the aircraft fuselage is too big to fit in a wind tunnel. A forebody simulator is used in conjunction with the inlet to characterize its flow field. The forebody simulator is designed to produce a flow field at the inlet reference plane (IRP) similar to the flow field produced by the aircraft.

Parallel compressor theory has been used successfully to develop an understanding of compressor performance with inlet distortion. Parallel compressor theory models the compressor with multiple circumferential segments and a uniform exit back boundary condition. Parallel compressor theory is restricted to simple inlet distortion patterns and is consistently conservative at estimating the stability limit. There is a need for a 3D compression system to investigate the effects of complex inlet distortion on a high speed compression systems.

#### CITED EXAMPLE(S)

**3.78** Hale, A. A., "A Three-Dimensional Turbine Engine Analysis Compressor Code (TEACC) for Steady-State Inlet Distortion." Ph.D Dissertation, Virginia Polytechnic Institute and State University, Blacksburg, VA, 1996.

**3.79** Hale, A. A., and W. F. O'Brien, "A Three-Dimensional Turbine Engine Analysis Compressor Code (TEACC) for Steady-State Inlet Distortion," Journal of Turbomachinery, Vol. 120, July 1998, pp. 422-430.

**3.80** Hale, Alan, Chalk, Jacqueline, Klepper, Jason, and Kneile, Karl, "Turbine Engine Analysis Compressor Code, Part II: Multi-stage Compressors and Inlet Distortion", AIAA-99-3214, July 1999.

#### MODELING TECHNIQUE

A numerical simulation of inlet distortion has been developed and is called the Turbine Engine Analysis Compressor Code (TEACC, [Section 4.7](#)). TEACC ([Figure 3.102](#)) solves the compressible three-dimensional (3D) Euler equations over a finite-volume grid domain through each blade row. The Euler equations are modified to include turbomachinery source terms which model the effect of the blades. The turbomachinery source terms are bleed, blade forces in the three Cartesian directions, and shaft work. The source terms are calculated for each

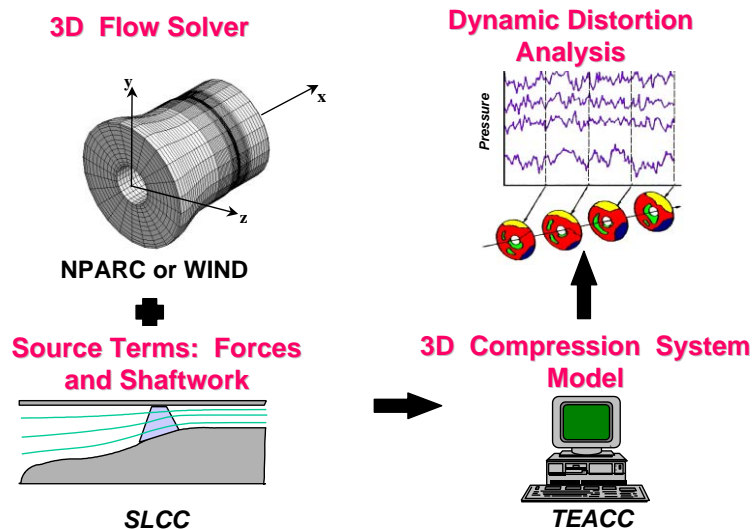


**Figure 3.102 Overall TEACC Approach**

system with a thorough analysis of clean and distorted inlet. Rotor 1B is a high-performance transonic rotor similar to those found in modern high-speed aircraft. The rotor was designed with a multiple circular-arc blade shape which was applied over the top 40 percent of the blade while a double circular-arc construction was employed for the bottom 60 percent of the blade. With a hub-to-tip ratio at the rotor inlet of 0.5, the blade sections were long enough to require a mid-span damper to maintain structural integrity during operation. Rotor 1B consisted of 44 blades, producing a moderate solidity of 1.3 at the rotor tip.

### Clean Inlet Validation of TEACC

**TEACC** was tailored to simulate Rotor 1B by calibrating the streamline curvature code (**SLCC**) used to calculate the turbomachinery source terms. The calibration was done by specifying a radial distribution of loss and exit relative flow angle from experimental data as a function of corrected mass flow and by specifying a radial distribution of blockage as a function of corrected mass flow. Calculated overall total pressure map of Rotor 1B with a clean inlet is presented in

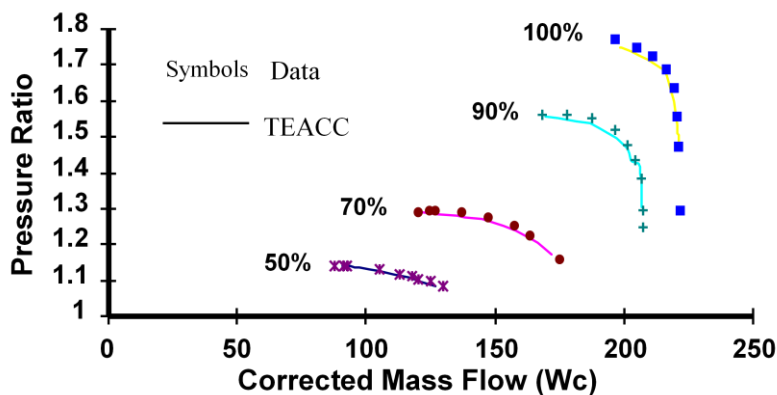


**Figure 3.103 Clean Inlet Overall Pressure Ratio Compared with Experimental Data**

circumferential grid section of each blade row by the application of a streamline curvature code. A methodology was developed for distributing the turbomachinery source terms axially, radially, and circumferentially through the bladed region. The following application was done for validation purposes of the technique.

### APPLICATION TO A SINGLE ROTOR, R1B

Rotor 1B [3.81] was chosen as the validation vehicle because it offered simplicity in the number of stages (1 blade row), and it represented a compression

**Figure 3.103** and compared with experimental data. Four corrected speeds (50, 70, 90, and 100 percent) were available for comparison, with symbols presented for the experimental data and lines for the **TEACC** solution. In an overall sense, there is good comparison between **TEACC** and data. The maximum percent difference in total pressure ratio is less than 1-percent difference for each characteristic.

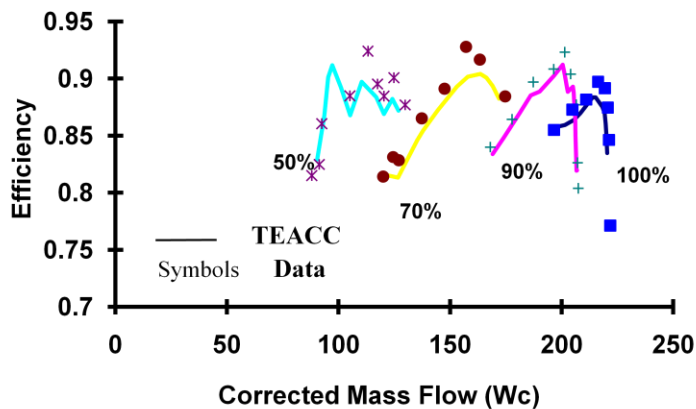


**Figure 3.104 Clean Inlet Efficiency Compared to Experimental Data**

**TEACC's** overall efficiency calculations for Rotor 1B are compared with experimental data in [Figure 3.104](#). The overall shape and character compares well with the experimental data. Each efficiency curve has a peak value which **TEACC** fails to reach, causing a maximum percent difference (for all speeds) between **TEACC** and experimental data of -2.9 percent occurring at the 50 percent corrected speedline.

#### Radial Comparison of TEACC with Data -- Clean Inlet

A radial comparison was made with exit total pressure and total pressure ratio as presented in [Figure 3.105](#) for the 100-percent speed point near the design throttle line. The overall shape is quite complicated for total pressure, increasing from hub to tip with the hub calculations deviating the most from experimental data by -1.34 percent. The tip and overall shape are in good agreement with the experimental data. The total pressure ratio is compared with data in [Figure 3.105](#), where a wide radial range in total pressure ratio can be seen. There is good agreement (1.0 percent difference) between **TEACC** and the experimental data.

The exit static pressure and exit Mach number consistently support the strong distribution in total pressure ratio. As shown in [Figure 3.105](#), the exit Mach number and the exit static pressure are in good agreement with the experimental data, and the exit Mach number is fairly uniform, but the exit static pressure varied consistent with the exit total pressure. The largest difference for both exit Mach number and exit static pressure with experimental data is at the tip, where Mach number is underpredicted by 2.7 percent and static pressure is overpredicted by 1.9 percent. The **SLCC** operates in the relative reference frame where the relative Mach number was observed to be transonic. The **TEACC** simulation remains in the absolute reference frame where Mach number remained subsonic.

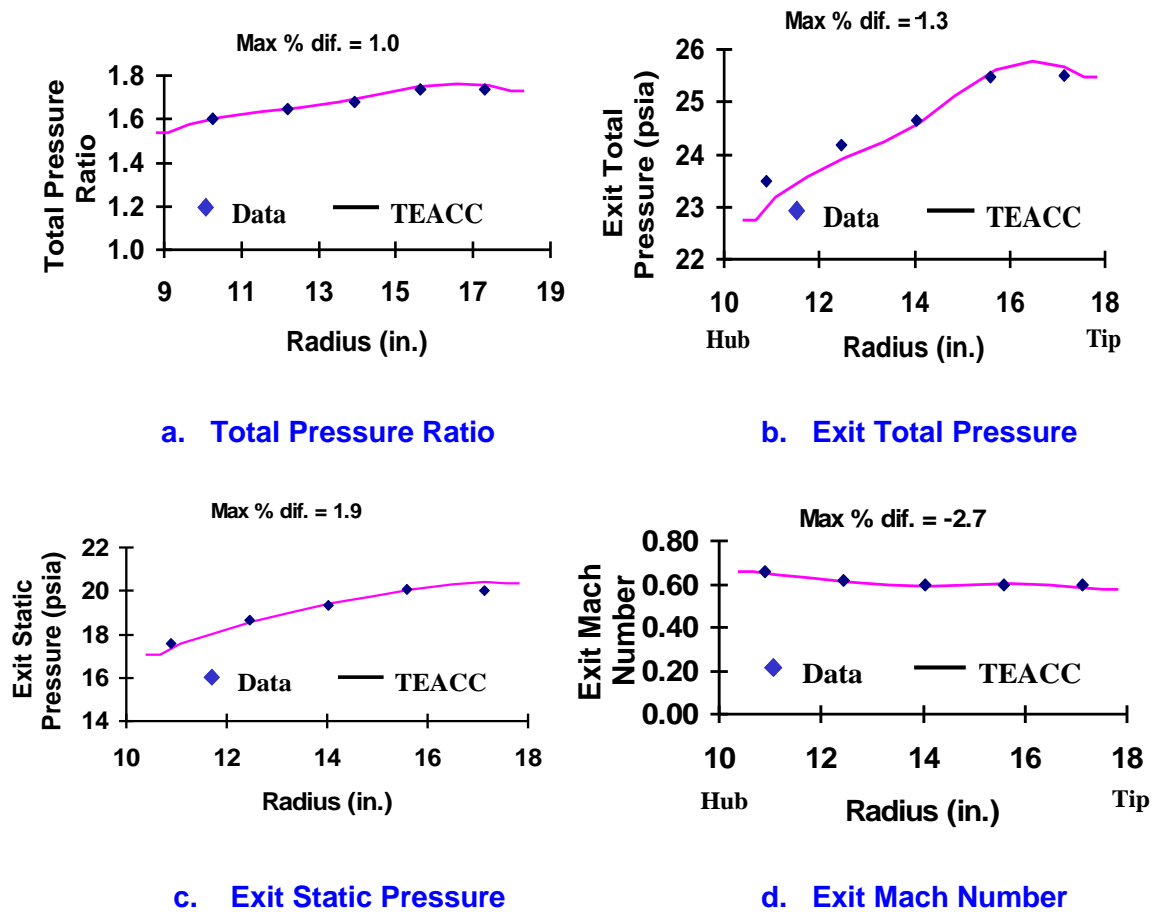
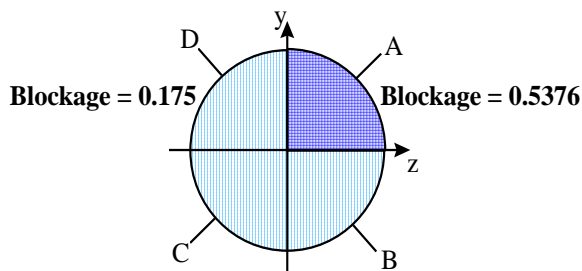


Figure 3.105 Clean Inlet Radial Comparisons

### Distorted Inflow Validation of TEACC

Rotor 1B was tested with an inlet screen to quantify the effects of inlet flow distortion on its performance. Because the distortion data provided with Rotor 1B was based on a  $90^\circ$ , one-per-revolution screen, a simulation of the screen was used in the **TEACC** simulation. For this study, **TEACC** was compared at three different corrected speedlines for a distorted inlet. A single distortion point on the 100-percent speedline was investigated in great detail because radial and circumferential data were available. Overall performance of the distorted compressor is compared to experimental data as well as radial and circumferential distributions.

**Distortion Screen Modeling.** To model the distortion screen, the porous wall boundary condition was used. The boundary condition is semi-empirical in that experimental data has been taken across a variety of screens to establish a loss in total pressure as a function of Mach number, porosity, and Reynolds number. The value of total pressure at the exit of the screen was calculated from the continuity, energy equations (total enthalpy equal to a constant), and an empirical pressure loss coefficient. This general technique to simulate the effect of a distortion screen was incorporated for all inlet distortion calculations.



**Figure 3.106 Screen Location and Labeling**

The compressor rotates clockwise, causing air to swirl in the direction of increasing quadrant letter (A, B, C, and D).

A single screen with a  $90^\circ$ , one-per-revolution pattern was designed to give a classical circumferential inlet total pressure inlet distortion to Rotor 1B. At the 100-percent speed, the experimental data showed that the screen produced a total pressure loss of 15 percent from the clean inlet which was duplicated for the **TEACC** simulation. Investigations were conducted through the middle of the four circumferential quadrants where the experimental data was taken. The screen was located in quadrant A (**Figure 3.106**).

### Overall Rotor 1B Performance Comparison –Circumferential Distortion

An overall total pressure ratio performance map for Rotor 1B is presented in **Figure 3.107** for three corrected speeds of 50, 70, and 100 percent. The clean speedlines are presented to give a proper orientation of the distorted data, with stall depicted for each speedline at its lowest corrected mass flow rate. A conservative, but simple, stalling criterion was imposed on the **TEACC** simulation. When any one of the circumferential segments acquired a corrected mass flow which exceeded stall for the clean inlet, the compressor was considered stalled. Likewise, the **TEACC** simulation was halted when any one of the circumferential segments exceeded the clean inlet data on the choked end of the speedlines. These two restrictions define the distortion calculation limits presented for each speed in **Figure 3.107**.

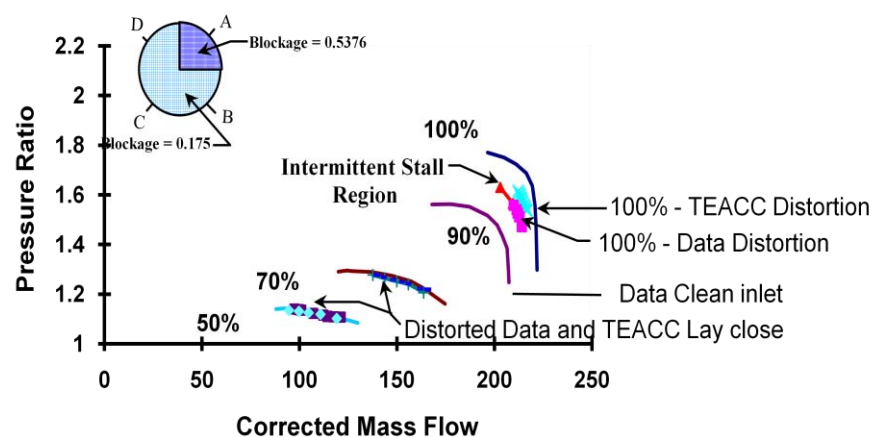


**Figure 3.107 Distorted inlet, Overall Performance Map with Total Pressure Ratio at 100% Corrected Speed.**

remained stable with the imposed inlet distortion screen. The **TEACC** simulation predicted the corrected mass flow rate differently from reported experimental data by a maximum of 3

For the two low-speed cases, the clean and distorted data lay close together. The extent in corrected mass flow rate is about the same for the simulation and the experimental distortion data. The maximum percent difference between **TEACC** results and experimental data at the lower speeds was approximately 2 percent. The 100-percent speed is more interesting because the experimental data presented a region where the compressor intermittently stalled or

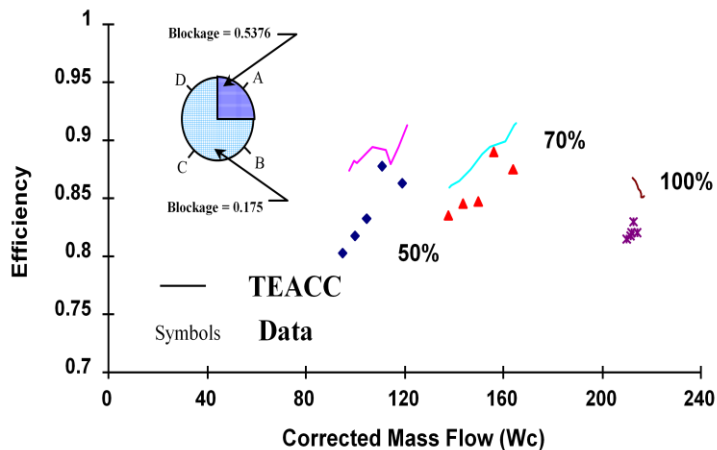


**Figure 3.108 Distorted Inlet Overall Performance Map with Efficiency at 100% Corrected Speed.**

difference between **TEACC** results and data are 6.9, 4.5, and 5.9 percent difference for 50-, 70-, and 100-percent speeds, respectively.

### Radial Comparison of Compressor with Experimental Data -- Distorted Inlet

This investigation now turns to an examination of **TEACC** results compared to experimental data behind the compressor. Exit total pressure (defined by the ratio of exit total pressure over the average screen inlet total pressure) versus compressor radius is presented and compared to experimental results in **Figure 3.109**. Pressure ratio is characterized by a division between

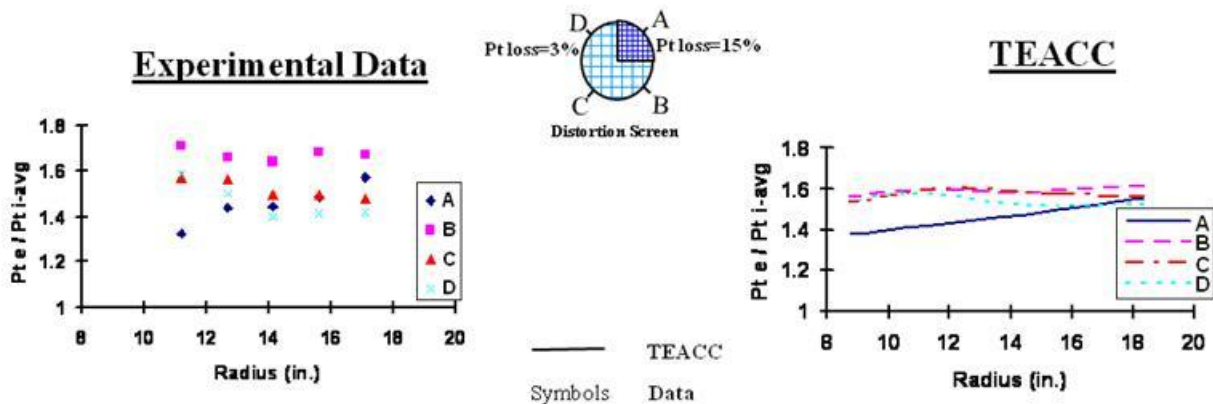


**Figure 3.109 Distorted Inlet Exit Total Pressure on 100% Speedline**

Quadrant A and the other three quadrants. **TEACC** does a good job of matching the character of the exit total pressure in Quadrant A with experimental data. **TEACC** results agree with the experimental data in the general character of the other three quadrants and identifies Quadrant B with the largest exit total pressure. The experimental data also confirms the **TEACC** results and shows that exit total pressure decreases steadily from Quadrant B to Quadrant D. Although the shapes of the other three quadrants are moving in the correct direction, the extent and scatter with pressure ratio is missing. The **TEACC** results in Quadrant A compare well to the



experimental data, except for the hub point, which causes the maximum percent difference with pressure ratio equal to 6.15 percent. **TEACC** results compared to experimental data are too low for Quadrant B (6.82 percent) and too high for Quadrants C (5.86 percent) and D (8.64 percent). The highest maximum percent difference is within 8.7 percent in Quadrant D.

The final comparison with experimental data is also behind the compressor (same reference location as exit total pressure). The ratio of total temperature at the compressor exit divided by the average total temperature at the screen inlet is compared to experimental data with data presented in [Figure 3.110](#). Quadrant A is again characterized as having a greater slope than the other three quadrants, and **TEACC** does a good job identifying this overall flow character. **TEACC** correctly identifies that, in the non-distorted region, the exit total temperature was the highest in Quadrant B, with the other quadrants decreasing in value from Quadrants B-D. **TEACC's** calculations for the total temperature at the compressor exit have a greater spread in Quadrants B-D than for the exit total pressure. Comparisons also show that the hub of Quadrant A is not as steep a slope as the experimental data, but the tip matches the data very well. Quadrants C and D match the data well, within 1.81 percent and 2.19 percent, respectively, and even Quadrant B matches the data well, except at a single tip point. The largest percent difference of **TEACC** with experimental data for exit total temperature is 6.60 percent.

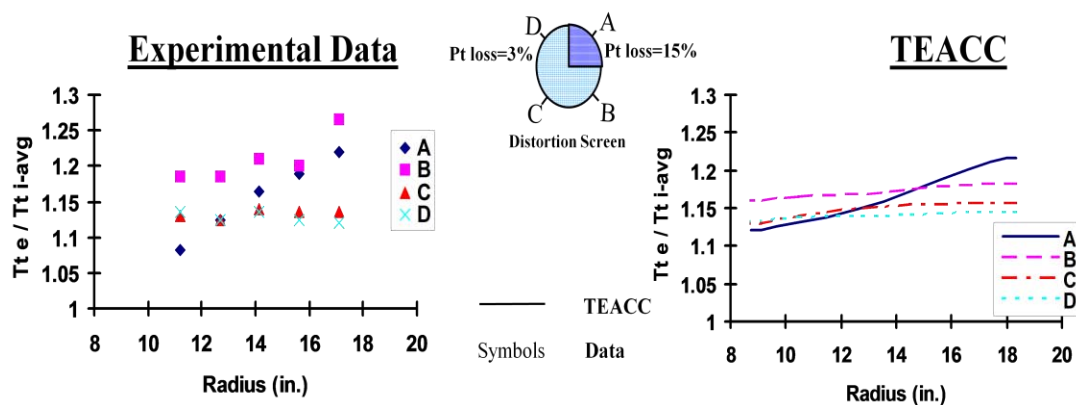


**Figure 3.110 Distorted Inlet Exit Total Temperature on 100% Speedline**

### Overall Rotor 1B Performance Comparison –Radial Distortion

Rotor 1B was tested with an inlet screen to quantify the effects of inlet flow distortion on its performance. The effects of circumferential and radial total pressure distortion were investigated. The radial distortion tests employed a radial screen that covered the outer 40-percent of the annulus. For the present study, **TEACC** was compared at three different corrected speed lines for a radially distorted inlet. A single distortion point on the 100-percent speed line was investigated in great detail. Overall performance of the distorted compressor is compared to experimental data as well as radial and circumferential distributions.

A coarse grid was used to model Rotor 1B. This grid, including the rotor location, is illustrated in [Figure 3.111a](#). As with the previously discussed grids, the stations in the circumferential

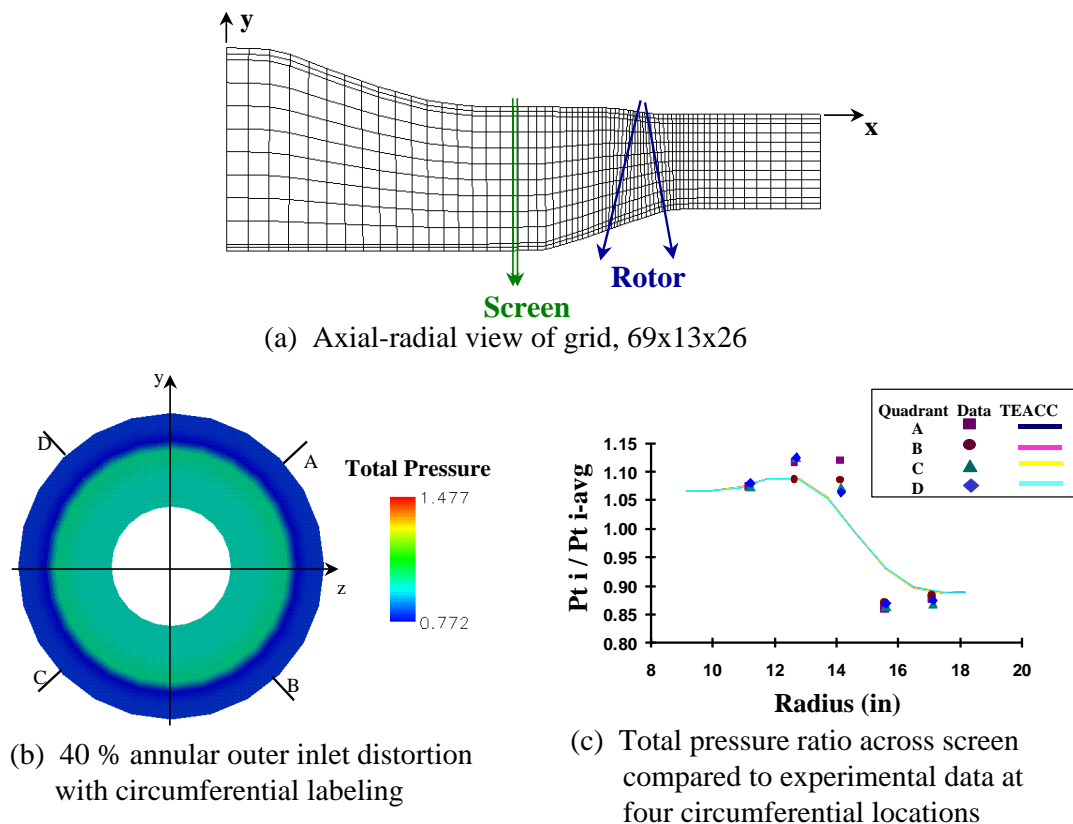


**Figure 3.111 Grid and Distortion Screen Modeling for Rotor 1B**

direction were comprised of equally-spaced  $15^\circ$  segments. A single screen covering the outer 40-percent of the compressor annulus was designed to give a classical radial inlet total pressure distortion to Rotor 1B. The location of this screen, relative to the rotor, is also denoted in [Figure 3.111a](#). At 100-percent speed, the experimental data showed that the screen produced a total pressure loss of 15% from the clean inlet, which was duplicated for the **TEACC** simulation. Investigations were conducted through the middle of the four circumferential quadrants where the experimental data was taken. The annular screen was the same for all quadrants ([Figure 3.111b](#)). The compressor rotates clockwise, causing air to swirl in the direction of increasing quadrant letter (A, B, C, and D). The radial characteristics of the distortion screen simulation compared with experimental data are illustrated in [Figure 3.111c](#). The character of the flow field behind the screen has certainly been captured. The individual pressure drops in each quadrant calculated by the screen-simulator are clustered together and represent the mean of the data. Some fidelity across the screen was lost due to the coarseness of the grid in the radial direction.

Like the fan and core, empirical loss and deviation correlations from open-literature were used to cross the bladed regions. Since the correlations are designed to be general, they may not accurately model all machines. For instance, because they were developed from earlier designs, the correlations may not accurately model more modern blade profiles. The correlations used in this research are for double-circular-arc and NACA 65-(A<sub>10</sub>) series blades. However, Rotor 1B has combination double-circular-arc/multiple-circular-arc profiles. In addition, these open-literature correlations are limited to performance away from choked

conditions. Furthermore, the correlations are un-calibrated for the clean and distorted inlet flow conditions.

Calculated overall pressure ratio and total temperature ratio for Rotor 1B with radial total pressure distortion is compared to experimental data in [Figure 3.112a](#) and [Figure 3.112b](#), respectively. Three corrected speeds (50-, 70-, and 100-percent) were available for comparison. The **TEACC** predicted values for total pressure ratio are typically higher than the data for all speeds, especially near choked conditions. However, the extent of corrected mass flow rate is similar between the simulation and the data. The deviation in total pressure ratio is explained by the fact that the **TEACC**-predicted clean inlet performance is also elevated. With respect to the predicted clean inlet, the distorted results have approximately the same delta as

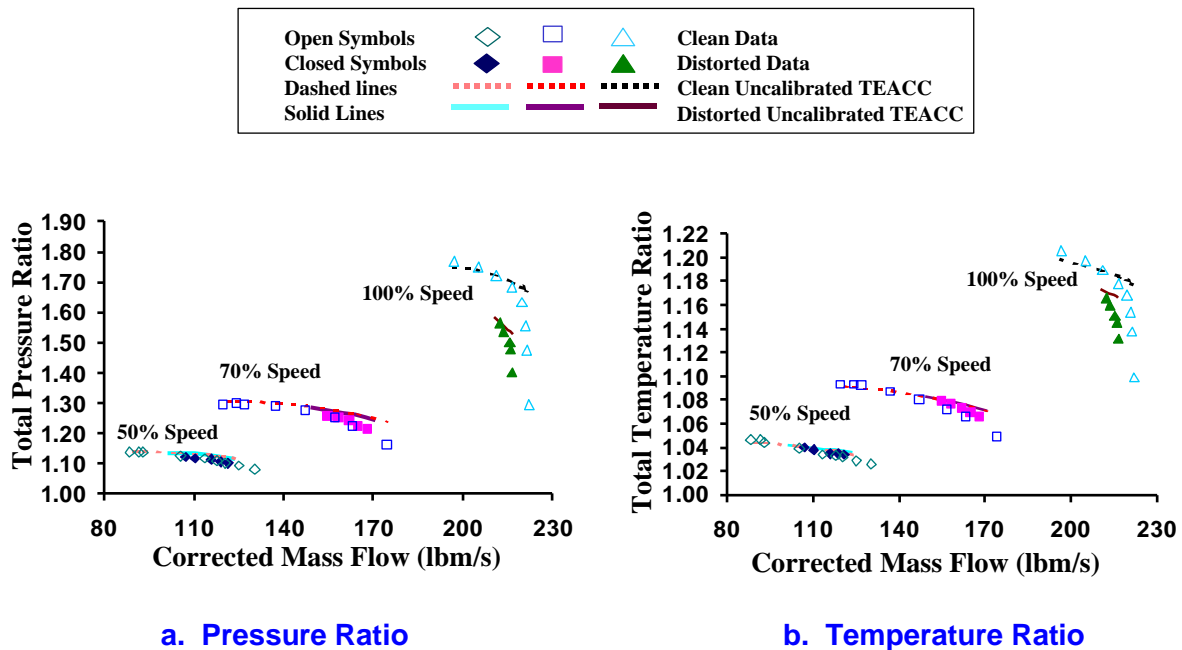


**Figure 3.112 Overall Performance Maps for Rotor 1B with Radial Inlet Total Pressure Distortion**

the distorted and clean experimental data. The trend in predicted total temperature ratio follows that of the total pressure ratio. As compared to data, **TEACC** typically over-predicts the overall total temperature ratio, but this is to be expected since it also over-predicts the clean inlet total temperature ratio.

The total pressure ratio (defined as the ratio of exit total pressure to the average screen-inlet total pressure) as a function of compressor radius is plotted in [Figure 3.113a](#). The total pressure ratio exhibits the same character in all quadrants. **TEACC** results match the character of the experimental total pressure ratio in all quadrants. Both **TEACC** results and data show that the exit total pressure increases from hub to tip. The maximum difference between **TEACC** results and experimental data in any quadrant is 2.7%. Total temperature ratio (total temperature at the compressor exit divided by the average total temperature at the screen inlet) as a function of radius is plotted in [Figure 3.113b](#).

The temperature ratio is practically identical in all quadrants. **TEACC** identifies the overall flow character, but the magnitude is slightly raised at the hub compared to the experimental data. All quadrants match the data within 1.8-percent.

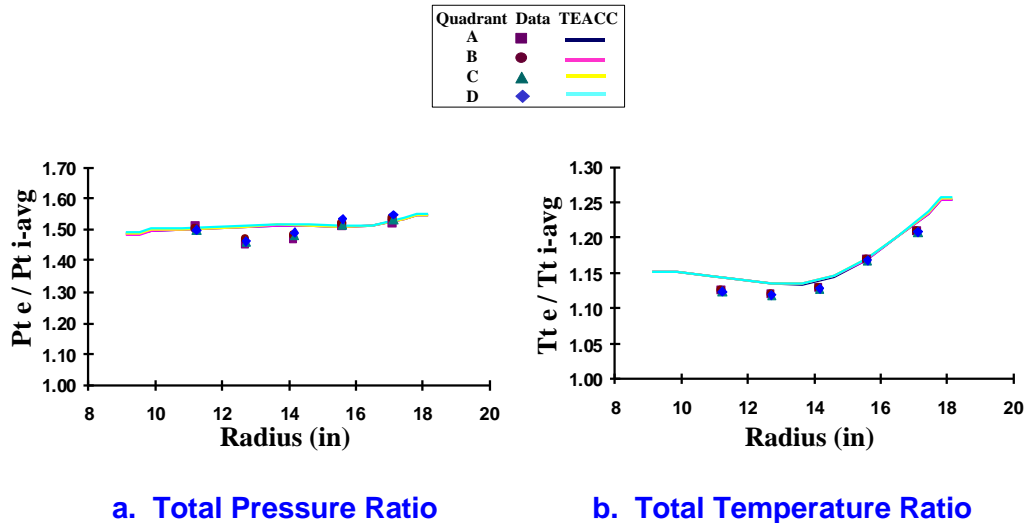


**Figure 3.113 Radial Comparisons of TEACC with Experimental Results for Rotor 1B with Radial Inlet Distortion at 100% Corrected Speed**

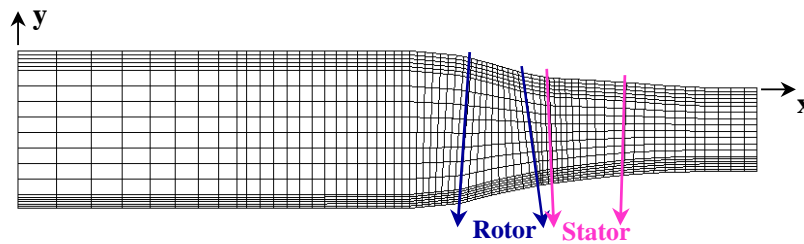
### **APPLICATION OF TEACC TO MULTIPLE BLADE ROW COMPRESSORS**

The expansion of **TEACC** from one blade row to multiple blade rows followed a logical progression. A single stage was modeled following the single-blade-row machine and the results were compared to experimental data. An analysis of a three-stage fan and a nine-stage high pressure compressor follows the single-stage model. The results for each of these cases are discussed in the following sections.

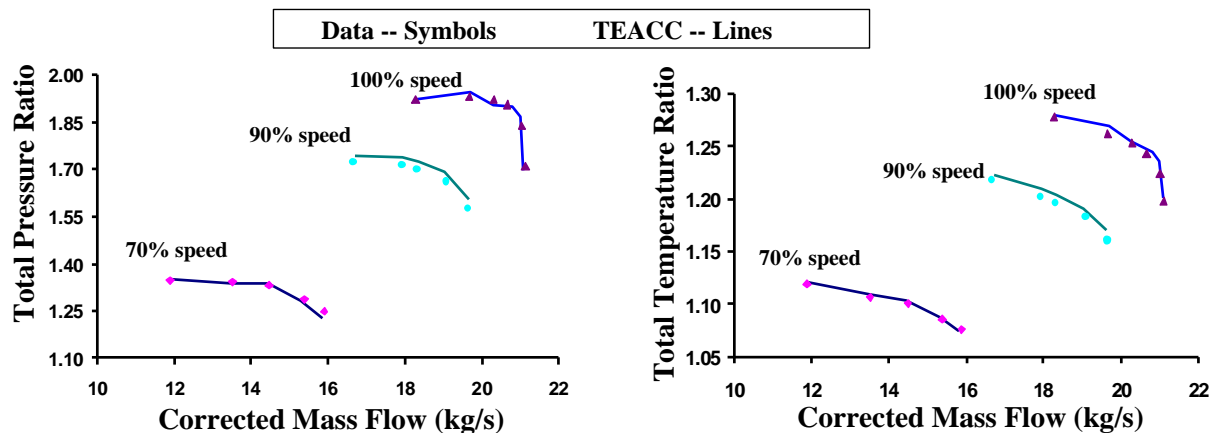
#### **Single Stage**

NASA Stage 35 [3.82] was the first multiple-blade-row machine modeled. Stage 35 is a single-stage, axial-flow transonic compressor designed in the mid-1970's as the first stage of a core compressor. It has two blade rows, comprised of highly loaded, low aspect-ratio blades with multiple-circular arc profiles. The rotor has a tip speed of 455 m/sec (1492 ft/sec) and a hub-tip ratio of 0.7. Stage 35 was designed to have a stage total pressure ratio of 1.82 at a mass flow of 20.2 kg/s (44.5 lbm/sec). Experience with other **TEACC** simulations suggest a relatively coarse grid could be used to model Stage 35 as shown in **Figure 3.114a**.

Loss and deviation correlations are needed to calculate the turbomachinery source terms in bladed regions using the streamline curvature code. For Stage 35, maps of radial distributions of loss and deviation data as functions of corrected speed and mass flow were used. Maps were used as a simple means to verify the modeling technique without the complexity and uncertainty of using correlations. Calculated overall total pressure ratio and total temperature ratio for Stage 35 with clean inlet conditions are compared to experimental data in **Figure 3.114b** and **Figure 3.114c**, respectively.



(a) Axial-radial view of grid, 69x20x26



(b) Total pressure ratio as a function of corrected mass flow

(c) Total temperature ratio as a function of corrected mass flow

**Figure 3.114 Grid and Overall Performance for Stage 35**

Three corrected speeds (70-, 90-, and 100-percent) were available for comparison. Symbols represent the experimental data, and lines denote the **TEACC** solution. The **TEACC** results compare well with the data for all speeds, with a maximum percent difference of 1.2-percent in overall total pressure ratio and 0.9-percent in overall total temperature ratio, both at 90-percent speed.

Radial comparisons of **TEACC** results and experimental data at 70% speed are presented in **Figure 3.115**. The exit total pressure of the rotor and the stator are shown in **Figure 3.115a**. The maximum percent differences in rotor exit total pressure and stator exit total pressure are 1.7% and 1.2%, respectively. **TEACC** over-predicts the exit total pressure at the tip for both blade rows. The values at the hub are slightly low compared to the data, but the overall shapes of the pressure profiles match the data for both blade rows. The exit static pressure of the rotor and the stator are plotted in **Figure 3.115b**. The rotor exit static pressure matches the data very well, except at the tip, where **TEACC** predicts a value about 1.2% below the data. **TEACC** predicts the exit static pressure of the stator within 1.1% of the data. Experience tells us that there should be a rise in static pressure at the tip, which has not been captured by the simulation. The absolute exit Mach number in **Figure 3.115c** further illustrates the failure of the tip to diffuse the flow properly. The static pressure is too low and the Mach number is too high near the tip of the stator. The total pressure ratio and total temperature ratio for rotor and stator are presented in **Figure 3.115d** and **Figure 3.115e**, respectively. The results for both blades

match the experimental data within 2.1% for total pressure ratio and 0.7% for total temperature ratio.

### Three-Stage Fan

The three-stage fan modeled in this effort represents a modern, high-performance military fan. It consists of a structural strut, a variable inlet guide vane (IGV) attached to the back of the strut, and three rotor/stator pairs. Unlike Stage 35, only overall experimental performance data were available for comparison; no blade-row by blade-row or radial distribution of flow quantities were available. As a result, only overall performance is compared with data. An axial-radial representation of the grid used for the three-stage fan is shown in [Figure 8a](#). The three-dimensional grid on which the flow field solution was obtained was uniformly spaced in the circumferential direction at 15-degree intervals.

The fan was executed with clean, standard-day inlet conditions. The results of the **TEACC** fan

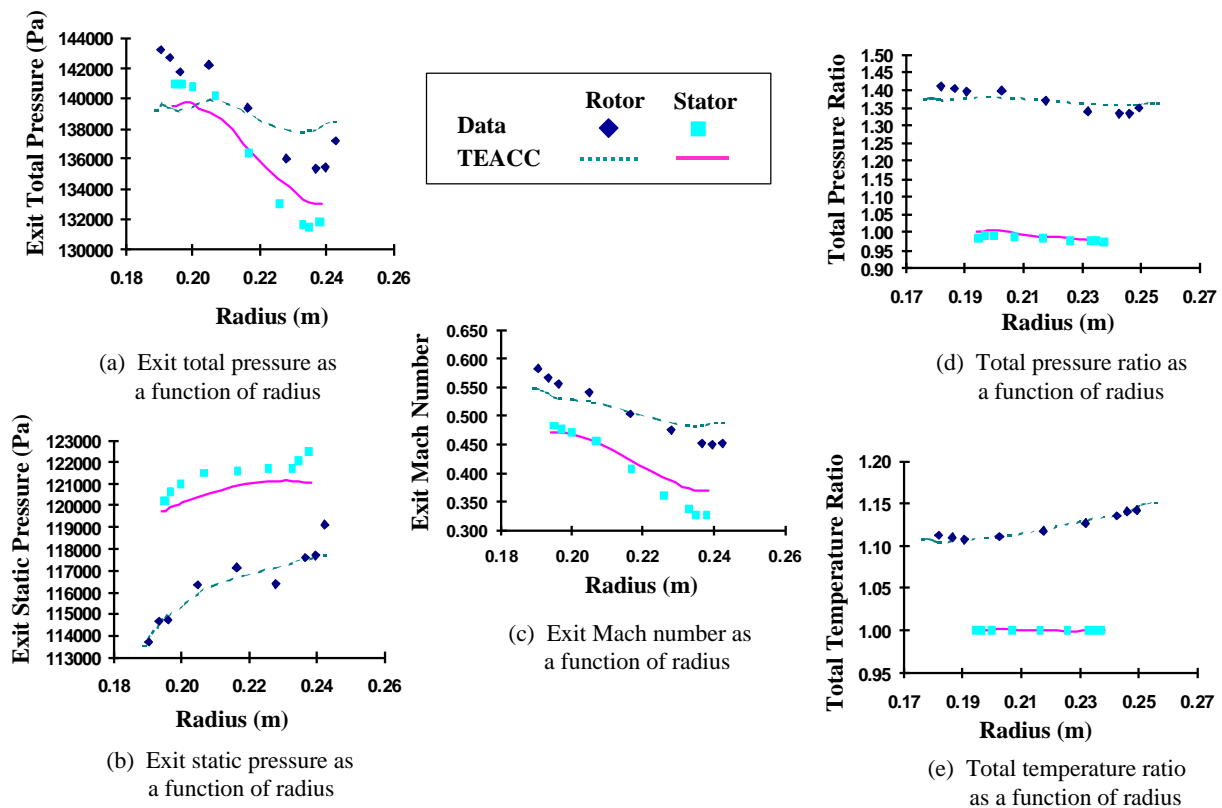


**Figure 3.115 Radial Comparisons of TEACC Results and Data for Stage 35 at 70% Corrected Speed**

simulation are at 68-percent of the design corrected mass flow on the 80-percent speed line. Both the normalized pressure ratio and the normalized temperature ratio achieved at this point were within 0.5-percent of the experimental data. These results were achieved with uncalibrated loss and deviation correlations obtained from the open literature [[3.83](#) & [3.84](#)]

Axial-radial slices of the normalized total pressure and normalized total temperature can be seen in [Figure 3.116b](#) and [Figure 3.116c](#), respectively. As expected, there is an increase in both total pressure and total temperature through the machine. [Figure 3.116](#) provides an



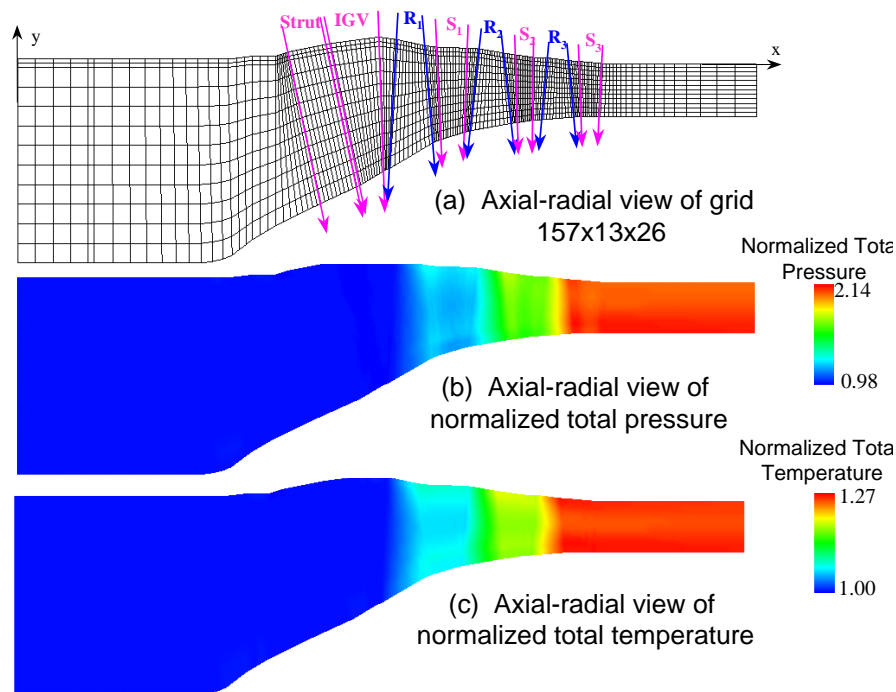
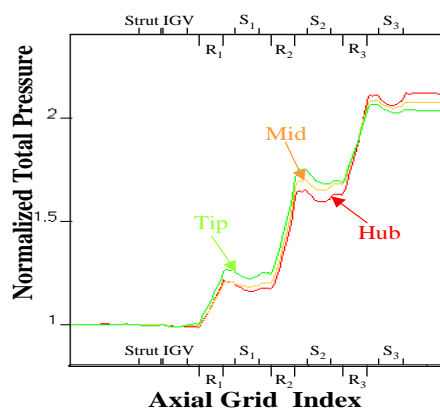


**Figure 3.116 Grid and Performance for Three-Stage Fan at 80% Corrected Speed**

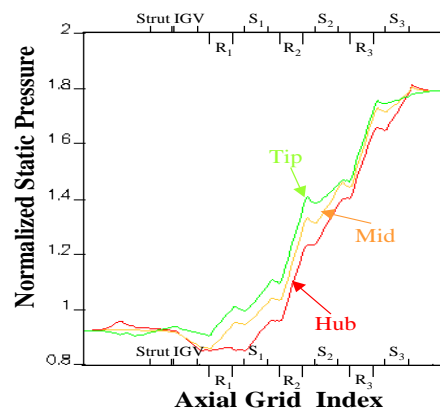
points can be seen in [Figure 3.116a](#). The pressure profiles at hub, tip, and mean are all shown in [Figure 3.117a](#). As expected, there is an increase in total pressure across each of the rotors, and a small decrease in total pressure across each of the stators. The total pressure is highest

insight into the general character of how the total pressure and temperature vary radially and axially throughout the machine.

[Figure 3.117](#) illustrates in much more detail the character of total and static pressure. [Figure 3.117a](#) shows the normalized total pressure as a function of axial station. This figure is presented with the axial grid points equally spaced for ready comparison of the hub, mean and tip performance. In actuality, the axial stations are not equally spaced. The relative spacing of the axial grid



**a. Normalized Total Pressure**



**b. Normalized Static Pressure**

**Figure 3.117 Total and Static Pressure for Three-Stage Fan at 80% Corrected Speed**

at the tip and lowest at the hub through most of the fan. The normalized static pressure is illustrated in [Figure 3.117b](#). Again, the value of static pressure is typically highest at the tip

and lowest at the hub. It can also be seen, by the continual increase in static pressure, that the flow is being diffused in both the rotors and the stators. The rise in static pressure across the stators can be attributed to the fact that stators not only turn the flow to direct it to the next rotor, but also act as diffusers. Illustrated in **Figure 3.118** are streamlines, colored with Mach number, through the fan. This figure clearly illustrates the rotors turning the flow and the stators straightening the flow.

The total turning of the flow through the entire machine is about 45 degrees. The figure also demonstrates the increase in Mach number across the rotors and the decrease in Mach number across the stators. The maximum Mach number throughout the fan is achieved at the hub of the first rotor. This can be attributed to the flow being accelerated by the turning of the rotor and the large decrease in area occurring at the first rotor. The hub has the highest Mach number through the entire fan. The streamlines illustrate that the flow is almost completely axial at the exit of the fan.

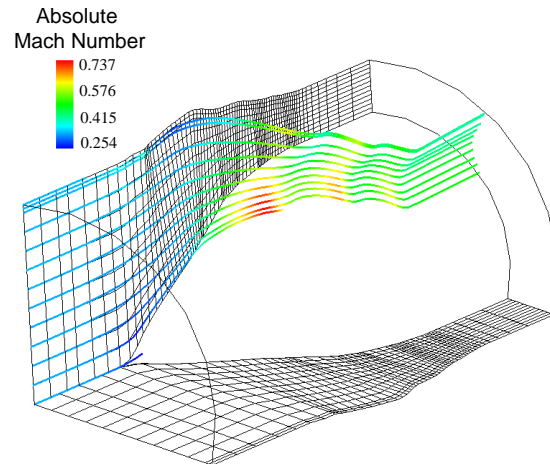


**Figure 3.118 Mach Number Associated Streamlines for the Three-Stage Fan at 80% Speed**

### Nine-Stage High-Pressure Compressor

The nine-stage high-pressure compressor, HPC, simulated in this paper is representative of a modern high-performance, military high-pressure compressor. It consists of a variable IGV followed by nine rotor/stator pairs of which the first three stators are variable. As with the fan presented above, the only data available for comparison was overall performance data; no blade-row by blade-row or radial distributions of data were available. Therefore, only overall performance was compared. **Figure 3.119a** shows an axial-radial depiction of the core grid geometry. As was the case with the three-stage fan, the grid for HPC was uniformly spaced in the circumferential direction at 15-degree intervals.

Although the HPC normally operates behind a fan, with the inlet total temperature and total pressure above standard-day conditions, for this simulation the HPC operated with clean inlet, standard-day conditions. The point used in the presentation is a typical point on the 90-percent speed line at a mass flow of 69-percent of the design corrected mass flow. The simulation results differed from experimental data by approximately 5% for normalized total pressure ratio and 3% for normalized total temperature ratio. The difference between the **TEACC** solution and experimental data can be attributed to the un-calibrated, open-literature correlations used in this simulation. The same correlations discussed for the fan were used in simulating the core.

Axial-radial slices of the normalized total pressure and normalized total temperature for the HPC are shown in **Figure 3.119b** and **Figure 3.119c**, respectively. As expected, both total pressure and total temperature increase through the machine. To verify correct operation, a closer examination of total pressure and static pressure was performed.

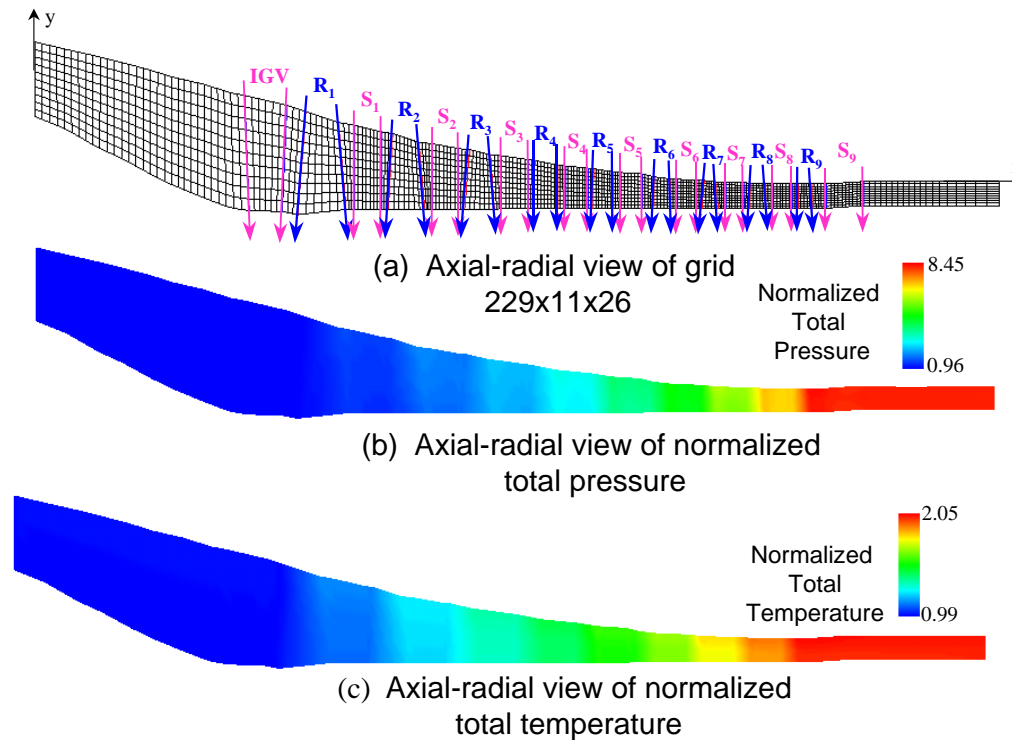


**Figure 3.119 Grid and Performance for Nine-Stage High-Pressure Compressor at 90% Corrected Speed**

**Figure 3.121a** shows the increase in the total pressure across the HPC as a function of axial station. As with the fan, the axial grid points in the figures are shown as equally spaced, but in reality, they are not. Again, the spacing between the axial grid points can be seen in **Figure 3.121a**. As expected, the total pressure increases across each of the rotors and slightly decreases across each of the stators. The tip consistently has a higher value of total pressure throughout the HPC. The normalized static pressure is shown in **Figure 3.121b** to continually increase throughout the machine. **Figure 3.121a** and **Figure 3.121b** show that the back half of the machine experiences a much greater increase in aerodynamic loading. This can be seen by the larger increases of both the total and static pressures across the last four rotors.

The fact that the static pressure rises almost linearly across the first five stages implies that the rotors and stators are diffusing the flow equally. **Figure 3.120** shows the streamlines colored with absolute Mach number for the nine-stage HPC. The turning of each of the rotors and flow straightening of each of the stators is illustrated in this figure. Compared to the fan, the HPC achieves much more flow turning. The fan turned the flow about  $45^\circ$ , while the core turns the flow more than  $100^\circ$ . The streamlines clearly demonstrate how the rotors turn the flow in the circumferential direction, while the stators turn the flow back toward the axial direction. Again, as with the fan, the flow is almost completely axial out the back of the HPC.

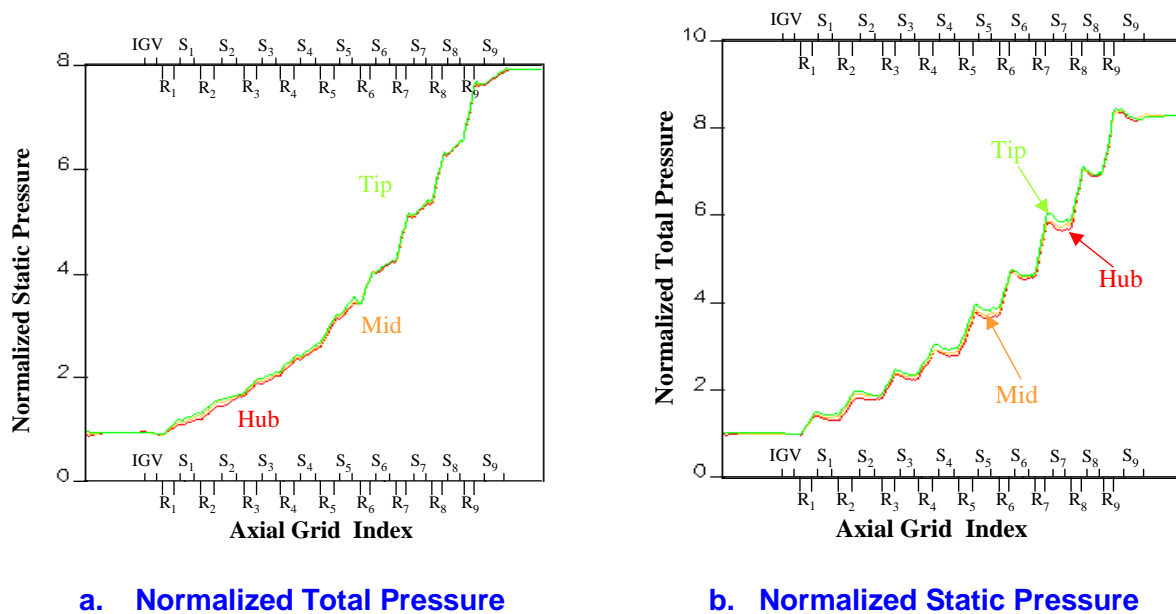


**Figure 3.121 Total and Static Pressure Profiles for a Nine-Stage High-Pressure Compressor at 90% Corrected Speed**

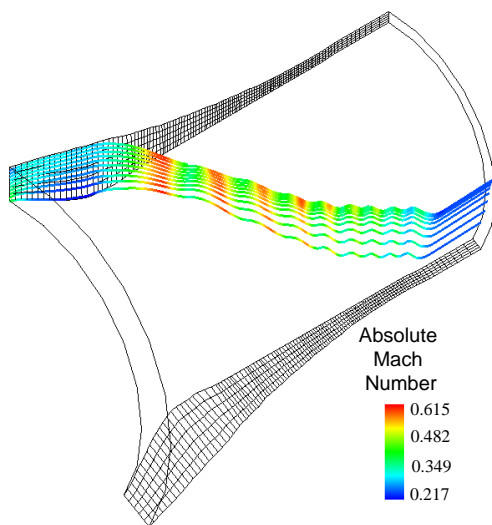


**Figure 3.120 Mach Number Associated Streamlines for the Nine-Stage High-Pressure Compressor at 90% Speed**

#### ADDITIONAL REFERENCES:

**3.81** Seyler, D. R. and Gestolow, J. P. "Single Stage Experimental Evaluation of High Mach Number Compressor Rotor Blading Part 2- Performance of Rotor 1B." NASA-CR-54582, September 1967.

**3.82** Reid, L. and Moore, R. D. "Design and Overall Performance of Four Highly Loaded, High-Speed Inlet Stages for an Advanced High-Pressure-Ratio Core Compressor." NASA-TP-1337, 1978.

**3.83** Lieblein, S. "Chapter VI: Experimental Flow in Two-Dimensional Cascades." Aerodynamic Design of Axial-Flow Compressors, NASA-SP-36, 1965, pp.183-226.

**3.84** Robbins, W. H., Jackson, R. J. and Lieblein, S. "Chapter VII: Blade-Element Flow in Annular Cascades." Aerodynamic Design of Axial-Flow Compressors, NASA-SP-36, 1965, pp. 227-254.

**3.85** SAE Aerospace Information Report AIR-1419, "Inlet Total-Pressure Distortion Considerations for Gas Turbine Engines," May 1983.

### 3.2.3 Inlet Total Pressure Distortion – TEACCSTALL, Higher Fidelity Simulation

During the development process of **TEACC**, it became obvious that some form of stall model or technique was going to be necessary for the determination of compression system instability. As **TEACC** moved from predicting system performance with inlet distortion, a primitive stall model based upon Diffusion Factor was first employed. The problem with this stall criteria was that one had to calibrate to a specific Diffusion Factor thus negating any predictive capability. The developers decided that a new formulation would be necessary that uses a form of 3D characteristic based upon CFD results would be necessary. After a thorough literature search, it was determined that an existing technique and code existed developed by Chima of NASA Glenn Research Center could be imported to AEDC and modified to provide a stalling criteria. Thus, was born **TEACCSTALL** which is heavily derived from Chima's **CSTALL** code [3.90]. Within a couple of months, the AEDC development team had **CSTALL** configured to applications of interest and modified to take advantage of both codes, **TEACC** and **CSTALL**. Without Chima's **CSTALL** code and his help, our efforts would have certainly taken at least a year to get to the same place as Chima **CSTALL** code provided us.

#### CITED EXAMPLE(S)

The HTSC effort cited in this example has not previously been published. The High Tip Speed Compressor (HTSC) has been previously used in other efforts by Gorrell, Sharokhi, and Hah [3.87, 3.88. & 3.89].

**3.86** Davis, Milt, et.al., “Demonstration of an Integrated Test and Evaluation (IT&E) Process for Airframe-Propulsion Systems as Applied to a Current Weapon System Program”, Presented at the 2010 AIAA Aerospace Sciences Meeting, January 2010.

#### MODELING TECHNIQUE

**TEACCSTALL** (Section 4.7) is converted from an Euler duct flow solver to a compressor simulation complete with stall prediction through the judicious use of source terms. The force of the simulated blades on to air is captured through the change in entropy and the flow turning through the bladed region. The dynamic effects of the blades moving in and out of distortion are accounted for with a 1<sup>st</sup> order lag equation. The thickness of the blades is accounted for through a blockage term and this term has the effect of accelerating the flow through the blades.

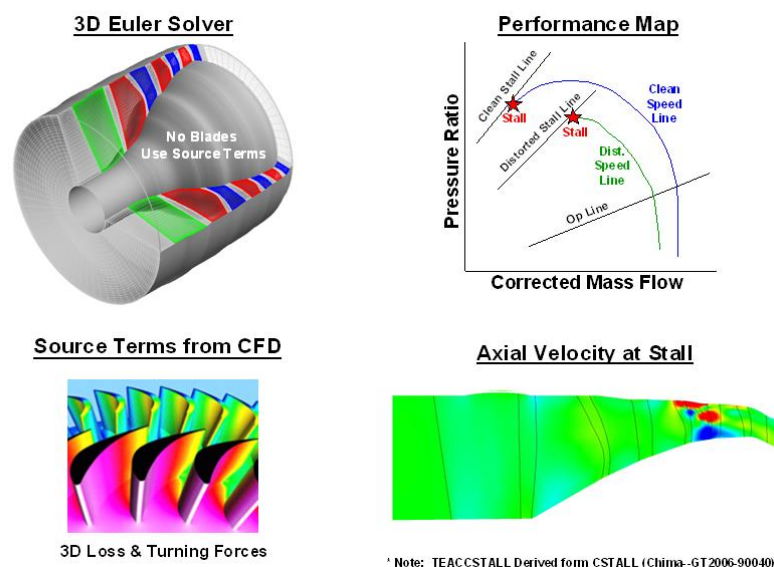


**Figure 3.122 TEACCSTALL Technical Approach.**

The operation of **TEACCSTALL** is represented in [Figure 3.122](#). The 3D Euler code solves the governing equations and represents the bladed regions with source terms. The source terms are provided by characteristics that come from a pre-processing step (usually radial distribution of CFD characteristics from a series of single passage clean inlet CFD solutions). The characteristics, along with the Euler solver give a time-accurate solution of the turbomachinery up through the stall inception point.

### APPLICATION TO THE HIGH TIP SPEED COMPRESSOR FOR VALIDATION

**TEACCSTALL** ([Section 4.7](#)) results are discussed in this section. **TEACCSTALL** has been applied to several different machines, including a single rotor, single stage, and multi-stage modern military fan. For this section, the application of **TEACCSTALL** to the High-Tip Speed Compressor (HTSC) is discussed. The HTSC is a two-stage, highly transonic fan design whose aerodynamic and aeromechanical characteristics are well documented with an extensive database of experimental measurements. Fan configuration has varied throughout the 15 years (and continuing) of experimental programs conducted at the Air Force Research Laboratory's Compressor Research Facility (CRF) – these include IGV/no IGV, swept/unswept, smooth tip casing/casing treatments.

### HTSC Description

[Figure 3.123](#) provides a schematic of the test setup and fan configuration used in the present work – no IGV, unswept rotor blades, and smooth tip casing. Design parameters of the first-stage rotor (R1) are summarized in [Table 3.4](#). Rotor 1, shown in [Figure 3.124](#), is a state-of-the-art, integrally-bladed disk (blisk), low aspect ratio design.

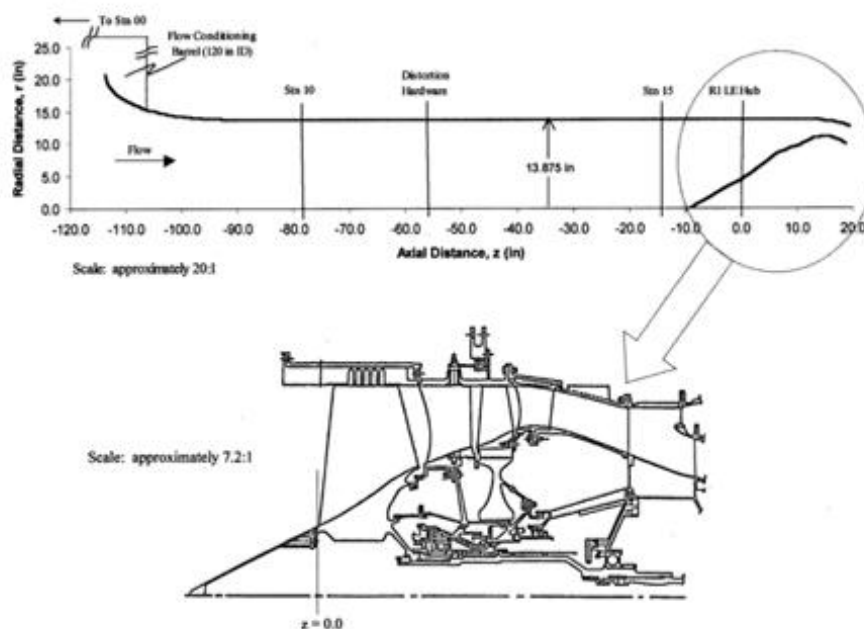


**Figure 3.123 HTSC Two-Stage Fan Schematic**



The variable first stage stator (S1) contains 41 vanes in an overlapped, tandem configuration - the forward section is fixed and the aft flap variable. The vanes of the S1 forward section are a bowed, swept design. Rotor two (R2) is a slot bladed disk containing 40 blades with tip solidity and  $(t/c)_{\max}$  very close to that of R1. Both rotors employ pre-compression tip section airfoils over the outer 30-40% span and tailored controlled diffusion airfoils (CDA) throughout the remainder of the blade. A view looking down the stacking axis of R1 is provided in [Figure 3.125](#). The pre-compression tip profile is clearly shown in [Figure 3.125](#) as is the hub section which turns the flow approximately 50 degrees. Stator two (S2) contains 60 vanes at fixed stagger and leaned counter to the direction of rotor rotation.

Parameter	Value
Aspect ratio (average span/hub axial chord)	1.0
Inlet radius ratio	0.33
Tip radius (ft)	1.16
Tip solidity	1.50
Tip $(t/c)_{\max}$	0.028
Tip speed (ft/s)	1609
Corrected flow (lbm/s)	158.6
Total pressure ratio	2.50
Adiabatic Efficiency	0.889
Corrected speed (rpm)	13,288

**Table 3.4 Design Parameters of the First-Stage Rotor**

The fan was extensively instrumented with 600-800 individual measurements taken, depending on the test program objectives. Only the measurements most pertinent to the present work are discussed here – refer to the individual references for additional details. The station references are those used by the Compressor Research Facility.

Inlet total temperature was measured with 49 thermocouples (station 00) located in the CRF



**Figure 3.124 HTSC First Rotor**

flow conditioning barrel about 13.5 feet upstream of the bellmouth inlet (see [Figure 3.123](#)). The bellmouth inlet (Stn 10) and distortion measurement plane (Stn 15) instrumentation are shown in [Figure 3.126](#) and [Figure 3.127](#), located about 78 and 14.5 inches, respectively, upstream of the R1 hub leading edge ([Figure 3.123](#)). The TT00 and station 10 measurements were used to calculate bellmouth mass flow rate. The total pressure transducers at station 15 were arranged in a typical pattern to determine distortion, as recommended by SAE AIR 1420 - eight rakes with five radially distributed measurements equally spaced around the circumference. Rotor exit total pressure and temperature measurements were made at the leading edges of both stators. As seen

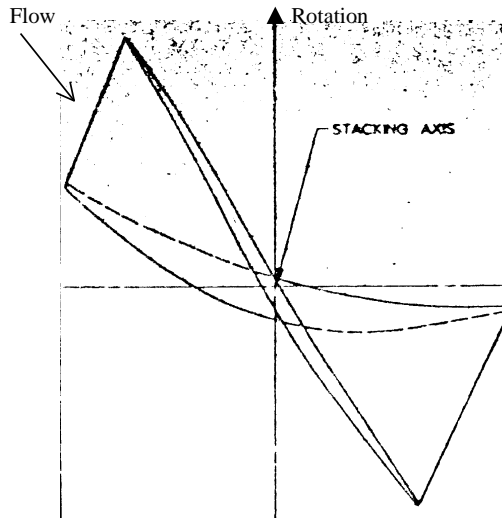


**Figure 3.125 Radial View of Rotor 1  
Showing Hub Section and Pre-  
Compression Tip Profile**

in **Figure 3.128** (representative of both S1 and S2), three stator vanes were instrumented at seven radial locations, approximately equally spaced around the circumference. Seven arc rakes, each containing 11 total pressure and temperature measurements (**Figure 3.129**), were used to obtain discharge measurements at 7 radial locations about one inch downstream of the stator two trailing edge. The rakes were designed to span two S2 passages to obtain wake-averaged calculations, ideal for the present application. These data, along with station 15 measurements, were used to determine overall machine performance. In all cases, area-averages were used to determine overall performance characteristics. Overall mass flow rate was calculated from venturi measurements located about 98 feet downstream of the fan. Hub and tip casing static pressure measurements were made at numerous axial locations through the fan.

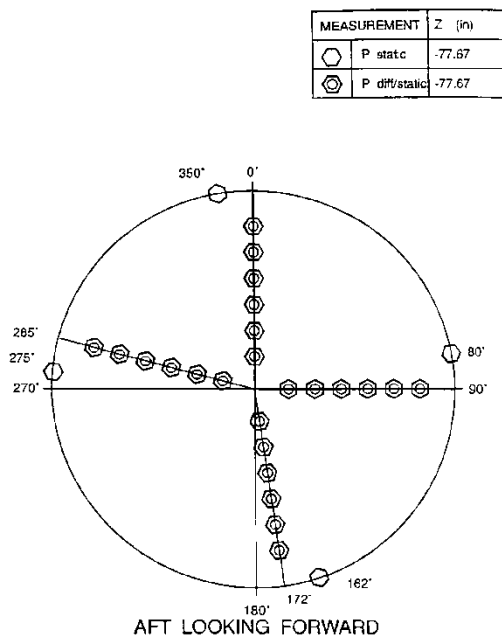


**Figure 3.126 CRF Inlet Station 10  
Instrumentation**

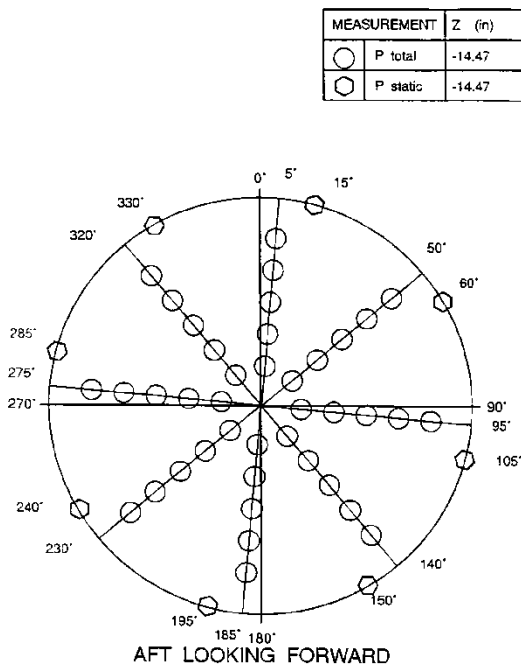


**Figure 3.127 CRF Distortion  
Measurement Station 15  
Instrumentation**

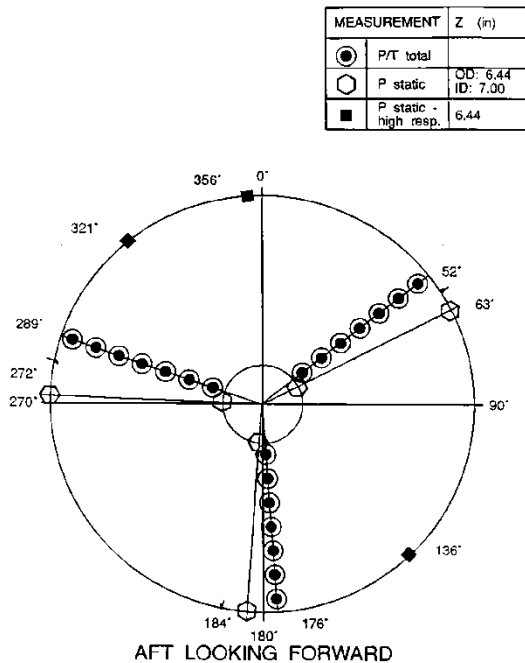
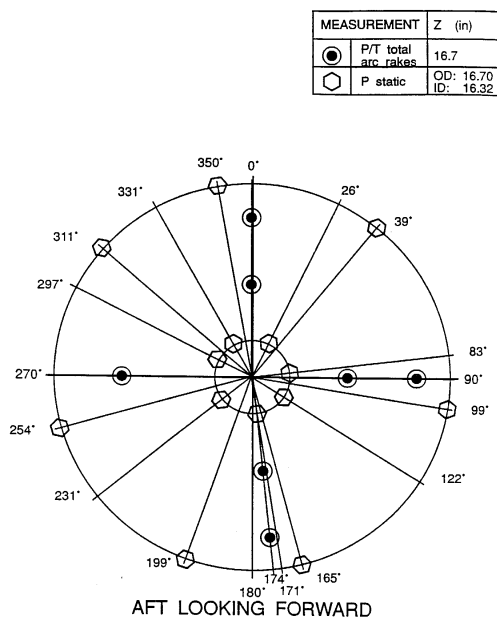


**Figure 3.128 Stator 1 Leading-Edge Instrumentation**

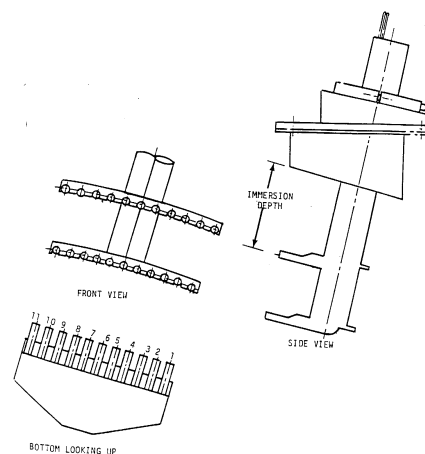
inlet total pressure to calculate the pressure ratio. After examining the data, the authors did not trust the inlet total pressure used, since the distorted total pressure ratio is higher and goes

Throughout its test history, this fan has been subjected to a variety of inlet distortion patterns – hub radial, tip radial, 1/rev, 2/rev, 3/rev, 8/rev – all generated by screens. As indicated in [Figure 3.123](#), distortion screen hardware was located approximately 56 inches upstream of the R1 hub leading edge. Hardware consisted of a one-inch square mesh backing screen used for mounting the different porosity screens of desired strength and pattern. Depending on the test program, the hardware was rotated – manually or remote automatically – to increase circumferential measurement resolution.

During HTSC testing, many configurations, speeds, and distortion patterns were tested. For this comparison of **TEACCSTALL** to data, only the 68.0% speed will be presented. Also, the only distortion pattern used in the comparison is the 180° circumferential pattern. The clean and distorted data points are shown in [Figure 3.130](#). To take the distortion data at 68.0% speed, the inlet total pressure rakes were removed. The CRF used a calibration to estimate the average



a. discharge instrumentation



b. arc rake schematics

**Figure 3.129 Fan Discharge Instrumentation**

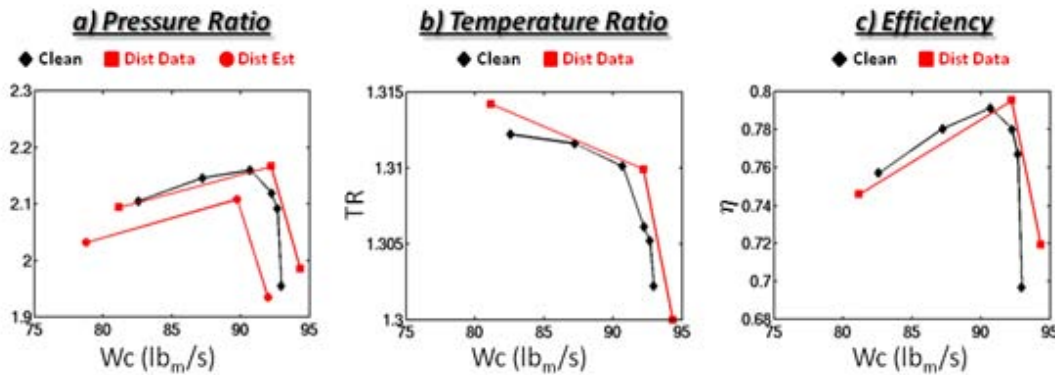


**Figure 3.130 HTSC Clean and Distorted Data Points for 68.0% Speed**

farther into choke than the clean at the same speed. This seems to not be possible. The inlet total pressure was adjusted in the pressure ratio and corrected mass flow calculations until the distorted choke point match the **TEACCSTALL** predicted choke point. The new estimated pressure ratio and corrected flow characteristic can be seen in **Figure 3.130a**.

To get the information needed to drive **TEACCSTALL**, the **SLCC** (**Section 4.3**) was calibrated to the radial data for the HTSC compressor at 68.0% speed. The SLCC solutions were then reduced down to the radial distribution of total pressure, total temperature, and velocity components at each of the mass flow points. **Figure 3.131** is the reduced non-dimensional

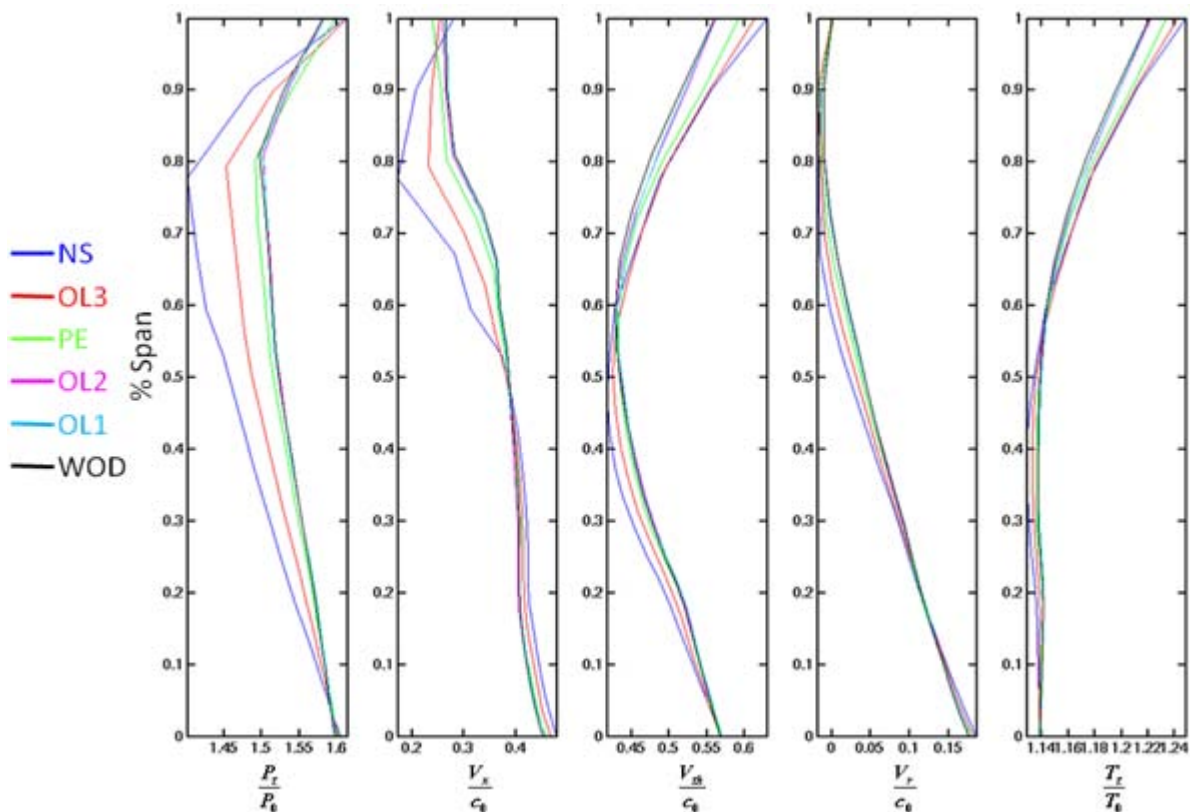


**Figure 3.131 HTSC Rotor 1 Non-Dimensional OSPAN File Data**

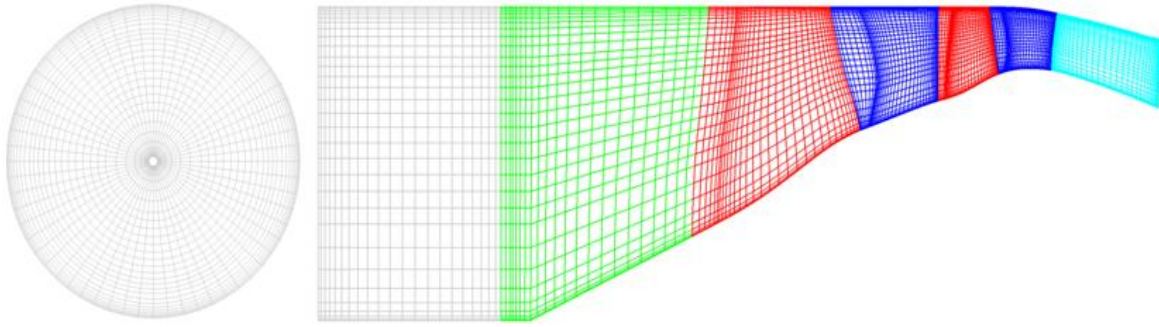


**Figure 3.132 Axisymmetric HTSC TEACCSTALL Grid**

SLCC solutions for Rotor 1. This is representative of the other blade rows in the HTSC. These are then used as the characteristic inputs to **TEACCSTALL** as the OSPAN file. The grid used to run the **TEACCSTALL** HTSC solutions is shown in **Figure 3.132**. The figure shows an axial-radial slice of each of the zones in the solution, along with a circumferential, radial slice to show the circumferential density. Overall, the grid is 7 zones with a total of 420,360 nodes. There are 62 circumferential stations and 30 radial stations in each zone.

The overall clean solution of **TEACCSTALL** is shown in **Figure 3.133**. This figure shows the overall 1-D total pressure ratio, temperature ratio, and efficiency including data, SLCC calibrated solutions, and **TEACCSTALL** solution. The **TEACCSTALL** solution was started at the steady-state choke point (WOD point) and ran time-accurately to stall inception by ramping the exit Mach number down until the machine stalled. **Figure 3.133** shows the **TEACCSTALL** predicted stall inception point that occurs at about 1.3% higher corrected mass flow than data. The **TEACCSTALL** characteristic follows closely the data characteristic for both total pressure and total temperature, with about a 0.4% error in temperature ratio at stall.

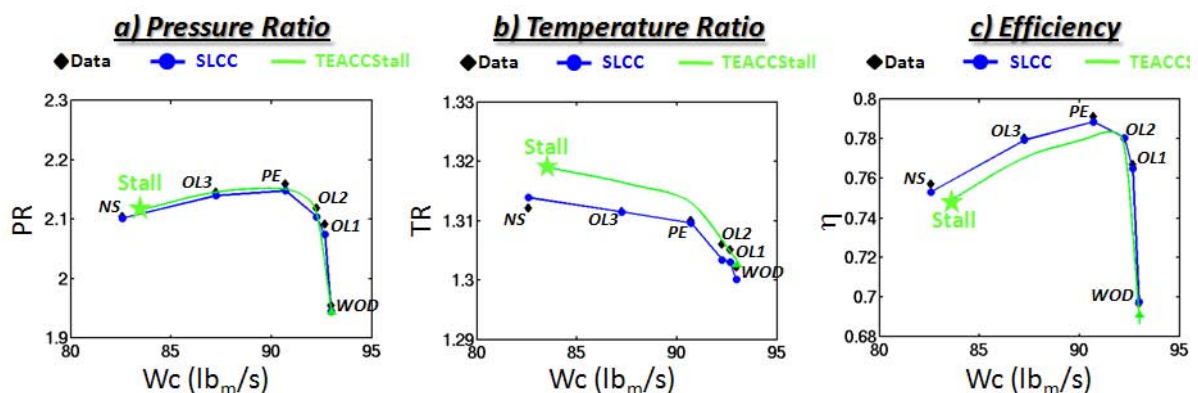
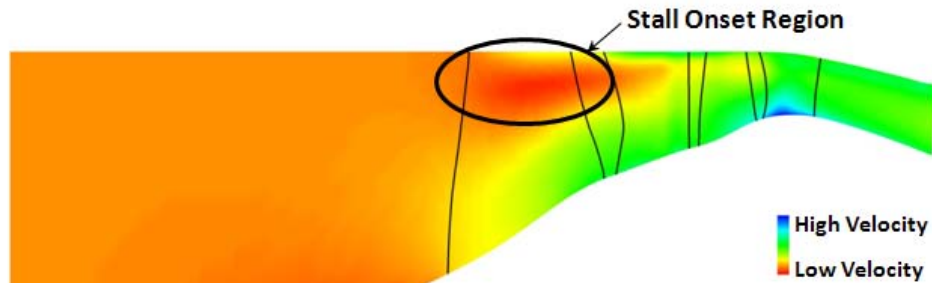


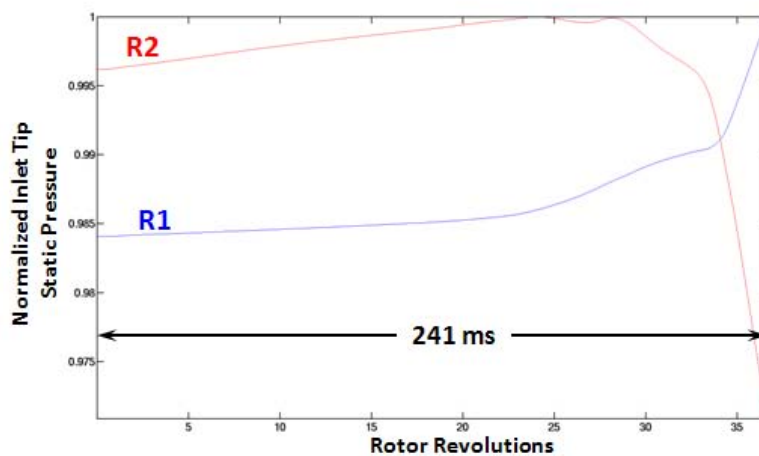
**Figure 3.133 Axisymmetric Overall 1-D Characteristic of HTSC – Clean**

**Figure 3.134** shows the **TEACCSTALL** solutions around the stall inception point. **Figure 3.134a** is a contour plot of the axial velocity around stall. The red regions show a very low velocity. The tip of Rotor one has a very low velocity at this point, illustrating the region where the rotor stalls. **Figure 3.134b** is a rotor inlet tip static pressure trace for the entire solution. The tip static pressures have been normalized to be about the same starting value. This figure shows how Rotor 1 inlet tip static pressure starts to rise sharply around rotor revolution 35 as





**a) Axial Velocity Contours at Stall**



**b) Normalized Tip Static Pressure Traces**

**Figure 3.134 TEACCSTALL Solution at Stall**

the Rotor 2 inlet tip static pressure falls sharply at the same time. This indicated that Rotor 1 stalled around 35 rotor revolutions of the simulation. These 35 rotor revolutions represent about 241 milliseconds of simulation time.

The WOD (Choke) point is illustrated in [Figure 3.135](#) and shows total pressure as a function of radius for Stators one and two inlet and Plane 23. The **TEACCSTALL** solution is compared to the data available at this flow point. Overall, the **TEACCSTALL** solution compares favorably to the data taken at the CRF.

**TEACCSTALL** was then run with the inlet total pressure pattern derived from data and shown in [Figure 3.136](#). This pattern shows a max loss in total pressure of about 8%. This distortion patterns generated the characteristic shown in [Figure 3.137](#). These figures show the total pressure ratio, total temperature ratio, and efficiency for data and **TEACCSTALL** for both clean and distorted. As stated early, the distortion data at 68.0% speed looked a little suspect since the total pressure ratio was higher with distortion than clean, and the fact that the inlet total pressure rakes were removed during testing, so the inlet total pressures were calculated from a calibration. The authors re-estimated the inlet total pressure and those results are also seen in [Figure 3.137](#) as the data.



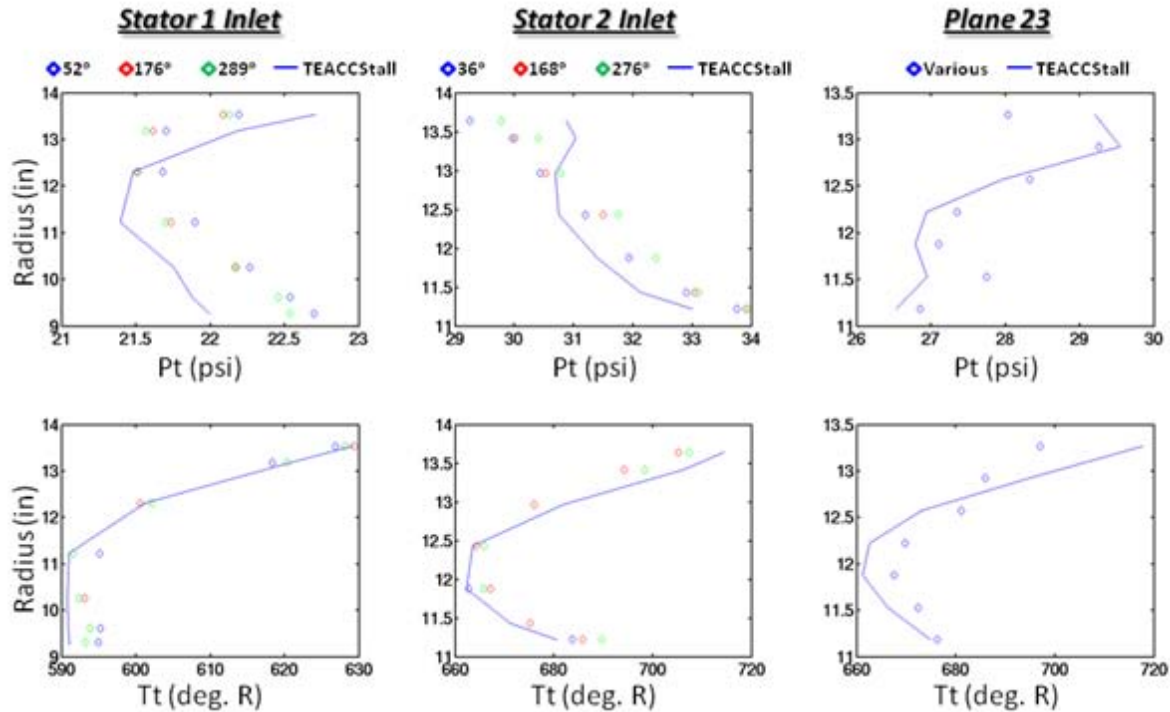


Figure 3.135 TEACCSTALL Clean Steady Results around WOD:  $W_c = 93.01 \text{ lb}_m/\text{sec}$

Figure 3.137 shows the TEACCSTALL solution that started with the steady-state choke solution and ramped the exit Mach number toward stall. The solution is time-accurate and shows the stall inception of the distorted run occurs at about 0.4% higher corrected flow than the estimated data. As with the clean, the total temperature ratio at stall is slightly higher than the data.

Figure 3.138 shows the distorted solution at stall. The circumferential location is in the center of the transition from the distorted region to the clean region. This appears to be the location that stall occurs. Figure 3.138a illustrates the axial velocity contours at stall. It shows a stall cell developing in the first rotor out near the tip. This region extends back into the first stator; while the second rotor is also starting to develop a stalling region. The normalized tip static pressure traces are also shown in Figure 3.138b. It shows the Rotor 1 and Rotor 2 inlet tip static pressure traces from the beginning of the simulation until Rotor 1 stalls about 238 milliseconds into the transient.

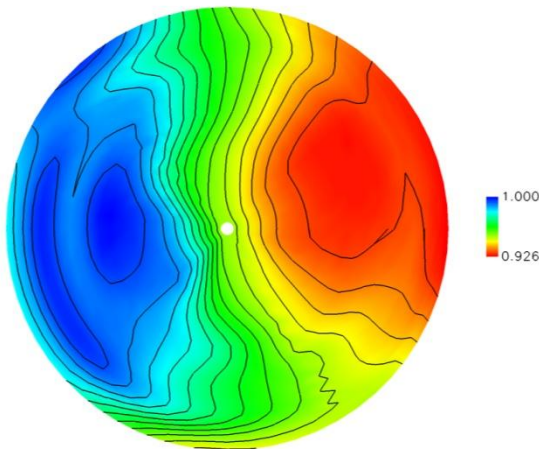


Figure 3.136 Inlet Distortion Pattern

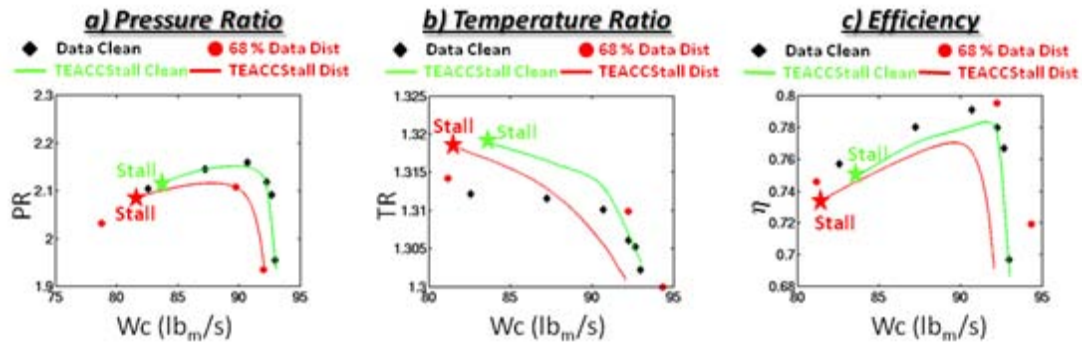


Figure 3.137 Overall 1-D Characteristics of the HTSC – Distortion

The radial comparison to data at the stator inlets around WOD is shown in [Figure 3.139](#). This illustrates that **TEACCSSTALL** does a good job of matching the radial and circumferential results

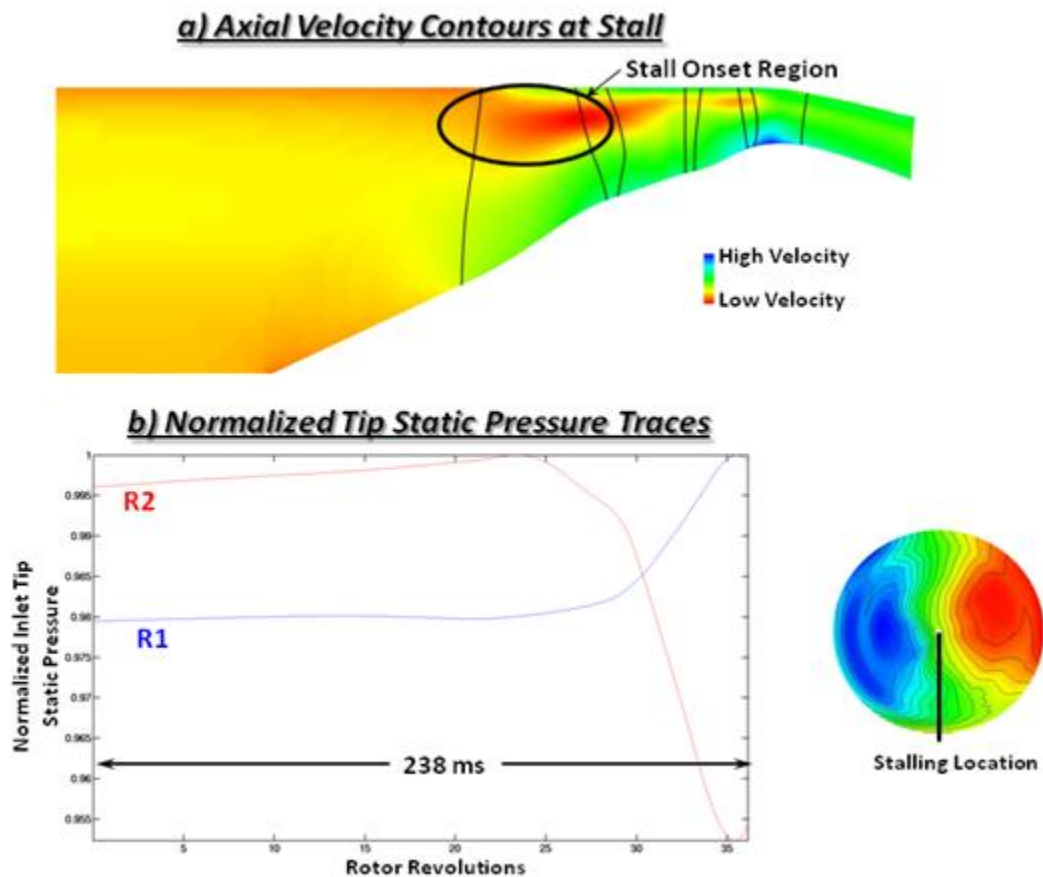


Figure 3.138 TEACCSSTALL Distorted Solution at Stall

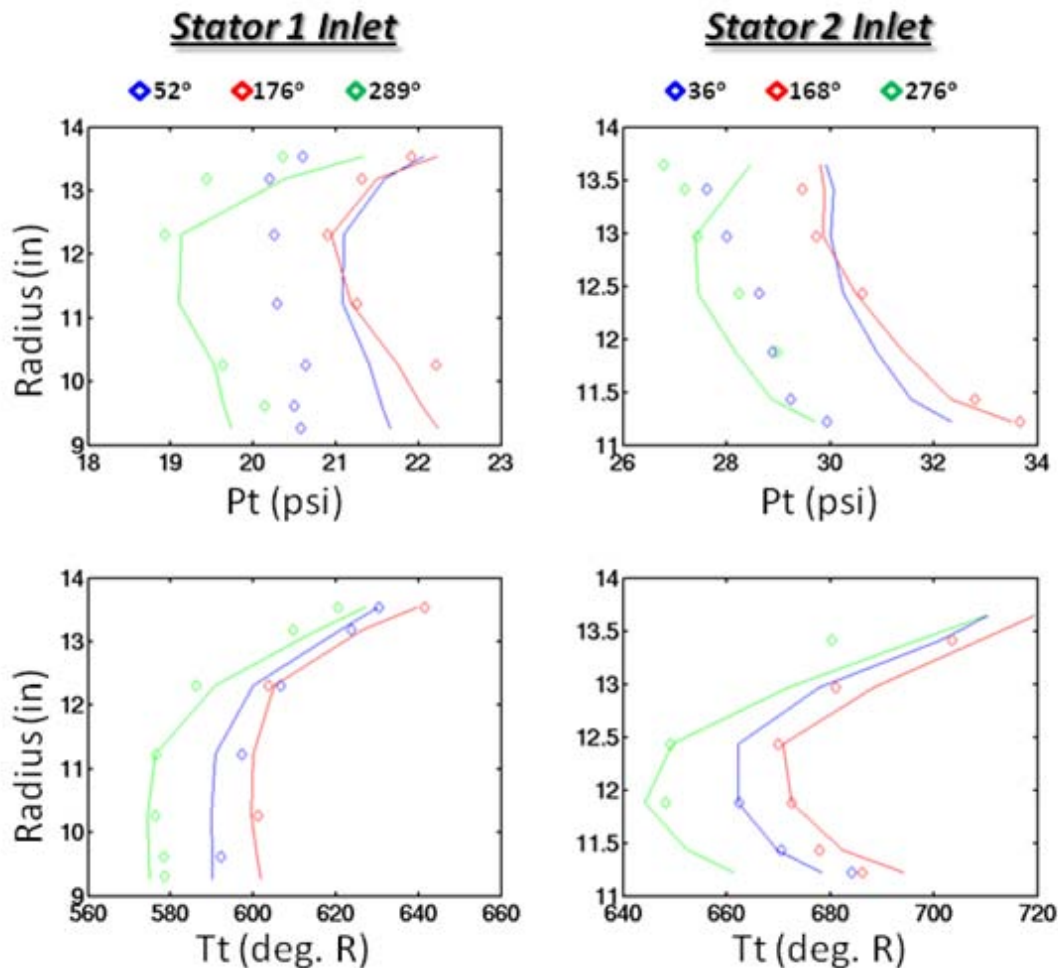


Figure 3.139 TEACCSTALL Distorted Steady Results around WOD:  $W_c = 92.04 \text{ lb}_m/\text{sec}$

demonstrated with the data for both radial and circumferential content.

#### APPLICATION TO AN ADVANCED THREE-STAGE FAN

**TEACCSTALL** was configured to model an advanced fan. The fan is a three-stage fan with a variable IGV and low-bypass ratio. Three main inputs are needed for the fan simulation in **TEACCSTALL**. The grid (first input) is an axisymmetric representation of the flow field from the fan inlet, through the seven blade rows, and out a splitter with two exits. One exit is the fan bypass duct, while the second is the high-pressure compressor inlet. The grid contains 7 blade rows with a total of about 900,000 points distributed over 12 zones. The second input is an axial and radial distribution of blade radial blockage. This is the physical blockage of the blades in the flow path. Finally, a series of clean, single-passage CFD solutions at several mass flows on the design speed line (third input) is used to build a file containing a radial distribution of total pressure, total temperature, and axial, radial, and circumferential velocities at the fan inlet, at the fan exit, and between each blade row.

To validate the **TEACCSTALL** code's ability to determine stall inception, the fan model was compared against ground-test simulated inlet distortion data taken at AEDC for a variety of engine builds. The following configurations were used in validating the fan:

- Clean
- Tip-Radial
- Hub-Radial
- 180° Circumferential
- Complex Pattern CX1
- Complex Pattern CX2M
- Complex Pattern CX3

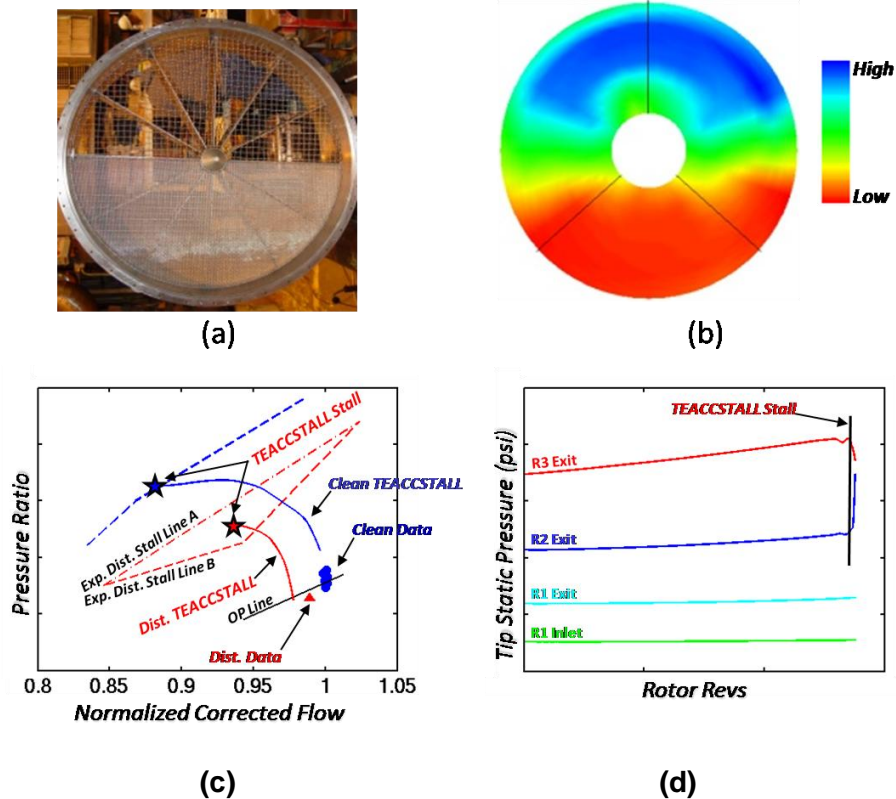


**Figure 3.140 180-deg Distortion Results.**

Even though all configurations were validated, for the purposes of this effort, a simple circumferential 180-deg distortion pattern and the complex CX3 distortion pattern will be presented. Each of the results presented were run the same way. A steady-state solution of **TEACCSTALL** was obtained on the operating line with a total pressure distortion pattern imposed on the fan (simulated by an inlet distortion screen during test). A transient run was then initiated on the operating line, and the exit Mach number in the fan bypass duct was ramped down for a time approaching that of approximately 100 rotor revolutions until the solution indicated that a stall occurred. **Figure 3.140** shows the results from the simple circumferential 180-deg distortion runs. Included in **Figure 3.140a** is an image of the screen that was run in front of the engine. **Figure 3.140b** shows the resulting total pressure pattern implemented in **TEACCSTALL**. The performance map (**Figure 3.140c**) shows where the stall

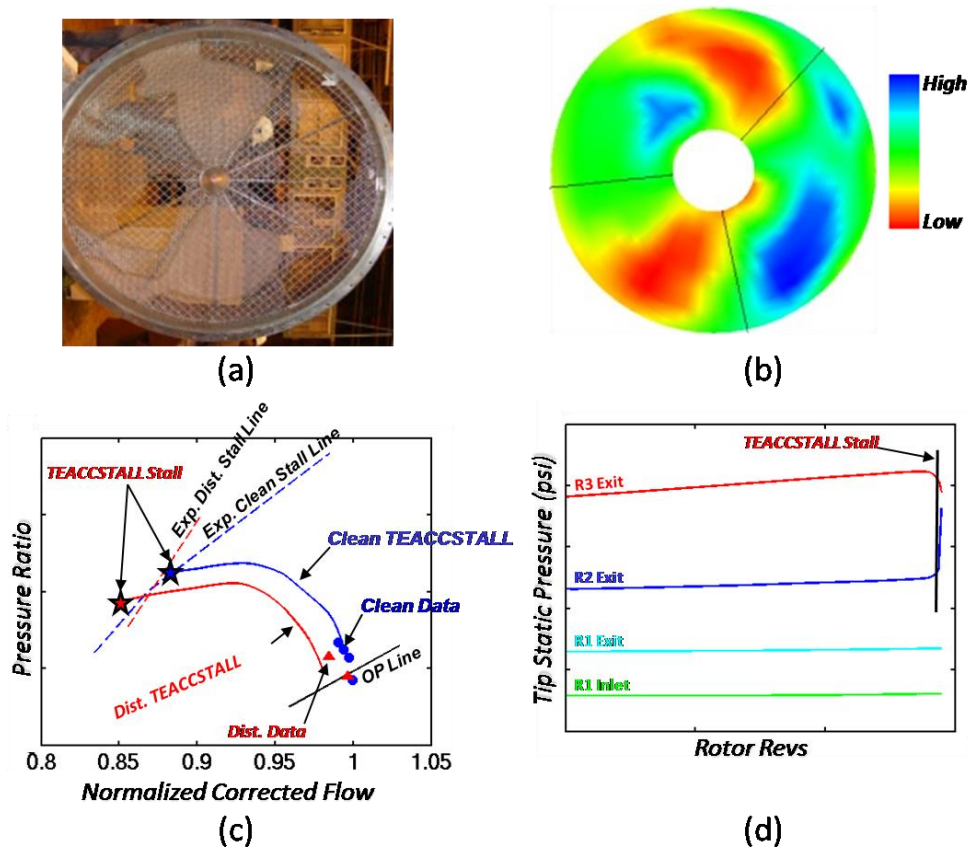


Figure 3.141 CX3 Distortion Results.

occurred, and the static pressure traces (Figure 3.140d) indicate how stall was determined. Figure 3.140c shows the performance of the clean data and TEACCSTALL solutions with respect to the 180-deg distortion solutions for reference. Since the 180-deg pattern was run on two separate engine builds, there are two stall lines from the ground-test data. As shown in Figure 3.140c, the TEACCSTALL solution predicts the stall to occur in between the two separate engine builds. Figure 3.140d illustrates the tip static pressures at the exit of each rotor and shows where the stall causes a blockage at the tip between the exit of rotor 2 and the exit of rotor 3.

Figure 3.141 shows the results from the complex CX3 distortion runs. Included in Figure 3.141a is an image of the screen that was run in front of the engine. Figure 3.141b shows the resulting total pressure pattern implemented in TEACCSTALL.

As shown in Figure 3.141c, the TEACCSTALL solution predicts the stall at a lower mass flow than the ground-test data indicate, but within reasonable expectations. Figure 3.141d illustrates the tip static pressures at the exit of each rotor and shows how the stall causes a blockage at the tip between the exit of rotor 2 and the exit of rotor 3.



### **ADDITIONAL REFERENCES**

**3.87** Gorrell, S. E. and M. W. Davis, Jr., "Application of a Dynamic Compression System Model to a Low Aspect Ratio Fan: Casing Treatment and Distortion", AIAA Paper # AIAA-93-1871, Presented at the 29th Joint Propulsion Conference and Exhibit, Monterey, CA, June 1993.

**3.88** Shahroghi, K. A., and M. W. Davis, Jr., "Application of a Modified Dynamic Compression System Model to a Low-Aspect Ratio Fan: Effects of Inlet Distortion," AIAA-95-0301, January 1995

**3.89** Hah, C., et. al., "Effects of Inlet Distortion on the Flow Field in a Transonic Compressor Rotor", **Transaction of the ASME, Journal of Turbomachinery**, Vol 120, April 1998, pp. 233-246.

**3.90** Chima, R. V., "A Three-Dimensional Unsteady CFD Model of Compressor Stability", ASME GT2006-90040, ASME Turbo Expo 2006, Barcelona, Spain, May 2006.



### 3.2.4 Inlet Total Temperature Distortion Analysis -- Parallel Compressor Theory

The issue of transient temperature distortion effects on airframe-propulsion integration stems from two key flight regimes: (1) fighter aircraft combat maneuvers with in-flight weapon launches (Figure 3.142) and (2) Vertical Takeoff and Landing Aircraft (VSTOL) during takeoff and landing operations (Figure 3.143). Such distortion originates from the ingestion of hot exhaust from the weapon itself.



**Figure 3.142 Aircraft with Gun Gas Ingestion**

problems. The lift-jet approaches typically applied in fighter VSTOL concepts produce concentrated high-temperature flows in the vicinity of the aircraft inlet. Any exhaust-gas diffusion benefits that the helicopter derives from the main rotor is typically absent in the fighter system. Furthermore, the high propulsive efficiency in the hover mode provided by the low disk loading of the helicopter often permits engine operation with sufficient surge margins to prevent operability problems. Conversely, the high disk loadings of the fighter VSTOL yields lower efficiency in the hover mode. As a result, the system demands peak thrust-to-weight ratios from the propulsion system and cannot tolerate performance losses associated with simply operating further from the surge limits.

During hover operation in ground effect, the engines of VSTOL aircraft can be subjected to extremes in steady and transient temperature distortion. In this case, the distortion originates from the re-ingestion of hot engine exhaust following interaction with the ground plane. Although the exhaust-gas re-ingestion is certainly a concern for helicopters, the advent of fixed-wing VSTOL aircraft with lift jets directed at the ground and very high disk loadings, present new and unique opportunities for temperature-related operability



**Figure 3.143 Aircraft in Hover Re-ingesting Exhaust Gas**

The aerospace community has observed that total temperature distortion affects turbine engine operability by degrading the surge margin. Steady-state spatial temperature distortion adversely shifts the turbomachine stability limit. Furthermore, time-variant temperature distortion including uniform temperature ramps, degrades stability margin by shifting the turbomachine operating point.

Historically, the effects of such degradations on the aircraft mission were controlled by avoiding hot-gas ingestion or by accommodating hot-gas ingestion with a performance loss. Mounting stores at locations remote from the aircraft inlet often allowed avoidance of hot-gas ingestion. Operating further from the surge line permitted accommodation of the surge loss due to temperature distortion at the cost of performance. However, the advent of new generation highly integrated aircraft render these methods obsolete. For example, bay-launched missiles necessarily decrease the distance between the launch point and the aircraft inlet location invalidating the accommodation approach. The advent of supermaneuverability and tactics involving weapon launches at high angle of attack adds to the diminishing likelihood of avoiding weapon exhaust ingestion.

Furthermore, the thrust demanded during the supermaneuver may not allow the accommodation of performance losses resulting from a shift in the operating point. Finally, the addition of VSTOL capabilities to fighter aircraft systems may result in unavoidable temperature distortion in a regime where performance degradation cannot be accommodated. These issues have renewed concerns in the entire arena of temperature distortion effects on airframe-propulsion integration.

### **CITED EXAMPLE(S)**

**3.91** Davis, M. W., Jr., "Parametric Investigation into the Combined Effects of Pressure and Temperature Distortion on Compression System Stability", AIAA Paper # AIAA-91-1895, Presented at the 27th Joint Propulsion Conference, Sacramento, CA, June 1991.

**3.92** Davis, Milt and Kidman, David, "Prediction and Analysis of Inlet Pressure and Temperature Distortion on Engine Operability from a Recent T-38 Flight Test Program", Presented at the 2010 ASME International Gas Turbine Institute Turbo Expo, June 2010.

### **MODELING TECHNIQUE**

A one-dimensional modeling technique known as **DYNTECC** ([Section 4.4](#)) and as described by Hale and Davis in [Ref 3.93](#) has been modified for the analysis of distorted inflow using parallel compressor theory ([See Section 4.6](#)) [[3.91](#), [3.92](#)]. As indicated in [Figure 3.144](#), a parallel compressor model uses a multi-segmented circumferential compressor concept. Each circumferential segment is modeled using the one-dimensional technique described in [Ref. 3.93](#). Each segment operates independently except at the exit boundary where the specification of either uniform static pressure or uniform Mach number is imposed. This is the only location where the modeling technique transfers information from one segment to another. Different levels of temperature distortion may be imposed upon the inlet, and each segment will operate to its own limit. In this classical form, when one segment reaches the instability limit the entire compression system is considered to be unstable. Using this approach, the mean operating point at instability is a weighted average of the low flow sector operating at the uniform flow stability boundary, and the high flow sector operating at some other point far from the stability limit as shown in [Figure 3.144](#).

The greatest loss in stability margin occurs with the narrowest distorted sector inlet. This leads to predictions that are inconsistent with experimental observations. For example, the theory would indicate that the whole compression system would be unstable for a 1-degree sector if that sector were stalled.

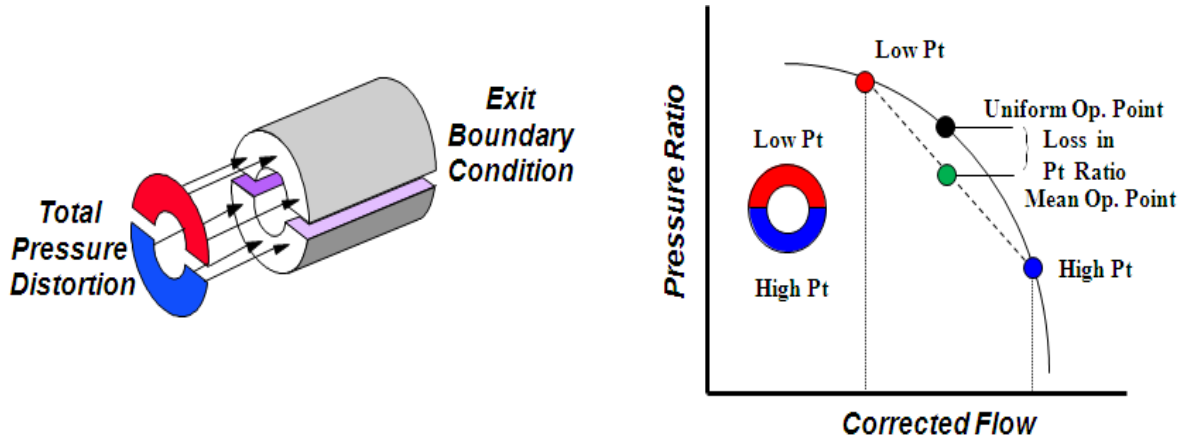


Figure 3.144 Parallel Compressor Concept

#### APPLICATION TO A TEN-STAGE SINGLE-SPOOL COMPRESSOR

**Steady State Temperature Distortion** - While a moderate amount of pressure distortion has only a moderate effect on the overall stability limit, temperature distortion has a much more pronounced effect. The effect of 180-deg circumferential temperature distortion on overall performance and stability limit is shown in Figure 3.145. A distortion magnitude of 10 percent (10 percent higher temperature in Segment 1 than in Segment 2) was imposed upon the inlet total temperature boundary condition. Increasing the Segment 1 inlet total temperature was conducted over a short period of time. The system was then allowed to settle at a new steady-state condition. Since the inlet temperature was changed, the corrected rotor speed was changed as well. This can be seen in Figure 3.145 as a lateral movement of the initial operating point. Once steady operation was verified at this new operating point, the exit static pressure was increased at a rate of 50 psia/sec until system instability was indicated. Approximately half of the stability margin was lost as a result of a 10-percent temperature distortion. Inspection of the static pressure signature at the time of stall indicated at that stage 7 of the distorted segment (Segment 1, higher temperature region) initiated the stall.

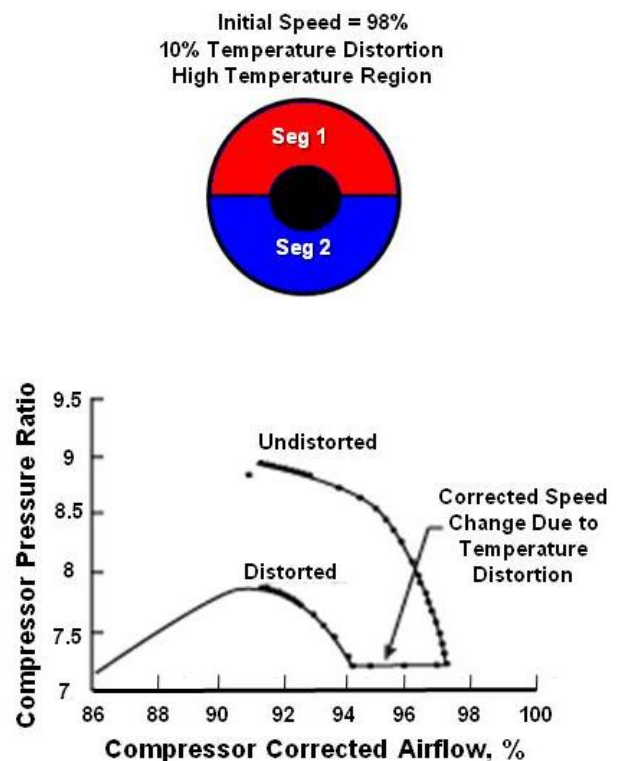
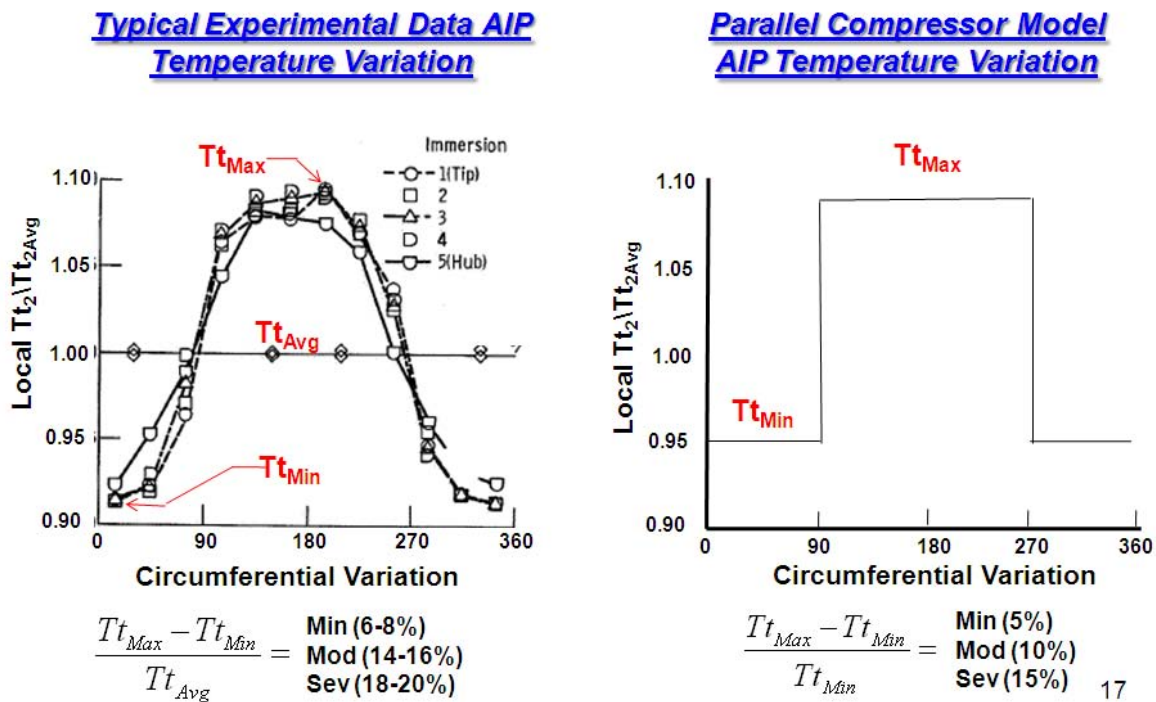


Figure 3.145 Aircraft in Hover Re-ingesting Exhaust Gas

### APPLICATION TO THE J85 EIGHT STAGE COMPRESSOR

The J85-13 engine was also tested with inlet temperature distortion as reported by Mehalic in [Ref. 3.96](#). A typical temperature distortion pattern as generated using a hydrogen burner is shown in [Figure 3.146](#). Since temperature measurements were not provided within the original report [3.96], the overall temperature distortion as measured by the maximum Temperature minus the minimum temperature divided by a face average was used as a figure of merit.



**Figure 3.146 Comparison of a Typical Experimental Temperature Profile to That Used with the Parallel Compressor Model**

For implementation into the parallel compressor model, a simpler variation along the lines of a square wave was used to implement the temperature distortion as illustrated in [Figure 3.146](#). Since a different figure of merit was necessary, exact comparisons to the experimental results is not possible. However, the experimental data was taken with three levels of temperature distortion: minimum, moderate, and severe. What those levels mean are presented also in [Figure 3.146](#) for both the experimental results and how they were used in the parallel compressor simulation. All three levels were experimentally analyzed but only the minimum level is presented in [Figure 3.147](#).

This is appropriate since it is these levels of temperature distortion that are present within the experimental flight test data presented later in this paper. Presented in [Figure 13](#) are the parallel compressor predictions to a minimum level temperature distortion. Although, the experimental stability limit is not presented on the figure, one can see by inspection between [Figure 3.147](#) and [Figure 3.148](#) that the level of loss in stability pressure ratio is approximately the same for this minimum level of distortion.



### 180 Degree Circumferential Temp Distortion – Minimum Level

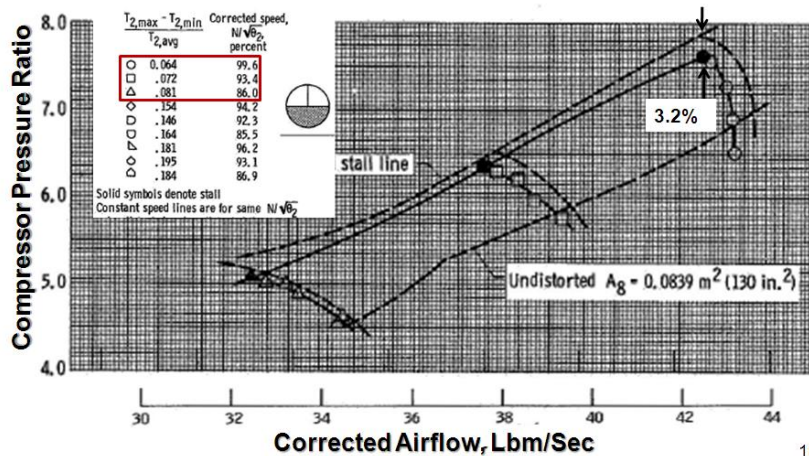


Figure 3.147 Reproduced Figure [3.96] Indicating the Effect of Temperature Distortion on the Stability Limit

the physical speed was increased.

Presented in Figure 3.149 are other experimental data indicating loss in stability pressure ratio at higher temperature distortion levels than the minimum level, but at lower corrected speeds. Also, in Figure 3.149 are comparisons of the parallel compressor model predictions to those observed experimentally. In general, the comparisons are quite favorable except for one point near the 92-93% speed.

### 180 Degree Circumferential Temp Distortion – Minimum Level (5%)

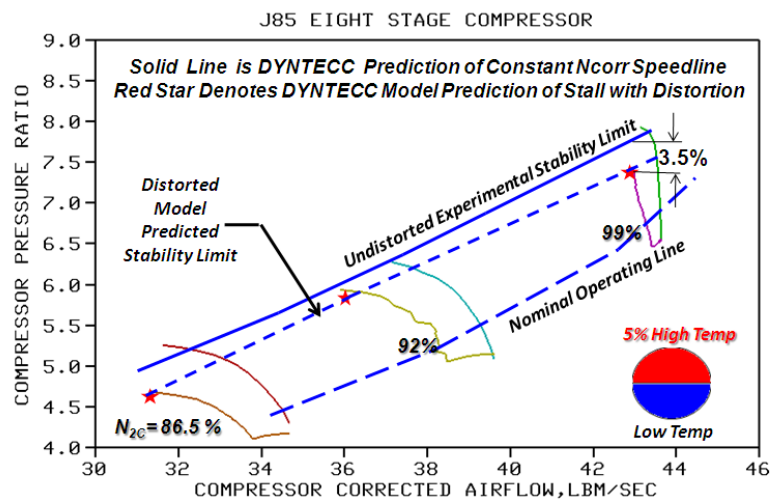
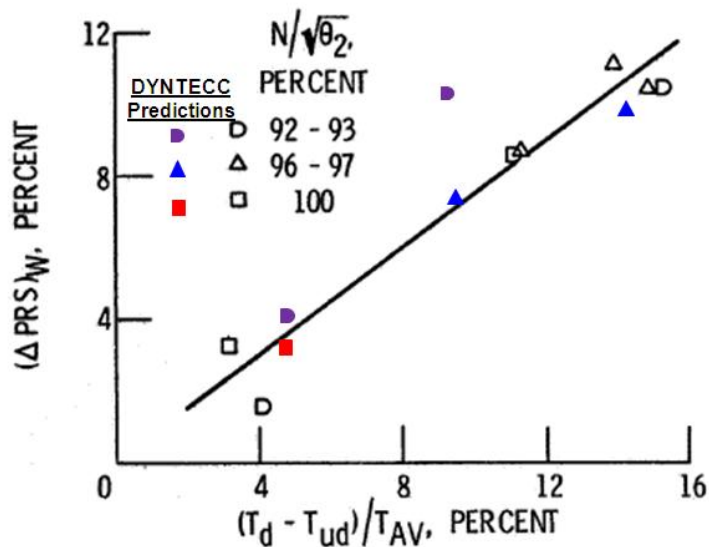


Figure 3.148 Parallel Compressor Model Results of the Effects of Temperature Distortion on Compressor Operability for Minimum Level of 5%



**Figure 3.149 Comparison of DYNTTECC Parallel Compressor Results for Total Temperature Distortion to Those Observed Experimentally**

#### ADDITIONAL REFERENCES

- 3.93** Hale, A. A. and M. W. Davis, Jr., "DYNAMIC Turbine Engine Compressor Code: DYNTTECC -- Theory and Capabilities", AIAA Paper # AIAA-92-3190, Presented at the 28th Joint Propulsion Conference and Exhibit, Nashville, TN, July 1992.
- 3.94** Shahroohi, K. A., and M. W. Davis, Jr., "Application of a Modified Dynamic Compression System Model to a Low-Aspect Ratio Fan: Effects of Distortion," AIAA-95-0301, Presented at the 33rd Aerospace Science Meeting, Reno, NV, January 1995.
- 3.95** Milner, E. J., "Analytical Prediction of the Performance and Stability of a J85-13 Compressor with distorted Inlet Flow", NASA TM X-3515, May 1977.
- 3.96** Mehalic, C. M., & Lottig, R. A., "Stead-State Inlet Temperature Distortion Effects on the Stall Limits of a J85-GE-13 Turbojet Engine", NASA TM X-2990, February 1974.
- 3.97** Braithwaite, W. M., Graber, E.J., & Mehalic, C., M., "The effects of Inlet Temperature and Pressure Distortion on TurboJet Performance" NASA TM X-71431, November 1973.



### 3.2.5 Combined Pressure and Temperature Distortion Analysis

Temperature distortion encountered in some aircraft operations may be accompanied by total pressure distortion as well. Several experimental and analytical investigations have been conducted to examine these steady-state effects [3.100-3.102]. These investigations have indicated that the loss in stall margin attributable to the combined distortions is dependent upon the orientation of the high-temperature and low-pressure regions. These investigations established that the largest loss in stall margin resulted when the high-temperature and low-pressure regions coincided while diametrically opposed distortions had the smallest effect on stall margin.

During weapon firings, exhaust gas may be ingested into the inlet, causing the compression system to experience rapid temperature ramps. At the same time because of aircraft maneuvers, the compression system may also experience total pressure distortion. This section also looks at the possibility of rapid temperature ramps in conjunction with steady-state pressure distortion both in opposition and concurrently.

#### CITED EXAMPLE(S)

**3.98** Davis, M. W., Jr., "Parametric Investigation into the Combined Effects of Pressure and Temperature Distortion on Compression System Stability", AIAA Paper # AIAA-91-1895, Presented at the 27th Joint Propulsion Conference, Sacramento, CA, June 1991.

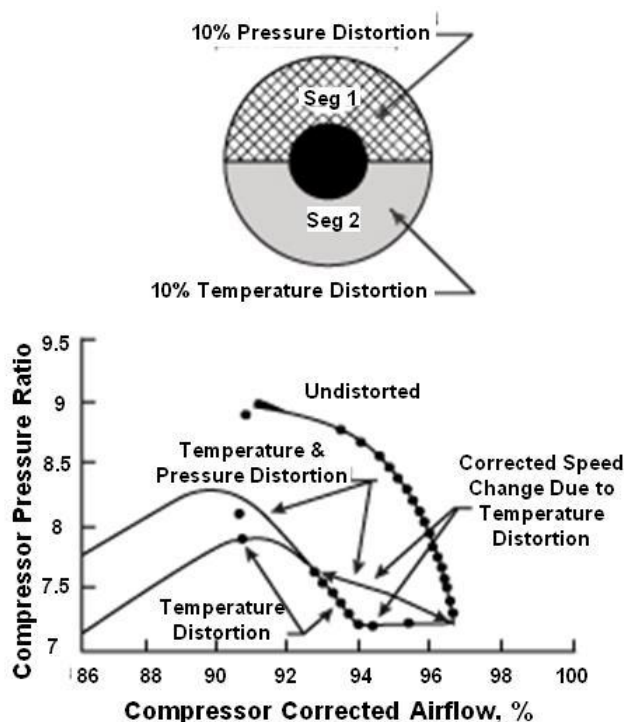


**Figure 3.150 Model Prediction with 180° Opposing Pressure and Temperature Distortion – Initial Speed = 98%**

**3.99** Davis, Milt and Kidman, David, "Prediction and Analysis of Inlet Pressure and Temperature Distortion on Engine Operability from a Recent T-38 Flight Test Program", Presented at the 2010 ASME International Gas Turbine Institute Turbo Expo, June 2010.

#### MODELING TECHNIQUE

A one-dimensional modeling technique known as **DYNTECC** ([Section 4.4](#)) and as described by Hale and Davis in [Ref. 3.103](#) has been modified for the analysis of distorted inflow using parallel compressor theory ([See Section 4.6](#)) [3.104, 3.105].

#### APPLICATION TO A 10-STAGE SINGLE-SPOOL COMPRESSOR

All model studies with combined distortion effects were configured in the same manner as was the study with a single distortion. In the case of steady-state pressure and temperature

distortion, both distortion patterns were set and the compression system allowed to come to a new steady-state operating point. The exit static pressure was then increased at a rate to simulate a fuel pulse until system instability occurred.

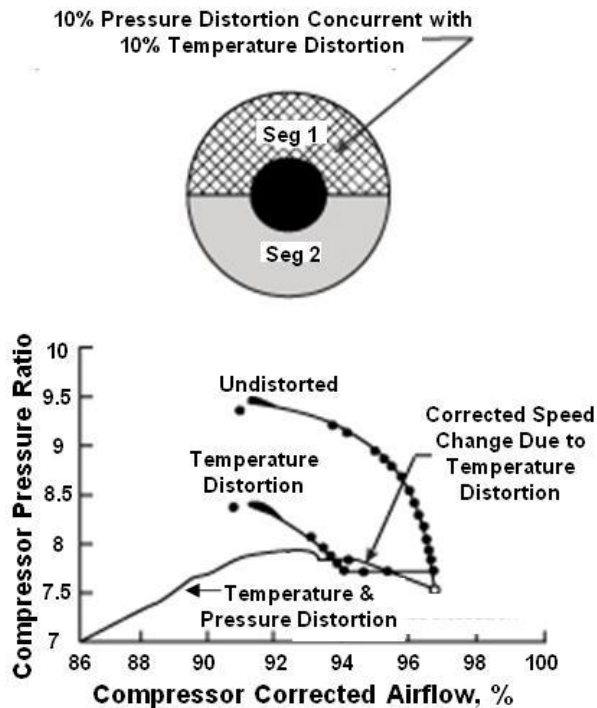


**Figure 3.151 Model Prediction with 180° Opposing Pressure and Temperature Distortion – Initial Speed = 98%**

However, when high temperature and low pressure are concurrent in the same 180-deg circumferential segment, the stability characteristics are much worse, as seen in **Figure 3.151**. In this case, the stability limit and the initial operating point are almost on top of each other (i.e., zero steady-state stall margin). To get a viable solution, the initial operating point was lowered from a pressure ratio of 7.2 to 7.0. Model results with concurrent pressure and temperature distortion are qualitatively comparable with that observed experimentally, mentioned above. Analysis of the static pressure signature at time of instability for both opposing and concurrent events indicate that the 7th stage of the segment with temperature distortion present triggered the instability.

Presented in **Figure 3.150** is the effect of 180-deg circumferential combined temperature and pressure distortion on compression system stability limit. In this case the high-temperature region is opposing the low-pressure region (out of phase). Comparison with the clean inlet indicates that the stability limit pressure ratio decreased approximately 8 percent (i.e., a loss of one third of the stability margin). Comparison with the stability limit of that obtained with temperature distortion only of the same magnitude shows that opposing pressure distortion improved the stability characteristics of the compression system (i.e., a loss of approximately two-thirds of the stability margin for temperature only versus one-third for the opposing combination).

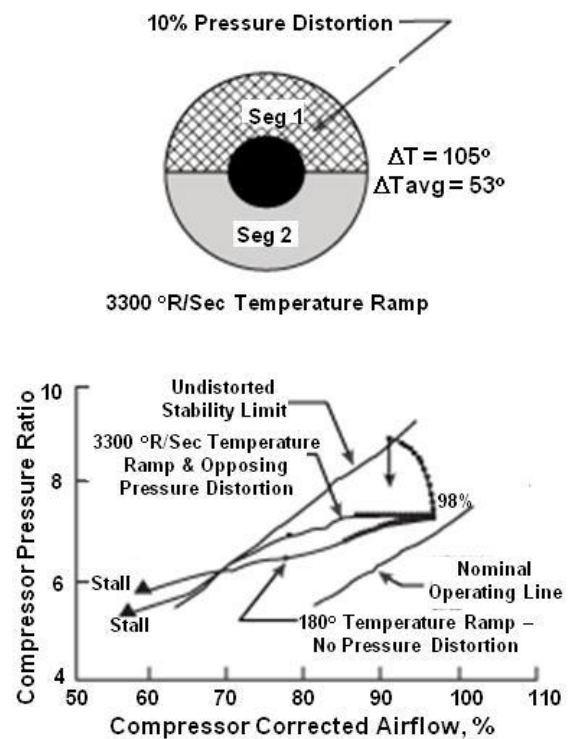


**Figure 3.152 Model Prediction with 180° Opposing Pressure and Temperature Ramp – Initial Speed = 98%**

The model predictions in **Figure 3.152** is the result of imposing a 3,300 degree/sec inlet temperature ramp on a 180-deg segment (Segment 1) and a 10% total pressure distortion in the opposite 180-deg segment (Segment 2). Also presented on the compression system map is the results of only a 180-deg temperature ramp of the same magnitude. As illustrated, the trajectories are similar but the magnitude of the inlet temperature increase is much smaller (105 °R versus 156 °R) for the combined distortions.

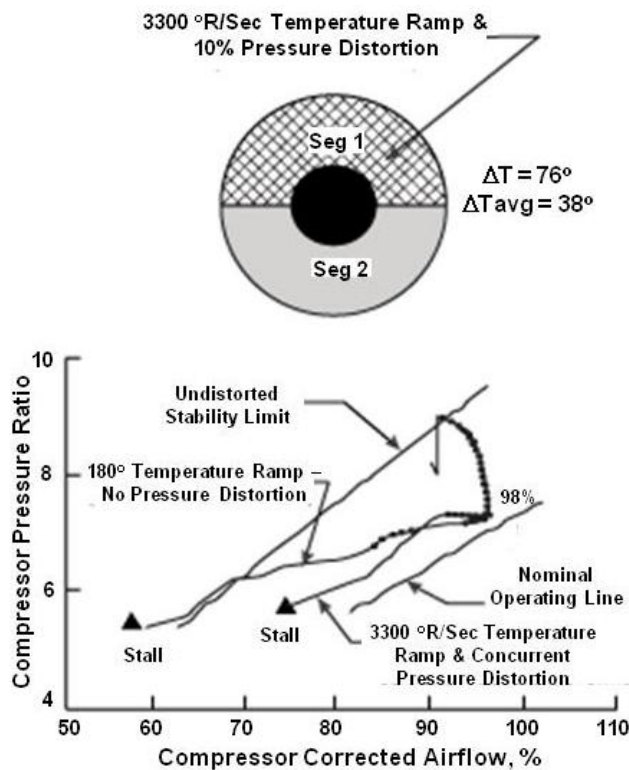


**Figure 3.153 Model Prediction with 180° Concurrent Pressure and Temperature Ramp – Initial Speed = 98%**

Imposing the pressure distortion concurrently with the temperature ramp causes further inlet temperature ramp sensitivity, as illustrated in **Figure 3.153**. The trajectory does not even get to the clean instability limit, indicating that the stability limit has been lowered by the pressure distortion. The amount of temperature increase was much smaller than that predicted in the opposing case (76 °R versus 105 °R).

Analysis of the static pressure signature indicates that the 7th stage of the segment with temperature ramps initiated system instability whether in opposition or in conjunction with total pressure distortion.

#### **APPLICATION TO THE J85 EIGHT STAGE COMPRESSOR**

The Northrop Grumman T-38, Talon (**Figure 3.154**), has been the US Air Force's major jet trainer for nearly fifty years. The T-38 was first flown in April of 1959, powered by two afterburning General Electric J85 turbojet engines and in March of 1961, the T-38A was delivered to Randolph AFB, Texas for the 3510<sup>th</sup> Flying Training Wing [3.106].

The J85-GE-5 with afterburner (**Figure 3.155**) was installed in the first production aircraft and began flight testing in 1960. Closely following the development of the T-38, was the single-seat fighter known as the F-5. The production F-5A/B was equipped with the J85-GE-13 a variant of the J85 with slightly higher thrust levels due to increased turbine inlet temperature, Tt4. In the



**Figure 3.154 The Northrop Grumman T-38, Talon, Trainer**

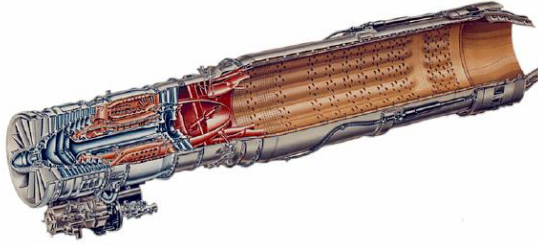


**Figure 3.155 The J85-GE-5 Afterburning Turbojet Engine**

implemented to address the life of the compressor rotor since an investigation into the 1995 mishap revealed that an uncontained failure of an 8<sup>th</sup> stage compressor disk had occurred. Because the USAF wanted to minimize the costs and overall risks, no major aircraft modifications were allowed, thus restricting the new J85 rotor design to be a drop-in replacement to ensure maximum compatibility with existing engine components. The rotor redesign resulted in a split rotor using Inco 718 which provided excellent resistance to corrosion. This redesign resulted in a reduction in projected maintenance and eliminated high stress concentration in rim bolt holes. In addition, the airflow characteristics and aeromechanics of the J85-5 were found to be exceptionally sound and thus there were no changes to the flowpath or blade designs for this new design.

The success of the initial update to the J85 prompted the USAF to consider other updates to the engine that later became known as the Propulsion Modernization Program or PMP. The major change was (described earlier), the eight stage spooled compressor rotor but other improvements were made to the combustor, the nozzle flaps and seals, fuel pumps, afterburner fuel control, the digital engine control, T2 sensors and compressor bleed valves to name a few [3.107].

Since the J85 engine is but one component of the T-38 aircraft, another evaluation was conducted to see what technology options were available for improvements in performance and reductions in the cost of ownership. Two specific improvements that

1990's various studies by the US Air Force led to the development of a comprehensive T-38 upgrade program. The improvements were significant enough to warrant an aircraft designation change to the T-38C. Initially, limited effort was devoted to addressing propulsion system reliability and performance; however, due to an engine failure causing loss of a T-38 in 1995 the propulsion system began a modernization process as well [3.107].

The improvements to the J85-5 engine were

**Modified ejector**



**T-38A**



**T-38C PMP**

**Figure 3.156 New PMP Ejector Nozzles to Reduce Drag Associated with Overexpansion [3.108]**



**T-38A**



**T-38C PMP**



**Figure 3.157 New PMP Inlet Nozzle to Increase Takeoff Thrust [3.108]**



were made were in the area of the ejector nozzle and inlet lip modification. The original configuration of the T-38 exhaust nozzle was sized for max afterburning operation. This nozzle exit area resulted in overexpansion of the exhaust plume at military power which resulted in increased drag and lower overall net thrust. A new system was designed that incorporated free floating doors in an ejector (**Figure 3.156**) which resulted in an effective variable nozzle size at all power conditions [3.107, 3.108]. In addition to the variable ejector flaps, it was concluded that an increase in performance could be realized by the incorporation of a revised inlet lip contour. Using Northrop's experience, a new inlet shape incorporating a fatter lip with a squarer profile was developed (**Figure 3.157**). This new design was initially tested on a NASA T-38 using an add-on glove to simulate the new inlet design. This new inlet design resulted in an increase in take-off thrust of 22% [3.107, 3.108].

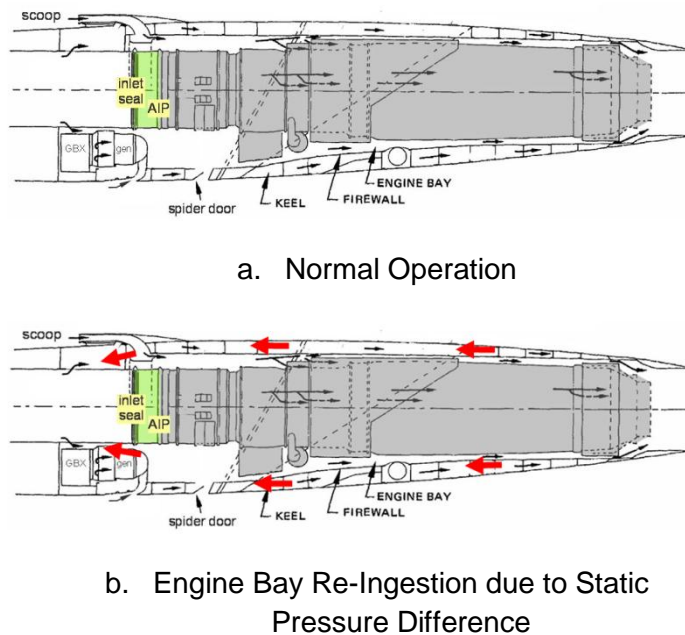


**Figure 3.158 Engine Bay Cooling and the Potential for Flow Re-Ingestion**

flow reversal moving hot air from the engine bay to the inlet as schematically shown in **Figure 3.158b** which is then ingested near the tip of the compression system.

Temperature hot gas re-ingestion causing inlet temperature distortion is not a new one for the T-38/J85 since it was noted in 1959 during the YT-38 flight tests.

*"The investigation was conducted with the engine installed in the airplane with different airframe configurations. The stalls were traced to one major problem: hot exhaust gases were drawn forward between the engine and the fuselage and into the engine inlet. The hot gases expanded the compressor casing, opening up the rotor tip-to-case clearance, and caused the engine to stall while it was running on the ground at high speed. In addition to various engine and airframe modifications, the primary fix was to install suck-in (vacuum breaker) doors in the fuselage near the compressor face which prevented the recirculation of hot air during ground running."* [3.109]

As a result of the 2007 IRT findings, a series of flight tests were conducted in 2008 to investigate the causes and magnitude of the problem and to quantify the temperature distortion associated with engine bay re-ingestion. In addition to T-38 flight tests there would be a future engine ground test to quantify measured and/or predicted pressure and temperature distortion effects on the J85 engine.

As a part of the flight test analysis process and subsequent to the ground engine test, a numerical investigation was undertaken to predict the effect of observed or calculated pressure and temperature distortion on the operability of the J85 compression system. The purpose of this paper is to report the results of the numerical investigation and predict the effect of the observed/calculated pressure and temperature distortion on the J85 engine.

### J85-13 Validation

During flight test, the inlet may have both pressure and temperature distortion in combination. For the parallel compressor model to predict the effects of combined pressure and temperature distortion, it must be validated against experimental results.

As it turns out, that independent experimental pressure and temperature data was taken in the 1970's on the J85-GE-13 engine [3.116]. However, the current SAE methodologies associated with both pressure and temperature distortion alone [3.119, 3.120 & 3.121] does not provided a suitable procedure for combining them.

#### 180 Degree Circumferential Temp & Pressure Opposed Distortion – Min Level

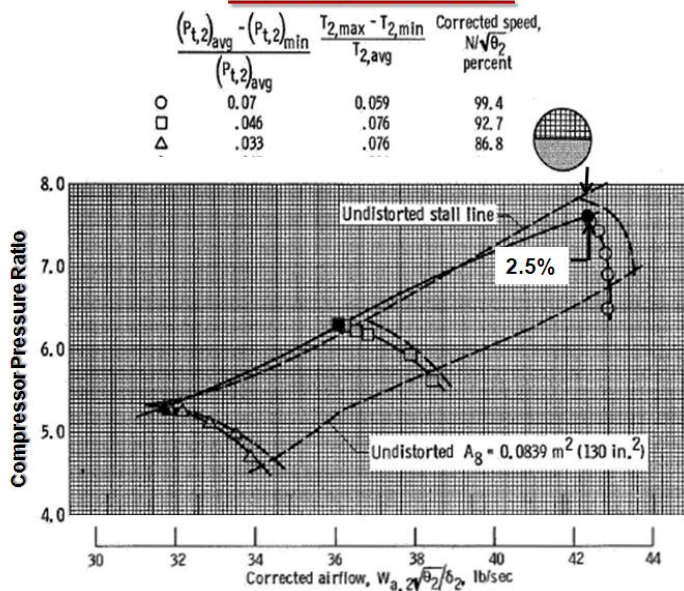


**Figure 3.159 Reproduced Experimental Results [3.116] for Combined Pressure and Temperature Distortion -- Opposed**

Using the guidance of experimental results from Ref. 3.116, the parallel compressor model was validated for the combination. Inherently, when combining both pressure and temperature distortion, one has to consider whether the temperature distortion is concurrent with the pressure distortion or opposite to the pressure distortion. This was investigated experimentally and reported in Ref. 3.116. Presented in Figure 3.159 is the case when pressure and temperature are in opposite 180° sections.

As can be seen, the effect of the temperature and pressure distortion almost cancel each other's effect out with an ultimate effect of having nearly no effect on the stability pressure ratio limit. The opposite situation, however, does not provide such a benign result.



### 180 Degree Circumferential Temp & Pressure Concurrent Distortion – Min Level

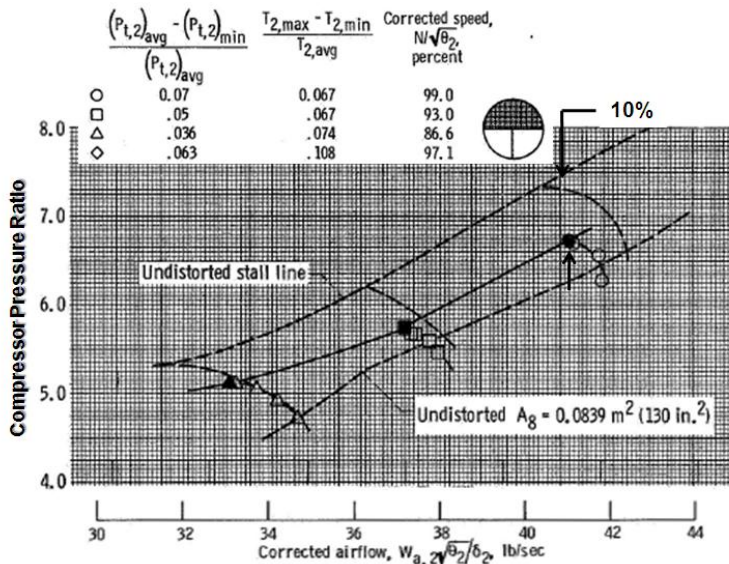


**Figure 3.160 Reproduced Experimental Results [3.116] for Combined Pressure and Temperature Distortion – Concurrent**

Presented in **Figure 3.160** is the case when pressure and temperature are in the same 180° section. As evident in the figure, the individual effects seem to be more severe than the linear combination of both effects. These two cases were also executed within the parallel compressor model and were also found to have similar effects as presented in **Figure 3.161** and **Figure 3.162**.

In summary, the **parallel compressor model** was validated for the J85-GE-13 eight stage system. Comparisons of the effect of circumferential pressure and temperature distortions, separately and in combination, agreed well

with what had been observed experimentally. Thus, use of the parallel compressor model seems appropriate for more complex distortions especially if they can be tailored to some

### 180 Degree Circumferential Temp & Pressure Opposed Distortion – Min Level

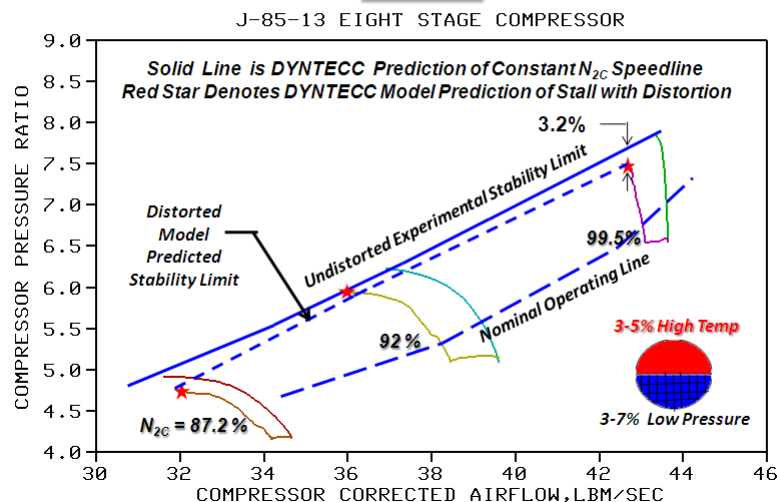


**Figure 3.161 Parallel Compressor Model Results of Temperature and Pressure Distortion – Opposed**

equivalent form of circumferential distortion.

**180 Degree Circumferential Temp & Pressure Concurrent Distortion –  
Min Level**

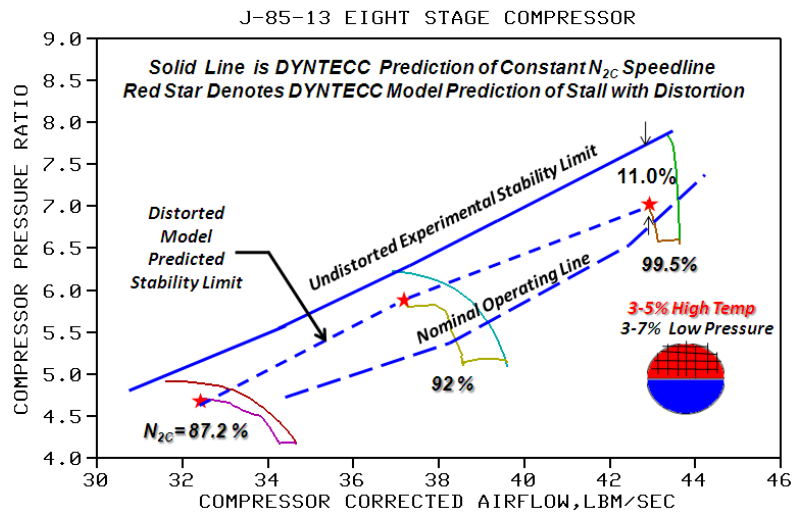


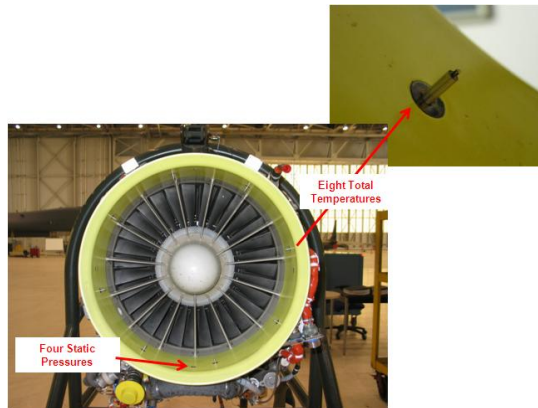
**Figure 3.162 Parallel Compressor Model Results of Temperature and Pressure Distortion -- Concurrent**

### Specific T-38 Inlet Distortion Patterns

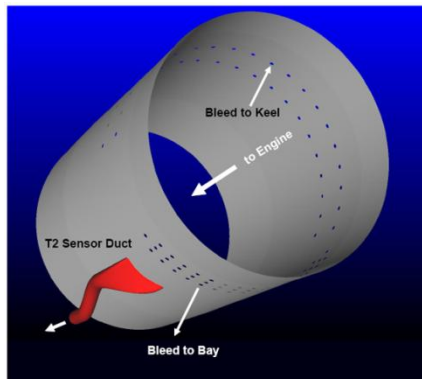
During the 2008 flight tests, a series of thermocouples (**Figure 3.163a**) were installed in the inlet of the T-38 just prior to the engine face and after the cooling holes as shown in **Figure 3.163b**. These thermocouples measured the reverse flow temperature and provided a measure of the temperature distortion present during bay re-ingestion. However, no pressure measurements were obtained and a quantitative assessment of pressure distortion during particular flight maneuvers was not obtained. To approximate what pressure and temperature distortion might be present during certain maneuvers, RANS steady state CFD calculations were run at two flight conditions using an approximation of the reverse flow from the cooling holes and the new blunter inlet. A representative total pressure and temperature inlet distortion pattern at the Aerodynamic Interface Plane, (AIP) is shown in **Figure 3.164** for a typical cruise altitude - Mach number condition.

A visual inspection of the CFD indicates that the pressure distortion pattern is nearly a one-per-rev 180° circumferential pattern. The temperature pattern is confined to a 90° segment near the tip of the machine and in the same quadrant as the pressure distortion. Because of these observations, a simplification of the pattern for use within the parallel compressor model was made as illustrated in **Figure 3.165**.

As indicated by the steady state CFD predictions, a single average pressure defect of 15% was chosen to represent the pressure distortion in the low pressure region. In addition, the temperature distortion was averaged to be a single increase in temperature of approximately 4% in a 90° quadrant out near the tip which was also based upon the CFD results. In addition, these two patterns were made to occur in the same regions (or concurrent) which as shown previously would be more detrimental than if they were not in the same quadrants.



a. Thermocouple Arrangement



b. Bay Cooling System

**Figure 3.163 T-38 Inlet Interface Hardware to the J85 Engine**

In addition to the altitude condition, steady state CFD calculations were also run at Sea-Level-Static case as shown in [Figure 3.167](#). By inspection, the CFD pattern is similar to that observed at the cruise altitude flight condition and a similar approximation was used to provide an appropriate set of total pressure and temperature distortion patterns for the parallel compressor model (10% pressure defect and 2.5% increase in temperature in the distorted regions).

The parallel compressor model was executed with clean inlet, 15% pressure defect for 180° inlet total pressure distortion, 4% increase in temperature distortion in the 90° tip location, and with both the pressure and temperature distortion present as indicated in [Figure 3.166](#).

The loss in stability pressure ratio is given for comparison for all cases. With 180° circumferential pressure distortion of 15% degradation in the low pressure area, the loss in stability pressure ratio was 6.3%. With 4% increase in temperature in a 90° quadrant near the tip, the loss in stability pressure ratio was 3.8%. However, with both temperature and pressure distortion in a concurrent segment, the loss in stability pressure ratio was 10.1 % as shown. This particular amount of loss would put the stability limit near the nominal operating line as indicated in [Figure 3.166](#). Because of temperature distortion, the corrected speed for both the temperature distortion alone and the combination cases are no longer at 100% but between 97-98% speeds and are shifted to the left of the clean inlet case. In addition, with pressure distortion alone, the speedline is also shifted to the left as a result of circumferential flow redistribution due to pressure differences between the two segments.

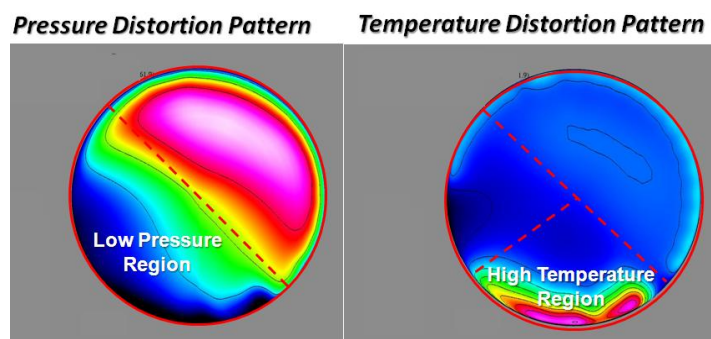


**Figure 3.164 Representative Steady State CFD AIP Pressure and Temperature Distortion Patterns at a Typical Cruise Flight Condition**

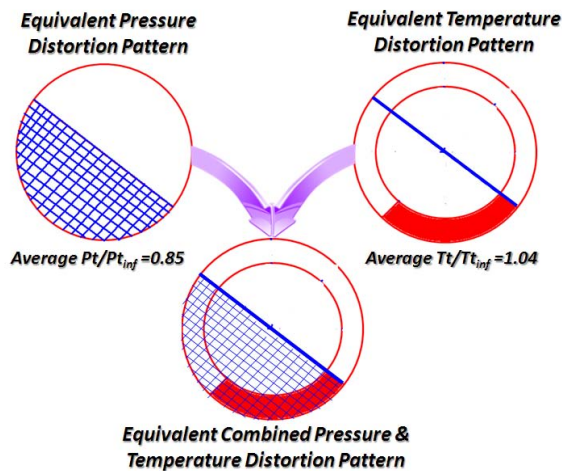


**Figure 3.165 Simplified Pressure and Temperature Distortion Patterns for Use within the Parallel Compressor Model**

Using the concept of  $180^\circ$  circumferential pressure distortion and a concurrent overlapping  $90^\circ$  segment of temperature distortion near the tip of the compressor, the patterns were setup to the inlet of the parallel compressor model which was then ramped via an exit pressure pulse to system instability. The result of that investigation is presented in [Figure 3.168](#).

As in the case of the cruise altitude condition, the effect of pressure and temperature distortion was investigated separately and then in combination. With an average 10% pressure defect for  $180^\circ$  circumferential pressure distortion alone, the stability limit pressure ratio was decreased by 5%

over that of clean inlet.

When the temperature was increased 2.5% in the  $90^\circ$  quadrant near the tip of the machine, a loss in stability pressure ratio of 3.2% was noted. However, when the pressure and temperature were concurrent there was a loss of 8.3% in stability pressure ratio. As in the previous case when temperature distortion was present, the corrected speed is no longer at 100% but between 97-98% speeds and has been shifted to the left of the clean inlet case. In addition, with pressure distortion alone, the speedline is also shifted to the left as a result of circumferential flow redistribution due to pressure differences between the two segments.

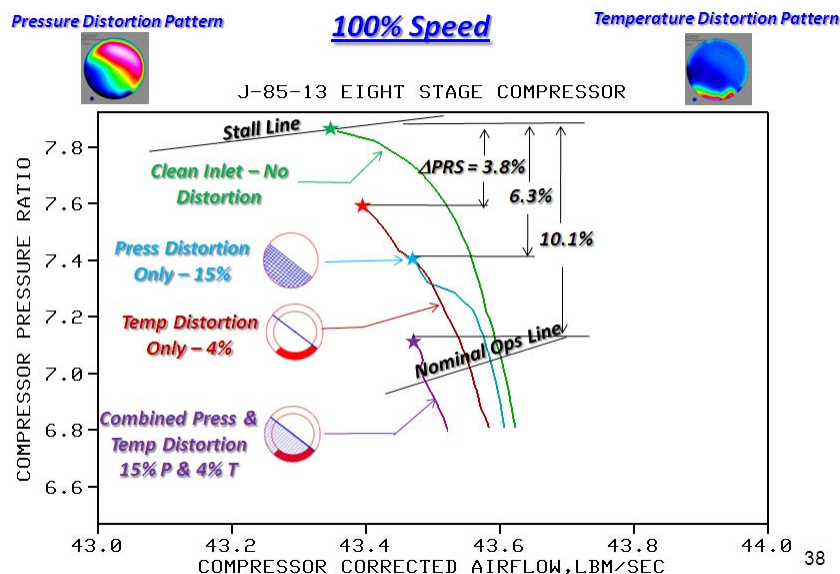


**Figure 3.166 Parallel Compressor Model Prediction of the Loss in Stability Limit for Pressure and Temperature Distortion Separately and in Combination for the Altitude Condition**



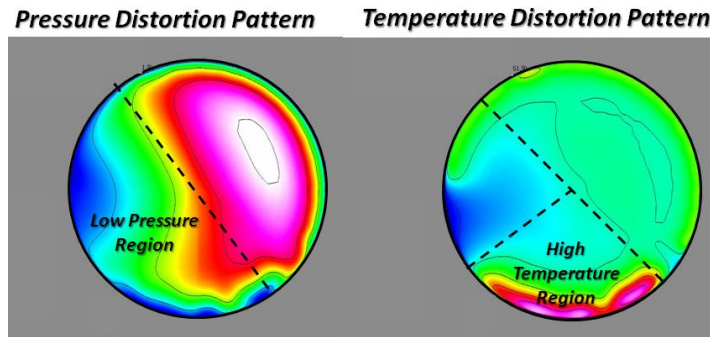


**Figure 3.167 Representative Steady State CFD AIP Pressure and Temperature Distortion Patterns at SLS**

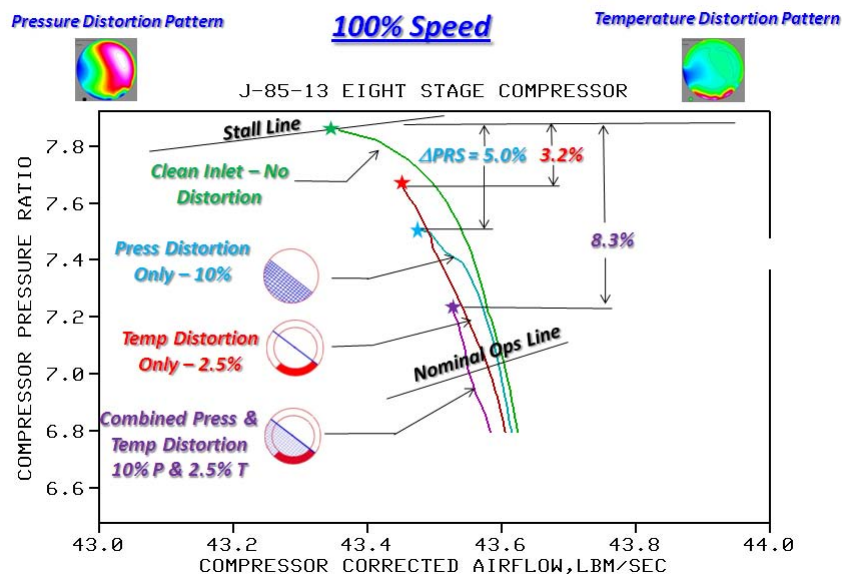


**Figure 3.168 Parallel Compressor Model Prediction of the Loss in Stability Limit for Pressure and Temperature Distortion Separately and in Combination at SLS**

### **Evaluation of the Specific Combinations of Pressure & Temperature Distortion Effects**

To effectively evaluate the combined effects of total pressure and temperature inlet distortion on compression system operability, an experimental investigation using the system of interest would need to be done. As it turns out, such an investigation was conducted and reported in **Ref. 3.117** on a J85-GE-13 engine. The results were restricted to those obtained with circumferential, one-per-rev, 180° extent distortion. The results were further restricted to corrected speeds of 90 to 100% where the bleeds were closed and the inlet guide vanes were fixed. A simple set of algorithms were developed for combining both total pressure and temperature with allowances for when that combination was concurrent or in opposite segments. Based upon that set of algorithms, a graphical representation of the expected loss in stability pressure ratio for 97% speed is presented in **Figure 3.169**.

Superimposed on the graph is what the algorithm would produce for both the altitude and the SLS cases in terms of the separate levels of pressure and temperature distortion. Also presented in Figure 25 for comparison purposes is what the parallel compressor code produced also in terms of the loss in stability pressure ratio. For both cases, the parallel compressor code results were in excellent agreement to that predicted by the algorithm (10.1% versus 10% altitude and 8.3% versus 7.0% @ SLS). This verification, although not exact does give confidence in the results from the parallel compressor code such that a prediction using actual temperature distortion from flight test data and an estimate of the expected pressure distortion can be made.

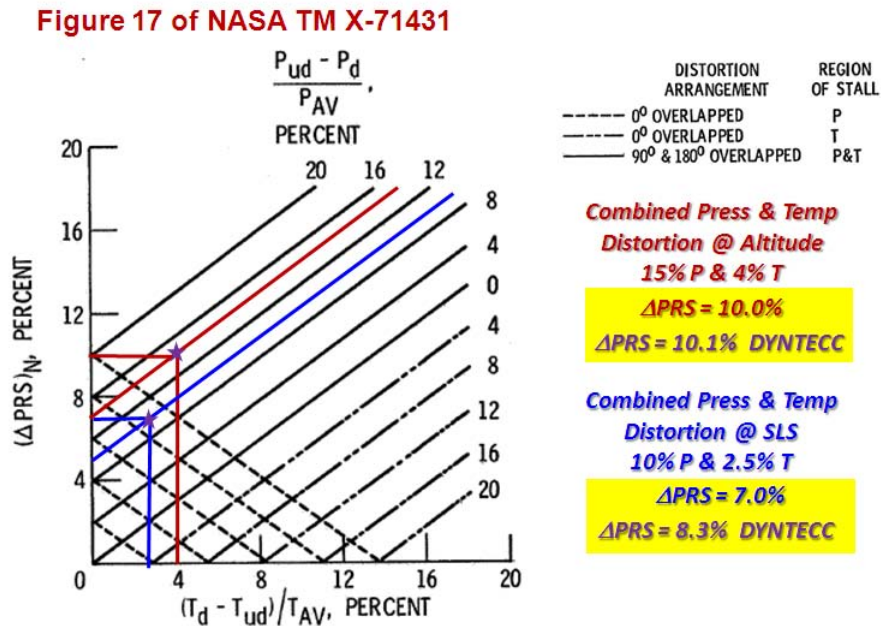


**Figure 3.169 Comparison of the Parallel Compressor Results to that Predicted by the NASA Algorithm Based Upon Experimental Results**

### Parametric Investigation

Since the parallel compressor model has been shown to provide reasonable results with both temperature and pressure distortion separately and in combination, an investigation into the effects of distortion on what could be expected during a typical flight may be conducted. During the flight test program, temperature instrumentation was available near the engine face on the outer casing providing a temperature profile as illustrated in [Figure 3.170](#).

This particular profile was representative of the highest levels of temperature distortion resulting from the combined effects of re-ingestion and inlet duct heat transfer and was extensively analyzed as reported by Hale in [Ref. 3.121](#). To make the profile amenable to the parallel compressor model, simplification of the pattern was necessary. This simplification is also presented in [Figure 3.170](#).

During the flight test, no total pressure measurements at the AIP were made and as such the level of pressure distortion was not quantitatively known. However, based upon the steady



state CFD predictions as presented earlier in this paper, an estimate of the level of pressure distortion can be made and predictions of their effect along with the known temperature distortion can be made using the parallel compressor model. Using the CFD predictions as a guide, a parametric study was conducted to determine the effect on the stability limit of various levels of pressure distortion in combination with the actual observed temperature distortion. The results of that parametric investigation are presented in **Figure 3.170**.

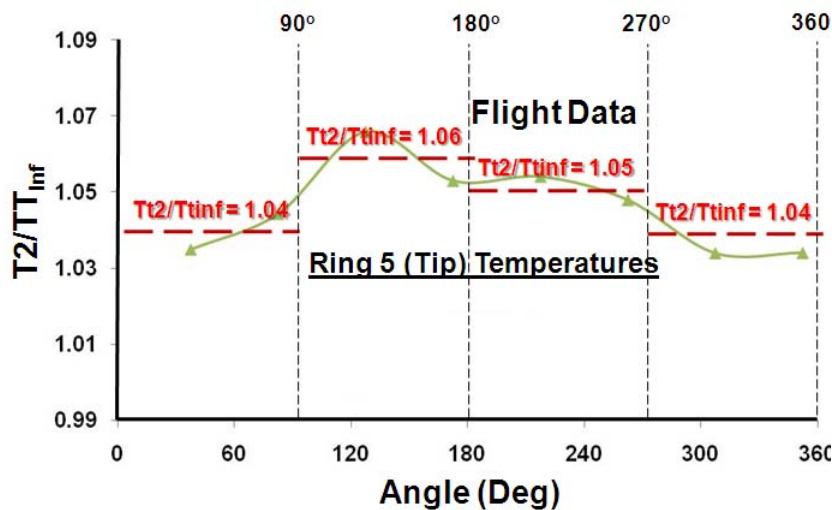


**Figure 3.170 Measured Temperature Distortion Near the Tip of the Compressor and a Representation of the Simplification Necessary for the Parallel Compressor Model**

segments. Verification of these predictions can only be made when adequate instrumentation (i.e. addition of AIP dynamic total pressure measurements) is provided. However, this set of

The loss in stability pressure ratio for the temperature distortion alone was 8.3%. When increasing amounts of pressure distortion (5, 10 & 15%) were added, the loss in stability pressure ratio increased to 9.5, 11.4 and 11.4%, respectively. Although there was no change between 10 and 15% pressure defect cases in terms of loss in stability limit, there was a shift in the speedline due to the additional crossflow terms as a result of the larger pressure difference between the parallel

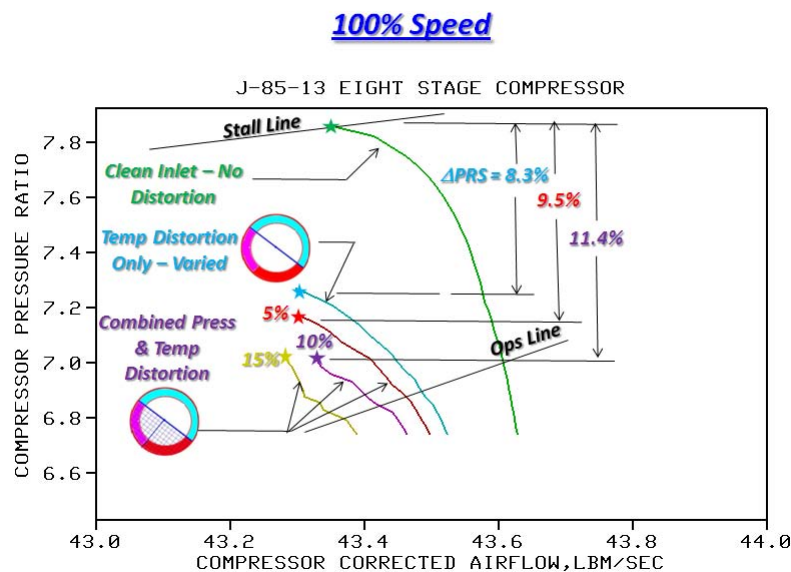


**Figure 3.171 Parallel Compressor Model Prediction of the Effect on System Operability Due to Various Levels of Pressure Distortion and the Measured Temperature Distortion**

predictions can be used to provide a sense of what is important to the operability of the J85 engine and what potential solutions might be attractive to reduce the temperature and pressure distortion levels or their effect on operability.

### Summary and Conclusions for the J85 Investigation

The **parallel compressor model** has been validated for the J85-GE-13 compression system using extensive experimental results obtained by NASA during the 1970's for both clean and distorted inlets caused by both total pressure and temperature separately and in combination. Since the J85-GE-13 system is similar to the J85-GE-5 at least up to 100% speed, the validated parallel compressor model can be used to predict trends and effects of inlet distortion for the current J85 system (R/S version) without being overly concerned about the differences between the current version and the original J85 for the T-38 application. The validated model was then used to predict the effects of combined total pressure and temperature effects on the stability pressure ratio using CFD predictions of the distortion. When those results were compared to an experimentally determined algorithm for combined pressure and temperature distortion, they were found to be in good agreement. In addition, predictions of actual flight temperature profiles and estimated total pressure profiles effects on system operability were calculated and were judged to be consistent with other predictions.

### ADDITIONAL REFERENCES

**3.100** Brithwaite, W. M. and R. H. Soeder, "Combined Pressure and Temperature Distortion Effects on Internal Flow of a turbofan Engine." AIAA Paper No. AIAA-79-1309, Presented at the AIAA/SAE/ASME 15th Joint Propulsion Conference, Las Vegas, NV, June 1979.

**3.101** Soeder, R. H., and G. A. Bobula, "Effects of Steady-State Temperature and Combined Distortion 6n Inlet Flow to a Turbofan Engine." NASA-TM79237, August 1979.

**3.102** Soeder, R. H., and C. M. Mehlic, "Effect of Combined Pressure and Temperature Distortion Orientation on High-Bypass-Ratio Turbofan Engine Stability." NASA-TM-83771, October 1984.

**3.103** Hale, A. A. and M. W. Davis, Jr., "DYNamic Turbine Engine Compressor Code: DYNTECC -- Theory and Capabilities", AIAA Paper # AIAA-92-3190, Presented at the 28th Joint Propulsion Conference and Exhibit, Nashville, TN, July 1992.

**3.104** Davis, M. W., Jr., "Parametric Investigation into the Combined Effects of Pressure and Temperature Distortion on Compression System Stability", AIAA Paper # AIAA-91-1895, Presented at the 27th Joint Propulsion Conference, Sacramento, CA, June 1991.

**3.105** Shahrohi, K. A., and M. W. Davis, Jr., "Application of a Modified Dynamic Compression System Model to a Low-Aspect Ratio Fan: Effects of Distortion," AIAA-95-0301, Presented at the 33rd Aerospace Science Meeting, Reno, NV, January 1995.

**3.106** Eden, R. M., "The Northrop Grumman T-38 Talon: 40 Years Plus & Still Teaching Pilots to Fly", AIAA 2001-0313, 39<sup>th</sup> Aerospace Science Meeting & Exhibit, 8-11 January 2001, Reno, Nevada.

**3.107** Briskin, T. A., Howell, P. N., & Ewing, A. C., "J85 Rejuvenation Through Technology Insertion", RTO EN-14, October 2000.

- 3.108** Wimer, R. & Hall, A., "Computer Modeling to Solve Problems with the T-38 Propulsion Modernization Program", Paper/Presentation Presented on October 25, 2007 at the NDIA 10<sup>th</sup> Annual System Engineering Conference.
- 3.109** Leyes, R. A., **The History of North American Small Gas Turbine Aircraft Engines**, Chapter 6, General Electric Small Aircraft Engine, "The J85 Turbojet Engine", AIAA Library of Flight Series, 1999, pp. 261-279
- 3.110** Hale, A. A. and M. W. Davis, Jr., "DYNamic Turbine Engine Compressor Code: DYNTECC -- Theory and Capabilities", AIAA Paper # AIAA-92-3190, Presented at the 28th Joint Propulsion Conference and Exhibit, Nashville, TN, July 1992.
- 3.111** Davis, M. W., Jr., "Parametric Investigation into the Combined Effects of Pressure and Temperature Distortion on Compression System Stability", AIAA Paper # AIAA-91-1895, Presented at the 27th Joint Propulsion Conference, Sacramento, CA, June 1991.
- 3.112** Shahrooki, K. A., and M. W. Davis, Jr., "Application of a Modified Dynamic Compression System Model to a Low-Aspect Ratio Fan: Effects of Distortion," AIAA-95-0301, Presented at the 33rd Aerospace Science Meeting, Reno, NV, January 1995.
- 3.113** Milner, E. J., "Analytical Prediction of the Performance and Stability of a J85-13 Compressor with distorted Inlet Flow", NASA TM X-3515, May 1977.
- 3.114** Tesch, W. A., & Steenken, W. G., "Blade Row Dynamic Digital Compression Program – Volume I: J85 Clean Inlet Flow and Parallel Compressor Models", NASA CR-134978, March 1976.
- 3.115** Calogeras, J. E., Mehalic, C. M., & burstadt, P. L., "Experimental Investigation of the Effect of Screen-Induced Total Pressure Distortion on Turbojet Stall Margin", NASA TM X-2239, March 1971.
- 3.116** Mehalic, C. M., & Lottig, R. A., "Stead-State Inlet Temperature Distortion Effects on the Stall Limits of a J85-GE-13 Turbojet Engine", NASA TM X-2990, February 1974.
- 3.117** Braithwaite, W. M., Graber, E.J., & Mehalic, C., M., "The effects of Inlet Temperature and Pressure Distortion on TurboJet Performance" NASA TM X-71431, November 1973.
- 3.118** SAE S-16 Committee, ARP 1420, Revision B,"Gas Turbine Inlet Flow Distortion Guidelines," Society of Automotive Engineers, February 2002.
- 3.119** SAE Aerospace Information Report AIR-1419, "Inlet Total-Pressure Distortion Considerations for Gas Turbine Engines," May 1983.
- 3.120** Society of Automotive Engineers, "A Current Assessment of the Inlet/Engine Temperature Distortion Problem," Aerospace Resource Document AIR 5867, 2009.
- 3.121** Hale, A. A., et.al., "An Investigation into the Effects of Highly Transient Flight Maneuvers on Heat and Mass Transfer on the T38 Air Force Trainer Inlet", ASME GT2010-YYYYY, To be Presented at the 2010 IGTI Conference, June 2010.

### 3.2.6 Inlet Swirl Distortion Analysis

Historically, swirl has not been a major performance or operability concern on any U.S. fighter or bomber application, largely because those military aircraft have engines fitted with inlet guide vanes (IGVs). There are no documented cases in the open literature where swirl has had to be considered for engines with IGV's. However, some installations do not use IGV's and consequently exhibit a higher sensitivity to swirl than engines with IGV's. Furthermore, new inlet concepts designed for low observables (stealth) feature sharp s-bends that can induce significant swirl. Flows with severe swirl may cause separation on IGV's and produce unwanted pressure distortion to the first rotor and thus contribute to an additional loss of stability margin unaccounted for in the established inlet distortion methodology. These issues prompted the Society of Automotive Engineers (SAE) S-16 Committee to embark on the development of a methodology for considering swirl as part of the inlet-engine compatibility assurance process.

Swirl can be categorized by type as: paired, bulk, wrapping inlet swirl, and tightly wound vortices. Paired swirl is produced when a flow containing vorticity normal to the flow direction is turned in the plane of the vorticity. Paired swirl is the most common case of swirl and is associated with flow in an S-duct. Low velocity fluid moves

inward in boundary layers at the left and right of the duct (when the turn is in the vertical plane). This results in two vortices rotating in opposite directions at the exit of the turn. When the two vortices have equal magnitude and opposite rotation, this is termed twin swirl. Twin swirl has zero circumferential average around the annulus. In the more general case of flow with non-symmetric boundary layers, two vortices are formed of opposite rotation but different magnitude. In this case, the swirl has non-zero circumferential average around the annulus. Two examples of paired swirl are shown in Figure 3.172.

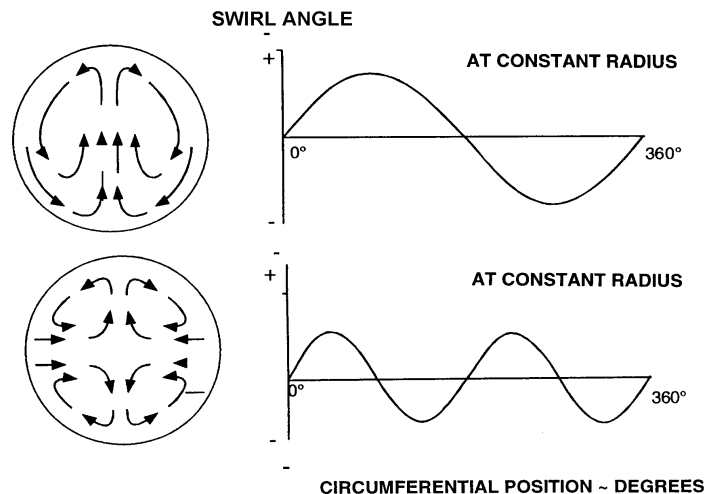


**Figure 3.172 Projected Velocity Vectors Produced with Paired Swirl [3.124]**

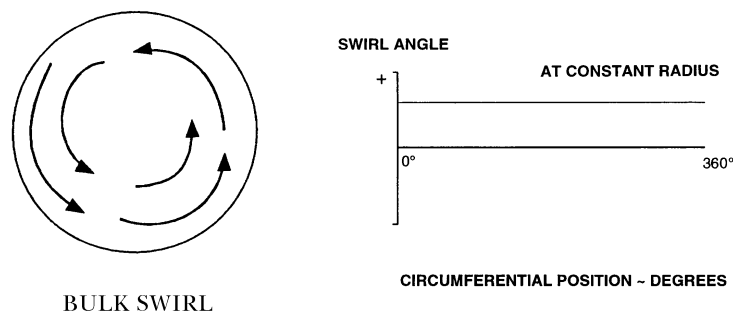


**Figure 3.173 Projected Velocity Vectors Produced with Bulk Swirl [3.124]**

Bulk swirl is a special case of paired swirl in which the magnitude of one of the swirls greatly exceeds that of the other and is shown schematically in Figure 3.173.

Bulk swirl can be generated either externally to the inlet or internally from non-axisymmetric total-pressure gradients through a turn

in the inlet ducting. Bulk swirl has non-zero average circumferential velocity around the annulus. Bulk swirl can be caused by S-bend induced pressure gradients acting on a locally separated flow which separated upstream of the bend. For an S-shaped inlet, the swirl process is initiated when a total pressure deficit region occur out-of-plane with the bend (e.g. left and right for a vertical S-duct).

### **CITED EXAMPLE(S)**

**3.122** Davis, Milt, Hale, Alan, "A Parametric Study on the Effects of Inlet Swirl on Compression System Performance and Operability using Numerical Simulations," ASME Paper #GT2007-27033, 2008 ASME Turbo Expo, May 2007.

**3.123** Davis, Milt, Beale, Dave, Sheoran, Yogi, "Integrated Test and Evaluation Techniques as Applied to an Inlet Swirl Investigation Using the F109 Gas Turbine Engine," ASME Paper #GT2008-50074, June 2008.

### **MODELING TECHNIQUE**

The following section will discuss work done at AEDC involving inlet swirl distortion. This section will include analysis done with the dynamic **parallel compression system models**, **DYNTECC** ([Section 4.6](#)), **meanline** model ([Section 4.2](#)), and the **TEACC** 3D Euler model ([Section 4.7](#)). Analysis will be presented for 3 separate cases, Rotor 1B (Single Rotor Configuration), F109 fan (Single Stage Configuration), and the HTSC (Multiple Stage Configuration).

### **APPLICATION TO TWO RESEARCH COMPRESSORS, ROTOR 1B AND THE HIGH TIP SPEED COMPRESSOR**

To conduct a numerical parametric investigation, two compression systems were chosen: one system representing technology of the 60's and 70's and the other system representing technology of the 80's, 90's and current systems. Both systems have design aspects of compression systems in use in modern-day military turbofan engines. The first system was a single rotor (Rotor 1B) tested by NASA and the other a two-stage, advanced-design (low aspect ratio, high solidity) fan (High Tip Speed Compressor, HTSC). The primary reason these machines were selected was because neither system had an IGv. Therefore, the first rotor of each system was exposed to the swirl distortion, unaltered.

Rotor 1B [\[3.129\]](#), [Figure 3.174](#), was chosen as one of the compression systems because it offered simplicity in the number of stages (1 blade row), and enough experimental data to construct reliable rotor characteristics. Rotor 1B is a high-performance transonic rotor similar to those found in modern high-speed aircraft. The rotor was designed with a multiple circular-arc blade shape which was applied over the top 40 percent of the blade while a double circular-arc construction was employed for the bottom 60 percent of the blade. With a hub-to-tip ratio at the rotor inlet of 0.5, the blade sections were long enough to require a mid-span damper to maintain structural integrity during operation. Rotor 1B consisted of 44 blades, producing a moderate solidity of 1.3 at the rotor tip. Rotor 1B was designed for a total pressure ratio of 1.6 at design speed and flow rate.

The more advanced system, a two-stage fan, was tested at the Compressor Research Facility (CRF) in the 80's and 90's under a variety of programs (HTSC, ADLARF, CRFER). The specific version of the 2-stage fan used in this analysis was designated the High Tip Speed



Compressor, HTSC and was configured with no IGV, un-swept rotor blades, and smooth tip casing (**Figure 3.175**).

The system was designed to provide a total pressure ratio of 2.5 at design speed and flow rate. The first rotor is a state-of-the-art, integrally-bladed disk (blisk), low aspect ratio design. The variable first stage stator (S1) contains 41 vanes in an overlapped, tandem configuration - the forward section is fixed and the aft flap variable. The vanes of the S1 forward section are bowed, swept design. Rotor two (R2) is a slot bladed disk containing 40 blades with tip solidity and  $(t/c)_{max}$  very close to that of R1. Both rotors employ pre-compression tip section airfoils (see discussion in Section 2-3) over the outer 30-40% span and tailored controlled diffusion airfoils (CDA) throughout the remainder of the blade. Stator two (S2) contains 60 vanes at fixed

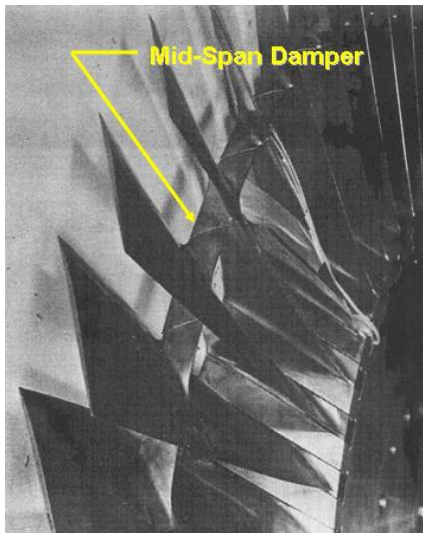


**Figure 3.174 Single-Stage Rotor 1B**



**Figure 3.175 Two-Stage HTSC as Tested at the Compressor Research Facility [3.125]**

stagger and leaned counter to the direction of rotor rotation. Details of the 2-stage fan can be found in Boyer's Dissertation [3.125].

### Blade Row Analysis -- Rotor 1B

To predict the effects of Co-and Counter swirl on blade row performance, the **meanline code** described above was applied to the specific compression systems using required blade and annulus geometry and a set of loss and deviation correlations based upon cascade tests of NACA 65 Series blades and Double Circular Arc blades as reported in **Ref. 3.128**.

The **meanline** code was calibrated to the experimental results for both systems so that an accurate representation of the clean inlet performance was assured. Calibration was only conducted at the design speeds to provide a proof-of-concept. For complete analysis on these systems, calibrations would need to be conducted at a variety of speeds. For both applications investigated an inlet swirl representing 5 degrees of angular deviation from straight flow in both a Co-and Counter-rotation direction was applied to the **meanline** inlet boundary condition.



The results of the calibration of Rotor 1B at 100 percent speed is presented in [Figure 3.176](#). The **meanline** model was only calibrated at 100 Percent speed so that Since the system is a single blade row, overall total pressure and temperature ratios were specified in the calibration process. The loss and deviation obtained by the correlations were modified by an iterative process until the desired total pressure and temperature ratios were obtained. As can be seen in [Figure 3.176](#), the calibration process produced a meanline that reproduces the measure experimental results at 100% speed.

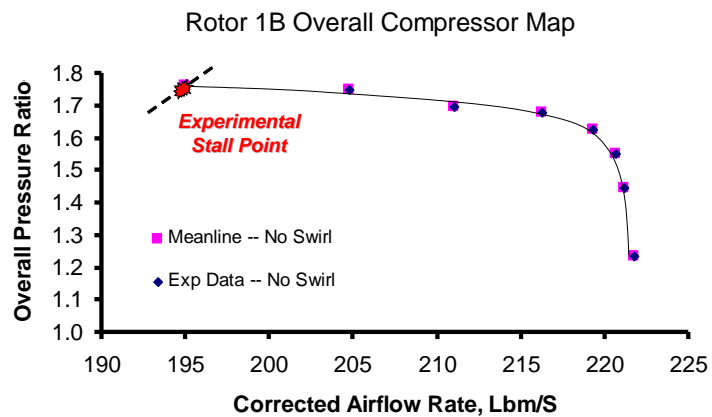


**Figure 3.176 Results of R1B Meanline Calibration Process at 100% Speed**

Using the **meanline** code, each flow point was recalculated with an inlet flow angle of plus or minus 5 degrees from axial. That is the flow was given an angular velocity in the direction of rotor rotation (Co-swirl) or in the opposite direction of rotor rotation (Counter-swirl) thus producing a circumferential swirl component to the inlet flow. During this process, the correlations used within the **meanline** code were not adjusted as they had been in the calibration process but were allowed to reflect the change in both loss and deviation due to the change in inlet flow conditions (i.e. the addition of swirl). The results of the co-and counter-swirl blade row analysis using the **meanline** code produce the new co-and counter-swirl rotor characteristics presented in [Figure 3.176](#) together with the clean inlet rotor characteristics.

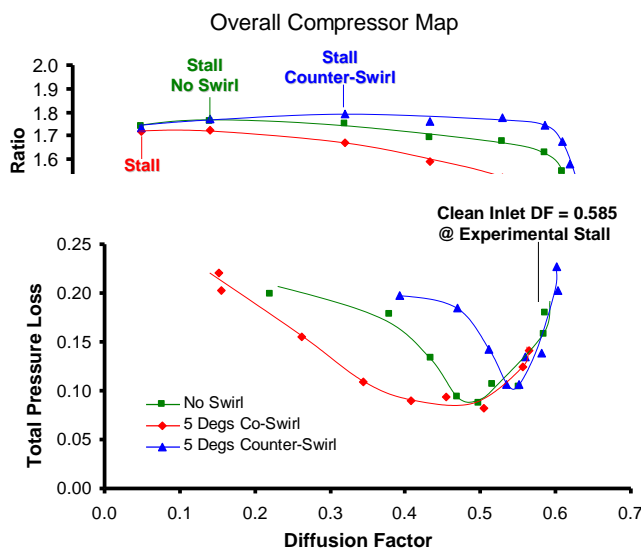


**Figure 3.177 Effect of Swirl on Rotor 1B Loss and Diffusion Factor**

The effect of a positive swirl angle (i.e. Co-swirl) is to reduce the rotor pressure ratio at all flow points because there has been a reduction in the blade incidence angle. The reduction in total pressure ratio is more pronounced away from stall and near choke. The effect of negative swirl angle (i.e. Counter-swirl) is to increase total pressure ratio at all flow points because there has been an increase in incidence angle. However, the point at the clean inlet stall point is near the same level of pressure ratio as the clean value because the losses have increased enough to lower the performance even though the incidence angle is higher.

The **meanline** code does not currently have a stall criteria built into the code itself. It is up to the user to make a determination when and if the blade row becomes stalled. One criterion that has been used in the past is the diffusion factor.

*“Values of DF (Diffusion Factor) in excess of 0.6 are thought to indicate blade stall and a value of 0.45 might be taken as a typical design choice.” [3.126]*

The diffusion factor is a measure of the velocity diffusion taking place in the channel between blades and a value near 0.6 has been observed to indicate where total pressure losses begin to dramatically increase. Diffusion factors near or above 0.6 are indicative of stalling behavior (flow separation resulting in under-turning of the flow) and has been used in the past to indicate stalled flow. The diffusion factor is presented in **Figure 3.177** as a function of total pressure loss for all three cases (clean inlet, co-swirl, and counter-swirl) for the full range of airflows.

For the clean inlet, the diffusion factor at the experimental stall point was observed to be 0.585 which is near the recommended value of 0.6 [3.126]. That value was used to determine the stall points for both the co-and counter-swirl cases. For counter-swirl, the stalling airflow rate was approximately 205 lb<sub>m</sub>/sec and for the co-swirl, the stalling airflow rate occurred at approximately 190 lb<sub>m</sub>/sec, much lower than that observed for clean inlet (195 lb<sub>m</sub>/sec). Those stall points are shown in **Figure 3.176** and will be used in the bulk and twin swirl investigations in a latter section.

### Blade Row Analysis -- High Tip Speed Compressor (HTSC)

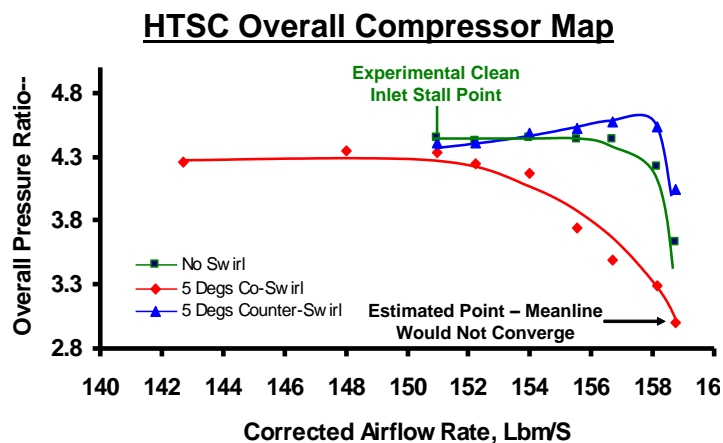


**Figure 3.178 The Effect of +/- 5 deg of Swirl on HTSC Overall Performance**

from axial. That is the flow was given an angular velocity in the direction of rotor rotation (Co-swirl) or in the opposite direction of rotor rotation (Counter-swirl) thus producing a circumferential swirl component to the inlet flow. As was the case in the Rotor 1B application, the correlations used within the **meanline** code were not adjusted as they had been in the calibration process but were allowed to reflect the change in both loss and deviation due to the change in inlet flow conditions

To investigate the effects of swirl on a multi-stage compression system, the High Tip Speed Compressor (HTSC) was chosen since it represented a fan system that has features similar to systems being implemented in today's military turbofan engines. A similar process was conducted using the **meanline** code as was conducted with Rotor 1B. First the application of the HTSC to the **meanline** code was calibrated to the experimental results at 98.6% speed as published by Boyer in **Ref 3.125**.

Using the **meanline** code, each flow point was recalculated with an inlet flow angle of plus or minus 5 degrees

The effect of swirl on the overall performance ([Figure 3.178](#)) is not as easily discerned as was the case for the single rotor system (Rotor 1B) because of the multi-stage re-matching. In general, the effect of a positive swirl angle (i.e. Co-swirl) on system performance is to reduce the rotor pressure ratio at all flow points. The reduction in total pressure ratio is more pronounced away from stall and near choke. Also in general, the effect of negative swirl angle (i.e. Counter-swirl) on system performance is to increase total pressure ratio at all flow points except for points nearer to stall.

However, the generalization is not uniform across the whole flow spectrum in the case of the counter-swirl case. Since the **meanline** code can calculate beyond blade row stall, one must

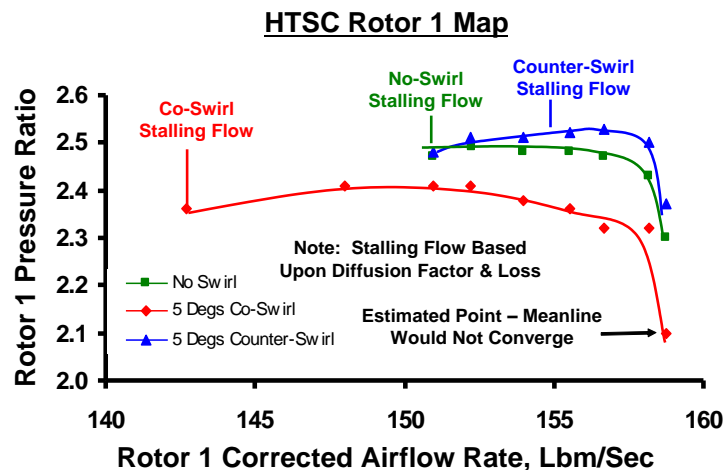


**Figure 3.179 The Effect of +/- 5 deg of Swirl on HTSC First Rotor Performance**

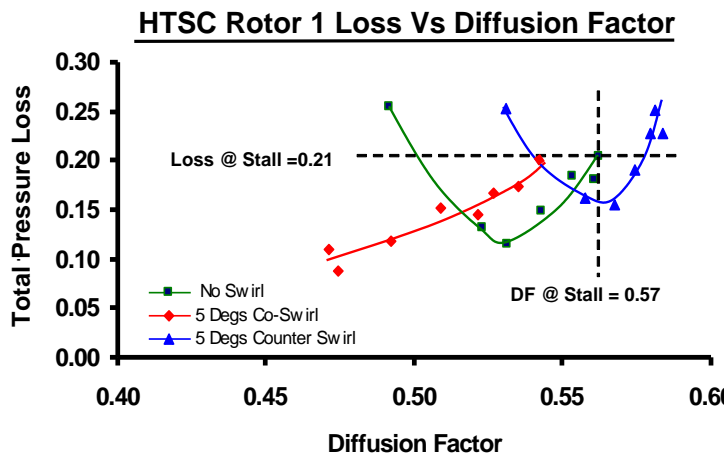


**Figure 3.180 Effect of +/- 5 deg of Swirl on HTSC First Rotor Loss and Diffusion Factor**

evaluate the individual rotor performance and make a determination as to blade row stall and consequently system stall. Using the same approach as was done with Rotor 1B, individual rotor performance was analyzed to determine the effects of swirl on both performance and operability in [Figure 3.179](#) - [Figure 3.181](#).

Presented in [Figure 11](#) is the effect of swirl on the first rotor performance. As can be seen within the figure, the effect of swirl does follow what was observed with Rotor 1B. Also indicated on [Figure 3.179](#) are blade row stalling flow points which were estimated using the diffusion factor method similar to what was done with Rotor 1B.

The diffusion factor for the first rotor is presented in [Figure 3.180](#) as a function of total pressure loss for all three cases (clean inlet, co-swirl, and counter-swirl) for the full range of airflows. For the clean inlet, the diffusion factor at the experimental stall point was observed to be 0.57 which is near the recommended value of 0.6 [[3.126](#)]. That value and the corresponding loss (0.21) was used to determine the first blade row stall points for both the co- and counter-swirl cases as indicated in [Figure 3.179](#).

Presented in [Figure 3.181](#) is the effect of swirl on the second rotor performance. As can be seen within the figure, the effect of swirl does not seem to follow the trend as was observed within the first rotor. In fact, as might be expected, the effect of swirl has been “washed out” and

certainly doesn't affect the counter-swirl case at all. In the case of the co-swirl, it may be postulated that the effect of swirl is minimal. An average rotor performance is indicated in **Figure 3.181** to use in Bulk and Twin swirl parametric investigations reported in a latter section of this paper.

The diffusion factor for the second rotor is presented in **Figure 3.182** as a function of total pressure loss for all three cases (clean inlet, co-swirl, and counter-swirl) for the full range of airflows.

For the clean inlet, the diffusion factor at the experimental stall point was observed to be 0.45 which is near the recommended value for design [3.126]. Even though the losses are higher than those observed for the first rotor, the diffusion factor suggests that the second rotor is operating near its design point for all cases and is not a contributing factor in system stall.

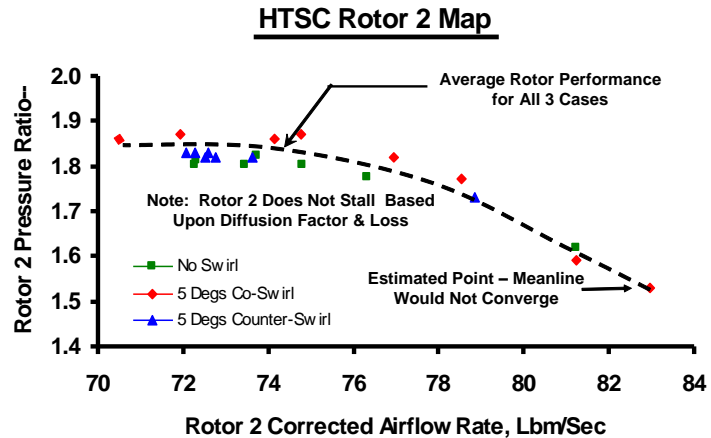


**Figure 3.181 Effect of +/- 5 deg of Swirl on HTSC Second Rotor Performance**

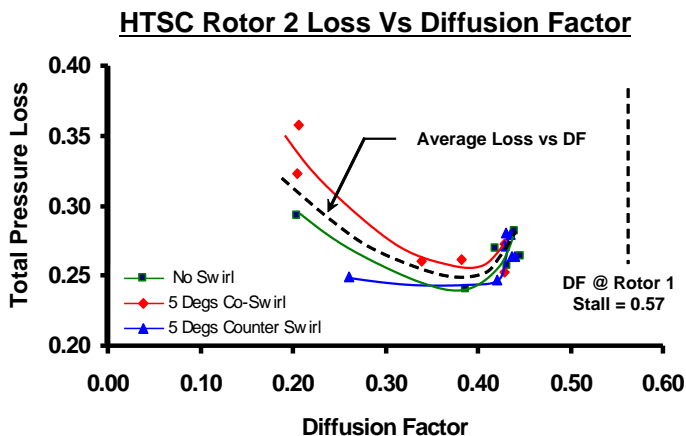


**Figure 3.182 Effect of +/- 5 deg of Swirl on HTSC Second Rotor Loss and Diffusion Factor**

characteristics was performed when bulk swirl was imposed on the inlet control volume. A scale-factor on the stage pressure ratio characteristic was applied to simulate what was deduced with the **meanline** code. Bulk swirl in the co-swirl direction tends to lower the pressure ratio and extend the stalling flow rate while swirl in the counter-swirl direction tends to increase the pressure ratio and decrease the stalling flow rate. The stall criteria for clean inlet (the flow at which the stage pressure characteristic has a zero slope) was also modified to reflect what was discovered with the **meanline** code and the diffusion factor investigation when either co or counter-swirl was present.

## Compression System Analysis

Using a **parallel compression system numerical simulation** as described in a previous section, a parametric investigation was conducted to qualitatively determine the effects of both bulk and paired swirl has on both the Rotor 1B and the HTSC compression systems performance and operability. Bulk swirl was investigated first to determine if the model would produce similar results as that obtained by the **meanline** code for both compression systems. To simulate the effects of bulk swirl, a simple modification to the affected clean inlet input stage(s)

When twin-paired swirl was investigated, the parallel compressor simulation was divided into two equal circumferential segments. To simulate twin-paired swirl, one sector was required to use the co-swirl characteristics while the other sector was required to use the counter-swirl characteristics. When pressure distortion along with swirl was investigated, the same two circumferential segments were used and one segment was reduced in inlet total pressure while the other was held at the initial pressure.

The following procedure was used to investigate the effects of swirl and pressure distortion on system performance and operability. The parallel compressor model was first allowed to come to a steady condition. If swirl was to be implemented on the system, it was initiated abruptly after the steady condition was established. This caused some numerical instability which quickly settled out and the system was allowed to reach a new steady condition again. Once steady conditions were assured, the exit static pressure which had been held constant for steady operation was ramped at a quasi-steady rate to back pressure the system and drive the system to its instability point. If pressure distortion was to be implemented along with swirl, it was ramped on over a short time interval and the system was allowed to reach a new steady operating point before implementing swirl and the final exit static pressure ramp.

### Compression System Analysis -- Rotor 1B

The results of co- and counter bulk swirl on the performance and operability of the single rotor system, Rotor 1B, are presented in [Figure 3.183](#). Although the results are not identical to that obtained with the **meanline** code due to the scale factor approach, ([Figure 3.177](#)), they have an appropriate spread in stalling mass flow and a similar range in pressure ratio. Therefore, the scale factor approach for creating co-and counter-swirl characteristics within the parallel compressor simulation is adequate for investigating the effects of paired swirl distortions as presented in [Figure 3.172](#).

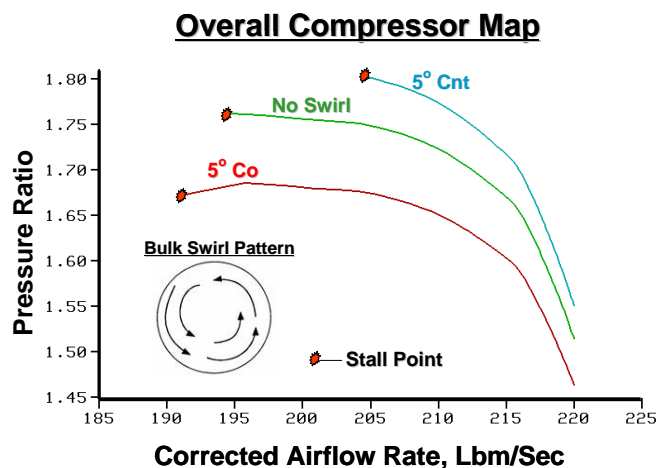


**Figure 3.183 The Effects of Co- and Counter Bulk Swirl on Rotor 1B Performance and Operability**

Similar to the bulk swirl case, twin-paired swirl was investigated with the parallel compressor model by applying the appropriate swirl compressor characteristic for each parallel tube. The results for Rotor 1B are presented in [Figure 3.184](#).

As can be seen, the twin-swirl performance in terms of Pressure Ratio is lower than both the no-swirl and counter-swirl bulk swirl cases. In addition, the stall point is between the counter and co-swirl cases. By examining the individual sector flow coefficients ([Figure 3.185](#)) which is indicative of the corrected flow that would exist in that sector if the sector where operating with full flow, one can determine that the co-swirl stall

point is controlling the overall stall point of the system when subjected to twin swirl. This result does not seem intuitive but can readily be explained by viewing where each segment ends up after swirl is implemented on the inlet during steady state operation. Because the parallel



compressor model is holding the same static pressure back boundary condition as existed during clean inlet flow, the mass flow in each segment must adjust to the new inlet conditions.

In the co-swirl case, the massflow decreases for that same static pressure, while the counter flow massflow slightly increases. This condition sets the co-swirl sector in a position to be much closer to the stall side of the operating characteristic and thus when a rapid static pressure increase is applied to the exit boundary, the co-swirl sector reaches its stalling airflow rate much sooner than the counter-swirl sector. For parallel compressor theory, when one sector reaches its stall point, the full compression system is said to be stalled.

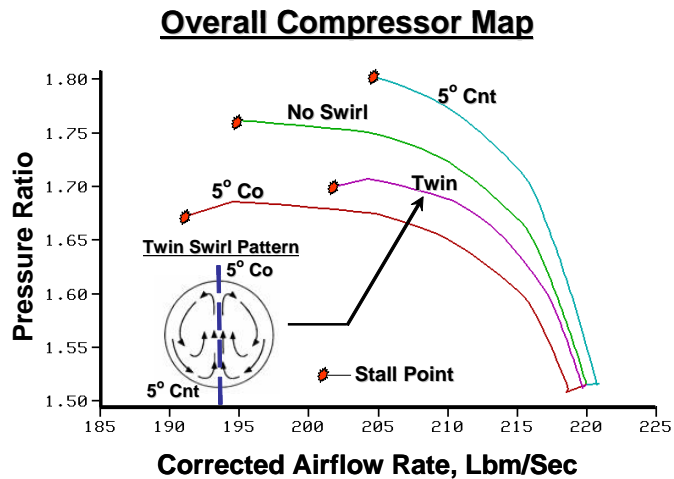


**Figure 3.184 The Effects of Twin Bulk Swirl on Rotor 1B Performance and Operability**

A final analysis was conducted with Rotor 1B which investigated the effects of swirl and pressure distortion in combination as alluded to previously and in **Ref. 3.131**. In fact, if swirl is present, it will be accompanied by total pressure distortion as well and it will be hard to separate out the individual effects in an actual experiment. Using the parallel compressor model, it was easy to implement two different possibilities. One possibility has the low pressure region concurrent with the count-swirling flow and the other possibility has the low pressure region concurrent with co-swirling flow. For this investigation, 5 degrees of co-and counter-swirl were implemented along with a 5 percent reduction in total pressure in one sector at a time. The results of that investigation are presented in **Figure 3.186**.

Both the performance and stall point were affected by which combination of swirl and pressure distortion was implemented. When the low pressure region was concurrent with the counter-swirl region, the pressure ratio was higher than that calculated with only swirl, but obviously lower than the clean inlet case. When the low pressure region was concurrent with the co-swirl region, the exact opposite was true (i.e. the pressure ratio was lower than that calculated with swirl alone). In both cases with pressure distortion, the co-swirl sector drove the compression system to the stability limit

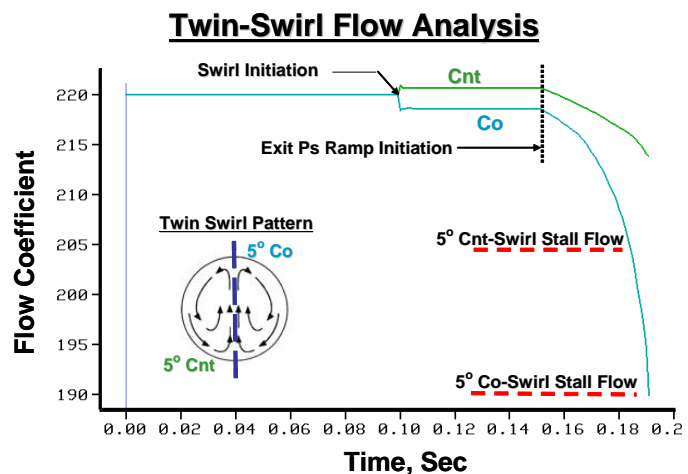


**Figure 3.185 The Effects of Twin Bulk Swirl on Rotor 1B Performance and Operability**



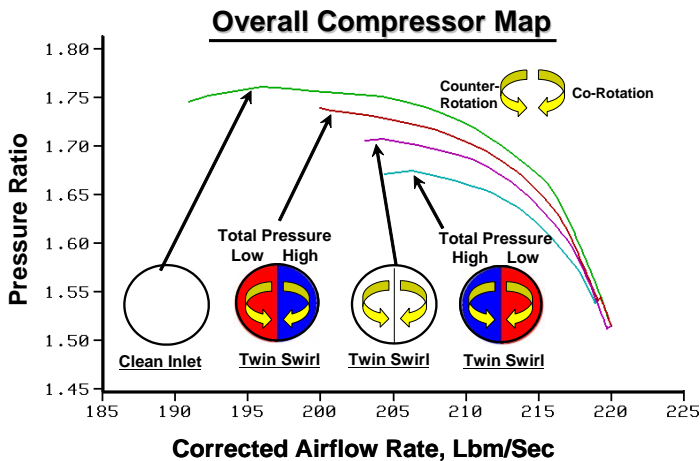


**Figure 3.186 The Effects of Twin Bulk Swirl In Combination with Total Pressure Distortion on Rotor 1B Performance and Operability**

### Compression System Analysis -- High Tip Speed Compressor

The results of co- and counter bulk swirl on the performance and operability of the HTSC are presented in [Figure 3.187](#). Although the results are not identical to that obtained with the **meanline** code due to the scale factor approach, ([Figure 3.178](#)), they have an appropriate spread in stalling mass flow and a similar range in pressure ratio. Therefore, the scale factor approach for creating co- and counter-swirl characteristics within the parallel compressor simulation is adequate for investigating the effects of paired swirl distortions as presented in [Figure 3.172](#).

The overall map ([Figure 3.187](#)) shows the effect on the system and equally important is the effect on each stage as presented in [Figure 3.188](#) and [Figure 3.189](#). To simulate the effects of swirl, the first rotor characteristic was adjusted while the second rotor characteristic was not adjusted. Thus the shift in overall performance is solely due to the simulated effect of swirl on the first rotor while the second rotor rematches to the new conditions as was observed when applying the **meanline** code.

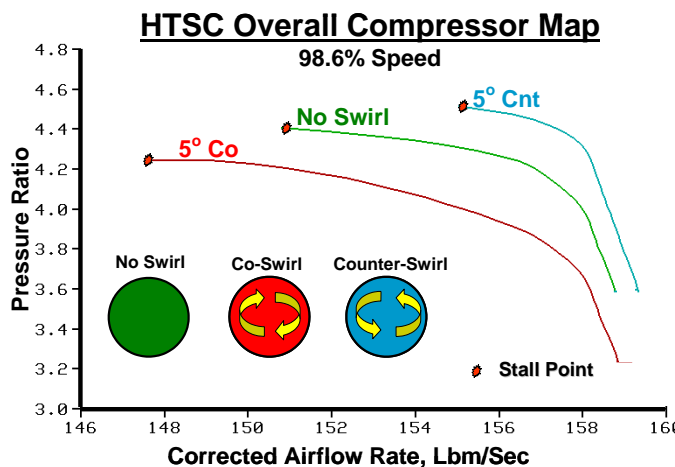


**Figure 3.187 The Effects of Co-and Counter Bulk Swirl on HTSC Performance and Operability**

The effect of twin-swirl was also investigated with the HTSC in a similar fashion as presented with Rotor 1B. As can be seen in [Figure 22](#), the twin-swirl performance in terms of Pressure Ratio is lower than both the no-swirl and counter-swirl bulk swirl cases. In addition, the stall point is between the counter and co-swirl cases. As was the case with Rotor 1B, examination of the individual sector flow coefficients indicate that the co-swirl stall point controls the overall stall point of the system when subjected to twin swirl.

For this investigation, 5 degrees of co- and counter-swirl were implemented along with a 5 percent reduction in total pressure in one sector at a time. The results of that investigation are presented in [Figure 3.190](#)

A final analysis was also conducted with HTSC which investigated the effects of swirl and pressure distortion.

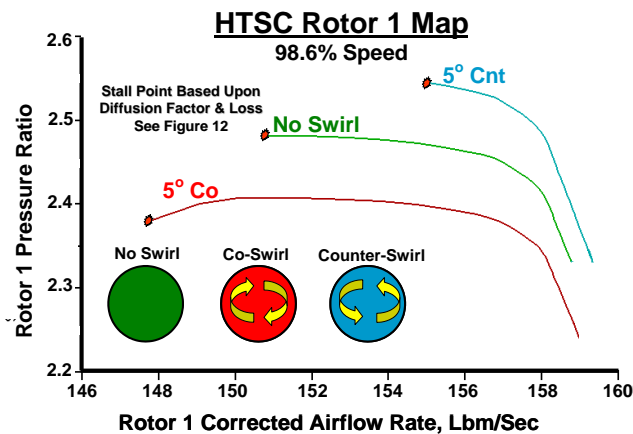


**Figure 3.188 The Effects of Co-and Counter Bulk Swirl on HTSC Rotor 1 Performance and Operability**

ratio was lower than that calculated with swirl alone). In both cases with pressure distortion, the co-swirl sector drove the compression system to the stability limit

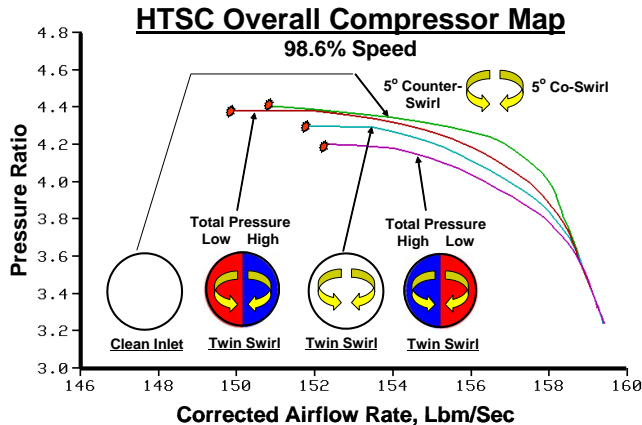


**Figure 3.190 The Effects of Twin Bulk Swirl In Combination with Total Pressure Distortion on HTSC Performance and Operability**

blade row or stage characteristics as input. Once the effect on blade row performance was determined with the **meanline** code, a simple scale factor method was used on the stage characteristics within the **parallel compressor** model to provide an effective means for changing the stage characteristic appropriately for the effect of either co- or counter-swirl. Predictions of the effect of twin swirl with and without inlet pressure distortion was conducted on

As was observed with Rotor 1B, both the performance and stall point were affected by which combination of swirl and pressure distortion was implemented. When the low pressure region was concurrent with the counter-swirl region, the pressure ratio was higher than that calculated with only swirl, but obviously lower than the clean inlet case. When the low pressure region was concurrent with the co-swirl region, the exact opposite was true (i.e. the pressure

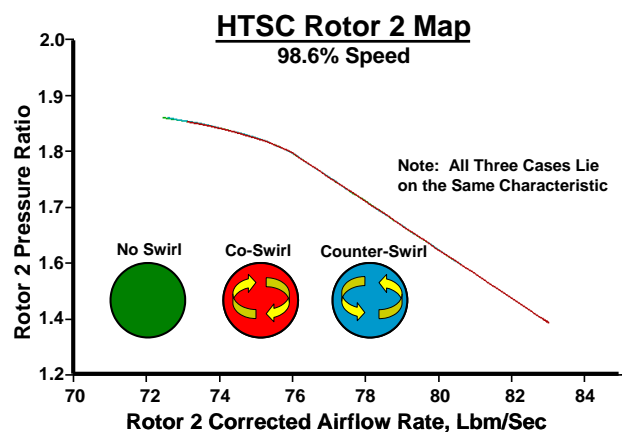


**Figure 3.189 The Effects of Co-and Counter Bulk Swirl on HTSC Rotor 2 Performance and Operability**

### Summary and Conclusions for Rotor 1B and HTSC

In summary, a parametric investigation into the effects of bulk and twin swirl was conducted using simple but effective numerical simulations (a **meanline** and **parallel compressor** codes). The **meanline** code was used to determine the effects of swirl on blade row performance which could then be implemented into a parallel compressor model which must have

a single blade row system and a 2-stage advanced compression system. The results from both systems appear reasonable. Since this section does not compare any of the swirl distortion results to experimental data, the numerical analysis should only be viewed as a guide in determining future experimental or numerical investigations.

### APPLICATION TO THE F109 TURBOFAN ENGINE SINGLE STAGE FAN

For the application to the F109 fan, the **meanline** code was initially calibrated to the experimental results so that an accurate representation of the clean inlet performance was assured. Once the F109 fan application of the **meanline** code was calibrated to the clean flow solution, that solution was used to investigate the effects of swirl on performance and operability. Inlet swirls representing 5° and 10° of angular deviation from straight flow in both a co- and counter-rotation direction were applied at the **meanline** inlet boundary condition.

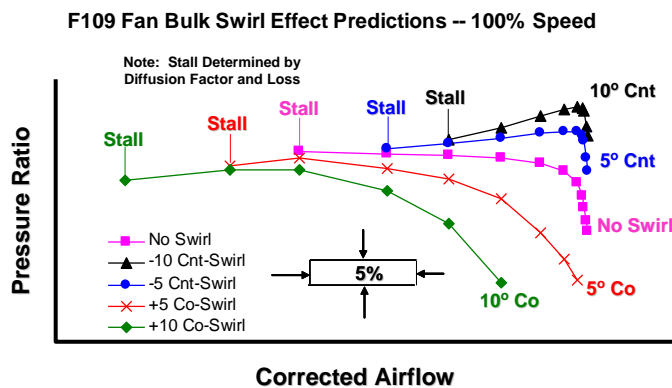


**Figure 3.191 Predictions of the Effect of Swirl on F109 Fan Performance**

The results of the co-and counter- swirl blade row analysis using the **meanline** code produce the new co- and counter-swirl rotor characteristics presented in **Figure 3.191** together with the clean inlet rotor characteristics. Although the numerical scales have been stripped, the spatial relation of the scales have been maintained to provide the reader a way of comparing.

The effect of a positive swirl angle (i.e., co-swirl) is to reduce the rotor pressure ratio at all flow points because there has been a reduction in the blade incidence angle. In addition, there is a shift in the full speedline to lower levels of flow rate. The reduction in total pressure ratio is more pronounced away from stall and near choke. The effect of negative swirl angle (i.e., counter-swirl) is to increase total pressure ratio at all flow points because there has been an increase in incidence angle. There is also a shift in the full speedline to higher levels of flow rate. Near the stalling flow rates, the pressure ratio decreases to values near that of the clean inlet due to the higher level of losses and incidence which is indicative of flow separation.

The **meanline** code does not currently have a stall criteria built into the code itself. It is up to the user to make a determination when and if the blade row becomes stalled. One criterion that has been used in the past is the diffusion factor. Values of DF (Diffusion Factor) in excess of 0.6 are thought to indicate blade stall and a value of 0.45 might be taken as a typical design choice [3.126].

The diffusion factor is a measure of the velocity diffusion taking place in the channel between blades, and a value near 0.6 has been observed to indicate where total pressure losses begin to dramatically increase. Diffusion factors near or above 0.6 are indicative of stalling behavior (flow separation resulting in under-turning of the flow) and has been used in the past to indicate stalled flow. The use of the diffusion factor as a stalling criterion has been well documented, but its use within a numerical simulation was first brought to the attention of the authors by members of the S-16 subcommittee on swirl distortion.

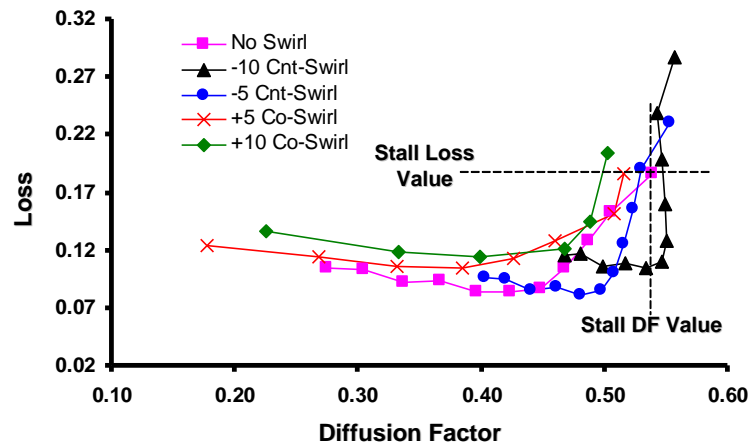


**Figure 3.192 Determination of Stall Point Using Diffusion Factor and Loss**

The diffusion factor is presented in **Figure 3.192** as a function of total pressure loss for all five cases (clean inlet, 5° and 10° co-swirl, and 5° and 10° counter-swirl) for the full range of airflows.

For clean inlet flow, the diffusion factor of 0.54 and associated loss of 0.19 corresponds to the diffusion factor associated with the experimental stall point. These values were chosen to provide the stalling criteria for cases when inlet swirl is present. For counter-swirl of both -5° and -10°, the DF was used to determine the stall point. For Co-swirl (both 5° and 10°), it was decided that stall occurred at the level of loss associated with the clean inlet stall point even though the DF had not reached a critical value.

### Predictions of Twin Swirl Effects on the F109 Fan Simulation Using a Parallel Compressor Simulation

Using a **parallel compression system numerical simulation**, an investigation was conducted to qualitatively determine the effects of both bulk and paired swirl on F109 fan system performance and operability. Bulk swirl was investigated first to determine if the model would produce results similar to those obtained by the **meanline** code.

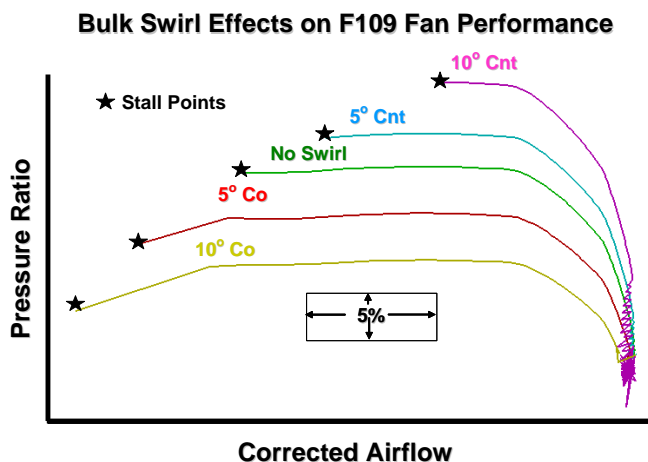


**Figure 3.193 The Effects of Bulk Swirl on F109 Fan Performance and Operability**

Bulk swirl was investigated first to determine if the model would produce results similar to those obtained by the **meanline** code.

To simulate the effects of bulk swirl, a simple modification to the affected clean inlet input stage(s) characteristics was performed when bulk swirl was imposed on the inlet control volume. A scale-factor on the stage pressure ratio characteristic was applied to simulate what was deduced with the **meanline** code. Although the bulk swirl characteristics using a scale-

factor algorithm are not identical to those predicted with the **meanline** code, they reproduce the major effects observed with the **meanline** as illustrated in **Figure 3.193** and thus are reasonable to use for relative comparisons.

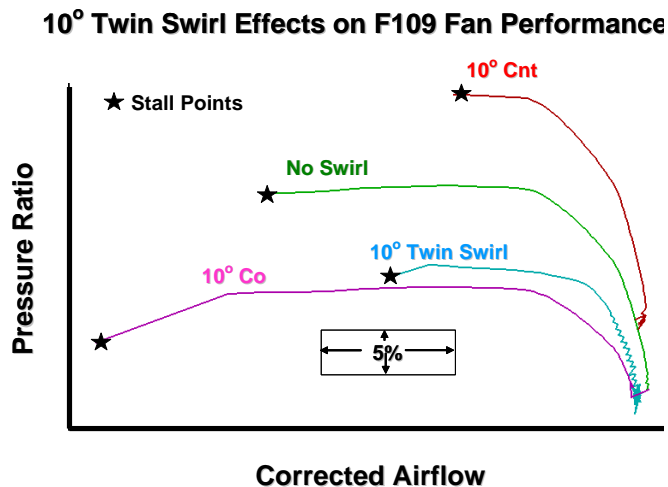


**Figure 3.194 The Effects of Twin Paired Swirl on F109 Fan Performance and Operability**

to lower the pressure ratio and extend the stalling flow rate while swirl in the counter-swirl direction tends to increase the pressure ratio and decrease the stalling flow rate. The stall criteria for clean inlet (the flow at which the stage pressure characteristic has a zero slope) was also modified to reflect what was discovered with the **meanline** code and the diffusion factor investigation when either co or counter-swirl was present. When twin-paired swirl was investigated, the parallel compressor simulation was divided into two equal circumferential segments. To simulate twin-paired swirl, one sector was required to use the co-swirl characteristics while the other sector was required to use the counter-swirl characteristics.

Similar to the bulk swirl case, twin-paired swirl was investigated with the parallel compressor model by applying the appropriate swirl compressor characteristic for each parallel tube. The results for the F109 fan are presented in **Figure 3.194**.

As can be seen, the twin-swirl performance in terms of Pressure Ratio is lower than both the no-swirl and counter-swirl bulk swirl cases. In addition, the stall point is between the counter and co-swirl cases. Comparisons of predicted bulk swirl performance between the parallel

The following procedure was used to investigate the effects of swirl on system performance and operability. The parallel compressor model was first allowed to come to a steady condition. If swirl was to be implemented on the system, it was initiated abruptly after the steady condition was established. This caused some numerical instability that quickly settled out, and the system was allowed to reach a new steady condition. Once steady conditions were assured, the exit static pressure, which had been held constant for steady operation, was ramped at a quasi-steady rate to back-pressure the system and drive the system to its instability point.

Bulk swirl in the co-swirl direction tends

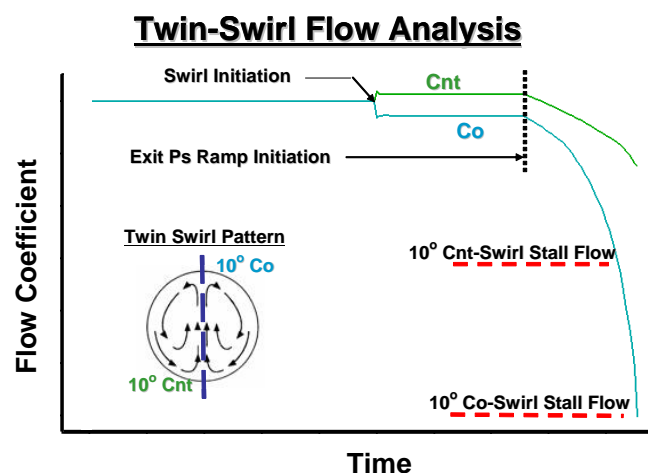


**Figure 3.195 The Effects of Twin Bulk Swirl on F109 Performance and Operability**

compressor and **meanline** codes ([Figure 3.191](#) and [Figure 3.192](#)) showed excellent agreement.

By examining the individual sector flow coefficients ([Figure 3.195](#)) which is indicative of the corrected flow that would exist in that sector if the sector were operating with full flow, one can determine that the co-swirl stall point is controlling the overall stall point of the system when subjected to twin swirl.

This result does not seem intuitive but can readily be explained by viewing where each segment ends up after swirl is implemented on the inlet during steady-state operation. Because the parallel compressor model is holding the same static pressure back boundary condition as existed during clean inlet flow, the mass flow in each segment must adjust to the new inlet conditions.

In the co-swirl case, the mass flow decreases for that same static pressure while the counter flow mass flow slightly increases, moving the sector into the choked region of the stage map. This condition sets the co-swirl sector in a position to be much closer to the stall side of the operating characteristic, and thus when a rapid static pressure increase is applied to the exit boundary, the co-swirl sector reaches its stalling airflow rate much sooner than the counter-swirl sector. For parallel compressor theory, when one sector reaches its stall point, the full compression system is said to be stalled. This unexpected result collaborates what was also noted by other members of the S-16 subcommittee on swirl in the development of the unpublished document on swirl effects

**Different Amounts of Twin Swirl Effects on F109 Fan Performance**

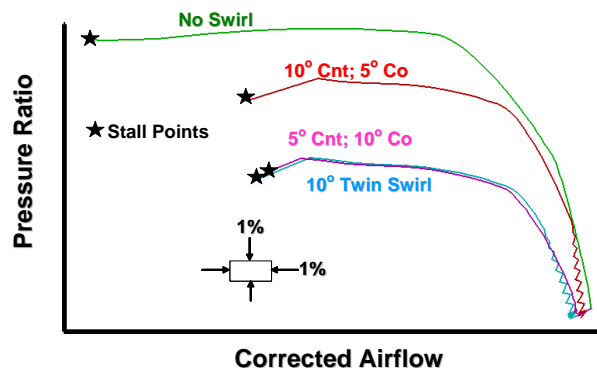


**Figure 3.196 The Effects of Differing Amounts of Twin Swirl on F109 Performance and Operability**

Another perturbation for twin swirl is to have uneven amounts of swirl in each twin sector. Using the **parallel compressor simulation**, twin swirl patterns of  $10^\circ$  of counter-swirl were added in one sector while  $5^\circ$  of co-swirl was added in the other sector. To bound the effect, the opposite investigation was also conducted (i.e.,  $5^\circ$  of counter swirl in one sector versus  $10^\circ$  of co-swirl in the other). Both of these predictions are presented in [Figure 3.196](#).

When co-swirl is dominant (i.e.,  $10^\circ$  of co-swirl versus  $5^\circ$  of counter-swirl), the performance and the stall point are nearly identical to those predicted with identical swirl sectors (i.e.,  $10^\circ$  of co-swirl and  $10^\circ$  of counter-swirl). When the co-swirl sector has a lesser magnitude of swirl (i.e.,  $5^\circ$  of co-swirl), the performance and operability degradation is less severe.

### Prediction of Swirl Effects on the F109 Fan Using a 3D Euler Compressor Simulation

**TEACC** was applied to the F109 fan and calibrated to the clean inlet flow for 100% speed. To verify that **TEACC** would provide a reasonable prediction of swirl effects, co-and-counter bulk



swirl were implemented on the F109 fan. The results of that investigation are presented in **Figure 3.197** and compared to the clean inlet values.

When the results from the **TEACC** solution (**Figure 3.197**) are compared with those from the meanline prediction (**Figure 3.191**), it is observed that there are similarities and differences.

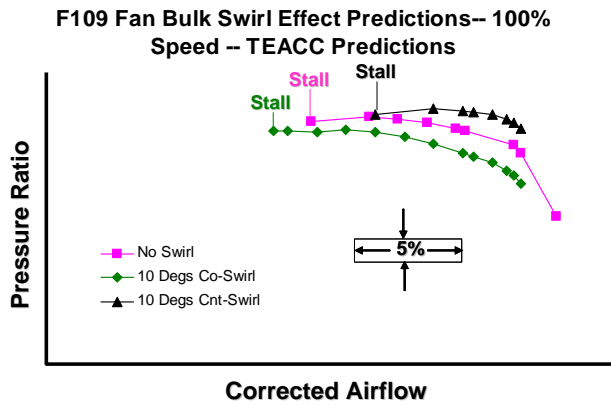


**Figure 3.197 Predictions of the Effect of Bulk Swirl Using a 3-D Euler Compression System Simulation**

Although the numerical scales have been stripped, the spatial relation of the scales have been maintained to provide the reader a way of comparing. The trends are similar (i.e., counter-swirl moves the characteristic to higher pressure ratios and flow rates, and co-swirl lowers the pressure ratio and flow rates), but the magnitude of the change is not the same. Because the **TEACC** solution is three-dimensional in nature, it potentially has enough of the physics to produce a more correct prediction. However, these simulations are only predictions and will have to be verified and validated with experimental results from the F109 test.

#### **ADDITIONAL REFERENCES:**

- 3.124** Boulding, B. and Sheoran, Y., "Inlet Flow Angularity Descriptors Proposed for Use with Gas Turbine Engines", SAE Paper # 2002-01-2919
- 3.125** Boyer, Keith, "An Improved Streamline Curvature Approach for Off-Design Analysis of Transonic Compression Systems", PhD Dissertation, Virginia Polytechnic and State University, Blacksburg, VA, April 2001.
- 3.126** Cumpsty, N. A., **Compressor Aerodynamics**, Longman Scientific & Technical, 1989, pp.47-48.
- 3.127** Hearsey, R.M., *Program HT0300, NASA 1994 Version*, The Boeing Company.
- 3.128** NASA SP-36, *Aerodynamic Design of Axial-Flow Compressors*, edited by Johnsen, I.A. and Bullock, R.O., 1965.
- 3.129** Seyler, D. R. and Gestolow, J. P. "Single Stage Experimental Evaluation of High Mach Number Compressor Rotor Blading Part 2- Performance of Rotor 1B." NASA-CR-54582, September 1967.
- 3.130** Smith, S. L., "1-D Meanline Code Technique to Calculate Stage-by-Stage Compressor Characteristics," M.S. Thesis, University of Tennessee, Knoxville, TN, 1999
- 3.131** Schmid, N. R., Leinhos, D. C., and Fottner, L., "Steady Performance Measurements of a Turbofan Engine with Inlet Distortions Containing Co- and Counterrotating Swirl from an Intake Diffuser for Hypersonic Flight," **Journal of Turbomachinery**, Vol. 123, April 2001, pp. 379-385

### 3.3 AIRFRAME-PROPULSION INTEGRATION VIA NUMERICAL SIMULATIONS

The integration of the airframe and its propulsion system is a key design issue in the development and deployment of military aircraft. Many disciplines comprise this issue, one being the aerodynamic interaction between the inlet system and the engine. The external airframe and inlet system must capture flow from the freestream and deliver it to the installed engine at Mach numbers commensurate with fan or compressor requirements. Unfortunately, the modification of the flow to meet engine requirements generally results in flow distortion that can degrade engine performance, operability, and durability. Such degradations may include loss of thrust, loss of stability margin with the potential for surge or even flameout, and the reduction of fan or compressor life due to high cycle fatigue (HCF). Therefore, such degradations introduce serious issues both in the success of the weapon system during combat and in the cost of maintaining system readiness. Therefore, the aircraft developer and the test community must consider the compatibility of the inlet and the engine throughout the full acquisition process.

For over 30 years, the Society of Automotive Engineers (SAE) S-16 committee (Turbine Engine Inlet Flow Distortion Committee, [Figure 3.198](#)) has been providing methodologies and standards for the aircraft/engine community to use in testing and analyzing inlet distortion effects on gas turbine engines, focusing on the performance and operability aspects of inlet/engine compatibility. The existing SAE S-16 methodologies have traditionally been used

## SAE S-16 Committee Developed Test & Evaluation Standard



**Figure 3.198 The Society of Automotive Engineers S-16 Committee for Turbine Engine Inlet Flow Distortion**

to characterize inlet distortion by consideration of total pressure distortion, total temperature distortion, or planar waves, either singularly or in combination [3.132-3.135]. However, many gas turbine installations can generate significant flow angularity as well as total pressure distortion at the Aerodynamic Interface Plane (AIP). This technical effort has been prompted by the potential limitation of the current SAE S-16 developed methodologies to address combined total pressure and flow angularity issues associated with advanced inlets such as exists with the F-35 aircraft. The use of the integrated numerical simulation described within this paper will demonstrate the potential for enhancing the current methodology as well as ground and flight test processes.

A primary objective of the Arnold Engineering Development Center (AEDC) test and evaluation (T&E) mission is centered on integrating weapon system airframe and propulsion systems. Airframe-propulsion integration encompasses a number of issues ranging from aircraft stability and control to inlet-engine compatibility (Figure 3.199). Consequently, the integration involves a wide range of technical disciplines with implications to the T&E environment. Examples include external aerodynamics with the characterization of forces and moments, inlet performance, engine operability, engine performance, controls, and structures. To address the



**Figure 3.199 Aircraft-Propulsion Integration Issues**

disciplines, the T&E process requires the application of a variety of test resources as well as analytical and computational tools. Testing for airframe-propulsion integration, and in particular inlet-engine compatibility, generally requires the coupling of component tests conducted in wind tunnels and engine altitude facilities [3.136, 3.137].

The advent of technologies for providing controlled flight at extremely high angles of attack and sideslip have enabled weapon system developers to consider post-stall maneuvers as combat tactics. As a result, future fighter aircraft may be required to execute maneuvers containing drastic and transient changes in flight conditions at the high power settings demanded by combat (See [Ref 3.136](#) for an overview of the airframe-propulsion integration issue). Large and transient changes in angle of attack can produce hysteresis and therefore deviations from the steady-state condition. As a result, future direct-connect engine or compressor tests may require distortion generators capable of producing a rapid sequence of distortion patterns to provide a time history corresponding to a transient maneuver.

Stealth has produced inlets highly integral with the airframe including blended inlets. High speed cruise and stealth have both motivated designers to adopt bay-launched munitions in fighter aircraft designs. Together, these features have increased the proximity between the aircraft inlet and the weapon to be launched in flight. Furthermore, the use of the post-stall maneuver as a combat tactic in the point-and-shoot concept will result in weapon launches at angles of attack and sideslip outside current flight envelopes. These factors increase the likelihood that hot weapon exhaust gases will enter the aircraft inlet.

Another type of inlet distortion that may appear in future operability and performance assessments involves flow angularity. The current total-pressure methodology neglects flow angularity as a separate distortion parameter. However, experience with a number of systems showed that flow angularity could affect both operability and performance. In an aircraft inlet, flow angularity generally appears in the form of swirling flow. A rotation of the entire flow about the engine or compressor hub constitutes a bulk swirl and either increases or decreases engine performance depending on the direction of rotation with respect to the machine. Localized swirl, in the form of vortices appearing in various regions of the AIP, can affect surge margin. Engines lacking inlet guide vanes have demonstrated the highest sensitivity to inlet swirl. Inlet swirl can originate at the aircraft forebody or it can be generated in s-shaped inlet diffuser ducts. Therefore, the advent of stealth systems, with blended inlets and s-ducts, may introduce requirements to address swirl in future inlet-engine compatibility tests and evaluation.

The intent of this section is to portray how coupled airframe and propulsion systems numerical analysis tools may be used to enhance the information stream necessary for development and acquisition of an aircraft weapon system. The Joint Strike Fighter (F-35 and F135 fan) was chosen for demonstrating the potential benefits of the numerical simulations because of its relevance to a current weapon system acquisition process and technologies. While the application of this present analytical technique to current weapon systems in development enhances the acquisition process it does limit the ability to report the details of the findings of the effort.

The integration of the airframe and its propulsion system is a key design issue in the development and deployment of military aircraft. The external airframe and inlet system must capture flow from the freestream and deliver it to the installed engine at Mach numbers commensurate with fan or compressor requirements. Unfortunately, the modification of the flow to meet airframe requirements generally results in flow distortion that can degrade engine performance, operability, and durability. Therefore, such degradations introduce serious issues both in the success of the weapon system during combat and in the cost of maintaining system readiness. The aircraft developer and engine manufacturer must consider the compatibility of the inlet and the engine throughout the design process.



Currently, the airframe-propulsion integration process is handled by an established methodology. This process has been derived by consensus of industry and government experts over the last 30 years and reported by the Society of Automotive Engineers (SAE) in an Aerospace Recommended Practice (ARP-1420) [3.132]. This document was developed by the SAE Technical Committee, S-16 (Turbine Engine Inlet Flow Distortion), published in 1978 and updated in 2002. The S-16 committee is still in existence working on other airframe-engine compatibility issues such as model-to-full-scale comparisons and a recommended methodology for inlet swirl effects on engine operability and performance. This existing process lends itself to surprises and often extends the acquisition cycle due to unexpected integration issues and can be improved via M&S of the full aircraft-inlet-propulsion system.

Integration of a weapon system airframe and its propulsion system encompasses a number of issues ranging from aircraft stability and control to inlet-engine compatibility. To address these issues, the test and evaluation (T&E) process requires the application of a variety of test resources as well as a wide range of analytical and computational tools. Testing for airframe-propulsion integration, and in particular inlet-engine compatibility, generally requires the coupling of component tests conducted in both wind tunnels and engine altitude facilities.

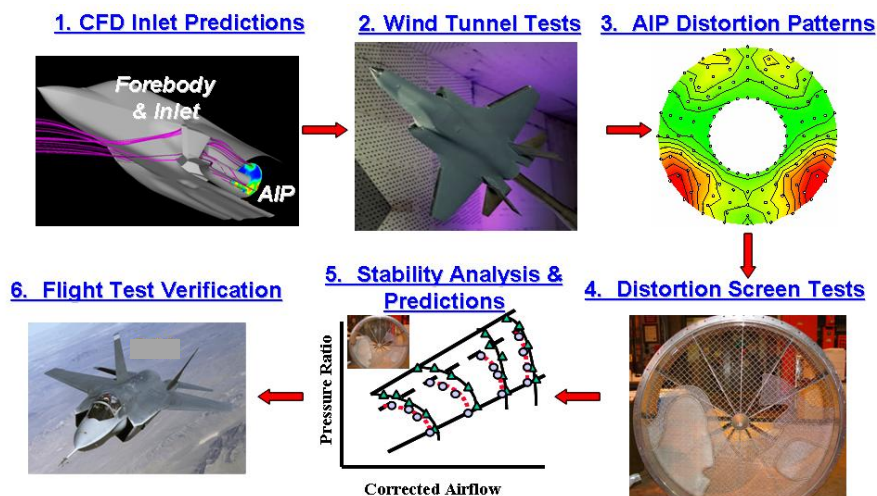


**Figure 3.200 Current Weapons System Integration Process.**

(Step 1). Subscale inlet tests are then conducted in a wind tunnel to determine the conditions that must be simulated at the face of a full-scale engine (Step 2). Thus, subscale inlet tests in a wind tunnel are used to select the conditions that must be simulated at the face of a full-scale engine. These conditions, although a function of angle of attack, sideslip, and flight condition, are characterized by a distortion-indexing methodology (Step 3).

Similarly, the engine test methodology measures the effect of a series of distortion patterns based upon distortion screens (Step 4) on engine operability and performance. Keeping with one of the fundamental precepts of the recommended practice set forth in the ARP-1420 and in its companion document, AIR-1419 [3.133] (namely, that engine stability can be defined by tests using equivalent levels of steady-state distortion), aircraft manufacturers, engine manufacturers, and testing organizations have implemented testing procedures which reflect that premise.

The inlet-engine integration test methodology currently is based on engine tests that show that the engine experiences distortion patterns that last for a time of the order of one engine RPM as if they were steady-state conditions. Although the ARP-1420 methodology does not address aerostructural effects on the engine (e.g., high-cycle fatigue), testing is often done with multiple-per-rev distortion screens for aeromechanical purposes. The accuracy of this distortion-indexing methodology is dependent upon the thoroughness of dedicated engine tests with classic distortion patterns and realistic distortion patterns for the particular application.

Once engine testing for distortion has been completed, analysis techniques are used to determine the sensitivity of the particular compressions system to both circumferential and radial distortion separately. These sensitivities are then combined via the ARP-1420 methodology to produce an estimate of the loss in stability for a particular complex pattern. To validate the ARP-1420 methodology, a complex total pressure pattern (via screen) will be imposed on the compression system to verify the predicted results (Step 5). The final step in the process is to validate the integration of the airframe and propulsion system during flight tests (Step 6). In this phase, the system is exposed to the actual environment and conditions in which it must operate. The disadvantage is that the risk is higher that a failure may occur with loss of the aircraft.

The advent of technologies allowing for controlled flight at extremely high angles of attack and sideslip has enabled weapon system developers to consider post-stall maneuver capabilities as combat tactics. As a result, fighter aircraft may be required to execute maneuvers containing drastic changes in flight conditions at the high power settings demanded by combat. Such maneuvers bring forth the question of what role the distortion time history might play in the inlet-engine integration task. The current methodology does not take into account the time history of the patterns and thus may not accurately capture an important aspect of airframe-propulsion integration. Large and transient changes in angle of attack can produce hysteresis and, therefore, deviations from the steady-state condition. Clearly the volume of issues facing future integrations of inlet and engine into viable aircraft systems demands improved test techniques coupled with dynamic numerical simulations.

Of primary concern is to identify how to enhance the existing engine-inlet compatibility analysis and design methodology (ARP-1420) through the use of modeling and simulation (M&S) that integrates the aircraft and propulsion system in a single computation process domain for the purpose of identifying system level interactions and potential improvements. This section describes an improved test and evaluation process that integrates propulsion system numerical simulations (inlet-engine 3D aerodynamic codes) into the current test and evaluation process.

This integrated process then can be utilized to guide test planning so that the most relevant conditions are tested and the benign conditions are relegated to the numerical simulation. This will provide a means for the test program to consider reducing certain tests and thus reduce cost and schedule. If a problem is discovered in flight testing, it may produce a major acquisition cost overrun since a redesign may become necessary. Use of a validated airframe-propulsion system simulation may be able to indicate potential integration issues well before flight testing when redesign or modification is simpler. This product could then be used in future test programs to:

- **Provide pretest prediction and posttest assessment of engine operability test matrix to optimize altitude propulsion testing**



- Provide pretest prediction and posttest assessment of aircraft test matrix to optimize wind tunnel inlet testing
- Provide connectivity between ground-test engine/inlet performance/operability test results with the actual flight-test environment
- Provide an analysis capability for assessing full propulsion system performance and operability issues.

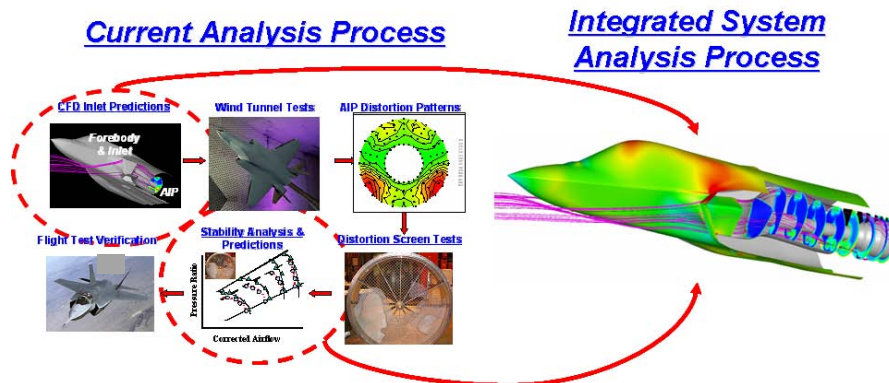


**Figure 3.201 Improved Test and Evaluation Process Through Numerical Simulations**

approach, the full aircraft-propulsion system can now be evaluated much earlier in the current weapon system acquisition process as illustrated in **Figure 3.201**. Predictions of the effect of various inlet distortion phenomena which include total pressure, swirl, and total temperature distortion can now be realistically evaluated using the computational approach and then later validated via flight test. This provides less risk, potentially lowers costs, and has the potential to reduce the weapon system acquisition schedule.

#### **ADDITIONAL REFERENCES**

- 3.132** SAE S-16 Committee, ARP 1420, Revision B, "Gas Turbine Inlet Flow Distortion Guidelines," Society of Automotive Engineers, February 2002.
- 3.133** SAE Aerospace Information Report AIR-1419, "Inlet Total-Pressure Distortion Considerations for Gas Turbine Engines," May 1983.
- 3.134** SAE S-16 Committee, ARD50026, "A current Assessment of Planer Waves," Society of Automotive Engineers, September 1995.
- 3.135** Society of Automotive Engineers, "A Current Assessment of the Inlet/Engine Temperature Distortion Problem," Aerospace Resource Document ARD50015, 1991.
- 3.136** Davis, M. W., Jr., et al. "A Proposal for Integration of Wind Tunnel and Engine Test Programs for the Evaluation of Airframe-Propulsion Compatibility Using Numerical Simulations." **Journal of Engineering for Gas Turbines and Power**, July 2002, pp. 447-458.
- 3.137** Hale, Alan, Milt Davis, and Jim Sirbaugh, "A Numerical Simulation Capability for Analysis of Aircraft Inlet-Engine Compatibility", **Journal of Engineering for Gas Turbines and Power**, Vol. 128, July 2006, pp. 473-481.

### 3.3.1 Aircraft –Propulsion Integration – One-Dimensional Analysis

Traditionally, aircraft inlet performance and propulsion performance have been designed separately and latter mated together via flight-testing. In today's atmosphere of declining resources, it is imperative that more productive ways of designing and verifying aircraft and propulsion performance be made available to the aerospace industry. One method of obtaining a more productive design and evaluation capability is with numerical simulations. Numerical simulations can provide insight into physical phenomena that may not be understood by test data alone. Simulations can fill information gaps and extend the range of test results to areas not tested. In addition, once a simulation has been validated, it can become a numerical experiment and the analysis engineer can conduct 'what-if' studies to determine possible solutions to performance or operability problems.

The economic viability of a commercial supersonic transport, such as the High Speed Civil Transport (HSCT), is highly dependent on the development of a high-performance propulsion system. Typically, these propulsion systems mate a supersonic mixed-compression inlet with a turbojet or turbofan engine. The nature of such propulsion systems offers the potential for undesirable component interactions, which must be thoroughly understood for proper design. Therefore, it is imperative to have tools that allow investigation of inlet-engine integration issues.

The inlet must provide the engine with the correct mass flow rate at the highest possible pressure with minimum drag. Additionally, flow angularity and distortion must be minimized at the compressor face if the engine is to function appropriately. Maximum thrust with a minimum of fuel consumption will not be obtained without the inlet operating close to peak performance. Unfortunately, operating near peak performance can result in an inlet unstart (expulsion of the normal shock) followed by engine stall and possibly surge. When that happens, proper control action must be taken to recover the system as quickly as possible. Thus the operability of the overall system must also be addressed, because stable time dependent operation of the system must be ensured for both scheduled and nonscheduled events.

Because of the complexity of the inlet and engine systems, and the high cost of experimentally determining overall performance, numerical simulations of the components can be of significant benefit. For example, dynamic simulations provide a means for investigating the potential interactions mentioned above, as well as providing a test bed for guiding the design, testing and validation of propulsion controls.

#### **CITED EXAMPLE(S)**

**3.138** Garrard, G. D., Davis, M. W., Jr., Wehofer, S., and G. Cole, "A One-Dimensional, Time Dependent Inlet/Engine Numerical Simulation for Aircraft Propulsion Systems", ASME Paper # 97-GT-333, June 1997.

## MODELING TECHNIQUE

The simulation system, operating under the Application Portable Parallel Library, **APPL**, closely coupled a supersonic inlet with a gas turbine engine. The supersonic inlet was modeled using the Large Perturbation Inlet, **LAPIN**, computer code, and the gas turbine engine was modeled using the Aerodynamic Turbine Engine Code, **ATEC** ([Section 4.5](#)), as illustrated in [Figure 3.202](#).

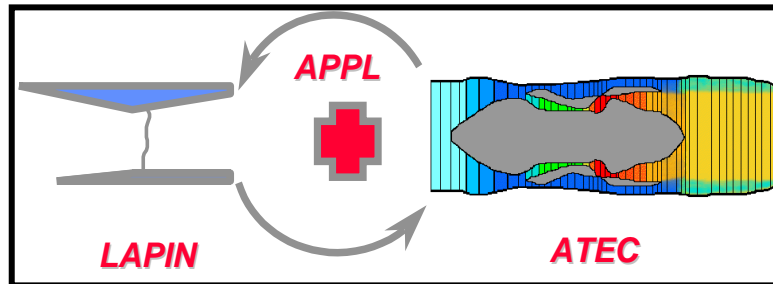


**Figure 3.202 Schematic of the Coupled Inlet-Engine Codes**

## APPLICATION TO THE HIGH SPEED CIVIL TRANSPORT

In order to demonstrate the capabilities of the coupled inlet / engine simulations, a representative test case has been selected from the available literature. The coupled LAPIN / ATEC simulation system has been exercised for a supersonic inlet with 60 percent internal compression (a 4060 Inlet) and a General Electric J85-13 turbojet. The inlet and engine have been actively tested at the LeRC since the mid-1960's, both together and separately, and have been the subject of several technical reports [[3.142](#), [3.145](#), [3.140](#), [3.139](#), [3.143](#)]. The combined system is shown installed in the LeRC 10x10 supersonic wind tunnel in [Figure 3.203](#). A cross-sectional sketch is presented in [Figure 3.204](#).

The 4060 inlet is an axisymmetric mixed-compression inlet with 40 percent effective supersonic area contraction occurring externally and 60 percent supersonic area contraction occurring internally. The design free-stream Mach number is 2.5. The inlet has a translating centerbody to provide start/restart capability. High-response bypass doors were used for normal shock control by matching inlet airflow to engine airflow requirements. An ejector bypass provided air for engine cooling. The J85-13 turbojet consists of an eight stage axial flow compressor, a

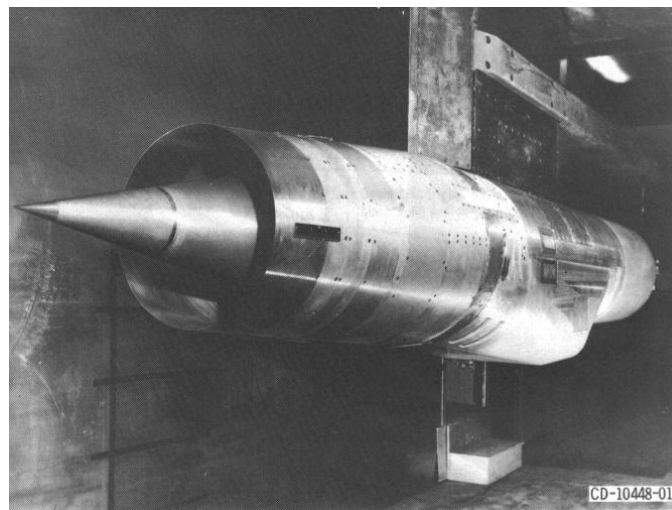


**Figure 3.203 A 4060 Inlet and J85-13 Turbojet Installed in the LeRC 10x10 Supersonic Wind Tunnel [[3.140](#)]**

combustor, and a two stage axial turbine. An afterburner is attached to the engine. The compressor operates with a nominal pressure ratio of 7:1 at a design flow rate of 44 lbm/sec.

The purpose of the test case is to demonstrate the utility of the coupled simulation system. It is

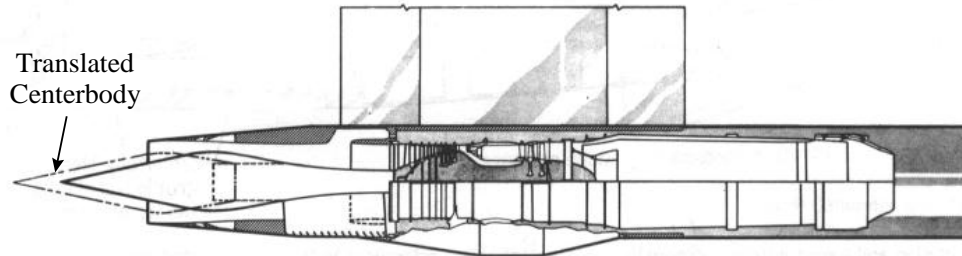


**Figure 3.204 Cross-Sectional View of the 4060 Inlet and J85-13 Turbojet Installation [3.140]**

intended to exercise the system through an inlet unstart. Previously, a **LAPIN** simulation of the 4060 inlet was shown to give good agreement with experimental data [3.148] for both steady-state, transient, and dynamic operation. In those cases the effects of an engine were approximated by an appropriate time-varying exit boundary condition. The **ATEC** simulation has also been shown to accurately simulate this class of gas turbine engine [3.144]. For the J85-13, the **ATEC** simulation results have been compared to steady state cycle program output for a nominal J85-13 operating at sea level static conditions. The model was found to compare reasonably well, and the simulation was tuned until the maximum difference in the key parameters was less than 5 percent. Because of the many modifications that have been made to the specific LeRC J85-13 turbojet engine, adjustments to both the compressor and turbine characteristic maps were required to bring the simulation results in line with the test data. For example, it was stated in Cole, et. al., 1969, that the first stage nozzle of the axial flow turbine had been reduced to 86 percent of its original value to move the engine operating point closer to the compressor surge limit. Several modifications to the compressor have also occurred, such as the various casing treatments reported in Ref. 3.145. Because the available engine data for the configuration considered in the test case are limited, the tuning of the engine model was less

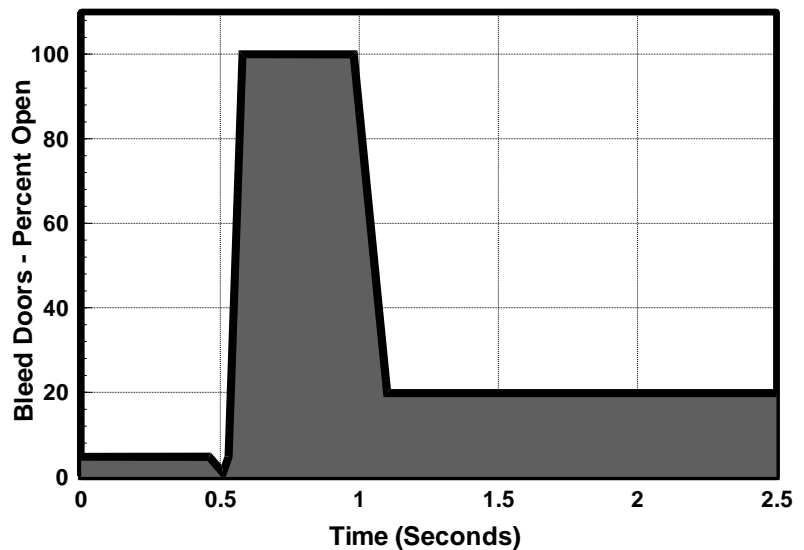


**Figure 3.205 Bleed Bypass Doors Percent Open as a Function of Time**

accurate than for the steady state case. The simulation results presented herein will reflect this inaccuracy.

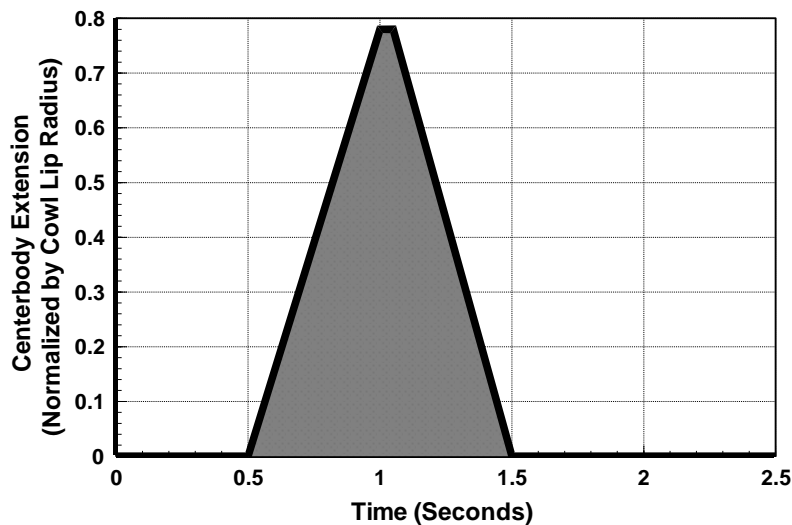


**Figure 3.206 Centerbody Extension (Values Normalized by Cowl Lip Radius)**

The test case selected for this study [3.141] was conducted at a tunnel test section Mach number of 2.5 (called free stream Mach number in the test data). The engine shaft rotational speed was adjusted to 85 percent of the design corrected speed. Centerbody and bypass-door control loops [3.142] were closed during the test. The transient event was initiated by pulsing the bypass doors in the closed direction. The result is an inlet unstart followed by an engine compression system stall. Upon sensing the inlet

unstart, the control loop actions are to open the bypass doors and extend the centerbody. The centerbody continues to translate forward until the normal shock is re-ingested, after which the centerbody is retracted to its initial position. The bypass doors modulate continuously throughout the transient to maintain the commanded value of the control pressure (scheduled as a function of centerbody position). The inlet recovers from unstart to its initial condition in about 1.5 seconds. The control loops were not implemented in the simulation. Therefore, the bypass door area and centerbody position were scheduled as functions of time, as shown in Figure 3.205 and Figure 3.206, respectively, to approximate the control action.

Before presenting the results of the computations, the test data will be discussed first. This will be done to establish the trends and characteristics that should also be present in the simulation results. The computational results for both the inlet and engine will then be presented. The presentation of the results will conclude with information from the computations that are not obtainable from the test data.

The first parameter that will be considered is the compressor inlet total pressure normalized by the free stream total pressure. This parameter provides a measure of how well the inlet provided total pressure recovery. Data for the test case are shown plotted as a function of time in Figure 3.207. At the start of the transient, the total pressure recovery falls off significantly. The total pressure ratio across the inlet drops from an initial value of 0.93 to approximately 0.33. A 65 percent loss of total pressure recovery occurs during the inlet unstart. Only after the shock is reswallowed does the inlet total pressure ratio recover to the pre-transient level.



The ratio of the compressor exit total pressure to free stream total pressure from test data is plotted in 08 The drop in compressor inlet total pressure forces the pressure ratio across the entire system from the inlet entrance to the compressor exit to drop dramatically. The ratio of compressor exit total pressure to free stream total pressure falls from an initial value of 3.58 to

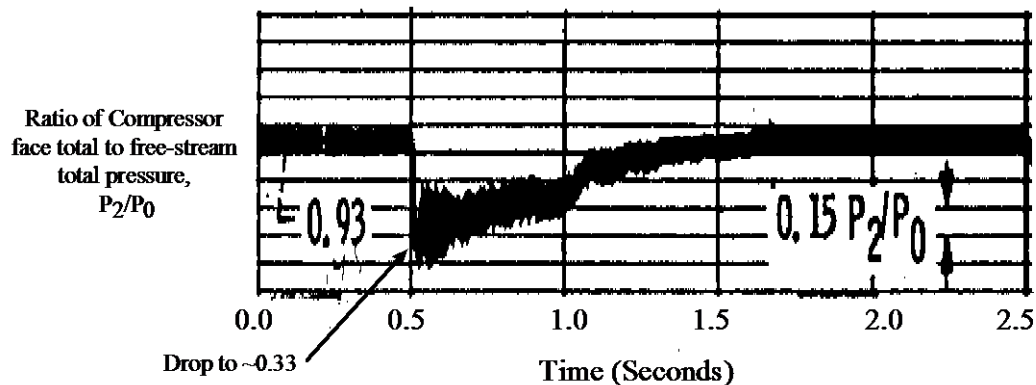


**Figure 3.207 Test Data: Ratio of Compressor Inlet Total Pressure to Freestream Total Pressure [3.141]**

approximately 0.9. Recovery is obtained only after the shock is repositioned downstream of the inlet throat. Unlike the inlet, however, the engine compressor does not recover back to the original pre-transient level during the allotted time period due to the reduction in shaft rotational speed.

The shaft rotational speed of the engine during the transient is shown plotted as a function of time in **Figure 3.209**. As would be expected, the engine speed decreases during the transient due to the flow instabilities. The original data shown in **Ref. 3.141** indicated a drop in rotation speed of approximately 200 revolutions per minute. Data shown in **Ref. 3.142**, however, indicated that for the same transient event, the engine shaft rotational speed dropped by approximately 2000 revolutions per minute. It was judged by the authors that for the inlet to recover as shown in **Figure 3.207** with the bleed bypass door schedule as shown in Fig. 9, engine shaft rotation speed would be required to drop significantly more than 200 revolutions

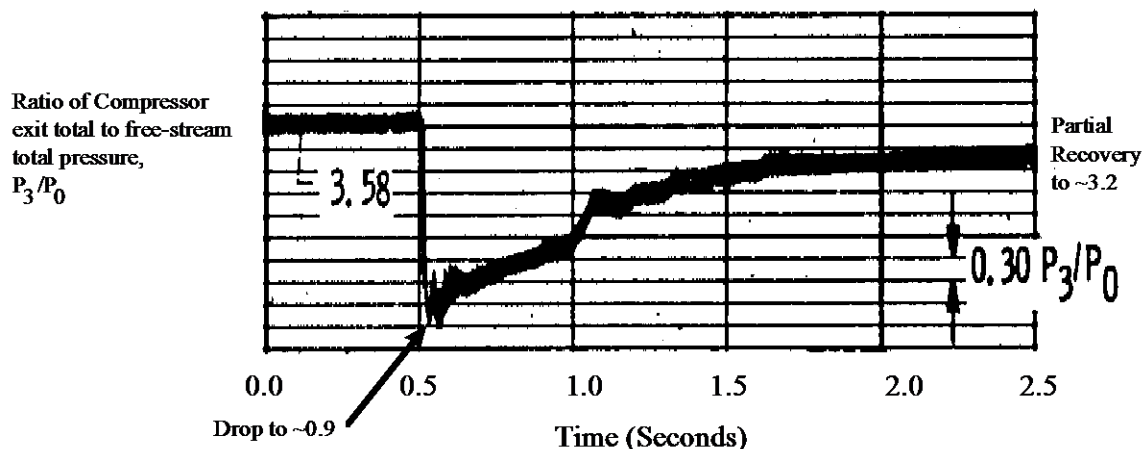


**Figure 3.208 Test Data: Ratio of Compressor Exit Total Pressure to Freestream Total Pressure [3.141]**



per minute. It was therefore concluded that by the end of the transient, the rotor speed had dropped from 14,335 rpm to approximately 12,050 rpm.

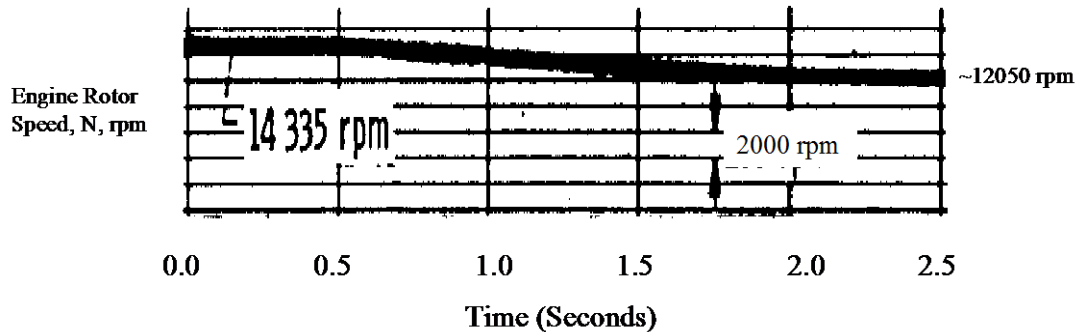


**Figure 3.209 Test Data: Engine Shaft Rotational Speed [3.141, with reference to 3.142]**

Model results for the ratio of compressor face total pressure to free stream total pressure are shown in **Figure 3.210**. Although the absolute values of the compressor face total pressure to free stream total pressure ratio are not exact, the overall trends of the test data and model do

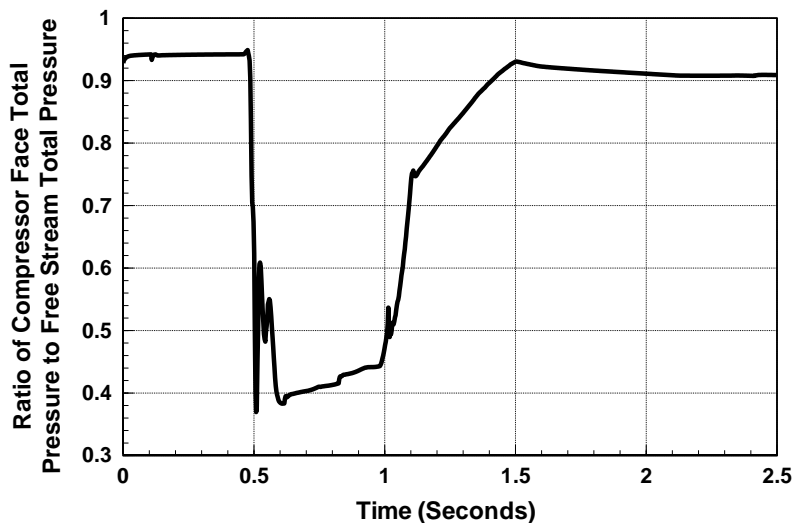


**Figure 3.210 Model Predictions: Ratio of Compressor Face Total Pressure to Freestream Total Pressure**

agree. As with the test data shown in **Figure 3.207**, the model results show that the face total pressure recovery falls significantly as the shock is expelled from the inlet. Beginning with a pressure ratio of 0.94, the pressure ratio drops to 0.38 within a tenth of a second. This is a loss of approximately 60 percent in total pressure recovery. After the inlet shock is re-swallowed, the total pressure at the compressor face returns back to near its original level. Because of the previously discussed mismatch between the engine simulation performance and the actual test data, the model results show a reduction in inlet total pressure recovery as time progresses. Additional work is planned to investigate the differences between the test data and the simulation results.

Model results for the ratio of compressor exit total pressure to free stream total pressure are shown in **Figure 3.211**. As is shown in the test data in **Figure 3.208**, the inlet unstart forces the compressor exit total pressure to free stream total pressure to drop significantly. The model predicted a pressure ratio drop from 4.0 to approximately 0.3. As was shown in the test data,

the engine compression system does not fully recover back to the original total pressure ratio. A maximum compressor exit total to free stream total pressure ratio of approximately 2.4 was reached at 1.5 seconds.

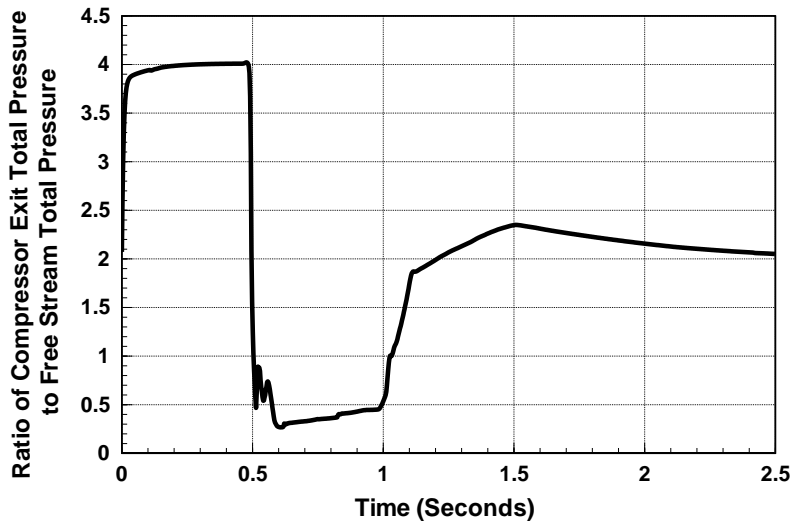


**Figure 3.211 Model Predictions: Ratio of Compressor Exit Total Pressure to Freestream Total Pressure**

numerical simulations. The remainder of the paper will focus on presenting several parameters that were not presented in the test data, but provide an interesting view of the system operation.

During the given transient, the majority of the system instabilities can be traced to the fact that the normal shock, located initially downstream of the inlet throat, was expelled outside of the inlet. The location of the shock is plotted as a function of time in [Figure 3.213](#). The shock location is normalized by the inlet cowl lip radius, and referenced to the centerbody tip. The cowl lip is axially located two cowl lip radii downstream of the centerbody tip. The act of closing the bypass valve (shown in [Figure 3.205](#)) forces the shock structure to be expelled from the inlet. Moving the centerbody forward in conjunction with proper modulation of the bypass doors allows the shock to be reingested.

The total pressure through the inlet during the transient is shown in [Figure 3.214](#). The

Model results for engine rotor speed are shown in [Figure 3.212](#). As with the test data shown in [Figure 3.209](#), the engine shaft rotational speed decreases in time. Over the two second time interval, the model rotation speed dropped by approximately 2000 revolutions per minute.

Although the above presentation does not represent a full validation of the coupled inlet / engine simulation system, it does demonstrate that the 4060 inlet and the GE J85-13 turbojet can be successfully represented by the given

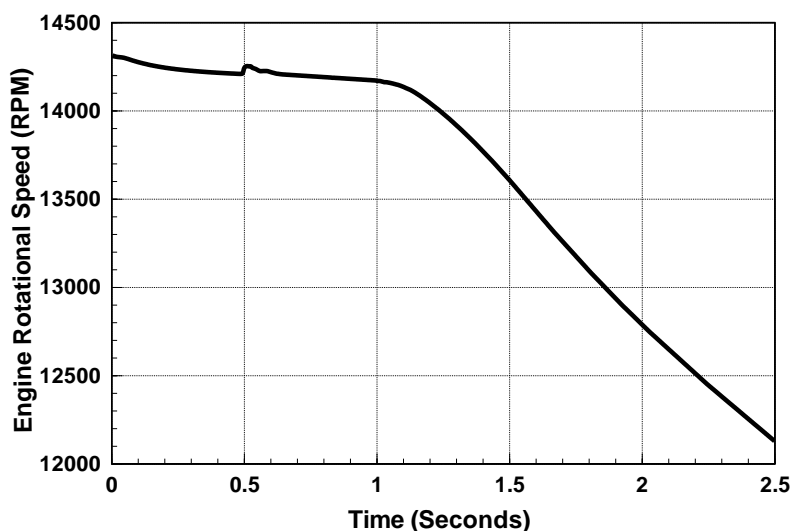


**Figure 3.212 Model Predictions: Engine Rotational Speed**

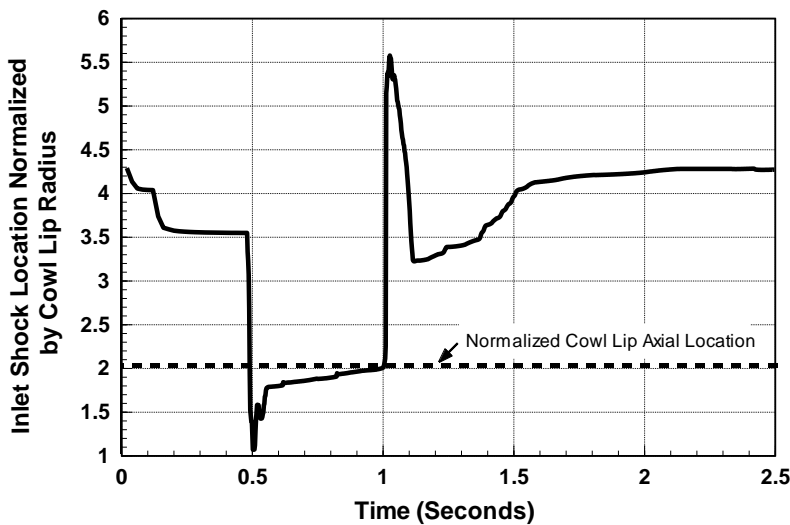


**Figure 3.213 Inlet Shock Location Normalized by Cowl Lip Radius**

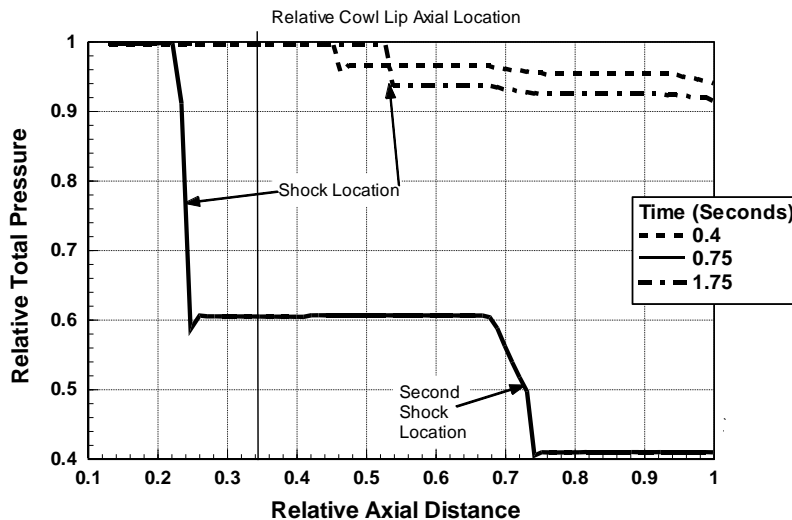


**Figure 3.214 Relative Total Pressure in the Inlet at Three Different Times**

data set is axially referenced to 0.0 at the inlet centerbody tip and is normalized by the distance from the centerbody tip to the inlet exit. The total pressure values are normalized by the maximum level obtained in the **LAPIN** computational domain. Three total pressure curves are shown, representing the axial distribution of total pressure through the system at times of 0.40 seconds, 0.75 seconds, and 1.75 seconds. These times correspond to instants before unstart, while unstarted, and after recovery of the initial started condition.. The total pressure falls dramatically during the unstarted portion of the transient due to the high losses associated with the expelled shock. It is interesting to note that the total pressure plot at 0.75 seconds indicates the presence of another shock structure in the inlet, located at approximately 85 percent distance. This is an expected result of opening the bypass doors which chokes the throat. Due to the closed-loop inlet control, the total pressure recovers to essentially the pre-transient level, while the engine speed is still undergoing changes.

The Mach number through the inlet is presented in **Figure 3.215** for the same three instants in time. The axial scale is the same as for **Figure 3.214**. Note the jump in Mach number from supersonic to subsonic at the 85% axial location for the time plot at 0.75 seconds. This confirms the presence of the second normal shock that was indicated by the total pressure plot in **Figure 3.214**.

The relative total pressure in the engine is presented in **Figure 3.216** for the same three instants of time that were used with the inlet. The axial distance is normalized by the overall length of the engine and pressure is normalized by the maximum level obtained in the **ATEC** computational domain. Total pressure across the compressor is lost once the inlet system unstarts. The

compressor pressure ratio as a function of time is shown in [Figure 3.218](#). At the instant of unstart (time approx. .5 sec) there is as sharp spike in pressure ratio to value exceeding 5.0 which (probably) exceeds the steady-state stall line, resulting in stall. Although the system begins to recover the original level of compressor operating pressure ratio, the compressor total pressure ratio is lower.

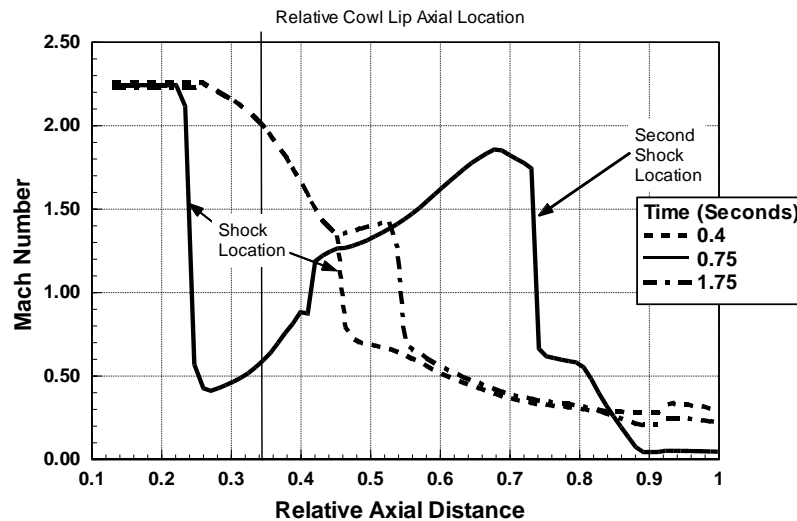


**Figure 3.215 Mach Number in the Inlet at Three Different**

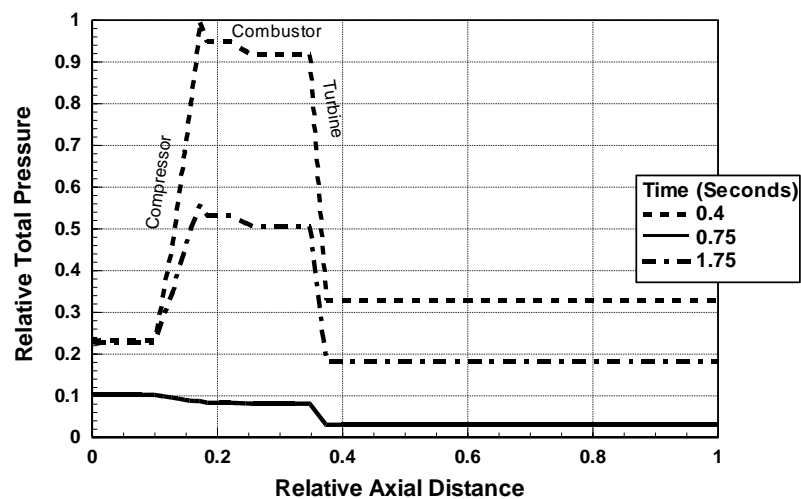


**Figure 3.216 Relative Total Pressure in the J85-13 Turbojet at Three Different Times**

The relative compressor pressure ratio is plotted as a function of the inlet corrected mass flow rate, expressed as a percentage of the design mass flow rate, in [Figure 3.217](#). It is evident from

the figure that there is one engine surge cycle, with a rotating stall event. Recovery takes place at a lower corrected inlet mass flow rate due to the lower engine shaft speed..

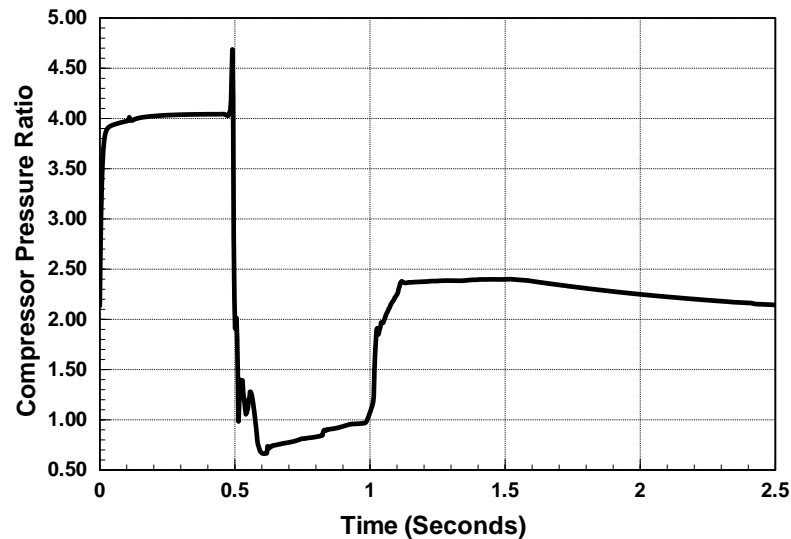


Figure 3.218 Compressor Pressure Ratio

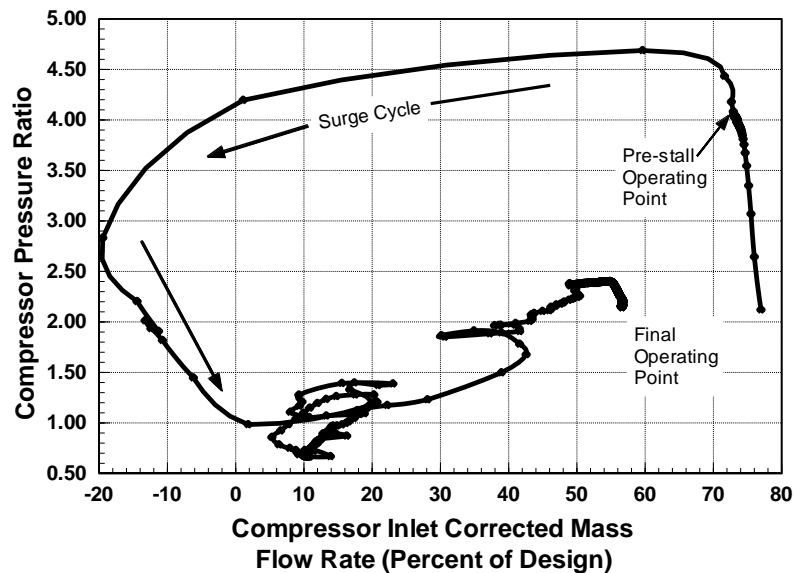


Figure 3.217 Compressor Pressure Ratio as a Function of Compressor Inlet Corrected Mass Flow Rate

## SUMMARY

A closely coupled computer simulation system that provides a one dimensional, high frequency inlet / engine numerical simulation for aircraft propulsion systems has been developed. The simulation system uses the **LAPIN** simulation to represent the inlet system, and the **ATEC**

simulation to represent the gas turbine engine. The **LAPIN** and **ATEC** simulations can simulate on- and off-design steady-state operation, as well as transient and dynamic engine responses to perturbations in a wide range of operational and control conditions. Operational verification of the simulation system has been conducted by comparing the trends and responses of the simulation system to test data. The system was exercised by imposing a sudden change in inlet overboard bypass conditions, resulting in an inlet unstart and engine surge cycle. The simulation showed reasonably good agreement with the data. Additional calibration of the simulations to additional test data is planned.

### **ADDITIONAL REFERENCES**

**3.139** Batterton, P. G., and Gold, H., "Experimental Test Results of a Generalized-Parameter Fuel Control," NASA TN D-7198, March 1973.

**3.140** Calogeras, J. E., "Experimental Investigation of Dynamic Distortion in a Mach 2.50 Inlet with 60 Percent Internal Contraction and its Effect on Turbojet Stall Margin," NASA TM X-1842, October 1969.

**3.141** Choby, D. A., Burstadt, P. L., and Calogeras, J. E., "Unstart and Stall Interactions Between a Turbojet Engine and an Axisymmetric Inlet with 60-Percent Internal-Area Contraction," NASA TM X-2192, March 1971.

**3.142** Cole, G. L., Neiner, G. H., and Crosby, M. J., "An Automatic Restart Control System for an Axisymmetric Mixed-Compression Inlet," NASA TN D-5590, December 1969.

**3.143** Costakis, W. G., and Wenzel, L. M., "An Experimental Investigation of Compressor Stall using an On-Line Distortion Indicator and Signal Conditioner," NASA TM X-3182, April 1975.

**3.144** Garrard, G. D., "ATEC: The Aerodynamic Turbine Engine Code for the Analysis of Transient and Dynamic Turbine Engine System Operations," Ph. D. Dissertation, The University of Tennessee, Knoxville, August, 1995.

**3.145** Hager, R. D., "Analysis of Internal Flow of J85-13 Multistage Compressor," NASA TM X-3513, April 1977.

**3.146** Moeckel, W. E., "Approximate Method for Predicting Form and Location of Detached Shock Waves Ahead of Plane or Axially Symmetric Bodies," NACA TN 1921, July 1949.

**3.147** Quealy, A., Cole, G. L., and Blech, R. A., "Portable Programming on Parallel/Networked Computers Using the Application Portable Parallel Library (APPL)," NASA TM-106238, July 1993.

**3.148** Varner, M. O., Martindale, W. R., Phares, W. J., Kneile, K. R., and Adams, J. C., Jr., "Large Perturbation Flow Field Analysis and Simulation for Supersonic Inlets," NASA CR 174676, September 1984.

**3.149** Ziemianski, J. A., and Ball, C. L. "Propulsion Technology Challenges for Turn-of-the-Century Commercial Aircraft," NASA TM-106192, June 1993.



### 3.3.2 Airframe-Propulsion Integration 3D Analysis

To adequately simulate the integration of the aircraft and propulsion system, it would be necessary to have high fidelity CFD simulations of both the aircraft forebody and the turbine engine propulsion system. In both cases, there are limitations due to status of the current state-of-the-art in computational capabilities. CFD simulations of aircraft-inlet systems need to be able to resolve the turbulence associated with shock-boundary layer interaction and in combination with separation due to serpentine inlets. Current Reynolds Averaged Navier Stokes (RANS) solution techniques will not be able to resolve the turbulent content of the flow in the inlet system, only the steady component of the flow.

Likewise, in the turbine engine, full-annulus CFD calculations would be required to simulate the effect of the distorted flowfield as presented by the inlet system. Current turbomachinery CFD using the RANS approach would not be able to resolve the effect of the turbulent content of the flow at the AIP. In addition, since there are many blades and multiple blade rows, the amount of calculations necessary to compute the effect of the inlet distortion on compression system performance and operability would be quite large and take a long time but not impossible to compute.

There have been other investigations into the coupling of inlets and fan systems numerically [3.152, 3.153, 3.154], however, these investigations have stayed in the realm of computational research and not been applied to a current system. The effort reported in this section has been applied to an advanced aircraft-propulsion system to show the potential for interaction with the acquisition process.

The computational simulation of inlets, especially for advanced fighter aircraft, requires modeling of complex geometries and physical phenomena. The inlets can be highly curved to hide observables such as hot engine parts and other inlet design details. This leads to inlets having become an essential part of the aircraft fuselage and thus being forced to have a wide range of cross-sectional shapes, introducing issues such as non-uniform flow, significant crossflow velocities, and flow separations prior to the engine face.

Simulating these complex geometries and the associated complex physical phenomena of engine inlets requires simulation tools capable of capturing unsteady, three-dimensional (3D), turbulent flow fields. Because of the highly 3D nature of the flow and the potential for significant flow separation, either the full Navier-Stokes equations must be solved or the use of a hybrid system of RANS with Large Eddy Simulations (LES) or Direct Eddy Simulations (DES) must be solved.

The Navier-Stokes solver needs to have the capability to model unsteady phenomena such as the time history of fluctuating pressures at the compressor face, inlet unstart, and inlet buzz. Also, the simulation tool needs to have the capability to solve for or model the effects of the presence of the engine, in particular the first stages of the compressor, on the inlet flow field.

Current RANS CFD capabilities do not include resolution of the total pressure fluctuations of the flow; only the “steady-state” total pressures are obtained. In spite of these limitations, RANS CFD solutions of inlet duct flows are useful in understanding inlet/engine integration challenges and will be used in this investigation. Of particular interest are the effects of the aircraft forebody on the flow field at the Aerodynamic Interface Plane (AIP) as presented in [Figure 3.219](#).

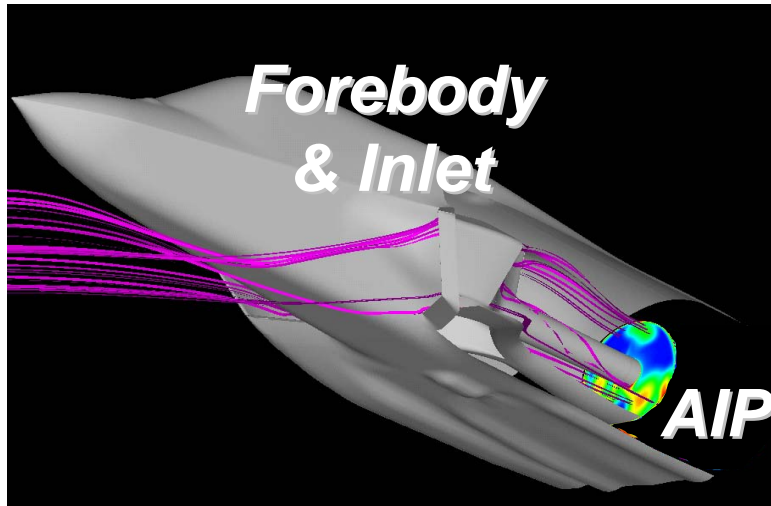


**Figure 3.219 CFD Flow-Field and Inlet Computations of**

whether to obtain computations that give a very detailed flow analysis such as with CFD or to use approximate methods that provide appropriate trends but depend upon a higher level of empiricism. The choice may be more dependent upon the amount of computational resources necessary and the amount of time it takes to obtain a solution. All these factors must be weighed to provide the right analysis tool for system evaluation. Presented in **Figure 3.220** are different types of compression system simulations and how they fit within the complexity spectrum and an approximate timeframe for computations.

On the low end of the complexity spectrum reside compression system techniques such as parallel compressor theory [3.155] and streamline curvature models [3.156]. Although these techniques can provide turn around in a matter of seconds, the capability to solve complex distortion patterns does not exist.

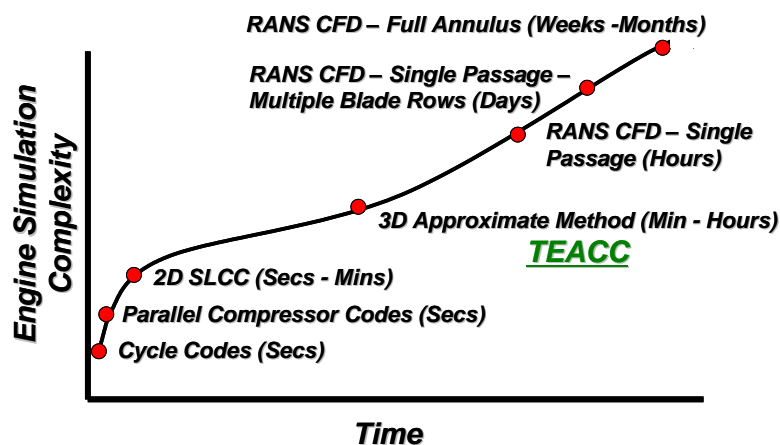


**Figure 3.220 Computational Techniques Complexity as a Function of Approximate Computational Time**

Inlet calculations can characterize the steady flow field at the AIP that the propulsion system must be able to accept but the effect of that pattern on the engine requires engine testing and analysis. To augment testing and analysis, numerical simulations capable of calculating compression system and eventually engine performance and/or operability are required.

Compression system simulation technology ranges from simple concepts based upon textbook theory to very complex CFD simulations. The analysis engineer has to make a choice

The more complex form of modeling for inlet distortion effects uses 3-D turbomachinery Navier-Stokes codes as illustrated in **Figure 3.221**. Although these types of codes require an extremely fine computational grid or mesh to solve the Reynolds Averaged Navier-Stokes (RANS) equations, there have been several investigations that compute the effects of a distorted inlet flowfield on compression system performance [3.157].

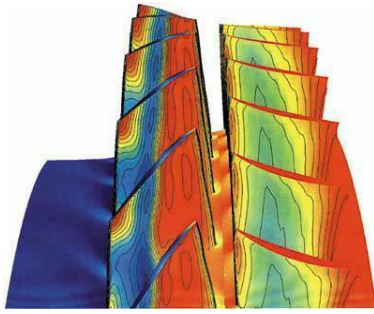


**Figure 3.221 Complex Flow-Field Calculation using RANS CFD for Turbomachinery**

It is also known that numerical solutions based on the RANS equations do not always predict absolute values of the aerodynamic loss in turbomachinery. However, it is widely accepted that the most important flow physics are properly captured and thus this method can be used to understand the flow mechanisms found within the turbomachinery. Navier-Stokes analyses typically require at least several weeks or months to solve a single complex distorted flow field because of the amount of computational space (in terms of grid points) that is associated with full annulus geometry.

### **CITED EXAMPLE(S)**

**3.150** Davis, Milt, Hale, Alan, Vining, Charles, and Cousins, William, "Application of Numerical Analysis Tools for Airframe-Propulsion Integrated Test and Evaluation," ASME Paper #GT2008-50194, 2008 ASME Turbo Expo, June 2008.

**3.151** Davis, Milt, Hale, Alan, Klepper, Jason, Dubreus, Terrance, and Cousins, William, "Demonstration of an Integrated Test and Evaluation (IT&E) Process for Airframe-Propulsion Systems as Applied to a Current Weapon System Program," AIAA Paper, 2010 Aerospace Science Conference, January 2010.

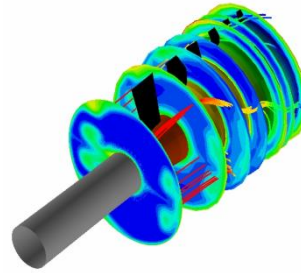
### **MODELING TECHNIQUE**

An alternate approach to parallel theory and RANS Navier-Stokes equation for distorted inflow is the numerical solution of the full three-dimensional Euler Equations. This technique allows for circumferential and radial control volumes to interact directly with each other via Euler equations with body forces representing the forces associated with a blade row. This technique allows the direct exchange of mass, momentum, and energy. One technical approach for the development of this technique is illustrated in [Figure 3.222](#) and is known as the Turbine Engine Analysis Compressor Code, **TEACC** [[3.158](#), [3.159](#), [3.160](#)] ([Section 4.7](#)).

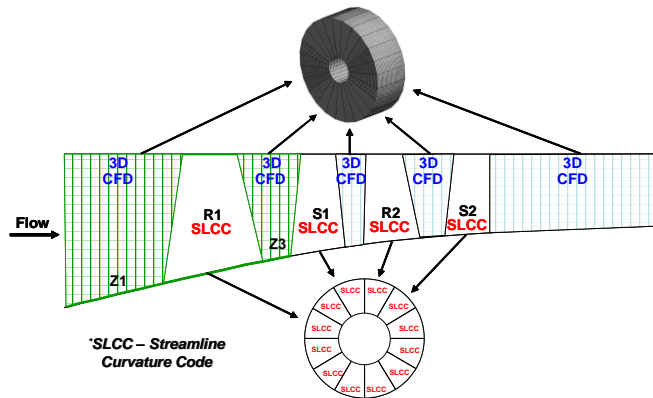
Because the airframe/inlet geometry and angle of attack can present various total pressure and swirl distortion patterns to a compression system, it is necessary to model the entire airframe/inlet-propulsion system together in a single, high fidelity model to determine the operability effects on the compression system. AEDC has developed and applied this technique on several occasions. This section will report the work on integrating an advanced airframe-propulsion system with two different techniques. The first example uses the **USM3D** unstructured code for airframe/inlet portion of the model and the **TEACC** code for the compression system model. The second example will use the **OVERFLOW** CFD package for the airframe/inlet model, while using the **TEACCSTALL** code for the compression system model.

To compute time-dependent, complex inlet distortion effects on the compressor flow field and vice versa in a timely manner, one must accept more empiricism in the modeling approach. The approach discussed in this paper is the development of a 3D compression system model which can compute complex inlet distortion effects on the compressor flow field and vice versa in a

timely manner. **TEACC** is a 3D compression system model that uses a Streamline Curvature Code to represent turbomachinery blades instead of the traditional turbomachinery CFD approach. A general purpose 3D flow simulation computer code has been modified to accept turbomachinery information on boundaries that represent the inlet and exit of each blade row.



a. TEACC Computational Flow Field Results



b. TEACC Computational Domain

Figure 3.222 Technical Approach for 3D Euler Turbomachinery Code for the Analysis of Inlet Distortion

Information is passed at these boundaries each time step until convergence is acquired. As such, **TEACC** transports the macro details of the flow (e.g. massflow, temperature, and pressure) and does not try to explicitly calculate turbulence, boundary layer thickness or shock structure as might be calculated with a turbomachinery CFD code.

#### APPLICATION TO AN ADVANCE AIRFRAME-PROPULSION SYSTEM –USM3D AND TEACC

Using a CFD representation of the aircraft forebody and inlet with USM3D [3.164] and a 3D numerical simulation of the fan (**TEACC**), an aircraft-propulsion simulation was developed by integrating these separate simulations together at the Aerodynamic Interface Plane, AIP. Integration was obtained in one of three ways:

- Using the same CFD Software for both the aircraft and **TEACC**, in this case, **OVERFLOW**
- Integrating at the AIP via a message passing routine using different codes for aircraft and **TEACC**
- Integration using the software package known as **STEPNET** [3.163].

Full interaction was achieved and solutions of both the inlet flow and the fan performance with inlet distortion were obtained and analyzed. In the first case where the same software package was used for both the airframe and the fan was a default case. **TEACC** uses the **OVERFLOW** CFD solver in the Euler mode as the baseline solver. Thus, it was simple to hook up more computational zones representing the aircraft and inlet system.

In the second case, **TEACC** was connected to an unstructured CFD code, **USM3D**, representation of the forebody and inlet system. This proved challenging since information had to be interpolated between a structured grid in the **OVERFLOW** system to an unstructured grid

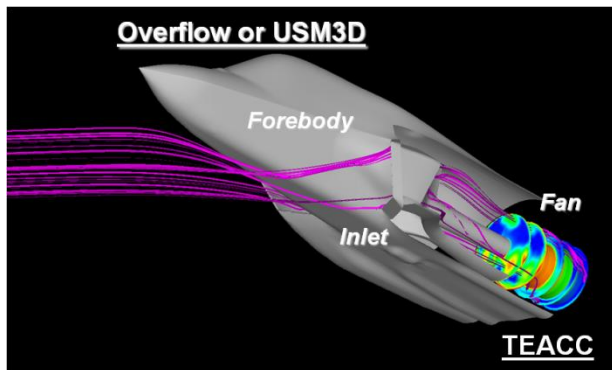


**Figure 3.223 Solution of the Integrated Aircraft – Propulsion System**

in the **USM3D** system. Message passing at the boundary was conducted with a routine that passed the dependent variables in an overlapping manner. Since two different codes were used, a means to determine when one code was ready to receive information had to be implemented. This procedure would also be used in the third method describe below.

The third method uses **STEPNET**, which is a code which was used as a means to connect different codes and execute them on multi-processors in a parallel computing environment. For this case, **USM3D** and **TEACC** were connected in a similar

manner as in case two, but **STEPNET** controlled the message passing process and determine the appropriate processors for each code. In all three cases, solutions were obtained as presented in **Figure 3.223**.

The aircraft was set at an angle-of-attack and a small amount of side-slip at a flight condition of interest. In addition, the appropriate boundary condition for the inlet calculation is now present (i.e. the engine fan operating at a specified speed and airflow) making the inlet CFD results more realistic. The presented solution not only gives the distortion pattern at the AIP but with the fan connected provides the performance of the fan in terms of the compressor map as shown in **Figure 3.224**.

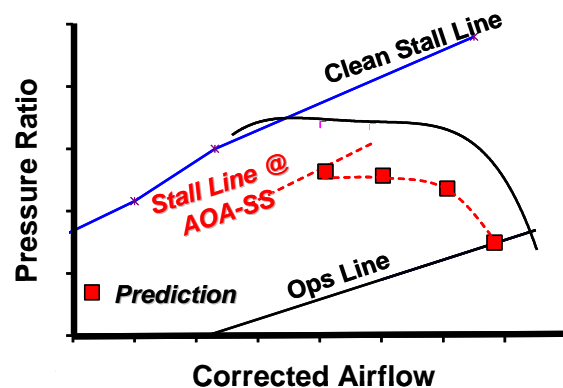


**Figure 3.224 Prediction of Fan Stall at a Typical Flight Condition**

In this case there is no validation data to substantiate the results and is thus a prediction. But of course this is the objective of the effort: to provide a predictive capability. To fully validate this system analysis capability, the integrated system model now needs to be compared with flight test data.



## APPLICATION TO AN ADVANCE AIRFRAME-PROPULSION SYSTEM –OVERFLOW AND TEACCSTALL

This section not only describes the application of **OVERFLOW/TEACCSTALL** to the advanced airframe-propulsion system, but also provides details on the CFD model validation to wind tunnel data for the inlet.

A modern military aircraft performing attack and evasive flight maneuvers causes the flow entering through the inlets and traveling through S-ducts to be highly distorted and unsteady at the aerodynamic interface plane (AIP). The AIP is a location that logically marks the end of the airplane inlet immediately followed by the engine. Typically, the inlets and the engine are designed, built, and tested separately with engineers having only a general knowledge of the other component. Since the flow field across the compressor and turbine blades does not scale uniformly with geometry, the engine must be tested in a full-scale configuration. The inlet geometry, however, can be proportionally reduced producing a subscale model of the inlet. The subscale model results can be manipulated through scaling rules to determine the full-scale inlet behavior. With increased emphasis on engine performance, thermal efficiency, and engine stability, aircraft and engine manufacturers as well as test organizations are teaming to improve the inlet/engine integration.

The purpose of this section is to outline the overarching issue with direct comparison of wind tunnel data to flight data, the use of the ARP-1420 methodology to calculate loss in stability margin, and various ways numerical simulations may be combined with wind tunnel/flight data to predict loss in engine stability margin.

Wind tunnels are used for inlet testing because the incoming conditioned air can be specified and controlled and the subsequent effect of the inlet on the air can be measured accurately. The inlet is usually scaled down from full size. The reduction in size allows the inlet to be manipulated within the test section of the wind tunnel independent of wall influences. Typically, a flow point is identified by specifying the angle of attack ( $\alpha$ ), the angle of side slip ( $\beta$ ), the flight Mach number (MN), and the mass flow corrected to the area weighted totals at the AIP. The final scaling parameter sufficient for converting subscale to full-scale results is Reynolds number. Unfortunately, the correct Reynolds number is seldom obtained with subscale tests because the wind tunnel energy requirements to achieve the necessary static pressure are prohibitive. The inability of the wind tunnel test to achieve the correct Reynolds number is the primary difficulty in comparing wind tunnel and flight-test results.

Flight Reynolds numbers range from 20 to 40 million with typical wind tunnel operation delivering Reynolds numbers an order of magnitude less (2 to 6 million). The Reynolds number is important because it directly effects boundary-layer growth, shock/boundary-layer interaction, location of flow separation, and the location of transition from laminar to turbulent flows. However, experience with wind tunnel results shows that even though the inlet boundary layer grows proportionally faster in the subscale model, artificial boundary-layer tripping techniques can be effectively used to minimize the effect of not matching Reynolds number.

The S16 document ARP-1420 outlines a methodology for calculating engine stability limits using an array of unsteady total pressures obtained on a rake at the AIP. Since this methodology hinges on the accurate collection of unsteady total pressures at the AIP, an approach for obtaining unsteady total pressures from wind tunnel data will be presented. The methodology continues by obtaining circumferential and radial intensities from an array of filtered unsteady total pressures which can be plotted on a “doghouse” plot ([Figure 3.225](#)).



Circumferential intensity is plotted on the ordinate, and radial intensity is plotted on the abscissa, with tip intensity plotted as positive and hub intensity plotted as negative. The doghouse plot gets its name from the shape of the stability boundary also shown on the doghouse plot. These intensities are then combined with engine specific sensitivities, obtained from the engine manufacturer, to predict the loss in stability margin due to an unsteady inlet distortion.

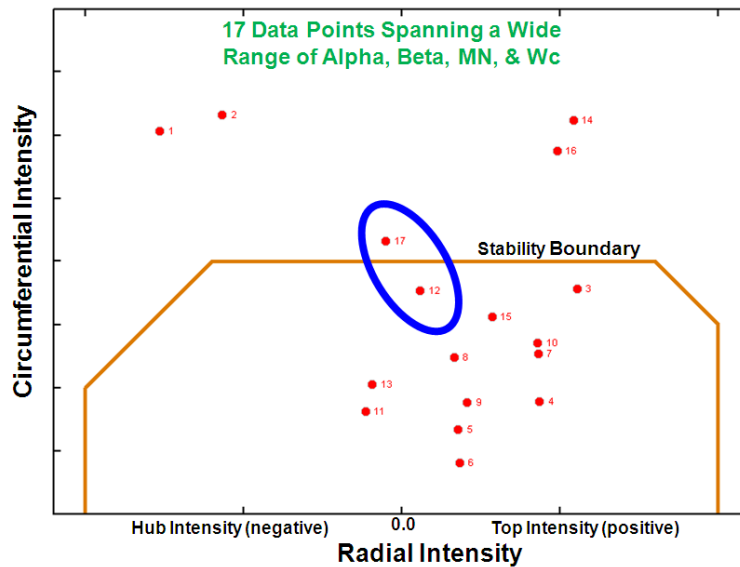


**Figure 3.225 Doghouse Plot.**

obtained at each of the 120 instrumentation locations specified by the 24 rakes and 5 rings. In addition, high-response pressure probes were located at the same ring locations with only half of the rake density (every other rake) as that of the steady-state probes. Therefore, 60 unsteady total pressures were obtained circumferentially 30 deg apart (12 rakes) by adding the high-response pressure to the adjacent steady-state pressure at each of the locations specified by 12 rakes and 5 rings.

A 12.05% subscale model of the forebody/inlet was tested in the 16-Ft Transonic Wind Tunnel located at Arnold Air Force Base as shown attached to a sting in [Figure 3.226](#). Also presented in [Figure 3.226](#) is a rake supporting instrumentation which is located at the AIP of that subscale model.

The rakes are separated circumferentially 15 deg apart (24 rakes, 12 major rakes 30 deg apart and 12 minor rakes in-between), and the instrumentation on the rakes is spaced radially on the rakes at equal area locations (5 rings). A steady-state total pressure was

#### **Subscale Model in Wind Tunnel**



#### **Aerodynamic Interface Plane, AIP Instrumentation**



**Figure 3.226 Wind Tunnel Installation and Total Pressure Probes at AIP.**

Many configurations were tested at AEDC; however, for the focus of this investigation only the most aerodynamic configuration is considered. This configuration is specified by clean (no stores hanging from the aircraft and the wheels up) conventional takeoff and landing (CTOL).

Wind tunnel data points consisted of taking data at a rate of 8,000 samples per second over a 4-sec time interval. Wind tunnel testing to date has produced over 10,000 clean CTOL data points. Part of the ARP-1420 methodology assumes that a distortion pattern that lasts less than a rotor revolution will have no effect on the stability of the compressor; however, a distortion pattern lasting on the order of a rotor revolution or longer may cause the compressor to become unstable and stall.

To eliminate the influence of distortion patterns lasting less than a rotor revolution, the wind tunnel data are filtered to eliminate higher frequencies. AEDC filters the data using a five-pole Bessel cut-off filter. Analog Bessel filters are characterized by almost constant group delay across the entire pass-band, thus preserving the wave shape of the filtered signals. The full-scale cutoff frequency was set at 150 Hz which translates to a cutoff frequency of 1,244 Hz for a 12.05% subscale inlet model. Each sample of filtered wind tunnel data spanning the 4 sec can be investigated to determine the maximum intensities. The ARP-1420 methodology provides a technique (not outlined in this work) for obtaining circumferential and radial intensities from the array of 60 filtered, unsteady total pressures. Circumferential intensity is a measure of loss in total pressure relative to its mean on a ring-by-ring base. Radial intensity is the largest of the hub or tip loss in total pressure relative to the face average.

Therefore, intensities are calculated on a given sample (60-probe pattern) containing an array of filtered, unsteady total pressures. In contrast, sensitivities are obtained from direct-connect engine ground testing where classical distortion screens are placed in front of the engine and the sensitivity of the engine to the distortion pattern is assessed for a wide range of mass flows. For example, circumferential sensitivities could be obtained by placing a circumferential distortion screen (180 or 90 deg, 1 deg per revolution) in front of the engine and determining the sensitivity of the engine to a purely circumferential distortion. The radial sensitivities are obtained in a similar manner by placing a hub radial or tip radial distortion screen in front of the engine and determining the sensitivity of the engine to a purely radial distortion.

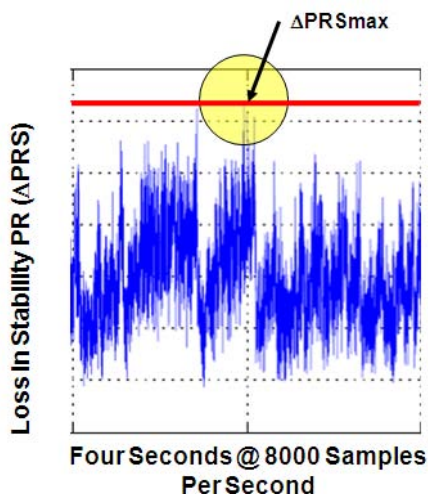


**Figure 3.227 Calculated Loss in Stability Pressure Ratio for a 4-sec Transient.**

The ARP-1420 methodology defines the loss in stability total pressure ratio to be relative to the clean stability line instead of the engine operating line because in the early design phase of the engine the operating line may not yet be defined. For a given corrected mass flow, an inlet distortion sample (60-probe pattern) may have a loss in stability margin or  $\Delta PRS$ . Alternatively, the loss in stability margin or  $\Delta PRS$  can be calculated from the ARP-1420 methodology which uses the previously defined circumferential and radial sensitivities combined with the circumferential and radial intensities. The object is to evaluate each sample of filtered wind tunnel data for a given data point, as shown in [Figure 3.227](#), and determine the maximum loss in stability margin and corresponding circumferential and radial intensities.

The intensities that correspond to the maximum loss in stall margin are usually not the maximum circumferential intensity and maximum radial intensity occurring during the data point. Since the sensitivities are strongly variant with mass flow, a similar distortion pattern may produce a very different loss

in stall margin. Nevertheless, intensities without the influence of sensitivities are often plotted on a “doghouse” plot (**Figure 3.225**).

Seventeen data points were selected from the large CTOL wind tunnel data base with a diverse range of alphas, betas, Mach numbers, and corrected mass flows. These data point were processed through **Eqn. 3-6**

$$\Delta PRS = \frac{PR1 - PRDS}{PR1} \times 100$$

**Eqn. 3-6**

with the maximum loss in stall margin plotted in **Figure 3.228** and the corresponding intensities plotted in **Figure 3.225**. The stability limit for each of the 17 data points is appropriately located between the clean stability limit line and the engine operating line. Also plotted on the performance map (**Figure 3.228**) is an engine acceleration transient initiated at a low engine speed (low corrected mass flow) and transitioned to a high engine speed (high corrected mass flow). This transient traces a path above data point number 12 and below data point number 17. This means that during the engine acceleration transient the unsteady inlet distortion represented by data point 12 would cause the engine to stall, but the engine would continue stable operation when exposed to the unsteady inlet distortion specified by data point 17.

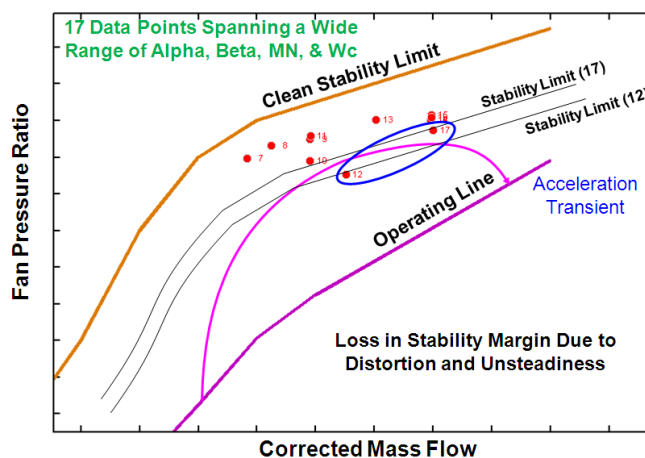


**Figure 3.228 ARP-1420 Estimated Loss in Stability Pressure Ratio for Selected Wind Tunnel-Produced Inlet Distortion Patterns.**

The dangers of using the doghouse plot in isolation of the sensitivities for drawing conclusions about engine stability is evident by returning to

**Figure 3.225** and focusing again on data points 12 and 17. The stability boundary is plotted between data point 12 and 17 incorrectly, suggesting that the unsteady intensities of data point 17 would produce engine instability and the unsteady intensities of data point 12 would result in engine stability. Although the doghouse may be a useful guide for a quick-look assessment of a data point, failure to properly include the engine sensitivities could produce misleading results.

The final purpose of this section is to outline various ways numerical simulations may be combined with wind tunnel/flight data to predict loss in engine stability margin. **Figure 3.229a** represents the traditional ARP-1420 methodology previously described. The significant features of this approach are that an array of unsteady total pressures are obtained on a rake at the AIP from either wind tunnel or flight data and processed through the previously defined ARP-1420 methodology to obtain the maximum loss in stall margin. A significant limitation of this approach is the need for engine sensitivities. Both the steady-state and the maximum unsteady stability limits are plotted as solid dots in **Figure 3.229e**.

**Figure 3.229b** outlines an alternative approach to obtain an array of total pressures at the AIP. The flow field over the forebody and through the inlet was simulated with **OVERFLOW**, which

used the Reynolds Averaged Navier Stokes equations (RANS) to obtain steady-state solutions. When rakes are used to collect arrays of total pressures at the AIP, the rest of the flow-field information is lost because the ARP-1420 methodology ignores this information. Similarly,

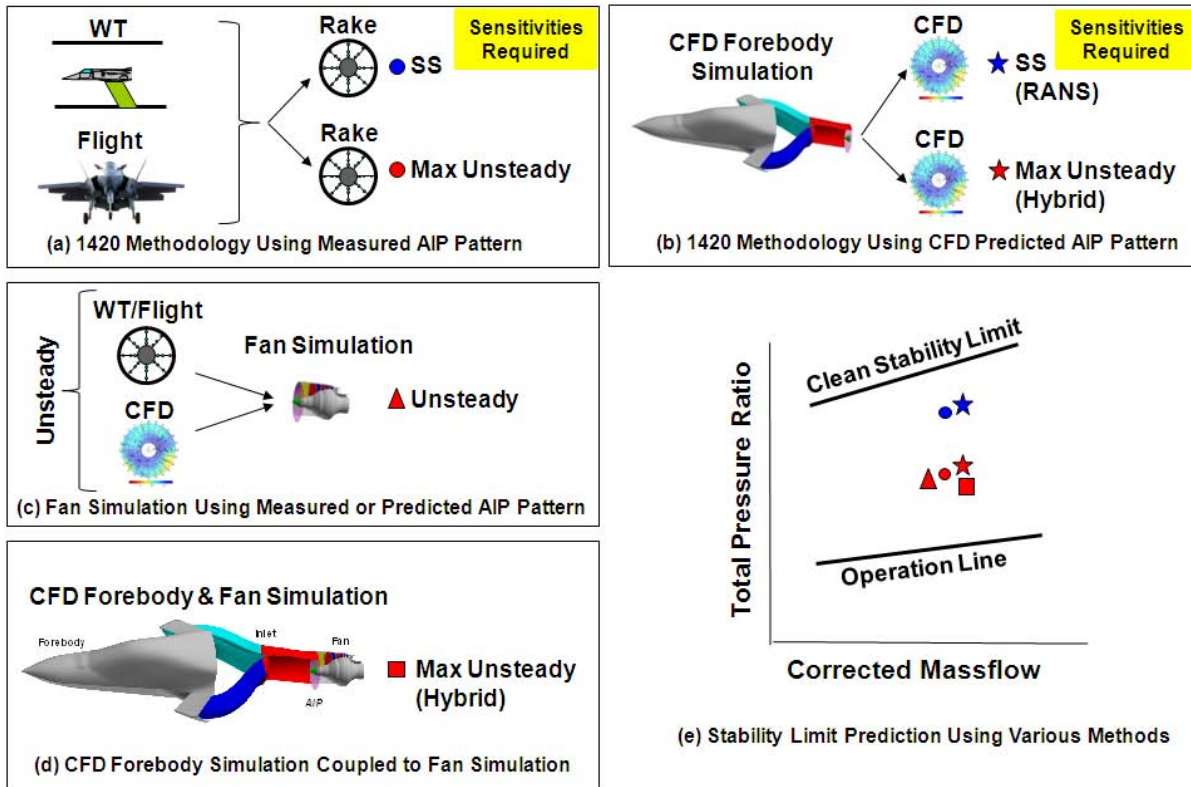


**Figure 3.229 Methods for Determining Loss in Stability Pressure Ratio.**

additional information, such as swirl, generated by the CFD solution at the AIP is also ignored. The ARP-1420 methodology can then be used to calculate the steady-state loss in stall margin as represented by the blue star on the fan performance map. A recommendation for future work is to calculate the flow field over the forebody/inlet using a hybrid CFD technique. This would provide unsteady total pressures at the AIP. The hybrid CFD system generates an unsteady solution by resolving some of the turbulent length scales on the computation grid and the remainder of the length scales through large eddy simulations. The unsteady total pressures obtained at the AIP are processed as before through the ARP-1420 methodology to obtain the unsteady stability limit depicted by the red star plotted in [Figure 3.229e](#).

The numerical stability prediction capability embodied in [Figure 3.229c](#) provides an alternative to the ARP-1420 methodology to predict the loss in stability margin. The fan simulation eliminates the need for engine sensitivities to obtain engine stability limits. An array of unsteady total pressures obtained from wind tunnel data, flight data, or CFD forebody/inlet simulations are provided to fan simulation as inlet boundary conditions, which predicts the loss in stability margin.

The final technique for calculating the loss in stall margin is outlined in [Figure 3.229d](#) and is completely numerical. A coupling technique is used to connect the CFD of the airframe forebody/inlet with a fan simulation to predict a steady-state loss in stall margin. **OVERFLOW** as previously defined is used to calculate the flow field over the forebody and through the inlet



to the AIP. The advantages of numerically calculating the flow field at the AIP are that other parameters such as swirl are immediately accounted for in the solution. The ARP-1420 methodology ignored the effects of swirl, but this influence is immediately accounted for through the coupling of the simulations. In addition, the numerical fan simulation eliminates the need for engine sensitivities. A recommendation for future work would be to couple a hybrid CFD code used to calculate the forebody/inlet flow field with the fan simulation to generate an unsteady loss in stall margin.

### Validation of OVERFLOW for Airframe-Inlet Forebody

The purpose of the section is to outline the effectiveness of current CFD to calculate the flow field over the forebody and through the inlet. The approach is to compare steady-state CFD solutions of the forebody/inlet to their corresponding steady-state wind tunnel data point in recovery, radial and circumferential intensity, radial and circumferential total pressure, and finally loss in stall margin on a performance map.

The flow field over the forebody and through the inlet was simulated with **OVERFLOW**, which used the Reynolds Averaged Navier Stokes equations (RANS) to obtain steady-state solutions. **OVERFLOW** uses an upwind differencing scheme developed by Harton, Lax, and Van Lear along with a Van Albada flux limiter. The spatial differencing of the convection terms is third-order accurate, and the spatial difference of the diffusion terms is second-order accurate. All of the CFD solutions were obtained using a shear stress transport two-equation turbulent transport model. Solutions were accelerated to steady-state through local time stepping. **OVERFLOW**'s native chimera grid (overset grid) capability was extensively used in the grid construction simulating of the forebody/inlet; the simulation consisted of 20 zones totaling 10 million grid points. Typical CFD solutions were achieved in 24 hr using 16 processes by adjusting exit static pressure until the desired corrected mass flow was achieved.

Seventeen data points were selected from the large CTOL wind tunnel data base with a diverse range of alphas, betas, Mach numbers, and corrected mass flows.

**OVERFLOW** produced a converged, steady-state solution for each of the 17 selected wind tunnel data points. A comparison of CFD results to wind tunnel data in total pressure inlet recovery is presented in **Figure 3.230**. The 17 flow points are compared in increasing corrected mass flow from left to right as reflected by the positive or zero slope of the magenta line. **Eqn. 3-7** listed below was used to process both the CFD results and the wind tunnel data to generate recovery.

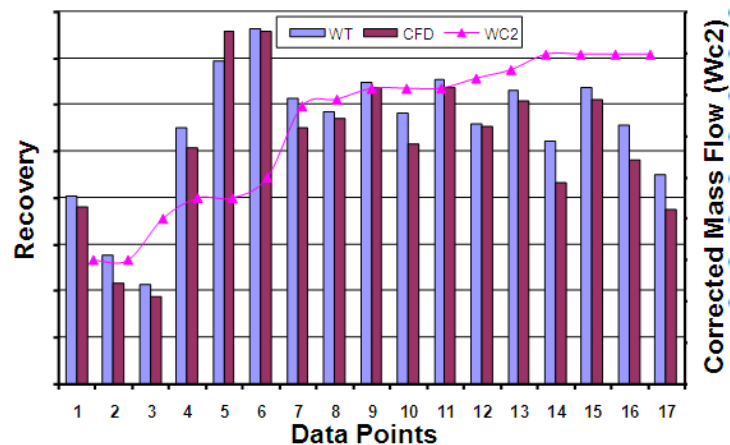


**Figure 3.230 Inlet Total Pressure Recovery for the 17 Chosen Data Points.**

$$Recovery = \frac{1}{(i_{max} * j_{max})} \sum_{i=1}^{i_{max}} \sum_{j=1}^{j_{max}} \frac{P_{t_{ij}}}{P_{t_{freestream}}} \quad \text{for } i_{max}=5; j_{max}=24 \quad \text{Eqn. 3-7}$$

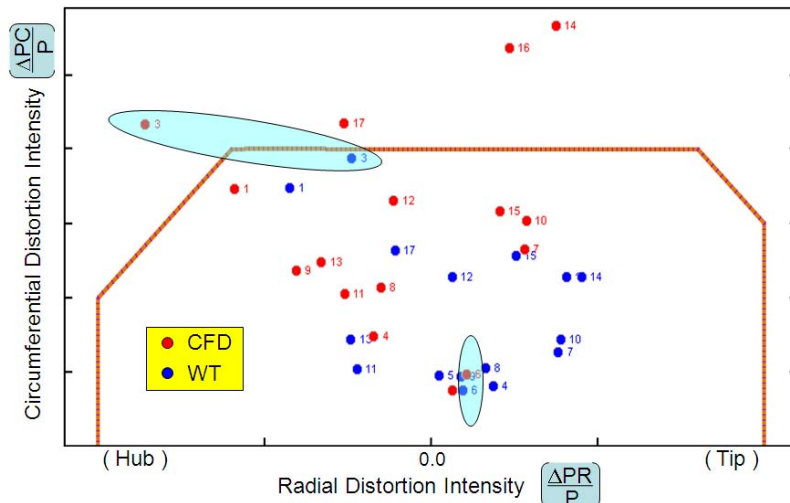


**Figure 3.231 Comparison of Steady-State CFD Generated Inlet Distortion Intensities to Wind Tunnel Data for the Airframe/Inlet on a Doghouse Plot.**

For consistency in the comparison, the CFD results were interpolated to the wind tunnel equivalent locations of 5 rings and 24 rakes also producing 120 steady-state total pressures. The overarching trend in the comparison is that the CFD results consistently overpredicted the loss of total pressure at the AIP.

The SAE ARP-1420 methodology provides a technique (previously presented) for calculating radial and circumferential intensities. The wind tunnel steady-state intensities are calculated from

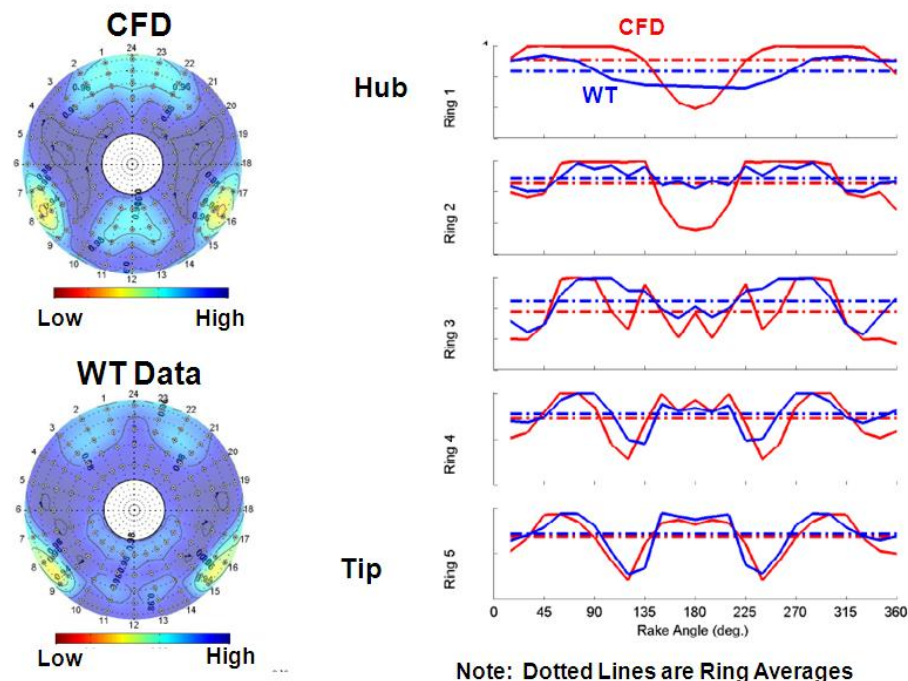


**Figure 3.232 Total Pressure Distortion Intensity Comparison for Chosen Data Point 6.**



the array of 120 steady-state total pressures located at the AIP. The CFD steady-state intensities are calculated using the same steady-state total pressure used to calculate the previously defined recovery. Radial and circumferential steady-state intensities for the same 17 wind tunnel data points previously referenced are present in [Figure 3.231](#) (doghouse plot) with CFD intensities plotted in red and wind tunnel intensities plotted in blue. A general trend is the CFD intensities are shifted higher and to the left of the wind tunnel intensities. This means that the CFD solutions are producing greater circumferential distortion with an elevated hub distortion. Two data points, numbers 6 and 3, will be investigated to provide additional insight.

The wind tunnel and CFD intensities compare favorably for data point number 6 with a modest amount of circumferential and tip radial intensity. Total pressure plots are presented in [Figure 3.232](#) using a polar technique for a qualitative view of AIP distortion and a circumferentially unwrapped ring-by-ring technique for a quantitative view of AIP distortion.

The polar plots reveal that the general character of the total pressure distortion is captured both in location and in extent. The ring-by-ring unwrapped CFD total pressures compare well to the wind tunnel total pressures at the outer ring (tip area). However, the quality of the comparison steadily deteriorates with decreasing ring number (tip-to-hub). The CFD solution produces a large dip in total pressure near the 180-deg circumference for both ring 1 and ring 2 (hub area) with only a modest drop in total pressure arising from the wind tunnel data at ring 1. Clearly something is causing an elevated distortion pattern in the CFD results.

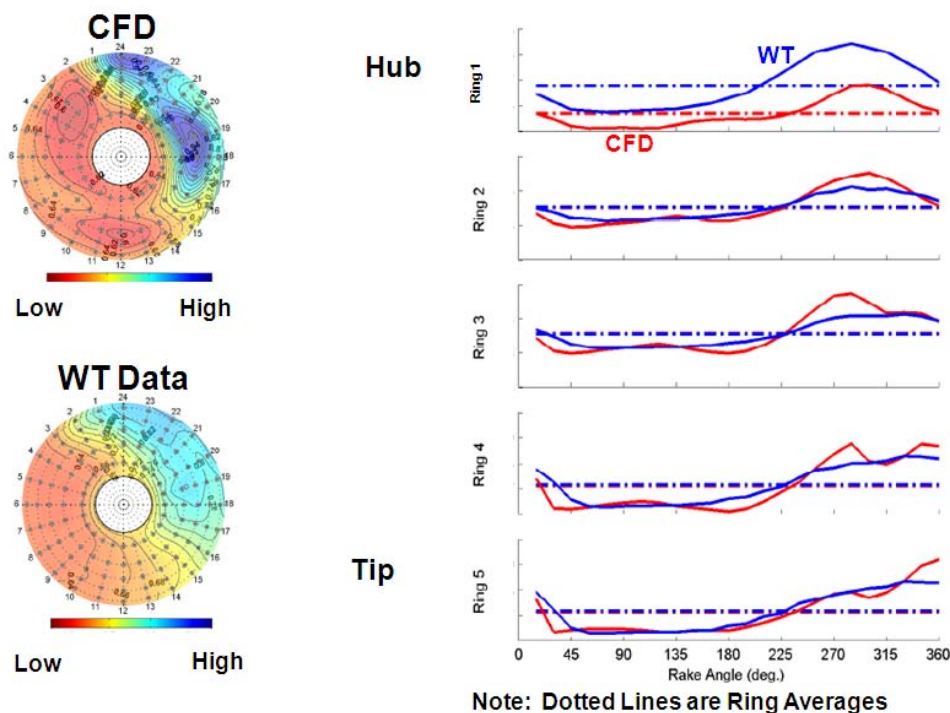


**Figure 3.233 Total Pressure Distortion Intensity Comparison for Chosen Data Point 3.**

**Figure 3.233** shows detail associated with data point 3 comparing CFD results to wind tunnel data at the AIP through specially analyzing the steady-state total pressure. The polar plots

show that the overall character of the CFD results are very similar to the wind tunnel data in extent, and that the distortion is located in the correct part of the annulus (not shifted radial or circumferentially).

The detailed view of steady-state total pressure presented in the unwrapped ring-by-ring comparison of CFD results to wind tunnel results shows very good agreement in all of the rings except for the first ring. The CFD results have the same shape as the wind tunnel results in the first ring, but the CFD results are significantly shifted down indicating that CFD is predicting an elevated distortion level near the hub.

The ARP-1420 methodology, previously outlined, combined the intensities calculated from an array of steady-state total pressures and combined them with fan sensitivities to make a prediction of loss in fan steady-state stall margin. The previous comparison of CFD results to wind tunnel data showed that CFD generally predicted a lower recovery and overpredicted the circumferential and hub radial intensities. Nevertheless, what really matters is whether these differences, when combined with fan sensitivities, cause a measurable loss in stall margin on a fan performance map. **Figure 3.234** is a fan performance map showing a comparison of CFD results to wind tunnel data for the high mass-flow group from the previously selected 17 data points. The prediction of CFD loss in fan stall margin across all mass flows is on the order of twice that predicted by the wind tunnel loss in fan stall margin.

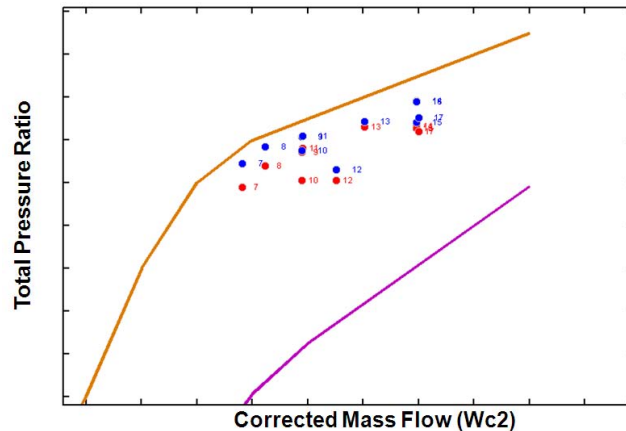


**Figure 3.234 Comparison of the CFD Stability Pressure Ratio Loss Using the ARP-1420 Methodology to Steady State Inlet WT Data.**

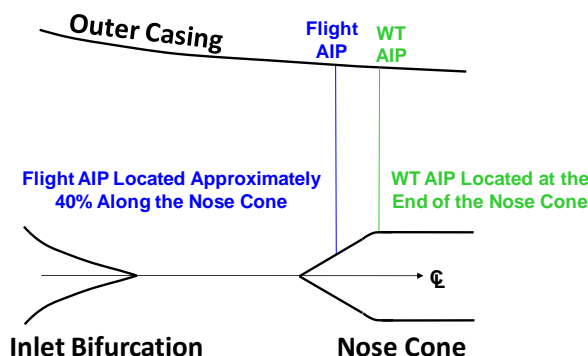


**Figure 3.235 Nosecone Differences Between WT Model and CFD Calculations.**

Since the differences in fan stall margin between CFD and wind tunnel data are significant, effort should be focused on improving the CFD simulation. The previously focused investigation with data points 3 and 6 revealed that the CFD results compared favorably to the wind tunnel data everywhere except the hub. This suggested that there may be a change in geometry between what was tested in the wind tunnel and the flight-ready geometry simulated by the CFD. **Figure 3.235** is a sketch of the final part of the inlet bifurcation, the nosecone region just before the fan

blades, and some ducting connecting these two components. Some significant geometry differences were observed. The wind tunnel data were taken with the rake located after the

nosecone slope change ended; however, the CFD results corresponding with flight geometry identified the AIP at a location approximately 40% along the nosecone angle change.

These hub geometry changes could make a significant difference since a highly distorted flow field is experiencing a large cross-sectional area change. Additionally, the CFD results may be improved through grid modification and choice of turbulence modeling.

## Compression System

**TEACCSTALL** (Figure 3.236) is an AEDC derivative of the **CSTALL** [3.165] code and the previous AEDC effort, **TEACC** [3.159, and 3.160]. **TEACCSTALL** is a 3D, time-accurate Euler code for modeling turbomachinery with an emphasis on determining stall inception. Instead of representing each blade passage with an appropriate grid, the effects of each bladed region are modeled by using turbomachinery source terms (relative total pressure loss, change in angular momentum, and radial blade blockage). The code is used to model both steady-state performance and dynamic stall inception. The stalling of the compressor is determined by an

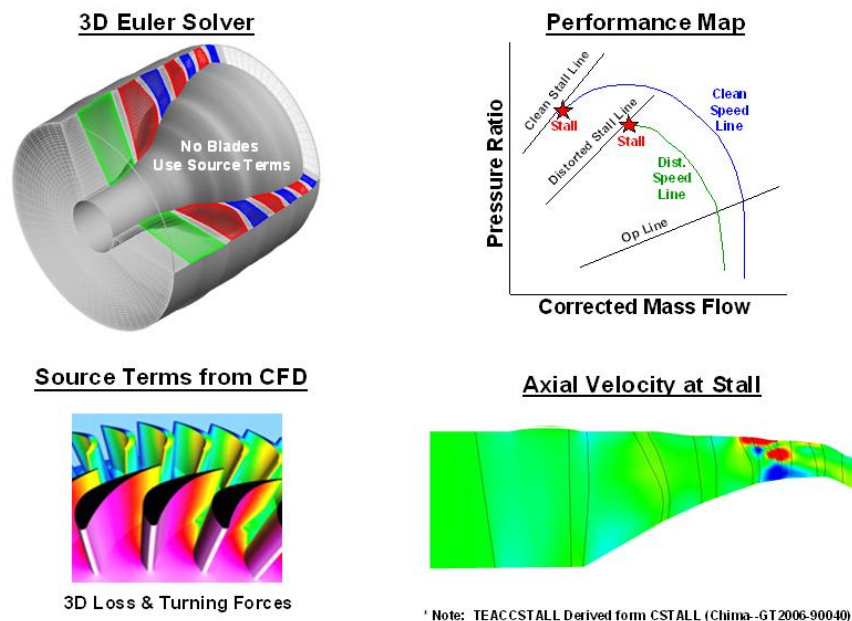


**Figure 3.236 TEACCSTALL Technical Approach.**

imbalance of the forces based on the local flow field and source terms. **TEACCSTALL** uses a cylindrical coordinate system. The equations are discretized by either a central difference with second- and fourth-order artificial dissipation or an ASUM<sup>+</sup> upwind finite-difference scheme. For steady-state solutions, **TEACCSTALL** uses a two-stage explicit Runge-Kutta scheme with spatially varying time stepping and implicit residual smoothing for acceleration to solution. For time-accurate solutions, **TEACCSTALL** uses a four-stage explicit Runge-Kutta scheme with constant time steps.

## OVERFLOW-TEACCSTALL Integration

Another goal of this effort was to develop an integrated airframe forebody-inlet-engine simulation. This would provide the ability to determine stall inception of the fan through aircraft maneuvers with realistic, time-dependent distortion patterns generated by the airframe

forebody-inlet combination. Since AEDC previously developed the forebody and inlet simulation in **OVERFLOW**, it was decided to couple **TEACSTALL** with **OVERFLOW** for the overall integration mission.

A first-generation coupling method was prototyped several years ago with a previous version of **TEACC** and **OVERFLOW**. The previous integration was file-based and single-fringed, which limited computing efficiency, and this integration was unable to accept reverse flow and dynamic behaviors. It was determined that the same **DiRTlib** implementation used for multi-zone **TEACSTALL** would also facilitate communications with an external code (**OVERFLOW**).

To accomplish this, **DiRTlib** was implemented into a version of **OVERFLOW** using callbacks in **OVERFLOW** (similar to the multi-zone callbacks in **TEACSTALL**). These callbacks account for the difference in scaling and non-dimensionalization of the flow variables in each code. **Figure 3.237** show the concept of integration of the two codes. **OVERFLOW** is used to solve the airframe forebody-inlet up to the aerodynamic interface plane (AIP), and **TEACSTALL** solves from the AIP through the fan exit. **DiRTlib** facilitates not only the communication of the flow variables between the codes at the AIP, but also at the **TEACSTALL** zone interfaces. Currently, a simplified inlet running in **OVERFLOW** connected to the fan **TEACSTALL** simulation has been implemented and converged to solution.

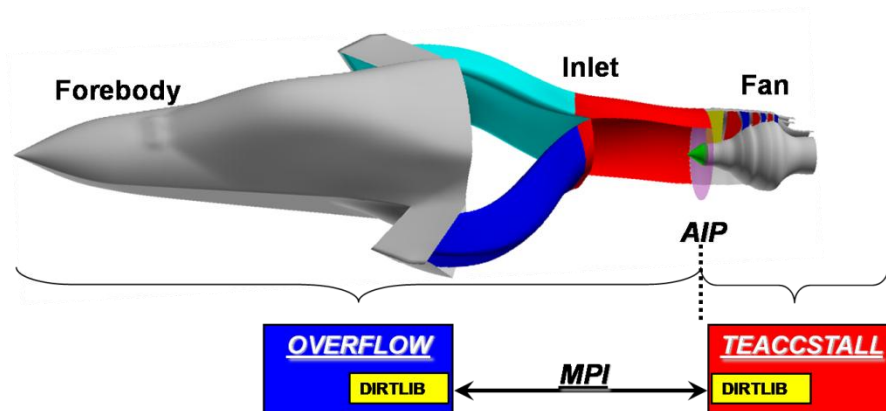


**Figure 3.237 Integration of OVERFLOW and TEACSTALL Using DiRTlib.**

#### **ADDITIONAL REFERENCES:**

**3.152** Suresh, A., Townsend, S.E., Cole, G.L., Slater, J.W., Chima, R. "Analysis of Compressor-Inlet Acoustic Interactions Using Coupled Component Codes" AIAA Paper 99-0749, 1999.

**3.153** Numbers, K., and Hamed, A., 1997, "Development of a Coupled Inlet-Engine Dynamic Analysis Method," AIAA Paper No. 97-2880.

**3.154** Numbers, K., and Hamed, A., "Conservative Coupling Technique for Dynamic Inlet-Engine Analysis", **Journal of Propulsion and Power**, Vol. 19, No. 3, May-June, 2003, pp. 444-455.

- 3.155** Davis, M. W., Jr. "Parametric Investigation into the Combined Effects of Pressure and Temperature Distortion on Compression System Stability," AIAA-91-1895, June 1991.
- 3.156** Hearsey, R. M. "HTO300 – A Computer Program for the Design and Analysis of Axial Turbomachinery," March 1970.
- 3.157** Yao, J., Gorrell, S., and Wadia, A., "Unsteady RANS Analysis of Distortion Transfer Through Two Military Fans", To Be Published in the Journal of Turbomachinery in 2007
- 3.158** Hale, A. A., and O'Brien, W. F. "A Three-Dimensional Turbine Engine Analysis Compressor Code (TEACC) for Steady-State Inlet Distortion," *Journal of Turbomachinery*, Vol. 120, July 1998, pp. 422-430.
- 3.159** Hale, Alan, et al. "Turbine Engine Analysis Compressor Code: TEACC – Part II: Multi-Stage Compressors and Inlet Distortion," AIAA-99-3214, June 1999.
- 3.160** Davis, Milt, Hale, Alan, and Beale, Dave. "An Argument for Enhancement of the Current Inlet Distortion Ground Test Practice for Aircraft Gas Turbine Engines," **Journal of Turbomachinery**, April 2002, pp. 235-241.
- 3.161** NASA SP-36, *Aerodynamic Design of Axial-Flow Compressors*, edited by Johnsen, I.A. and Bullock, R.O., 1965.
- 3.162** Buning, P.G., Jespersen, D.C., Pulliam, T.H., Chan, W.M., Slotnick, J.P., Krist, S.E., and Renze, K.J., OVERFLOW User's Manual- version 1.8, NASA Langley Research Center, February 1998.
- 3.163** Meilunas, R., "Overview of the Simulation, Test and Evaluation Process Network: STEPNET, AIAA-2007-6572, August 2007.
- 3.164** Pandya, M.J., Frink, N.T., and Noack, R.W.: "Progress Toward Overset-Grid Moving Body Capability for USM3D Unstructured Flow Solver", AIAA 2005-5118, June 2005.
- 3.165** Chima, Rod, "A Three-Dimensional Unsteady CFD Model of Compressor Stability," ASME Paper GT2006-90040.



### 3.3.3 Aero-Structural for System Interaction Analysis

Traditionally, aeropropulsive and structural performance have been designed separately and later mated together via flight-testing. In today's atmosphere of declining resources, it is imperative that more productive ways of designing, optimizing and verifying aeropropulsive performance and structural aerodynamic interaction are made available to the aerospace industry. One method of obtaining a more productive design and evaluation capability is through numerical simulations. Recent advances in turbomachinery design are leading to very high thrust, lightweight engines that challenge all fronts of technology development. High temperature super alloys with single crystal construction offer tremendous resilience in extremely harsh turbine engine operating environments. Similarly, the high-bypass wide-chord, lightweight hollow, or composite, fan blade offers tremendous strength during bird strikes, hail ingestion, and surge cycles.

#### CITED EXAMPLE(S)

**3.166** Nazir, J., Couch, R., and M. Davis, "An Approach for the Development of an Aerodynamic-Structural Interaction Numerical Simulation for Aeropropulsion Systems" ASME Paper # 96-GT-480, June 1996.

#### MODELING TECHNIQUE

There are two technical approaches for analyzing aerodynamic-structural interactions. The more traditional approach is to use a computational fluid dynamic code to obtain aerodynamic forcing functions, and then pass that information to a finite-element structural code. The second approach is to use a code that integrates both the structures and aerodynamics. This approach has been demonstrated with a code known as **ALE3D** [3.167] ([Section 4.8](#)) developed by Lawrence Livermore National Laboratory. This code is capable of characterizing fluid and structural interaction for components such as the combustor, fan and stators, inlet and nozzles. This code solves the 3D Euler equations and has been applied to several aeropropulsive applications, such as a supersonic inlet and a combustor rupture simulation.

The basic computational step consists of a Lagrangian step followed by an advection, or remap step. This combination of operations is formally equivalent to an Eulerian solution while providing increased flexibility and, in some cases, greater accuracy. In the Lagrangian phase, nodal forces are accumulated and an updated nodal acceleration is computed. Following **DYNA3D**, the stress gradients and strain rates are evaluated by a lowest order finite-element method. At the end of the Lagrangian phase of the cycle, the velocities and nodal positions are updated. At this point, several options are available. If the user wishes to run the code in a pure-Lagrangian mode, no further action is taken and the code proceeds to the next time step. If a pure-Eulerian calculation is desired, the nodes are placed back in their original positions. This nodal motion or relaxation generates inter-element fluxes that must be used to update velocities, masses, energies, stresses and other constitutive properties. This re-mapping process is referred to as advection. Second-order schemes are required to perform this operation with sufficient accuracy. In addition, it is not generally adequate to allow advection only within material boundaries. **ALE3D** has the ability to treat multi-material elements, thus allowing relaxation to take place across material boundaries.

Fan-blade-off events can create failure in the compressor leading to engine surge. Normally the fan performs work on the incoming air such that air is pumped from low pressure at the inlet to a higher pressure at the outlet. This work ensures that the flow stays in the direction from compressor inlet to exit.



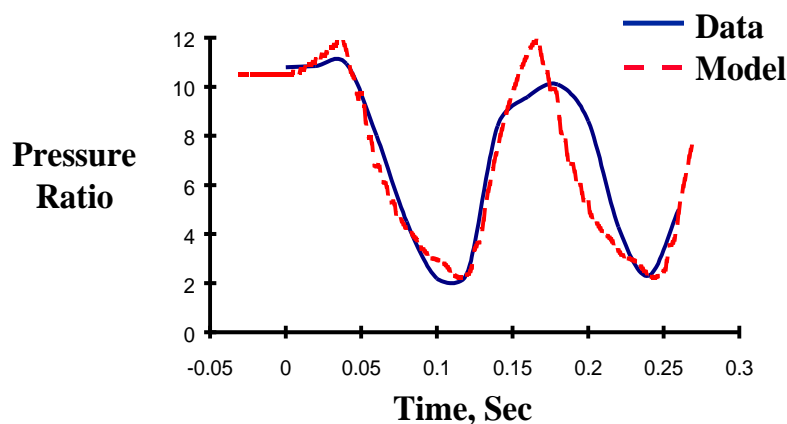
To model a fan-blade-off event both prior to and after the event analytically one can use a simulation that describes each blade and each stage exactly. The modeling of each blade in a discretized manner can employ many elements which once replicated to represent all the stage of high compressor, turbine, nacelle, casing, thrust reverser and other engine components can create a model that is so huge that analysis would take too long to run. This limitation requires an alternative strategy to the modeling of the fan-blade-off event other than discretizing and describing each blade and stage.

AEDC has been concerned with engine transient dynamics for over a decade and has been involved in testing various military engines. AEDC has accumulated a vast knowledge of engine transient dynamics and has applied that knowledge to analytical procedures which they use to complement test results and perform "what if" investigations. The AEDC numerical codes incorporate Euler equations of fluid motions along with turbomachinery source terms to simulate turbine engine performance and operability. These analytical codes have been successfully adapted not only to military engines, but also to high by-pass commercial turbine engines.

**DYNTECC** [3.168] (Section 4.4) is a one-dimensional, stage-by-stage, compression system mathematical model which is able to analyze any generic compression system. **DYNTECC** uses a finite difference numerical technique to simultaneously solve the mass, momentum, and energy equations with turbomachinery source terms (mass bleed, blade forces, heat transfer, and shaft work). The source terms are determined from a complete set of stage pressure and temperature characteristics provided by the user.

### SURGE CYCLE ANALYSIS

To illustrate the surge cycle analysis that can be conducted with **DYNTECC**, Boeing analyzed the aerodynamic behavior of a present-day commercial high pressure compressor (HPC) undergoing surge. System geometry was configured to include the fan and combustor geometry that interacts with the compressor during surge.



Stage characteristics were synthesized using a streamline curvature code for pre-stall characteristics while using experience from both low speed and high speed systems to estimate post-stall characteristics. The exit mach number was reduced at a rate simulating a combustor pressure pulse which initiates system surge.

**Figure 3.238 Comparison of Predicted Surge Frequency and Pressure Ratio to Experimental Results**

A comparison of **DYNTECC**'s prediction of aerodynamic behavior is presented **Figure 3.238**. The experimental pressure ratio presented represents component performance during surge of the HPC. **DYNTECC** reproduces that signature both in level and frequency. Since **DYNTECC** compares with the pressure ratio signature, the pressure at the inlet of the HPC is assumed to be accurate as presented in **Figure 3.239**. The pressure profile is what is required by the **ALE3D** code as a boundary condition.

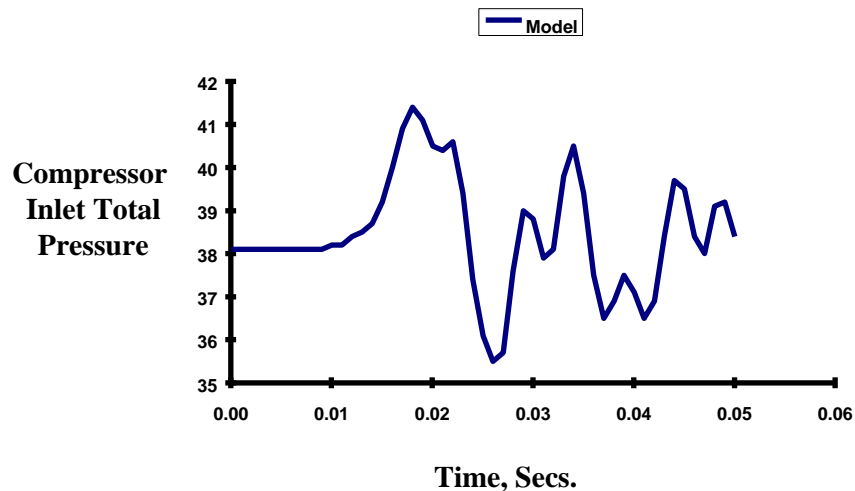


**Figure 3.239 Model Predicted Compressor Inlet Total Pressure During Surge Event**

#### **AERODYNAMIC – STRUCTURAL ANALYSIS**

An engine inlet configuration associated with the HSCT program that was scheduled for testing in 1996 was analyzed. A scale mock-up of the desired HSCT engine inlet was to be tested during an inlet unstart and its transient loading on the simulated scaled wing panel is to be measured. In addition to the plume size, intensity and pattern of the shock waves that are generated during an inlet-unstart is to be monitored. Inlet start is a complex three dimensional

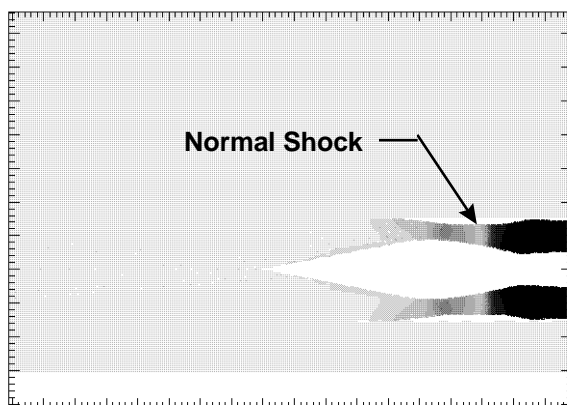


**Figure 3.240 Pressure Contours at Equilibrium with Imbedded Normal Shock During Steady Operation**

phenomena where a supersonic flow which comes through the inlet is stabilized to some acceptable subsonic conditions before entering the fan. This produces a shock wave that sits strategically somewhere in the inlet thus creating a transition zone from supersonic flow to sub-sonic flow within the HSCT inlet. Pressure contours at equilibrium and at plume peak are illustrated in **Figure 3.240**.

If for whatever reason the engine undergoes a transient such as an engine surge, the stable shock

wave will be disrupted and become unstable possibly spilling out around the engine. This bubble/plume will spread and produce loading on the surrounding structure such as wing and can produce considerable challenge to the aircraft attitude control surfaces which will try to compensate for such pulse loadings. In addition if the bubble/plume size is large enough it could be sucked in by the adjacent engine and thus perhaps causing it to unstart as well. This will obviously intensify the dynamics for the control system to compensate and thus requiring a thorough understanding of this phenomena.

The initial approach has been to analyze this coupled aerodynamic-structural interaction with a decoupled numerical technique. The decoupled approach that was taken was to model the surge cycle frequencies and intensity using **DYNTECC** for a typical high pressure turbine engine and correlate it with the SR-71 supersonic engine's surge data. This scaled pressure loading at the fan face was then introduced as a boundary condition to **ALE3D** which characterized the HSCT inlet steady state shock location in a three dimensional inlet. The boundary condition imposed in **ALE3D** from **DYNTECC** did not incorporate radial and theta variations because of **DYNTECC**'s one-dimensional formulation.

The appropriate boundary conditions were applied and the equilibrium flow was obtained as described in the previous section. The surge conditions were then applied as a time-varying one-dimensional pressure boundary condition. The time dependent boundary condition is illustrated in [Figure 3.241](#). The boundary condition captures the initial nature of the surge cycle as illustrated in [Figure 3.239](#). The initial spike and rapid drop-off occurs within the first 10 to 15 milliseconds after the event is initiated. The highly cyclic nature of the blowdown part of the cycle is not represented by the boundary condition. However, the inlet has already unstalled by that time and the cyclic oscillations no longer play a role in inlet unstart.

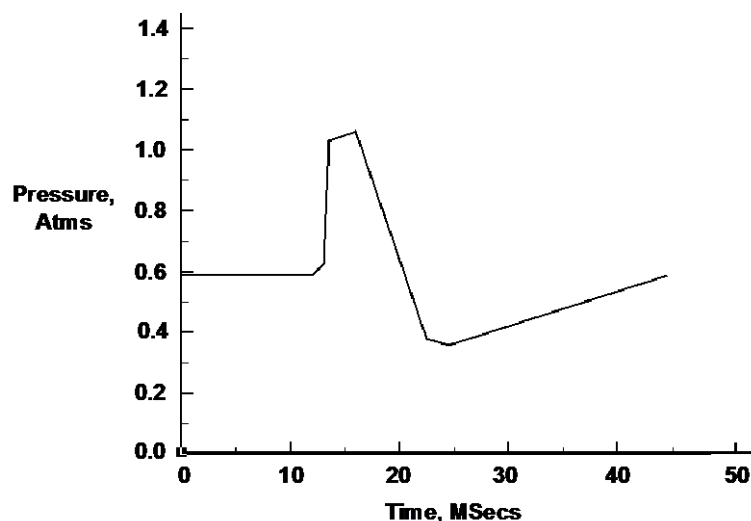


**Figure 3.241 Surge Pressure Boundary Condition for Mock HSCT Inlet**

The surge condition caused the shock to propagate out of the inlet with a finite plume size as illustrated in [Figure 3.242](#). [Figure 3.243](#) presents a plot of displacement on the wing-mock surface which indicates the dynamic response of the structure to the surge induced loading. The calculated results will be compared with data when the experimental results become available

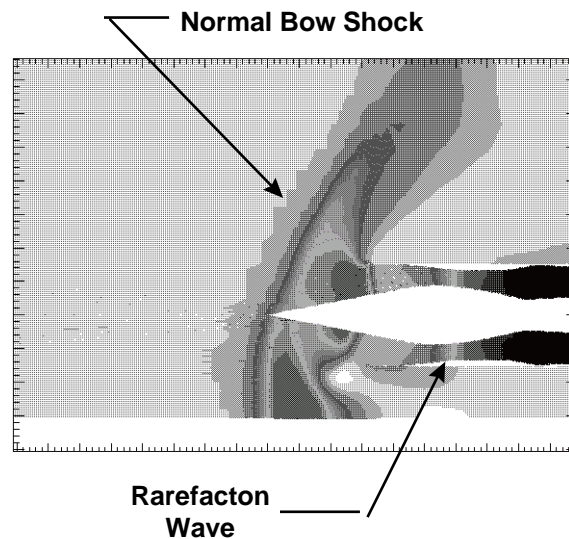


**Figure 3.242 Inlet Unstart Due to Engine Surge Cycle**

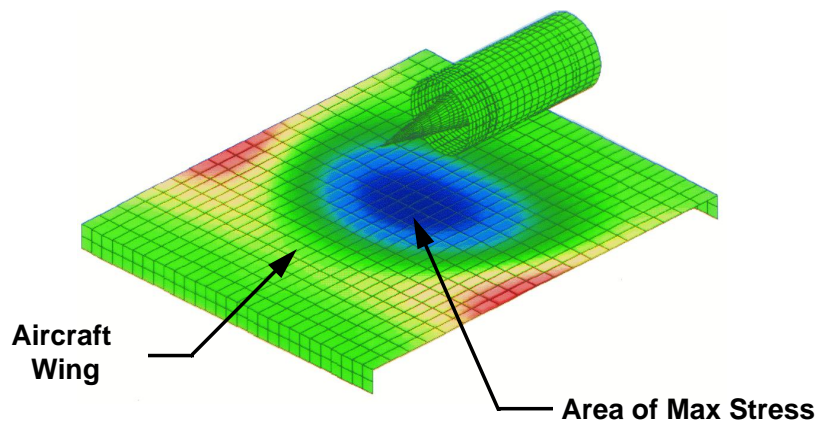


**Figure 3.243 Effect of Inlet Unstart on Aircraft Wing Assembly**

#### ADDITIONAL REFERENCES

**3.167** Sharp, R., Anderson, S., Dube, E., Futral, S., Otero, I., "User's Manual for ALE3D," Lawrence Livermore National Laboratory, unpublished, 1995.

**3.168** Hale, A. A. and M. W. Davis, Jr., "DYNamic Turbine Engine Compressor Code: DYNTTECC -- Theory and Capabilities", AIAA Paper # AIAA-92-3190, Presented at the 28th Joint Propulsion Conference and Exhibit, Nashville, TN, July 1992.

### 3.4 PROPULSION FACILITY ISSUES ADDRESSED BY NUMERICAL SIMULATIONS FOR OPERABILITY

Arnold Engineering Development Center (AEDC) is the most advanced and largest complex of flight simulation test facilities in the world ([Figure 3.244](#)). The center operates 58 aerodynamic and propulsion wind tunnels, rocket and turbine engine test cells, space environmental chambers, arc heaters, ballistic ranges and other specialized units.



**Figure 3.244 An Aerial View of the Arnold Engineering Development Center**

AEDC's Engine Test Facility (ETF) test cells are used for development and evaluation testing of propulsion systems for advanced aircraft and missiles. These propulsion systems include turbojet and turbofan air breathing engines and ramjets. Ground tests of air breathing engines provide information such as performance, operability and reliability and can help cut development time and the number of flight tests required for manned aircraft or unmanned weapon systems such as cruise missiles and unmanned aerial vehicles (UAVs). The tests may involve complete flight-type engines or heavier boilerplate versions in which inlets, compressors, combustors, nozzles or other components can be installed for experimental investigation.

The Aeropropulsion System Test Facility (ASTF, [Figure 3.245](#)) is part of AEDC's Engine Test Facility, (ETF) which has established the center as the USAF center of expertise in turbine engine testing. Located on a 57-acre site, ASTF is an open-circuit facility with two test cells, each 28 feet in diameter and 85-feet long. The facility's unique features permit data to be acquired in ground testing that was previously available only after extensive flight testing. ASTF provides the United States with the unique test capability of simulating flight conditions at



altitudes up to 100,000 feet, at speeds up to Mach 3.8, for engines rated up to 100,000 pounds of thrust. The air supply compressors can provide up to 1,500 pounds of air per second (more than one-million standard cubic feet per minute) into the test cell to simulate airspeeds up to 2,000 miles per hour. The compressors, totaling 215,000 horsepower, are started by one of the largest variable frequency starting systems in the world. An additional 600 pounds per second of airflow is available by drawing outside air directly into the test cell.



**ASTF Aerial**

Photo no 01-55503

### **Figure 3.245 An Aerial View of the Aeropropulsion System Test Facility, ASTF**

Providing properly conditioned air to the propulsion systems to simulate supersonic flight conditions calls into play the largest air heaters in the world. Exhaust gases can reach temperatures of nearly 3,500 degrees Fahrenheit and must be cooled before they go through the exhaust machinery and are vented into the atmosphere. Initial cooling is done by direct contact water spray, which reduces the temperature to 2,500 degrees Fahrenheit. The exhaust then passes through a 4,600-pipe heat exchanger that reduces the temperature to 350 degrees Fahrenheit, and another water spray cools and cleans the exhaust gas to less than 120 degrees Fahrenheit before it enters the exhaust compressors.

This section will provide a series of investigations that have been conducted to look at either compression system operability issues or the effect of facility geometry on turbine engine operability. In one case, the 1D dynamic model was applied to a closed circuit wind tunnel system as a means of investigating potential dynamic behavior from changes to aircraft model orientation.

#### **REFERENCES:**

**3.169** AEDC Fact Sheet, Release 2007-092, AEDC Website, [www.arnold.af.mil](http://www.arnold.af.mil)

**3.170** Aeropropulsion Systems Test Facility (ASTF) Fact Sheet, Release 2007-096, AEDC Website, [www.arnold.af.mil](http://www.arnold.af.mil)

**3.171** Engine Test Facility Fact Sheet, Release 2007-086, AEDC Website, [www.arnold.af.mil](http://www.arnold.af.mil)



### 3.4.1 Facility Duct Length Analysis for Test Article Post-Stall Behavior

A turbofan engine that was scheduled to be tested at the AEDC experienced non-recoverable stall during sea level testing at the manufacturer's test facility. It was determined by the manufacturer that the problem was the result of using a bellmouth inlet duct with a pressure drop screen on the engine. The bellmouth inlet duct included a pressure drop screen for the purposes of reducing the aero-structural loads on the engine systems. The screen also had the effect of closing the volume in front of the engine. Because of the reduced volume between the pressure drop screen and the engine face, the system volume dynamics were such that the compression system operated in the rotating stall regime.

The proposed test installation at the AEDC's Engine Test Facility (ETF) used a bellmouth inlet that was nearly identical to the sea level test bellmouth inlet. However, unlike the sea level test installation, the installation in the ETF did not place the entrance to the bellmouth in the ambient atmosphere. Rather, the bellmouth inlet ducting is located in a larger diameter supply plenum. The pressure loss screen (used for flow straightening in the ETF) was also located farther upstream from the engine inlet. A typical engine test cell installation in the ETF is shown in [Figure 3.246](#). Because of the manufacturer's concerns that the bellmouth inlet duct volume could unfavorably influence the test results in the ETF, a study was initialized to determine if the influence of the proposed test installation was minimal.

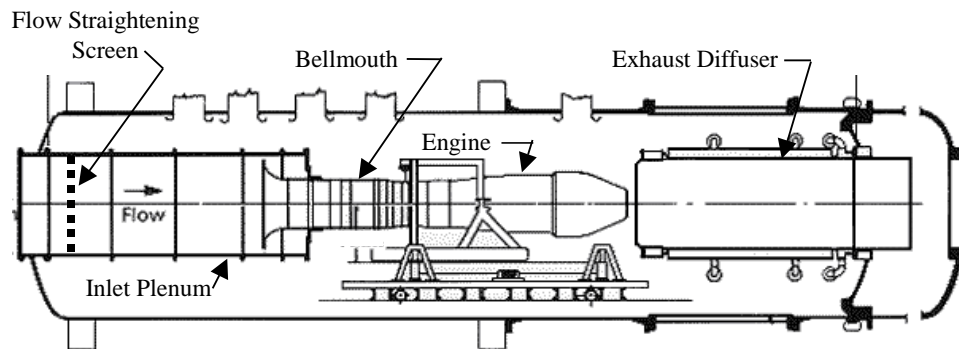


**Figure 3.246 Typical Test Cell Installation in the ETF**

#### CITED EXAMPLE(S)

**3.172** Garrard, D., Davis, M., Chalk, J., Savelle, S., "Analysis of Gas Turbine Engine Operability with the Aerodynamic Turbine Engine Code," ISABE97-7034, AIAA, September 1997.

#### MODELING TECHNIQUE

The **DYNTECC** compression simulation ([Section 4.4](#)) was configured to model a multi-stage fan system that closely matched the performance of the particular system of interest. Test cases were constructed that represented three possible geometric configurations:

Number	Configuration
1	Bellmouth with screen, ambient inlet
2	Bellmouth without screen, ambient inlet
3	Bellmouth without screen, plenum inlet

### DUCT LENGTH ANALYSIS

The results from the **DYNTECC** simulation for the first configuration showed that the fan system would enter rotating stall. The geometry of the **DYNTECC** computational domain and the initial pressure distribution are shown in [Figure 3.247](#). By reducing the mass flow rate exiting the system, the compression system was forced into the post-stall regime. The fan pressure ratio as a function of time is shown in [Figure 3.248](#) and as a function of percent of design corrected inlet flow rate in [Figure 3.249](#).

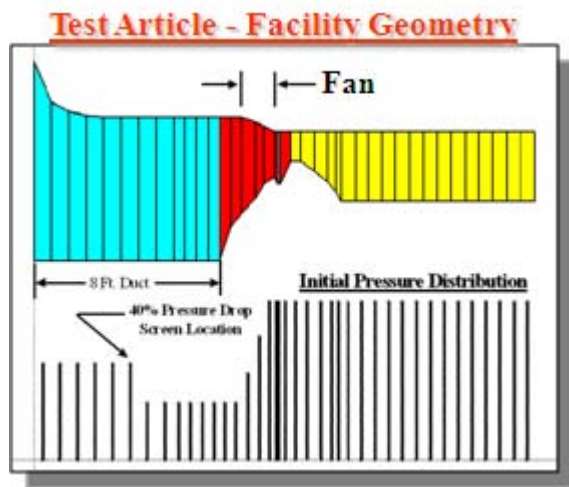


**Figure 3.247 Simulation Geometry and Initial Total Pressure Distribution for Configuration 1**

The second configuration confirmed that the additional volume facilitated by the removal of the pressure loss screen would permit the system to operate in recoverable surge cycles. The geometry of the second configuration and the initial total pressure distribution are shown in [Figure 3.250](#). The fan pressure ratio as a function of time is shown in [Figure 3.251](#) and as a function of percent design corrected inlet

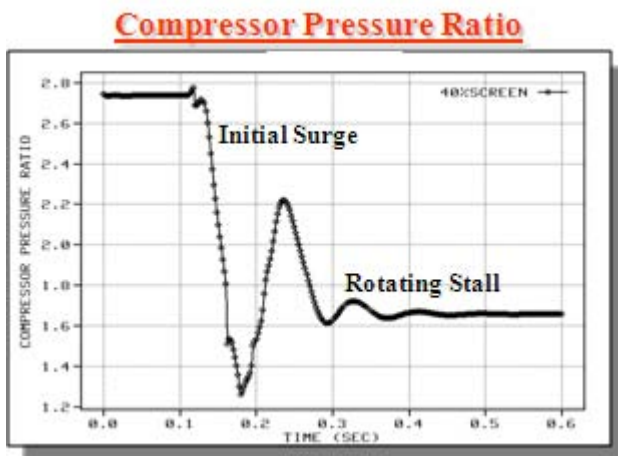


**Figure 3.248 Fan Total Pressure Ratio as a Function of Time for Configuration 1**

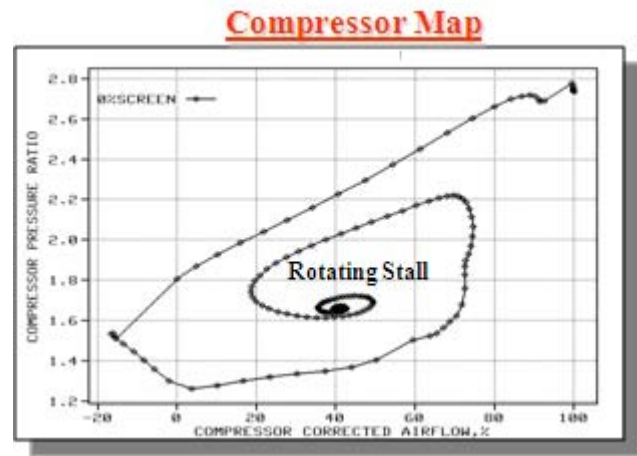


**Figure 3.249 Fan Pressure Ratio as a Function of Percent Design Corrected Airflow Rate for Configuration 1**

### Test Article - Facility Geometry

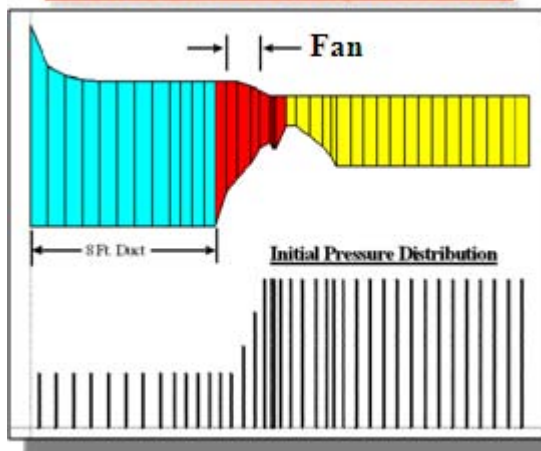


**Figure 3.250 Simulation Geometry and Initial Total Pressure Distribution for Configuration 2**

the actual system installed in an aircraft.

The third configuration, based upon the ETF test installation, likewise demonstrated that the compression system would operate with recoverable surge cycles. Because the flow straightening screen is located far upstream of the engine face, rather than near the engine face as was done in Configuration 1, the volume of the system was sufficient for favorable operation. The geometry of the system is shown in [Figure 3.253](#). The inlet boundary location coincides with the flow straightening screen location. The fan pressure ratio as a function of time is shown in [Figure 3.254](#).

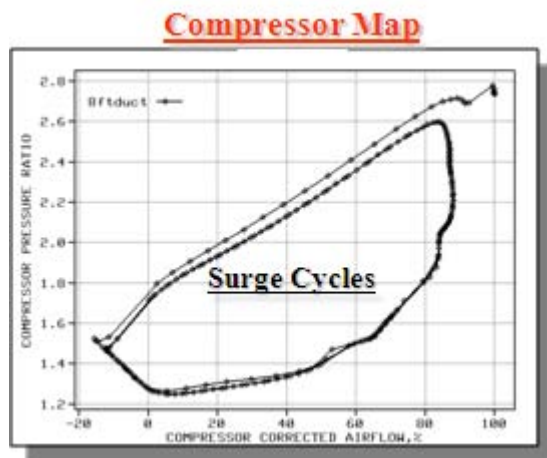


**Figure 3.252 Fan Pressure Ratio as a Function of Percent Design Corrected Airflow Rate for Configuration 2**

bellmouth inlet. This in turn ensured an acceptable simulation of the engine-operating environment.

### Compressor Pressure Ratio

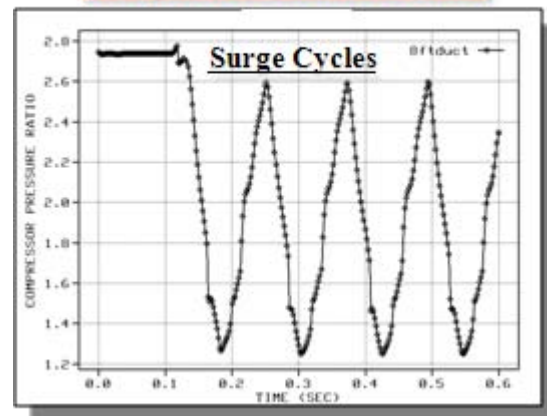


**Figure 3.251 Fan Pressure Ratio as a Function of Time for Configuration 2**

flow rate in [Figure 3.252](#). By removing the pressure drop screen, the volume dynamics of the system respond in a manner similar to

The fan pressure ratio as a function of percent design corrected air flow rate is shown in [Figure 3.255](#). Based on the results of this study, it was concluded that the standard inlet bellmouth used in the ETF would be sufficient for the planned testing. Both the manufacturer's test installation (without the pressure drop screen) and the planned ETF test installation used similar hardware. The volume that was provided by the ETF's inlet plenum was sufficient to represent an "infinite volume" boundary to the

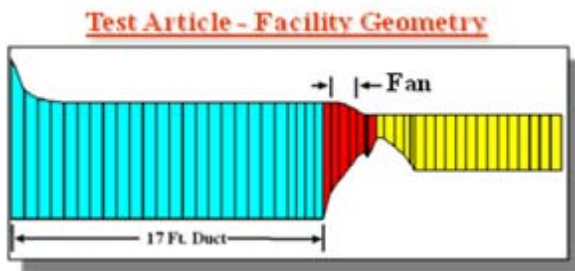


**Figure 3.253 Simulation Geometry and Initial Total Pressure Distribution for Configuration 3**

Based on the results of this study, it was concluded that the standard inlet bellmouth used in the ETF would be sufficient for the planned testing. Both the manufacturer's test installation (without the pressure drop screen) and the planned ETF test installation used similar hardware. The volume that was provided by the ETF's inlet plenum was sufficient to represent an "infinite volume" boundary to the bellmouth inlet. This in turn ensured an acceptable simulation of the engine-operating environment

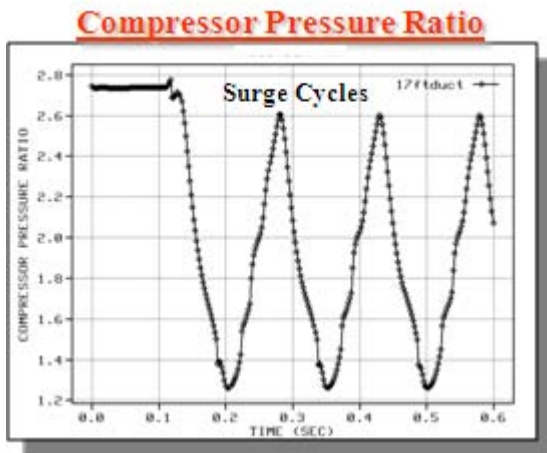


**Figure 3.254 Fan Pressure Ratio as a Function of Percent Design Corrected Airflow Rate for Configuration 3**



**Figure 3.255 Fan Pressure Ratio as a Function of Percent Design Corrected Airflow Rate for Configuration 3**

#### Additional References:

None

### 3.4.2 Facility Overpressure Analysis for Test Article Post-Stall Behavior

When a turbofan engine is tested at the AEDC and experiences surge cycles, the specific facility may experience over-pressure in the inlet ducting system. To understand the potential magnitude of that over-pressure, numerical simulations compression systems capable of producing a surge cycle and aerodynamically joined to an appropriate simulation of the facility have been used to analyze the facility pressure environment. A typical direct connect test cell is illustrated in [Figure 3.256](#). Called out on [Figure 3.256](#) is an expansion joint between the engine inlet ducting and the airflow measuring bellmouth. Of particular concern is the over-pressure forces on this expansion joint and was the objective of the investigation presented in this section.

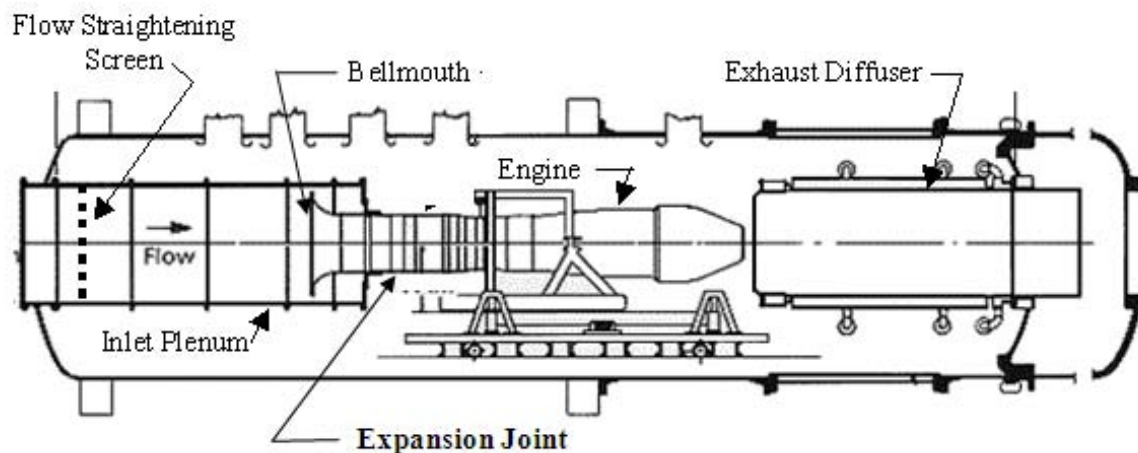


**Figure 3.256 Typical Test Cell Installation in the ETF**

#### CITED EXAMPLE(S)

None

#### MODELING TECHNIQUE

The **DYNTCC** compression simulation was configured to model a High Pressure Compressor system that closely matched the performance of the particular system of interest. Surge cycles were simulated using the post-stall capability of the **DYNTCC** code as described in [Section 4.4](#).

#### DUCT LENGTH ANALYSIS

A schematic of the test cell inlet ducting hooked to the HPC system is illustrated in

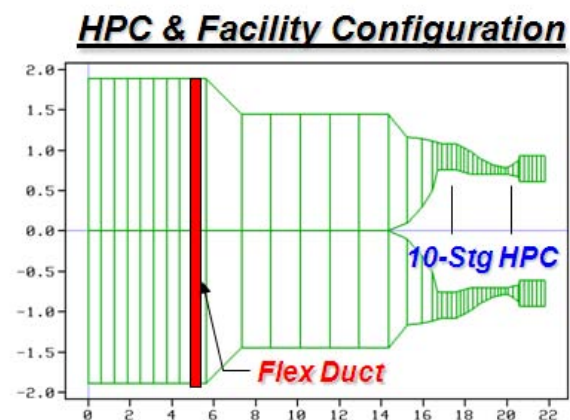


**Figure 3.257 Simulation Geometry with Flex Duct**



**Figure 3.257.** The expansion joint is shown as a control volume approximately 10 feet upstream of the HPC inlet. A specific test condition representing a High-Q (high speed near sea level) condition so as to analyze the potential worst case. Since only the HPC was being used, a fan pressure ratio of approximately 3 was assumed to provide HPC inlet conditions. The HPC was run near military power to provide an HPC pressure ratio near its highest value. By reducing the mass flow rate exiting the system, the compression system was forced into the post-stall regime. The results from the **DYNTTECC** simulation for surge cycles are shown in **Figure 3.258**. As noted the surge cycle experience reverse flow through the compression system setting up a reverse flow condition in the facility ducting. The reversed flow in the ducting experience not only total pressure and temperature excursions but static pressure excursions as well. These static pressure excursions can be used to calculate internal duct

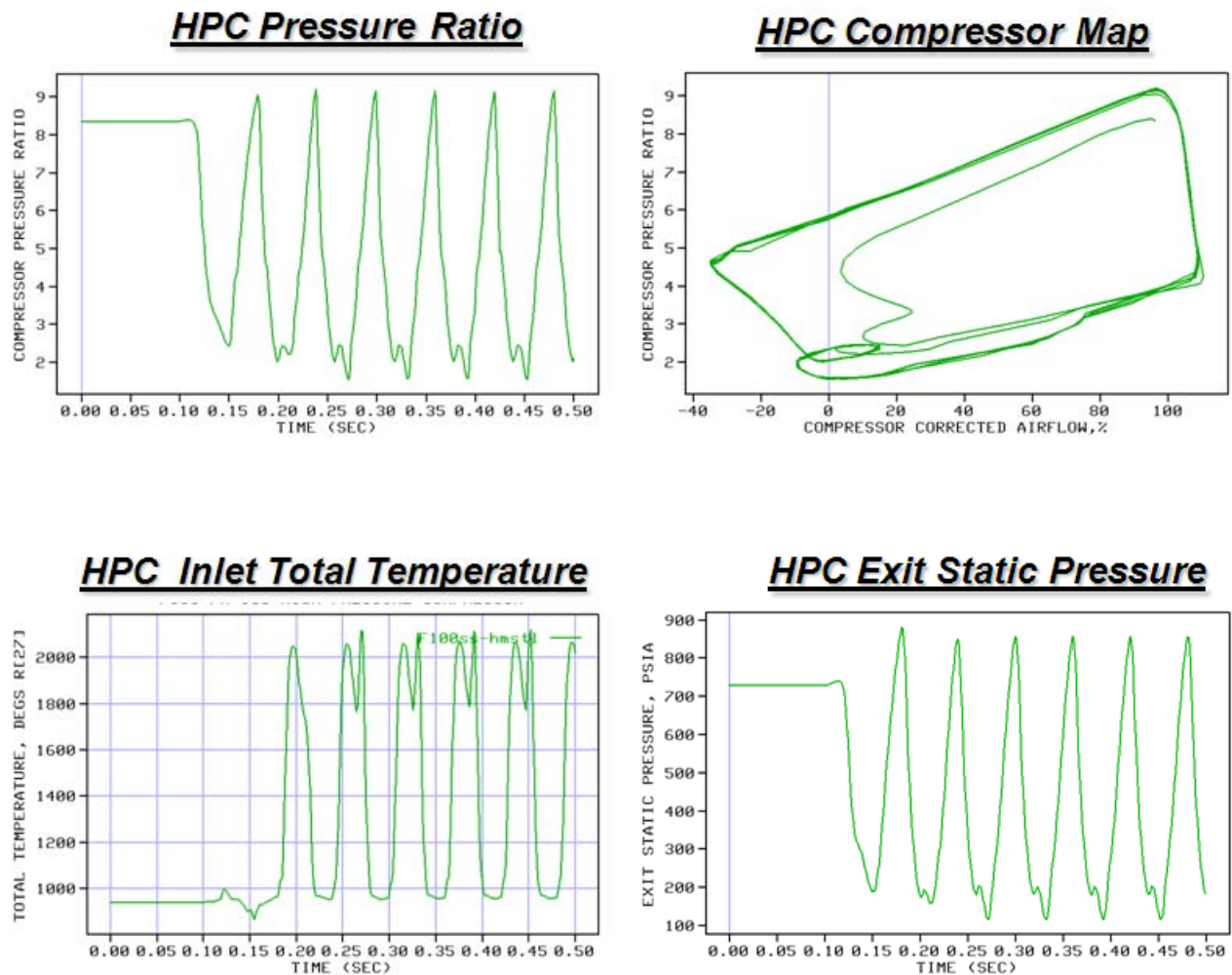


**Figure 3.258** DYNTTECC Predicted Results for Surge Cycle Behavior of a Typical Military HPC System

forces as applied to the flex duct control volume.

Analysis of the overpressure forces at the flex duct are presented in **Figure 3.259**. Whether these forces are high enough to cause concern was not evaluated at the time of this numerical



analysis. However, this analyses indicates the value of the **DYNTECC** simulation for this type of planar wave disturbance.

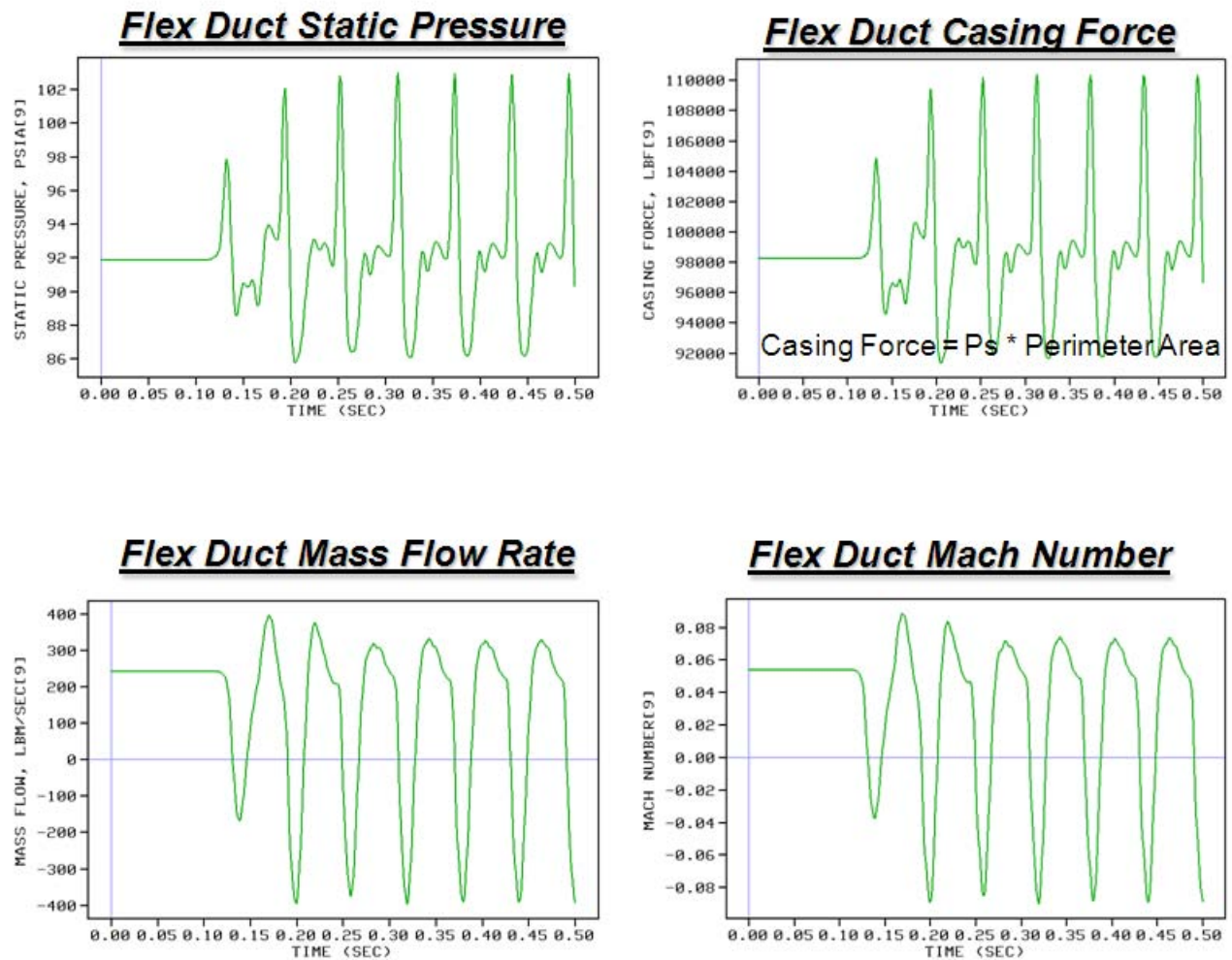


**Figure 3.259 Flex Duct Overpressure Force Analysis for Surge Cycle Behavior of a Typical Military HPC System**

**Additional References:**

None

### 3.4.3 E311 Distortion Analysis

Over the last two and one half decades since the operation of the Aeropropulsion System Test Facility, ASTF, began, there have been documented problems with the E311 exhaust compressor ([Figure 3.260](#)), and or the associated ducting with that compressor.



**Figure 3.260 ASTF Exhaust System**

E311 is the C-Plant third-stage exhauster drive train. Due to the duct configuration, it is the only one of the four high-stage (44,000 HP drive motor, able to exhaust to atmosphere) exhaust drive trains which can serve as the third stage. It is also important because it represents one-fourth of the exhaust plant maximum airflow capability (approximately 2200 lbm/sec total).

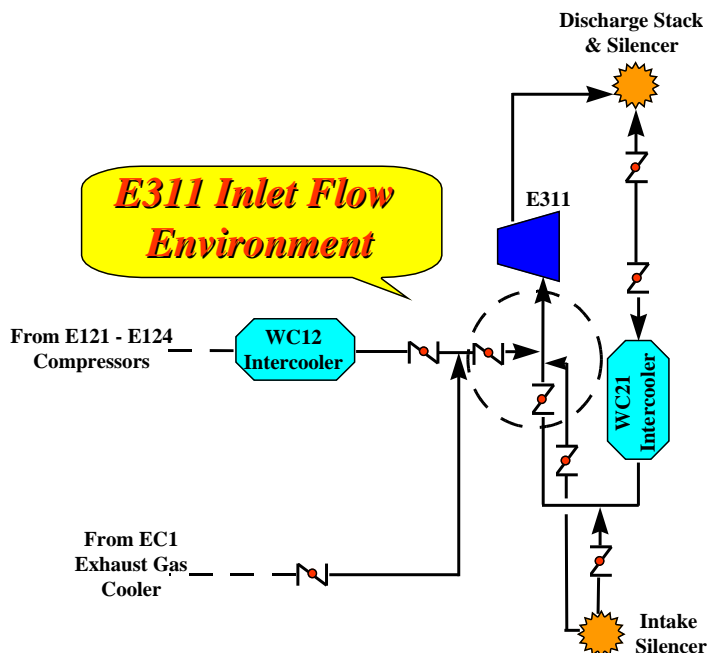


**Figure 3.261 Schematic of the E311 Inlet Flow Environment**

The E311 inlet duct is unique among the twelve exhauster drive trains due to its function as the third-stage exhauster. Because E311 can receive airflow from its individual surge stack, the exhaust header duct, and/or the discharge of the second-stage drive trains (through an interstage cooler), its inlet duct is intersected by an arrangement of branch ducts (See [Figure 3.261](#)). The intersection of greatest concern is the 180 degree opposed, but collinear, junction of the surge stack duct and the header connection duct with the E311 inlet duct. Simply stated, this intersection is a cross with three inlet ducts and one outlet duct.

The primary problem at this intersection is that the surge (hydraulic control) valve, located eleven feet above the intersection point, operates under a fully-choked flow condition. This extremely turbulent, high velocity, flow being drawn toward the exhauster inlet appears to

spill into the opposing lower duct (header connection duct) before flowing into the exhauster. This tortuous flow path increases the turbulence and nonuniformity of the flow field. The observable effects of this turbulence are that the E311 inlet duct vibrates excessively and the exhauster performance is degraded. However, the overall bearing vibration levels of E311 are consistent with those of the other exhausters. There is no evidence that the excessive duct vibration is affecting the machine vibration levels. It is both interesting and important to note that under conditions of exhaust header flow only; i.e. the surge valve is fully shut, the inlet duct vibration level and exhauster performance are both acceptable.

### **CITED EXAMPLE**

**3.173** Davis, M., "C-Plant Exhauster Study," Internal Sverdrup Technology, Inc. Memorandum, August 30, 1996.

### **MODELING TECHNIQUE**

Thus, based upon the comments about the flow quality issues in, **DYNTECC** in the parallel compressor mode ([Section 4.6](#)) was used to postulate the effects of temperature and pressure distortion on the E311 compressor stability limit.

The user must provide a set of stage characteristics as inputs into the **DYNTECC** code. These characteristics are usually in the form of pressure and temperature rise as a function of steady state mass flow. For the E311 nine-stage compressor, only the overall compressor performance had ever been measured. Thus, for this task to be completed, a set of stage characteristics was synthesized. The **SLCC** ([Section 4.3](#)) was used for the development of the stage characteristics.

The streamline curvature code uses blade geometry, annulus geometry, and a set of cascade aerodynamic correlations (pressure loss and exit flow deviation from the metal angle) to develop the aerodynamic states at discrete locations within the compressor flow field, usually at the entrance and exit of a blade row. The blade and annulus geometry were provided by the compressor manufacturer, Westinghouse, as inputs into the streamline curvature code. Although the streamline curvature code can provide blade aerodynamic behavior as a function of radius, **DYNTECC** only requires a lumped characteristic. Thus, the radial aerodynamic behavior was mass averaged across the radius at each calculating station. The blade row characteristics were combined into a set of stage characteristics for two speedlines, (100 and 97.5%) and implemented into **DYNTECC**.

During the activation of the ASTF C-Plant exhaust gas compressor system, two types of operational limitations were observed. The first type involves compressor surge phenomena including the surge pressure ratio limit, surge recovery, and surge characteristics. The second type involves thermal rotor bow.

### **E311 DISTORTION ANALYSIS**

It was specified that the exhaust compressor be able to operate stable at a corrected pressure ratio of 4.0. The actual corrected surge pressure ratio is approximately 3.6 (corresponds generally to an uncorrected surge pressure ratio of 3.90 +/- 0.05). Due to inherent instrumentation inaccuracies, the compressors are normally operated at an uncorrected surge pressure ratio of 3.6 or less. This surge pressure ratio deficiency reduces the minimum test cell pressure (maximum altitude) which can be obtained by the exhaust plant. Single-stage



operation provides a minimum test cell pressure of approximately 4.3 psia (30,000 ft.), two-stage figures are 1.3 psia (55,000 ft.), while three-stage operation has not yet been test.(as of 10/85)

### Parametric Investigation Results

In the process of investigating the performance of the E311 compressor, it was discovered that a comparison of all other ASTF exhaust compressors was made in the initial activation phase. These results are shown in [Figure 3.262](#).

A summary of that figure is presented in [Figure 3.263](#). It can be noted from the original [Figure 3.262](#), that in comparison to the initial Westinghouse design curve, all other compressors are under-designed (i.e. each is at a volumetric flow rate less than that predicted by the design code). In fact, the E311 compressor is the one with the most under-designed capability. An average performance curve was estimated that runs through the middle of the region bounded by the design curve and the E311 curve with an uncertainty of 4.4% bounding the whole region. The original presentation of [Figure 3.262](#) was set up to provide a measure of the uncertainty of the performance of the nine compressors. No attempt was made to quantify the reasons why there were differences between the design and between each compressor. One such explanation for the differences would be if there were differing levels of inlet pressure or temperature distortion at the entrance of each compressor.

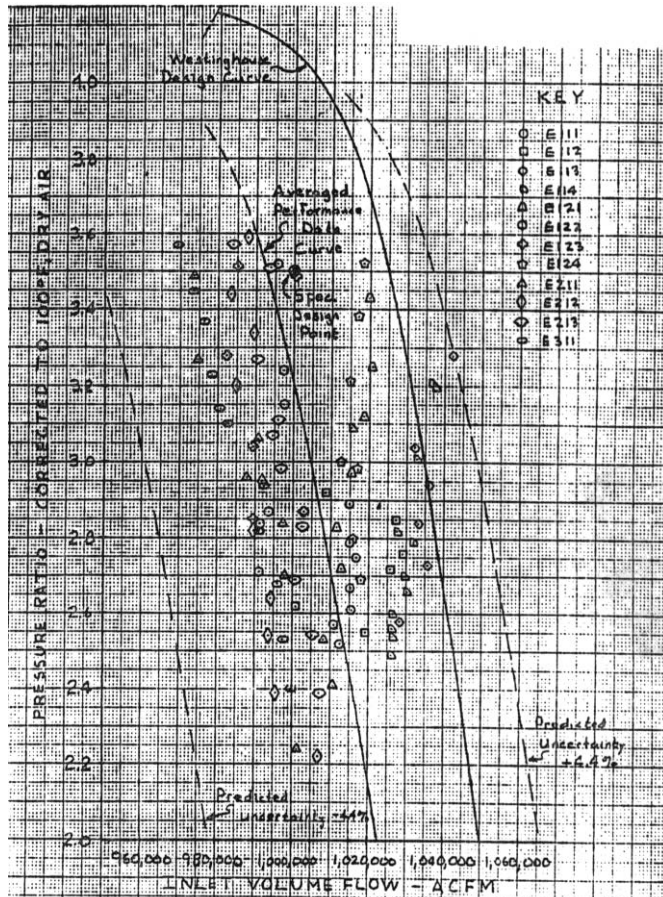


**Figure 3.262 Exhauster Compressor Volume Flow**

One way to quantify the effect of inlet distortion on the E311 compressor is to use a system model such as **DYNTTECC** and conduct a parametric investigation. However, prior to conducting the parametric investigation, one needs to know how good are the **DYNTTECC** calculated results for the non-distorted case. Using **DYNTTECC**, full compressor operation was achieved from some point near choke to system instability for two speeds. Westinghouse, probably using a streamline curvature code, has developed a full compression system performance map from which a comparison could be made. A comparison of the **DYNTTECC** results for non-distorted flow is presented in [Figure 3.264](#). The **DYNTTECC** model results are within 2% in volume flow rate at the 100% speed. The Westinghouse 95% speedline is shown for a relative comparison

for the **DYNTECC** 97.5% speedline. There is some differences in that the 97.5% doesn't fall midway between but more on the 95% side. However, for the parametric distortion evaluation, the two **DYNTECC** speedlines will provide enough of a map to give good trends.

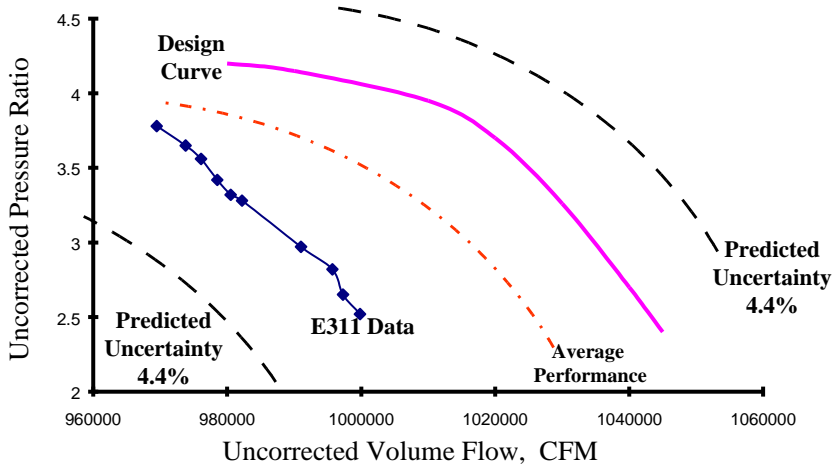


**Figure 3.263 Potential Effect of Inlet Pressure Distortion on the E311 Exhaust Compressor**

At 100% speed, a parametric investigation was conducted using the **DYNTECC** simulation of the E311 exhaust compressor to determine the sensitivity of the E311 compressor to various amounts of inlet total pressure. Not knowing what type of distortion may be present, a simple 180 degree circumferential, once per rev, distortion pattern was arbitrarily chosen. Levels of 5, 10, 15, and 20 percent total pressure distortion (e.g., the distorted segment being 5% lower in total

pressure than the non-distorted segment) were imposed upon the nominal operating point and allowed to come to a new steady state condition. Once steady state had been achieved, the exit static pressure was ramped in a quasi-steady manner until system instability was indicated. For these calculations, system instability was determined when one (1) stage in one of the segments (in this case it occurred in the distorted segment first) had reached its peak pressure performance. A comparison of each case with various levels of distortion is presented in **Figure 3.265**. Once the distortion was implemented, the compression system volumetric flow rate decreased to a new lower level due to the decrease in density. A new speedline was generated when the exit static pressure was increased. The reduction in the volumetric flow rate is the same effect as is noted in the experimental data (**Figure 3.262**) and lends support to the concept that some level of inlet total pressure distortion may be present. The pressure ratio has been degraded by as much as 15% from a level of 4.3 to 3.8 for a maximum investigated distortion level of 20%.

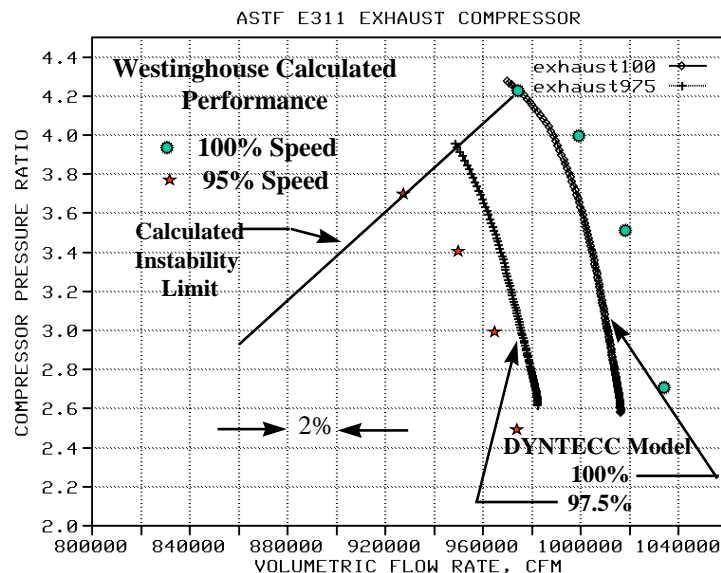


**Figure 3.264 DYNTECC Calculated Results vs. Westinghouse Calculated Performance**

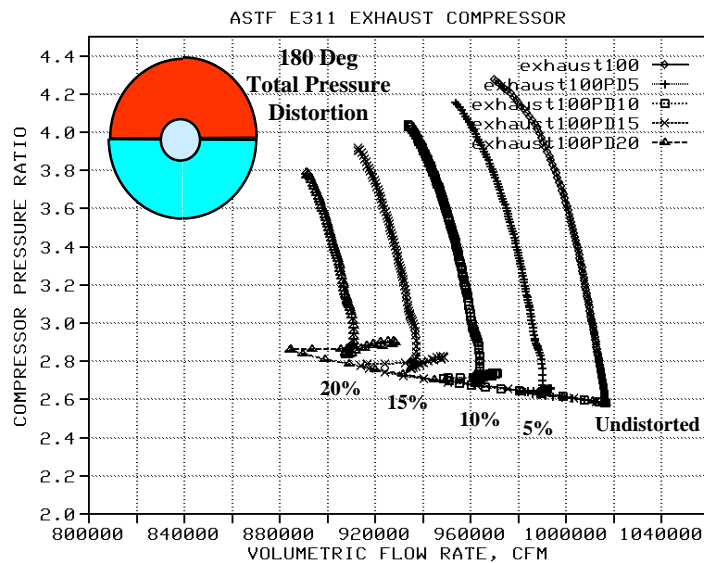


**Figure 3.265 Potential Effect of Inlet Pressure Distortion on the E311 Exhaust Compressor**

pressure ratio and certainly drives the volumetric flow rate lower due to the decrease in density. When a 5% total pressure distortion is combined with the 5% temperature distortion in the same segment (i.e. concurrently) a 15% decrease in pressure ratio is realized and the volumetric flow rate is reduced further. In this case, if there is even a little (5%) temperature distortion, it may have the same effect as 20% of pressure distortion.

#### **CONCLUSIONS AND RECOMMENDATIONS**

Based upon the parametric study, it appears likely that the E311 compressor performance degradation may be caused by some level of inlet pressure distortion with the possibility of some level of temperature distortion as well. Once compression system instability is encountered, the compressor moves into a rotating stall condition. Assuming that distortion is the culprit, several recommendations are set forth:

Because of the inference made about the turbulent flow path, pressure distortion is the main suspect for the performance degradation. However, since the flows are coming from different sources, (i.e. other compressors, coolers, surge lines, etc.) these flows may be coming with differing temperature levels that may produce some level of temperature distortion as well. To determine the potential sensitivity of the E311 compressor to temperature distortion, the DYNTECC simulation was subjected to a 5% temperature distortion (5% increase in inlet total temperature in one of the 180 degree segments) by itself and is compared to the undistorted case in Figure 3.266. A 5% increase of the inlet temperature in a single 180 degree segment may produce as much as a 10% drop in

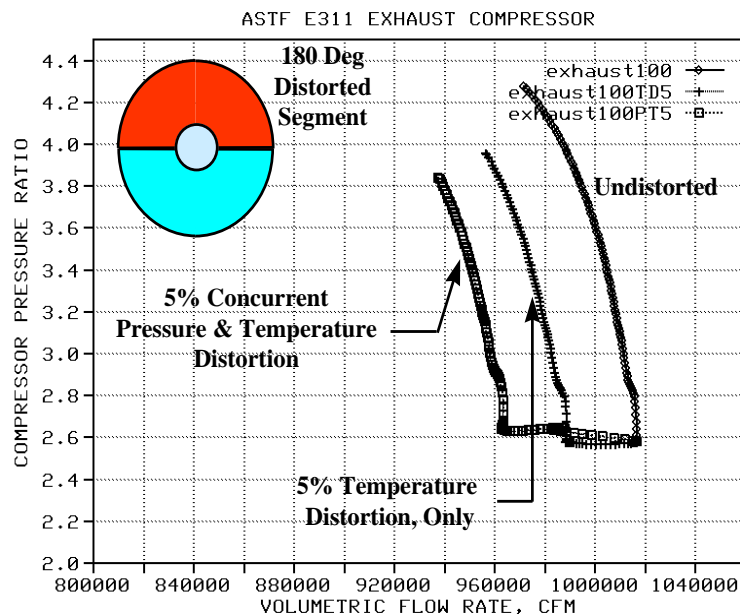


**Figure 3.266 Potential Effect of Temperature Distortion and Combined Effects of Temperature and Pressure Distortion on the E311 Compressor**



1. It is recommended that a set of pressure and temperature measurements, much like is done for inlet distortion testing in turbine engines, be made at the inlet of the E311 compressor to confirm whether distortion is present and how much.
2. If distortion is present, a study needs to be made to determine how to effectively reduce or eliminate the distortion.
3. If it becomes too expensive to implement pressure and temperature measurements into the inlet duct and fix the distortion, another solution as how to "live with it" must be devised. One solution might be to over-speed the compressor by gearing the motor. This would have the effect of increasing the volumetric flow rate as well as increasing the pressure ratio for any given throttling condition.

**ADDITIONAL REFERENCES:**

None

### 3.4.4 16T Wind Tunnel Dynamic Simulation

The PWT facility is composed of the 16-foot transonic (16T), 16-foot supersonic (16S) and the aerodynamic 4-foot transonic (4T) wind tunnels, **Figure 3.267**. The 16-foot supersonic wind tunnel is currently in inactive status. Devoted to aerodynamic and propulsion integration testing of large-scale aircraft models, PWT is used to provide AEDC's customers with complete testing and analysis capability. In some cases, the propulsion systems and inlets are tested simultaneously to make sure they are aerodynamically designed to provide adequate airflow to the engines. Other tests involve store separation investigations— making sure bombs, missiles or other externally carried stores separate cleanly from the parent aircraft when released.

The facility has two 16-foot-square, 40- foot long test sections, closed-circuit wind tunnels, one transonic (16T) and one supersonic (16S),. The 16T facility is capable of being operated at Mach numbers from 0.06 to 1.60. The inactive 16S facility is capable of operation from Mach numbers from 1.60 to 4.0. Both tunnels can be used for conventional aerodynamic tests and for combined aerodynamic/propulsion systems tests.

Pressure of the airflow through the test sections can be varied to simulate altitude conditions from sea level to about 150,000 feet. The large tunnel size also allows for full-scale missile installations to test engine performance and airframe aerodynamics.



**Figure 3.267 16T Wind Tunnel Circuit**

Some of the features of the 16-foot tunnels include a moveable support system called a strut. The strut is attached to the floor of the wind tunnel's test section. The tunnels are also equipped with a special movable support system, called a sting, for mounting additional models. To simulate change in flight attitudes or maneuvers, the support is yawed (moved side to side), rolled or pitched up or

down. The 16-foot tunnels can be used to examine the relationship between engine air inlets and the corresponding performance of and compatibility with the engine itself. This is done to determine the most efficient air-induction system design or to study how varying the geometrical shape of an inlet or propulsion nozzle can affect the aerodynamics of the flight vehicle. Both tunnels also have a scavenging system that removes combustion products when testing rocket motors or gas turbine (jet) engines.

#### **CITED EXAMPLE(S)**

**3.174** Bates, L. B, "Development of a Dynamic Model and Simulation of 16T (Job 2347)," Internal Sverdrup Technology, Inc. Memorandum, September 9, 1995.

## MODELING TECHNIQUE

A "proof-of-concept" dynamic model and simulation of the 16T Wind Tunnel facility has been developed using as a basis the **DYNTECC** dynamic compression system computer code. The resulting code is called **AFAST** (Aerodynamic Facility Analysis Simulation Technique). Sample runs have been made using the **AFAST** code and the results, along with recommendations for further development of the simulation, are presented in this section.

The **DYNTECC** ([Section 4.4](#)) is a one-dimensional, time-dependent, stage-by-stage axial compression system mathematical model and simulation which is able to analyze a generic compression system [3.176]. **DYNTECC** uses a finite difference numerical technique to simultaneously solve the mass, momentum, and energy equations (i.e., Euler equations) with turbomachinery source terms (mass bleed, blade forces, and shaft work).

When the need for a dynamic model of the 16T wind tunnel system was identified, it was recognized that the tunnel circuit is basically a compression system which could be modeled using **DYNTECC**. The **DYNTECC** code, however, had not been utilized to simulate a closed-circuit system, and some modifications to the code were made to enable this mode of operation. Additionally, modifications were made to the code input files to enable the user to input the 16T wind tunnel physical geometry parameters and operating characteristics.

The 16T wind tunnel system was modeled by dividing the circuit into a set of 24 control volumes as shown in [Figure 3.268](#). Geometric parameters describing each of the control volumes, including length, inlet equivalent diameter, and inlet hydraulic diameter, were obtained and input into the **AFAST** geometry file. The resulting volume and surface area calculations are made within the code. Total pressure loss coefficients for each of the control volumes are characterized as described by [Ref. 3.177](#). Losses modeled include those for the following elements: friction losses in straight ducts, corners, screens and honeycombs, heat exchangers, contractions, and diffusers. Heat transfer is currently modeled by input of a heat transfer rate for each volume. The 16T compressor is modeled using pressure ratio and efficiency as a function of inlet guide vane angle, which can be varied. The compressor characteristics currently used are for a rotational speed of 600 rpm only.

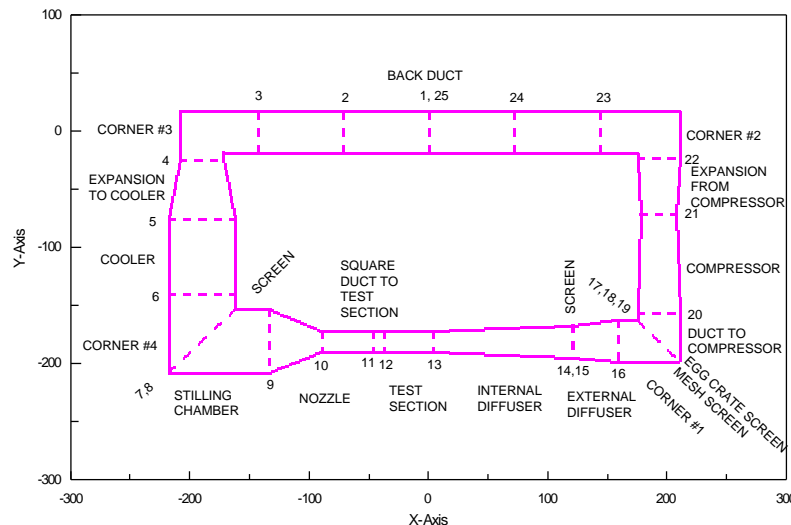


**Figure 3.268 16T Wind Tunnel Circuit**

### SIMULATION RESULTS FROM SAMPLE RUN

A sample run of the 16T model was made simulating steady-state operation at Mach = 0.8 and  $P_t = 2000$  psfa in the tunnel test section. The results of this run are presented in [Figure 3.269](#) – [Figure 3.272](#). [Figure 3.269](#) presents a plot of system total pressures as a function of time. It can be seen that, for this sample run, the system reaches a near-steady-state condition in approximately 9 seconds. [Figure 3.270](#), [Figure 3.271](#), and [Figure 3.272](#) show a comparison of the AFAST simulation results for total pressure, total temperature, and Mach number, respectively, with those for the 16T steady-state model at this test condition. Good agreement between the two calculations is indicated.

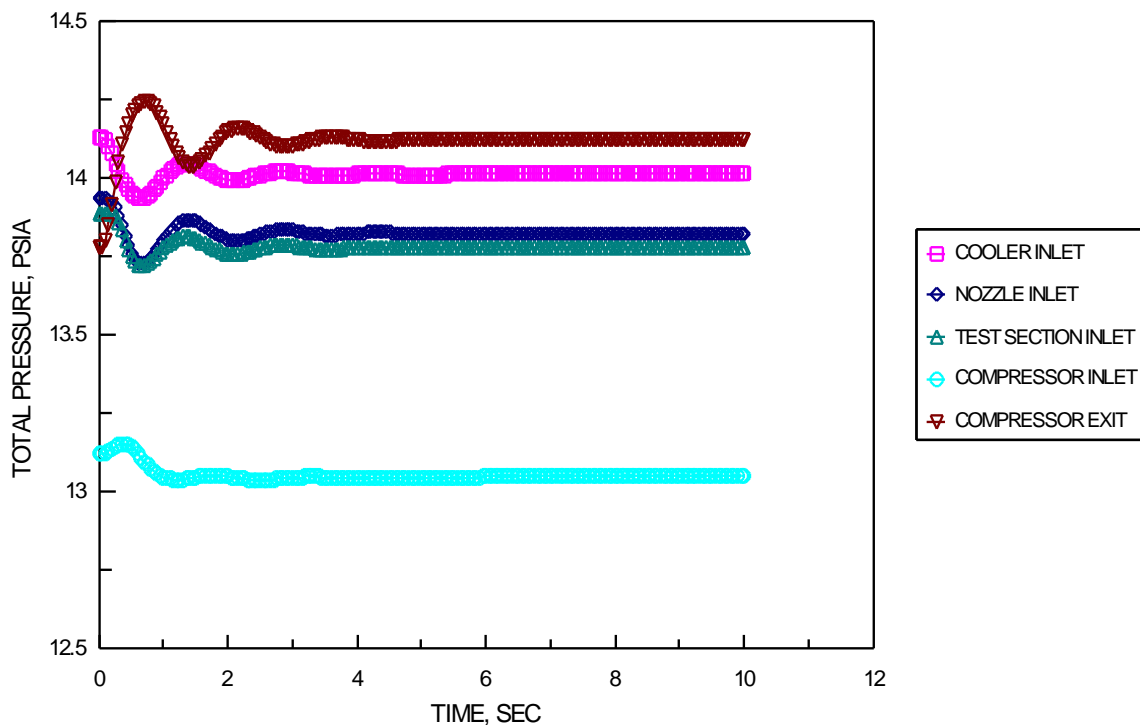


**Figure 3.269 AFAST 16T Wind Tunnel Total Pressure**

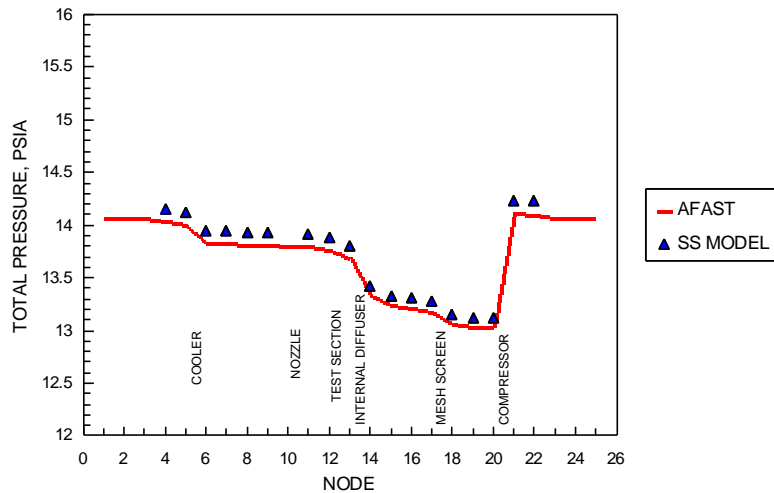


**Figure 3.270 Comparison of AFAST and SS Model Results for Total Pressure**

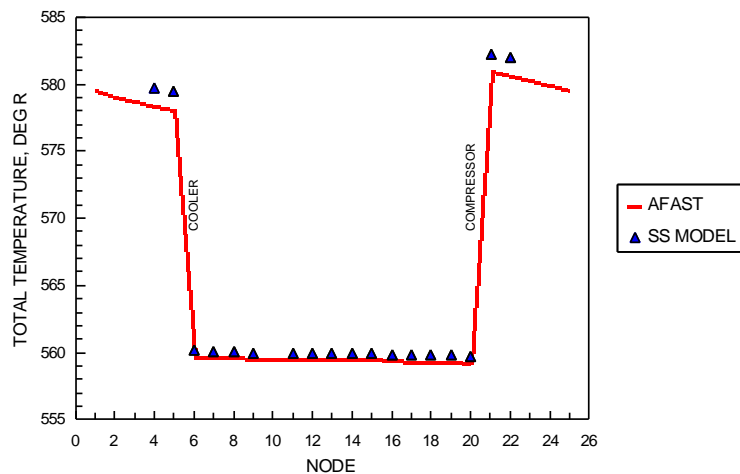


**Figure 3.271 Comparison of AFAST and SS Model Results for Total Temperature**

inputs. Additionally, the capability to model the humidity level in the tunnel components should be included.

4. The AFAST 16T simulation should be incorporated with a control system simulation for control algorithm development.

## **Conclusions**

1. A "proof-of-concept" dynamic model and simulation of the 16T Wind Tunnel facility has been developed using as a basis the **DYNTECC** dynamic compression system computer code. The resulting code is called **AFAST**.

2. Sample runs of the **AFAST** 16T simulation have been made and the results compare favorably with steady-state model results.

1. Additional checkout cases need to be made to exercise the model and simulation at various test conditions including some dynamic and transient events.

2. Optimization of control volume sizes should be made to reduce run times. In addition, the inclusion of an implicit, variable time step solver should be evaluated.

3. Equations for calculation of the heat transfer characteristics of the circuit should be incorporated into the model, rather than the current manual

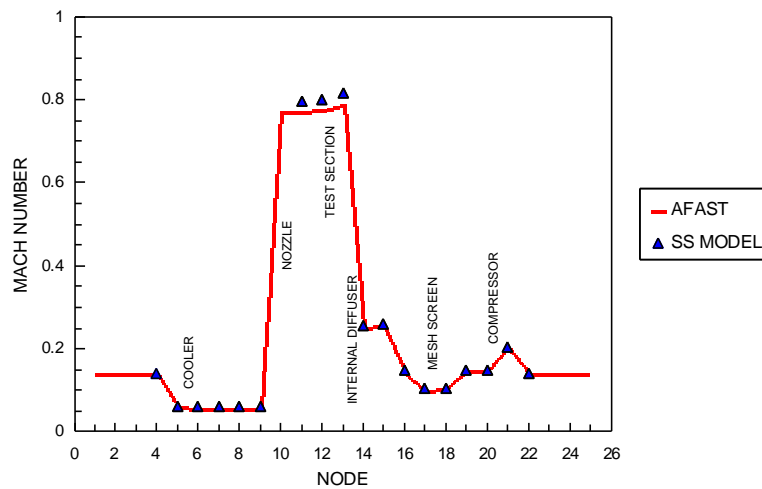


**Figure 3.272 Comparison of AFAST and SS Model Results for Mach Number**

#### **ADDITIONAL REFERENCES:**

**3.175** Propulsion Wind Tunnel Facility Fact Sheet, Release 2007-088, AEDC Website, [www.arnold.af.mil](http://www.arnold.af.mil)

**3.176** Hale, A.A. and Davis, M. W., "DYNamic Turbine Engine Compressor Code DYNTECC – Theory and Capabilities", AIAA/SAE/ASME/ASEE 28th Joint Propulsion Conference, Nashville, TN, July 6-8, 1992, AIAA-92-3190.

**3.177** Cunningham, D. H., Memo for Record, "Wind Tunnel Static Model Equations", February 6, 1984, Revised, May 3, 1984.



### 3.5 STEAM AND WATER INGESTION ISSUES

The United States Navy currently launches aircraft from carrier decks with a steam-driven catapult. As the seals on a steam catapult wear, high-pressure steam leaks from the catapult and becomes ingested by a launching aircraft (**Figure 3.273**). By the time the steam reaches the aircraft inlet, it is typically expected to have quality less than 100 percent. Quality is defined



**Figure 3.273 Carrier Launched Aircraft with Steam Ingestion [3.178]**

as the ratio of the mass of vapor present to the total mass of the two-phase liquid-vapor mixture (100-percent quality has 100-percent vapor and 0-percent liquid, while 0-percent quality has 0-percent vapor and 100-percent liquid). Because of the high power demands, and the criticality of the compressor performance during launch, it is important to understand how steam ingestion affects the performance and stability of the gas turbine engine compression system.

Although the industry standard for water ingestion, the AGARD report "Recommended Practices for the Assessment of the Effects of Atmospheric Water Ingestion on the

Performance and Operability of Gas Turbine Engines," [3.179] did not directly address steam ingestion, it did provide insight into the effects of water (in liquid, solid, and gaseous forms) on gas turbine engine compression systems. The trends dealing with vaporization in the compression system in this AGARD report will be used to evaluate the results of the work presented in this paper since no experimental data were identified at the time of writing. Steam ingestion, as considered in the current analysis, typically has quality less than 100 percent. The quality is in the form of liquid water droplets condensed in the flow. These particles vaporize as they move through the system because of the increasing temperature caused by compression of the working fluid.

Three separate efforts for modeling operability effect of water/steam ingestion have been undertaken at AEDC. These efforts were an initial capability demonstration on a generic multistage High Pressure Compressor System (HPC), analysis and comparison to data on a Pratt and Whitney FT8 ground based turbine, and prediction of results on a three-stage military fan. These results are presented in this section.

#### REFERENCES:

**3.178** [http://www.news.navy.mil/view\\_single.asp?id=2114](http://www.news.navy.mil/view_single.asp?id=2114) U.S. Navy photo by Photographer's Mate Jessica Davis, July 27, 2002.

**3.179** "Recommended Practices for the Assessment of the Effects of Atmospheric Water Ingestion on the Performance and Operability of Gas Turbine Engines," Propulsion and Energetics Panel Working Group 24, Advisory Group for Aerospace Research and Development (AGARD), NATO, 1995.

### 3.5.1 Steam Ingestion for a Generic HPC

Steam ingested into a gas turbine engine compression system has three major effects. First, the addition of water causes changes in the gas properties. For example, at standard temperature and pressure the specific ratio,  $\gamma$ , for water is 1.31 and for air is 1.4. Second, if some portion of the steam has condensed into liquid water before being ingested into the compressor inlet (steam with quality less than 100 percent), the increase in temperature occurring through the compressor is expected to cause the water to go through a phase change from liquid to vapor. This process, which involves heat transfer and a change in the density of the gas, will force incidence changes on the blades, causing a stage rematch effect on the overall compression system.

Finally, the hot steam ingestion causes a temperature distortion that can change the stage balance. Each of these changes may lead to some change in performance and the possibility of a reduction in the stability margin of the compression system. Although each of these effects is important, the scope of this work is limited to the first two effects: gas property changes and vaporization effects.

#### EXAMPLE(S) CITED

**3.180** Klepper, Jason, Hale, Alan, and Davis, Milt, "A Numerical Investigation of Steam Ingestion on Compression System Performance," ASME Paper #GT2004-54190, 2004 ASME Turbo Expo, June 2004.

#### MODELING TECHNIQUE

Development of a steam ingestion modeling technique required a one-dimensional (1-D) **multiphase code** [3.181] and a 1-D compressor **meanline code** [3.182]. An in-depth discussion of these codes can be found in [Section 4.10](#).

A modeling and simulation technique has been developed to use a one-dimensional (1-D) multiphase code and a 1-D compressor **meanline code (MLC)** to investigate the effects of water ingestion. The **multiphase code (MPC)** primarily accounts for the heat transfer associated with the phase change of water, and the **meanline code** uses the heat transfer and gas properties to model the flow properties through a compression system.

#### GENERIC MULTISTAGE HPC

Because steam ingestion testing is uncommon, a data set for comparing analytical results was not available at the time of writing. Therefore, the analytical results will be evaluated against the observed compressor behavior as outlined in the AGARD report [3.183] since it is regarded as the industry standard for water ingestion.

To provide a suitable parametric study, a generic representation of an eight-stage, high-pressure core compressor (HPC) was selected. The eight rotors were constructed using double-circular-arc profiles, and the eight stators used NACA 65 series profiles. For simplicity, no bleeds were included. The compressor is typical of a 1970s-vintage technology high-pressure core compressor. The actual HPC inlet total conditions were determined on the assumption that a fan of similar technology with a pressure ratio of 3.00 and a temperature ratio of 1.30 preceded the HPC. The fan inlet conditions were assumed to be sea-level-static

conditions. The HPC design pressure ratio was around 11.0, and the design temperature ratio was around 2.30.

The analytical results of the compression system alone used the generic HPC at constant inlet physical gas mass flow and at a constant physical speed. The decision to hold the inlet gas mass flow constant for this preliminary analysis was made because time constraints prohibited the inclusion of the exit boundary condition necessary to run the simulation at a constant exit gas mass flow that would represent compressor rig behavior.

Two separate sets of parametric results are presented. One parametric study was done using varying quantities of steam, while the second parametric study was done using varying qualities of steam. Both studies are compared to a “dry” case. The “dry” case has no water present in either vapor or liquid phases. As mentioned in the introduction, this study does not include the effects of temperature distortion. Since the temperature of the steam is not known, the overall gas temperature is assumed not to be elevated by the presence of steam. Also, several assumptions were made regarding the liquid water particle parameters. For these results, the initial single particle diameter chosen for steam was 15 microns. This diameter was chosen because it is on the same order of magnitude of droplets of condensation discussed in the AGARD report [3.183]. The initial particle velocity was assumed to be the same as the inlet gas velocity. This assumption was made on the basis of the fact that particles of this size closely follow the streamlines of the gas.

### Quantity of Steam Parametric Study

For the “quantity of steam” parametric study, three cases were run and compared to the “dry” case. These cases were run at 1, 3, and 5 percent of the total inlet mass flow in steam. The overall inlet physical gas mass flow (“dry” air + water vapor) was held constant for each case. Although air, water vapor, and liquid water are accounted for in the **MPC**, only water vapor and air are accounted for in the **MLC**. Also, for each of these cases the quality of the steam was set to 50 percent. The initial conditions of the steam particles also remained the same for each test case.

**Figure 3.274** illustrates how the fluid properties change as a function of the percentage of axial distance traveled through the machine. **Figure 3.274a** shows how the gas mass flow is increasing through the machine as the liquid water is vaporized and becomes water vapor. As the percentage of inlet steam is increased, the total amount of gas mass flow increases by nearly 2.5 percent in the 5-percent steam condition.

**Figure 3.274b** shows the liquid water loading factor decreasing through the machine in each case. Although with the increasing amount of inlet steam comes an increasing amount of liquid water at the inlet, each case shows the liquid water being vaporized near the exit of the HPC. However, it does not completely vaporize at exactly the same location for each case. The complete vaporization occurring close to the same location is due to the fact that particle vaporization is largely dependent on surface area of the particle. Since initial liquid particle diameters are the same, initial exposed surface areas are the same. So even though there are more liquid water particles present in the cases with more inlet steam, the vaporization rate will be similar for each particle, leading to complete vaporization at similar locations in the HPC. The slight differences in location are due mainly to increased energy transfer for vaporization and higher overall water vapor concentration in the cases with more inlet steam.

**Figure 3.274c** presents the gas constant as a function of axial distance. Increasing inlet steam increases the amount of water vapor coming into the machine. This decreases the molecular weight of the gas and increases the gas constant. As more liquid water is vaporized through the machine, the gas constant increases because of the decreasing molecular weight of the mixture for each case investigated. The “dry” case shows no increase in the gas constant since no water vapor is present. The specific heat ratio (**Figure 3.274d**) also changes through the machine. In each case, including the “dry” case, the specific heat ratio decreases across each rotor because of increasing temperature occurring in the rotors. However, the specific heat ratio is also decreasing for each case as more steam is introduced into the system. Since the inlet temperature is the same for each case, this initial offset in specific heat ratio is caused by the difference in mass fraction of water vapor, which causes a change in both the mixture gas

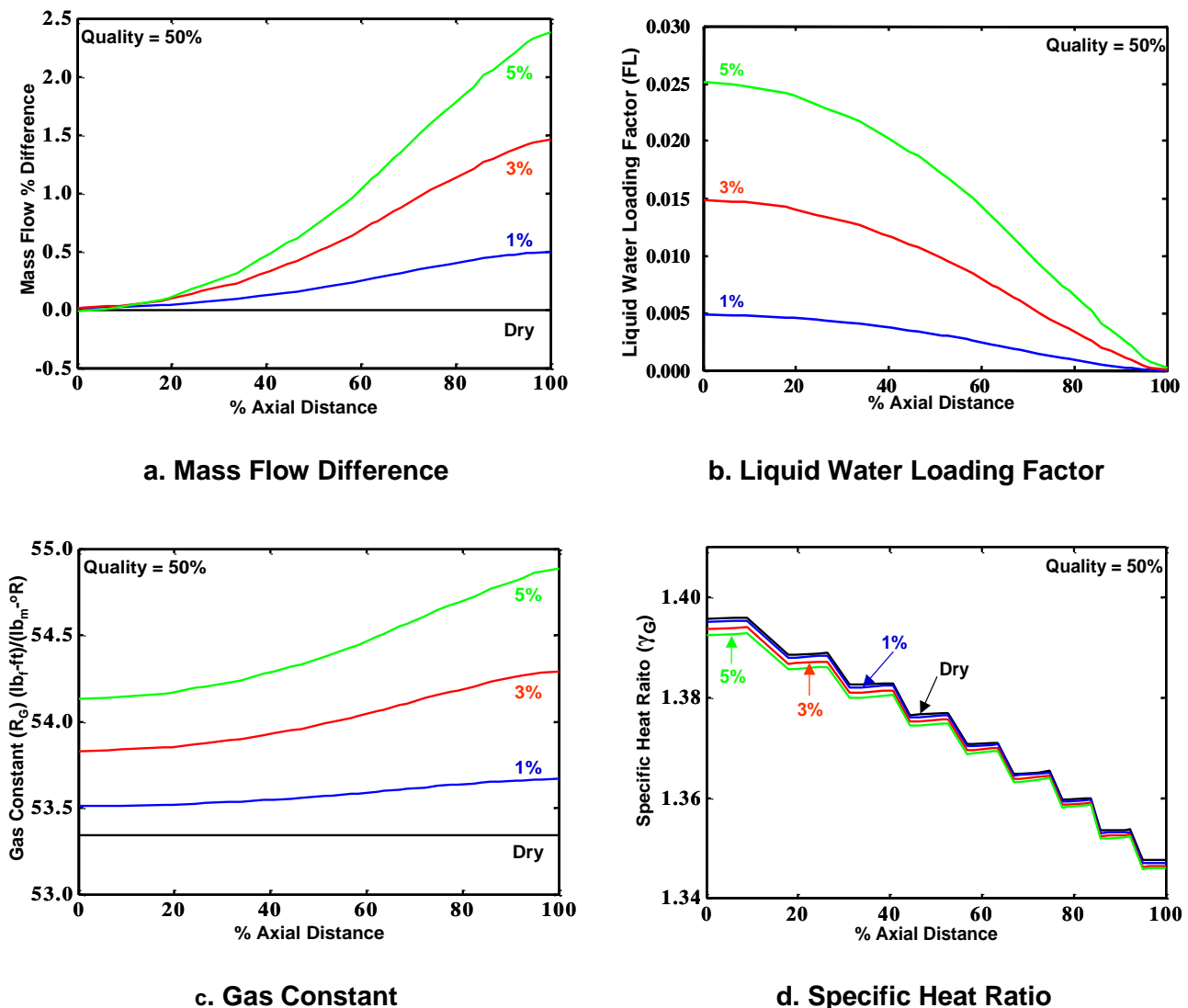


**Figure 3.274 Parametric Study Results – Changes in Fluid Properties as a Function of Percentage of Steam and Axial Distance with Constant Quality of 50%**

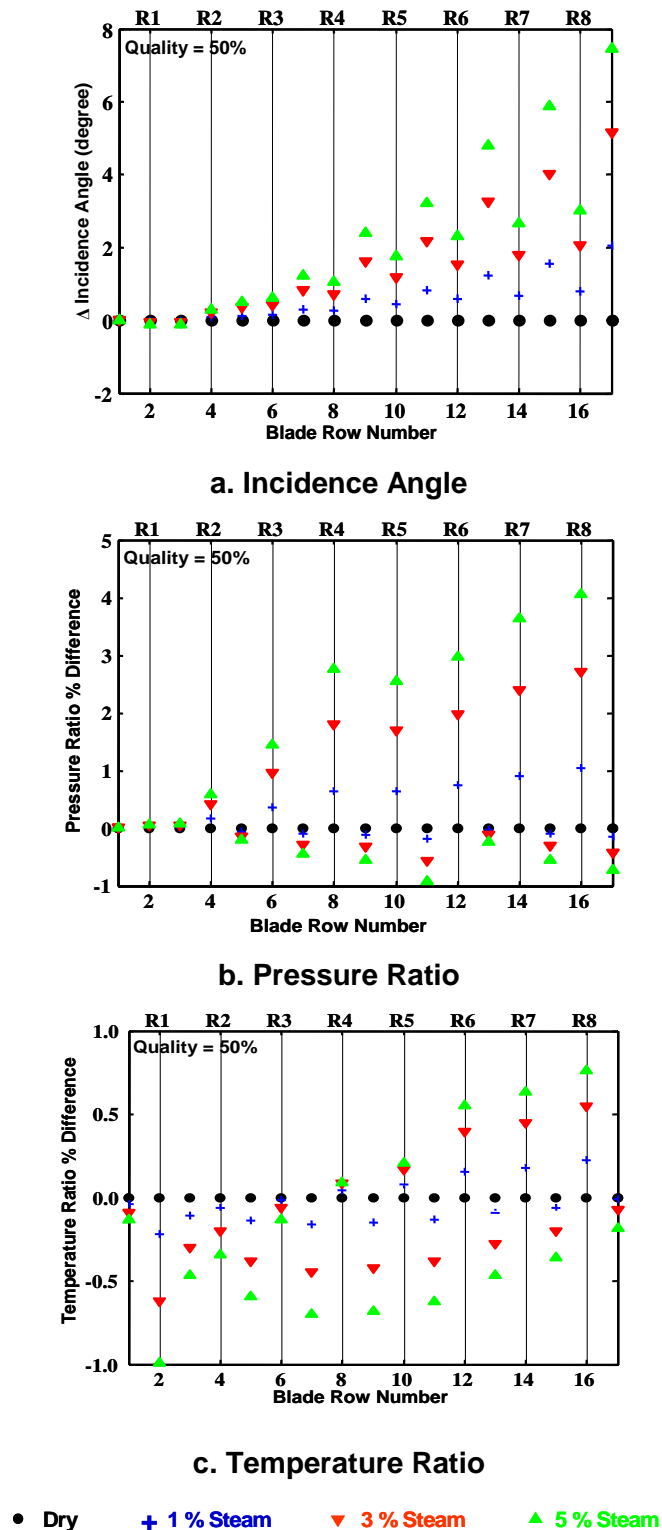


**Figure 3.275 Parametric Study: Effect of Amount of Steam at 50-Percent Quality on Compressor Stage Performance**

decrease in total pressure ratio for 5-percent steam.

constant, due to the change in molecular weight, and the specific heat at constant pressure.

The data in [Figure 3.275](#) are presented in a slightly different form. They are presented as a function of blade row, with the even blade numbers being rotors (labeled across the top of each figure), and odd blade numbers being stators (except for blade number 1, which is an inlet guide vane). The best way to look at these data is to pick a particular blade row and look bottom to top. The more steam introduced into the compressor, the more dramatic the effect is on incidence ([Figure 3.275a](#)), especially for the rear part of the machine. For the last stator (S8, blade number 17) at 1-, 3-, and 5-percent steam, the incidence change from the “dry” case is near 2.0, 5.0, and 7.5 deg, respectively. This is explained by the lower temperature of the gas mass flow due to the evaporation process. This reduced temperature increases the stage corrected speed, thereby increasing the stage pressure rise and density, and reducing the stage axial velocity. The reduced blade axial velocity causes an increased incidence angle, therefore taking the blade toward stall. This observed phenomenon is consistent with trends identified in the AGARD report [\[3.183\]](#).

Since there is an increase in incidence on the rotors at the rear of the machine and therefore an increased load on the rear rotors, the pressure ratio across each rotor increases as the quantity of steam increases ([Figure 3.275b](#)). However, along with an increase in incidence at each stator there comes an increase in losses, which results in a decrease in the pressure ratio across the stators with additional amounts of steam. The maximum increase in pressure ratio for a single rotor occurs at the last rotor (R8, blade 16) and shows over 4-percent increase in total pressure ratio for 5-percent steam. The largest decrease in pressure ratio occurs at stator 5 (S5, blade 11), which shows almost 1-percent



**Figure 3.275c** shows the percent difference in temperature ratio across each blade with steam compared to the temperature ratio across each blade row in the “dry” case. From looking at the stators (odd blade row numbers), the figure shows the temperature ratio decreases across the blade rows. This is because the stators are adding no work into the system and vaporization is causing evaporative cooling; thus the temperature ratio must decrease. However, there is a different effect on the rotors. Several different things are affecting the temperature ratio across the rotors. Vaporization seems to affect the temperature ratio more in the front part of the machine than toward the back of the machine. The vaporization across the first three rotors actually causes the temperature ratio to decrease. With increased loading and incidence in the back part of the machine, the back rotors’ work increases. This increase in work is able to overcome the vaporization effects. As there is also less liquid water available to be vaporized in the back part of the machine, the vaporization effect is less significant for these rotors.

The previous discussion has focused on effects inside the HPC. **Figure 3.276** describes the overall compressor performance effects in terms of compressor performance maps. Isentropic efficiency maps are not presented since heat transfer exists in this analysis; therefore, temperature ratio maps are presented as an alternative.

With the amount of steam introduced into the system increased and with the overall physical gas mass flow and speed held constant, **Figure 3.276** shows the pressure ratio of the machine increased advancing the machine toward stall, while the overall temperature ratio of the machine decreased. The changes in pressure ratio can be attributed to the increased loading on the blades caused by the fluid changes as vaporization occurred. The decrease in total temperature illustrated in **Figure 3.276** can be attributed to the heat transfer taking place between the gas and the water particles during vaporization.

For the parametric study of quantity of steam (with constant quality) for the compression system only, the following conclusions can be drawn:

- 1) The more steam at constant quality, the more dramatic the effects on fluid properties;
- 2) The more steam at constant quality, the greater the rematching and loading (evidenced by the increase in incidence and by the increase in rotor pressure ratios as shown in **Figure 3.275**), and the closer to stall the compression system is

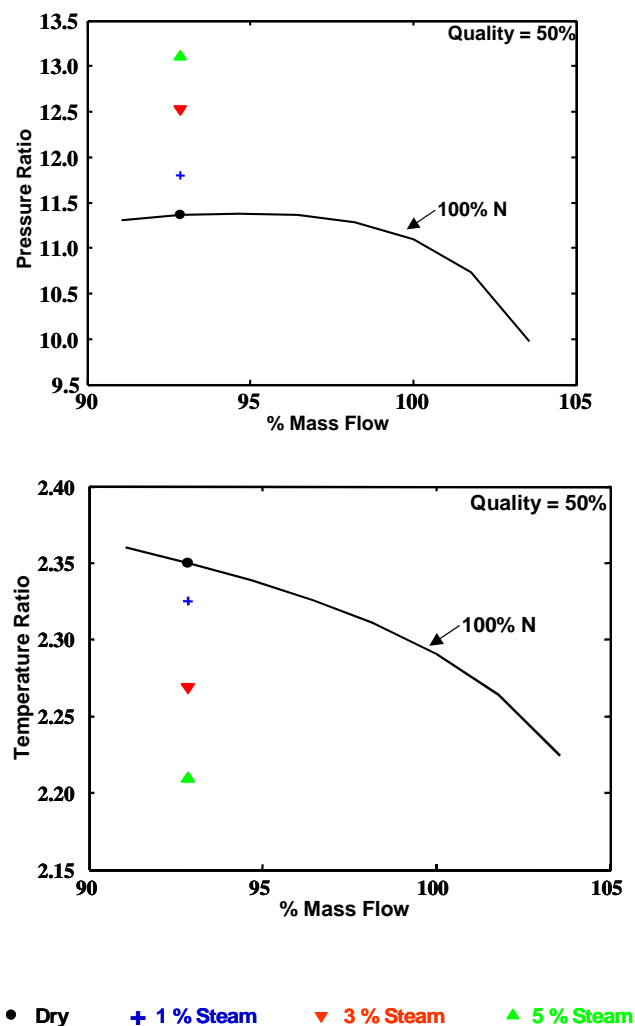


**Figure 3.276 Parametric Study: Effect of Amount of Steam at 50% Quality on Overall Compressor Performance**



driven, particularly the rear stages. This is consistent with the statement in the AGARD report [183 that at high speeds, evaporation “will tend to advance this process (stalling of the rear stages) by re-matching these stages closer to stall.”

### Quality of Steam Parametric Study

For the “quality of steam” parametric study, five cases were run and compared to the “dry” case. These cases were run at 0-, 25-, 50-, 75- and 100-percent initial quality. For each of these cases the quantity of the steam was held constant to 1 percent of the total inlet mass flow in steam. The overall inlet physical gas mass flow (“dry” air + water vapor) and the initial conditions of the steam particles also remained the same for each test case.

**Figure 3.277** illustrates how the fluid properties change through the machine. **Figure 3.277a** shows the percent difference in mass flow compared to the “dry” case as a function of axial distance. For the case of 100-percent quality, the gas mass flow is constant because there was no liquid water to vaporize through the machine. The largest increase in mass (at the exit of the machine) occurs for the 0-percent quality case, where nearly 1 percent of additional gas mass flow was added because of vaporization through the machine.

**Figure 3.277b** illustrates the liquid water loading factor. For the 100-percent quality case, since no liquid was present, the value is zero throughout the machine. However, for the 0-percent quality case, 1 percent of the gas mass flow was in liquid water at the inlet of the machine. For each of the cases with quality less than 100 percent, nearly all of the water was vaporized by the exit of the machine. This is the same vaporization behavior seen in the “quantity of steam” parametric study and is discussed in the previous section.

**Figure 3.277c** depicts how the gas constant changes through the machine. As the inlet quality of the steam increases, the inlet gas constant value increases. Similarly, as the amount of vaporization increases through the machine, the value of the gas constant increases through the machine. Since in every case the amount of water vapor present at the exit of the machine is nearly the same, the value of the gas constant is also nearly the same at the exit of the machine. **Figure 3.277d** illustrates how the specific heat ratio changes through the machine. For each case, the value of the specific heat ratio is decreasing through the rotors because of the increasing temperature. However, as the percent quality increases from case to case (more water vapor present at the inlet), the lower the overall value of the specific heat ratio.

The data in **Figure 3.278** are presented in the same fashion as the data in **Figure 3.275**. Again, one can best interpret these data by looking at each individual blade row separately. One interesting thing to note about **Figure 3.278a** is the 100-percent quality case. Since this case contains no liquid water, no vaporization takes place (and therefore, there is no heat transfer). This case has the opposite effect on the incidence (moving more toward choke, at the rear, instead of toward stall) than do the cases where vaporization occurs. Therefore, this effect is attributed to the change in fluid properties caused by the presence of water vapor only (changes in  $R_G$  and  $\gamma_G$ ). In the cases where liquid water is present (0, 25, 50, and 75 percent) the vaporization drives the rear stages in the direction of stall (increasing incidence). For the 0-percent quality case, the change in incidence of the last blade row is over 4.0 deg in the stall direction.

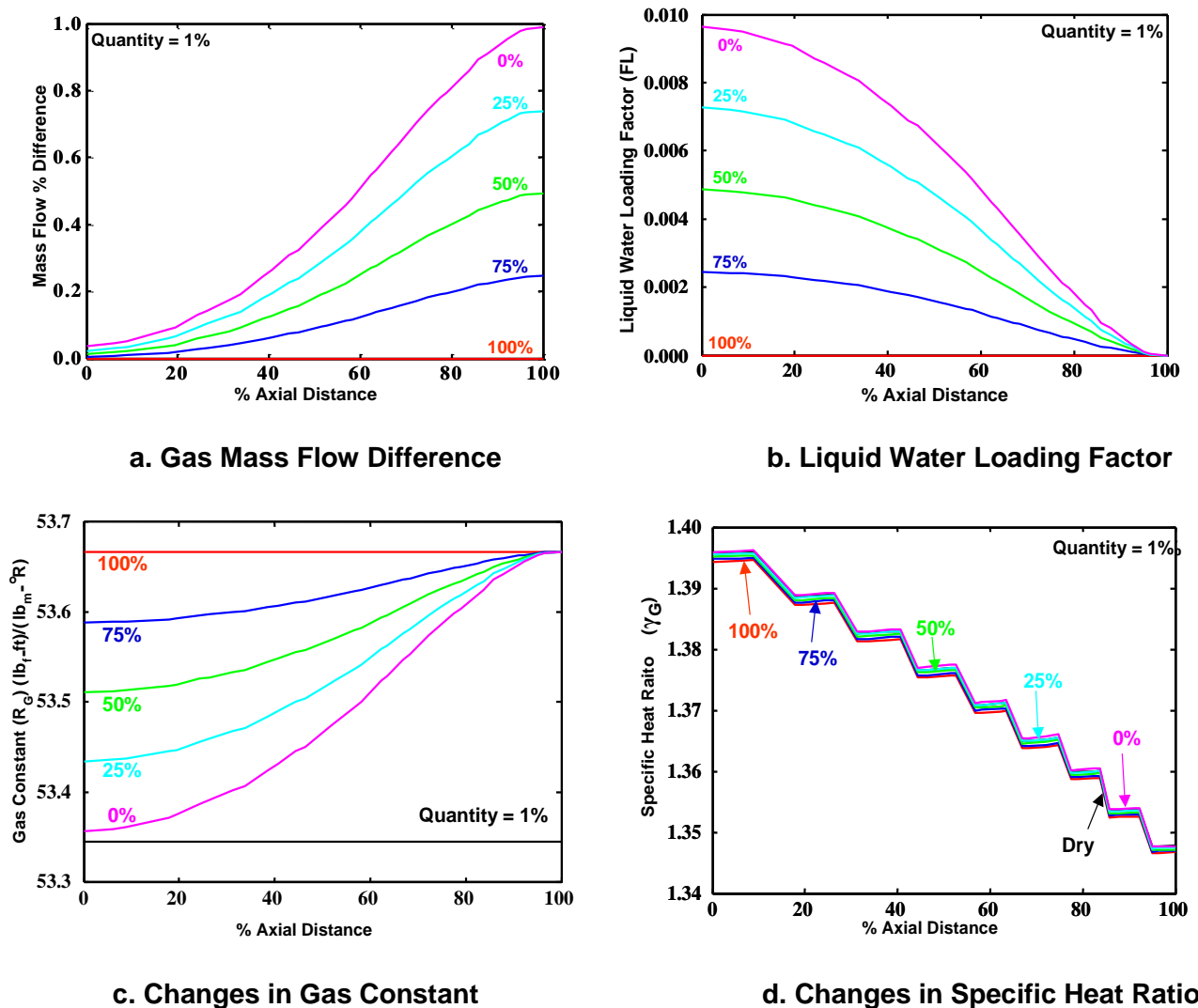


**Figure 3.277 Parametric Study Results: Changes in Fluid Properties as a Function of Steam Quality and Axial Distance for Constant Amount of Steam of 1%**

**Figure 3.278b** shows the percent change in pressure ratio across each of the blade rows individually. Similar to the incidence, in the case where no vaporization occurs (100-percent quality), the pressure ratio moves in the opposite direction of the cases with vaporization. Therefore, this effect is attributed to the change in fluid properties caused by the presence of water vapor only (changes in  $R_G$  and  $\gamma_G$ ). For the cases with liquid water (and therefore heat transfer occurring during vaporization), the pressure ratio across the rotors increases, while the pressure ratio across the stators decreases. The effects are greatest for the 0-percent quality case (the case with the most vaporization occurring). The pressure ratio across the last rotor (R8, blade row 16) increases by more than 2 percent for the 0-percent quality case.

**Figure 3.278c** represents the percent difference in temperature ratio across each blade row, individually, when compared to the “dry” case. The effects on temperature ratio for this quality

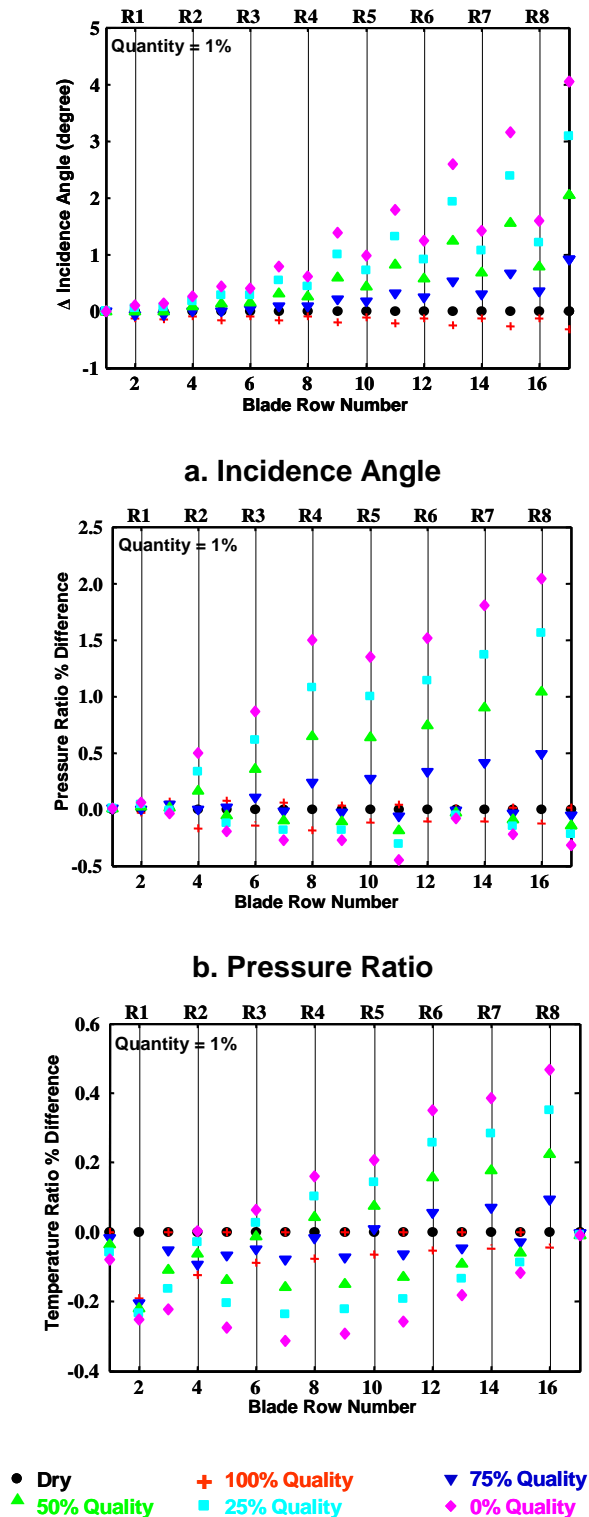


**Figure 3.278 Parametric Study: Effect of Quality of Steam for an Amount of 1% on Compressor Stage Performance**

study are similar to the effects for the quantity study discussed previously. The temperature of the stators must decrease because the stators are adding no work and vaporization is causing heat transfer from the gas. Also interesting to note is that the 100-percent quality case (no vaporization) and the “dry” case are nearly identical for the stators.

Again, as in the previously presented quantity study ([Figure 3.275](#)), the rotors behave differently from the stators. In the front part of the machine, vaporization seems to affect the temperature ratio more than it does toward the back of the machine. The vaporization across the first two rotors actually causes the temperature ratio to decrease. With the increased loading and incidence in the back part of the machine, the back rotors’ work increases and is able to overcome the vaporization effects. Also, since there is less water to vaporize in the back part of the machine, the vaporization effect is less significant for these rotors. For the 100-percent quality case (no vaporization), the temperature ratio across the rotors actually decreases by comparison to the “dry” case. This means that the gas property changes (without vaporization) have an opposite effect from when these effects are combined with vaporization. [Figure 3.279](#) shows that incidence changes caused by water vapor alone cause the performance across the rotors to decrease, thus resulting in the lower temperature ratio across all rotors.

[Figure 3.279](#) depicts the overall compressor performance maps for this particular machine at the 100-percent speed. The effects of quality on the performance maps can be seen in each of these cases. For constant physical speed and flow, the more liquid water present (lower quality), the higher the overall pressure ratio and, because of the vaporization and the change in fluid properties, the lower the overall

temperature ratio of the machine. As discussed previously, since the analysis included heat transfer and thus this was no longer an isentropic process, isentropic efficiency maps are not included.

For the parametric study of the quality of steam (at constant quantity) for the compression system only, the following conclusions can be drawn:

- The lower the quality, the more vaporization (heat transfer) occurs, and the more dramatic are the effects on compression system performance.
- The lower the quality, the greater the rematching and loading (evidenced by the increase in incidence and the increase in rotor pressure ratios shown in Figure 6), and the closer to stall the compression system is driven, especially the rear stages. This is consistent with the statement in Ref. 3.183 that at high speeds, evaporation “will tend to advance this process [stalling of the rear stages] by rematching these stages closer to stall.”

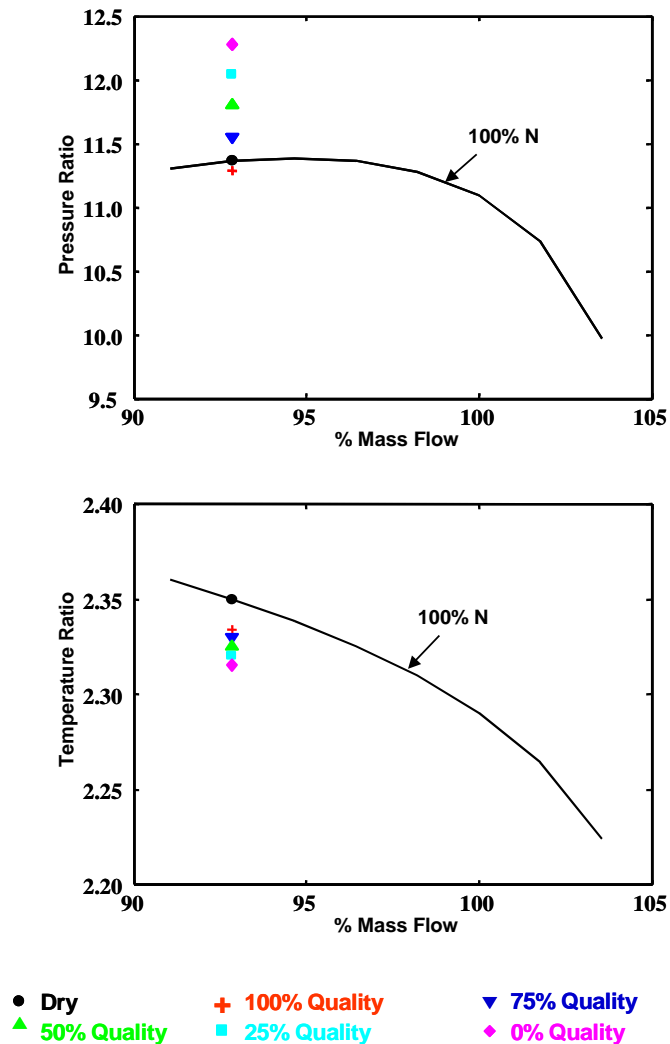


**Figure 3.279 Parametric Study: Effect of Quality of Steam for an Amount of 1 Percent on Compressor Performance**

### Conclusions for Generic HPC

By loosely coupling a vaporization code and a compressor performance code, the investigators developed a technique that could be used to discover the effects and trends of steam ingestion on compression system performance and stability. This coupling provides the ability to model vaporization and the effects of vaporization on fluid properties and stage rematch caused by the changes in fluid properties and heat transfer.

The analysis presented in this section demonstrates that steam ingestion has an effect on compressor performance and potentially on the stability margin. That effect is reflected in stage rematching caused by blade incidence changes that tend to drive the rematched stages closer to stall. This effect also seems to be more pronounced at the back of the machine.

In addition, the heat transfer caused by the vaporization of liquid water has more of an effect than the property changes caused by the presence of water vapor alone. Therefore, it is concluded

that, excluding the effect of a temperature distortion, that the presence of liquid water in steam (steam with quality less than 100 percent) has more of an effect than water vapor alone. Therefore, the effects of steam ingestion with some quality are attributed more to the vaporization than to the fluid property changes.

**ADDITIONAL REFERENCES:**

**3.181** Willbanks, C.E. and Schulz, R.J. "Analytical Study of Icing Simulation for Turbine Engines in Altitude Test Cells." AEDC-TR-73-144 (AD-770069), November 1973.

**3.182** Smith, S.L. "1-D Meanline Code Technique to Calculate Stage-by-Stage Compressor Characteristics." M.S. Thesis, The University of Tennessee, Knoxville, TN, 1999.

**3.183** "Recommended Practices for the Assessment of the Effects of Atmospheric Water Ingestion on the Performance and Operability of Gas Turbine Engines," Propulsion and Energetics Panel Working Group 24, Advisory Group for Aerospace Research and Development, NATO, 1995.

### 3.5.2 Water Ingestion Analysis for the FT8

To validate the steam ingestion modeling technique ([Section 4.10](#)), it was decided to use experimental data obtained during fogging water ingestion tests of an FT8 engine ([Figure 3.280](#)). The FT8 is a 25-MW gas turbine consisting of a gas generator derived from the JT8D aircraft engine and a separate power turbine. Power turbines available are optimized for electric power generation (3000 or 3600 RPM) or mechanical drive (5500 RPM nominal speed). An experimental data set with dry, non-fogging water and fogging water results was provided for the eight-stage, low-pressure compressor (LPC) of the FT8 compression system. Included with these data was cycle code generated information. A decision as to how much of the test cell and LPC should be simulated was based upon the available experimental data and the cycle code results.



**Figure 3.280 FT8-2 Gas Turbine Engine for Power Production**

#### EXAMPLE(S) CITED

**3.184** Hale, Alan, Klepper, Jason, and Hurwitz, Wayne, "A Numerical Capability to Analyze the Effects of Water Ingestion on Compression System Performance and Operability," ASME Paper #GT2005-68480, 2005 ASME Turbo Expo, June 2005.

#### MODELING TECHNIQUE

Development of a steam ingestion modeling technique required a one-dimensional (1-D) **multiphase code** [[3.185](#)] and a 1-D compressor **meanline code** [[3.186](#)]. An in-depth discussion of these codes can be found in [Section 4.10](#).

A modeling and simulation technique has been developed to use a one-dimensional (1-D) multiphase code and a 1-D compressor **meanline** code to investigate the effects of water ingestion. The **multiphase** code primarily accounts for the heat transfer associated with the phase change of water, and the **meanline** code uses the heat transfer and gas properties to model the flow properties through a compression system. The combination of the **meanline** and the **multiphase** code will be known as the **MLC/MPC**.

#### TEST CELL ANALYSIS

As shown in [Figure 3.281](#), the plenum chamber leading up to the bellmouth is 6 ft (2.18 m) long and has a corresponding inlet Mach number of 0.03. The distance from the bellmouth to the LPC inlet is less than 2 ft (0.73 m), and this is a significantly elevated Mach number of 0.4 at the LPC inlet. These conditions in the test cell suggest that there is a long response time for changes in heat transfer and evaporation/condensation in the long plenum region and less opportunity for heat transfer and evaporation/condensation changes to occur in the short, fast-flowing bellmouth area leading to the LPC inlet.



Experimental data of static pressure and static temperature were provided at Station 1.7. The location of these data in the plenum chamber was such that the velocity was nearly zero, allowing the static's to approximate the totals at Station 1.7. No cycle code results were available at Station 1.7, but they were available at Station 2.0.

The experimental data provided only limited boundary conditions for simulation of the FT8 LPC. However, from the cycle model results provided, the following boundary conditions could be discerned at station 2:

- Gas mass flow (air and water vapor)
- Remaining liquid water mass flow
- Inlet totals (pressure and temperature)

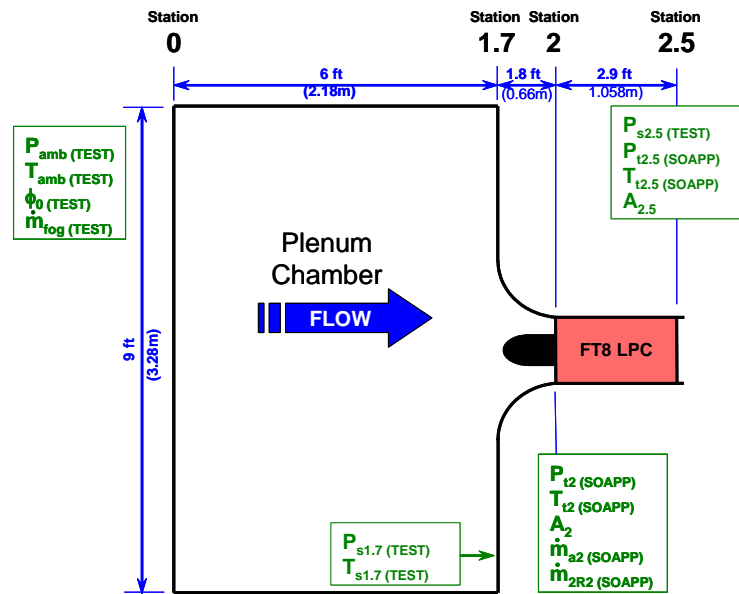


Figure 3.281 Test Cell and FT8 as Modeled

The boundary conditions at the inlet of the LPC not provided by data or the cycle code were water droplet temperature, velocity, and diameter. Cycle code calculations assumed that the liquid water evaporated until the saturated condition was reached. To simulate the LPC only, the water droplet parameters would have to be estimated based upon how water droplets would change as a result of vaporization/condensation occurring in the plenum chamber and bellmouth. The water diameter is a critical unknown in the preferred simulation of modeling the LPC only. In the absence of a well-defined set of boundary conditions, a different modeling approach was developed.

The new modeling approach was to model simultaneously the plenum chamber, bellmouth, and LPC where previously unknown water parameters' boundary conditions are better defined. Additional information was obtained from Pratt and Whitney (manufacturer of the FT8) to facilitate construction of a simulation of the plenum chamber and bellmouth. The new experimental and cycle code boundary conditions available to support this modeling approach at station 0 were:

- Dry air mass flow calculated from cycle code
- Liquid fogging water mass flow
- Ambient conditions (pressure and temperature)
- Water droplet diameter

Even though there were still some unknown parameters (water droplet temperature and velocity), these were judged to be less significant and easier to approximate.

This plenum chamber, bellmouth, and LPC modeling approach required a gas mass flow defined at the inlet of the plenum chamber. The only gas mass flow provided was from the cycle code at the inlet of the LPC after the evaporation through the plenum chamber and

bellmouth had been accounted for. Therefore, the gas mass flow provided by the cycle code at the inlet of the LPC included water vapor from both the ambient relative humidity and the previously mentioned evaporation. Based upon an assumption of saturation, the cycle code determined the amount of water evaporated through the plenum chamber and bellmouth. For the MLC/MPC simulation, the gas mass flow at the inlet to the plenum chamber was determined by subtracting the cycle code's approximation of the fogging water vaporized in the plenum chamber and bellmouth from the gas mass flow at the LPC inlet. To determine the accuracy of the assumption of saturation, the researchers performed an analysis of the plenum chamber.

### Analysis of Plenum Chamber

Two analytical tools, the lumped volume approach and the **meanline-multiphase code, (MLC/MPC)** were compared to experimental data and used to corroborate cycle code's prediction of water (liquid and vapor) mass flows entering the LPC inlet. The lumped volume analytical tool is used to analyze the constant cross-sectional area plenum chamber from plenum inlet to the bellmouth inlet. This tool solves the steady-state, 1-D conservation of mass, momentum, and energy along with ideal gas equations of state for the air and water vapor phases. The **MLC/MPC** used to model the FT8 LPC can also be used to model the vaporization/condensation in the plenum chamber.

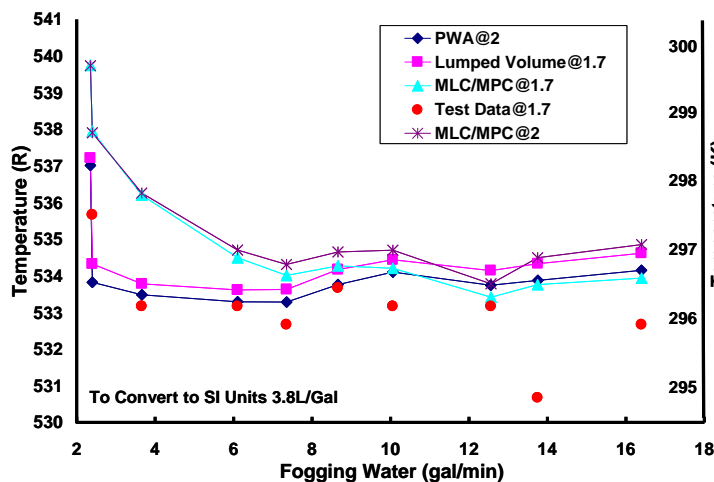


**Figure 3.282 Reduction in Total Temperature Due to Fogging Water Evaporation in Plenum Chamber**

was provided with the experimental data in addition to the water vapor associated with the relative humidity. The results of the two analytical tools for mass flow compared to the cycle code results are presented in **Figure 3.282**.

Vapor mass flow entering the plenum chamber with the air mass flow for the fogging test cases is depicted on the figure and ranges from 2.63-2.88 lbm/sec (1.19-1.31 kg/sec) and is proportional to the relative humidity which varies from 57.9-69.1%. The amount of liquid water entering the plenum chamber varies from 2.35-16.4 gal/min (0.33-2.28 lbm/sec or 0.15-1.05 kg/sec). The amount of liquid water added to the system in every case is less than the water vapor already present from relative humidity.

The results of the two previously specified analytical tools and cycle code's predictions of total temperature are compared with experimental data in **Figure 3.282** as a function of inlet to the plenum chamber liquid fogging water. The results of all of the techniques together span a max of 1% difference in total pressure (not shown) and total temperature.

The only mass flow calculations available for any analysis of the test cell leading up to the LPC inlet was provided by the cycle code. The mass flow of the air provided by the cycle code is combined with relative humidity and ambient day temperature and pressure to calculate the vapor mass flow entering the plenum chamber. Fogging water mass flow

The cycle code results for evaporation are similar to the evaporation predicted by the lumped volume approach. Liquid water can be seen to evaporate for each fogging test case. For example, using the lumped volume technique, [Figure 3.282](#), shows that the evaporation ranges from 0.33-0.54 lbm/sec (0.15-2.5 kg/sec). The water predicted to evaporate by each technique can be seen to be accounted for by an increase in the water vapor. Only the lowest fogging water test case does not provide enough liquid water to bring the flow field to saturated equilibrium. The lumped volume evaporation techniques over-predict the amount of evaporation compared to the **MLC/MPC** technique associated with the lowest fogging water test cases. Therefore, the simplified lumped volume evaporation technique appears more accurate for the higher fogging water test cases.

By modeling this geometry with the **MLC/MPC**, it was shown that total pressure, total temperature, and water mass flows varied by less than 1% between Station 1.7 (bellmouth inlet) and Station 2 (LPC inlet). These results serve as a means to validate that the totals remain approximately unaffected by heat transfer and evaporation/condensation due to the speed of the flow and the short distance between the bellmouth inlet and the LPC inlet face. These totals become important in calculated corrected speed and corrected flow used in the LPC validation.

We conclude that the assumption of saturation at station 2 is adequate to calculate an inlet gas mass flow from the cycle code. In addition, the following section uses the **MLC/MPC** simulation of the constant area plenum chamber to provide insight as to the nature of the evaporation process before presenting the more complex problem of evaporation with turbomachinery.

### Investigation of the Plenum Chamber Evaporation Process

The evaporation process is not instantaneous; rather, it is a balance between heat transfer, mass concentration, and velocity differences occurring between the water droplet and the gas mixture along the length of the plenum chamber. Since the **MLC/MPC** has the ability to predict the flow field throughout the plenum chamber, this tool was used to provide insight into the evaporation process through the plenum chamber.

Using the **MLC/MPC**, the investigators explored the evaporation process for the lowest and highest fogging water test cases. The liquid water droplets were added at Station 0, as shown in [Figure 3.281](#). The liquid water droplet temperature was assumed to enter the gas mixture at the same static temperature as the gas mixture and the water droplets were all specified to be 11 microns, as specified in the data. Since the mixture and the water droplets were the same temperature, there was no initial net heat transfer between them; however, the water vapor concentration between the surface of the water droplets and the mixture was far from being in a state of equilibrium. When the water droplets were introduced into the gas mixture, a cloud of air and water vapor immediately formed around the droplet at the saturated partial pressure corresponding to the temperature of the water droplets. The following analysis assumed the temperature of the water droplets to be the same as the surface temperature of the water droplets and that all heat transfer thus occurs at the surface of the droplets.

Initially, evaporation occurs rapidly at the water droplet surface, increasing the water vapor concentration in the gas mixture. The evaporation process is accomplished when random kinetic energy in the water droplets combines to give a water molecule enough energy to convert it from liquid to vapor at the temperature of the droplets. This reduces the energy of the water droplets and results in a corresponding temperature reduction of the water droplets. The evaporation process of the fogging water was tracked through the constant area plenum chamber of the test cell and characterized on a temperature-entropy (T-S) diagram in

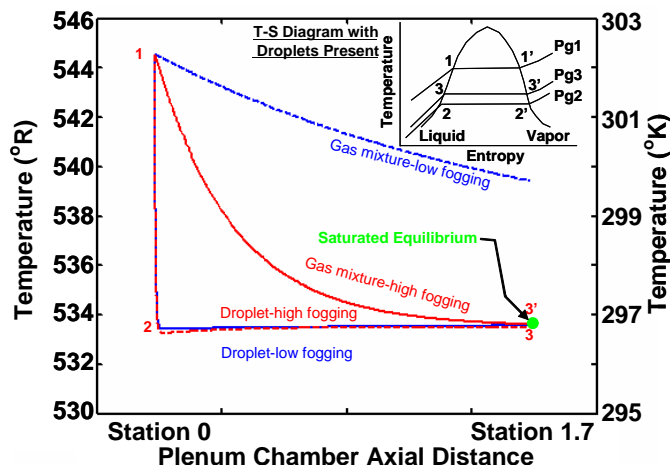


**Figure 3.283 Temperature of the Gas Mixture and Liquid Water Droplets**

associated with this temperature difference is zero, but the energy transfer is large because of the evaporation process associated with a large partial pressure difference between the particle and the gas mixture. As the droplet temperature continues to decrease below the gas mixture temperature, the convective heat transfer caused by temperature differences increases. The rate of temperature reduction of the water droplets begins to slow down as the convective heat transfer increases.

The liquid droplet temperature, however, continues to decrease until the convective heat transfer from the gas mixture to the water droplets balance the evaporation energy transfer as depicted by the 2-2' equilibrium condition on the T-S diagram of [Figure 3.283](#). Since the liquid water proceeds from location 1 to location 2 on the T-S diagram quickly, very little of the liquid water actually evaporates by location 2. The 2-2' location on the T-S diagram is specified by the temperature of the droplet and the partial pressure,  $P_{g2}$ , of the water vapor surrounding the droplet.

Since the diameter of the water droplets from the test cell fogger is a uniform 11 microns, an increase in fogging water increases the total surface area of the collective water droplets. The additional surface area of the water droplets exposed to the low concentration of water vapor in the gas mixture increases the rate of evaporation. The effect of these two high and low water test cases is most evident by investigating the change in temperature of the gas mixture.

The temperature of the gas mixture immediately begins to reduce during the evaporation process. The primary reason for this temperature reduction is the convective heat transfer from the higher gas mixture temperature to the cooler water droplets. Another reason for the reduction in gas mixture temperature is that the evaporation process takes place at the temperature of the water droplets, and heat is required to transform the lower temperature water vapor to the temperature of the gas mixture.

Even though the convective heat transfer and evaporative energy transfer are nearly balanced, and opposite in sign after state 2 is reached, mass transfer continues and the gas mixture temperature reduces until the water is completely evaporated or saturated equilibrium is reached.

**Figure 3.283.** The water droplets enter the plenum chamber for both test cases saturated at the mixture temperature, with vapor partial pressure ( $P_{g1}$ ) in the immediate vicinity of the water droplet, denoted by 1-1' on the T-S diagram. The droplet temperature quickly drops because of the loss of internal energy associated with the evaporation process.

Convective heat transfer also occurs as a result of the temperature difference between the water droplet and the free stream gas mixture along the length of the plenum chamber. At first, the convective heat transfer

Saturated equilibrium is obtained when the temperature of the mixture stream is equal to the temperature of the water droplets and the vapor concentration of the mixture is equal to the vapor concentration around the water droplets. This means that the partial pressure of the vapor in the mixture and around the water droplets is the saturated partial pressure at the temperature of the mixture and the temperature of the droplets.

The highest fogging water test case provides an example of saturated equilibrium at the 3-3' location on the T-S diagram where the temperature and vapor partial pressure,  $P_{g3}$ , are the same in the mixture as around the water droplet. For both fogging test cases, the evaporation process of the **liquid water** from 1-1' to 3-3' is very similar. However, the rate of temperature decrease of the **gas mixture** for the max fogging water test case is much greater than that of the lowest fogging water test case.

The greater drop in gas mixture temperature for the high fogging water test case corresponds to a large increase in heat transfer from the gas mixture to the liquid water droplets. Yet, even with this large heat transfer being added to the water droplets for the high fogging water test case, the water droplet temperature for the fogging water test case changes very little. The explanation is observed in [Figure 3.284](#) where the energy transfer caused by evaporation is nearly balanced by the convective heat transfer to the water droplets.

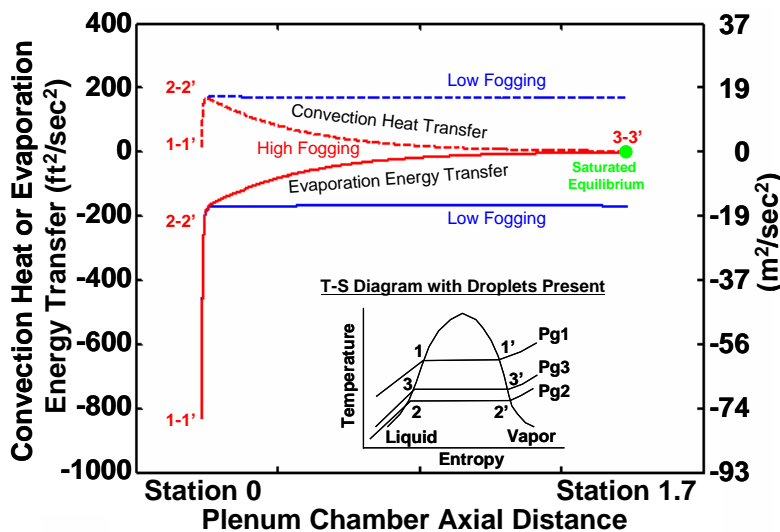


**Figure 3.284 Evaporative Energy Transfer from Liquid Droplets to Gas Mixture and Convective Heat Transfer from Gas Mixture to Liquid Water Droplets**

The convective heat transfer caused by temperature differences between the gas mixture and the water droplets balanced by evaporation energy transfer forms a mirror image plot from the 2-2' to 3-3' for both the lowest and highest fogging water cases. The low fogging water test case is observed not to reach saturated equilibrium before the exit of the plenum chamber because the evaporative energy transfer and convective heat transfer do not reduce to zero. However, for the high fogging water test case, both evaporative energy transfer and

convective heat transfer reduce to zero, resulting in saturated equilibrium at 3-3'. This balance in energy transfers will continue until changed by an external influence such as an area change.

#### **VALIDATION OF THE MLC/MPC WITH FT8 DATA AND CYCLE CODE RESULTS**

After a thorough analysis of the FT8 information, it was determined that an inconsistency in the information provided and the ability to execute the FT8 version of the AEDC MLC at those



points would cause problems in the validation process. A description of those inconsistencies is outlined below.

- The **MLC/MPC** was calibrated, blade-row-by-blade-row, to what appears to be the dry design point of the FT8 with standard day inlet total temperature and total pressure.
- The experimental data were provided at very different inlet conditions of nominally 65-percent relative humidity, inlet total temperature of 533°R and inlet total pressure of 14.13 psia.
- The **MLC/MPC** is known to perform well only within the immediate neighborhood of a calibrated point. The fogging and non-fogging points from the experimental and/or cycle code data are outside this neighborhood for the MPC/MLC code's one (1) calibrated point.

A scheme was therefore devised to operate the **MLC/MPC** near its calibration point and compare fogging water results with cycle code results and experimental data. Since the experimental data were obtained at different speeds and corrected flows from that of the **MLC/MPC** calibration point, comparisons can be obtained only by constructing non-dimensional performance maps. The FT8 cycle code (CYCLE CD) results for fogging, a non-fogging point, and a dry point (provided for the calibration of the **MLC/MPC**) are plotted on a corrected performance map, and the results are depicted either as red dots or a red oval in **Figure 3.285**.

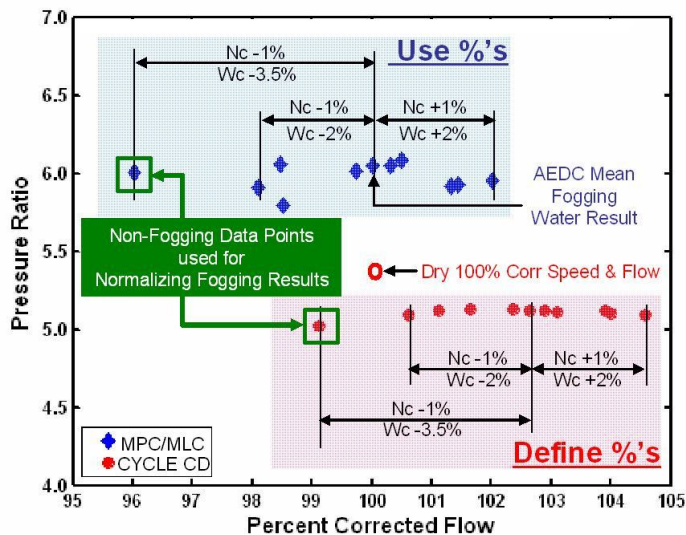


**Figure 3.285 Corrected Map Relating Percent Differences in Fogging Results About the Mean Fogging Point for Speed and Flow**

A review of the experimental data revealed that the engine controls caused the engine components to rematch, with the ingestion of fogging water, and resulted in an increased corrected wheel speed and corrected flow of the LPC. Ten experimental data points were provided, with fogging water varying between 2.35 and 16.40 gal/min.

This variation in fogging water caused the engine to operate with a range of  $\pm 1$  percent difference in corrected speed and a range of  $\pm 2$  percent difference in corrected flow from the mean fogging water point of 7.35 gal/min, and these percent differences are defined among

the red dots in **Figure 3.285**. The **MLC/MPC** dry blade-row-by-blade-row calibration was corrected to the mean fogging water inlet totals to take advantage of the detailed calibration, and then 65 percent relative humidity water vapor along with the 7.35 gal/min of fogging water was added to the simulation; the result from the MLC/MPC simulation is plotted in **Figure 3.284** as the blue diamond in the “AEDC Mean Fogging Water Result.”



This means that the **MLC/MPC** operated at the mean fogging water point, using the fan inlet totals of the experimental data, with a physical speed and flow corresponding to 100-percent design corrected speed and flow before the relative humidity vapor and fogging water were added. The previously calculated percent differences in corrected speed and corrected flow

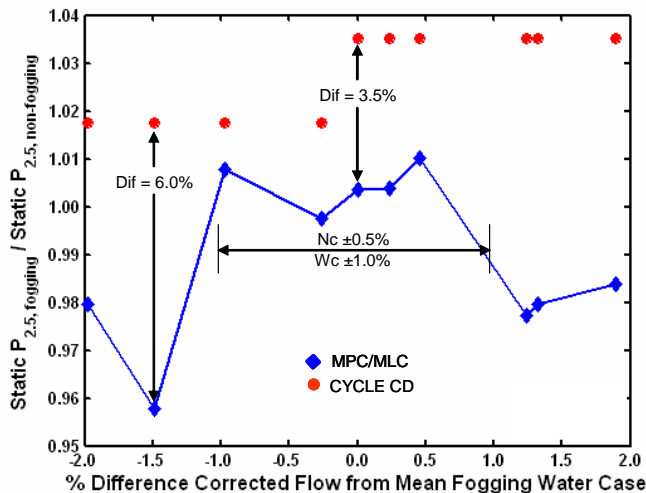


**Figure 3.286 Normalized Static Pressure for FT8 Validation with Fogging Water**

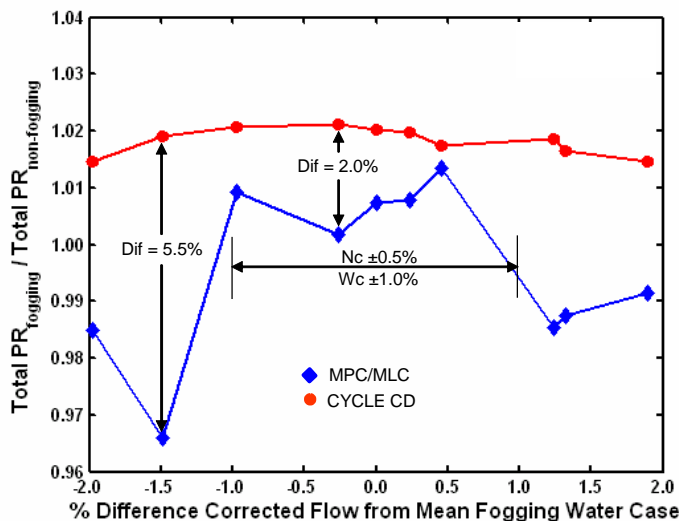


**Figure 3.287 Normalized Total Pressure Ratio for FT8 Validation with Fogging Water**

and the **MLC/MPC** simulation are depicted within green boxes in [Figure 3.285](#). The neighborhood of confidence about the mean fogging water point is defined in [Figure 3.285](#) as  $\pm 0.5$  and  $\pm 1.0$  percent difference in speed and flow, respectively. Within this neighborhood, there is a difference of 3.5 percent in exit static pressure ratio between experimental data and the **MLC/MPC** simulation and a maximum overall difference of 6.0 percent.

were applied to the **MLC/MPC's** 100-percent design corrected speed and flow simulation of the mean fogging water point to obtain proportional excursions in speed and flow for the remainder of the fogging water points. This process allowed the **MLC/MPC** to operate within a neighborhood of its calibrated point and simulate the adjacent fogging water data points at a specified speed and flow from the mean fogging data point. The only experimental data available at the exit of the LPC were static pressures for each fogging point. In the absence of additional experimental data, the cycle code results were used to provide exit total temperature and pressure to the LPC.

Static pressure from experimental data was provided at the exit of the LPC, station 2.5 of [Figure 3.281](#), for the fogging and the non-fogging water data points. A pressure ratio was constructed by normalizing the exit fogging water static pressure by the non-fogging water exit static pressure, and results of this exit pressure ratio are presented in [Figure 3.286](#). Additionally, the **MLC/MPC** simulations of the fogging and non-fogging water as defined previously in percent differences in corrected speed and flow were used to develop a normalized exit fan static pressure ratio, which is also presented in [Figure 3.286](#). The points used to obtain the normalizing exit static pressure for the experimental data

Exit total pressure and temperature for the LPC experimental data were unavailable; therefore, cycle code simulations with fogging water were used to provide predictions for exit total pressure and temperature for comparison with results from the **MLC/MPC**. The same non-fogging water point defined earlier, specifying relative humidity and ambient conditions similar to those of the fogging water experimental data points, was used to construct an LPC pressure ratio and temperature ratio to normalize the cycle code pressure ratio and temperature ratio, respectively.

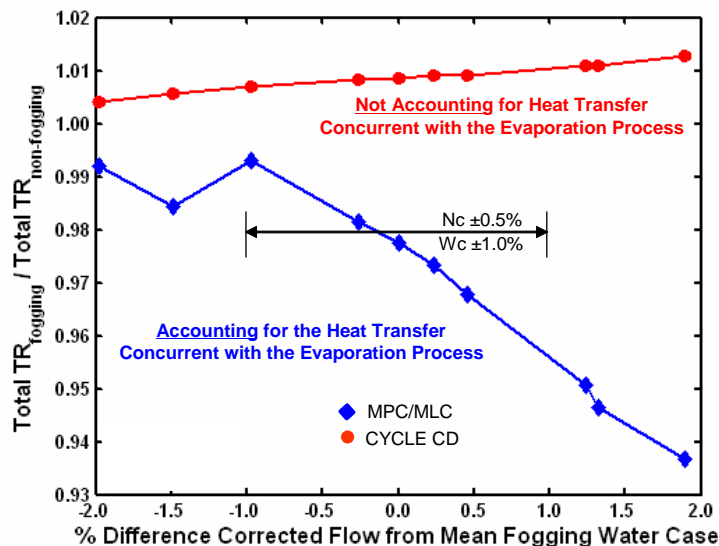


**Figure 3.288 Normalized Total Temperature Ratio for FT8 Validation with Fogging Water**

The results obtained are presented in [Figure 3.287](#) and [Figure 3.288](#). Similarly, the **MLC/MPC** was executed with the same ambient conditions as the non-fogging water experimental data and resulted in a non-fogging water LPC pressure and temperature ratio used to normalize the **MLC/MPC** simulation of the fogging water. The normalized LPC total pressure and temperature ratios are also plotted in [Figure 3.287](#) and [Figure 3.288](#).

The normalized total pressure ratio of [Figure 3.287](#) shows a result that is very similar to that of the exit static pressure ratio already discussed and previously presented in [Figure 3.286](#). The open literature correlations of the **MLC/MPC** restrict predictions away

from a calibrated point to be within a neighborhood of  $\pm 1$  percent difference in corrected flow and  $\pm 0.5$  percent difference in corrected speed. The results for the normalized total pressure ratio between the two simulations are within 2.0 percent at the mean fogging water point with a max overall difference of 5.5 percent.

A comparison of normalized total temperatures between the **MLC/MPC** simulation and the cycle code simulation for each of the fogging water points is presented in [Figure 3.288](#). The results are very different, and this difference becomes more pronounced as the simulation processes increasing amounts of fogging water. **The cycle code results do not account for the effects of heat transfer concurrent with the evaporation process through the LPC simulation while the MLC/MPC does account for these effects.** The **MLC/MPC** tracks the evaporation process through the LPC and accounts for the heat transfer between the water vapor and the air entering the LPC (defined by the gas-only control volume) to the evaporating liquid (defined by the two-phase control volume) throughout the simulation. The evaporation process has the effect of cooling the water vapor and the air of the working fluid moving through the LPC, thus causing a decrease in the exit total temperature with an increase in fogging water.

#### **ADDITIONAL REFERENCES:**

**3.185** "Willbanks, C.E. and Schulz, R.J. "Analytical Study of Icing Simulation for Turbine Engines in Altitude Test Cells." AEDC-TR-73-144 (AD-770069), November 1973.

**3.186** Smith, S.L. "1-D Meanline Code Technique to Calculate Stage-by-Stage Compressor Characteristics." M.S. Thesis, The University of Tennessee, Knoxville, TN, 1999.

### 3.5.3 Steam Ingestion Predictions for a Modern Military Compression System

This capability was produced to provide predictions of the effects of steam ingestion on military compression system performance and operability, especially for Navy aircraft operating from carriers. To provide an example, an analysis of the effects of steam on both a typical modern fan and a HPC was conducted.

#### EXAMPLE(S) CITED

**3.187** Hale, Alan, Klepper, Jason, and Hurwitz, Wayne, "A Numerical Capability to Analyze the Effects of Water Ingestion on Compression System Performance and Operability," ASME Paper #GT2005-68480, 2005 ASME Turbo Expo, June 2005.

#### MODELING TECHNIQUE

Development of a steam ingestion modeling technique required a one-dimensional (1-D) **multiphase code** [3.188] and a 1-D compressor **meanline code** [3.189]. An in-depth discussion of these codes can be found in [Section 4.10](#).

A modeling and simulation technique has been developed to use a one-dimensional (1-D) multiphase code and a 1-D compressor **meanline** code to investigate the effects of water ingestion. The **multiphase** code primarily accounts for the heat transfer associated with the phase change of water, and the **meanline** code uses the heat transfer and gas properties to model the flow properties through a compression system. The combination of the **meanline** and the **multiphase** code will be known as the **MLC/MPC**.

#### FAN ANALYSIS – CORRECTED MAPS WITH AIR AND WATER

With the inclusion of water for turbomachinery, traditional corrected performance maps obtained through similitude relationships are modified to include the effects of water. The relationships used to correct the mass flow and speed with the inclusion of water are represented in [Eqns. 3-8](#) and [3-9](#), respectively.

$$\dot{m}_c = \frac{\dot{m}_G \sqrt{\frac{R_G}{\gamma_G} \frac{T}{T_{ref}}}}{\frac{P}{P_{ref}}} \quad \text{Eqn. 3-8}$$

$$N_c = \frac{N}{\sqrt{\gamma_G R_G \frac{T}{T_{ref}}}} \quad \text{Eqn. 3-9}$$

There are five parameters that could be varying with the addition of vaporization occurring in turbomachinery, each of which could change the incidence on a blade row either more positive (toward stall) or more negative (toward choke). To understand how each of these parameters affects incidence and, therefore, performance, the following discussion assumes only one parameter varies at a time. As **gas mass flow** increases, the incidence will tend to move toward choke, while a reduction in gas mass flow would move the incidence toward stall. An

increase in the **gas constant** will increase the corrected flow and decrease the corrected speed, thus moving the incidence toward choke. A change in the **specific heat ratio** will cause the same proportional change in corrected flow and corrected speed, resulting in no change in the incidence. A decrease in the **total temperature** will cause a decrease in the corrected flow and an increase in the corrected speed, and thus an increase in the incidence moving the blade toward stall. An increase in **total pressure** will have no effect on corrected speed, but it will decrease the corrected flow and cause the incidence to move toward stall.

In a compression system, all of the parameters could be changing at the same time, making it difficult to account for the effects of each individual parameter. Generally, however, when water vapor only is included (no vaporization occurring), the incidence tends to move toward choke, reflecting the changes that occur with the increase in the gas constant. Also, with vaporization of liquid water particles in the compressor, the trend is to lower the temperature in front of a rotor, thereby increasing the incidence as is consistent with the decrease in inlet temperature from the dry fan.

Predictions of the corrected maps are presented to obtain an understanding of how the fan would behave dry and in the presence of vapor and liquid water. **Figure 3.289** and **Figure 3.290** show a single-speed line on these corrected pressure- and temperature-ratio maps. In the figures, same symbols represent constant corrected gas mass flow, while same colors represent same liquid water mass flow. The heavy black line is a portion of the **MLC/MPC** predicted dry speed line. The only calibrated point is the military power point, and this calibration is held constant for all other points on the corrected maps.

For each of the four corrected mass flow settings, five varying water cases were run. Two corrected mass flows are less than the military power point, and one is greater. The first varying water case (black) is the dry case with no water (liquid or vapor). All subsequent varying water cases are run with a relative

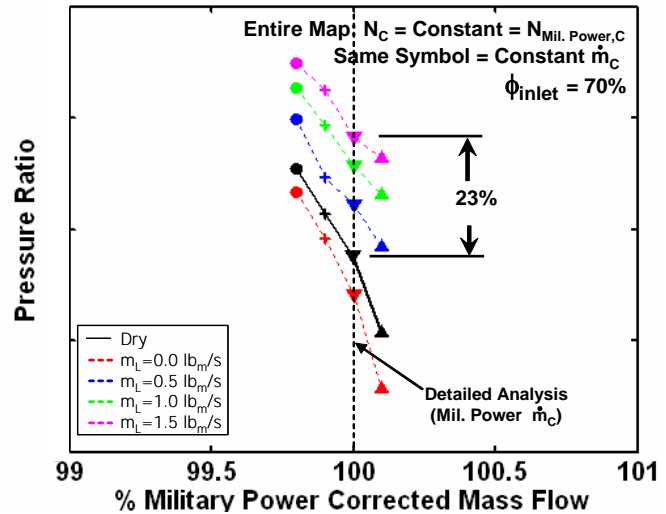


**Figure 3.289 Predicted Fan Pressure Ratio vs. Corrected Gas Mass Flow for Various Liquid Water Loading Factors**

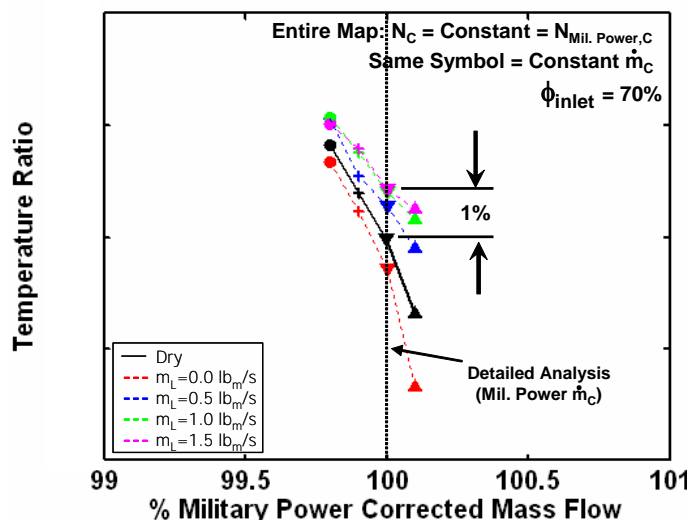


**Figure 3.290 Predicted Fan Temperature Ratio vs. Corrected Gas Mass Flow for Various Liquid Water Loading Factors**

humidity,  $\phi_{\text{inlet}}$ , of 70 percent at the fan inlet. This translates to 1.2 lb<sub>m</sub>/sec (0.544 kg/sec) of water vapor, which corresponds to a mass fraction of water vapor of  $3.65 \times 10^{-3}$ . The second varying water case (red) includes the specified water vapor only. The next three varying water cases include both the specified water vapor and uniformly increasing liquid water mass flows of 0.5 lb<sub>m</sub>/sec (0.227 kg/sec) (blue), 1.0 lb<sub>m</sub>/sec (0.454 kg/sec) (green), and 1.5 lb<sub>m</sub>/sec (0.68 kg/sec) (magenta). For each of the varying water cases, the same four inlet corrected gas mass flows are used. For the three varying liquid water cases, the initial water particle temperature is 560°R (311.1 °K), the initial particle velocity is equal to the local inlet gas velocity, and the initial particle diameter is 15 microns.

On a pressure ratio performance map, the addition of only water vapor causes each dry point to shift the corrected speed line to the left and results in both a decrease in performance and a movement toward choke. For each vapor-only point, as additional liquid water is included, the corrected speed shifts to the right, resulting in both an increase in performance and a reduction in stall margin. Meacock, et. al [3.190] observed a similar trend in pressure ratio performance with liquid water injection and describes the effect as an apparent increase in corrected speed. Similarly to the pressure ratio map, the water vapor-only case causes a decrease in temperature ratio. As liquid water is included, the temperature ratio is always greater than the vapor-only case. However, at the lower mass flows, additional liquid water may not cause a continual increase in temperature ratio because of vaporization.

### Fan Analysis: Liquid Water Parametric Study

A detailed analysis of the military power point is presented in [Figure 3.291](#) through [Figure 3.295](#) to show how the fan performance varied (five cases) through the machine for a constant corrected mass flow and constant corrected speed for a dry case, a water vapor-only case, and three varying amounts of liquid water cases. The location of the inlet guide vanes and rotors R1 through R3 are explicitly highlighted in [Figure 3.291](#) through [Figure 3.295](#).

Indicated in [Figure 3.291](#) is the mass fraction of water vapor for each of the cases in the parametric study. The dry case has a mass fraction of water vapor of zero throughout the entire compression system (and thus it lies on the abscissa of [Figure 3.291](#)) since no

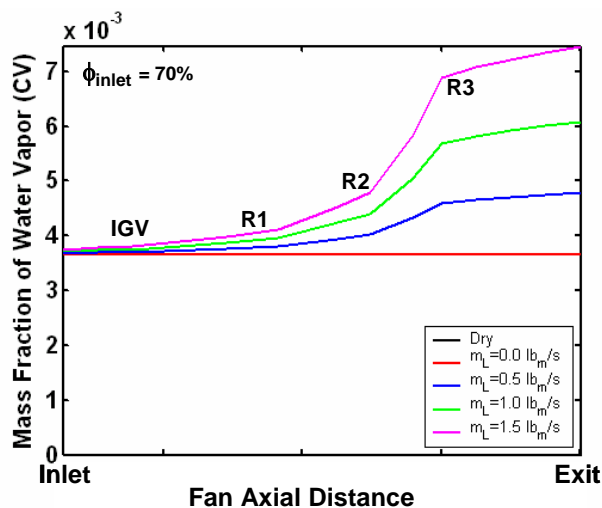


**Figure 3.291 Mass Fraction of Water Vapor vs. Axial Distance**

water in liquid or vapor form is present. For each of other cases, the inlet mass fraction of water vapor is held constant to a value of  $3.65 \times 10^{-3}$ . For the case with no liquid water ( $m_L = 0.0$  lb<sub>m</sub>/s), the mass fraction of water vapor is constant through the entire fan since no liquid water is present to be vaporized. For each of the other cases where liquid water is included, more liquid water is available to be vaporized, thus increasing the mass fraction of water vapor through the fan.

[Figure 3.292](#) illustrates what happens to the liquid water content through the fan. For the dry and vapor-only case, no liquid water is present; therefore, the liquid water loading factor is zero through the

entire fan. For the three water cases, the liquid water loading factor is decreasing through the fan as more vaporization occurs. For each of the liquid water cases, only a small portion of the inlet liquid water amount is still present at the exit of the fan.

To get a better idea of the effects of the water ingestion on compressor performance, it is best to examine [Figure 3.293](#) through [Figure 3.295](#) together. First, the performance with the inclusion of water vapor only is examined; then, the results with liquid water are analyzed.

For the case with water vapor only, the general effect on the entire fan is to decrease the incidence and move the overall machine more toward choke. Because no liquid water is included at the inlet, no vaporization occurs in the fan. This has the effect of changing only the properties of the gas because of the less dense water vapor present. The gas constant increases (as is the case with the addition of water vapor), the corrected gas mass flow will increase, and the corrected speed will decrease, resulting in the incidence moving more in the choke direction. This is evidenced by looking at [Figure 3.293](#) and discovering that the incidence decreases. This results in a decrease in pressure ratio ([Figure 3.294](#)) and a corresponding decrease in temperature ratio as well ([Figure 3.295](#)) for Rotor 3.

With the inclusion of liquid water in addition to the inlet vapor water, vaporization occurs, and the effect on the fan is different. Because the liquid water drops are warmer than the surrounding gas, heat is transferred to the gas, causing it to warm slightly at the inlet to both the IGV and Rotor 1. This causes a very slight decrease in incidence for Rotor 1. However, some vaporization does occur across Rotor 1, causing a slight increase in total pressure ratio ([Figure 3.294](#)), and a slight decrease in temperature ratio ([Figure 3.295](#)).

As the vaporization continues across Stator 1, the inlet temperature to Rotor 2 for most of the water cases is decreased to a value below that of the dry inlet. The lower temperature at the inlet of Rotor 2 should cause an increase in the incidence of Rotor 2, which is shown in [Figure](#)

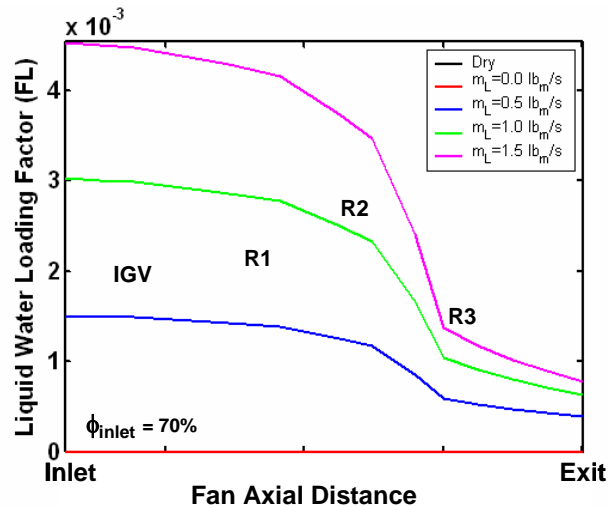


**Figure 3.292 Liquid Water Loading Factor vs. Axial Distance**

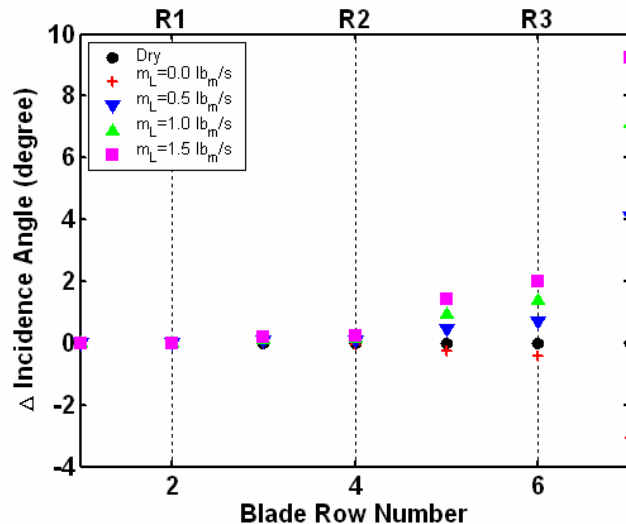


**Figure 3.293 Change in Blade Incidence Angle from Dry vs. Blade Row**



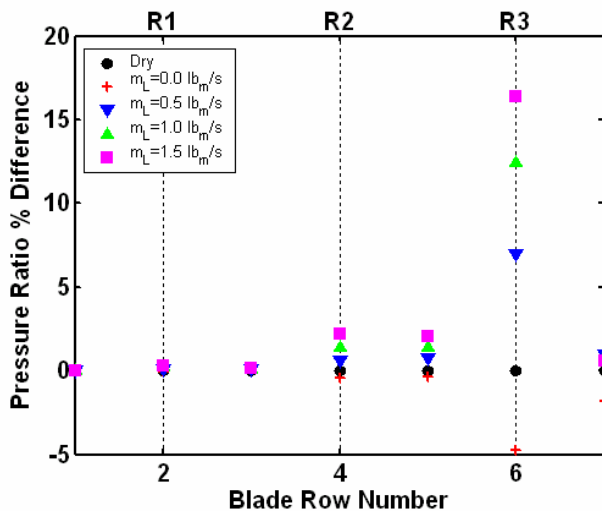


**Figure 3.294 Per Blade Row Pressure Ratio Percent Difference from Dry vs. Axial Distance**

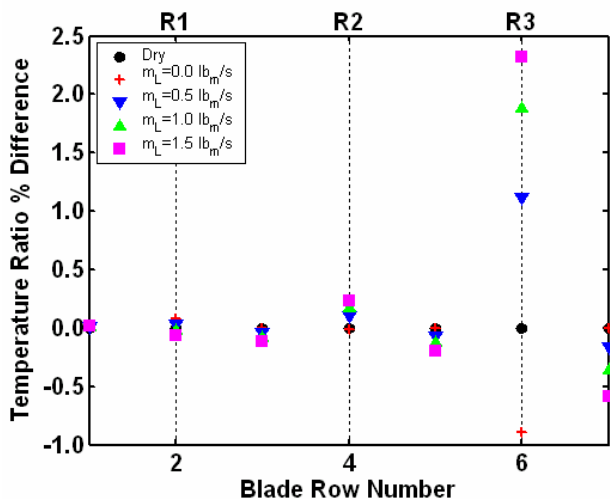


**Figure 3.295 Per Blade Row Temperature Ratio Percent Difference from Dry vs. Axial Distance**

**3.293.** Because Rotor 2 moved off design, the pressure ratio illustrated in [Figure 3.294](#) increases. This off-design performance will also overcome the vaporization cooling effect on the temperature ratio, as seen in [Figure 3.295](#), and actually cause an increase in total temperature ratio across Rotor 2. Even if no further vaporization occurred, resulting change in exit flow conditions of Rotor 2 will cause a change in performance of all subsequent blade rows.

Rotor 3 behaves similarly to Rotor 2 but with a more pronounced effect. Because of the higher exit temperature of Rotor 2, the evaporation rate increases. By the time the flow has moved through Stator 2, the inlet total temperature to Rotor 3 is once again below the dry condition for most water cases. Because of this effect and the change in flow conditions caused by the off-design performance of previous blade rows, the incidence for Rotor 3 increases in the stall direction. This change in incidence (about 2 deg as shown in [Figure 3.293](#)), results in a pressure ratio ([Figure 3.294](#)) change of over 16 percent for Rotor 3 alone, and a temperature ratio change of nearly 2.5 percent.

## Fan Analysis Conclusions

Several conclusions can be drawn from the fan liquid water parametric study.

- Adding water vapor alone causes a change in the gas properties that results in a decrease in incidence on the blades and moves the fan off-design in the choke direction.
- As vaporization occurs with the inclusion of liquid water in addition to the water vapor, the effect is to reduce the temperature at the inlet of the rotors and, therefore, to drive the fan toward stall by increasing the incidence angle. This effect is more pronounced toward the back of the fan, where the temperatures are higher, allowing more vaporization. The off-

design movement of the previous blades continues to have the effect of moving the fan performance off-design. The more liquid water included, the more the effect on incidence and, therefore performance.

### **HPC ANALYSIS**

In addition to the fan analysis, a similar analysis of the corresponding high performance compressor (HPC) was also conducted. Results for the HPC were obtained and are summarized below.

- Adding water vapor alone causes a change in the gas properties that results in a decrease in incidence on the blades and moves the HPC off design in the choke direction. The same phenomenon was observed in the fan.
- As vaporization occurs with the inclusion of liquid water in addition to the water vapor, the effect is to reduce the temperature at the inlet of the rotors and, therefore, to drive the HPC toward stall by increasing the incidence angle. After all the liquid water is evaporated, the HPC continues to move toward stall. This appears to happen because the off-design behavior of the blade rows that had vaporization tends to cause the downstream blade rows to continue to move off-design in the stall direction to increase both the pressure ratio and temperature ratio of each rotor.

### **ADDITIONAL REFERENCES:**

**3.188** Willbanks, C.E. and Schulz, R.J. "Analytical Study of Icing Simulation for Turbine Engines in Altitude Test Cells." AEDC-TR-73-144 (AD-770069), November 1973.

**3.189** Smith, S.L. "1-D Meanline Code Technique to Calculate Stage-by-Stage Compressor Characteristics." M.S. Thesis, The University of Tennessee, Knoxville, TN, 1999.

**3.190** Meacock, A. J., and White, A. J., "The Effect of Water Injection on Multi-Spool Gas Turbine Behavior", ASME Paper GT2004-53320, June 2004.

## CHAPTER 4 TABLE OF CONTENTS

4	Numerical Simulations – Technical Details .....	273
4.1	An Overview of Codes and Technical Approaches.....	274
4.2	Meanline Code (MLC) Technical Approach.....	283
4.3	Streamline Curvature Code, SLCC, Technical Approach .....	286
4.4	1D Dynamic Compression System Technical Approach,.....	304
4.3.1	Single Spool DYNMOD & DYNTTECC .....	305
4.3.2	Dual Spool DYNMOD & DYNTTECC .....	318
4.5	1D Dynamic Engine Code, ATEC, Technical Approach .....	321
4.6	Parallel Compression System Code.....	345
4.7	3D Euler Code, TEACC & TEACCSTALL Technical Approach .....	351
4.8	ALE3D Technical Approach .....	366
4.9	Turbomachinery CFD Codes, Turbo & Overflow, Technical Approach .....	369
4.10	Water/Steam Ingestion Technical Approach .....	376
4.11	Integration of ML & DYNTTECC, Technical Approach .....	383

### 4 NUMERICAL SIMULATIONS – TECHNICAL DETAILS

The two predominant means of evaluating new compressor designs are experimental and computational. The advantages of experimental testing are more accurate and reliable results. Therefore, physical testing is required prior to implementation of a new design. The advantages of computational simulation are speed, reduced cost, more data, and rapid design modifications. Due to time and cost considerations involved in experimental testing of new compressors, computational simulations have been used more extensively in recent years. Through the use of advanced and accurate computer simulations, much of the preliminary experimental testing may be reduced to a minimum level.

When an operability capable model is used, the model capability and fidelity is generally limited by the model characteristics available for the system. The simulation will often be a trade-off between what is desired for model capability and fidelity and what can be achieved with the available operability models.

Model characteristics important for consideration are:

- **Accuracy** - Does it match reality for overall component-performance?
- **Detail** - Does it provide all parts of the model at the required level?
- **Fidelity** - Does it model all of the components at the required level of detail? (Average, Radial Profile, 3-D, Boundary Layer)
- **Functionality** - Does it have the required capability? (Stall Performance, Dynamic Effects, Recoverability, Distortion Analysis, 3D Effects)
- **Complexity** - Execution speed, data required, model expertise required, computer limitations
- **Range of Operation** - Off-design, low and high speed
- **Compatibility with System Model and Other Component Models** - Installation and use in system simulation, development overhead, consistency with accuracy and functionality of other models

Since nearly the beginning, AEDC has been involved in turbine engine operability testing. To gain a better understanding of operability, AEDC began to develop numerical simulation techniques to model compression system operability. Since then, several codes with various complexities and abilities have been developed to investigate operability issues. The codes range from steady-state to dynamic, lumped component to fully three dimensions. This chapter provides a brief overview followed by specific technical detail of each type of modeling technique.

#### 4.1 AN OVERVIEW OF CODES AND TECHNICAL APPROACHES

Advances in physical knowledge of fluid flow, rotating machinery and combustion, coupled with advances in computational speed and capacity have resulted in improvements in turbine engine computational models. These models are generally combinations of empirical data and computational methods with a multitude of computational paths dependent on operating conditions. These models have a range of computational fidelity that allow the user to pick an appropriate simulation capability based upon his understanding of the accuracy requirements and the timing of the required information. This section provides a brief overview of the models developed or co-developed at AEDC for this purpose. In general, the codes are presented from the simplest to the most complex formulation.

##### MEANLINE AND STREAMLINE CURVATURE PERFORMANCE SIMULATIONS

Although the **Meanline code**, **MLC**, and Streamline Curvature code, **SLCC** identified in this sub-section may have limited capability to predict the effects of spatial or temporal inlet flow distortion by themselves, they have been used in combination with other techniques that use what these codes produce and as such should be mentioned in this document.

A **Meanline** code is, in general, a compressible, 1-D, steady state, row-by-row characteristics solver [4.1]. The purpose of a **meanline** code is to provide a rough estimate of the overall performance of a compression system that is characterized by the blade geometry at the mean radius. A meanline code generally assumes a perfect gas with constant properties, inviscid flow and adiabatic walls upstream and downstream of the blades and constant rothalpy within the single streamtube through the blades. Semi-actuator disks replace the blade rows, and all of the losses and inefficiencies that are manifested in the span of the blade are modeled by loss and deviation correlations associated at the mean radius as illustrated in **Figure 4.1**. In addition, losses due to hub and casing boundary layers are negligible at the meanline, as are many secondary flow effects. It is also beneficial that because radial effects can be neglected, the radii of the meanline streamline remains relatively constant as opposed to the radii of hub and tip streamlines. Blade row stall is generally approximated by using empirically determined methods such as diffusion factors or DeHaller velocity ratios.

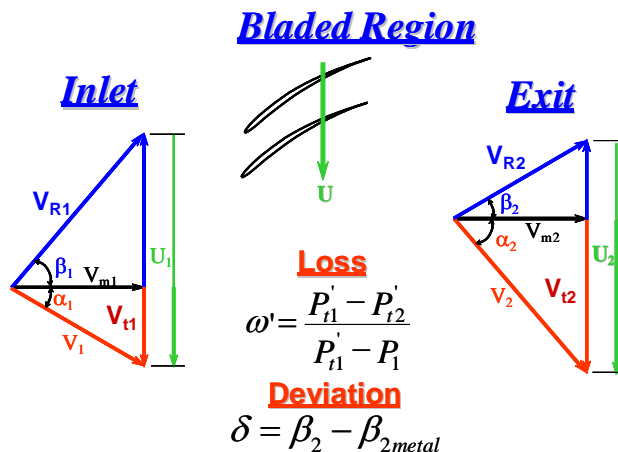


**Figure 4.1 Meanline Theory In Terms of Velocity Diagrams**

A streamline curvature code is a computer program that solves an axisymmetric, annular flow field [4.2 and 4.3]. The flow is assumed to be an inviscid, perfect gas with no transfer of mass, momentum, or energy between adjacent streamlines. Streamlines are defined as lines, which are tangent to the velocity vectors throughout the flow field. A **SLCC** method assumes an inviscid, axisymmetric, adiabatic, steady state flow with no body forces. The governing equations are continuity, circumferential momentum, axial momentum, radial momentum, energy, entropy and the ideal gas Eqn. of state. The inputs required by a **SLCC** are the overall annulus geometry, blade geometry, and a radial distribution of inlet total temperature, total pressure, swirl angle, and loss and deviation correlations which are sensitive to the local flow field. The annulus geometry is divided into a series of axial stations that need not necessarily be radial but may be leaned, or inclined, at an angle with respect to the radial direction to facilitate placement at locations of interest, such as the leading- and trailing-edge blade angles. Initial estimated streamlines are then set up radially to create a computational grid. The slopes of the streamlines are assumed to be zero far from the bladed regions at the inlet and exit. A schematic of **SLCC** inputs and how the annulus is divided into a computational grid is illustrated in Figure 4.2.

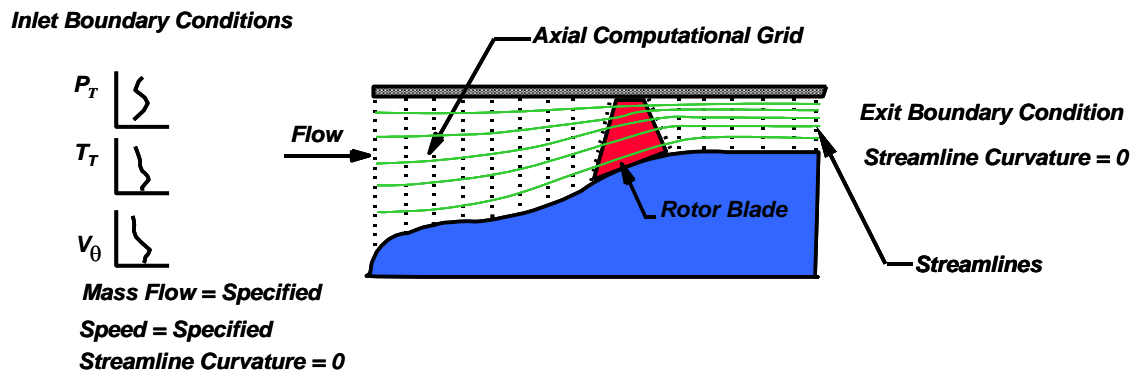


Figure 4.2 Streamline Curvature Code Computational Grid

Because of the complexity of the flows involved in the bladed region, the **SLCC** does not directly model the bladed region. Empirically derived loss and deviation correlations provide the relative total pressure loss coefficient and flow deviation across a bladed region. The correlations for both loss and deviation are generally experimentally derived. With loss and deviation provided by the correlations at each streamline, the closure relations that specify the change in enthalpy, entropy, and angular momentum across a blade row are obtained. The exit parameters calculated by the **SLCC** method are exit swirl velocity, exit total temperature, and exit total pressure. A major deficiency of the **SLCC** method is that there is not a prior method for determining blade stall. Generally, that information is supplied by experimental data. The correlations for blade loss and deviation generally do not supply specific information about blade stall for other than simple blade shapes.

An excellent example of a Streamline Curvature Code is one developed by Hearsey [4.3]. Another reference that provides a bit more of the technical details can be found in Cumpsty's textbook [4.2]. Loss and deviation correlations are the heart of both the **MLC** and **SLCC** techniques. Correlations developed for NACA 65 Series, and Double Circular Arc can be found in NASA SP-36, Ref. 4.4. Recent improvements to some of the loss correlations and subsequent improvement in the prediction capability of the **SLCC** method were made by Boyer [4.5].

## ONE-DIMENSIONAL DYNAMIC MODEL

To aid in the analysis of engine performance and operability, one-dimensional gas turbine compression system mathematical models and simulations have been developed that can provide insight into physical phenomena, which may be difficult to understand using test data alone. The best-known effort that spawned a multitude of follow-on investigations was the original effort published by Greitzer [4.6 and 4.7] in 1976. His initial effort presents an instability theory based on system response to compressor stall and in addition presents test data to show the credibility of the theory. Greitzer's 1D theory of compression system instability addresses the system response once it has undergone an initial instability. It does not address the stall structure, cell propagation speed, interstage matching or any other aerodynamic feature of compressor stall. It simply uses the overall performance characteristic to obtain response similar to rotating stall and to surge. Greitzer's model uses the fact that the typical compressor instability limit is the cause of system instability because of the discrete change in performance characteristics. The system model postulated by Greitzer consists of a compressor followed by a length of duct leading to an exhaust plenum. The plenum is connected to an exhaust duct with a throttle valve at the exit of the duct. The flow is discharge to the atmosphere. Greitzer model is based upon the conservation of mass, momentum and energy with the following major assumptions:

- The compressor performance is represented by a single map (i.e no breakout for blade rows or stages)
- The compressor volume is negligible
- The compressor is represented by an actuator disk
- The flow is incompressible

During the 80's many investigators used the concepts formulated by Greitzer's simple model and embellished upon those concepts. Stage-by-stage or row-by-row models were developed and were used during the "Nonrecoverable Stall" investigations of the 1980's and are detailed in Refs. 4.8 - 4.13.

A short overview of the AEDC modeling technique [4.8] is provided in the following paragraphs. This modeling technique uses a finite difference numerical scheme to simultaneously solve the mass, momentum, and energy equation with or without **turbomachinery** source terms (mass bleed, blade forces, heat transfer, and shaft work).

The compression system source terms are determined from a complete set of stage pressure and temperature characteristics provided by the user. The combustor system source terms are determined from a complete specification of the fuel energy content, flammability limits, and combustion efficiency. A representative, single-spool, multi-stage compressor and combustor system is illustrated below. An overall control volume models the compressor and combustor system as illustrated in Figure 4.3. The overall control volume is

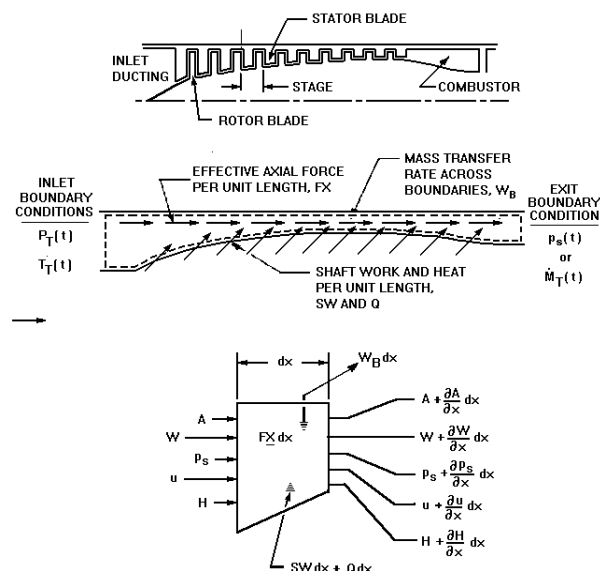


Figure 4.3 Control Volume Technique



subdivided into a set of elemental control volumes. Typically, the compressor section is subdivided by stages either as rotor-stator or stator-rotor, depending on how the experimental stage characteristics are obtained. Acting on the fluid control volume is an axial force distribution,  $FX$ , attributable to the effects of the compressor blading and the walls of the system. These effects are lumped together due to the difficulty of separately distilling the effect of each from experimental data. Appropriate inlet and outlet boundary conditions are applied at the inflow and outflow boundary locations. Energy supplied to the control volume includes the rate of heat added to the fluid,  $Q$ , and shaft work done on the fluid,  $SW$ . Mass transfer rates across boundaries other than the inlet or exit (e.g., interstage bleeds) are represented by the distribution,  $w_B$ .

Time dependent boundary conditions can be specified either at the entrance or the exit of the overall control volume. Inlet total pressure or temperature time history may be linearly ramped, varied cyclically, or remain constant. The same is true for the overall control volume exit pressure, Mach number, and airflow rate. At the entrance, both total pressure and total temperature must be specified. At the exit, however, only one parameter may be specified, usually static pressure or exit Mach number.

### **PARALLEL COMPRESSOR MODEL**

The one-dimensional modeling technique can also be modified for the analysis of distorted inflow via parallel compressor theory [4.14 - 4.18]. As indicated below, a parallel compressor model uses a multi-segmented circumferential compressor concept. Each circumferential segment is modeled using the one-dimensional technique. Each segment operates independently except at the exit boundary where the specification of either uniform static pressure or uniform Mach number is imposed. This is the only location where the modeling technique transfers information from one segment to another. Different levels of pressure or temperature distortion may be imposed upon the inlet, and each segment will operate to its own limit. In this classical form, when one segment reaches the instability limit the entire compression system is considered to be unstable. Using this approach, the mean operating point at instability is a weighted average of the low flow sector operating at the uniform flow stability boundary, and the high flow sector operating at some other point far from the stability limit as shown in Figure 4.4.

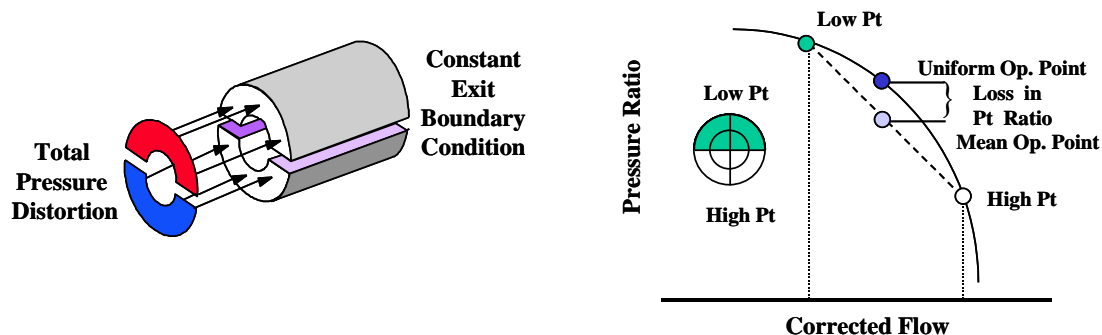


**Figure 4.4 Parallel Compressor Theory Concept**

The greatest loss in stability margin occurs with the narrowest distorted sector inlet. This leads to predictions that are inconsistent with experimental observations. For example, the theory would indicate that the whole compression system would be unstable for a 1-degree sector if that sector were stalled. Evidence indicates that there is a critical angle of extend that this

theory will work with. Some investigators suggest that 60 degrees or 6 segments is the limit. The implication is that it is possible for a small portion of the compressor annulus to operate beyond the observed stability limit provided that there is enough of the annulus operating on the stable side to maintain overall stability. Modifications to the pure parallel compressor theory to allow for circumferential crossflow between segments have been attempted by Sharokhi [4.17] with limited success. Extensions of the parallel concept for radial distortion require knowledge of the radial distribution of the flow and have thus far not proved to be fruitful. However, the parallel modeling technique has proven to work well for both classical pressure and temperature circumferential distortion as reported in Refs. 4.19 and 4.20, by Cousins and Hymes, respectively.

Parallel compressor models have also been used to analyze the effects of swirl on compression systems. For the parallel compressor approach to be utilized for the analysis of swirl, stage, blade-row or overall system maps must be generated that include the effects of swirl. These swirl-maps allow the different sectors of the parallel compressor containing different input swirls to operate at an appropriate operating point of the given off-design speed line. These swirl maps can be generated using a meanline code, a streamline curvature code or through experimentation. Examples of using a parallel compressor simulation for the analysis of swirl can be found in Refs. 4.21, & 4.22 by Davis and in Ref. 4.23 by Bouldin.

### THREE-DIMENSIONAL EULER MODEL.

An alternate approach to parallel theory for distorted inflow is the numerical solution of the full three-dimensional Euler Equations. This technique allows for circumferential and radial control volumes to interact directly with each other via Euler Equations with body forces representing the forces associated with a blade row. This technique allows the direct exchange of mass, momentum, and energy. One technical approach for the development of this technique is illustrated in Figure 4.5 as reported in Ref. 4.24 by Hale.

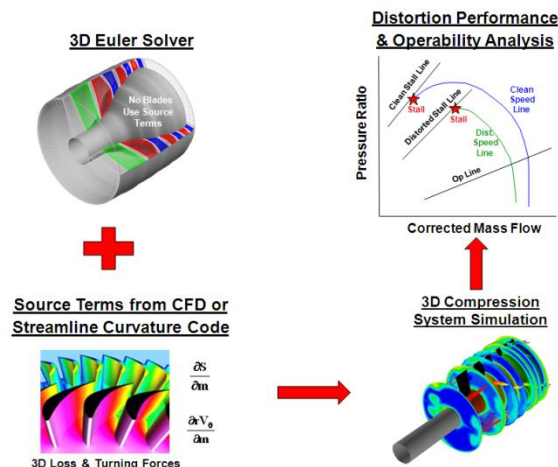


**Figure 4.5 3D Euler Technical Approach**

The governing equations used in the Euler technique are developed by applying the conservation of mass, momentum, and energy principles. In **turbomachinery** flows, the viscous effects predominate mostly along the wall, making accurate simulation of the flow field away from the wall possible by using the Euler equation with **turbomachinery** source terms. Three-dimensional blade force and rate of shaft work terms must be supplied by some other means. One method is the use of a streamline curvature code (**SLCC**) as detailed by Hearsey in Ref. 4.3. The **SLCC** is based on a radial redistribution of blade forces and shaft work, producing an “axisymmetric flow with swirl” in the form of streamlines. Necessary

inputs include overall geometry, blade geometry, and loss and deviation correlations. Blade row characteristics as a function of radius are another method used by Chima in [Ref. 4.25](#). The codes are used to model both steady-state performance and dynamic stall inception. Generally, the stalling of the compressor is determined by an imbalance of the forces based on the local flow field and source terms.

### THREE-DIMENSIONAL NAVIER-STOKES MODEL

The most complex form of modeling for inlet distortion effects uses 3-D **turbomachinery** Navier-Stokes codes. Although these types of codes require an extremely fine computational

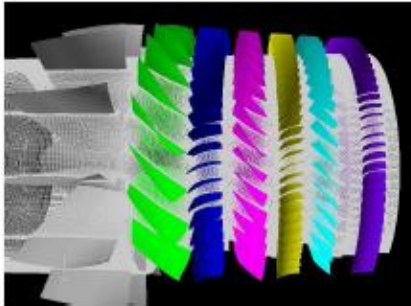


Figure 1. Computational domain and grid of the first multistage fan (not drawn to scale)

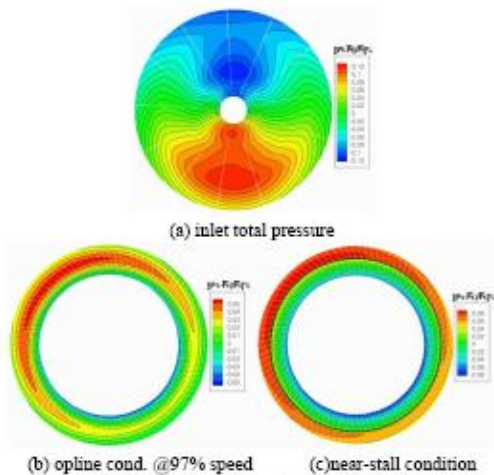


Figure 2. Boundary conditions of the first multistage fan. 1/rev total pressure distortion at inlet (a), and the static pressure distribution at stator-3 exit (b) and (c).  $[(P_t - \bar{P}_t)/\bar{P}_t]\%$  is plotted in (a),  $[(P_s - \bar{P}_s)/\bar{P}_s]\%$  is plotted in (b) and (c).

**Figure 4.6 Typical CFD Grid and Results with Inlet Distortion Taken from [Ref. 4.29](#)**

grid or mesh to solve the Reynolds Averaged Navier-Stokes, RANS, Eqn.s, there have been several investigations that compute the effects of a distorted inlet flowfield on compression system performance. It is also known that numerical solutions based on the RANS equations do not always predict absolute values of the aerodynamic loss in **turbomachinery**. However, it is widely accepted that the most important flow physics are properly captured and thus can be used to understand the flow mechanisms found within the **turbomachinery**. For analysis of inlet distortion using RANS CFD, full annulus simulations must be represented. Investigations into the use of RANS CFD and its accuracy was conducted by Yao, Gorrell, and Wadia and documented in [Refs. 4.28](#) and [4.29](#) and illustrated in [Figure 4.6](#). That work highlighted the distortion transfer process for two separate three-stage fans. A summary of some of their conclusions is presented below:

High fidelity CFD was demonstrated to be able to predict the distortion transfer accurately for multistage fans. The work split among the stages was accurately predicted as well. Even with inlet total pressure distortion alone, both fans investigated were able to see the distortion of total temperature and swirl generated in the multi-stage environment. Detailed analysis of the CFD results lead to a thorough understanding of the total

temperature distortion generation and transfer mechanism, especially for the spatial phase difference of total pressure and total temperature profiles.

**REFERENCES:**

- 4.1** Cohen, H., Rogers, G. F. C., and H. I. H. Saravanamuttoo, **Gas Turbine Theory**, Longman, Third Edition, 1987.
- 4.2** Cumpsty, N. A, **Compressor Aerodynamics**, Longman Scientific and Technical, 1989
- 4.3** Hearsey, R. M., "HTO300 – A Computer Program for the Design and Analysis of Axial turbomachinery", 1970
- 4.4** NASA SP-36 **Aerodynamic Design of Axial-Flow Compressors**, edited by Johnsen, I. A. and R. O. Bullock, 1965
- 4.5** Boyer, K.M. and W. F. O'Brien, "An Improved Steamline Curvature Approach for Off-Design Analysis of Transonic Axial Compression Systems", **Transaction of the ASME, Journal of Turbomachinery**, July 2003, Vol. 125, pp 475-481.
- 4.6** Greitzer, E. M., "Surge and Rotating Stall in Axial Flow Compressors, Part I: Theoretical Compression System Model", **ASME Journal of Engineering for Power**, Vol. 98, April 1978, pp.190-198.
- 4.7** Greitzer, E. M., "Surge and Rotating Stall in Axial Flow Compressors, Part II: Experimental Results and Comparisons with Theory", **ASME Journal of Engineering for Power**, Vol. 98, April 1978, pp 199-217.
- 4.8** Hale, A. A. and M. W. Davis, Jr., "DYNAmic Turbine Engine Compressor Code: **DYNTECC** -- Theory and Capabilities", AIAA Paper # AIAA-92-3190, July 1992.
- 4.9** Reynolds, G. G., and W. G. Steenken, "Dynamic Digital Blade Row Compression Component Stability Model: Model Validation and Analysis of Planar Pressure Pulse Generator and Two-Stage Fan Test Data", AFAPL-TR-76-76, August 1976.
- 4.10** Hosney, W. M., Bitter, S. J., and Steenken, W. G., "Turbofan Engine Non-recoverable Stall Computer Simulation Development and Validation", AIAA Paper # 85-1432, July 1985.
- 4.11** Ward, G. G., "Compressor Stability Assessment Program (Techniques for Constructing Mathematical Models of Compression Systems and Propulsion Systems)", Air Force Aero Propulsion Laboratory, TR-74-107, Vol. II, Wright-Patterson Air Force Base, OH, December 1974.
- 4.12** Davis, M. W., Jr., "A Stage-by-Stage Dual-Spool Compression System Modeling Technique", ASME Paper 82-GT-189, March 1982.
- 4.13** Hosney, W. M., and W. G. Steenken, "Aerodynamic Instability Performance of an Advanced High-Pressure-Ratio Compression Component", AIAA Paper # AIAA-86-1619, June 1986.
- 4.14** Mazzawy, R. S. "Multiple Segment Parallel Compressor Model for Circumferential Flow Distortion." **Transactions of the ASME, Journal of Engineering for Power**, April 1977, pp. 288-296.

- 4.15** Tesch, W. A., and Steenken, W. G., "Blade Row Dynamic Digital Compressor Program, Vol. 1, J85, Clean Inlet Flow and Parallel Compressor Models", NASA CR-134978, Lewis Research Center, Cleveland, OH, March 1976
- 4.16** Longley, J. P. and Greitzer, E. M. "Inlet Distortion Effects in Aircraft Propulsion System Integration." AGARD-LS-183. Advisory Group for Aerospace Research & Development Lecture Series, May 1992.
- 4.17** Shahrooki, K. A., and M. W. Davis, Jr., "Application of a Modified Dynamic Compression System Model to a Low-Aspect Ratio Fan: Effects of Inlet Distortion," AIAA-95-0301, January 1995
- 4.18** Davis, M., Jr., "Parametric Investigation into the Combined Effects of Pressure and Temperature Distortion on Compression System Stability", AIAA Paper # AIAA-91-1895, June 1991.
- 4.19** Cousins, William T., et. al., "Inlet Distortion Testing and Analysis of a High-Bypass Ratio Turbofan Engine" Presented at the 16<sup>th</sup> International Symposium on Air Breathing Engines" Paper # ISABE-2003-1110, August, 2003.
- 4.20** Hynes, T. P. and E. M. Greitzer, "A Method for Assessing Effects of Inlet Flow Distortion on Compressor Stability", Transaction of the ASME, Journal of Turbomachinery, Vol. 109, pp 371-379.
- 4.21** Davis, Milt, and Hale, Alan, "A Parametric Study on the Effects of Inlet Swirl on Compression System Performance and Operability Using Numerical Simulations", GT2007-27033, May 2007
- 4.22** Davis, Milt, Jr., Beale, Dave, and Sheoran, Yogi, "Integrated Test and Evaluation Techniques as Applied to an Inlet Swirl Investigation Using the F109 Gas Turbine Engine", GT2008-50074, June 2008.
- 4.23** Bouldin, B. and Sheoran, Y., "Impact of Complex Swirl Patterns on Compressor Performance and Operability Using Parallel Compressor Analysis", ISABE2007-1140, September 2007
- 4.24** Hale, A. A., and W. F. O'Brien, "A Three-Dimensional Turbine Engine Analysis Compressor Code (TEACC) for Steady-State Inlet Distortion, " Transaction of the ASME, Journal of Turbomachinery, Vol. 120, July 1998, pp. 422-430.
- 4.25** Chima, R. "A Three-Dimensional Unsteady CFD Model of Compressor Stability" , ASME Paper GT2006-90040, May 2006.
- 4.26** Davis, Milt, Hale, Alan, and Beale, Dave. "An Argument for Enhancement of the Current Inlet Distortion Ground Test Practice for Aircraft Gas Turbine Engines," Transaction of the ASME, Journal of Turbomachinery, April 2002, pp. 235-241.
- 4.27** Hale, Alan, Milt Davis, and Jim Sirbaugh, "A Numerical Simulation Capability for Analysis of Aircraft Inlet-Engine Compatibility", Journal of Engineering for Gas Turbines and Power, Vol. 128, July 2006, pp. 473-481.

**4.28** Yao, J., Gorrell, S. E., and Wadia, A. R., “High-Fidelity Numerical Analysis of Per-Rev-Type Inlet Distortion Transfer in Multistage Fans – Part I: Simulations with Selected Blade Rows”, ASME Paper GT2008-50812, June 2008. – To Be Published in the Journal of Turbomachinery -- 2009

**4.29** Yao, J., Gorrell, S. E., and Wadia, A. R., “High-Fidelity Numerical Analysis of Per-Rev-Type Inlet Distortion Transfer in Multistage Fans – Part II: Entire Component Simulation and Investigation” ASME Paper GT2008-50813, June 2008. -- To Be Published in the Journal of Turbomachinery -- 2009



## 4.2 MEANLINE CODE (MLC) TECHNICAL APPROACH

The objective of this section is to define terminology, definitions, notation, and sign convention used in 2-D linear cascade analysis. **Figure 4.7** illustrates the absolute and relative flow velocities in an axial flow cascade.

As the cascade blades are moving with velocity  $U$  in the  $-\theta$  direction, it is convenient to view the fluid velocity from the perspective of a cascade blade in order to simplify blade row performance evaluation. This is known as switching from the absolute to the relative frame of reference. The absolute velocities and flow angles are expressed as  $V_i$  and  $\alpha_i$ , respectively, and the relative velocities and flow angles are expressed as  $W_i$  and  $\beta_i$ , respectively. In order to relate absolute

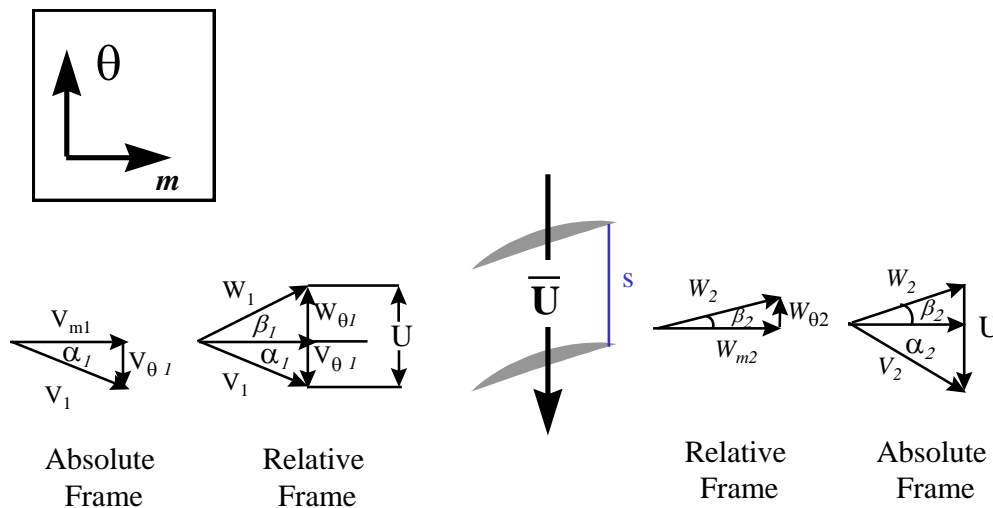


**Figure 4.7 Axial Flow Compressor Cascade Geometry and Velocity Triangles**

to relative reference frames or vice versa, one need only apply the vector sum as shown in **Eqn 4.-1**

$$\bar{W} = \bar{V} - \bar{U}$$

**Eqn. 4-1**

Loss and deviation correlations are presented as functions of blade geometry. Therefore, it is critical to understand blade terminology in order to correctly apply the correlations. **Figure 4.8** is a schematic of a blade with several definitions noted.

In **Figure 4.8**, the chord ( $c$ ) is the distance from the leading edge to the trailing edge of the airfoil. The leading edge radius (LER) and trailing edge radius (TER) are used to measure the blade thickness at the inlet and exit of the blade. The camber line is that line which represents the mid-thickness of the blade between its pressure and suction sides at every point along the airfoil. The length of the camber line is often referred to as the camber length. The blade angles  $\beta'_1$  and  $\beta'_2$ , also called the metal angles, are those between the meridional axis ( $m$ ) and the line tangent to the camber line at the blade leading and trailing edges, respectively. Deviation ( $\delta$ ) is defined as the difference between the exit relative flow angle  $\beta'_2$  and the blade exit metal angle  $\beta'_2$  (see **Eqn 4.-3**). The angle formed between the chord line and the meridional axis is referred to as the stagger angle ( $\xi$ ). The maximum thickness between the pressure and suction sides of the airfoil is  $t_{\max}$ . Although not shown in **Figure 4.8**,  $a$  is the distance along the chord from the leading edge of the blade to the point of maximum camber,

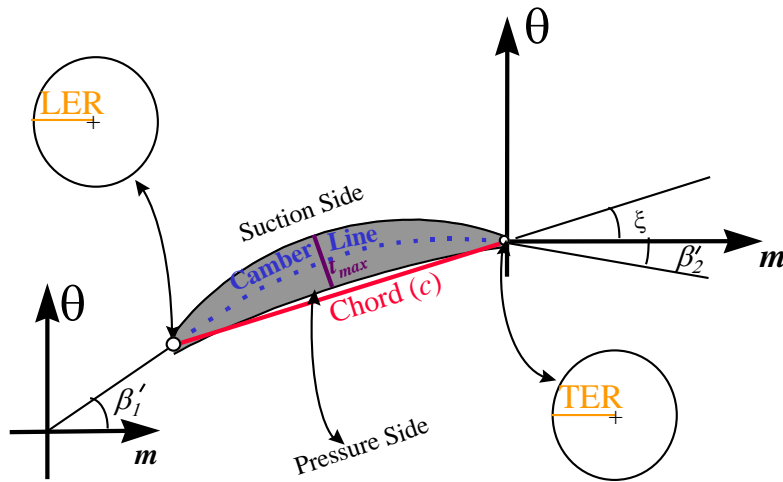


**Figure 4.8 Axial Flow Compressor Blade Geometry**

$$\theta' = \beta'_1 - \beta'_2$$

$$\sigma = \frac{s}{c}$$

which occurs where there is maximum displacement between the camber line and the chord line. The spacing ( $s$ ) is the distance between blades in the  $\theta$  direction. **Eqn.s 4-2** through **4-6** represent some blade geometry definitions as expressed in Eqn. form:

$$i = \beta_1 - \beta'_1 \quad \text{Eqn. 4-2}$$

$$\delta = \beta_2 - \beta'_2 \quad \text{Eqn. 4-3}$$

$$\alpha^* = \beta_1 - \xi \quad \text{Eqn. 4-4}$$

$$\theta' = \beta'_1 - \beta'_2 \quad \text{Eqn. 4-5}$$

$$\sigma = \frac{s}{c} \quad \text{Eqn. 4-6}$$

These geometry definitions include the incidence angle ( $i$ ), deviation angle ( $\delta$ ), angle of attack ( $\alpha^*$ ), camber angle ( $\theta'$ ), and cascade solidity ( $\sigma$ ).

The 1-D compressor meanline code used is the AEDC Meanline Code (**MLC**) [4.30]. The **MLC** works by taking the blade inlet total pressure, total temperature, and geometry to calculate the static conditions on the basis of isentropic relationships. Velocity triangles are developed from these static parameters. Next, flow conditions in the relative-to-the-blade-row frame of reference are determined.

Loss and deviation correlations [4.31] are then used to step across the bladed region. These correlations are the same Hearsey correlations used in the **SLCC** (Section 4.3). The relative total pressure loss coefficient and the blade deviation calculated by the correlations, along with the given geometry, are used to determine relative total pressure and total temperature ratios. The inlet mass flow function ( $MFF_1$ ) is then calculated by **Eqn 4-7**.

$$MFF_1 = \frac{\dot{m}_G \sqrt{T'_{t1}}}{P'_{t1} A_1} \quad \text{Eqn. 4-7}$$

The relative total pressure ratio, relative total temperature ratio, and area ratio are then used to calculate the blade exit mass flow function ( $MFF_2$ ) with the relationship presented in **Eqn 4-8**.

$$MFF_2 = MFF_1 \left( \frac{P'_{t1}}{P'_{t2}} \right) \sqrt{\frac{T'_{t2}}{T'_{t1}}} \left( \frac{A_1}{A_2} \right) \quad \text{Eqn. 4-8}$$

The exit mass flow function now can be used to determine the exit relative Mach number using **Eqn. 4-9**.

$$\text{MFF}_2 = \sqrt{\frac{\gamma_g}{R_g}} M_2' \left[ 1 + \frac{(\gamma_g - 1)}{2} M_2'^2 \right]^{-\frac{(\gamma_g + 1)}{2(\gamma_g - 1)}} \quad \text{Eqn. 4-9}$$

Next, isentropic relationships are again used to calculate exit static conditions. Finally, from these static conditions, exit velocity triangles are determined and are used to define the absolute exit total pressure and exit total temperature. The blade exit conditions are then used to proceed to the inlet of the next blade row.

#### **REFERENCES:**

- 4.30** Smith, S. L. "1-D Meanline Code Technique to Calculate Stage-by-Stage Compressor Characteristics." M.S. Thesis, The University of Tennessee, Knoxville, TN, 1999.
- 4.31** Hearsey, R.M. *Program HT0300, NASA 1994 Version*, The Boeing Company.
- 4.32** Hale, A., Klepper, J., Hurwitz, W., "A Numerical Capability to Analyze the Effects of Water Ingestion on Compression System Performance and Operability," GT2005-68480, ASME Turbo Expo, Reno-Tahoe, Nevada, June 2005.

### 4.3 STREAMLINE CURVATURE CODE, SLCC, TECHNICAL APPROACH

The inputs required by the **SLCC** are the overall annulus geometry, blade geometry, and a radial distribution of inlet total temperature, total pressure, swirl angle, and loss and deviation correlations which are sensitive to the local flow field. The annulus geometry is divided into a series of axial stations that need not necessarily be radial but may have a complex radial profiles to facilitate placement at locations of interest, such as the leading- and trailing-edge blade profiles. Initial estimated streamlines are then set up radially to create a computational grid. The slope of the streamlines is assumed to be zero far from the bladed regions at the inlet and exit. A schematic of the **SLCC** inputs and how the annulus is divided into a computational grid is illustrated in **Figure 4.9**.

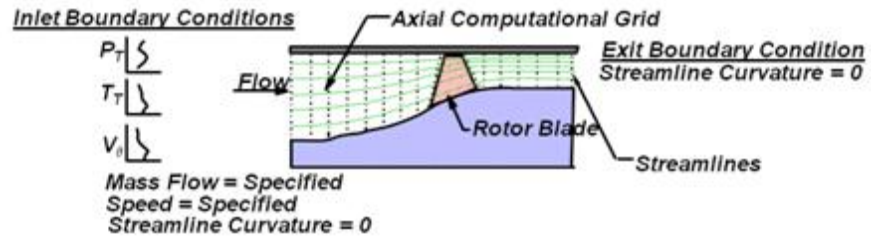


**Figure 4.9 Schematic of SLCC Inputs**

A computing station is defined by the computational grid. A sketch of the computing station is shown in **Figure 4.10**. In this figure,  $r$  is the radial direction,  $z$  is the axial direction,  $l$  is the computing station direction,  $m$  is the meridional direction,  $r_c$  is the radius of curvature of the streamline,  $\gamma$  is the station lean angle, and  $\phi$  is the streamline slope angle.

The velocity triangle nomenclature used in the **SLCC** is presented in **Figure 4.11**. The meridional velocity ( $V_m$ ) is the base velocity, defined as the vector sum of the axial and radial velocity components. One limitation of the streamline curvature method [4.47] is that the velocities in the absolute reference plane must be subsonic. The relative Mach numbers have no restrictions. Alpha ( $\alpha$ ) is the absolute flow angle and is defined as the angle between  $V_m$  and the absolute velocity,  $V$ . Beta ( $\beta$ ) is the relative flow angle and is defined as the angle between  $V_m$  and the relative velocity ( $W$ ).  $U$  represents the wheel rotational velocity.

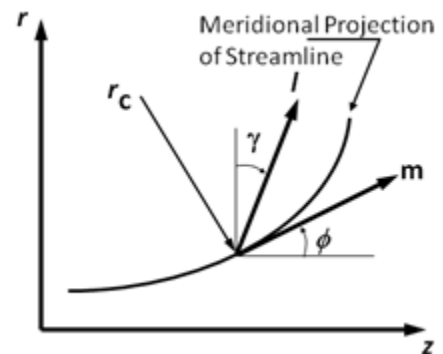


**Figure 4.10 Geometry of Computing Station [4.41]**

The governing Equations for the **SLCC** are derived from the Navier-Stokes Equations. With the assumptions of Inviscid, Axisymmetric, No body forces, Adiabatic and Steady-state

the Equations reduce to

$$\frac{\partial(\rho r \lambda V_r)}{\partial r} + \frac{\partial(\rho r \lambda V_z)}{\partial z} = 0$$

**Continuity**

**Eqn. 4-10**

$$V_r \frac{\partial V_\theta}{\partial r} + V_z \frac{\partial V_\theta}{\partial z} + \frac{V_r V_\theta}{r} = 0$$

**Circumferential Momentum**

**Eqn. 4-11**

$$V_r \frac{\partial V_z}{\partial r} + V_z \frac{\partial V_z}{\partial z} = -\frac{1}{\rho} \frac{\partial P}{\partial z}$$

Axial Momentum

Eqn. 4-12

$$V_r \frac{\partial V_r}{\partial r} + V_z \frac{\partial V_r}{\partial z} - \frac{V_\theta^2}{r} = -\frac{1}{\rho} \frac{\partial p}{\partial r}$$

Radial Momentum

Eqn. 4-13

$$\rho \frac{Dh_t}{Dt} = 0$$

Energy

Eqn. 4-14

$$\frac{Ds}{Dt} = 0$$

Entropy

Eqn. 4-15

$$P = \rho RT$$

Ideal Gas Eqn. of State

Eqn. 4-16

For use in the **SLCC**, the conservation equations were mapped to the non-orthogonal  $m$  and  $l$  coordinate system shown in **Figure 4.10**. The  $m$  direction is the meridional, or streamline, direction. The  $l$  direction is the computing station direction that can be leaned to better

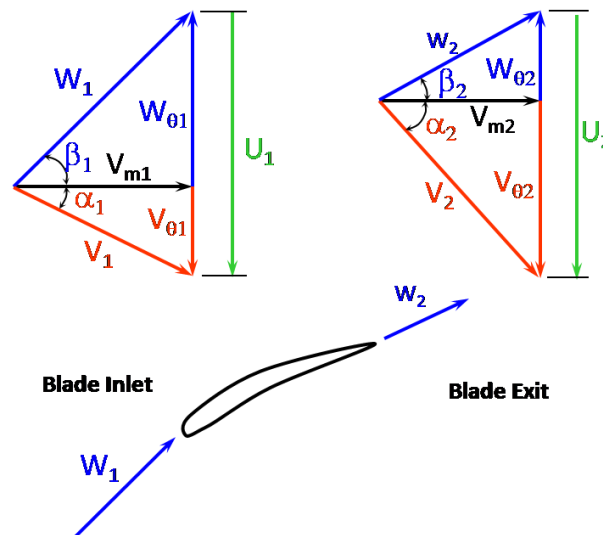


**Figure 4.11 Velocity Triangle Nomenclature Used in SLCC**

approximate leading and trailing edges of blades.

Mapping **Eqn. 4-11** to these coordinates gives

$$\frac{\partial}{\partial m}(rV_\theta) = 0.$$

Eqn. 4-17

This states that the angular momentum is constant along a streamline.

Eqn. 4-12 maps to

$$V_m \left(1 + \tan^2 \beta\right) \frac{dV_m}{dm} = \sin(\phi + \gamma) V_m \frac{dV_m}{dm} - T \frac{dS}{dl} + \frac{dH}{dl} + \frac{V_m^2 \cos(\phi + \gamma)}{r_c} - \frac{V_m^2}{r} \tan^2 \beta \cos \gamma - V_m^2 \tan^2 \beta \frac{d(\tan \beta)}{dl} + \frac{\cos \gamma}{\sin \phi} \left( T \frac{dS}{dm} - \frac{dH}{dm} \right) \quad \text{Eqn. 4-18}$$

Eqn. 4-13 maps to

$$V_m \left(1 + \tan^2 \beta\right) \frac{dV_m}{dm} = \sin(\phi + \gamma) V_m \frac{dV_m}{dm} - T \frac{dS}{dl} + \frac{dH}{dl} + \frac{V_m^2 \cos(\phi + \gamma)}{r_c} - \frac{V_m^2}{r} \tan^2 \beta \cos \gamma - V_m^2 \tan^2 \beta \frac{d(\tan \beta)}{dl} + \frac{\sin \gamma}{\cos \phi} \left( \frac{dH}{dm} - T \frac{dS}{dm} \right) \quad \text{Eqn. 4-19}$$

Upon close inspection of Eqn.s 4-18 and 4-19, they are identified as identical except for the last terms with enthalpy and entropy. By mapping Eqn.s 4-14 and 4-15 to the meridional direction, entropy and enthalpy are shown to remain constant along a streamline. Therefore, the last terms of Eqn.s 4-18 and 4-19 are identically zero. Therefore, Eqn.s 4-18 and 4-19 are equivalent to each other. Therefore, one of the Eqn.s can be discarded. It is decided to discard

the axial momentum Eqn.. The unknowns in Eqn. 4-19 are  $V_m$ ,  $\beta$ ,  $\phi$ ,  $T$ ,  $S$ ,  $H$ ,  $r_c$ , and  $\frac{dV_m}{dm}$ .

The next few steps will be presented to reduce the number of unknowns to the ones that can be solved.

By using the rules of differentiation and annulus geometry, it is discovered that

$$\frac{dV_m}{dm} = (1 - \tan \phi \tan \gamma) \frac{\partial V_z}{\partial z} + \frac{V_m \tan \phi}{r_c} - \frac{V_m \sin^2 \phi \cos \phi}{\cos \gamma} \frac{d(\tan \phi)}{dl} + \frac{\sin \phi}{\cos \gamma} \frac{dV_m}{dl} \quad \text{Eqn. 4-20}$$

However, we have introduced another unknown, the axial gradient of axial velocity. From continuity this can be shown to be

$$\frac{\partial V_z}{\partial z} = \frac{\sin \phi \sin \gamma}{\cos(\phi + \gamma)} \frac{dV_m}{dm} + \frac{\sin \gamma \cos \phi}{\cos(\phi + \gamma)} \frac{V_m}{r_c} - \frac{V_m}{\rho} \frac{d\rho}{dm} - \frac{V_m \sin \phi}{r} - \frac{\cos \phi \sin \phi}{\cos(\phi + \gamma)} \frac{dV_m}{dl} - \frac{V_m \cos^4 \phi}{\cos(\phi + \gamma)} \frac{d(\tan \phi)}{dl} - \frac{V_m}{\lambda} \frac{d\lambda}{dm} \quad \text{Eqn. 4-21}$$



This however introduces another unknown,  $\frac{d\rho}{dm}$ , which by assuming perfect gas and knowing that entropy and enthalpy are constant along a streamline can be shown as

$$\frac{1}{\rho} \frac{d\rho}{dm} = -M_m^2 \left( \frac{1}{V_m} \frac{dV_m}{dm} - \frac{\tan^2 \beta \sin \phi}{r} \right) \quad \text{Eqn. 4-22}$$

Then, by combining Eqn.s 4-19, 4-20, 4-21, and 4-22, the radial momentum becomes

$$\frac{dV_m^2}{dl} + A(l)V_m^2 = B(l) \quad \text{Eqn. 4-23}$$

where

$$\begin{aligned} A(l) = & -2 \cos^2 \beta \left[ \frac{1 - \cos^2(\phi + \gamma) M_m^2}{\cos(\phi + \gamma)(1 - M_m^2)} - \frac{\tan \beta}{rT} \frac{d}{dl} (r \tan \beta) - \right. \\ & \left. \frac{1}{1 - M_m^2} \left[ \cos^2 \phi \tan(\phi + \gamma) \frac{d \tan \phi}{dl} + \frac{\sin(\phi + \gamma)}{\gamma} \frac{d\lambda}{dm} \right] - \right. \\ & \left. \frac{\sin \phi \sin(\phi + \gamma)(1 + M_m^2)}{r(1 - M_m^2)} \right] \quad \text{Eqn. 4-24} \end{aligned}$$

and

$$B(l) = 2 \cos^2 \beta \left[ c_p \left( 1 - \frac{T}{T_t} \right) \frac{dT_t}{dl} - \frac{1}{\rho} \frac{P}{P_t} \frac{dP_t}{dl} \right] \quad \text{Eqn. 4-25}$$

The continuity Eqn. is

$$W = \int_{hub}^{case} dW = \int_{hub}^{case} \rho V_m \cos(\phi + \gamma) \lambda dA \quad \text{Eqn. 4-26}$$

Duct flow regions and bladed regions are solved by different equations. Both methods use the radial momentum Eqn., continuity Eqn., ideal gas Eqn. of state, definition of static temperature, and the isentropic relationship for static pressure. The other equations involved are used to calculate three closure parameters. These parameters are exit swirl velocity, exit total temperature, and exit total pressure.

## DUCT FLOW REGIONS

The duct flow region is described first. The duct flow case involves no bladed region. The eight unknowns for this case are:  $V_{m2}$ ,  $\phi_2$ ,  $V_{\theta 2}$ ,  $P_{t2}$ ,  $T_{t2}$ ,  $P_2$ ,  $T_2$ ,  $\rho_2$ . The eight equations that solve these unknowns are:

$$\frac{dV_m^2}{dl} + A(l)V_m^2 = B(l)$$

Radial Momentum

Eqn. 4-27

$$\frac{\partial}{\partial n}(rV_\theta) = 0$$

Circumferential Momentum

Eqn. 4-17

$$W = \int_{hub}^{case} dW = \int_{hub}^{case} \rho V_m \cos(\phi + \gamma) \lambda dA$$

Continuity

Eqn. 4-26

$$\rho \frac{Dh_t}{Dt} = 0$$

Energy

Eqn. 4-14

$$\frac{Ds}{Dt} = 0$$

Entropy

Eqn. 4-15

$$P = \rho RT$$

Ideal Gas Eqn. of State

Eqn. 4-16

$$T = T_t - \frac{V_m^2 + V_\theta^2}{2c_p}$$

Static Temperature

Eqn. 4-28

$$P = P_t \left( \frac{T}{T_t} \right)^{\frac{\gamma}{\gamma-1}}$$

Isentropic Relationship

Eqn. 4-29

where the radial momentum, circumferential momentum, continuity, energy, entropy, and ideal gas equation. of state were defined earlier in this section. The three closure parameters needed to resolve the flow field are exit swirl velocity, exit total temperature, and exit total pressure. By inspection of [Eqns. 4-14, 4-15, and 4-17](#), it is known that enthalpy, entropy, and angular momentum are conserved along a streamline. Therefore, the exit swirl velocity can be resolved by integrating the circumferential momentum Eqn. ([Eqn. 4-17](#)) to give

$$V_{\theta 2} = \left( \frac{r_1}{r_2} \right) V_{\theta 1}.$$

Eqn. 4-30

Then, the exit total temperature is found by integrating the energy Eqn. ([Eqn. 4-14](#)) to give

$$T_{t2} = T_{t1}.$$

Eqn. 4-31

Finally, by integrating the entropy Eqn. ([Eqn. 4-15](#)), the exit total pressure relation becomes

$$P_{t2} = P_{t1} \cdot \quad \text{Eqn. 4-32}$$

With these closure relations and the conservation equations listed at the beginning of this section, the entire flow field for a non-bladed region can be resolved.

### **BLADED REGIONS**

Resolving the flow field in the bladed region is more complicated. The unknowns and several of the governing equations are the same as the duct flow case. The closure relations are the only Equations that change. Therefore, the radial momentum (Eqn. 4-23), continuity equation. (Eqn. 4-26), ideal gas equation of state (Eqn. 4-16), static temperature equation. (Eqn. 4-28), and the isentropic relationship (Eqn. 4-29) are all the same for the duct flow and bladed region cases. The new closure relations are developed because entropy, enthalpy, and angular momentum are no longer constant along a streamline and must be specified. Because of the complex flow involved when crossing a bladed region, the **SLCC** does not directly model the bladed regions. For the closure relations to be specified, loss and deviation across a bladed region must be known. For the **SLCC** used in this investigation, the loss and deviation were specified using loss and deviation correlations. Loss and deviation are defined in one of the following sections.

With deviation specified by the correlations and the velocity triangles and exit streamline angles known at the exit radius, the first of the closure relations, exit swirl velocity, can be calculated from

$$\tan \beta_2 = \frac{W_{\theta 2}}{V_{m2}} \quad \text{Eqn. 4-33}$$

$$\cos \phi_2 = \frac{V_{z2}}{V_{m2}} \quad \text{Eqn. 4-34}$$

$$V_{\theta 2} = V_{m2} \tan \beta_2 \cos \phi_2 + U_2 \cdot \quad \text{Eqn. 4-35}$$

The second closure relation uses two relationships for work to calculate the exit total temperature. By equating the Euler **turbomachinery** equation,

$$w = U_2 V_{\theta 2} - U_1 V_{\theta 1}, \quad \text{Eqn. 4-36}$$

to the first law of thermodynamics with the assumptions of steady-state and isentropic flow with no heat addition,

$$w = h_{t2} - h_{t1}, \quad \text{Eqn. 4-37}$$

the Eqn. for exit total temperature is determined to be

$$T_{t2} = T_{t1} + U_2 \left[ V_{\theta 2} - \frac{r_1}{r_2} V_{\theta 1} \right] \frac{1}{c_p} . \quad \text{Eqn. 4-38}$$

The final closure relation is used to calculate the exit total pressure. This relationship uses the thermodynamic quantity rothalpy, defined as

$$I = h + \frac{W^2}{2} - \frac{U^2}{2} . \quad \text{Eqn. 4-39}$$

For rothalpy to be conserved in a moving passage, the flow must be steady in the rotating frame, no work can be performed in the rotating frame, and no heat transfer can occur to or from the flow. Then, using the isentropic relations, the relative total pressure loss coefficient, and the conservation of rothalpy, the exit total pressure is determined to be

$$P_{t2} = P_{t1} \left( \frac{T_{t2}}{T_{t1}} \right)^{\frac{\gamma}{\gamma-1}} \left[ 1 - \left( \frac{P'_{t1}}{P'_{t2}} \right)_{id} \bar{\omega}' \left( 1 - \left[ \frac{1}{1 + \frac{\gamma-1}{2} (M_1')^2} \right]^{\frac{\gamma}{\gamma-1}} \right) \right] \quad \text{Eqn. 4-40}$$

where

$$\left( \frac{P'_{t1}}{P'_{t2}} \right)_{id} = \left\{ 1 + \frac{\gamma-1}{2} M_{T1} \left[ \left( \frac{r_2}{r_1} \right)^2 - 1 \right] \right\}^{-\frac{\gamma}{\gamma-1}} \quad \text{Eqn. 4-41}$$

and

$$M_{T1} = \frac{U_1}{\sqrt{\gamma R T'_{t1}}} . \quad \text{Eqn. 4-42}$$

With the three closure Equations defined, **Eqn.s 4-35, 4-38, and 4-40**, the conservation Eqn. listed at the top of this section can be solved to develop the flow field for a bladed region.

### **CORRELATIONS**

Because of the complex physical flow occurring in a compressor stage, it is very difficult to model the flow phenomena exactly. For this reason, empirical correlations are typically used to approximate the actual physics involved. Most of the correlations used in the **SLCC** were originally derived from 2-D linear cascade flow results and are found in NASA SP-36 [4.44]. These correlations were developed from databases acquired from machines of 1950's and 1960's design. Because they were developed on earlier designs, the correlations may have trouble when modeling machines with more modern blade profiles. However, some correlations have been modified to better approximate modern high speed turbomachines.

Before the loss and deviation correlations can be used, several geometric quantities must be known. These are the blade inlet and exit metal angles, solidity, camber, blade maximum thickness to chord ratio, and location of maximum camber point as a fraction of chord. With these quantities defined, two reference values are calculated using the equations found in NASA SP-36 [4.44]. The first parameter is the low-speed reference minimum-loss incidence angle given by

$$i_{ref} = (k_i)_{shape} (k_i)_{th} (i_0)_{10} - n \theta \quad , \quad \text{Eqn. 4-43}$$

where  $(k_i)_{shape}$  and  $(k_i)_{th}$  are correction factors for blades with shapes other than NACA 65-(A<sub>10</sub>)-series blades and  $(i_0)_{10}$  is the variation of zero-camber incidence angle for the 10-percent-thick 65-series thickness distribution.  $(i_0)_{10}$  is a function of inlet air angle,  $\beta_1$ . This value is unknown at the time of calculation of  $i_{ref}$ , so it is found iteratively. The term  $n$  is the minimum-loss-incidence slope factor.

The last reference value that must be found is the reference minimum-loss air inlet angle. Assuming the minimum-loss incidence angle is zero, the reference minimum-loss air inlet angle would be equal to the inlet blade metal angle. However, Eqn. 4-43 calculates a reference minimum-loss incidence angle, so a better initial estimate of the reference minimum-loss air inlet angle is

$$\beta_{1ref} = \beta_{1m} + i_{ref} \quad . \quad \text{Eqn. 4-44}$$

## Loss Correlations

For applications to highly transonic fans, individual loss components can be broken down into one of three broad categories:

- Profile loss – includes blade boundary layer and wake
- Shock loss – due to non-isentropic shock process in the core flow
- Secondary losses – includes passage secondary flows and endwall interactions between annulus boundary layer and blade rows (tip gap flows and hub vortices)

The loss correlations calculate the relative total pressure loss coefficient,  $\overline{\omega}'$ , are defined by

$$\overline{\omega}' = \frac{(P'_{t2})_{id} - P'_{t2}}{P'_{t1} - P_1} \quad \text{Eqn. 4-45}$$

The **SLCC** calculates loss at a given compressor operating point by developing a "loss bucket". A loss bucket is the graphical representation of loss as a function of incidence for constant Mach number. The curve normally has a U-shape or bucket shape with the middle of the bottom of the bucket being the minimum-loss incidence point. The equation that develops the loss bucket for the **SLCC** is

$$\bar{\omega}' = \left[ \left( \bar{\omega}_{\min} + \bar{\omega}_M + \bar{\omega}_{hub} + \bar{\omega}_{tip} \right) \left[ 1 + \left( \frac{i - i_M}{W} \right)^2 \right] \right]$$

Eqn. 4-46

The first four terms are magnitudes of different loss values,  $i$  is the actual incidence,  $i_M$  is the minimum loss incidence, and  $W$  is an arbitrarily defined width of the loss bucket.  $i_M$  is a function of inlet relative Mach number and  $i_{ref}$  (defined by Eqn. 4-43). An example of the loss bucket and how each term affects the bucket shape is shown in Figure 4.12. The solid line represents a baseline bucket. The baseline bucket is an arbitrary bucket that will be used as a baseline to depict how the other variables affect the bucket. With increasing minimum incidence ( $i_M$ ), the bucket shifts to the right. With increasing magnitude of loss terms ( $\bar{\omega}_{\min}$ ,  $\bar{\omega}_M$ ,  $\bar{\omega}_{hub}$ ,  $\bar{\omega}_{tip}$ ), the bucket shifts up. As the width term ( $W$ ) decreases, the bucket width decreases.

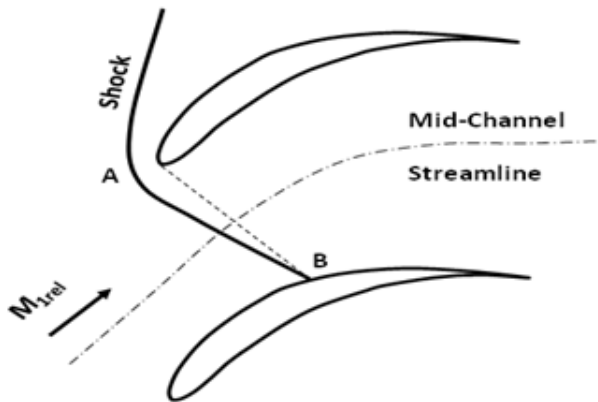


Figure 4.13 Schematic of Lewis, Miller, Hartman Shock Model

The minimum loss term,  $\bar{\omega}_{\min}$ , is essentially the profile loss, or friction loss, caused by viscous forces on the blade. The one used for this investigation is proposed by Robbins et. al. [4.46] in NASA SP-36. The correlation for minimum profile loss is given as

$$\bar{\omega}_{\min} = \bar{\omega}_{\text{loss}} \left( \frac{2P\sigma}{\cos \beta_{2ref}} \right)$$

Eqn. 4-47

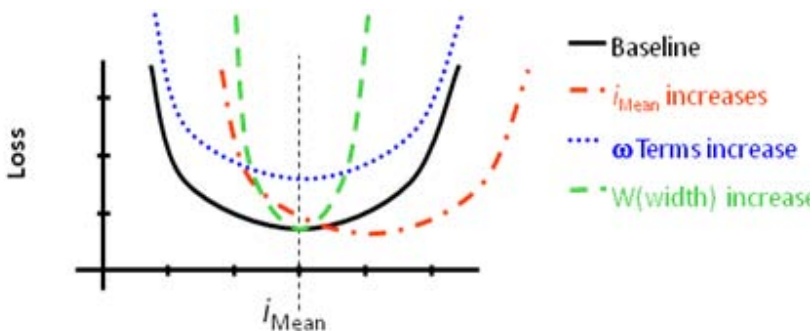


Figure 4.12 Representative Loss Bucket



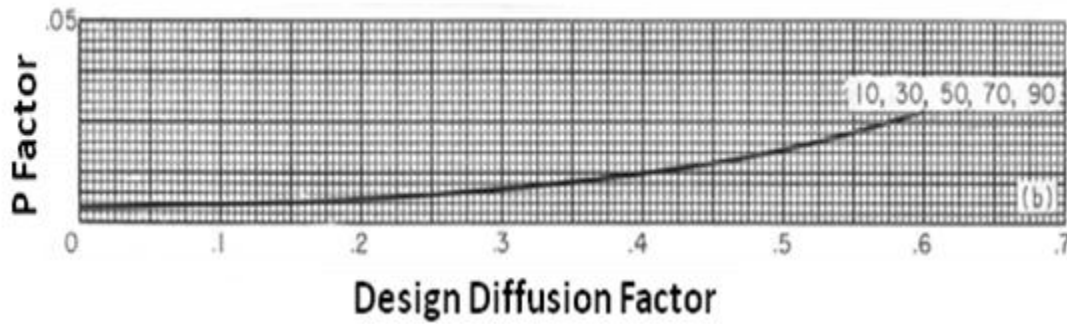


Figure 4.14 P Factor for Minimum Loss Calculation [4.46]

where  $\bar{\omega}_{vloss}$  is an input loss modification term. The P term in Eqn. 4-47 is interpolated from a data set developed from Figure 4.14. The abscissa for Figure 4.14 is the design diffusion factor,  $D_{des}$ . The diffusion factor used in the SLCC is based on flow-weighted mean inlet and exit axial velocities and the outlet flow angle plus the deviation due to mean axial velocity changes. Eqn. 4-48 shows this relationship

$$D_{des} = 1 - \frac{V_{a2}}{V_{a1}} \frac{\cos \beta_{1ref}}{\cos(\beta_{2ref} + \delta_{vamn})} + \left[ \frac{2(r_1 V_{a1} \tan \beta_{1ref} - r_2 V_{a2} \tan(\beta_{2ref} + \delta_{vamn}))}{r_1 + r_2} + \frac{2\pi N_s}{30} (r_2 - r_1) \right] \times \left[ \frac{\cos \beta_{1ref}}{2V_{a1} \sigma} 2(0.45 + 0.5(t/c)_{max}) \right] + 5.0(t/c)_{max}^2$$

Eqn. 4-48

where  $V_a$  is the axial velocity,  $\delta_{vamn}$  is the deviation due to mean axial velocity, and  $N_s$  is the rotational wheel speed in terms of revolutions per minute (rpm).

Two shock loss models are available, the original Miller, Lewis, and Hartman model and the more recent Boyer model. The first shock loss model described is the Miller, Lewis and Hartman model shock loss due to a strong shock in the passage. The model for shock loss is the one presented by Miller, Lewis, and Hartman [4.45]. The inlet critical Mach number is defined as the value of the inlet Mach number that will give supersonic flow somewhere in the blade passage. This value is found by assuming that the pressure coefficient corresponding to the minimum pressure point on the blade suction surface remains practically unchanged up to the critical Mach number [4.40]. From this assumption, the following equation for critical inlet Mach number was derived [4.35]

$$M_{1c}'^2 = \left\{ \frac{\left( \frac{V_{\max}'}{V_1'} \right)^2}{\left( \frac{V_{\max}'}{V_1'} \right)^2 + \left( \frac{2}{\gamma+1} \right)^{\frac{\gamma}{\gamma+1}} - 1} \right\}^{\frac{\gamma-1}{\gamma}} - 1 \left\{ \frac{2}{\gamma-1} \right\}. \quad \text{Eqn. 4-49}$$

Because **Eqn. 4-49** requires the ratio of maximum relative velocity to inlet relative velocity, the following correlation **[4.43]** was developed

$$\frac{V_{\max}'}{V_1'} = 1 + 5 \left( \frac{t}{c} \right)^2 + \frac{[0.45 + 0.5 \left( \frac{t}{c} \right)] [\cos \beta_{1ref} (\tan \beta_{1ref} - \tan \beta_{2ref})]}{\sigma}. \quad \text{Eqn. 4-50}$$

A schematic of the shock loss model is shown in **Figure 4.13**. If the inlet relative Mach number is larger than its critical value, a shock will exist somewhere in the blade passage. The shock will be a detached bow shock but, to simplify the problem, it is assumed to be a normal shock. The normal shock extends from the tip of the blade, normal to the mid-channel streamline, and intersects the following blade on the suction side, shown in schematically in **Figure 4.13**. The Mach number at point A in **Figure 4.13** is assumed to be the inlet relative Mach number. The Mach number at B is found by using a Prandtl-Meyer expansion from the blade tip to the point of shock impingement. The expansion angle is approximated by assuming the blade is a double-circular-arc (DCA) section. The shock Mach number,  $M_s$ , is an average of the inlet relative Mach number and the Mach number at point B. Solidity is important in this correlation because blade spacing will directly affect the point of shock impingement; hence affect the Prandtl-Meyer expansion angle. With the shock Mach number known, the loss coefficient associated with the shock given by Lewis, Miller, and Hartman is developed from normal shock and isentropic relations and is given as

$$\varpi_M = \frac{\left( \frac{(\gamma+1)M_s^2}{(\gamma-1)M_s^2 + 2} \right)^{\frac{\gamma}{\gamma-1}} \left( \frac{\gamma+1}{2\gamma M_s^2 - (\gamma-1)} \right)^{\frac{1}{\gamma-1}} - 1}{\left( 1 + \frac{(\gamma-1)}{2} M_1'^2 \right)^{\frac{\gamma}{\gamma-1}} - 1}. \quad \text{Eqn. 4-51}$$

The second shock loss model was developed by Boyer **[4.33]** and based on the method of Bloch **[4.36]**. This shock loss model, while simplified to be consistent with the overall current approach, is based on the known flow physics – loss is a function of  $M_{1rel}$ , operating condition, solidity, leading edge radius, and blade suction surface profile. It was developed specifically with off-design performance prediction in mind. Key features of the model are summarized below.

- Dual-shock system assumed between peak efficiency and choked flow operating conditions that transitions to single, detached, normal shock as stall approached (**Figure 4.16**).

- Basic principles used to determine hyperbolic shape of detached shock dictated by Mach number and blade leading edge radius.
- Numerical integration for detached bow shock loss included for operating conditions between peak efficiency and stall.
- Single point calculation for passage shock system loss with:
  - Shock angle at sonic point on Moeckel hyperbola taken as “average.”
  - Average elevated Mach number calculated from  $M_{1rel}$  and peak suction surface Mach number (for precompression tip sections,  $M_{1rel}$  is used).
  - Between peak efficiency and stall, if oblique first shock and supersonic downstream conditions, second normal shock assumed.

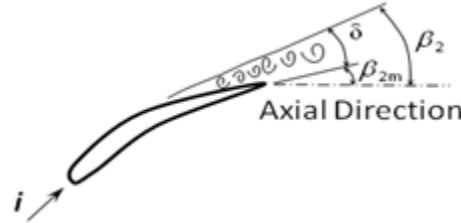


Figure 4.15 Schematic of Deviation

The last two loss terms in **Eqn. 4-46** are the losses due to hub and tip effects, such as intense and concentrated vorticity in the flow. Because the rotors centrifuge some boundary-layer/wake flow radially outwards, increased losses appear at the tip **[4.41]**. Hearsey also states that some experimental data shows an increase in the loss coefficient near the hub that is not accounted for by the other correlations. Therefore, he includes the  $\varpi_{hub}$  term. Both  $\varpi_{tip}$  and  $\varpi_{hub}$  are simply cubic functions of radius that add loss at both the hub and tip in proportion to user inputs,  $H_{loss}$  and  $T_{loss}$ . The equations for hub and tip loss are given as

$$\varpi_{hub} = \varpi_{min} H_{loss} \left( 1 - 2 \frac{r - r_{hub}}{r_{tip} - r_{hub}} \right)^3, \quad \text{Eqn. 4-52}$$

$$\varpi_{tip} = \varpi_{min} T_{loss} \left( 2 \frac{r - r_{hub}}{r_{tip} - r_{hub}} - 1 \right)^3. \quad \text{Eqn. 4-53}$$

Hearsey suggests both  $H_{loss}$  and  $T_{loss}$  to be zero for stationary blade rows. For a rotor, he suggests  $H_{loss}$  be set to match experimental data and  $T_{loss}$  be set to one for the first rotating blade row and decreased by 0.2 for each rotating blade row afterwards until it also is zero.

### Deviation Correlations

The deviation correlations represent the deviation in flow angle from the actual blade trailing edge or exit metal angle (**Figure 4.15**). Such deviations are caused by thick or separating boundary-layers, usually on the suction side of the blade. Like loss, there are several different reasons for deviation to occur. Five specific reasons will be investigated in this section. The total deviation is assumed to be representable as a linear combination of the five reasons. The total deviation is given as

$$\delta = \delta_{ref} + \delta_{va} + \delta_{3D} + \delta_m + \delta_i. \quad \text{Eqn. 4-54}$$

The first deviation correlation investigated [4.44] is the low-speed reference minimum loss deviation angle

$$\delta_{ref} = (k_s)_{shape} (k_s)_{th} (\delta_0)_{10} + \theta \frac{m + \frac{1}{2}(\alpha_c - \frac{1}{2})}{\sigma^{\delta}} \quad \text{Eqn. 4-55}$$

where  $(k_s)_{shape}$  and  $(k_s)_{th}$  are correction factors for blades with shapes other than NACA 65-(A<sub>10</sub>)-

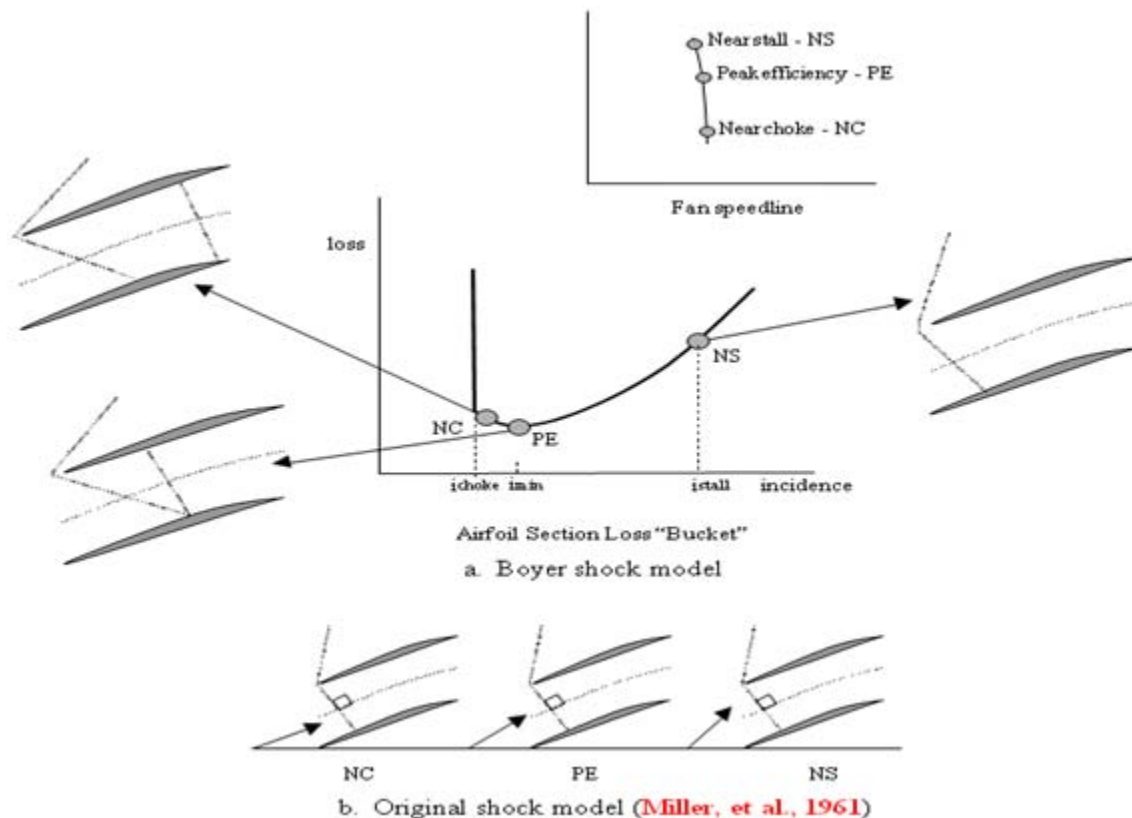


**Figure 4.16 Schematic of Boyer Shock Model [4.33]**

series blades and  $(\delta_0)_{10}$  is the variation of zero-camber deviation angle for the 10-percent-thick 65-series thickness distribution.  $(\delta_0)_{10}$  is a function of inlet air angle,  $\beta_1$ . The term  $m$  is the deviation slope factor and  $b$  is the solidity exponent. The equation for  $\delta_{ref}$  varies from the original one presented by Lieblein. A modification to it based on previous empirical data [4.38] made  $\delta_{ref}$  a function of  $(a/c)$ , the point of maximum camber as a fraction of chord.

The next deviation correlation is based on axial velocity ratio [4.42]. Horlock states that because of the growth of end wall boundary layers, the pressure increase (by diffusion) in the blade row is decreased, resulting in an axial velocity ratio that is different from the design. Thus, the axial velocity ratio will, in general, not be unity. Figure 4.17 shows how the streamline contraction across a blade row causes the streamtube area to change. With mass not allowed to cross a streamline, the streamtube area contraction requires that the axial velocity must increase (i.e. diffusion is reduced). With the axial velocity ratio larger than one, he noted the deviation actually decreases. Therefore, he presented this correlation

$$\delta_{va} = 10 \left( 1 - \frac{V_{m2}}{V_{m1}} \right). \quad \text{Eqn. 4-56}$$

The third deviation correlation is the deviation due to streamline radial location. Because of complex, three-dimensional flows at the blade hub and tip, the deviation at these locations can be different from the deviation at the mid-span. This correlation [4.46],  $\delta_{3D}$ , accounts for some of these effects. For high-speed sections, or blades with a DCA profile,  $\delta_{3D}$  is interpolated from Figure 4.18.

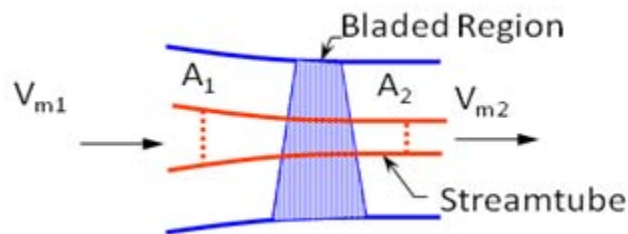


**Figure 4.17 Schematic of Streamtube Geometry Change Due to Axial Velocity Variation**

In this figure,  $\delta_{3D}$  is a function of the inlet relative Mach number and percent of blade height from compressor tip. For low-speed sections, or blades with NACA 65-(A<sub>10</sub>)-series sections,  $\delta_{3D}$  is equal to  $-0.5$  degrees for blade height greater than 50-percent of blade height from compressor hub. For all other radial locations of NACA 65-(A<sub>10</sub>)-series sections,

$$\delta_{3D} = -\frac{1}{2} + 9\frac{3}{8} \left( \frac{\frac{1}{2} - \frac{r - r_{hub}}{r_{tip} - r_{hub}}}{\frac{1}{2} - \frac{r_{hub}}{r_{tip} - r_{hub}}} \right)^2 \quad \text{Eqn. 4-57}$$

The existence of a shock in the blade passage is another source of deviation. This correlation is only used if the inlet relative Mach number is larger than one. The development of this

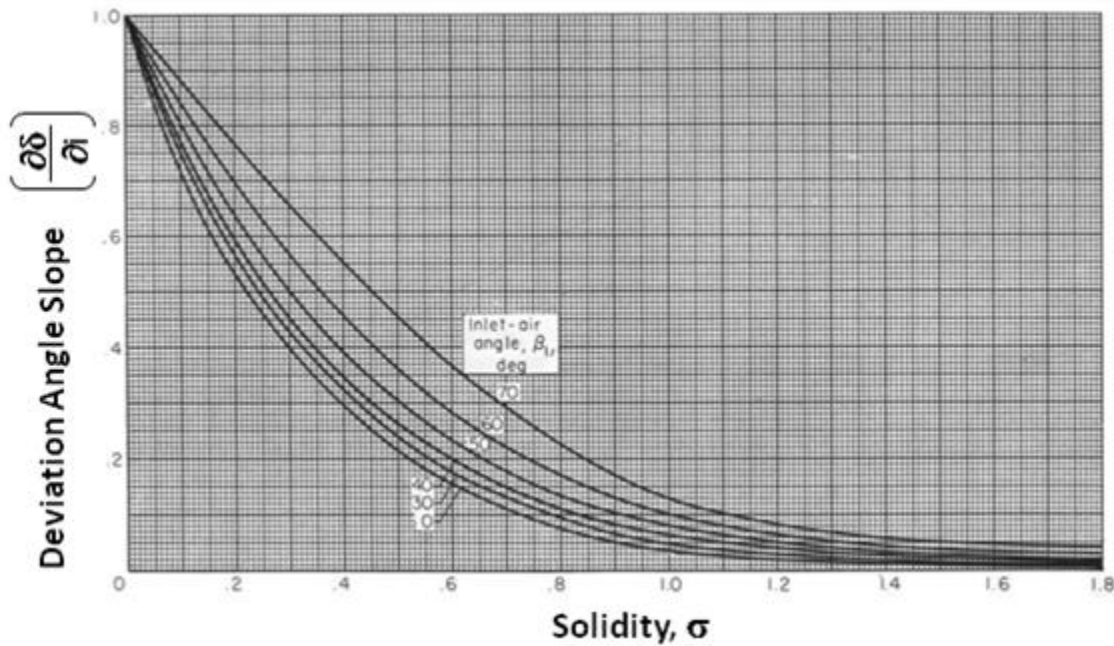


**Figure 4.18 Deviation Angle Slope Versus Solidity [4.46]**

correlation involves knowledge of the inlet and exit critical Mach numbers and the inlet and exit axial velocities. The inlet critical Mach number is presented in Eqn. 4-49. In the same paper [4.43], the exit critical Mach number, the inlet and exit critical velocities, and the inlet and exit axial velocities are derived. The exit critical Mach number,

$$M'_{2c} = M'_{1c} \frac{A_1 \cos \beta_{1ref}}{A_2 \cos \beta_{2ref}} \left[ \frac{1 + \frac{\gamma-1}{2} M'^2_{2c}}{1 + \frac{\gamma-1}{2} M'^2_{1c}} \right]^{\frac{\gamma+1}{2(\gamma-1)}} \quad \text{Eqn. 4-58}$$

is solved iteratively across the blade and used to calculate the exit critical velocity. The exit critical Mach number is also used to calculate the exit axial velocity. The inlet and exit critical velocities given by Jansen and Moffat are



$$V_{1c}' = \frac{\sqrt{\gamma R T_t'}}{\sqrt{\frac{1}{M_{1c}'^2} + \frac{\gamma - 1}{2}}} \quad \text{Eqn. 4-59}$$

and

$$V_{2c}' = \frac{\sqrt{\gamma R T_t'}}{\sqrt{\frac{1}{M_{2c}'^2} + \frac{\gamma - 1}{2}}}, \quad \text{Eqn. 4-60}$$

where  $T_t$  is the local relative total temperature.

The inlet axial velocity is found from

$$V_{1a} = \frac{\sqrt{\gamma R T_t'}}{\sqrt{\frac{1}{M_1'^2} + \frac{\gamma - 1}{2}}}. \quad \text{Eqn. 4-61}$$

Jansen and Moffat [4.43] state that the relative velocity ratio is assumed unchanged for Mach numbers above the critical value, hence the exit axial velocity ratio can be found from

$$V_{2a} = V_{1a} \frac{V_{2c}'}{V_{1c}'}. \quad \text{Eqn. 4-62}$$

Finally, the exit relative Mach number can be calculated from

$$M_2'^2 = \frac{1}{\frac{1}{\left(\frac{V_{2a}}{\sqrt{\gamma R T_t'}}\right)^2} - \frac{\gamma - 1}{2}}. \quad \text{Eqn. 4-63}$$

The actual outlet flow angle caused by the inlet Mach number above the critical value is given by

$$\cos \beta_{2M} = \cos \beta_{1ref} \frac{A_1}{A_2} \frac{V_{1a}}{V_{2a}} \left[ \frac{1 + \frac{\gamma - 1}{2} M_2'^2}{1 + \frac{\gamma - 1}{2} M_1'^2} \right]^{\frac{1}{\gamma - 1}}. \quad \text{Eqn. 4-64}$$

The deviation due to the Mach number greater than one in the blade passage is then simply

$$\delta_M = \beta_{2M} - \beta_{2ref} \quad \text{Eqn. 4-65}$$

The final deviation component is the deviation due to off-design incidence. To determine this value, the stalling and choking incidences must be known. The stalling incidence is the incidence at which a boundary-layer separation occurs over a large part of the blade, causing the blade to stall. The choking incidence is the flow incidence at which the flow in the blade passage becomes choked. The equations for stalling and choking incidence [4.39] are

$$i_{stall} = i_{ref} + 1.5 \left[ 10 + \frac{\theta(55 - \beta_{1m})}{150} \right] (0.5 + 5.0(i/c)_{max}) \quad \text{Eqn. 4-66}$$

and

$$i_{choke} = i_{ref} - \left[ 10 - \frac{\theta(\beta_{1m} - 40)}{450} \right] (0.5 + 5.0(i/c)_{max}) \quad \text{Eqn. 4-67}$$

The equations for deviation due to incidence were constructed by Hearsey using existing cascade data [4.42]. These equations are divided into four parts, depending on the actual incidence angle. They are

$$\delta_i = \frac{1}{2} \frac{\partial \delta}{\partial i} (i_{choke} - i_{ref}), \quad i \leq i_{choke} \quad \text{Eqn. 4-68}$$

$$\delta_i = \frac{\partial \delta}{\partial i} \frac{(i - i_{ref})(i + i_{ref} - 2i_{choke})}{2(i_{ref} - i_{choke})}, \quad i_{choke} < i \leq i_{ref} \quad \text{Eqn. 4-69}$$

$$\delta_i = (i - i_{ref}) \left[ 1 + \frac{\left(1 - \frac{\partial \delta}{\partial i}\right)(i + i_{ref} - 2i_{stall})}{2(i_{stall} - i_{ref})} \right], \quad i_{ref} < i < i_{stall} \quad \text{Eqn. 4-70}$$

$$\delta_i = i - i_{stall} + \frac{1}{2} \left( \frac{\partial \delta}{\partial i} + 1 \right) (i_{stall} - i_{ref}), \quad i \geq i_{stall} \quad \text{Eqn. 4-71}$$

where  $\frac{\partial \delta}{\partial i}$  is interpolated as a function of  $\sigma$  and  $\beta_{1ref}$  from a data set developed from [Figure 4.18](#).

**REFERENCES:**

- 4.33** Boyer, K. M., "An Improved Streamline Curvature Approach for Off-Design Analysis of Transonic Compression System," Ph. D. Dissertation, Virginia Polytechnic Institute and State University, Blacksburg, VA, April 2001.
- 4.34** Klepper, J., "Technique to Predict Stage-By-Stage, Pre-Stall Compressor Performance Characteristics Using a Streamline Curvature Code With Loss and Deviation Correlations," MS Thesis, University of Tennessee, Knoxville, TN, August 1998.
- 4.35** Al-Daini, A. J. "Loss and Deviation Model for a Compressor Blade Element." *Int. J. Heat & Fluid Flow*, March 1986.
- 4.36** Bloch, G. S., Copenhaver, W. W. and O'Brien, W. F., "A Shock Loss Model for Supersonic Compressor Cascades," *Transactions of the ASME, Journal of Turbomachinery*, Vol. 121, January 1999, pp. 28-35.
- 4.37** Boyer, K. M., "An Improved Streamline Curvature Approach for Off-Design Analysis of Transonic Compression System," Ph. D. Dissertation, Virginia Polytechnic Institute and State University, Blacksburg, VA, April 2001.
- 4.38** Carter, A. D. S. and Hughes, H. P. "A Theoretical Investigation into the Effects of Profile Shape on the Performance of Aerofoils in Cascades." British A.R.C,R&M No. 2384, 1946.
- 4.39** Emery J. C., Herrig, L. J., Erwin, J. R., and Felix, A. R. "Systematic Two-Dimensional Cascade Tests of NACA 65-Series Compressor Blades at Low Speeds." NACA Report No. 1368, 1958
- 4.40** Grewe, K. H. "Pressure Distribution Measurements on Two-Dimensional Cascades at High Subsonic Mach Numbers," Part 1. DFL report 57/6a, AFOSR TN 57-289, Institut für Strömungs-mechanik, Technische Hochschule, Braunschweig, Germany, March 1957.
- 4.41** Hearsey, R.M. "Program HT0300 NASA 1994 Volume 2." The Boeing Company, 1994. Horlock, J. H. *Axial Flow Compressors*. Butterworth Publications Limited, 1958.
- 4.42** Horlock, J. H. "Some Recent Research in Turbo-Machinery." *Proceedings of the Institute of Mechanical Engineers*, Volume 182, Part 1, No. 26, 1967-68, pp.571-586.
- 4.43** Jansen, W. and Moffat, W.C. "The Off-Design Analysis of Axial-Flow Compressors." *Transactions of the ASME, Journal of Engineering for Power*, October 1967, pp. 453-462.
- 4.44** Lieblein, S. "Chapter VI: Experimental Flow in Two-Dimensional Cascades." *Aerodynamic Design of Axial-Flow Compressors*, NASA-SP-36, 1965, pp. 183-226.
- 4.45** Miller, G. R., Lewis Jr., G. W. and Hartman, M. J. "Shock Losses in Transonic Compressor Blade Rows." *Transactions of the ASME, Journal of Engineering for Power*, July 1961, pp. 235-242.
- 4.46** Robins, W. H., Jackson, R. J. and Lieblein, S. "Chapter VII: Blade-Element Flow in Annular Cascades." *Aerodynamic Design of Axial-Flow Compressors*, NASA-SP-36, 1965, pp. 227-254.
- 4.47** Smith, L. H., Jr. "The Radial-Equilibrium Eqn. of Turbomachinery." *Transactions of the ASME, Journal of Engineering for Power*, January 1966.

#### 4.4 1D DYNAMIC COMPRESSION SYSTEM TECHNICAL APPROACH,

During operation of axial-flow multistage compression systems, instability phenomena known as surge and/or rotating stall have been observed. Surge is a violent planar disturbance in which the flow in the compressor reverses direction and empties the compressor volumes. This flow reversal relieves the back pressure on the compression system so that correct pumping action can take place. If, however, the original cause of surge has not been corrected, the compression system will undergo re-pressurization until it reaches the instability limit at which time surge will occur again. Surge typically occurs in a frequency range of 3-to-15 Hz.

Rotating stall on the other hand is not as apparently violent as surge but is more damaging to engine operation. Rotating stall occurs when a portion of the circumferential annulus is locally stalled by some destabilizing event such as a low-pressure region. Flow separation on a portion of the blades causes the angle of attack to increase on the adjacent blades, thus stalling them. The stalled region progresses from one blade passage to the next giving the appearance that the stalled region rotates in the direction of rotation. When rotating stall is present in a compressor rig, recovery can be produced by opening a throttle valve. When rotating stall occurs in an engine, no such throttle valve is possible. In fact, combustion has the effect of closing the turbine nozzle area, which appears as a throttle to the compressor. Thus, recovery from rotating stall is usually possible in an engine only by stopping the fuel flow and restarting the engine. With continued engine operation, rotating stall is "non-recoverable". Rotating stall has been a known phenomenon since the 1950's. In the late 70's and 80's a renewed interest was generated with the "Stagnation Stall" problem associated with the F100 turbofan engine, the propulsion system for both the F-15 and F-16 aircraft. The Stagnation Stall or as it came to be known, "Nonrecoverable Stall" produced the strongest incentive for the understanding of compression system instability.

Not only was AEDC involved in the testing of both the F100 and ultimately the F110 turbofan engines for understanding of "Nonrecoverable Stall", it was also involved with the development of compression system numerical simulations that were developed to provide insight into the problem, test techniques, and ultimately "fixes" or recovery from rotating stall.

Over the years, AEDC has developed various capabilities to model the operability of compression systems. The first code developed was the 1D code by Kimzey ([See Chapter 2](#)) followed by **DYMOD** which was followed by the **DYNAMIC Turbine Engine Compressor Code, DYNTTECC**. **DYMOD** and **DYNTTECC** were used to model both single and dual spool compression systems with various levels of total pressure and total temperature distortions. These codes cannot only handle the pre-stall characteristic, but can also model the compressor behavior during post-stall events. These capabilities are discussed in the next two sections.

#### 4.4.1 Single Spool DYNMOD & DYNTTECC

**DYNMOD** and its successor, **DYNTTECC**, are one-dimensional, stage-by-stage, compression and combustion system mathematical models and simulation which is able to analyze any generic flow system [4.48, 4.49, 4.50, 4.51]. It is a versatile code capable of modeling a variety of flow systems (e.g., high bypass dual spool compression, "inline" zero bypass dual spool compression, and single spool compression; each with or without a combustor). For systems involving flow bypass, the flow streams can be recombined after combustion into a single stream. Use is not limited to propulsive devices -- one application that has been made is the simulation of a wind tunnel facility.

**DYNMOD** and **DYNTTECC** use a finite difference numerical technique to simultaneously solve the mass, momentum, and energy equations with or without **turbomachinery** source terms (mass bleed, blade forces, heat transfer, and shaft work). The compression system source terms are determined from a complete set of stage pressure and temperature characteristics provided by the user. The combustor system source terms are determined from a complete specification of the fuel energy content, flammability limits, and combustion efficiency. A

representative, single-spool, multi-stage compressor and combustor system is illustrated below (Figure 4.19).

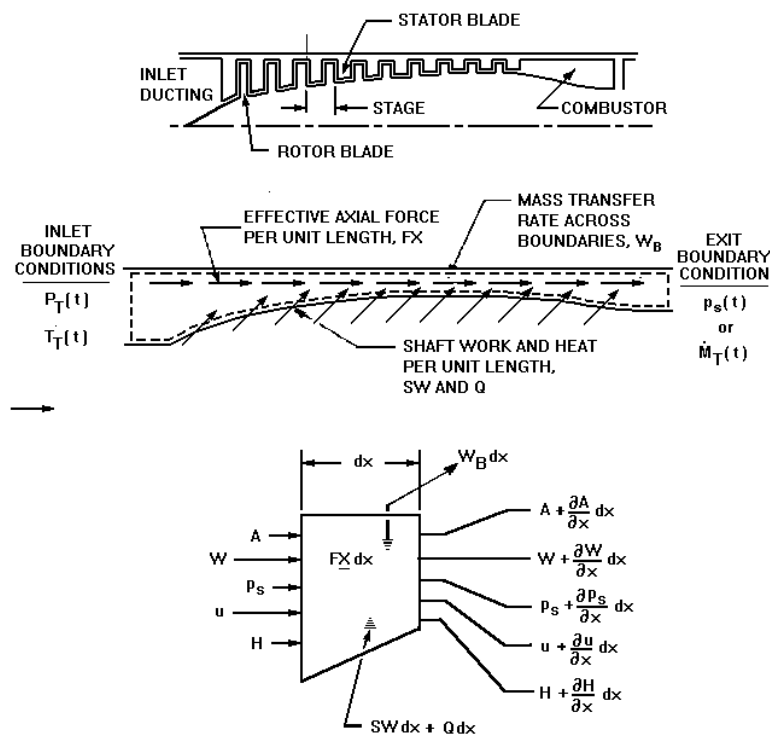


Figure 4.19 DYNTTECC Control Volume Technique

across boundaries other than the inlet or exit (e.g., interstage bleeds) are represented by the distribution,  $W_B$ .

The overall control volume is subdivided into a set of elemental control volumes. Typically, the compressor section is subdivided by stages either as rotor-stator or stator-rotor, depending on how the experimental stage characteristics are obtained. All other duct control volumes are divided to ensure an appropriate frequency response. The governing equations are derived

from the application of mass, momentum, and energy conservation principles to each elemental control volume. These equations can be expressed as:

$$\frac{\partial}{\partial t}(\bar{Q}A) + \frac{\partial}{\partial x}(\bar{F}A) = \bar{S} \quad \text{Eqn. 4-72}$$

where

$$\bar{Q} = \begin{Bmatrix} \rho \\ \rho U \\ e + \frac{U^2}{2} \end{Bmatrix}; \quad \bar{F} = \begin{Bmatrix} \rho U \\ \rho U^2 + P \\ \rho U \left( e + \frac{P}{\rho} + \frac{U^2}{2} \right) \end{Bmatrix}; \quad \bar{S} = \begin{Bmatrix} -W_{Bx} \\ F_x \\ Q_x + S_x - H_{Bx} \end{Bmatrix} \quad \text{Eqn. 4-73}$$

To provide compressor stage force ( $F_x$ ) and shaft work ( $S_x$ ) inputs to the momentum and energy equations, a set of quasi-steady stage characteristics must be available for closure. Likewise, providing the combustor heat addition ( $Q_x$ ) to the energy Eqn. requires a set of quasi-steady flammability limits and combustion efficiency maps. The models used to provide this information to the flow solver will be discussed in the Source Term Section below.

Both **DYNMOD** and **DYNTCC** are formulated as an initial condition boundary value problem. Initial conditions for the dependent variables ( ) are provided by an internal steady state stacking routine. Major inputs to the stacking routine are included in the data input file and geometry file. These inputs include the corrected rotational speed of the rotor, the initial airflow rate, and the boundary condition type and magnitude. A set of initial conditions for control volume entrance is calculated using steady-state flow physics and pre-stall compressor stage characteristics. This allows a steady flow situation from which the dynamic model starts.

Time dependent boundary conditions can be specified either at the entrance or the exit of the overall control volume. Inlet total pressure or temperature time history may be linearly ramped, varied cyclically, or remain constant. The same is true for the overall control volume exit pressure, Mach number, and airflow rate. At the entrance, both total pressure and total temperature must be specified. At the exit, however, only one of these parameters should be specified. The other parameter is set depending on the type of exit boundary condition selected in the data input file.

**Since the DYNMOD code has been superseded by the DYNTCC code**, the specifics of the **DYNMOD** technical approach will not be presented but can be found in **Ref.4.50** by Davis.

### VARIABLE TIME-STEP ROUTINE

In order to provide efficient flow solutions for transient problems, the **DYNTCC** simulation uses a combination of an explicitly formulated numerical solver and an implicitly formulated numerical solver. Both of these numerical solvers are discussed in detail by Garrard in **Ref. 4.53**. Through the combination of the two different solvers, efficient flow solutions using large time step sizes were obtained for all non-dynamic simulations while maintaining the capability of using only the explicit flow solver (with the resulting small time step size) during dynamic events. The approach used to provide this capability will now be developed.



A common measure of the stability of a given explicit numerical solution is given by the stability criteria of Courant, Friedrichs, and Lewy (CFL). The CFL stability criteria states that for a stable numerical solution of a linear system, a sound wave should not propagate farther than one elemental control volume length during a time step. In other words, the CFL criteria is a measure of how far a sound wave travels during a given time step on the grid:

$$\frac{(|u| + a)\Delta t}{\Delta x} \leq \text{CFL}_{\text{limit}} \leq 1.0 \quad \text{Eqn. 4-74}$$

where  $a$  is the speed of sound in the flow. For a linear system, the CFL is limited to 1.0. Due to the nonlinear nature of the turbomachinery simulation, particularly when simulating a choked turbine, experience has shown that a more realistic limit is 0.6. If the CFL limit is exceeded, the explicit method becomes numerically unstable and the resulting flow solution meaningless. For a given grid and flow, the maximum time step size that can be taken is given by:

$$\Delta t_{\text{max}} = \frac{\text{CFL}_{\text{limit}} \Delta x}{a + |u|_{\text{max}}} \quad \text{Eqn. 4-75}$$

The implicitly formulated numerical solver is not restricted by the CFL limit since the solution is obtained by solving all equations simultaneously at the current time step. For a purely linear system, a CFL approaching infinity is possible using an implicit numerical solver. Because the implicit flow solver used in the present work solves for the flow field solution simultaneously across the entire computational domain at the current time step, it takes more computational effort than an explicit solver that is also used.

The implicit numerical solver used in **DYNTECC** takes four times the amount of solution time than the explicit numerical solver requires for the same overall time step size.

Experience has shown that a CFL on the order of 500 is possible. This means that the implicit solver can use a time step 500 times larger than the explicit solver during steady state conditions.

Greater efficiency in calculating a flow solution can therefore be obtained by using the explicit numerical solver whenever the CFL criteria for the implicit numerical solver is less than four times the maximum CFL limit using the explicit numerical solver.

During transient events, the use of the implicit numerical solver reduces the accuracy of the flow field solution because the value of the CFL criteria is greater than one. In other words, because a sonic wave can propagate farther than one elemental control volume length during a given time step, certain characteristics of the flow solution may be missed by the implicit numerical solver. To minimize the computational errors when implementing the implicit numerical solver, a unique variable time step routine was developed and implemented into the **DYNTECC** simulation. The technique, discussed in detail in the following paragraphs, sets the time step size based on a user defined rate-of-change limit in the dependent variable time derivatives. The technique also takes advantage of the greater efficiency of the explicit solver at small time step sizes.

The following variable time step routine has been developed and implemented into the **DYNTECC** simulation:

1. After the initial conditions and boundary conditions have been specified, the first time step is integrated using the explicit numerical solver. The time step size is calculated based upon the flow field velocities calculated in the initial conditions routine and a user provided explicit numerical solver CFL limit.
2. Based upon the solution obtained by the explicit numerical solver, the time derivatives of the dependent variables are linearly extrapolated to the maximum time step size as provided by the user.
3. If the extrapolated values of the time derivatives do not exceed a user defined limit (expressed as a percentage of the dependent variable), the next time integration is taken using the maximum time step size with the implicit numerical solver.
4. If one or more of the time derivatives of the dependent variables changes more than allowed, the time step size is reduced to keep the time derivative change equal to the limit:

$$\Delta t_{\text{new}} = \frac{(\text{Derivative Change Limit})(\text{Time Step Size from Explicit Solution})}{\text{Maximum Derivative Change Extrapolated from Explicit Solution}} \quad \text{Eqn. 4-76}$$

5. For each implicit numerical solver time step, the variable time step routine checks to see if using the explicit numerical solver would be more efficient than using the implicit numerical solver. First, a maximum CFL for the next time integration of the flow field solution, based upon the current flow field solution and the time step size determined is calculated:

$$\text{CFL}_{\text{check}} = \frac{(\text{Maximum CFL from Explicit Solution})\Delta t_{\text{new}}}{(\text{Time Step Size from Explicit Solution})} \quad \text{Eqn. 4-77}$$

6. If  $\text{CFL}_{\text{check}}$  is greater than or equal to four times the maximum CFL allowed by the explicit numerical solver, the implicit solver is used. Otherwise, the explicit solver is used.
7. If the implicit numerical solver is used, the next time step integration uses the explicit solver to again calculate the time derivatives for the flow field solution. If the explicit numerical solver is used, the technique re-enters the procedure at the second bullet above. This process is repeated until an imposed simulation time limit is reached.

The variable time step routine is graphically depicted in **Figure 4.20**. The line identified as Case 1 represents a solution wherein the maximum rate of change of the dependent variables do not exceed the user imposed limit. Therefore, the full implicit time step size would be used for the next time integration. The line identified as Case 2, on the other hand, does exceed the derivative limit when linearly extrapolated. For this case, the implicit time step size would be limited to keep the derivatives from exceeding the imposed limit. A case where the implicit time step size is restricted sufficiently enough to warrant using the explicit solver is not shown above.

## **SOURCE TERMS**

In the governing equations there are terms that must be modeled by the user in order to obtain closure. These terms are: Blade Forces; Shaft Work; Bleed Flows; and Energy Addition or Subtraction as heat transfer. If these terms are set to zero, the standard Euler equations appear for non turbomachinery components. The source terms provide the performance and characteristics of the turbine engine component system. Each type of source term will be discussed below.

## **Compressor Stage Characteristics**

To provide the momentum and energy equations with stage forces and shaft work, a set of stage characteristics must be provided as input. **DYNTECC** has the capability to accept stage characteristics in one of four forms.

The first form is the classical definition. A stage flow coefficient,  $\phi$ , is classically defined as

$$\phi = u / U \quad \text{Eqn. 4-78}$$

where  $u$  is the axial velocity and  $U$  is the wheel speed at the mean-blade radius. Pressure and temperature coefficients,  $\Psi^P$  and  $\Psi^T$  respectively are defined as:

$$\Psi^P = PR, \quad \text{Eqn. 4-79}$$

$$\Psi^T = TR - 1$$

## **Eqn. 4-80**

The form of the flow coefficient defined above does not lend itself to terms that are easily measured. By using the concepts of Mach number, flow function, and critical reference state, stage characteristics can be manipulated to produce the second form, which differs from the classical definition by a constant.

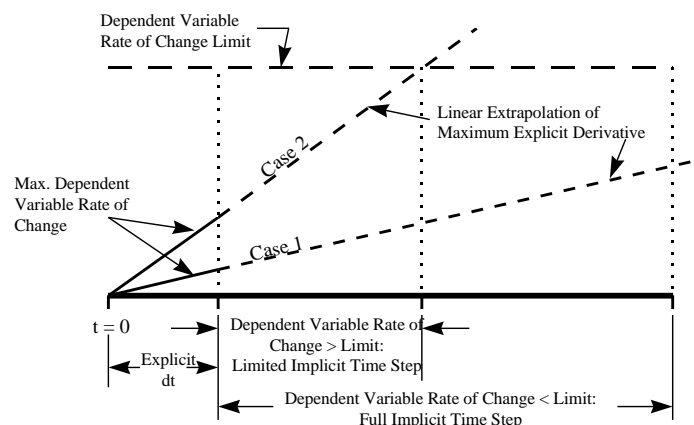


**Figure 4.20 Schematic of Variable Time-Step Routine**

$$\phi = \frac{W_{\text{cor}} * \text{NR}_{\text{cor}}}{W_{\text{cor}}^{**}} \quad \text{Eqn. 4-81}$$

where

$$W_{\text{cor}} = \frac{W * (T_T)^{1/2}}{P_T * A} \quad \text{Eqn. 4-82}$$

$W$ = Actual physical airflow, lbm/sec

$T_T$ = Total temperature (°R)

$P_T$ = Total pressure, psf

$A$ = Area, ft<sup>2</sup>

$$\text{NR}_{\text{cor}} = \frac{\text{Design Corrected Speed}}{\text{Actual Corrected Speed}} \quad \text{Eqn. 4-83}$$

$W_{\text{cor}}^{**}$  = Mass flow function representing sonic conditions = Constant = 0.5318

and

$$\Psi^P = (PR^{\gamma-1/\gamma} - 1) * (\text{NR}_{\text{cor}})^2 \quad \text{Eqn. 4-84}$$

$$\Psi^T = (TR - 1) * (\text{NR}_{\text{cor}})^2 \quad \text{Eqn. 4-85}$$

**A third form** of characteristics is a derivative of the second type and is defined as follows:

$$\phi = W'_{\text{cor}} * \text{NR}_{\text{cor}} \quad \text{Eqn. 4-86}$$

where

$$W'_{\text{cor}} = \frac{W * (TR_{\text{ref}})^{1/2}}{(PR_{\text{ref}})}; TR_{\text{ref}} = \frac{T_T}{T_{T_{\text{ref}}}}; PR_{\text{ref}} = \frac{P_T}{P_{T_{\text{ref}}}} \quad \text{Eqn. 4-87}$$

and

$$\Psi^P = (PR - 1) * (\text{NR}_{\text{cor}})^2$$

$$\Psi^T = (TR - 1) * (\text{NR}_{\text{cor}})^2 \quad \text{Eqn. 4-88}$$

**A fourth form** of the characteristics is a variation of the third type, and is defined by removing the influence of speed directly. Each stage characteristic is, however, a function of speed explicitly:

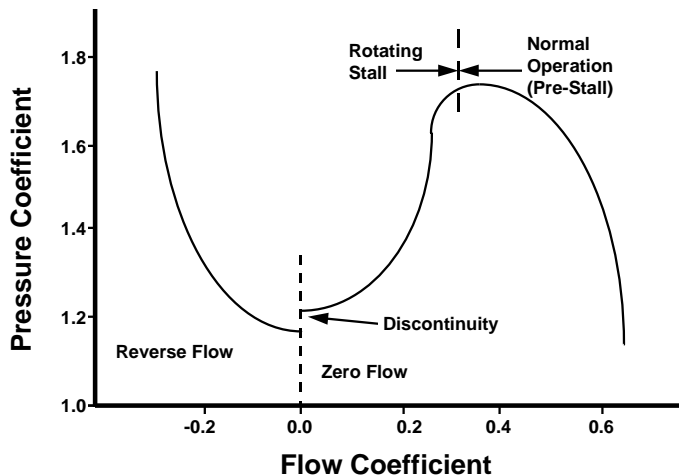
$$\phi = W'_{\text{cor}}$$

Eqn. 4-89

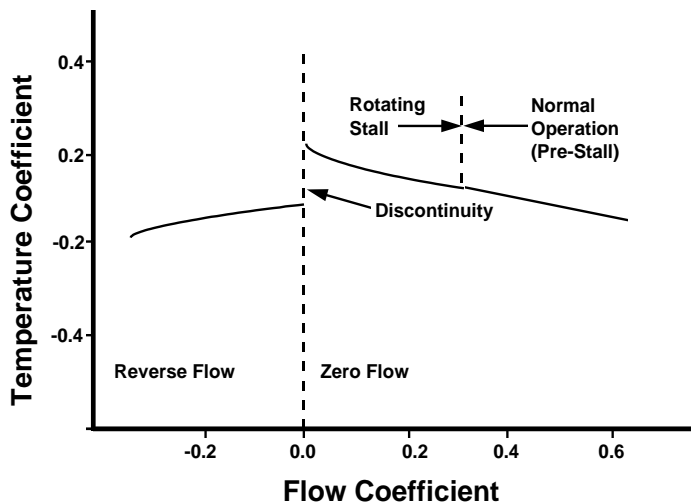
where

$$W'_{\text{cor}} = \frac{W * (TR_{\text{ref}})^{1/2}}{(PR_{\text{ref}})}; TR_{\text{ref}} = \frac{T_T}{T_{T_{\text{ref}}}}; PR_{\text{ref}} = \frac{P_T}{P_{T_{\text{ref}}}}$$

Eqn. 4-90



a. Pressure Coefficient



b. Temperature Coefficient

Figure 4.21 Typical Stage Characteristics

and

$$\Psi^P = (PR - 1)$$

$$\Psi^T = (TR - 1)$$

Eqn. 4-91

The preceding definitions of stage characteristics may be selected by choosing

**TYPECHAR = 1, 2, 3, or 4,**

respectively. After the stage characteristic definition has been chosen and the characteristics have been specified in the proper form (as described in Appendix B), the code will automatically return steady total pressure ratio, PR, and total temperature ratio, TR, as a function of any airflow, W.

A typical set of steady-state characteristics for both pre- and post-stall operations is presented in Figure 4.21. The stage characteristics are divided into three distinct regions: pre-stall, rotating stall, and reversed flow. The pre-stall characteristic represents the performance of a blade

row in normal operation. The transition to a rotating stall characteristic is approximated as a continuous characteristic along a postulated throttle line. The performance in the rotating stall

region is based upon a flow-weighted average of a fully developed rotating stall cell. The pressure and temperature ratios in this region represent the average pressure and temperature rise across the stage for both stalled flow and unstalled flow. The reversed-flow characteristic region represents the pressure loss and temperature rise associated with full-annulus reversed flow. The discontinuity at zero flow has been experimentally shown to exist for a three-stage low-speed compressor. This aspect of the quasi-steady flow characteristic has been incorporated into the modeling technique and can be chosen by the user if so desired.

With the steady total pressure ratio and temperature ratio at an assumed steady flow, the code uses the steady-state version of the conservation equations and backs out the appropriate steady-state control volume forces and shaft work. These values are then used in the dynamic equations as the necessary values of forces in the momentum equation, and shaft work in the energy equation.

This approximation is crucial to the understanding of the development of compressor source terms for the dynamic equations. The foregoing discussion of the stage characteristic has described the principal features of the pre-stall and reversed-flow steady-state performance, and the globally steady rotating stall average performance. For pre-stall and post-stall reversed flow, steady characteristics can be used as they exist. However, for a dynamic event such as rotating stall or surge, the use of steady characteristics is not necessarily correct. In the rotating stall region, rotating stall develops very rapidly and the globally steady characteristic is no longer applicable. To provide a dynamic stage characteristic, a first order time lag on the stage forces has been incorporated into the modeling technique in the rotating stall region only. The first order lag equation, used is:

$$\tau \frac{dFX}{dt} + FX = FX_{SS} \quad \text{Eqn. 4-92}$$

where

$FX$  = blade force and pressure area force of the casing,

$FX_{SS}$  = steady-state force, and

$\tau$  = time constant.

### Combustor Source Terms

The dynamic combustor model used by **DYNTECC** is a simple heat release model. Given the flow conditions in the control volumes that are defined by the user to be the combustor, the amount of energy generated by the combustion of the fuel is calculated and passed to the overall **DYNTECC** flow solver. The energy added to the flow is treated as a source term just as heat transfer is treated in the compressor. Several less important variables also appear in the equations; these have been identified in the discussions on user inputs.

The equivalence ratio of the flow in the combustor is a function of the airflow rate, the fuel flow rate, and the stoichiometric fuel air ratio of the fuel. It is assumed that the fuel is similar to JP-4, and the stoichiometric fuel air ratio is assumed to be 0.067. The user has the option of mixing the fuel with only part of the airflow. In an attempt to model the effect of the liner flow in the combustor, the user can specify the fraction of the overall airflow involved in the combustion process. For example, if the actual engine has a combustor where 50 percent of the airflow



enters the primary zone and 50 percent goes into the liner, the equivalence ratio calculation will use only  $\frac{1}{2}$  of the airflow rate.

The amount of heat released is a function of combustor equivalence ratio, combustion efficiency, upper and lower flammability limits and the lower heating value of the fuel.

The combustor flammability limits are determined by using steady-state engineering correlations developed by Herbert [4.54]. In order for stable combustion to occur, the primary zone equivalence ratio ( $\phi_{pz}$ ) must fall within a rich limit and a lean limit:

$$\phi_L \leq \phi_{PZ} \leq \phi_R \quad \text{Eqn. 4-93}$$

Based on experimental data, Herbert defined a Combined Air Loading Factor to calibrate the lightoff and blowout data.

$$CALF = \frac{\dot{m}_{pz}}{V_{pz} P_{t3}^2 e^{\frac{T_3}{n}}} \quad \text{Eqn. 4-94}$$

where

$$n = 220 \left[ \sqrt{2} \pm \ln \left( \frac{\phi_{pz}}{1.03} \right) \right] \quad \text{Eqn. 4-95}$$

The plus sign corresponds to  $\phi_{pz} \geq 1.03$ . A polynomial curvefit of Herbert's flammability data for a generic can type combustor is used in the model.

Combustion efficiency is determined by using steady-state engineering correlations developed by Lefebvre [4.55]. Lefebvre assumed that the overall combustion efficiency is limited by the efficiency of fuel evaporation and the reaction efficiency.

$$\eta_c = \eta_e * \eta_r \quad \text{Eqn. 4-96}$$

where

$$\eta_e = 1 - \exp \left[ \frac{-36 * 10^6 P_3 V_C \beta}{\dot{m}_{pz} D_0^2 T_c} \right] \quad \text{Eqn. 4-97}$$

$$\eta_r = 1 - \exp \left[ \frac{-0.022 P_3^{1.3} V_C \exp(T_c/400)}{\dot{m}_{pz}} \right] \quad \text{Eqn. 4-98}$$

Further modification to the Lefebvre work following Derr and Mellor [4.56] is made such that  $V_C = V_{pz}$  and  $T_C = T_{pz}$ . In turn,  $T_{pz}$  is estimated by averaging the temperatures at the faces of the primary zone control volumes.

Because of the dynamic operation of the combustor, it is possible for heat release to occur for a short period of time even though the combustor equivalence ratio may lie outside the steady-state flammability limits. Likewise, the heat release process may not resume immediately after the combustor equivalence ratio reenters the flammability bounds. To account for these affects, a first order lag on the heat release rate as proposed by Davis, [4.52], is incorporated in the model:

$$\tau \frac{d\dot{Q}}{dt} + \dot{Q} = \dot{Q}_{ss}(t) \quad \text{Eqn. 4-99}$$

Time constants are provided to lag both the blowout process and the lightoff process.

The pressure loss in the combustor is based upon a one dimensional, constant area analysis of the combustor stagnation pressure loss due to the energy release as given by Oates [4.57]. The model assumes the gases to be calorically perfect at the inlet and exit of the combustor, and that the mass addition of fuel is small relative to the airflow rate. The total pressure ratio across the combustor is given by:

$$\frac{P_{t4}}{P_{t3}} = \frac{\left(1 + \frac{\gamma_4 - 1}{2} Mn_4^2\right)^{\gamma_4/(\gamma_4 - 1)} P_4}{\left(1 + \frac{\gamma_3 - 1}{2} Mn_3^2\right)^{\gamma_3/(\gamma_3 - 1)} P_3} \quad \text{Eqn. 4-100}$$

where

$$\frac{P_4}{P_3} = \frac{1 + \gamma_3 Mn_3^2 [1 - (Cd/2)]}{1 + \gamma_4 Mn_4^2} \quad \text{Eqn. 4-101}$$

### Frictional or Lossy Ducts

For most problems of interest, inlet and exit ducting are associated with the compression system. **DYNTECC** has been formulated to provide as many isentropic ducts as the user specifies in the geometry input file. At times, however, it may be desirable to simulate frictional effects or some other pressure loss mechanism. A rudimentary capability has been provided that can drop the total pressure (or increase total pressure if so desired) across any control volume. Temperature can be affected in a like manner. By appropriate definition of the problem in the data input and geometry files, user specified percent changes in both total pressure and total temperature can be applied to the ducting volumes.

Isentropic duct simulation is the default situation with **DYNTECC**.

The user has the responsibility of determining a realistic value for pressure loss. There are

several prediction schemes for frictional loss based upon the Moody diagram, but the user must supply some information about the nature of the surface and the Reynolds number. Additionally, all pressure loss is applied instantaneously, thereby causing a spurious transient response within the modeling system. This response will be flushed out in a few hundred iterations.

## Bleed Flow Calculations

**DYNTECC** has the capability of specifying control volume bleed flow whether it be into or out of the control volume. This capability can be used to simulate start bleeds, customer bleeds, or surge bleeds. With this version of **DYNTECC** the user has the capability of specifying whether the bleed flow is a percentage of the inlet flow or is calculated from a bleed system geometry and flow properties. In addition, the user can specify a number of bleeds up to fifteen (15). The specification of how many and which control volumes those bleeds are located are specified in the geometry file as well as the Namelist input file.

If the user specifies the bleed flow as a percentage of the inlet flow, he does so by setting  $BLDVAL = 1$  in the BLEEDS Namelist option. If  $BLDVAL$  is any other value, the bleed flow is calculated by the following algorithm.

The user must provide the following inputs:

Constant Cross-sectional Area of the Bleed Pipe

Pressure drop across the bleed piping system (expressed as a pressure ratio less than 1)

Temperature Increase/Decrease across the bleed piping system (also expressed as a temperature ratio)

Controlling Pressure

Reservoir Static Pressure if Outflow

Reservoir Total Inlet Pressure if Inflow

Reservoir Total Inlet Temperature if Inflow

The mass flow associated with the bleed is calculated using

$$W_B = \frac{fm}{fg} \quad \text{Eqn. 4-102}$$

where

$$fm = \left( \frac{P_r A}{\sqrt{T_r}} \right) \sqrt{\frac{\gamma}{R}} M \quad \text{and} \quad fg = \left( 1 + \frac{\gamma - 1}{2} M^2 \right)^{\frac{\gamma + 1}{2(\gamma - 1)}} \quad \text{Eqn. 4-103}$$

$M$  = Mach Number and is calculated from the following expression:

$$M = \left\{ \frac{2}{\gamma - 1} \left[ \left( \frac{P_T}{P_S} \right)^{\frac{\gamma-1}{\gamma}} - 1 \right] \right\}^{\frac{1}{2}} \quad \text{Eqn. 4-104}$$

and goes to unity when choked.

Choking is checked by comparing the total-to-static pressure ratio to the choking pressure ratio as follows:

$$\frac{P_T}{P_S} \geq \left( \frac{\gamma + 1}{2} \right)^{\frac{\gamma}{\gamma-1}} \quad \text{Eqn. 4-105}$$

### **VARIABLE SPEED CAPABILITY**

This version of **DYNTECC** has the capability of changing physical speed. Speed can be varied by implementing a linear change as a function of time using the variables VALSP (with corresponding time variable TIMSP) in the TIMFUN Namelist input. If the geometry is such that the exit plane does not represent a physical choke point, then the user will need to vary the area or static pressure if he wishes to track a know speed condition as produced in a rig or engine system .

### **REFERENCES:**

**4.48** Hale, A. A. and M. W. Davis, Jr., "DYNamic Turbine Engine Compressor Code: **DYNTECC** -- Theory and Capabilities", AIAA Paper # AIAA-92-3190, Presented at the 28th Joint Propulsion Conference and Exhibit, Nashville, TN, July 1992.

**4.49** Davis, M. W., Jr., "A Post-Stall Compression System Modeling Technique", AEDC-TR-86-34, February 1987.

**4.50** Davis, M. W., Jr., "A Stage-by-Stage Post-Stall Compression System Modeling Technique: Methodology, Validation, and Application", Ph.D. Dissertation, Virginia Polytechnic Institute and State University, December 1986

**4.51** Davis, M. W. , Jr. and W. F. O'Brien, "Stage-by-Stage Poststall Compression System Modeling Technique", **Journal of Propulsion and Power**, Vol. 7, Number 6, November-December 1991, pp. 997-1005.

**4.52** Shahroki, K. A., "Application of a Modified Dynamic Compression System Model to a Low Aspect Ratio Fan: Effects of Inlet Distortion." Master's Thesis, Vanderbilt University, Nashville, TN, 1995.

**4.53** Garrard, G. D., "**ATEC**: The Aerodynamic Turbine Engine Code for the Analysis of Transient and Dynamic Turbine Engine System Operations," Ph.D. Dissertation, the University of Tennessee, Knoxville, August, 1995

**4.54** Herbert, M. V., "A Theoretical Analysis of Reaction Rate Controlled Systems - Part 1," Chapter 6 in **Combustion Research and Reviews, 1957**, Agardograph No. 15, Butterworths Scientific Publications, London, England, February, 1957.

**4.55** Lefebvre, A. H., "Fuel Effects on Gas Turbine Combustion - Ignition, Stability, and Combustion Efficiency." **Journal of Engineering for Gas Turbine and Power**, Vol. 107, January, 1985, pp. 23-37.

**4.56** Derr, W. S. and Mellor, A. M., "Recent Developments" in **Design of Modern Turbine Combustors**. Edited by A. M. Mellor, Academic Press, Harcourt Brace Jovanovich, New York, NY, © 1990.

**4.57** Oates, G. C. **Aerothermodynamics of Gas Turbine and Rocket Propulsion**. AIAA Education Series, J. S. Przemieniecki, Series Editor-in-Chief, American Institute of Aeronautics and Astronautics, Inc., Washington, DC, USA, © 1988.

#### 4.4.2 Dual Spool DYNMOD & DYNTECC

**Figure 4.22** illustrates the dual-spool model **DYNMOD** solution procedure outlined by Davis [4.58, 4.59] and adopted later for **DYNTECC**. At time equal zero (Step A), initial values of the dependent variables ( $\rho A$ ,  $W$ , and  $EA$ ) are specified for every calculating station. With the specification of boundary conditions, all thermodynamic variables can be calculated (Step B) at the inlet, interior and exit planes. Using the method-of-characteristics scheme or sonic exit condition scheme, the inlet and exit conditions for the next step in time can be calculated (Step C). With the interior thermodynamic properties from Step B known, the force and work terms

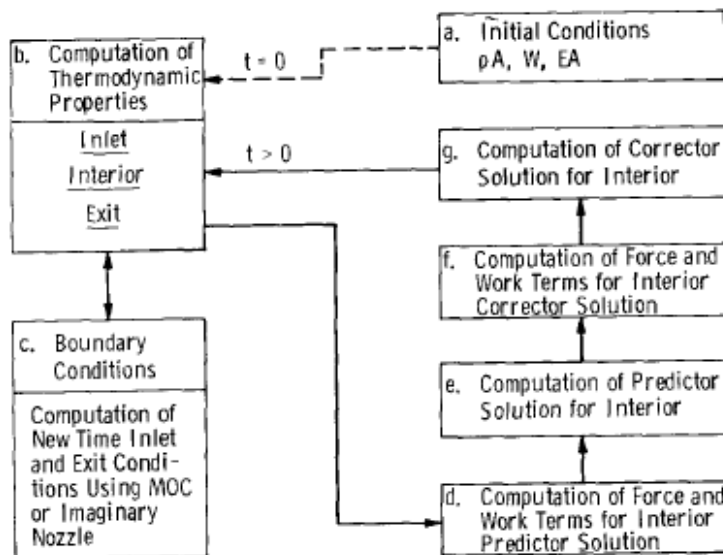


**Figure 4.22 Time-Dependent Compressor Model Solution procedure, McCormick Formulation**

(Step D) necessary for the momentum and energy Eqn.s can be calculated from stage characteristics for input into the predictor step of McCormick's method (Step E). New values for force and work can be determined from the predicted solution (Step F) and then used in the corrector step of McCormick's method (Step G). The new values of the dependent variables determined in Step G are then used to compute the thermodynamic properties (Step B) for that time step. The sequence is repeated with the boundary conditions changing in

accordance with the specified event being simulated.

For modeling dual-spool compression systems, the modeling solution procedure was modified to account for dual-spool aerodynamic and mechanical interaction. A schematic of the dual-spool compression system modeled is presented in **Figure 4.23**. The dual-spool compression system consists of a three-stage fan and a ten-stage high-pressure compressor aerodynamically coupled. The model operates to a known compressor/fan speed ratio based on the nominally determined compression system operating line. Fan speed is furnished as an input, and high-pressure compressor speed is calculated from the known speed relationship. Fixing the speed relationship to this particular schedule limits the model to rapid transients (less than 1.0 sec) where physical rotor speeds do not have sufficient time to respond to the changing environment.

The solution procedure is the same as given in **Figure 4.22** with one exception. In the compression system, the fan airflow is split into two separate flow streams after compression has taken place in the fan. The flow divides by means of a splitter into a fan stream exhausting to ambient or an augmentor and a core stream to be further compressed by the high pressure compressor. These two streams are aerodynamically coupled (i.e., perturbations in one stream are felt by the other stream). A technique based on steady flow conditions and a pseudoflow area was used to Initially, the airflow rates of the fan stream and core stream are known



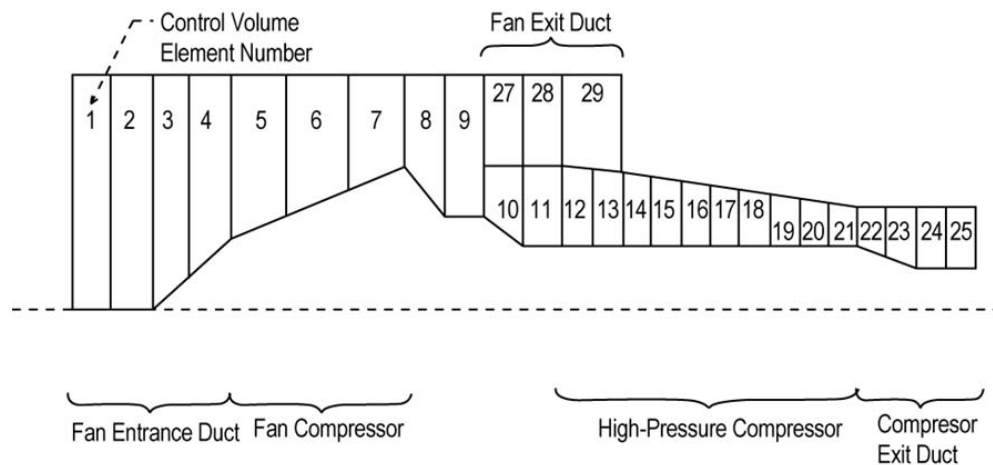


**Figure 4.23 Schematic of the 13-Stage, Dual-Spool Compression System Model**

because they are furnished as steady-state initial conditions. The calculating station just before the splitter plane is divided into two pseudoflow areas ( $A_{p1}$  and  $A_{p2}$ , see [Figure 4.24](#)). These areas are calculated by assuming that steady flow exists at any instant in time in the two artificially constructed control volumes (i.e., the control volume with entrance area  $A_{p1}$  and exit

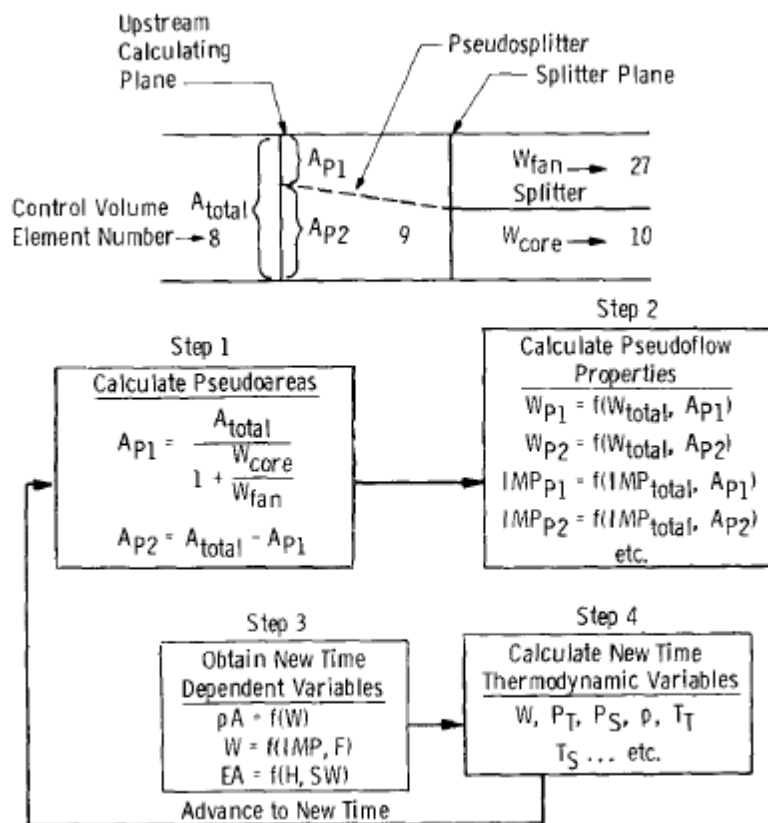


**Figure 4.24 Schematic Bypass Flow Calculation**

area corresponding to the fan duct entrance and the control volume with entrance area  $2A$ , and exit area corresponding to the core stream entrance). Airflow, impulse, forces, and enthalpy are calculated at each pseudoflow area by multiplying the instantaneous values of each term by the ratio of the pseudoflow area to the total flow area. This procedure divides the flow properties at the calculating station just before the splitter such that the McCormick differencing technique can be applied in the area of the splitter. If backward differencing is used at the calculating station just before the splitter, the pseudoflow area technique is not needed. If forward differencing is used, the pseudoflow area technique supplies the

proper flow properties for the forward differencing between the entrance to the fan stream and  $A_1$ , and for the forward differencing between the entrance to the core stream and  $A_{p2}$ . Thus, the flow properties at the calculating station before the splitter for the next instant in time become a flow-weighted average of the transmitted properties in the fan stream and core stream. At the splitter plane a similar procedure is applied. When backward differencing is used, each flow stream interacts with the appropriate pseudoflow area property (i.e., the fan stream properties are differenced with the properties existing at  $AD1$  and the core stream properties are differenced with the properties existing at  $A_{p2}$ ). When forward differencing is used the pseudoflow area technique is not needed. The process is repeated for each time step recalculating the pseudoflow area split based on the instantaneous airflows at the splitter plane. Using this technique, flow perturbations from either the fan duct or core stream can influence the upstream properties or each other.

#### **REFERENCES:**

**4.58** Davis, M. W., Jr., "A Stage-by-Stage Dual-Spool Compression System Modeling Technique", ASME Paper #82-GT-189, March 1982, Presented at the 1982 IGTI Conference, London, England.

**4.59** Davis, Milton W., Jr., "A Stage-by-Stage Compressor Modeling Technique for Single-and Dual-Spool Compression Systems", Unpublished Master's Thesis, University of Tennessee, Knoxville, Tennessee, August 1981

#### 4.5 1D DYNAMIC ENGINE CODE, ATEC, TECHNICAL APPROACH

The **Aerodynamic Turbine Engine Code, ATEC**, model as reported by Garrard [4.60, 4.61, 4.62] solves the one-dimensional Euler equations with turbomachinery source terms within a given domain of interest (such as a turboshaft engine). The overall system under consideration is separated into individual control volumes, as is represented by the compressor system sketched in **Figure 4.25**. The governing equations are derived by the application of mass, momentum, and energy conservation to the elemental control volume:

$$\frac{\partial \mathbf{U}}{\partial t} + \frac{\partial \mathbf{F}}{\partial x} = \mathbf{G} \quad \text{Eqn. 4-106}$$

where:

$$\mathbf{U} = \begin{bmatrix} \rho A \\ \rho u A \\ EA \end{bmatrix}; \quad \mathbf{F} = \begin{bmatrix} \rho u A \\ \rho u^2 A + PA \\ u(EA + PA) \end{bmatrix}; \quad \mathbf{G} = \begin{bmatrix} -W_{Bx} \\ F_x \\ Q_x + SW_x - H_{Bx} \end{bmatrix} \quad \text{Eqn. 4-107}$$

The specific flow variables are density  $\rho$ , static pressure  $P$ , total energy per unit volume  $E$ , and the axial flow velocity,  $u$ . The cross-sectional area of the flow path is defined as  $A$ . The turbomachinery source term for the conservation of mass Eqn. is the bleed flow rate distribution  $W_{Bx}$ . The conservation of momentum equation turbomachinery source term is  $F_x$ , which is the axial force distribution acting on the control volume. The conservation of energy Eqn. turbomachinery source terms include the heat transfer rate into the control volume fluid  $Q_x$ , the shaft work distribution applied to the control volume  $SW_x$ , and the enthalpy change due to the bleed flow distribution  $H_{Bx}$ .

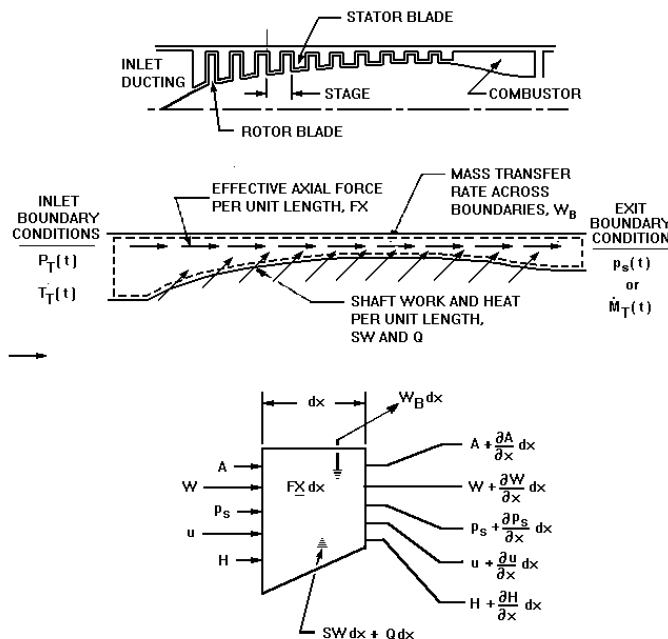


**Figure 4.25 ATEC Control Volume Technique**

To provide compressor and turbine stage force ( $F_x$ ) and shaft work ( $SW_x$ ) inputs to the momentum and energy equations, sets of steady-state stage characteristics must be provided. The combustor heat addition ( $Q_x$ ) to the energy Eqn. uses a set of steady-state flammability limits and combustion efficiency maps. Several other equations are required to obtain closure of the Eqn. set. These include the ideal gas Eqn. of state and the isentropic flow relationships. A constant ratio of specific heats is also assumed.

The model and simulation are formulated as an initial condition boundary value problem. Initial

conditions for the dependent variables ( $\rho A$ ,  $\rho u A$ ,  $EA$ ) are provided by an internal calculation routine that assumes steady-state flow conditions. Major inputs include the corrected rotational speed of the rotor, the initial airflow rate, and the boundary condition type and magnitude. A set of initial conditions for each control volume entrance is calculated using steady-state flow physics and pre-stall compressor stage characteristics. This develops a steady-state initial conditions set of data from which the time dependent model solution is initiated. Upon specification of boundary conditions, the simulation is ready for execution.

The time dependent flow field within the system of interest is obtained by solving the time dependent system of equations using either an explicit or implicit numerical approach. **ATEC** uses a flux-difference splitting scheme based upon characteristic theory [4.63] expressed in both an explicit and implicit formulation to solve for the face fluxes. The explicit numerical solver uses a first order Euler method to integrate the solution from the current time step to the next time step. The implicit numerical solver uses a first order Runge-Kutta scheme for the time integration. In order to improve the computational efficiency during transient events, but to ensure that dynamic flow phenomena are not missed, a variable time step routine has been developed and implemented into **ATEC**. The variable time step routine will also be discussed in the following sections

### COMPRESSOR MODEL

The **ATEC** simulation is based upon the dynamic compressor model and simulation **DYNTECC** [4.64]. **DYNTECC**, and hence **ATEC**, provides a stage-by-stage model and simulation of the compressor system under consideration. Steady-state compressor stage characteristics provide the necessary source terms to solve the governing equations discussed in the previous section.

A typical set of steady-state characteristics for both pre-and post-stall operation is presented in Figure 4.26. The stage characteristics are given as pressure and temperature ratios as functions of a flow coefficient for lines of constant corrected rotor speed. The stage characteristics are divided into three distinct regions: pre-stall, rotating stall, and reversed flow. The pre-stall characteristic represents the performance of a blade row in normal operation. The

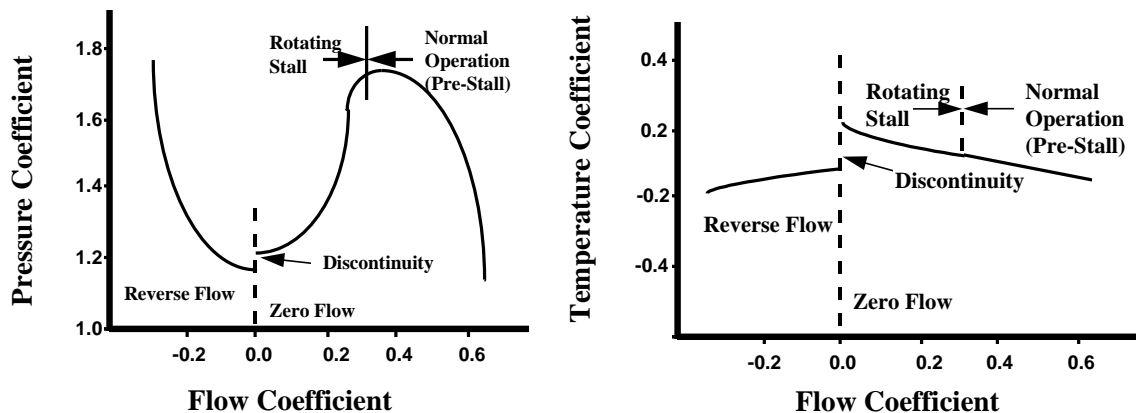


**Figure 4.26 Typical Compressor Pressure and Temperature Stage Characteristics**

transition to a rotating stall characteristic is approximated as a continuous characteristic along a postulated throttle line. The performance in the rotating stall region is based upon flow-weighted averages of the pressures and temperatures in a fully-developed rotating stall cell.

The pressure and temperature ratios in this region represent the average pressure and temperature rise across the stage for both stalled flow and unstalled flow. The reversed-flow characteristic region represents the pressure loss and temperature rise associated with full-annulus reversed flow.

With the steady-state total pressure ratio and temperature ratio at an assumed steady flow rate, the simulation uses the steady-state version of the conservation Eqn.s to compute the appropriate steady-state control volume forces and shaft work. These values are then used in the time dependent Euler equations as the necessary values of the forces in the momentum Eqn. and shaft work in the energy equation.

The foregoing discussion of the stage characteristic has described the principal features of the pre-stall and reversed-flow steady-state performance, and the globally-steady rotating stall average performance. For pre-stall and post-stall reversed flow, steady characteristics can be used as they exist. However, for a dynamic event such as rotating stall or surge, the use of steady characteristics is not adequate. In the post-stall region, the stall cell develops very rapidly and the globally steady characteristics are no longer applicable. To provide a dynamic stage characteristic, a first order time lag on the stage forces has been incorporated into the modeling technique in the post-stall stall region only as used by Davis [4.65]. The first order lag Eqn. used is:

$$\tau_{comp} \frac{dF_x}{dt} + F_x = (F_x)_{ss} \quad \text{Eqn. 4-108}$$

where  $F_x$  is the blade force and pressure area force,  $\tau_{comp}$  is a time constant used to define the compressor response time, and  $(F_x)_{ss}$  is the steady-state value of the blade force and pressure area force obtained from the steady-state compressor characteristics.

Time constants are provided for two portions of the compressor stage operation during the dynamic event. As shown in Figure 4.27, a time constant is provided for the time period that the compressor is just starting to reverse flow (pressure is high and flow rate derivative as a function of time is negative).

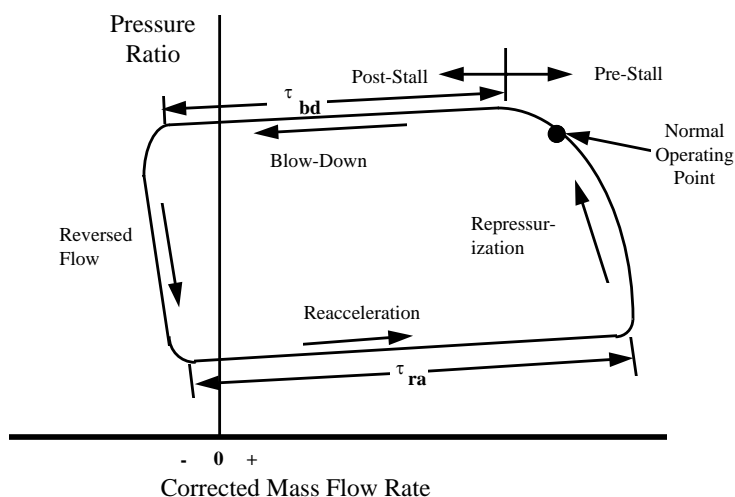


**Figure 4.27 Application of Time Constants During Post-Stall Operation**

After the flow reaches its maximum negative value and the pressure has been relieved, a separate time constant is supplied to control the reacceleration process. The steady-state characteristics are used "as-is" during the reversed flow and repressurization processes. Time constants are determined for a given compression system by matching simulation results to experimental data.

The use of time constants in describing the performance of the system volume dynamics

during post-stall operation is similar to the use of the B parameter as given by Greitzer [4.66]:

$$B = \frac{U}{2\omega L_c} \quad \text{Eqn. 4-109}$$

where  $U$  is the rotor speed,  $L_c$  is an effective length of the compressor volume, and  $\omega$  is the Helmholtz resonator frequency of the system. Depending on a value of  $B$ , the compression system responds differently during post-stall operation. A critical value of  $B$  can be determined that defines the operational point at which the compression system either enters into surge cycles or rotating stall. The value of the  $B$  parameter, however, is difficult to determine for a realistic compression system due to the difficulty of defining the characteristic length and the Helmholtz resonator frequency. The time constant  $\tau_{\text{comp}}$  is likewise difficult to predict analytically, but can readily be determined by matching simulation results to experimental data for a given system. In this sense, the transient and dynamic model is calibrated by experimental data.

### COMBUSTOR MODEL

The combustor model used in the **ATEC** simulation was derived from the **VPICOMB** model and simulation [4.67]. As with **VPICOMB**, the magnitude of the heat release source term in the governing energy Eqn. is defined by the fuel energy content, whether the combustor is lit, and, if it is burning, how well it is burning.

The combustor flammability limits, which define where the combustor provides stable combustion, are determined by using steady state engineering correlations developed by Herbert [4.68]. In order for stable combustion to occur, the primary zone equivalence ratio ( $\phi_{PZ}$ ) must fall within a rich and lean limit:

$$\phi_L \leq \phi_{PZ} \leq \phi_R \quad \text{Eqn. 4-110}$$

Based on experimental data, Herbert defined a combined air loading factor to calibrate the light off and blow off data, as shown in Figure 4.28. A polynomial curve fit of Herbert's flammability data for a generic can type combustor is used in the **ATEC** combustor model. Specific combustor characteristics for a given engine system can be easily implemented in

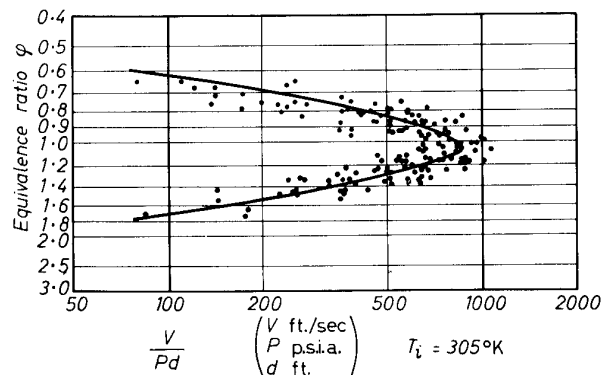


Figure 4.28 Flammability Data as Given By Herbert [4.68]

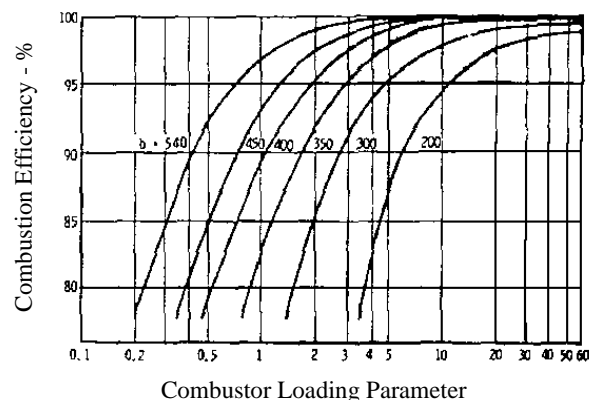


Figure 4.29 Combustion Efficiency Correlation as Given by Lefebvre [4.69]



**ATEC** through the appropriate definition of the polynomial coefficients.

Combustion efficiency is determined by using steady state engineering correlations developed by Lefebvre [4.69]. Lefebvre assumed that the overall combustion efficiency is limited by the efficiency of fuel evaporation and the reaction efficiency. As with Herbert, Lefebvre correlated the combustion efficiency as a function of a loading factor, as shown in Figure 4.29. Further modification to the Lefebvre work is made following Derr and Mellor [4.70] in which the volume of the primary zone of the combustor is replaced by the overall volume.

Because of the dynamic operation of the combustor, it is possible for heat release to occur for a short period of time even though the combustor equivalence ratio may lie outside the steady state flammability limits. Likewise, the heat release process may not resume immediately after the combustor equivalence ratio reenters the flammability bounds. To account for these effects, a first order lag on the heat release rate as proposed by Davis [4.65] is incorporated in the model:

$$\tau \frac{d\dot{Q}}{dt} + \dot{Q} = \dot{Q}_{ss}(t) \quad \text{Eqn. 4-111}$$

As with the compressor model, the combustor time constant is found by matching the simulation results to representative experimental data. Pressure loss in the combustor is based on a one-dimensional, constant cross-sectional area analysis of the combustor stagnation pressure loss due to the energy release, as given by Oates [4.71]. The model assumes that the combustion gases generated are calorically perfect at the inlet and exit of the combustor, and that the mass addition rate of the fuel is small relative to the air flow rate. The total pressure ratio across the combustor is given by:

$$\frac{P_{t4}}{P_{t3}} = \frac{\left(1 + \frac{\gamma_4 - 1}{2} \text{Mn}_4^2\right)^{\gamma_4/(\gamma_4 - 1)} P_4}{\left(1 + \frac{\gamma_3 - 1}{2} \text{Mn}_3^2\right)^{\gamma_3/(\gamma_3 - 1)} P_3} \quad \text{Eqn. 4-112}$$

where

$$\frac{P_4}{P_3} = \frac{1 + \gamma_3 \text{Mn}_3^2 [1 - (C_D/2)]}{1 + \gamma_4 \text{Mn}_4^2} \quad \text{Eqn. 4-113}$$

The influence of the pressure loss coefficient  $C_D$  and the combustor inlet Mach number  $\text{Mn}_3$  is shown in Figure 4.30.

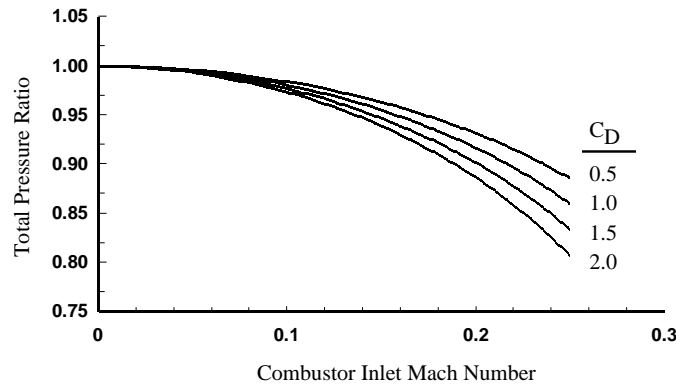


**Figure 4.30 Combustor Total Pressure Ratio as a Function of Inlet Mach Number and Pressure Loss Coefficient**

### **TURBINE MODEL**

Consistent with the approach taken to formulate and construct the compressor model, turbine performance characteristics are defined which have a particular format. The turbine stage forces and shaft work are determined from a set of turbine performance characteristics as sketched in **Figure 4.31**. The turbine flow function is:

$$TFF = \frac{W_4 \sqrt{T_{t4}}}{P_{t4}} \quad \text{Eqn. 4-114}$$

For flow conditions in which the turbine stage nozzle is not choked, a given value of turbine flow function explicitly defines a value for the turbine work done factor ( $w_{DF}$ ):

$$WDF = \frac{h_4 - h_5}{T_{t4}} \quad \text{Eqn. 4-115}$$

Once the turbine work done factor is known for the given inlet flow conditions and rotor speed, the turbine stage exit temperature is found. Given the total temperature ratio across the turbine, the second plot shown in **Figure 4.31** is used to obtain the total pressure ratio across the turbine stage. At this point, sufficient information has been obtained about the turbine to obtain the steady-state blade forces and shaft work terms required to integrate the Euler Eqn.s to the next point in time.

For flow conditions in which the turbine stage nozzle is choked, a given value of turbine flow function cannot be used to explicitly define the turbine work done factor. In the one-dimensional **ATEC** representation of the engine, the physical blockage of the nozzles is not modeled. The engine is typically modeled using the overall flow passage geometry with no reduction in area made for blading. The mass flow through the turbine, however, cannot exceed the limit given by the turbine flow function. The total temperature and total pressure ratio across the choked turbine stage is calculated by assuming that the downstream, rather than upstream, total pressure is known from the previous time step. The solution is iterated until a convergence of exit total temperature, inlet mass flow function, and total pressure ratio is obtained. Steady-

state blade forces and shaft work for the **turbomachinery** source terms are then calculated to use in the integration of the Euler Eqn.s to the next point in time.

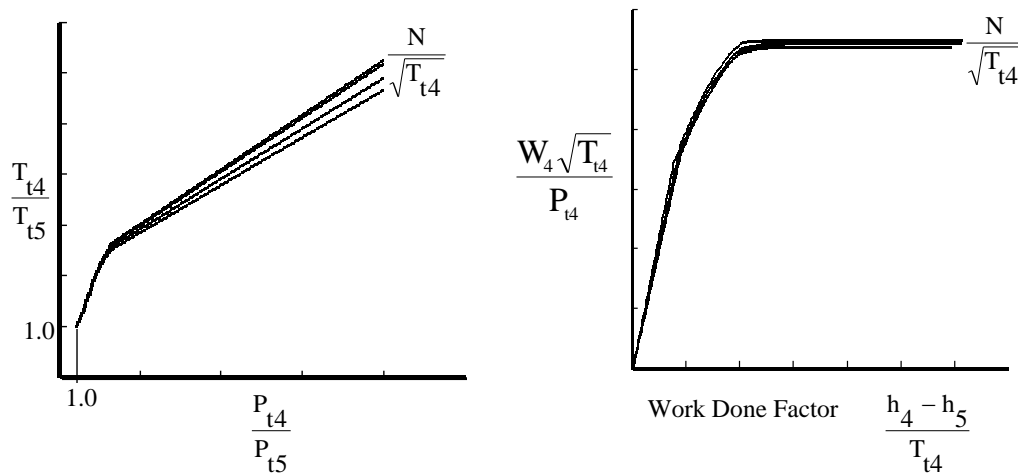


**Figure 4.31 Typical Turbine Performance Specification Curves**

### **ROTOR DYNAMICS MODEL**

The dynamics of the rotating shaft play an important function in the transient operation of a gas turbine engine. For both the compressor and turbine models, the rotor rotational speed determines where, on the given operational maps, the operating condition is located.

The rotor rotational speed is given as part of the initial conditions. Once the time integration process is started, the change in rotational speed is given by:

$$\frac{d\omega}{dt} = \frac{1}{I} (\Gamma_t - \Gamma_c - \Gamma_v - \Gamma_p + \Gamma_s) \quad \text{Eqn. 4-116}$$

where  $I$  is the rotor polar moment of inertia,  $\omega$  is the shaft rotational speed,  $\Gamma_t$  is the torque produced by the turbine,  $\Gamma_c$  is the torque required by the compressor,  $\Gamma_v$  is the torque required to account for viscous losses,  $\Gamma_p$  is the torque required to satisfy any customer power requirements, and  $\Gamma_s$  is the net torque produced by the starter and delivered to the rotor. The rotor dynamics model is integrated into the overall simulation at the end of each time step.

The rotor dynamics model works with torque rather than power due to the requirements at zero speed. If power, which is the torque divided by the rotor speed, is used during an engine starting process, the initial rotor speed of zero will result in indeterminate power requirements.

For both the compressor and turbine components, the level of torque generated (or extracted) at a given moment in time is determined by first calculating the enthalpy change across the component control volumes:

$$\Delta H_{total} = \sum_1^N w_{inlet} (h_{exit} - h_{inlet}) \quad \text{Eqn. 4-117}$$

where N equals the number of control volumes in the particular component. The inlet and exit values correspond to each individual control volume. Torque is then determined by dividing the total enthalpy change across the component by the rotor rotational speed. At zero rotor speed, the torque model explicitly sets the compressor and turbine torque to zero. The level of torque provided to the rotating shaft by the viscous losses model, the customer power requirements model, and the starter model are determined by algebraic models that describe the particular characteristics of a given engine system.

### HEAT TRANSFER MODEL

During normal engine operation, heat transfer processes occur throughout the engine. The effects of this heat transfer on the gas turbine engine operation can be significant as reported by Crawford and Burwell [4.72]. During steady-state operation, however, the heat transfer effects are implicitly built into the component performance maps. Since the **ATEC** simulation is based upon steady-state performance maps, the heat transfer does not have to be considered and modeled to match the steady state operation.

Frequently, however, the engine is not operated at the conditions for which the steady-state performance maps were developed by MacCallum and Pilidis [4.73]. The **ATEC** model and simulation considers the effects of the heat transfer within the compressor, combustor, and turbine components. It is assumed that the overall engine operates adiabatically with the surroundings. The heat transfer source terms for each of the components are calculated using standard heat transfer engineering correlations by Sissom and Pitts, [4.74]. In the compressor, the heat can be convected from the air to the stator blades and then conducted to the outer engine casing. In a rotor row, the heat is likewise convected from the air to the rotor blading and then conducted to the rotor. To represent the convective and conductive flow paths, a simple representation of the system is used and is sketched in Figure 4.32. The heat transfer model tracks four temperatures. They are the rotor and stator blade temperatures, and the base metal for the respective blades. The convective heat transfer rate from a blade to the air is given by:

$$\dot{Q}_{b-a} = \bar{h} A_s (T_{blade} - T_{gas}) \quad \text{Eqn. 4-118}$$

where  $T_{gas}$  is the average total temperature of the air flow through the compressor stage. The conductive heat transfer rate from the blade to the base is given by:

$$\dot{Q}_{b-b} = (kL)_{eff} (T_{base} - T_{blade}) \quad \text{Eqn. 4-119}$$

where  $(kL)_{eff}$  is a measure of the potential for conduction heat transfer. It is a combination of the thermal conductivity of the blade material and the overall all length across which the conduction occurs. Given these two heat transfer rates, the metal temperatures are calculated using:

$$T_{blade}^n = T_{blade}^{n-1} + \frac{\left( \overset{\circ}{q}_{b-b} - \overset{\circ}{q}_{b-a} \right)}{m_{blade} C_{blade}} \Delta t \quad \text{Eqn. 4-120}$$

$$T_{base}^n = T_{base}^{n-1} - \frac{\overset{\circ}{q}_{b-b}}{m_{base} C_{base}} \Delta t \quad \text{Eqn. 4-121}$$

The combustor and turbine heat transfer models are similar to the compressor model. The

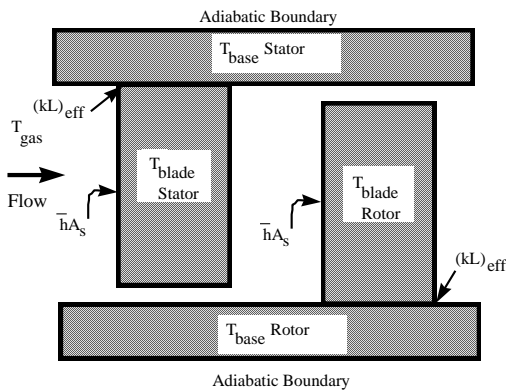


**Figure 4.32 Axial Compressor Heat Transfer Model**

combustor model tracks the combustor liner temperature, the combustor liner air flow temperature, and a case temperature. The turbine heat transfer model builds on the compressor model by adding heat transfer to the internal cooling flow. It is assumed in the models that the Biot modulus of the respective metal parts is sufficiently small to warrant the assumption of equal temperature throughout the metal masses. The average convective heat transfer coefficient is provided as a user input, rather than calculated.

## **NUMERICAL ALGORITHMS**

For a given integration of the flow solution in time, the Euler equations are used to define the fluxes and conservation variables on the faces of the individual control volumes interior to the boundaries. The source terms, provided by the various component models, are known on the control volume interval. The time rate of change of the dependent variables represents a change at some point within the control volume interval. It is assumed in the **ATEC** numerical formulation that this point is located at the center of the given control volume. In order to obtain a flow solution, the change in the dependent variables across the control volume interval must be converted into a change in the dependent variables on the control volume faces (or grid points) [4.64]. To achieve this redistribution, both the explicit and implicit numerical solvers split the change over the control volume interval to the control volume faces by using a flux difference splitting algorithm [4.75]. Both algorithms are based upon characteristic theory with modification to maintain strong conservation properties. The algorithms are robust and efficient, and can handle large changes in cross sectional area and nonuniform axial grid spacing with minimal numerical losses. The reader is referenced to Kneile, et al [4.63] for specific details concerning the numerical solvers.

**Explicit Numerical Solver:** A finite difference representation of the Euler equations with source terms is applied over an interval between grid points  $j$  and  $j+1$ . The fluxes are evaluated at the nodes and the sources are evaluated at the center of the volume. The finite difference representation is given by:

$$\left(\frac{\Delta U}{\Delta t}\right)_j = \Gamma^+_{j-\frac{1}{2}} \left(\frac{\Delta U}{\Delta t}\right)_{j-\frac{1}{2}} + \Gamma^-_{j+\frac{1}{2}} \left(\frac{\Delta U}{\Delta t}\right)_{j+\frac{1}{2}} \quad \text{Eqn. 4-122}$$

where:

$$\left(\frac{\Delta U}{\Delta t}\right)_{j-\frac{1}{2}} = \left[ \mathbf{G}_{j-\frac{1}{2}} - \frac{(\mathbf{F}_j - \mathbf{F}_{j-1})}{(x_j - x_{j-1})} \right] \quad \text{Eqn. 4-123}$$

$$\left(\frac{\Delta U}{\Delta t}\right)_{j+\frac{1}{2}} = \left[ \mathbf{G}_{j+\frac{1}{2}} - \frac{(\mathbf{F}_{j+1} - \mathbf{F}_j)}{(x_{j+1} - x_j)} \right] \quad \text{Eqn. 4-124}$$

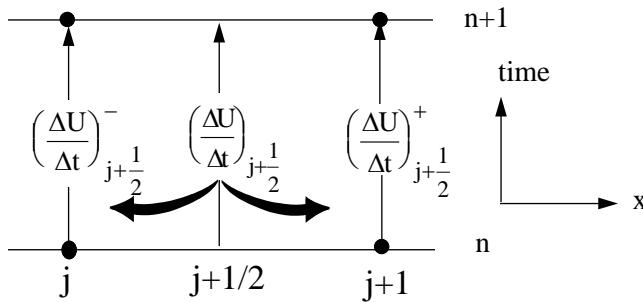


**Figure 4.33 Schematic of the Explicit Split Flux Differencing Scheme Used in ATEC**

Characteristic theory is used to develop weighting terms ( $\Gamma^+$ ,  $\Gamma^-$ ) for splitting the time derivatives to the adjacent nodes as illustrated in [Figure 4.33](#).

**Implicit Numerical Solver:** A finite difference representation of the Euler equations with source terms is applied over an interval that includes some part of the region outside of the interval between grid points  $j$  and  $j+1$ . For the explicit method, the

terms where shifted in

the direction of the characteristics to either the  $j^{\text{th}}$  or  $(j+1)^{\text{th}}$  node. In the implicit algorithm, this shift is extrapolated to points outside of the interval  $[j, j+1]$ , as shown in [Figure 4.34](#). The axial location of the shift, denoted by  $*$  in the following figure, is different for each eigenvalue. The distance of the shift is given by:

$$\alpha_i = \frac{(x^* - x_j)}{(x_{j+1} - x_j)} = \frac{\lambda_i \Delta t}{\Delta x}; \lambda_i < 0 \quad \text{Eqn. 4-125}$$

$$\alpha_i = \frac{(x^* - x_{j+1})}{(x_{j+1} - x_j)} = \frac{\lambda_i \Delta t}{\Delta x}; \lambda_i > 0 \quad \text{Eqn. 4-126}$$

where  $\lambda_i$  is the given characteristic.



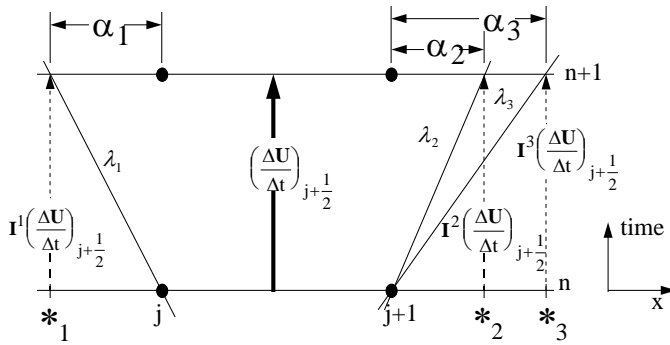


**Figure 4.34 Time Derivative Split to Adjacent nodes by Implicit Characteristic Based Split Flux Difference Scheme Used in ATEC**

**Boundary Conditions:** For both the explicit and implicit numerical solvers, the inlet boundary is applied at the physical inlet to the grid, and is assumed to be subsonic. Boundary conditions are developed using characteristics as developed above but with modifications to account for the fact that the algorithm is applied at the first node point. Through the linearization of the isentropic gas dynamic relationships and by specifying the change in total pressure and temperature,

appropriate information is along the characteristics to the interior grid. The exit boundary condition is developed in a similar manner, with the result being that only one parameter need be specified. The **ATEC** simulation requires that the user specify either exit static pressure, exit mass flow rate, or exit Mach number.

#### **VARIABLE TIME-STEP ROUTINE**

In order to provide efficient flow solutions for transient problems, the simulation uses a combination of an **explicitly formulated** numerical solver and an **implicitly formulated** numerical solver. Both of these numerical solvers are discussed in detail in Kneile, et al [4.63]. Through the combination of the two different solvers, efficient flow solutions using large time step sizes were obtained for all non-dynamic simulations while maintaining the capability of using only the explicit flow solver (with the resulting small time step size) during dynamic events. The approach used to provide this capability will now be developed.

A common measure of the stability of a given **explicit numerical solution** is given by the stability criteria of **Courant, Friedrichs, and Lewey (CFL)**. The **CFL** stability criteria states that for a stable numerical solution of a linear system, a sound wave should not propagate farther than one elemental control volume length during a time step. In other words, the **CFL** criteria is a measure of how far a sound wave travels during a given time step on the grid:

$$\frac{(|u| + a)\Delta t}{\Delta x} \leq \text{CFL}_{\text{limit}} \leq 1.0$$

**Eqn. 4-127**

where  $a$  is the speed of sound in the flow. For a linear system, the **CFL is limited to 1.0**. Due to the nonlinear nature of the **turbomachinery** simulation, particularly when simulating a choked turbine, experience has shown that a **more realistic limit is 0.6**. If the CFL limit is exceeded, the explicit method becomes numerically unstable and the resulting flow solution meaningless. For a given grid and flow, the maximum time step size that can be taken is given by:

$$\Delta t_{\text{max}} = \frac{\text{CFL}_{\text{limit}} \Delta x}{a + |u|_{\text{max}}}$$

**Eqn. 4-128**

The implicitly formulated numerical solver is not restricted by the CFL limit since the solution is obtained by solving all equations simultaneously at the current time step. For a purely linear system, a CFL approaching infinity is possible using an implicit numerical solver. Because the implicit flow solver used in the present work solves for the flow field solution simultaneously across the entire computational domain at the current time step, it takes more computational effort than an explicit solver that is also used.

The implicit numerical solver used in **ATEC** takes four times the amount of solution time than the explicit numerical solver requires for the same overall time step size.

Experience has shown that a CFL on the order of 500 is possible. This means that the implicit solver can use a time step 500 times larger than the explicit solver during steady state conditions.

Greater efficiency in calculating a flow solution can therefore be obtained by using the explicit numerical solver whenever the CFL criteria for the implicit numerical solver is less than four times the maximum CFL limit using the explicit numerical solver. During transient events, the use of the implicit numerical solver reduces the accuracy of the flow field solution because the value of the CFL criteria is greater than one. In other words, because a sonic wave can propagate farther than one elemental control volume length during a given time step, certain characteristics of the flow solution may be missed by the implicit numerical solver. To minimize the computational errors when implementing the implicit numerical solver, a unique variable time step routine was developed and implemented into the **ATEC** simulation. The technique, discussed in detail in the following paragraphs, sets the time step size based on a user defined rate-of-change limit in the dependent variable time derivatives. The technique also takes advantage of the greater efficiency of the explicit solver at small time step sizes.

The following variable time step routine has been developed and implemented into the **ATEC** simulation:

1. After the initial conditions and boundary conditions have been specified, the first time step is integrated using the explicit numerical solver. The time step size is calculated based upon the flow field velocities calculated in the initial conditions routine and a user provided explicit numerical solver CFL limit.
2. Based upon the solution obtained by the explicit numerical solver, the time derivatives of the dependent variables are linearly extrapolated to the maximum time step size as provided by the user.
3. If the extrapolated values of the time derivatives do not exceed a user defined limit (expressed as a percentage of the dependent variable), the next time integration is taken using the maximum time step size with the implicit numerical solver.
4. If one or more of the time derivatives of the dependent variables changes more than allowed, the time step size is reduced to keep the time derivative change equal to the limit:

$$\Delta t_{\text{new}} = \frac{(\text{Derivative Change Limit})(\text{Time Step Size from Explicit Solution})}{\text{Maximum Derivative Change Extrapolated from Explicit Solution}} \quad \text{Eqn. 4-129}$$

5. For each implicit numerical solver time step, the variable time step routine checks to see if using the explicit numerical solver would be more efficient than using the implicit numerical

solver. First, a maximum CFL for the next time integration of the flow field solution, based upon the current flow field solution and the time step size determined is calculated:

$$CFL_{check} = \frac{(\text{Maximum CFL from Explicit Solution})\Delta t_{new}}{(\text{Time Step Size from Explicit Solution})} \quad \text{Eqn. 4-130}$$

6. If  $CFL_{check}$  is greater than or equal to four times the maximum CFL allowed by the explicit numerical solver, the implicit solver is used. Otherwise, the explicit solver is used.
7. If the implicit numerical solver is used, the next time step integration uses the explicit solver to again calculate the time derivatives for the flow field solution. If the explicit numerical solver is used, the technique re-enters the procedure at the second bullet above. This process is repeated until an imposed simulation time limit is reached.

The variable time step routine is graphically depicted in **Figure 4.35**. The line identified as Case

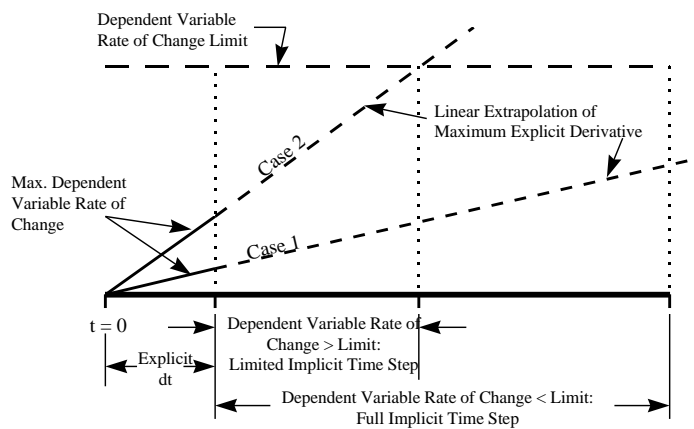


**Figure 4.35 Schematic of Variable Time-Step Routine**

1 represents a solution wherein the maximum rate of change of the dependent variables do not exceed the user imposed limit. Therefore, the full implicit time step size would be used for the next time integration. The line identified as Case 2, on the other hand, does exceed the derivative limit when linearly extrapolated. For this case, the implicit time step size would be limited to keep the derivatives from exceeding the imposed limit. A case where the implicit time step size is restricted sufficiently enough to warrant using the explicit solver is not shown above.

## **SOURCE TERMS**

In the governing equation there are terms that must be modeled by the user in order to obtain closure. These terms are: **Blade Forces; Shaft Work; Bleed Flows; and Energy Addition or Subtraction as heat transfer**. If these terms are set to zero, the standard Euler equations appear for non **turbomachinery** components. The source terms provide the performance and characteristics of the turbine engine component system. Each type of source term will be discussed below.

## **Compressor Stage Characteristics**

To provide the momentum and energy equations with **stage forces** and **shaft work**, a set of stage characteristics must be provided as input. **ATEC** has the capability to accept compressor stage characteristics in one of four forms.

The first form is the classical definition. A stage flow coefficient,  $\phi$ , is classically defined as

$$\phi = u / U \quad \text{Eqn. 4-131}$$

where  $u$  is the axial velocity and  $U$  is the wheel speed at the mean-blade radius. Pressure and temperature coefficients,  $\Psi^P$  and  $\Psi^T$  respectively are defined as:

$$\Psi^P = PR, \quad \text{Eqn. 4-132}$$

$$\Psi^T = TR - 1 \quad \text{Eqn. 4-133}$$

The form of the flow coefficient defined above does not lend itself to terms that are easily measured. By using the concepts of Mach number, flow function, and critical reference state, stage characteristics can be manipulated to produce the second form, which differs from the classical definition by a constant.

$$\phi = \frac{W_{cor} * NR_{cor}}{W_{cor}^{**}} \quad \text{Eqn. 4-134}$$

where

$$W_{cor} = \frac{W * (T_T)^{1/2}}{P_T * A} \quad \text{Eqn. 4-135}$$

$W$ = Actual physical airflow, lbm/sec

$T_T$ = Total temperature ( $^{\circ}R$ )

$P_T$ = Total pressure, psf

$A$ = Area,  $ft^2$

$$NR_{cor} = \frac{\text{Design Corrected Speed}}{\text{Actual Corrected Speed}} \quad \text{Eqn. 4-136}$$

$W_{cor}^{**}$  = Mass flow function representing sonic conditions = Constant = 0.5318

and

$$\Psi^P = (PR^{\gamma-1/\gamma} - 1) * (NR_{cor})^2 \quad \text{Eqn. 4-137}$$

$$\Psi^T = (TR - 1) * (NR_{cor})^2 \quad \text{Eqn. 4-138}$$

A third form of characteristics is a derivative of the second type and is defined as follows:

$$\phi = W'_{cor} * NR_{cor} \quad \text{Eqn. 4-139}$$

where

$$W'_{cor} = \frac{W * (TR_{ref})^{1/2}}{(PR_{ref})}; TR_{ref} = \frac{T_T}{T_{T_{ref}}}; PR_{ref} = \frac{P_T}{P_{T_{ref}}} \quad \text{Eqn. 4-140}$$

and

$$\begin{aligned} \Psi^P &= (PR - 1) * (NR_{cor})^2 \\ \Psi^T &= (TR - 1) * (NR_{cor})^2 \end{aligned} \quad \text{Eqn. 4-141}$$

A fourth form of the characteristics is a variation of the third type, and is defined by removing the influence of speed directly. Each stage characteristic is, however, a function of speed explicitly:

$$\phi = W'_{cor} \quad \text{Eqn. 4-142}$$

where

$$W'_{cor} = \frac{W * (TR_{ref})^{1/2}}{(PR_{ref})}; TR_{ref} = \frac{T_T}{T_{T_{ref}}}; PR_{ref} = \frac{P_T}{P_{T_{ref}}} \quad \text{Eqn. 4-143}$$

and

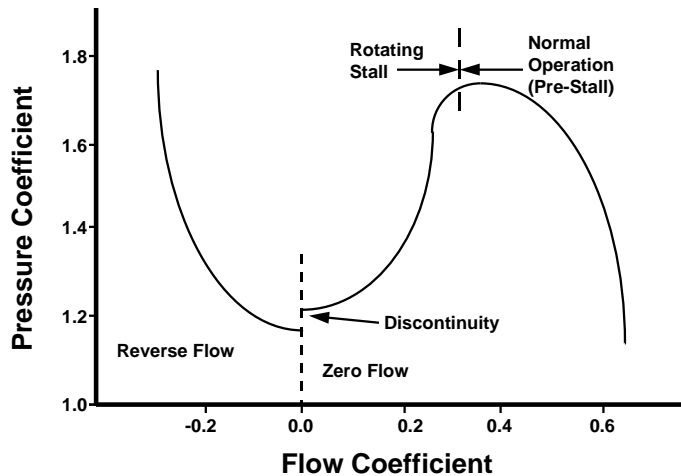
$$\begin{aligned} \Psi^P &= (PR - 1) \\ \Psi^T &= (TR - 1) \end{aligned} \quad \text{Eqn. 4-144}$$

The preceding definitions of stage characteristics may be selected by choosing

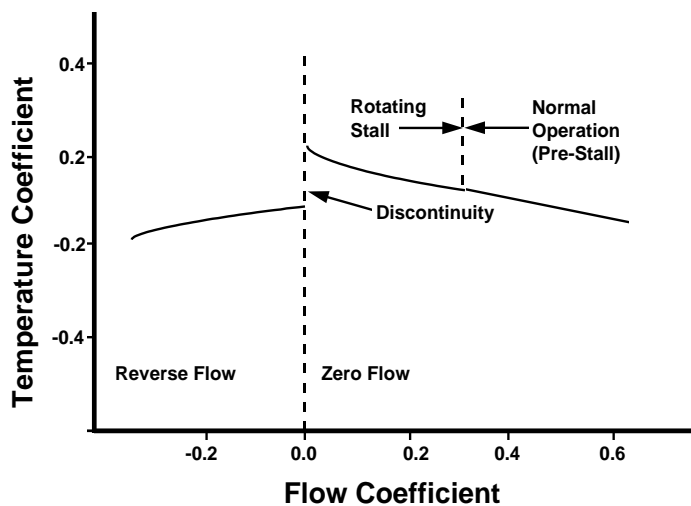
**TYPECHAR = 1, 2, 3, or 4,**

respectively. After the stage characteristic definition has been chosen and the characteristics have been specified in the proper form (as described in Appendix B), the code will automatically return steady total pressure ratio, PR, and total temperature ratio, TR, as a function of any airflow, W.

A typical set of steady-state characteristics for both pre-and post-stall operations is presented in **Figure 4.36**. The stage characteristics are divided into three distinct regions: pre-stall, rotating stall, and reversed flow. The pre-stall characteristic represents the performance of a blade row in normal operation. The transition to a rotating stall characteristic is approximated as a continuous characteristic along a postulated throttle line. The performance in the rotating stall region is based upon a flow-weighted average of a fully developed rotating stall cell. The pressure and temperature ratios in this region represent the average pressure and temperature rise across the stage for both stalled flow and unstalled flow. The reversed-flow characteristic region represents the pressure loss and temperature rise associated with full-annulus reversed flow. The discontinuity at zero flow has been experimentally shown to exist for a three-stage low-speed compressor. This aspect of the quasi-steady flow characteristic has been incorporated into the **ATEC** modeling technique and can be chosen by the user if so desired.



c. Pressure Coefficient



d. Temperature Coefficient

**Figure 4.36 Typical Stage Characteristics**

necessarily correct. In the rotating stall region, rotating stall develops very rapidly and the globally steady characteristic is no longer applicable. To provide a dynamic stage characteristic, a first order time lag on the stage forces has been incorporated into the modeling technique in the rotating stall region only. The first order lag equation used is:

$$\tau \frac{dFX}{dt} + FX = FX_{SS}$$

Eqn. 4-145

where

$FX$  = blade force and pressure area force of the casing,

$FX_{SS}$  = steady-state force, and

With the steady total pressure ratio and temperature ratio at an assumed steady flow, the code uses the steady-state version of the conservation equations and backs out the appropriate steady-state control volume forces and shaft work. These values are then used in the dynamic equations as the necessary values of forces in the momentum Eqn. and shaft work in the energy equation.

This approximation is crucial to the understanding of the development of compressor source terms for the dynamic equations. The foregoing discussion of the stage characteristic has described the principal features of the pre-stall and reversed-flow steady-state performance, and the globally steady rotating stall average performance. For pre-stall and post-stall reversed flow, steady characteristics can be used as they exist. However, for a dynamic event such as rotating stall or surge, the use of steady characteristics is not



$\tau$  = time constant.

This discussion of post-stall operation is only valid for the turbojet version of **ATEC**. Modeling enhancements for post-stall operation with a turbofan have yet to be made.

### Combustor Source Terms

The dynamic combustor model used by **ATEC** is a simple heat release model. Given the flow conditions in the control volumes that are defined by the user to be the combustor, the amount of energy generated by the combustion of the fuel is calculated and passed to the overall **ATEC** flow solver. The energy added to the flow is treated as a source term just as heat transfer is treated in the compressor. Several less important variables also appear in the Eqn.s; these have been identified in the discussions on user inputs.

The equivalence ratio of the flow in the combustor is a function of the airflow rate, the fuel flow rate, and the stoichiometric fuel air ratio of the fuel. It is assumed that the fuel is similar to JP-4, and the stoichiometric fuel air ratio is assumed to be 0.067627969. The user has the option of mixing the fuel with only part of the airflow. In an attempt to model the effect of the liner flow in the combustor, the user can specify the fraction of the overall airflow involved in the combustion process. For example, if the actual engine has a combustor where 50 percent of the airflow enters the primary zone and 50 percent goes into the liner, the equivalence ratio calculation will use only  $\frac{1}{2}$  of the airflow rate.

The amount of heat released is a function of combustor equivalence ratio, combustion efficiency, upper and lower flammability limits and the lower heating value of the fuel. The combustor flammability limits are determined by using steady-state engineering correlations developed by Herbert [Ref. 16]. In order for stable combustion to occur, the primary zone equivalence ratio ( $\phi_{PZ}$ ) must fall within a rich limit and a lean limit:

$$\phi_L \leq \phi_{PZ} \leq \phi_R \quad \text{Eqn. 4-146}$$

Based on experimental data, Herbert defined a Combined Air Loading Factor to calibrate the lightoff and blowout data.

$$CALF = \frac{\dot{m}_{pz}}{V_{pz} P_{t3}^2 e^{\frac{T_3}{n}}} \quad \text{Eqn. 4-147}$$

where

$$n = 220 \left[ \sqrt{2} \pm \ln \left( \frac{\phi_{pz}}{1.03} \right) \right] \quad \text{Eqn. 4-148}$$

The plus sign corresponds to  $\phi_{pz} \geq 1.03$ . A polynomial curvefit of Herbert's flammability data for a generic can type combustor is used in the model.

Combustion efficiency is determined by using steady-state engineering correlations developed by Lefebvre [4.69]. Lefebvre assumed that the overall combustion efficiency is limited by the efficiency of fuel evaporation and the reaction efficiency.

$$\eta_c = \eta_e * \eta_r \quad \text{Eqn. 4-149}$$

where

$$\eta_e = 1 - \exp \left[ \frac{-36 \cdot 10^6 P_3 V_C \beta}{\dot{m}_{pz} D_0^2 T_C} \right] \quad \text{Eqn. 4-150}$$

$$\eta_r = 1 - \exp \left[ \frac{-0.022 P_3^{1.3} V_C \exp(T_C/400)}{\dot{m}_{pz}} \right] \quad \text{Eqn. 4-151}$$

Further modification to the Lefebvre work following Derr and Mellor [4.70] is made such that  $V_C = V_{pz}$  and  $T_C = T_{pz}$ . In turn,  $T_{pz}$  is estimated by averaging the temperatures at the faces of the primary zone control volumes.

Because of the dynamic operation of the combustor, it is possible for heat release to occur for a short period of time even though the combustor equivalence ratio may lie outside the steady-state flammability limits. Likewise, the heat release process may not resume immediately after the combustor equivalence ratio reenters the flammability bounds. To account for these effects, a first order lag on the heat release rate as proposed by Davis, [4.65], is incorporated in the model:

$$\tau \frac{d\dot{Q}}{dt} + \dot{Q} = \dot{Q}_{ss}(t) \quad \text{Eqn. 4-152}$$

Time constants are provided to lag both the blowout process and the lightoff process.

The pressure loss in the combustor is based upon a one dimensional, constant area analysis of the combustor stagnation pressure loss due to the energy release as given by Oates (Ref. 19). The model assumes the gases to be calorically perfect at the inlet and exit of the combustor, and that the mass addition of fuel is small relative to the airflow rate. The total pressure ratio across the combustor is given by:

$$\frac{P_{t4}}{P_{t3}} = \frac{\left( 1 + \frac{\gamma_4 - 1}{2} M_{n4}^2 \right)^{\gamma_4/(\gamma_4 - 1)} P_4}{\left( 1 + \frac{\gamma_3 - 1}{2} M_{n3}^2 \right)^{\gamma_3/(\gamma_3 - 1)} P_3} \quad \text{Eqn. 4-153}$$

where

$$\frac{P_4}{P_3} = \frac{1 + \gamma_3 M_{n3}^2 [1 - (C_d/2)]}{1 + \gamma_4 M_{n4}^2} \quad \text{Eqn. 4-154}$$

## Frictional or Lossy Ducts

For most problems of interest, inlet and exit ducting are associated with the compression system. **ATEC** has been formulated to provide as many isentropic ducts as the user specifies in the geometry input file. At times, however, it may be desirable to simulate frictional effects or some other pressure loss mechanism. A rudimentary capability has been provided that can drop the total pressure (or increase total pressure if so desired) across any control volume. Temperature can be affected in a like manner. By appropriate definition of the problem in the data input and geometry files, user specified percent changes in both total pressure and total temperature can be applied to the ducting volumes.

Isentropic duct simulation is the default situation with **ATEC**.

The user has the responsibility of determining a realistic value for pressure loss. There are several prediction schemes for frictional loss based upon the Moody diagram, but the user must supply some information about the nature of the surface and the Reynolds number. Additionally, all pressure loss is applied instantaneously, thereby causing a spurious transient response within the modeling system. This response will be flushed out in a few hundred iterations.

## **BLEED FLOW CALCULATIONS**

**ATEC** has the capability of specifying control volume bleed flow whether it be into or out of the control volume. This capability can be used to simulate start bleeds, customer bleeds, or surge bleeds. With this version of **ATEC** the user has the capability of specifying whether the bleed flow is a percentage of the inlet flow or is calculated from a bleed system geometry and flow properties. In addition, the user can specify a number of bleeds up to fifteen (15). The specification of how many and which control volumes those bleeds are located are specified in the geometry file as well as the Namelist input file.

If the user specifies the bleed flow as a percentage of the inlet flow, he does so by setting  $BLDVAL = 1$  in the BLEEDS Namelist option. If  $BLDVAL$  is any other value, the bleed flow is calculated by the following algorithm.

The user must provide the following inputs:

- Constant Cross-sectional Area of the Bleed Pipe
- Pressure drop across the bleed piping system (expressed as a pressure ratio less than 1)
- Temperature Increase/Decrease across the bleed piping system (also expressed as a temperature ratio)
- Controlling Pressure
- Reservoir Static Pressure if Outflow
- Reservoir Total Inlet Pressure if Inflow
- Reservoir Total Inlet Temperature if Inflow

The mass flow associated with the bleed is calculated using

$$W_B = \frac{fm}{fg} \quad \text{Eqn. 4-155}$$

where

$$fm = \left( \frac{P_T A}{\sqrt{T_T}} \right) \sqrt{\frac{\gamma}{R}} M \quad \text{and} \quad fg = \left( 1 + \frac{\gamma - 1}{2} M^2 \right)^{\frac{\gamma + 1}{2(\gamma - 1)}} \quad \text{Eqn. 4-156}$$

$M$  = Mach Number and is calculated from the following expression:

$$M = \left\{ \frac{2}{\gamma - 1} \left[ \left( \frac{P_T}{P_S} \right)^{\frac{\gamma - 1}{\gamma}} - 1 \right] \right\}^{1/2} \quad \text{Eqn. 4-157}$$

and goes to unity when choked.

Choking is checked by comparing the total-to-static pressure ratio to the choking pressure ratio as follows:

$$\frac{P_T}{P_S} \geq \left( \frac{\gamma + 1}{2} \right)^{\frac{\gamma}{\gamma - 1}} \quad \text{Eqn. 4-158}$$

### **ATEC'S OPTIMIZATION OPTIONS**

**ATEC** now has an option for optimization of initial conditions. This was primarily developed for when a user may not know the optimum inlet mass flow rate for a given power setting and fuel flow rate. If a value far off optimum is chosen, wild variations in engine output can cause problems in the initial start-up of the **ATEC** code. As a result, an optimization procedure was developed to determine this optimum value before moving forward with the initial calculations in **ATEC**. This can save a great deal of time over a simple trial and error approach.

The optimization procedure developed uses the **REPLICAS** (Robust, Efficient Procedures and Logic for the Implementation of Computerized Analysis and Simulation) nonlinear solver. This solver was originally provided as a selectable option in Sverdrup Technology's Advanced Turbine Engine Simulation Technique (**ATEST**). Basically, it minimizes selected error terms by optimizing the defined iteration variables. Initially guesses for the iteration variables are provided to **REPLICAS**. By perturbing each of them, one at a time, a matrix of influence coefficients may be determined relating the change in each error term to the change in iteration variable. The matrix is then scaled and inverted providing a linear approximation describing the engine model behavior in the neighborhood of the initial set of iteration variables. This matrix is then updated during each iteration using Broyden's method, and the error terms are recalculated. This iteration process continues until the errors converge.

The method of C. G. Broyden is the key to the computational efficiency of **REPLICAS**. Using this method, the Jacobian matrix is corrected upon each iteration based on information obtained directly from the results of previous iterations. In this way, the reevaluation of the Jacobian during each iteration is no longer required. The following recursive relationship calculates each successive iteration variable:

$$X^i = X^{i-1} - E^{i-1} \cdot A^{-1}$$

Eqn. 4-159

where E is the error, A is the Jacobian matrix  $\Delta E / \Delta X$  and the superscripts are iteration indices. The delta is used to indicate that the quantity is the discrete approximation of a differential. Convergence is attained when all of the elements of E are smaller than a given tolerance value. Changes to iteration variables and the errors, as well as the elements of the current inverted Jacobian, all go into calculating a matrix of changes in the following manner:

$$\Delta A^{-1} = Z^T \cdot (\Delta X^i - A^{-i} \cdot \Delta E^i)$$

Eqn. 4-160

$$Z^T = \Delta X^{iT} \cdot A^{-i} / (\Delta X^{iT} \cdot A^{-i} \cdot \Delta E^i)$$

$$\Delta X^i = X^i - X^{i-1}$$

$$\Delta E^i = E^i - E^{i-1}$$

The updated matrix is then given by:

$$A^{-i+1} = A^{-i} + \Delta A^{-1}$$

The Jacobian is therefore evaluated only once during the initial iteration, and it is updated as described for all successive iterations.

A conditioning algorithm is utilized to insure reliable convergence properties. This leads to a scaling of the initial Jacobian by dividing each row by the largest value contained within it and each column by the resulting largest value contained within it. In this manner, no term in the initial Jacobian matrix remains with a value greater than one. The matrix is rescaled in this manner after each Broyden update. This procedure has the advantage that a constant tolerance value can be applied to the changes to the iterates as well as the errors in order to determine convergence.

### Turbojet Engine Optimization

For a turbojet engine, the appropriate error term would be the difference in mass flow entering the turbine compared with the mass flow it should optimally be getting to provide the necessary power output to drive the compressor. The following is an outline of the optimization procedure utilized for a turbojet engine:

- Guess a value for inlet mass flow rate
- Use **ATEC** initial calculations to determine the resulting mass flow rate entering the turbine.
- Calculate the optimum mass flow rate for the given power setting.
- Use the difference between these two mass flow rate values as an error term for **REPLICAS**.
- Vary inlet mass flow rate and calculate the Jacobian matrix of influence coefficients.
- Change the inlet mass flow rate and recalculate the error term.
- Update the Jacobian matrix using the Broyden method.
- Continue until the error term converges to very near zero.

In this way, the optimum inlet mass flow rate is found.

Modifications to **ATEC** and the **REPLICAS** solver needed to be made before applying it to this specific problem. The initial guess for inlet mass flow rate and subsequent iteration values must fall within specific boundaries for the engine to be capable of operation. If the mass flow rate is too low, the compressor stalls. Too high a mass flow rate can choke the grid. **ATEC** therefore was modified to feed the **REPLICAS** solver these specific boundaries. In turn, the **REPLICAS** solver was also modified to optimize only within these boundary values.

**ATEC** determines the proper optimization boundaries by using an iteration scheme to steadily increase mass flow rate from an initial value very near zero until the stall point for the compressor and choke point for the grid are found. An initial guess for inlet mass flow rate is then chosen midway between these boundaries, and this value along with the boundary values are passed to the **REPLICAS** solver.

The modification to the original **REPLICAS** routine took place within the iteration subroutine. **REPLICAS** still determines a new guess for inlet mass flow rate based on the updated matrix from previous iterations. However, before utilizing **ATEC** to recalculate the error term, **REPLICAS** checks that its new value for mass flow rate falls within the determined boundaries. If it is too high, then the increase is reduced and the check is made again. If it is too low, then the decrease is reduced and the check is made again. This process continues until a new value for inlet mass flow rate has been selected which falls within the boundaries. **ATEC** is then called for determination of the new error value. This allows for optimization to occur even if the optimum point lies near a boundary. Once an optimum value has been found, this mass flow rate is used to set **ATEC's** initial conditions.

### Turbofan Engine Optimization

Applying the optimization procedure to a turbofan engine requires two independent variables. The first is once again inlet mass flow rate. The second independent variable is bypass ratio. The correct amount of mass flow being passed into the engine must first be determined followed by the percentage of this allowed to pass through the core of the turbofan. The same procedure is applied to a turbofan as was outlined for a turbojet, however influence coefficients for the Jacobian matrix now include error variation with bypass ratio variation. The two required error terms are simply the differences in mass flow entering the turbines compared with the mass flow they should optimally be getting to provide the necessary power output to drive each compressor.



Boundaries for this optimization include the stall points for the fan and compressor, and the choked grid values for the inlet, core, and bypass ducts. Initial determination of these boundaries is done in the same manner as for the turbojet. However, **ATEC** was modified such that each of the three pieces are considered separately. The first piece includes the inlet, fan, and ducting up to the high pressure compressor and bypass inlet. First mass flow is varied from near zero until the fan stall point is found. It is then increased until the choke boundary for the grid is found. These values are converted to boundaries corrected for pressure and temperature and a point midway between is initially selected.

The second piece considered is the core of the turbofan. The stall point for the high pressure compressor is obtained and then the choke value for this section. The corrected values are stored, and a point midway between is initially selected. From this an initial bypass ratio is set as well.

Finally the choke point for the third piece, the bypass ducting, is determined, and that corrected flow boundary is stored. The flow through the bypass duct, based on the chosen inlet mass flow rate and the bypass ratio, is compared against the choke boundary. If it exceeds this limit, two options are available. First it looks at reducing the bypass ratio. This results in an increase to the core flow, so a check is performed to maintain the core flow below its choke boundary. If a point is reached such that a further decrease in bypass ratio would cause the core flow to exceed its choke limit, this is no longer an option. The only other solution is therefore to reduce the inlet mass flow selection, while checking that this does not drop below the stall point of the fan. Once an initial inlet mass flow rate and bypass ratio have been determined, such that the engine will operate within its boundaries, the Replicas optimization begins. The **ATEC** initial conditions are set once the optimum values have been found for inlet mass flow rate and bypass ratio.

### **ATEC'S NOZZLE BOUNDARY CONDITION**

**ATEC** now has a nozzle boundary condition. Users may input nozzle throat area as well as tables for modifying this area with time. Tables for pressure losses in the nozzle are allowed for as well. These involve entry of the nozzle discharge coefficient ( $C_D$ ) for various pressure ratios. An iteration routine is utilized to determine the correct value of  $C_D$  and thus pressure at the nozzle throat.

### **REFERENCES:**

**4.60** Garrard, G. D., "**ATEC**: The Aerodynamic Turbine Engine Code for the Analysis of Transient and Dynamic Turbine Engine System Operations," Ph.D. Dissertation, the University of Tennessee, Knoxville, August, 1995.

**4.61** Garrard, Doug, "**ATEC**, The Aerodynamic Turbine Engine Code for the Analysis of Transient and Dynamic Gas Turbine Engine System Operations, Part 1: Model Development", ASME Paper # 96-GT-193, June 1996.

**4.62** Garrard, Doug, "**ATEC**, The Aerodynamic Turbine Engine Code for the Analysis of Transient and Dynamic Gas Turbine Engine System Operations, Part 2: Numerical Simulations", ASME Paper # 96-GT-194, June 1996.

- 4.63** Kneile, K. R., and Hale, A. A., "Appendix C: Numerical Solution to the Governing Eqn.s," Appendix C in Garrard, G. D., "**ATEC**: The Aerodynamic Turbine Engine Code for the Analysis of Transient and Dynamic Turbine Engine System Operations," Ph. D. Dissertation, The University of Tennessee, Knoxville, August, 1995.
- 4.64** Hale, A. A. and Davis, M. W., "DYNamic Turbine Engine Compressor Code **DYNTECC** - Theory and Capabilities," AIAA-92-3190, Presented at the AIAA/SAE/ASME/ASEE 28th Joint Propulsion Conference and Exhibit, Nashville, TN, July 6-8, 1992.
- 4.65** Davis, M. W., "A Stage-by-Stage Post-Stall Compressor System Modeling Technique: Methodology, Validation, and Application," Ph. D. Dissertation, Virginia Polytechnic Institute and State University, August, 1986.
- 4.66** Greitzer, E. M., "REVIEW-Axial Compressor Stall Phenomena," Transactions of the ASME, Journal of Fluids Engineering, Vol. 102, June, 1980, pp. 134 - 151.
- 4.67** Garrard, G. D., Davis, M. W., Jr., and Hale, A. A., "Recent Advances in Gas Turbine Engine Dynamic Models Developed Through JDAPS," 95-GT-146, Presented at the 40th ASME International Gas Turbine and Aeroengine Congress and Exposition, Houston, TX, June 1995.
- 4.68** Herbert, M. V., "A Theoretical Analysis of Reaction Rate Controlled Systems - Part 1," Chapter 6 in *Combustion Research and Reviews, 1957*, Agardograph No. 15, Butterworths Scientific Publications, London, England, February, 1957.
- 4.69** Lefebvre, A. H., "Fuel Effects on Gas Turbine Combustion - Ignition, Stability, and Combustion Efficiency," Journal of Engineering for Gas Turbines and Power, Vol. 107, January 1985, pp. 24 - 37.
- 4.70** Derr, W. S., and Mellor, A. M., "Recent Developments," in Design of Modern Turbine Combustors, edited by A. M. Mellor, Academic Press, Harcourt Brace Jovanovich, New York, NY, © 1990.
- 4.71** Oates, G. C., Aerothermodynamics of Gas Turbine and Rocket Propulsion, AIAA Education Series, J. S. Przemieniecki, Series Editor-in-Chief, American Institute of Aeronautics and Astronautics, Washington, D. C., © 1988, pp. 218-220.
- 4.72** Crawford, R. A., and Burwell, A. E., "Quantitative Evaluation of Transient Heat Transfer on Axial Flow Compressor Stability," AIAA 85-1352, Presented at the 21st AIAA/SAE/ASME/ASEE Joint Propulsion Conference, Monterey, CA, July 8-10, 1985.
- 4.73** MacCallum, N. R. L., and Pilidis, P., "The Prediction of Surge Margins During Gas Turbine Engine Transients," ASME 85-GT-208, Presented at the Gas Turbine Conference and Exhibit, Houston, TX, March 18-21, 1985.
- 4.74** Sissom, L. E., and Pitts, D. R., Elements of Transport Phenomena, McGraw-Hill, Inc, New York, NY, © 1972, pp. 118-121.
- 4.75** Varner, M. O., Martindale, W. J., Phares, W. J., Kneile, K. R., and Adams, J. C., Jr., "Large Perturbation Flow Field Analysis and Simulation for Supersonic Inlets," NASA CR-174676, September, 1994.

#### 4.6 PARALLEL COMPRESSION SYSTEM CODE

**DYNTECC** can also be configured as a parallel compression system model as done by Hale and Davis, respectively [4.76, 4.77]. As indicated in Figure 4.37, a parallel compressor model uses a multi-segmented circumferential compressor concept. Each circumferential segment is modeled using the one-dimensional technique described above. This limitation is imposed since the post-stall technique has been developed only for the truly one-dimensional situation. The combustor model has not been investigated using a parallel system, but there is no fundamental problem that prevents such an approach. The model is not allowed to go into post-stall behavior. Post-stall behavior for multiple circumferential or radial segments has not yet been developed.

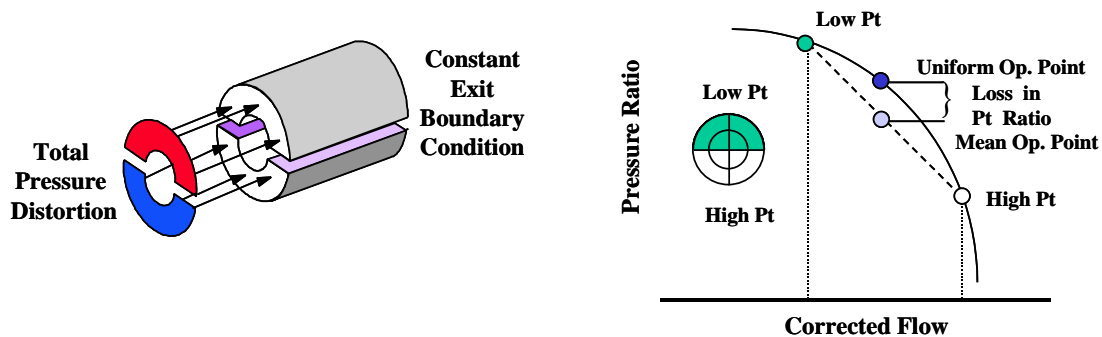


Figure 4.37 Classical Parallel Compressor Theory Concept

**DYNTECC** can use classical parallel compressor theory. Each segment operates independently except at the exit boundary where the specification of either uniform static pressure or uniform Mach number is imposed. This is the only location where the modeling technique transfers information from one segment to another. Different levels of pressure or temperature distortion may be imposed upon the inlet, and each segment will operate to its own limit. In this classical form, when one segment reaches the instability limit the entire compression system is considered to be unstable.

Calculations are halted when a set number of stages begin operating on the positive side of their pressure characteristic.

#### MODIFIED PARALLEL COMPRESSOR THEORY

The most recent research extends the **DYNTECC** model beyond the basic parallel compressor theory. The purpose of this extension is to provide a more accurate predictive tool for compressor performance and operability for cases involving inlet distortion. These modifications include circumferential mass redistribution, radial mass redistribution, dynamic blade response, and radial work redistribution. All of the modifications to the parallel compressor theory are based on research by Kimzey [4.78]. A detailed application of the modified parallel compressor theory was performed by Shahrokhi and Davis [4.79, 4.80].

## Circumferential Mass Redistribution

Inlet pressure distortions with circumferential non-uniformities can generate flow in the circumferential direction. The static pressure difference between two adjacent circumferential segments drives a flow in the circumferential direction (See [Figure 4.38](#)).

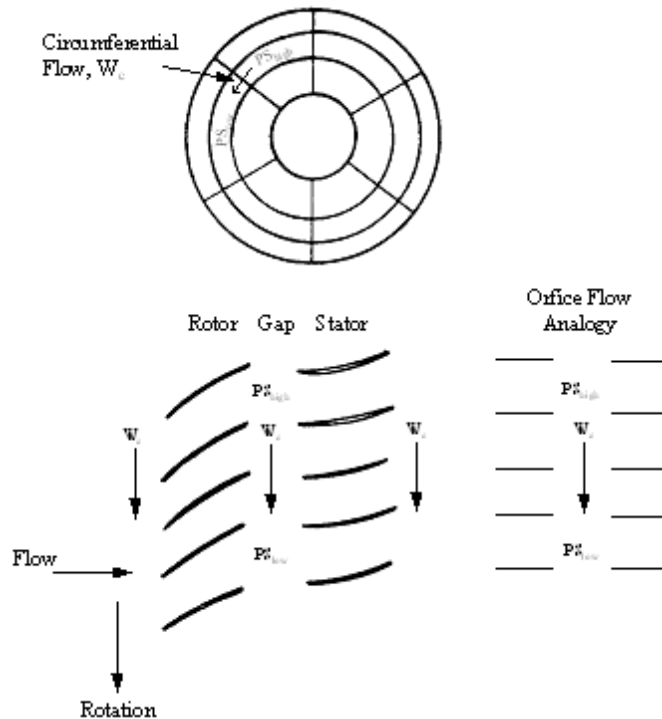


**Figure 4.38 Illustration of the Circumferential Mass Redistribution Model**

This flow occurs in the rotor-stator gap and can be approximated using a simple orifice flow analogy, a technique developed by Kimzey. In the analogy, the high and low pressure regions are seen as reservoirs and the rotor-stator gap as an orifice. Thus, the flow can be approximated utilizing a simple algebraic expression based on classic orifice flow.

To derive the circumferential mass redistribution expression, we begin with the basic assumption that flows with small pressure drops can be treated as incompressible. Therefore, the derivation begins with the continuity Eqn. and Bernoulli's Eqn. for steady flow. The Eqn. for the mass flow rate is expressed in terms of a pressure difference and an orifice flow coefficient.

$$W_c = \text{CXFC} * A_{\text{gap}} \sqrt{2\rho(P_{s,\text{high}} - P_{s,\text{low}})} \quad \text{Eqn. 4-161}$$

The crossflow coefficient, **CXFC**, is analogous to the orifice coefficient. For an orifice flow with a pronounced *vena contracta* and high Reynolds number, the value for the orifice coefficient converges to 0.6, which is used as a default in the **DYNTECC** model.

## Radial Mass Redistribution

Secondary radial mass flow can occur axially in the compressor through the passages between the compressor blades. The mass flux in the radial direction, referred to as the radial mass redistribution or crossflow, is similar in concept to the circumferential mass redistribution (See [Figure 4.39](#)). Both circumferential and radial mass fluxes across segment boundaries are due to differences in static pressure that drive the secondary flows.

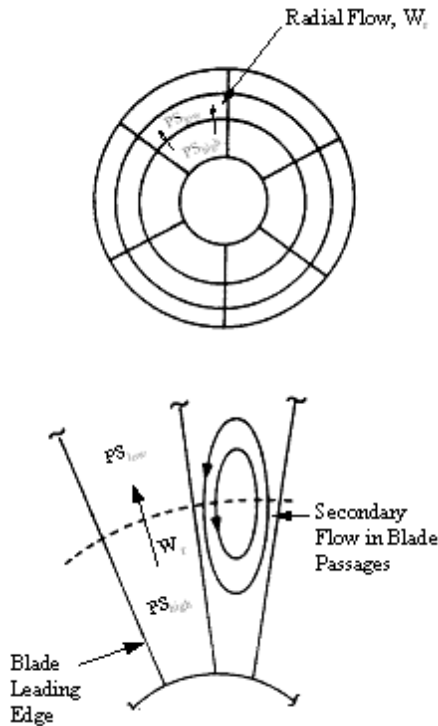


**Figure 4.39 Illustration of the Radial Mass Redistribution Model**

The expression for the radial mass redistribution has a similar derivation as the circumferential mass redistribution. Based on the Bernoulli equation, the theoretical mass flow rate driven by a radial static pressure gradient may be expressed as:

$$W_{r,net,theoretical} = \frac{A_{low}}{\sqrt{1 - \left( \frac{A_{low}}{A_{high}} \right)^2}} \sqrt{2\rho(P_{s,high} - P_{s,low})}$$

**Eqn. 4-162**

This Eqn. assumes steady, incompressible, frictionless flow. In order to determine the actual mass flow rate in the radial direction, a term is added to account for additional flow effects such as viscous and centrifugal forces.

$$W_{r,net,actual} = (1 + \kappa) W_{r,net,theoretical}$$

**Eqn. 4-163**

An Eqn. for the net mass flux in the radial direction is attained by setting the radial crossflow coefficient, CXFR, equal to the multiplier in the above Eqn.:

$$W_{r,net,actual} = CXFR * \frac{A_{low}}{\sqrt{1 - \left( \frac{A_{low}}{A_{high}} \right)^2}} \sqrt{2\rho(P_{s,high} - P_{s,low})}$$

**Eqn. 4-164**

### Dynamic Blade Response

Pressure distortions that are non-varying with time are referred to as steady distortions. However, from the perspective of an individual rotor blade encountering such a distortion, the distortion will vary with time. The rotor blade angle of attack,  $\alpha$ , due to the change in the relative velocity incident upon the blade leading edge. This is often referred to as an unsteady cascade effect. Goethert and Reddy [4.81] developed an effective frequency that the rotor blade experiences when a steady distortion is present. This frequency is called the reduced frequency,  $k$ , and is described as the ratio of the flow passage time over the disturbance stay time.

$$k = \frac{\Delta t_{passage}}{\Delta t_{disturbance}} = \frac{2\pi f C}{V_{rel}}$$

**Eqn. 4-165**

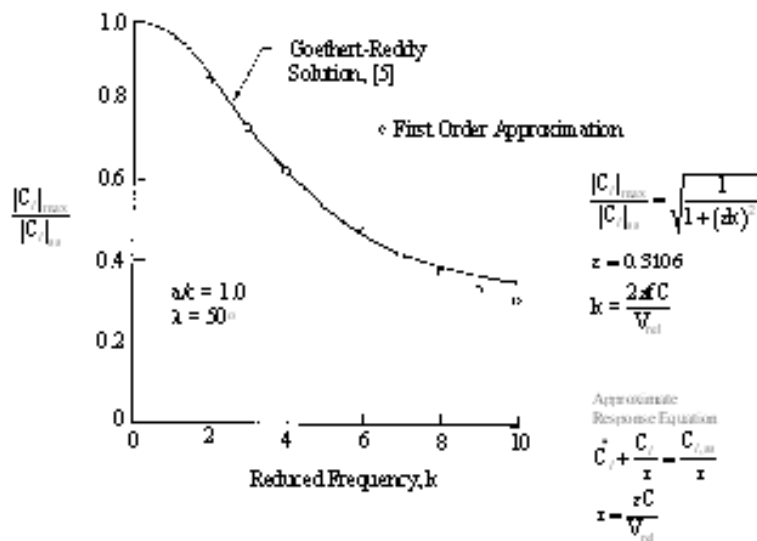


**Figure 4.40 Unsteady Lift Coefficient Magnitude Ratio**

Kimzey used the concept of reduced frequency to determine the response of a blade row to oscillating flow conditions. Based on the Goethert and Reddy analysis, the blade's response, in terms of the coefficient of lift, was approximated by a first-order solution (See [Figure 4.40](#)):

$$\frac{dC_l}{dt} + \frac{C_l}{\tau} = \frac{C_{l,ss}}{\tau} \quad \text{Eqn. 4-166}$$

The blade time constant,  $\tau$ , is a function of chord length and reduced frequency,  $k$ . Using the previously defined expression for  $k$  and simplifying:

$$\tau = \frac{\varepsilon C}{V_{rel}} \quad \text{Eqn. 4-167}$$

where  $\varepsilon$  is a constant dependent upon cascade geometry (i.e., stagger and solidity).

The approximation for the first-order lagging solution is:

$$\frac{|C_l|_{max}}{|C_l|_{ss}} = \frac{1}{\sqrt{1 + (\varepsilon k)^2}} \quad \text{Eqn. 4-168}$$

Kimzey showed that the dynamic value of the coefficient of lift is the same as the dynamic value of the stage loading parameter,  $\psi$ :



$$\frac{|\psi|_{\max}}{|\psi|_{ss}} = \frac{|C_l|_{\max}}{|C_l|_{ss}} = \text{DLR} \quad \text{Eqn. 4-169}$$

The dynamic lag algorithm developed by Kimzey introduces a dynamic lag ratio, DLR, into the stage characteristics:

$$\psi_{\text{present, c.v.}} = \text{DLR} \psi_{\text{present, ss, c.v.}} + (1 - \text{DLR}) \psi_{\text{previous, c.v.}} \quad \text{Eqn. 4-170}$$

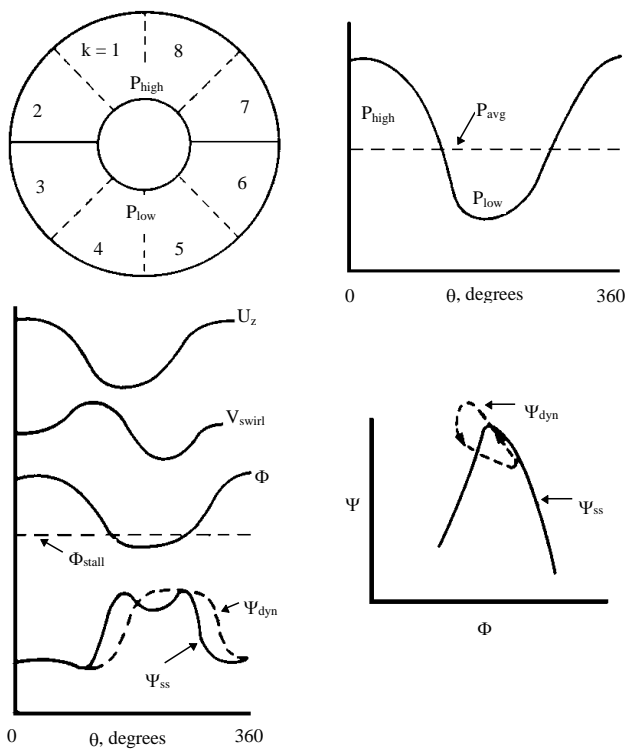


**Figure 4.41 Unsteady Blade Response to Circumferentially Nonuniform Flow**

The dynamic lag ratio damps the model's response to a flow disturbance (See [Figure 4.41](#)). The lag ratio is necessary because the characteristics used to determine the stage loading parameter are based on steady-state compressor operation. The DLR compensates for the dynamic response of the rotor blade.

### Radial Work Redistribution

Axial flow compressors do not have uniform blade loading in the radial direction. The work redistribution model seeks to radially distribute the work done across the blade to more accurately reflect experimental observations. The redistribution model uses scale factors to adjust the steady-state stage characteristics and thereby reflect the experimentally observed radial variations:

$$\text{PR} = \text{PR}_{ss} * \text{ScaleFactor} \quad \text{Eqn. 4-171}$$

An example of the effect of the scale factors is shown in [Figure 4.42](#).

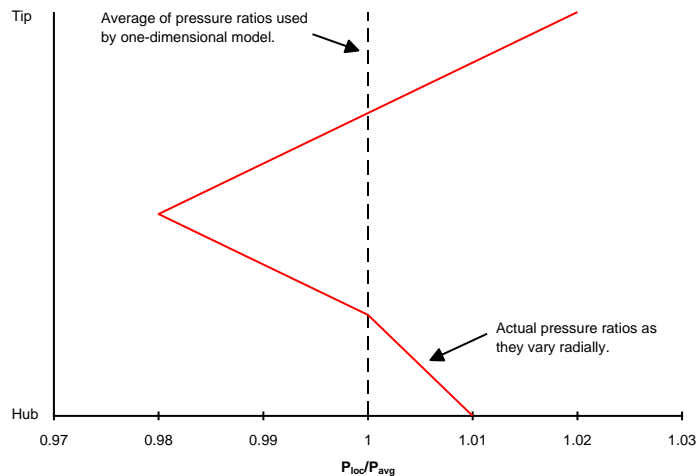


**Figure 4.42 Illustration of Work Redistribution Concept with Radial Variation of Pressure Ratios**

#### **REFERENCES:**

- 4.76** Hale, A. A. and M. W. Davis, Jr., "DYNamic Turbine Engine Compressor Code: **DYNTECC** -- Theory and Capabilities", AIAA Paper # AIAA-92-3190, Presented at the 28th Joint Propulsion Conference and Exhibit, Nashville, TN, July 1992.
- 4.77** Davis, M. W., Jr., "Parametric Investigation into the Combined Effects of Pressure and Temperature Distortion on Compression System Stability", AIAA Paper # AIAA-91-1895, Presented at the 27th Joint Propulsion Conference, Sacramento, CA, June 1991.
- 4.78** Kimzey, W. F., "An Analysis of the Influence of Some External Disturbances on the Aerodynamic Stability of Turbine Engine Axial Flow Fans and Compressors", AEDC-TR-77-80, August, 1977.
- 4.79** Shahroghi, K. A., "Application of a Modified Dynamic Compression System Model to a Low-Aspect Ratio Fan: Effects of Distortion," Unpublished Master's Thesis, Vanderbilt University, Nashville, Tennessee, May 1995.
- 4.80** Shahroghi, K. A., and M. W. Davis, Jr., "Application of a Modified Dynamic Compression System Model to a Low-Aspect Ratio Fan: Effects of Distortion," AIAA-95-0301, Presented at the 33rd Aerospace Science Meeting, Reno, NV, January 1995.
- 4.81** Goethert, B. H. and Reddy, K. C., "Unsteady Aerodynamics of Rotor Blades of a Compressor under Distorted Flow Conditions." AGARD paper presentation, Silver Springs, MD, September 1970.

#### 4.7 3D EULER CODE, TEACC & TEACCSTALL TECHNICAL APPROACH

The development of three-dimensional compressor simulation has taken several forms over the years, with the first being the Turbine Engine Analysis Compressor Code (**TEACC**) by Hale [4.82]. This code went through several iterations over the years. The **TEACC** code was determined to have several limitations that were not able to be overcome without a major re-write. At this time, another code (**CSTALL** by Chima, [4.84]) was picked up and blended with **TEACC** to remove the limitations and this blended code became **TEACCSTALL**. The description of both the **TEACC** and **TEACCSTALL** code are presented in the following section.

The original Turbine Engine Analysis Compressor Code (**TEACC**) started development in the early 1990's. It has undergone several different major modifications over the years. The algorithm uses a 3-D CFD code as its basis. Over the years, several different CFD codes have been used in the **TEACC** method, including **ARO1**, **NPARC**, **WIND**, and finally **OVERFLOW**. The following section describes in detail the technical approach to the **TEACC** code in two different iterations, the source term approach, and the boundary condition approach.

##### TEACC SOURCE TERM APPROACH

The source term approach is the original approach taken the **TEACC** code development history. This methodology is conceptually shown in Figure 4.43. A general purpose 3D flow simulation

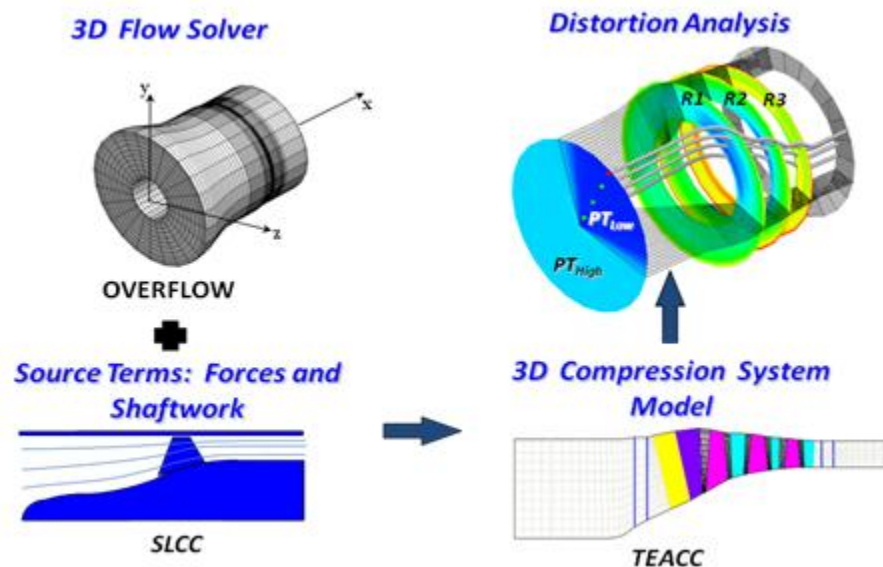


Figure 4.43 TEACC Source Term Methodology

computer code, **OVERFLOW**, is modified to accept turbomachinery source terms by semi-actuator disk theory. These turbomachinery source terms are calculated using the **SLCC** discussed in Section 4.3. **TEACC** is constructed by combining the technology of solving the Euler equations (**OVERFLOW**) modified to include source terms and the technology of calculating the source terms (**SLCC**) to produce a time-dependent turbomachinery simulation with the capability of analyzing inlet distortion.

The governing equation used in **TEACC** are developed by applying the conservation of mass, momentum, and energy. In turbomachinery flows, the viscous effects predominate mostly along the wall, making accurate simulation of the flow field away from the wall possible by using the Euler equations with turbomachinery source terms [4.83]. The equation of fluid motion using the thermally and calorically perfect ideal gas assumption with turbomachinery source terms are:

$$\frac{\partial \mathbf{Q}}{\partial t} + \frac{\partial \mathbf{E}}{\partial x} + \frac{\partial \mathbf{F}}{\partial y} + \frac{\partial \mathbf{G}}{\partial z} = \mathbf{S} \quad \text{Eqn. 4-172}$$

$$\mathbf{Q} = \begin{bmatrix} \rho \\ \rho u \\ \rho v \\ \rho w \\ (\rho e_t) \end{bmatrix}; \quad \mathbf{E} = \begin{bmatrix} \rho u \\ \rho u^2 + P \\ \rho uv \\ \rho uw \\ (\rho e_t + P)u \end{bmatrix}; \quad \mathbf{F} = \begin{bmatrix} \rho v \\ \rho uv \\ \rho v^2 + P \\ \rho vw \\ (\rho e_t + P)v \end{bmatrix}; \quad \mathbf{G} = \begin{bmatrix} \rho w \\ \rho vw \\ \rho wv \\ \rho w^2 + P \\ (\rho e_t + P)w \end{bmatrix}; \quad \mathbf{S} = \begin{bmatrix} S_{\dot{m}} \\ S_{\dot{x}} \\ S_{\dot{y}} \\ S_{\dot{z}} \\ S_{\dot{e}} \end{bmatrix} \quad \text{Eqn. 4-173}$$

$$e_t = e + \frac{1}{2} V^2$$

$$P = \rho R T$$

The volumetric turbomachinery source terms are: (1) bleed per volume, (2) forces in the x, y, and z direction per volume, and (3) rate of shaft work per volume. The technique for calculating these source terms from the **SLCC** are developed later in this section.

The time dependent Euler equations with source terms define a hyperbolic in time and an elliptic in space system of equations requiring a full set of boundary conditions specified at all boundaries. The boundary conditions used with **OVERFLOW** are explicit. The inflow boundary condition is based on reference plane characteristics, and the total pressure and total temperature at the inlet are specified. Inlet flow directions are assumed to be normal to the boundary. The exit boundary condition is a variable static pressure capable of supporting the exit profile of strong swirl. The exit static pressure is calculated by specifying a single value and imposing the static pressure profile of the adjacent upstream station on the exit. The wall boundary conditions are assumed to be slip wall; the normal velocity components are set equal to zero at the solid walls. A rotationally periodic (wrap-around) boundary condition is used in the circumferential direction, where the circumferential seam of the grid was overlapped by two circumferential segments.

Three-dimensional blade force and rate of shaft work terms are supplied by the **SLCC**. The **SLCC** is described in [Section 4.3](#). For the **TEACC** simulation to be responsive to the local change in total pressure due to inlet distortion and capable of modeling transients, the **SLCC** must be restricted to a small axial region on either side of the blades. Since the **SLCC** is a subsonic flow solver, it needs a full set of boundary conditions around its domain. The **SLCC** boundary conditions of inlet and exit curvature, overall mass flow, swirl angle, total temperature, and total pressure are calculated from the **TEACC** flow field. [Figure 4.44](#) is included to show the truncated grid in which the **SLCC** is restricted to operate.

Although the boundary conditions are of the same type in this new mode of operation as they were before the grid was truncated to the blades, they are now more complicated since they are no longer uniform but a function of the time dependent **TEACC** flow field around the blades.

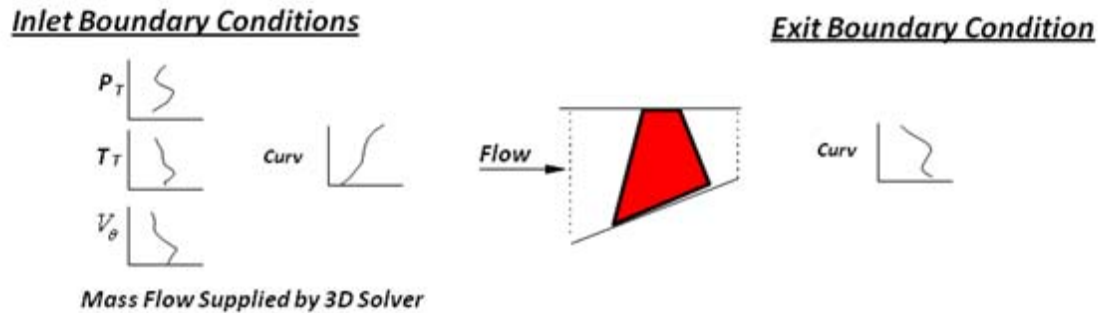
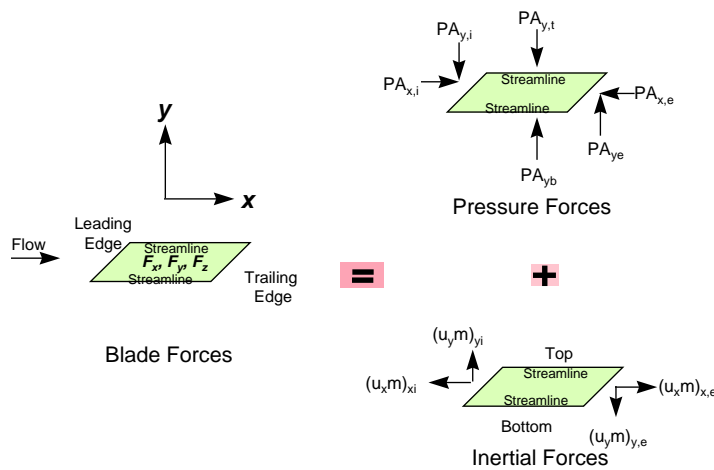


**Figure 4.44 Modifications to SLCC for Calculating Source Terms**

The boundary conditions for the modified **SLCC** technique are outlined below for the computational domain specified in [Figure 4.44](#). Inlet and exit curvature provided by the 3D integrator are calculated from a circumferential projection of the flow field onto a circumferential slice (axial-radial plane). This is effectively the same as calculating streamline curvature from only the axial and radial velocity components of the 3D transient velocity flow field. Curvature is calculated as a function of local velocity and acceleration. Overall mass flow rate as a boundary condition to the **SLCC** is calculated from the 3D flow field just upstream of the bladed region by the integration of mass for each circumferential segment. The mass flow rate of each circumferential segment is summed together to calculate overall mass flow. A radial distribution of swirl angle is calculated from the **TEACC** solution at the blade inlet and defined as the arc-tangent of tangential velocity divided by axial velocity. The total temperature and total pressure at the inlet are calculated by using the conservation variables, ideal gas relations, and the compressible form of the stagnation definitions at the inlet of each control volume.

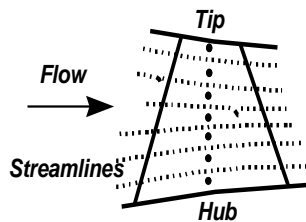
The source term calculations are performed after the **SLCC** converges to a steady-state solution through the bladed region. The technique for calculating turbomachinery source terms uses control volumes within the bladed region and applies steady-state conservation laws across each control volume. Since the conservation of angular momentum is maintained in the axisymmetric solution of the **SLCC**, a radial distribution of circumferential velocity vectors are produced. Cartesian control volumes are constructed over a circumferential segment of the bladed region from streamlines and overall blade geometry with velocities and pressures known on all surfaces from streamline calculations. A simplifying assumption that the top and bottom surfaces of each control volume are streamsurfaces is incorporated since mass, momentum, and energy does not cross a streamsurface. The turbomachinery forces are calculated from a control volume analysis and the streamsurface assumption by the pressure area forces and the inertial forces ([Figure 4.45](#)).

With the **TEACC**-supplied boundary conditions, the **SLCC** produces an axisymmetric solution through the bladed region in the form of streamsurfaces which are constructed into control volumes to calculate turbomachinery source terms. A methodology for distributing the sources radially, circumferentially, and axially through the grid packed region through the blade was developed.



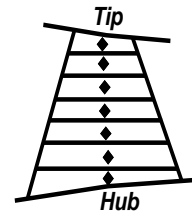
To implement these source terms into **TEACC**, a radial interpolation technique was derived. A radial distribution of sources is constructed by selecting the radius at the center of each **SLCC** source control volume ([Figure 4.46a](#)). This radius is non-dimensionalized by the radial extent of the inner and outer casing in the axial center of

### Streamline Curvature Solution

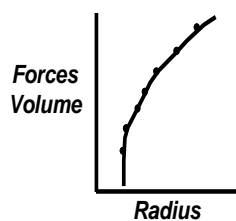


a. SLCC streamlines grid

### TEACC Solution

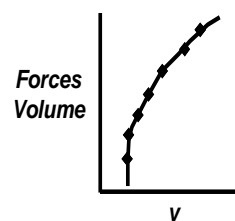


c. 3D Solver fixed grid



b. SLCC Volumetric Distribution

Interpolation



d. Interpolated Volumetric Distribution

**Figure 4.46 Interpolation of Radial Distribution of Source Terms**

the blade ([Figure 4.46b](#)).

A spline is used to interpolate these source terms to **TEACC** along a single circumferential segment of the bladed region. A radial distribution of **TEACC** control volumes is defined through the bladed region using the existing grid structure as shown in [Figure 4.46c](#). The radius is non-dimensionalized by the radial extent of the inner and outer casing in the middle of the bladed region. A radial distribution of **TEACC** source terms is acquired by interpolating the fixed



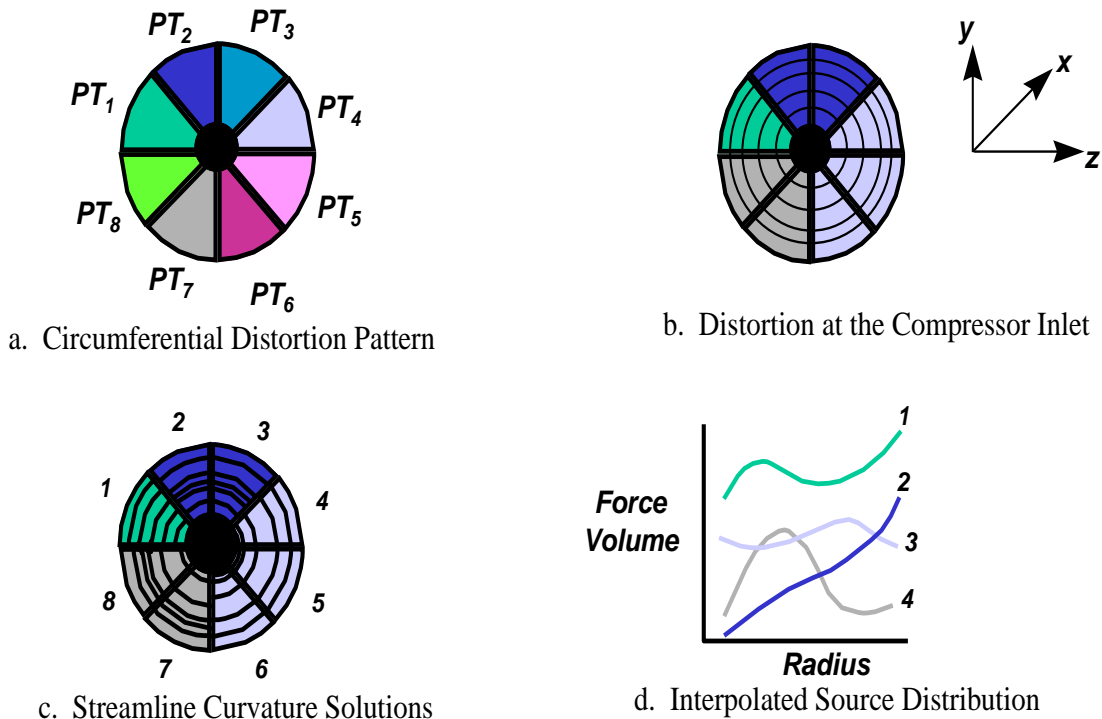


**Figure 4.47 Circumferential Distribution of Source Terms**

**TEACC** volume centers onto the function of sources developed earlier from the **SLCC** as shown in [Figure 4.46d](#).

The circumferential distribution of turbomachinery source terms is calculated by a direct application of the **SLCC** in each circumferential grid segment. For a distorted inlet upstream of the compressor, a circumferential inlet distortion is imposed on the system, as in [Figure 4.47a](#). According to Longley, this distortion affects the adjacent flow field, and [Figure 4.47b](#) shows that this circumferential distortion, ignoring viscous effects, will persist up to the compressor inlet [4.83]. The compressor's performance will be affected by this distortion, causing a non-uniform circumferential flow field. The modeling technique for acquiring a circumferential distribution of turbomachinery source terms applies the **SLCC** separately at each circumferential segment, as shown in [Figure 4.47c](#). The **SLCC** is sensitive to the changing demands to the flow field because it acquires its boundary conditions immediately upstream and downstream of each circumferential segment. Therefore, the **SLCC** interpolates a new radial distribution of turbomachinery source terms, sensitive to the changing flow field for each circumferential segment as shown in [Figure 4.47d](#). With a more complex inlet distortion pattern, the number of circumferential segments would be increased to maintain the high fidelity of the **TEACC** simulation.

The grid was packed through the bladed region to reduce the numerical error from strong flow gradients. This method means a great deal of freedom exists in how the sources should be distributed through the bladed region. The sources are distributed conservatively through the bladed region by requiring that the sum of the sources distributed through the **NPARC** grid must equal the sum of the sources developed in the **SLCC**. A simple technique to investigate this problem was incorporated by using a weighting function which could take on a variety of linear shapes. However, a uniform weighting function was found to be the most robust.

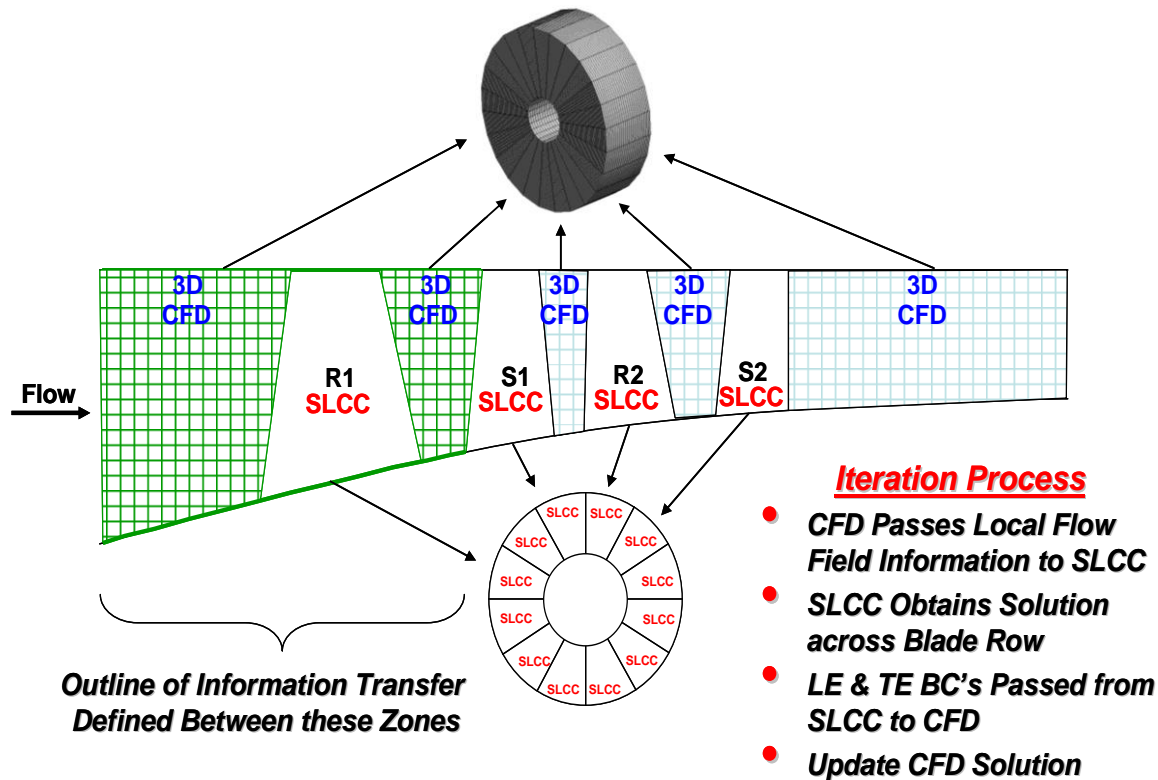


**Figure 4.48 Boundary Condition TEACC Overall Approach to Solution**

### **TEACC BOUNDARY CONDITION APPROACH**

A simplified version of **TEACC** was also developed that used the **SLCC** to generate boundary conditions instead of the blade forces as discussed in the previous section. The following section discusses the technical approach to the boundary condition version of **TEACC**.

**TEACC** is a method to perform inflow distortion analysis of a three dimensional compressor through the repeated application of a two-dimensional streamline curvature code (**SLCC**). The resulting system retains the ability to simulate a multiple blade row compression system in three-dimensions, without the need to explicitly model the blades, by modeling the bladed region through the use of a streamline curvature code (**SLCC**). Inflow distortion can be from variations in multiple flow properties, such as total pressure, total temperature, and swirl. The **TEACC** approach is characterized by alternating non-bladed and bladed zones as shown in **Figure 4.48**. The non-bladed zones are modeled using standard CFD techniques to advance the solution in time. Each bladed zone represents one blade row of the compressor system and the blade rows are modeled using repeated applications of the two-dimensional streamline curvature code around the circumference of the blade row. The solution from each application of the streamline curvature code is combined together to represent the potentially non-axisymmetric flow through the blade row.

The **TEACC** approach to fully three-dimensional compressor modeling depends on a CFD code (**OVERFLOW**) to provide the connectivity between the blade rows and multiple applications of the streamline curvature code (**SLCC**) within a blade row. The number of circumferential

applications of the **SLCC** is specified by the circumferential grid resolution of the non-bladed regions. The circumferential grid resolution is determined by the complexity of the inlet distortion pattern and the required resolution of the overall **TEACC** solution. Each **SLCC** solution receives its inlet boundary conditions from a segment of the upstream CFD zone and its exit boundary conditions from a segment of the downstream CFD zone. A bladed region is modeled through assembling each of the **SLCC** solutions. Therefore, a non-uniform circumferentially flow-field approaching a bladed region will contribute to an appropriately non-uniform turbomachinery effect through the bladed region.

The **SLCC** is used in two very different ways for a **TEACC** application. First, **SLCC** is used to initialize the bladed and non-bladed regions. The initialization approach is accomplished through an axial-radial **SLCC** solution encompassing the full axial extent of the **TEACC** application. The **SLCC** solution is then distributed circumferentially for each region, so that the three-dimensional **TEACC** grids are initialized with an axis-symmetric solution. Second, **SLCC** is used for all subsequent time steps, as discussed in the previous paragraphs, to be applied uniquely across each segment of each blade row.

Inlet distortion is stepped or ramped on to the inlet plane (AIP) of the **TEACC** simulation. This process allows the transport of inlet distortion through the bladed regions (simulated by the **SLCC**) and the non-bladed regions (simulated by CFD) to the exit of the simulation. The **TEACC** exit boundary condition is specified by setting the physical mass flow or by specifying an exit static pressure at a point and allowing the conservation equations to set the exit static pressure profile. The detailed technique to update the solution in time is pictorially represented in [Figure 4.49](#) by investigating the solution procedure for the first three zones of a **TEACC** application. [Figure 4.49](#) outlines a fringing strategy for passing conservation variables between the zones to make **TEACC** zonal analyzable. This means that each zone of a **TEACC** application can be updated one time step without being mindful of the zone order.

A blade zone comprises the geometry extent of the adjacent CFD zones. Boundary condition information is transferred between CFD zones and blade zones through fringing. At the beginning of a time step the adjacent CFD zone solutions are interpolated to the included blade zone (except for the leading and trailing axial stations), and the **TEACC** leading and trailing edge solutions are interpolated to the adjacent CFD zones. Therefore, each zone has all the boundary condition information necessary, through the fringing process, to advance that zone to the next time step.

The CFD zones are well defined by receiving updated inlet and exit blade boundary conditions (conservation variables) from the blade zones. A blade zone, however, is not a traditional CFD zone in that a CFD code is not deployed to update its solution in time. A blade zone is a zone designed as a convenient storage mechanism for bringing together, at the same time step, conservation variables from the adjacent CFD zones. The conservation variables in the blade zone are converted to boundary conditions for the **SLCC** at the BC locations. The previously stated **SLCC** inlet totals and inlet swirl angle boundary conditions are obtained only from conservation variables at the BC<sub>1</sub> location. However, curvature requires knowledge of conservation variables at five axial stations, which explains why so many stations are fringed from the adjacent CFD zones to the blade zone. Curvature is defined as the radius-of-curvature of an instantaneous axial-radial projection of a streamline passing through a given radius at the BC location.

A converged solution of the **SLCC** provides a flow-field solution at the leading and trailing edge of the blade. This solution is converted to conservation variables and interpolated to and stored

with the blade zone. The leading and trailing edge of the blades are the location of the CFD zone boundary conditions. At the beginning of the next time step, all fringing from the CFD zones and **TEACC** zone are performed. The technique of advancing a time step for each zone is continued until the **TEACC** solution is converged.

## ***BCs Transported between Zones by Fringing***

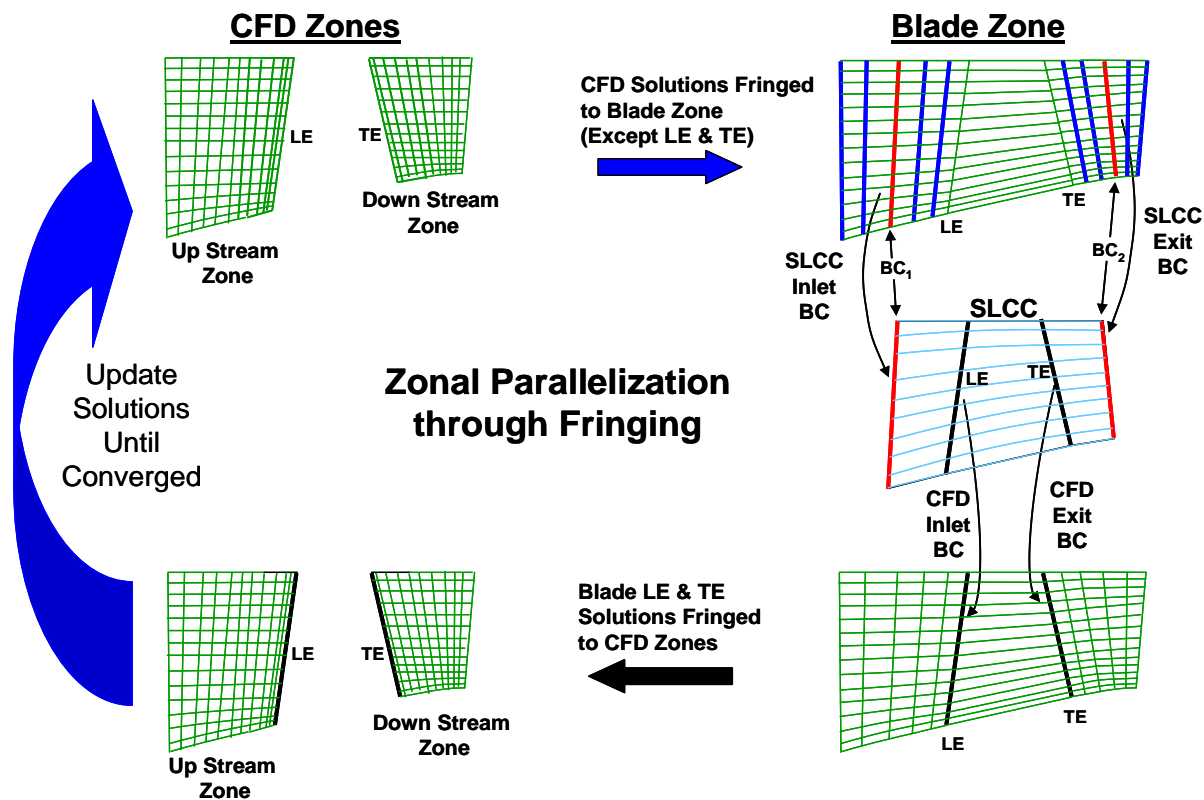


**Figure 4.49 Detailed Technique to Advance a Solution to Convergence**

### **Additional References:**

**4.82** Hale, A.A, O'Brien, W., "A Three-Dimensional Turbine Engine Analysis Compressor Code (**TEACC**) for Steady-State Inlet Distortion," Journal of Turbomachinery, Vol. 120, Number 3, July 1998, pp 422-430.

**4.83** Longley, J. P. and Greitzer, E. M. "Inlet Distortion Effects in Aircraft Propulsion System Integration." AGARD-LS-183. Advisory Group for Aerospace Research & Development Lecture Series, May 1992.

## TEACCSTALL

**TEACCSTALL** is an AEDC derivative of the Chima **CSTALL** code [4.84] developed at NASA Glenn. **TEACCSTALL** is a 3D time-accurate Euler code for modeling turbomachinery with an emphasis on determining stall inception. Instead of gridding up each blade passage, the effects of each bladed region are modeled by using turbomachinery source terms (loss, change in angular momentum, and radial blade blockage). The code is used to model both steady-state performance and dynamic stall inception. The stalling of the compressor is determined by an imbalance of the forces based on the local flow field and source terms.

**TEACCSTALL** uses a cylindrical coordinate system. The equations are discretized by either central difference with 2<sup>nd</sup> and 4<sup>th</sup> order artificial dissipation or ASUM<sup>+</sup> upwind finite difference scheme. For steady state solutions, **TEACCSTALL** uses a 2-stage explicit Runge-Kutta scheme with spatially-varying time stepping and implicit residual smoothing for acceleration to solution. For time-accurate solutions, **TEACCSTALL** uses a 4-stage explicit Runge-Kutta scheme with constant time steps.

**TEACCSTALL** is converted from an Euler duct flow solver to a compressor simulation complete with stall prediction through the judicious use of source terms. The force of the simulated blades on to air is captured through the change in entropy and the flow turning through the

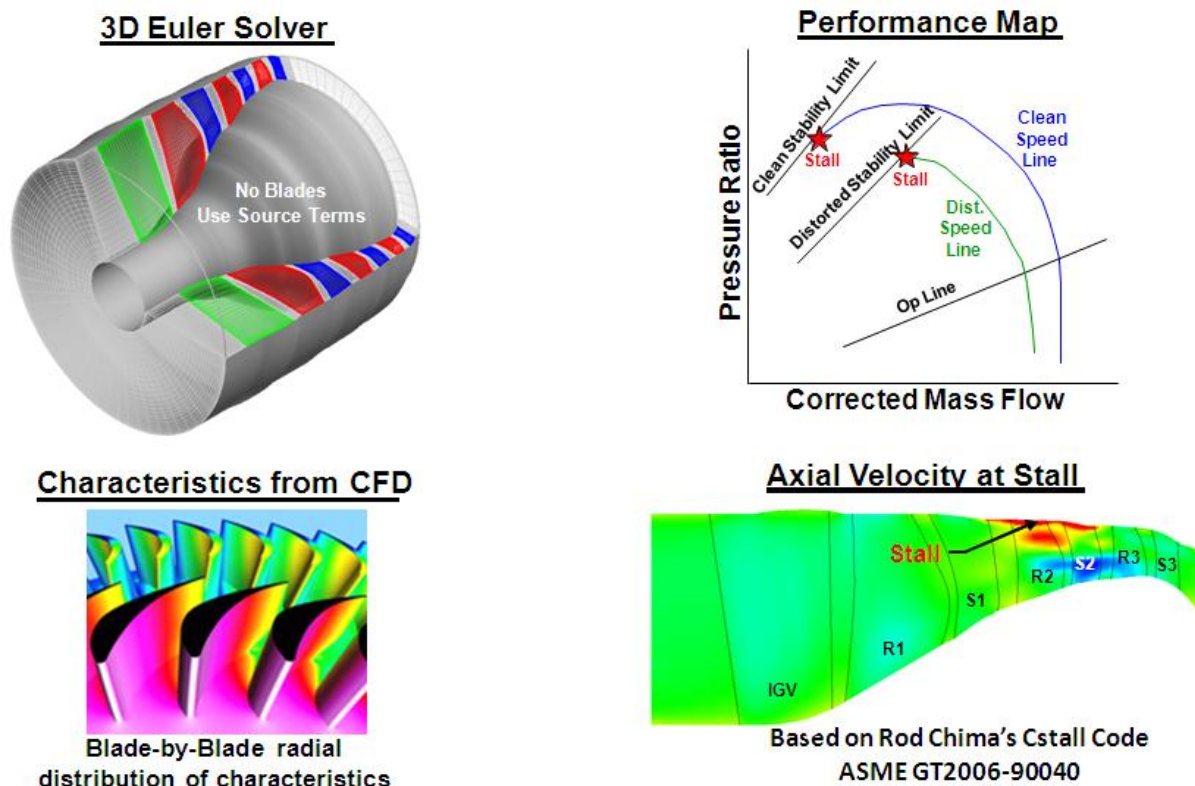


**Figure 4.50 Representation of TEACCSTALL**

bladed region. The dynamic effects of the blades moving in and out of distortion are accounted for with a 1<sup>st</sup> order lag Eqn.. The thickness of the blades is accounted for through a blockage term and this term has the effect of accelerating the flow through the blades.

The operation of **TEACCSTALL** is represented in [Figure 4.50](#). The 3D Euler code solves the governing Eqn.s and represents the bladed regions with source terms. The source terms are provided by characteristics that come from a pre-processing step (usually radial distribution of CFD characteristics from a series of single passage clean inlet CFD solutions). The characteristics, along with the Euler solver give a time-accurate solution of the turbomachinery up through the stall inception point.

**TEACCSTALL** has the ability to run as a multi-zone parallel code by the use of the **SUGGAR** (Structured, Unstructured, and Generalized Grid AssembleR), and **DiRTlib** (Donor interpolation Receptor Transaction Library).

The governing equations with source terms are presented as follows.

$$\frac{\partial q}{\partial t} + \frac{\partial E}{\partial x} + \frac{1}{r} \frac{\partial G}{\partial \theta} + \frac{\partial H}{\partial r} = K + \Phi \quad \text{Eqn. 4-174}$$

where

$$q = br \begin{bmatrix} \rho \\ \rho u \\ \rho v \\ \rho w \\ e \end{bmatrix} \quad K = \begin{bmatrix} 0 \\ rp\partial_x b \\ -b\rho vw \\ b(\rho v^2 + p) + (rp\partial_y b) \\ 0 \end{bmatrix} \quad \Phi = br \begin{bmatrix} 0 \\ \Phi_x \\ \Phi_\theta \\ \Phi_r \\ r\Omega\Phi_\theta \end{bmatrix}$$

$$E = br \begin{bmatrix} \rho u \\ \rho u^2 + p \\ \rho uv \\ \rho uw \\ u(e + p) \end{bmatrix} \quad G = br \begin{bmatrix} \rho v \\ \rho uv \\ \rho v^2 + p \\ \rho vw \\ v(e + p) \end{bmatrix} \quad H = br \begin{bmatrix} \rho w \\ \rho uw \\ \rho vw \\ \rho w^2 + p \\ w(e + p) \end{bmatrix}$$

where

$$\frac{1}{r} \frac{\partial G}{\partial \theta} = 0, \text{ in stator passages}$$

$$\frac{1}{r} \frac{\partial G}{\partial \theta} \rightarrow \Omega \frac{\partial q}{\partial \theta}, \text{ in rotor passages}$$

In [Eqn. 4-174](#),  $\Phi$  represents the blade forces and shaft work derived from the characteristics. The derivation of these terms is provided next. The forces applied and the work done by the compression blades to turn the flow and increase the pressure is obtained by developing traditional techniques like those outlined by Frank Marble [\[4.85\]](#). The approach combines two techniques, a global view which accounts for the influence of all blade rows and far field



boundary conditions along with a local view that provides the detailed blade loss and turning. The global view is modeled after the radial equilibrium theory with the additional assumption that the flow field is axially symmetric. These assumptions have the effect of numerically modifying the compressor geometry to consist of an infinite number of infinitely thin blades. In addition, the assumption of axial symmetry means that the blade wake vortex field is no longer in periodic discrete sheets but circumferentially uniform. The local view is focused on the details of the blade geometry and how the chordwise loading is calculated from cascade theory. Blade segments follow streamlines which introduces an additional assumption that each radial blade segment behaves independently.

The combined effect of axially symmetric throughflow theory and two-dimensional cascade theory offers an effective way to calculate turbomachinery source terms. The following steady, axially symmetric Euler equations written in non-conservative form are presented in a cylindrical coordinate system where the absolute velocity ( $V_z$ ,  $V_\theta$ ,  $V_r$ ) and axially symmetric force ( $\Phi_z$ ,  $\Phi_\theta$ ,  $\Phi_r$ ) have components in the  $z$ ,  $\theta$ , and  $r$  directions.

$$V_r \frac{\partial V_z}{\partial r} + V_z \frac{\partial V_z}{\partial z} = -\frac{1}{\rho} \frac{\partial p}{\partial z} + \Phi_z \quad \text{Eqn. 4-175}$$

$$V_r \frac{\partial V_r}{\partial r} + V_z \frac{\partial V_r}{\partial z} - \frac{V_\theta^2}{r} = -\frac{1}{\rho} \frac{\partial p}{\partial r} + \Phi_r \quad \text{Eqn. 4-176}$$

$$V_r \frac{\partial(rV_\theta)}{\partial r} + V_z \frac{\partial(rV_\theta)}{\partial z} = r\Phi_\theta \quad \text{Eqn. 4-177}$$

The momentum Eqn.s are conveniently recast through the following transformation along the meridional streamline  $m$ .

$$\frac{D(\cdot)}{Dm} = V_r \frac{\partial(\cdot)}{\partial r} + V_z \frac{\partial(\cdot)}{\partial z} \quad \text{Eqn. 4-178}$$

The derivative of any quantity can be evaluated along a streamline from the transformation.

$$V_m \frac{\partial(\cdot)}{\partial m} = \frac{D(\cdot)}{Dm} \quad \text{Eqn. 4-179}$$

$$V_m = \sqrt{V_r^2 + V_z^2} \quad \text{Eqn. 4-180}$$

The representation of the Euler equation is simplified through this transformation.

$$\frac{D(V_z)}{Dm} = -\frac{1}{\rho} \frac{\partial p}{\partial z} + \Phi_z \quad \text{Eqn. 4-181}$$

$$\frac{D(V_r)}{Dm} - \frac{V_\theta^2}{r} = -\frac{1}{\rho} \frac{\partial p}{\partial r} + \Phi_r \quad \text{Eqn. 4-182}$$

$$\frac{D(rV_\theta)}{Dm} = r\Phi_\theta \quad \text{Eqn. 4-183}$$

The Tds Eqn. is satisfied everywhere along a streamline with

$$T \frac{Ds}{Dm} = \frac{Dh}{Dm} - \frac{1}{\rho} \frac{Dp}{Dm} \quad \text{Eqn. 4-184}$$

where

$$\frac{Dh}{Dm} = \frac{De}{Dm} + \frac{D}{Dm} \left( \frac{p}{\rho} \right) \quad \text{Eqn. 4-185}$$

$$T \frac{Ds}{Dm} = \frac{De}{Dm} + \frac{D}{Dm} \left( \frac{p}{\rho} \right) - \frac{1}{\rho} \frac{Dp}{Dm} \quad \text{Eqn. 4-186}$$

Expand the pressure term.

$$\frac{1}{\rho} \frac{D(p)}{Dm} = \frac{V_r}{\rho} \frac{\partial(p)}{\partial r} + \frac{V_z}{\rho} \frac{\partial(p)}{\partial z} \quad \text{Eqn. 4-187}$$

Substitute the z- and r-momentum equations into the Tds pressure term.

$$\frac{1}{\rho} \frac{D(p)}{Dm} = V_r \left( \frac{V_\theta^2}{r} + \Phi_r - \frac{D(V_r)}{Dm} \right) + V_z \left( \frac{D(V_z)}{Dm} + \Phi_z \right) \quad \text{Eqn. 4-188}$$

$$\frac{1}{\rho} \frac{D(p)}{Dm} = V_r \Phi_r + V_z \Phi_z + V_r \frac{V_\theta^2}{r} - V_r \frac{D(V_r)}{Dm} - V_z \frac{D(V_z)}{Dm} \quad \text{Eqn. 4-189}$$

Substitute the pressure term into the Tds Eqn..

$$T \frac{Ds}{Dm} = \frac{De}{Dm} + \frac{D}{Dm} \left( \frac{p}{\rho} \right) - V_z \Phi_z - V_r \Phi_r - \frac{V_r V_\theta^2}{r} + V_r \frac{D(V_r)}{Dm} + V_z \frac{D(V_z)}{Dm} \quad \text{Eqn. 4-190}$$

Apply the following simplifications:

$$V_r \frac{D(V_r)}{Dm} = \frac{D}{Dm} \left( \frac{V_r^2}{2} \right) \quad \text{Eqn. 4-191}$$

$$V_z \frac{D(V_z)}{Dm} = \frac{D}{Dm} \left( \frac{V_z^2}{2} \right) \quad \text{Eqn. 4-192}$$

$$\frac{D}{Dm} \left( \frac{V^2}{2} \right) = \frac{D}{Dm} \left( \frac{V_r^2}{2} \right) + \frac{D}{Dm} \left( \frac{V_\theta^2}{2} \right) + \frac{D}{Dm} \left( \frac{V_z^2}{2} \right) \quad \text{Eqn. 4-193}$$

$$T \frac{Ds}{Dm} = \frac{D}{Dm} \left( e + \frac{p}{\rho} + \frac{V^2}{2} \right) - \frac{D}{Dm} \left( \frac{V_\theta^2}{2} \right) - \frac{V_r V_\theta^2}{r} - V_z \Phi_z - V_r \Phi_r \quad \text{Eqn. 4-194}$$

Simplify the Tds Eqn. by substituting  $V_\theta$  multiplied by the  $\theta$ -momentum Eqn..

$$V_\theta \left( \frac{DV_\theta}{Dm} + \frac{V_r V_\theta}{r} \right) = \Phi_\theta \quad \text{Eqn. 4-195}$$

$$T \frac{Ds}{Dm} = \frac{Dh_t}{Dm} - V_z \Phi_z - V_\theta \Phi_\theta - V_r \Phi_r \quad \text{Eqn. 4-196}$$

Rearrange and convert the Tds Eqn. to a relative-to-the-blade expression.

$$\frac{Dh_t}{Dm} - \omega r \Phi_\theta = T \frac{Ds}{Dm} + [V_z \Phi_z + (V_\theta - \omega r) \Phi_\theta + V_r \Phi_r] \quad \text{Eqn. 4-197}$$

The term in brackets is recognized as a dot product of relative velocity ( $\vec{W}$ ) and force ( $\vec{\Phi}$ ).

$$\vec{W} = V_z \vec{i} + (V_\theta - \omega r) \vec{j} + V_r \vec{k} \quad \text{Eqn. 4-198}$$

$$\frac{Dh_t}{Dm} - \omega r \Phi_\theta = T \frac{Ds}{Dm} + \vec{W} \cdot \vec{\Phi} \quad \text{Eqn. 4-199}$$

The forces are those generated by the blade accelerating the air and in the absence of friction these forces would be perpendicular to the blade. However, in the presence of friction a component of force is also generated parallel to the relative blade velocity but opposing the flow. These forces are conveniently represented by two forces, one perpendicular and the other parallel to the blade surface as shown in **Figure 4.51** and **Figure 4.52**.

$$\vec{\Phi} = \vec{F} + \vec{f} \quad \text{Eqn. 4-200}$$

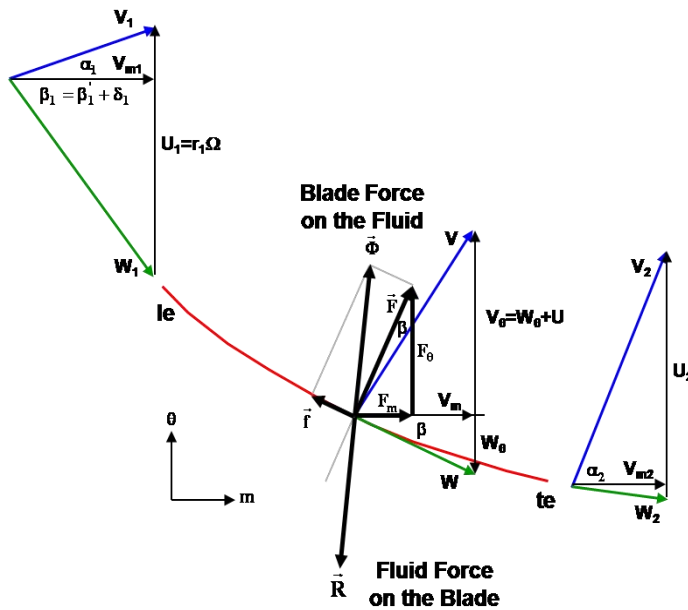


**Figure 4.51 Turning Forces Generated by the Rotor**

From the assumption that a blade row consists of an infinite number of infinitely thin blades, the rotor and stator in **Figure 4.51** and **Figure 4.52** respectively are represented by a curved red line. Velocity triangles are positioned at the leading edge (le), the trailing edge (te), and at an arbitrary part-span blade location with the fluid depicted as flowing from left to right. The loss force ( $\vec{f}$ ) is observed to be persistently parallel to the blade relative velocity but opposite in direction, and the turning force ( $\vec{F}$ ) is observed to remain perpendicular to the blade. The loss and turning force added together represents the cumulative blade force accelerating the fluid. The Tds Eqn. can be expanded by separating the cumulative force into the loss and turning forces.

$$\frac{Dh_t}{Dm} - r\Omega\Phi_\theta = T \frac{Ds}{Dm} + \vec{W} \cdot (\vec{F} + \vec{f}) \quad \text{Eqn. 4-201}$$

The Tds equation is significantly simplified by recognizing that the forces perpendicular to the blade is also perpendicular to the relative velocity.

$$\vec{W} \cdot \vec{F} = 0 \quad \text{Eqn. 4-202}$$

$$\frac{Dh_t}{Dm} - r\Omega\Phi_\theta = T \frac{Ds}{Dm} + \vec{W} \cdot \vec{f} \quad \text{Eqn. 4-203}$$

Each term on the RHS of the Tds equation. is recognized to be independently zero in the absence of losses allowing the LHS of the Tds equation to be set to zero. Therefore, the LHS of the Tds Eqn. provides a means to calculate the work produced by the blade.

$$\frac{Dh_t}{Dm} = r\Omega\Phi_\theta$$

Eqn. 4-204

A first law of thermodynamics analysis with or without losses for an adiabatic compressor relates the change of work to the change in total enthalpy. Therefore, the LHS of the Tds equation is immediately recognized as the work done by the blade on the fluid.

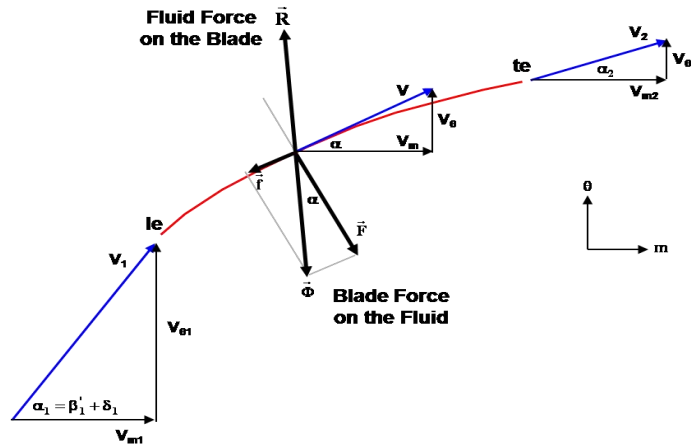


**Figure 4.52 Turning Forces Generated by the Stator**

$$\text{Work} = \frac{Dh_t}{Dm} = r\Omega\Phi_\theta$$

Eqn. 4-205

The Euler turbine Eqn. is readily derived by substituting the previously developed conservation or  $\theta$ -momentum Eqn. for the  $r\Phi_\theta$ .

$$\frac{Dh_t}{Dm} = \frac{D(r\Omega V_\theta)}{Dm}$$

Eqn. 4-206

Since the Euler turbine equation applies with or without the assumption of any losses, the right and left side of the Tds equation independently vanish to zero. The friction force is readily calculated through the observation of the friction force being parallel but opposite in direction to the relative velocity as

viewed in **Figure 4.51** and **Figure 4.52**

$$T \frac{Ds}{Dm} = -(\vec{W} \cdot \vec{f}) = -|\vec{W}| |\vec{f}| \cos 180$$

Eqn. 4-207

$$|\vec{f}| = \frac{T}{|\vec{W}|} \frac{Ds}{Dm} \quad \text{or} \quad |\vec{f}| = \frac{TV_m}{|\vec{W}|} \frac{\partial s}{\partial m}$$

Eqn. 4-208

$$\vec{f} = f_z \vec{i} + f_\theta \vec{j} + f_r \vec{k}$$

Eqn. 4-209

The friction force unit vector is equated with the negative of the relative velocity unit vector. Each coordinate direction provides an equation for calculating the components of the frictional force.

$$\frac{f_z}{|\vec{f}|} \vec{i} + \frac{f_\theta}{|\vec{f}|} \vec{j} + \frac{f_r}{|\vec{f}|} \vec{k} = - \left[ \frac{V_z}{|\vec{W}|} \vec{i} + \frac{(V_\theta - \omega r)}{|\vec{W}|} \vec{j} + \frac{V_r}{|\vec{W}|} \vec{k} \right]$$

Eqn. 4-210

$$f_z = - \frac{V_z |\vec{f}|}{|\vec{W}|} \quad f_\theta = - \frac{(V_\theta - \omega r) |\vec{f}|}{|\vec{W}|} \quad f_r = - \frac{V_r |\vec{f}|}{|\vec{W}|}$$

Eqn. 4-211

The circumferential component of the turning force can now be calculated from the conservation of  $\theta$ -momentum equation since the circumferential component of the friction force is known.

$$\Phi_\theta = \frac{1}{r} \frac{D(rV_\theta)}{Dm} = \frac{V_m}{r} \frac{\partial(rV_\theta)}{\partial m}$$

Eqn. 4-212

$$F_\theta = \Phi_\theta - f_\theta$$

Eqn. 4-213

The remaining components of the turning force are calculated by taking advantage of the fact that the turning force is everywhere perpendicular to the relative blade velocity and that the axial and radial components of the turning force are proportional to the streamline geometry depicted in **Figure 4.53**.

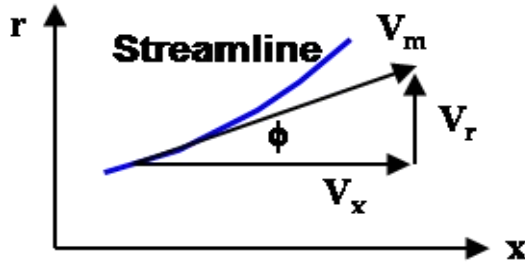


**Figure 4.53 Streamline Angles and Velocity Components**

$$\vec{W} \cdot \vec{F} = 0 \quad \text{Eqn. 4-214}$$

$$V_z F_z + (V_\theta - \omega r) F_\theta + V_r F_r = 0 \quad \text{Eqn. 4-215}$$

$$F_m = - \left[ \frac{(V_\theta - \omega r)}{V_m} \right] F_\theta \quad \text{Eqn. 4-216}$$

$$F_r = F_m \sin \phi \quad \text{Eqn. 4-217}$$

$$F_z = F_m \cos \phi \quad \text{Eqn. 4-218}$$

The cumulative forces (loss and turning) together with the shaft work define the steady portion of the turbomachinery source terms necessary to model the effect of the missing blades.

When operating through a distortion, viscous effects prevent the blade boundary layer from responding instantly to the change in incidence angle. If the distortion is small enough the compressor blade operating near stall may transiently exceed the steady-state stall limit and return without stalling. The dynamic blade forces are obtained from a 1<sup>st</sup> order lag of the turbomachinery steady-state derived in the previous section.

$$\tau \frac{\partial \Phi}{\partial t} + \Phi = \Phi_{ss} \quad \text{Eqn. 4-219}$$

A convent form of this Eqn. results in a simple force realization Eqn. with n representing iteration.

$$\Phi^{n+1} = r \Phi_{ss}^n + \Phi^n (1 - r) \quad \text{Eqn. 4-220}$$

where:

$$r = \frac{\Delta t}{\tau} \quad \text{Eqn. 4-221}$$

#### **REFERENCES:**

**4.84** Chima, R. V., "A Three-Dimensional Unsteady CFD Model of Compressor Stability", ASME Paper GT2006-90040.

**4.85** Marble, F. E., "Three-Dimensional Flow in Turbomachines," in *High Speed Aerodynamics and Jet Propulsion, Vol X, Aerodynamics of Turbines and Compressors*, Hawthorne, W. R., ed. Princeton University Press, Princeton, NJ., pp.83-165.

## 4.8 ALE3D TECHNICAL APPROACH

The development of 3D simulation tools at Lawrence Livermore National Laboratory (LLNL) in the areas of structural, fluid and thermal analysis has followed the traditional path of first developing capabilities limited to the particular topic of interest. **DYNA3D** [4.94] is the culmination of two decades of research in structural analysis. **TOPAZ3D** [4.90] is the equivalent tool for use in thermal transport simulations. **JOY** [4.87], a 3D pure-Eulerian finite-difference code and **CALE** [4.92], a 2D finite-difference arbitrary-Lagrangian-Eulerian code provide the heritage for the fluid mechanics capability that is being applied to the engine aero-structural analysis.

A 3D finite element code called **ALE3D** [4.91] has been developed as a means of merging many of the capabilities developed in the individual technology areas. **ALE3D** was developed from a version of **DYNA3D**. It uses the basic Lagrangian finite element techniques developed there but has not maintained an identical set of algorithms as the two code efforts evolved along different paths. The treatment of solid elements, where fluid dynamics is treated, has been completely rewritten. The coding and the available models for treating beam and shell elements, however have been kept consistent with the equivalent **DYNA3D** models, although only a subset are currently available. Fluid mechanics and ALE techniques from **JOY** and **CALE** were modified for application to unstructured meshes and incorporated into **ALE3D**. Thermal and structural analysis techniques are generally developed first in **DYNA3D** and **TOPAZ3D** then migrated to **ALE3D** as required.

**ALE3D** is a finite element code that treats fluid and elastic-plastic response on an unstructured grid. The grid may consist of arbitrarily connected hexahedral, shell and beam elements. The mesh can be constructed from disjoint blocks of elements which interact at the boundaries via slide surfaces or other types of boundary conditions. Nodes can be designated as relax nodes and **ALE3D** will adjust their position relative to the material in order to relieve distortion or to improve accuracy or efficiency. This relaxation process can allow nodes to cross material boundaries and create mixed or multi-material elements.

The basic computational step consists of a Lagrangian step followed by an advection, or remap step. This combination of operations is formally equivalent to an Eulerian solution while providing increased flexibility and, in some cases, greater accuracy. In the Lagrangian phase, nodal forces are accumulated and an updated nodal acceleration is computed. Following **DYNA3D** [4.88], the stress gradients and strain rates are evaluated by a lowest order finite element method.

At the end of the Lagrangian phase of the cycle the velocities and nodal positions are updated. At this point several options are available. If the user wishes to run the code in a pure-lagrangian mode, no further action is taken and the code proceeds to the next time step. If a pure-Eulerian calculation is desired, the nodes are placed back in their original positions. This nodal motion or relaxation generates inter-element fluxes which must be used to update velocities, masses, energies, stresses and other constitutive properties. This re-mapping process is referred to as advection. Second-order-accurate schemes are required to perform this operation with sufficient accuracy. In addition, it is not generally adequate to allow advection only within material boundaries. **ALE3D** has the ability to treat multi-material elements, thus allowing relaxation to take place across material boundaries.



The full potential of the ALE approach is realized when the code user has options available to tailor the evolution of the mesh to maximize either efficiency or accuracy. In the simplest implementation the code is instructed to relax nodes as required to eliminate distortions in the mesh. A more powerful approach has the code relax nodes on the basis of an optimization scheme. To this purpose **ALE3D** utilizes a finite element based equipotential method developed by R. Tipton [4.93]. This method accommodates weighting functions which can be used to optimize the mesh based on some defined criterion. **ALE3D** allows weighting by pressure, by artificial viscosity, by plastic strain, by material number and along designated slip surfaces. The solution will result in a more highly resolved mesh in the volumes containing the highest weights. This provides a form of dynamic mesh refinement. An illustration of this technique is presented in Figure 4.54 for diffuser geometry.

This technique has proved useful in improving the effective resolution in shock tracking simulations. There are also a number of options available for selecting predetermined or dynamically programmed mesh evolution in cases where that is appropriate.

A version of **TOPAZ3D** has been incorporated into **ALE3D** to provide a thermal transport capability. The **TOPAZ3D** package has been enhanced by the inclusion of a reaction chemistry module [4.89]. These capabilities are utilized in a split operator mode whereby the operator can be applied at a time interval that is appropriate for thermal effects and need not be consistent with the time step for the dynamics.

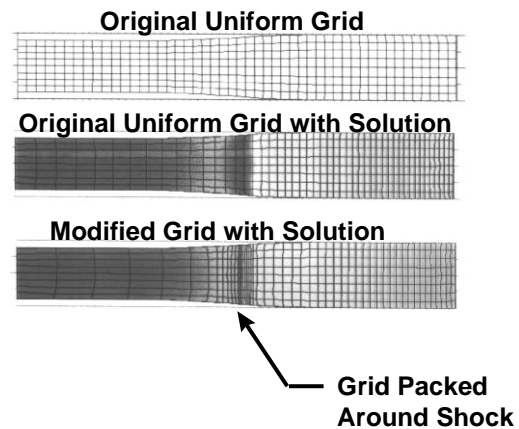


Figure 4.54 Grid Remapping Feature of ALE3D

A critical step in any type of transient analysis for rotating **turbomachinery** is to stabilize the configuration to steady state conditions in terms of both structural and fluid dynamics. Often it is required to follow many revolutions of structural components without perturbation from numerical integration errors. This places severe constraints on the techniques used to integrate the dynamic Eqn.s through time.

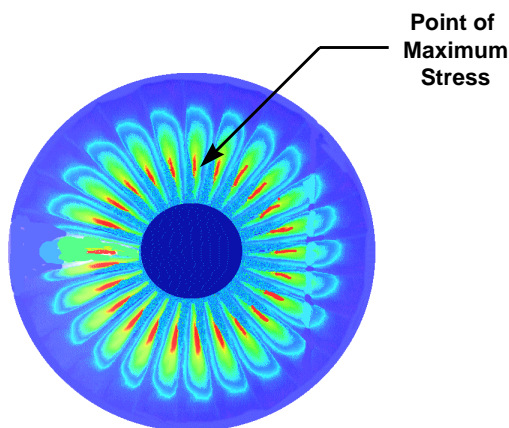


Figure 4.55 Single Fan Stage Structural Analysis Using DYNA3D

Pre-stressing a body in **DYNA3D** is performed in a fully dynamic mode. The technique involves an initial phase where body forces are applied to the unstressed configuration. Centrifugal forces are applied to represent the effect of rotation. The oscillatory response of the structure to this non-equilibrium loading is controlled by applying a viscous damping term. Judicious application of this damping term allows an efficient relaxation to the equilibrium configuration. When the kinetic energy in the structure falls to a value deemed negligible, the code replaces the explicit centrifugal forces with an equivalent rotational velocity field and the code begins the actual time integration. Figure 4.55 depicts a rotating structure for which this process has been applied.

This particular configuration represents the equilibrium state of the structure prior to blade release. This simulation is intended to be one phase in the computational sequence from blade release to surge to structural response. The von Mises stress in an element in a blade as it undergoes many revolutions was nearly constant for a full 100 revolutions. The stability of von Mises stress in an element is an indication of the accuracy of the numerical algorithms.

#### **Additional References:**

- 4.86** Nazir, J., Couch, R., Davis, M., "An Approach for the Development of an Aerodynamic-Structural Interaction Numerical Simulation for Aeropropulsion Systems," ASME Paper 1996-GT-480, 1996.
- 4.87** Couch, R. G., Albright, E., Alexander, N., "JOY Computer Code," Lawrence Livermore National Laboratory, UCID-19688, 1983.
- 4.88** Hallquist, J. O., "Theoretical Manual for DYNA3D," Lawrence Livermore National Laboratory, UCID-19401, draft, 1982
- 4.89** Nichols, A. L. III, Westerberg, K. W., "Modification of a Thermal Transport Code to Include Chemistry with Thermally Controlled Kinetics," Numer. Heat Transfer, Part B, Vol 24, pp 489-509, 1993.
- 4.90** Shapiro, A. B., "TOPAZ3D - A Three-Dimensional Finite Element Heat Transfer Code," Lawrence Livermore National Laboratory, UCID-20484, 1985.
- 4.91** Sharp, R., Anderson, S., Dube, E., Futral, S., Otero, I., "User's Manual for ALE3D," Lawrence Livermore National Laboratory, unpublished, 1995.
- 4.92** Tipton, R., "CALE User's Manual," Lawrence Livermore National Laboratory, unpublished, 1990.
- 4.93** Tipton, R., Lawrence Livermore National Laboratory, unpublished, 1992. Whirley, R. G., Engelman, B. E., 1993, A Nonlinear, Explicit, "Three Dimensional Finite Element Code for Solid and Structural Mechanics - User Manual", Lawrence Livermore National Laboratory, UCRL-MA-107254 Rev 1.
- 4.94** Whirley, R. G., Engelman, B. E., 1993, A Nonlinear, Explicit, "Three Dimensional Finite Element Code for Solid and Structural Mechanics - User Manual", Lawrence Livermore National Laboratory, UCRL-MA-107254 Rev 1.

#### 4.9 TURBOMACHINERY CFD CODES, TURBO & OVERFLOW, TECHNICAL APPROACH

AEDC started a serious effort in CFD turbomachinery several years ago. The first step in this process was to identify a multitude of commercial and government CFD codes that could model rotating machinery. During this effort three codes were identified to further evaluate for AEDC's turbomachinery modeling effort. The codes of interest were **ANSYS CFX**, **FLUENT**, and **TURBO**. Two of these codes, **ANSYS CFX** and **FLUENT**, were commercial codes; while **TURBO** was developed at Mississippi State University [4.96]. While the evaluation of the commercial codes were successful and provided good results, two major limitations were identified during this process- cost and ability to modify. The costs of the commercial codes were very high, especially when needing to run large problems with many processors. The ability to modify the source code was also seen as a need when applying these codes to operability problems at AEDC. Therefore, this effort at AEDC recommended the **TURBO** code as the code of choice to develop at AEDC.

After further evaluations continued, it was also decided to pursue the development of the **OVERFLOW** [4.95] turbomachinery capability. The **OVERFLOW** code is used extensively at AEDC for external aero applications. Several experts in **OVERFLOW** applications and development were also available at AEDC. In a previous effort, **OVERFLOW** had been modified and applied for analyzing turbomachinery at AEDC. Therefore, this section will describe both the **TURBO** and **OVERFLOW** approaches for modeling turbomachinery.

##### TURBO TECHNICAL APPROACH

This section will describe the basics of the **TURBO** code. Most of this information is from Chen and Briley [4.96]. The governing equations for **TURBO** are the unsteady Reynolds-averaged Navier-Stokes equations with a NASA/CMOTT k-ε turbulence model by Zhu [4.102]. The governing equations are formulated in a rotating frame attached to the blades, and with velocity retained in the absolute vector basis by Chen [4.98]. Two levels of sub-iteration at each time step are available in the implicit solver. The outer layer is an approximate Newton iteration to solve the nonlinear system obtained from discretizing the governing equations. For each Newton sub-iteration  $k$ , a linear Eqn. system can be formed:

$$(L + D + U)\Delta q^{k-1} = \frac{q^n - q^{k-1}}{\Delta t} + R^{k-1} \quad \text{Eqn. 4-222}$$

where  $L$  is a lower block triangular matrix,  $D$  is a block diagonal matrix, and  $U$  is an upper triangular matrix. The increment  $\Delta q^{k-1}$  is the change of the conservative variables  $q$  ( $\rho$ ,  $\rho u$ ,  $\rho v$ ,  $\rho w$ ,  $e$ ) between Newton sub-iterations, and  $R^{k-1}$  is the sum of the body forces and flux balance. The updated conservative variables,  $q^k$ , are exchanged across blade passages either after each time step (loose coupling) or after each Newton sub-iteration within a time step (close coupling). A symmetric Gauss-Seidel relaxation scheme is then used as the inner sub-iteration to solve the linear system for each Newton sub-iteration, i.e.,  $q^{k-1}$ . Details of this algorithm are reported in Chen and Whitfield [4.99] and Whitfield, et al. [4.101]. **TURBO** can be used to model single or multiple stages of complex turbomachinery flow. It can also be used to model the full circumference of the **TURBO** machine or a single blade passage. For single blade passage simulations, phase-lag boundary condition [4.100] has been implemented to model the unsteady blade row interactions. This is a superior boundary condition for stages of irreducible blade counts because it can simulate the unsteadiness at the adjacent blade passing frequency. This is reported by Chen and Barter [4.97]. To increase turn-around time, a parallel computing **TURBO** has been developed using the MPI parallel communication framework [4.96].

## **OVERFLOW TECHNICAL APPROACH**

**OVERFLOW 2.1** [4.95] is a three-dimensional time-marching implicit Navier-Stokes code that can also operate in two-dimensional or axisymmetric mode. The code uses structured overset grid systems. Several different inviscid flux algorithms and implicit solution algorithms are included in **OVERFLOW 2.1**. The code has options for thin layer or full viscous terms. A wide variety of boundary conditions are also provided in the code. The code may also be used for multi-species and variable specific heat applications. Algebraic, one-Eqn., and two-Eqn. turbulence models are available. Low speed preconditioning is also available for several of the inviscid flux algorithms and solution algorithms in the code. The code also supports bodies in relative motion, and includes both a six-degree-of-freedom (6-DOF) model and a grid assembly code. Collision detection and modeling is also included in **OVERFLOW 2.1**. The code is written to allow use of both MPI and OpenMP for parallel computing applications. Either **PEGASUS** or **SUGGAR** can be used to assemble the grids.

The **OVERFLOW 2.1** code does not inherently have the ability to simulate single passage Turbomachinery solutions. However, through a technology effort at AEDC, this capability was added a few years ago by Sirbaugh [4.103]. After looking at other freely available codes, it was decided that building the mixing plane approach to turbomachinery into **OVERFLOW** was more beneficial than acquiring and learning other codes.

The mixing plane approach to turbomachinery calculations is based on having a location between blade rows, the mixing plane, where the flow field is converted so as to present an axisymmetric steady-state flow field to adjacent blade rows. With the mixing plane approach only one blade per blade row must be included in the computational grids and non-time accurate flow solvers can be applied. Converged solutions can be generated for multiple blade row geometries very quickly. The inaccuracy is that an artificial constraint is imposed in the flow field. The utility of such a capability is case dependent.

### **Concept**

The approach pursued to achieving an **OVERFLOW** mixing plane capability is fairly straight forward in concept, unfortunately less straight forward in implementation. Consider a multiple block overlapping grid, one block per blade row, which has been constructed so that in cylindrical coordinates, the overlaps create a point-to-point correspondence in axial and radial coordinates. With uniform circumferential point spacing within each block and the same number of circumferential grid points for all blocks, a virtual point-to-point correspondence can be uniquely established. Chimera style data exchange is performed between grid blocks based on this overlapped point-to-point correspondence. Once the data has been exchanged, the flow field data on each circumferential running grid line, which is of constant radius, can be adjusted according to the mixing plane approach. The flow field equations are solved with rotation assumptions on the grid blocks containing rotors.

The chimera approach allows for the modeling of the blades with additional grids which are embedded within the previously described passage grids. Other than be limited to lie totally within the bounds of the passage grid, additional grids used to model blade details are not restricted in fashion. The user can add such details as tip clearance and base cavities using standard grid generation tools.

## Implementation

The concept is very straight forward, first construct the grid block with unique characteristics that establish a point-to-point correspondence in the block overlaps, second modify the chimera approach to recognize the point correspondence, third apply mixing plane assumptions at inflow and outflow boundaries of block, and lastly solve the flow equations with rotation terms were appropriate. The implementation of this approach required the development of a grid generation process to meet the unique grid requirements. A program was created that modified the chimera data file to reflect the virtual point-to-point correspondence. The flow solver already allowed for the entire grid system to simulate a rotating grid system, so changes to the flow solver were necessary to simulate only prescribed blocks as rotating. Lastly, boundary conditions that converted the chimera exchanged data into a mixing plane form were written.

The difficulty in implementing this concept lies in grid generation and creating the chimera data file. Grids could be constructed using commercial programs, but would be tedious and error prone. The success of this concept depends on strict compliance of the passage grid requirements. The chimera data file must reflect a point-to-point correspondence between adjacent passage grids that does not exist in physical space. No tools were available to modify the chimera data file to create a non-physical point-to-point correspondence.

## Grid Generation

Stringent passage grid requirements accompany the approach followed to create a mixing plane turbomachinery capability with **OVERFLOW**. A grid generation process and support tools were developed to construct the passage grids. The user must generate a single two-dimensional grid that will define the axial and radial grid spacing for all the blade passages. The user also must create a three-dimensional grid surface for each blade passage that passes through the blade's leading and trailing edges and generally follows the blade shape. The surface can be thought of as a stream surface that passages smoothly through the blade surface and extend upstream and downstream of the blade. A new tool is then used to form the three-dimensional passage grid from the user supplied two-dimensional grid and the set of three-dimensional

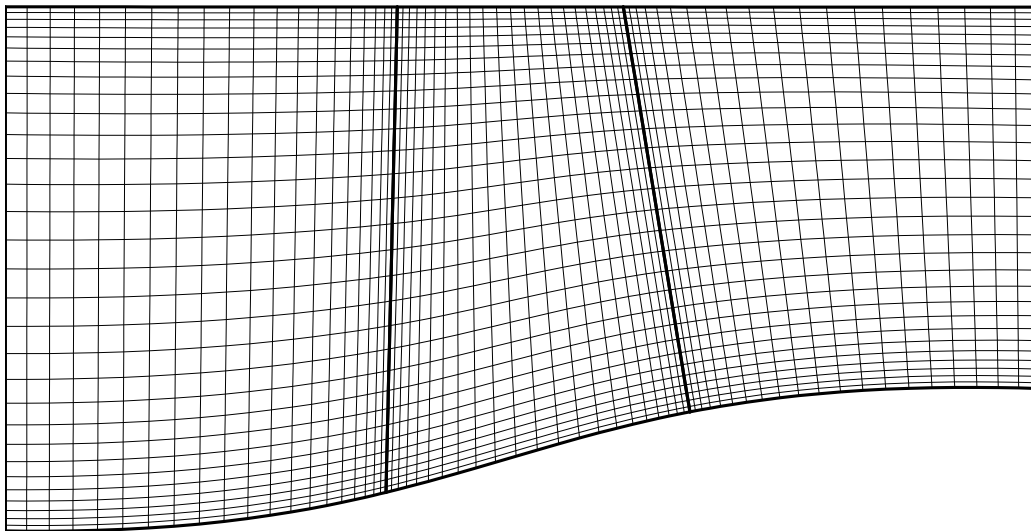


**Figure 4.56 Example Two-Dimensional Grid**



surfaces. The user can then use any means desired to create turbomachinery blade embedded in the passage grids.

The two-dimensional grid defines the grid spacing for the three-dimensional grid. The leading and trailing edges of all blades should be represented in the grid with grid packing around these locations to provide sufficient grid resolution to perform chimera embedded grid hole cutting using a Pegasus5. The individual passage grids are formed by sections of the two-dimensional grid and thus should have adequate grid resolution between adjacent blade rows to allow chimera style grid overlapping between passage grids. Adequate grid resolution is also required to capture shock waves near the blades. Grid packing toward the inner and outer casings is dependent on the boundary conditions applied and if the blade tip is modeled. An example of a two-dimensional grid is shown in [Figure 4.56](#). A table should be created that indicates the starting and ending streamwise indices in the two-dimensional grid that relates to the upstream and downstream boundaries of the passage grid. This information will be used in the passage grid generation step.

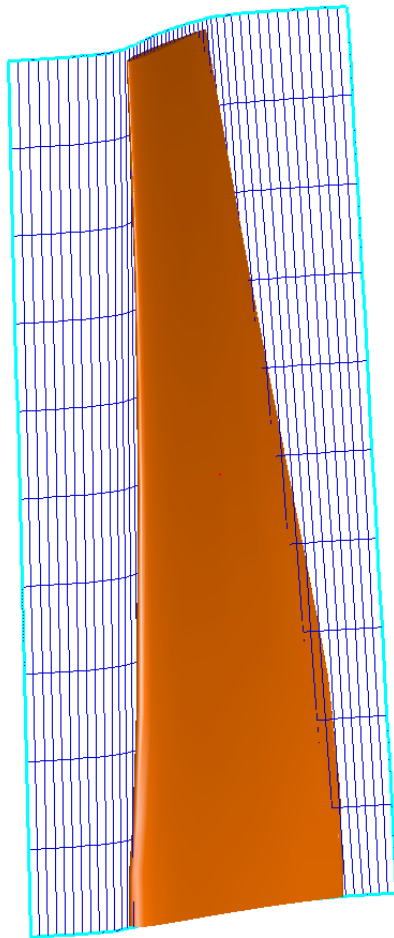


**Figure 4.57 Sample Mean Surface**

A three-dimensional surface must be generated for each blade that will be used to define the shape of grid planes in the passage grids. Shown in [Figure 4.57](#) is an example of such a surface. The surface passes through the blade leading and trailing edges and approximately follows the blade chamber surface shape. The surface extends upstream and downstream of the blade and tends toward being aligned with Turbomachinery axis away from the blade. In practice, the only portions of this surface that is used by the passage grid generation step are the edge curves along the inner and outer casings. The surface is defined as a surface grid and can be generated using grid generation software.

The passage grid is created by a tool called “build\_passage”. This tool is best utilized by creating a simple script that repeatedly executes the tool once for each passage grid.

The three-dimensional surface definition file is copied to a file named “mean\_surf.fmt”. The upstream and downstream grid indices from the two-dimensional grid is input, followed by the number of blades in the blade row, and lastly the number of circumferential grid points in the passage grid. As previously noted, the number of circumferential grid points must be the same for all passage grids. The tool stores the passage grid to a file which should be renamed.

The build\_passage tool creates the passage grid by first defining inner and outer casing curves along the three-dimensional surface. The casing curves axial grid point locations are directly copied from the axial location of the two-



dimensional user supplied grid. The inner and other casing curves are connected at the upstream and downstream ends with radial direction curves that are approximately normal to the casings. Using these four bounding curves, an interior grid is constructed using transfinite interpolation. An example of such a surface constructed from the three-dimension surface shown in [Figure 4.57](#) is shown in [Figure 4.58](#). Note that the two surfaces are similar, but not identical. The `build_passage` tool then creates the passage grid from this new grid surface by rotating copies of the surface grid in both the clockwise and counter-clockwise directions.

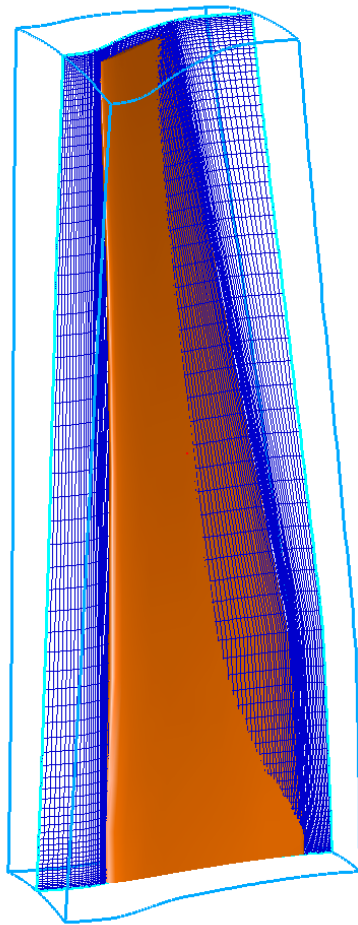


**Figure 4.58 Sample Passage Grid**

unique point-to-point correspondence between grid points in adjacent passage grids. The tool “`add_mixing_plane_to_XINTOUT`” was created that modifies the XINTOUT file to allow point-to-point data transfer between adjacent passage grids. The optimum fringe arrangement is an area for addition research. The tool is sufficiently versatile to allow exploring other fringe arrangements.

### New Boundary Conditions

A mixing plane boundary condition was added to **OVERFLOW**. The boundary condition is applied after the flow field data is exchanged through the chimera process. The boundary

Any number of grid blocks can be used to define the blade geometry and volume around the blade. Using Pegasus, the grids defining the blade and volume must be trimmed to remaining interior to the passage grid. Only the passage grid can be used to create data communication to adjacent blade rows.

### PEGASUS5 Input

**Pegasus5** is used to create the XINTOUT data file defining the chimera communication between the passage grid and any blade grids and prevent chimera boundaries on all outer boundaries of the passage grids. To prevent creation of these unwanted chimera boundaries the user can translate the grid blocks so as removing the overlap between passage grids. **OVERFLOW** boundary conditions can be set at all boundaries of the passage grids or the passage grids can be excluded from the automatic outer fringe creation in **PEGASUS5**. The chimera communication between passage grids will be established using a separate tool. The circumferential boundaries are handled using a periodic boundary condition created for that purpose.

### XINTOUT File Modifications

Once the XINTOUT file is created by **PEGASUS5**, the file must be modified to establish the passage-to-passage communication. Recall that the passage grids have been constructed to create a

condition averages data along each circumferential running grid line to create an axisymmetric inflow and outflow to each passage block. There are numerous variations of the mixing plane approach which could be attempted using this boundary condition as a starting point. The inflow boundary of each passage grid could be treated as a characteristic inflow boundary using the averaged total pressure, total temperature, and flow direction. The outflow boundary could be treated as a mass flux boundary or a variable static pressure boundary using the averaged values.

Only one blade per blade row is modeled in a passage block with the assumption of circumferentially periodic flow at the circumferential direction boundaries. A new boundary condition was created that defined the circumferential direction boundaries as the average of the flow from the grid planes adjacent the boundaries. This simple averaging approach is consistent with treatment of the wake-cut boundary condition. A higher order version of this boundary condition is a virtual overlap approach where the grid is extended and multiple grid planes of flow field data is rotated to opposite ends of the circumferential running grid lines. The higher order approach was not employed since it prevented the use of convergence acceleration techniques such as grid sequencing and multigrid. The accuracy of the simple averaging approach can be increased by increasing the number of circumferential direction grid points.

The compressor face outflow boundary condition used in inlet calculations at AEDC was modified to permit either spatially variable static pressure with a pressure set a single grid point, or to allow total mass flow rate be set as the outflow boundary condition.

## **OVERFLOW Modifications**

The majority of the modifications made to **OVERFLOW** have been previously mentioned. The modifications primarily were the addition of boundary conditions. Previously when rotation was indicated, the entire grid system was considered to be rotating. A new input variable was introduced that allows for specifying that flow equations should include the effect of solid body rotation for an individual block.

## **REFERENCES:**

- 4.95** "OVERFLOW 2.1t User's Manual", August 2008. Sirbaugh, J, "Turbomachinery Mods to OVERFLOW," Internal AEDC memo report, 2006.
- 4.96** Chen, J.P., Briley, W.R., "A Parallel Flow Solver for Unsteady Multiple Blade Row Turbomachinery Simulations," ASME Paper 2001-GT-0348, June 2001.
- 4.97** Chen, J.P., Barter, J.W., "Comparison of Time-Accurate Calculations for the Unsteady Interaction in Turbomachinery Stage," AIAA 98-3292, July 1998.
- 4.98** Chen, J.P., Ghosh, A.R., Sreenivas K., and Whitfield, D.L., "Comparison of Computations Using Navier-Stokes Eqn.s in Rotating and Fixed Coordinates for Flow Through Turbomachinery," AIAA-97-0878, 1997.
- 4.99** Chen, J.P., and Whitfield, D.L., "Navier-Stokes Calculations for The Unsteady Flowfield of Turbomachinery," AIAA-93-0676, Jan. 1993.

- 4.100** Erdos, J.I., Alzner, E., and McNally W., "Numerical Solution of Periodic Transonic Flow Through a Fan Stage," AIAA Journal 15 (11), pp 1559–1568, 1977.
- 4.101** Whitfield, D.L., Janus, J.M. and Simpson, L.B., "Implicit Finite Volume High Resolution Wave–Split Scheme for Solving the Unsteady Three– Dimensional Euler and Navier–Stokes Eqn.s on Stationary or Dynamic Grids," MSSU–EIRS–ASE–88–2, 1988.
- 4.102** Zhu J. and Shih, T.–H., "CMOTT Turbulence Module for NPARC," NASA CR 204143, Aug. 1997.
- 4.103** Sirbaugh, J, "Turbomachinery Mods to OVERFLOW," Internal AEDC memo report, 2006.

#### 4.10 WATER/STEAM INGESTION TECHNICAL APPROACH

This section will discuss a water/steam ingestion capability for compression system performance and operability developed at AEDC. Most of the information in this section was taken from a technical paper written by Hale and Klepper [4.104].

Steam ingested into a gas turbine engine compression system has three major effects. First, the addition of water causes changes in the gas properties. For example, at standard temperature and pressure the specific ratio,  $\gamma$ , for water is 1.31 and for air is 1.4. Second, if some portion of the steam has condensed into liquid water before being ingested into the compressor inlet (steam with quality less than 100 percent), the increase in temperature occurring through the compressor is expected to cause the water to go through a phase change from liquid to vapor. This process, which involves heat transfer and a change in the density of the gas, will force incidence changes on the blades, causing a stage rematch effect on the overall compression system.

Finally, the hot steam ingestion causes a temperature distortion that can change the stage balance. Each of these changes may lead to some change in performance and the possibility of a reduction in the stability margin of the compression system. Although each of these effects is important, the scope of this work is limited to the first two effects: gas property changes and vaporization effects.

Although the industry standard for water ingestion, the AGARD report "Recommended Practices for the Assessment of the Effects of Atmospheric Water Ingestion on the Performance and Operability of Gas Turbine Engines," [4.105] did not directly address steam ingestion, it did provide insight into the effects of water (in liquid, solid, and gaseous forms) on gas turbine engine compression systems. The trends related to vaporization in the compression system in this AGARD report are used to evaluate the results of the work presented in this paper where no experimental data was available. Steam ingestion, as considered in the current analysis, typically has quality of less than 100 percent. The quality is in the form of liquid water droplets condensed in the flow. Because of the increasing temperature caused by compression of the working fluid, these particles vaporize as they move through the system. The AGARD reference states that at high compressor speeds, as vaporization occur, the rear stages will rematch closer to stall.

Development of a steam ingestion modeling technique required a one-dimensional (1-D) multiphase code and a 1-D compressor **meanline** code. An in-depth discussion of these codes and the previous investigation can be found in Klepper, Hale, Davis [4.110]. These codes, and the methodology used to couple the codes, are briefly described in this section.

##### **AEDC MULTIPHASE CODE (MPC)**

Although the Arnold Engineering Development Center (AEDC) Multiphase Code (**MPC**) by Wilbanks and Schulz [4.109] was developed in the early 1970s, it has been consistently updated through the years. A brief listing of the assumptions used to develop the code follows.

- Air and water vapor are treated as ideal gases (i.e.,  $c_p$  and  $\gamma$  are functions of temperature only).
- The gas phase is homogenous at any axial station except in the droplet boundary layer.
- Drops remain entrained in the gas stream throughout the duct.

- Collisions and agglomerations are considered negligible.
- Drops are uniformly distributed at any cross section of the duct.
- Drops are spherical in shape.
- Vaporization is occurring at any instant in equilibrium.

The **MPC** is a steady-state, 1-D, multiphase code with vaporization and freezing phase-change models involving heat transfer and mass transfer. The code solves the conservation of mass, momentum, and energy equations for both gas and liquid phases and ties the two together with the Eqn. of state. It uses a 5<sup>th</sup>-6<sup>th</sup> order Runge-Kutta solver for solving the governing equations numerically.

The code tracks up to 10 different particle classes. These classes of particles may differ in surface temperature, droplet size, droplet velocity, and/or liquid water loading factor (FL, ratio of liquid water mass flow to “dry” air mass flow). As the particles move through the gaseous flow field, both heat and mass transfer occur, causing the particle and gas properties to change accordingly.

### **AEDC MEANLINE CODE (MLC)**

The 1-D compressor **meanline** code used in the analysis is the AEDC **Meanline** Code (**MLC**) as reported by Smith [4.108]. The **MLC** works by taking the blade inlet total pressure, total temperature, and geometry to calculate the static conditions on the basis of isentropic relationships. Velocity triangles are developed from these static parameters. Next, flow conditions in the relative-to-the-blade-row frame of reference are determined.

Loss and deviation correlations [4.106] are then used to step across the bladed region. The relative total pressure loss coefficient and the blade deviation calculated by the correlations, along with the given geometry, are used to determine relative total pressure and total temperature ratios. The inlet mass flow function (MFF<sub>1</sub>) is then calculated by Eqn. 4-223.

$$MFF_1 = \frac{\dot{m}_G \sqrt{T_{t1}'}}{P_{t1}' A_1} \quad \text{Eqn. 4-223}$$

The relative total pressure ratio, relative total temperature ratio, and area ratio (to be further developed in a following section) are then used to calculate the blade exit mass flow function (MFF<sub>2</sub>) with the relationship presented in Eqn. 4-224,

$$MFF_2 = MFF_1 \left( \frac{P_{t1}'}{P_{t2}'} \right) \sqrt{\frac{T_{t2}'}{T_{t1}'}} \left( \frac{A_1}{A_2} \right) \quad \text{Eqn. 4-224}$$

The exit mass flow function now can be used to determine the exit relative Mach number using Eqn. 4-225.

$$MFF_2 = \sqrt{\frac{\gamma_G}{R_G}} M_2' \left[ 1 + \frac{(\gamma_G - 1)}{2} M_2'^2 \right]^{-\frac{(\gamma_G + 1)}{2(\gamma_G - 1)}} \quad \text{Eqn. 4-225}$$

Next, isentropic relationships are again used to calculate exit static conditions. Finally, from these static conditions, exit velocity triangles are determined and are used to define the absolute exit total pressure and exit total temperature. The blade exit conditions are then used to proceed to the inlet of the next blade row.

### **MODIFICATIONS TO THE MLC/MP**

A requirement for this work was for the **MP** to interface with any **MLC**. This resulted in modifications and restructuring of the integrated **MLC/MP** code from the original code as reported in Klepper, Hale, Davis [4.110]. The previous iteration scheme was simplified to a two-step process to calculate **Turbomachinery** and heat transfer. Other improvements include more accurate modeling of gas properties and bleeds. In addition to these efforts, a better physical model for heat transfer was implemented that allows for the multiphase calculations to be performed relative to the blade row instead of in the absolute reference frame, as previously done.

### **Restructuring of the MLC/MP**

In the code originally developed [4.110], a main program was used to call both the **MLC** and the **MP**. This main routine also handled the integration of the two solutions. The AEDC **MLC/MP** code was restructured to allow the **MLC** to be the controlling code. This section describes how the codes were coupled together and the modeling decisions that were made to allow the combined **MLC** and **MP** to simulate **Turbomachinery** and multiphase flow in the same region. The **MLC/MP** uses a two-step process to account for **Turbomachinery** with heat transfer. The first step in the process of running the **MLC/MP** is initially to run the **MLC** through a region with no influence from the **MP**. Once the **MLC** reaches a solution without **MP** influence, a subset of geometry and flow parameters is passed to the **MP** to model the multiphase effects on the flow. The flow parameters passed to the **MP** for rotors are exit relative total pressure and temperature, relative flow angles, and the average of the inlet and exit relative Mach numbers. For stators and duct, the relative parameters are replaced by absolute parameters, and the Mach number is the inlet Mach number instead of an average Mach number. The geometry parameters include the cross-sectional area and the inlet and exit axial locations.

**Figure 4.59** represents the geometry of the blade passage. The cross-sectional areas ( $A_{1x}$  and  $A_{2x}$ ) passed by the **MLC** are converted to areas normal to the mean flow path ( $A_1$  and  $A_2$ ) by the appropriate flow angles. The inlet area is then scaled to match the average Mach number. The same geometric scaling factor is applied to the exit area. The axial distance is also rescaled to model the actual distance along the mean flow path.

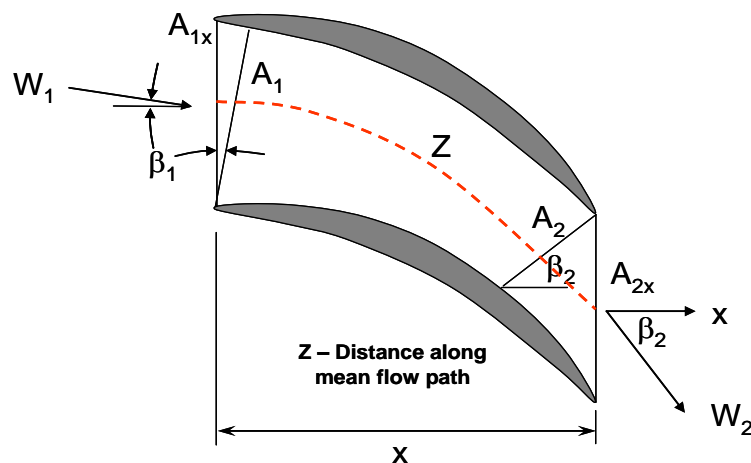


**Figure 4.59 Blade Passage Geometry**

The **MP** is then called to calculate the evaporation or condensation that occurs across the



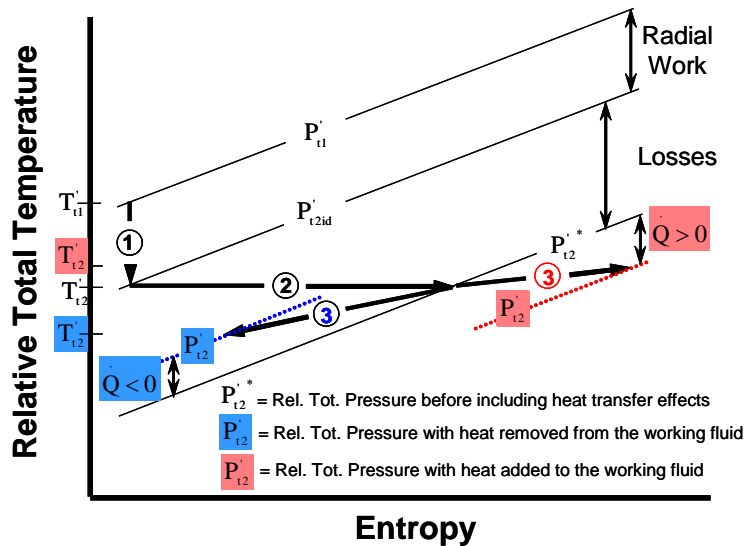


**Figure 4.60 Heat and Work Process Involved Within a Region Defined in a Relative Coordinate System**

region while following fluid particles. Therefore, the gas mass flow is increased or decreased by water vapor associated with evaporation or condensation, respectively. The heat transfer ( $\dot{Q}$ ) associated with evaporation or condensation is calculated and passed back to the **MLC**. The discussion of the  $\dot{Q}$  calculation is included in the following section.

### Modifications to the Meanline Code for Heat Transfer

The **MLC** is constructed to calculate flow through bladed and non-bladed regions, thus to account for heat transfer (**Figure 4.60**). Flow-field calculations for

stators and ducts are completed in the absolute reference frame, and rotor flow-field calculations are made in the relative-to-the-blade-row reference frame.

*In this section, figures and equations are cast in the relative-to-the-blade-row reference even though for ducts and stators the relative and the absolute are identical.*

**Figure 4.60** is a Temperature-Entropy (T-S) diagram with heat and work processes depicted in the relative-to-the-blade reference frame. The modeling of steam ingestion required that the meanline code be modified to further simulate the effect of heat transfer associated with the latent heat of vaporization and condensation through the compression system. An approximation technique was selected to include the effect of heat transfer to avoid the added complexity of simultaneously solving a system of ordinary differential equations. This process is also outlined in **Figure 4.60** on a T-S diagram applied to the relative-to-the-blade-row reference frame. The relative total pressure and temperature ratios are, therefore, obtained by stacking the radial work (rotors), the effect of losses (rotors, stators, and ducts), and the heat addition (red process) or heat subtraction (blue process) through the region (rotors, stators, and ducts). All three processes—radial work, losses, and heat transfer—are shown in **Figure 4.60**.

The first process shown is radial work, which applies to rotors only, and results in work being reversible and thus ideal by virtue of a radius change. Radial work increases when the streamline radius increases across the region, and radial work decreases when the streamline radius decreases across the region.

The second and third processes viewed on the same T-S diagram apply to the simulation of rotors, stators, and ducts. The second process shows the losses at constant relative total temperature represented by a drop in relative total pressure from the region inlet to exit. These losses include profile losses, shock losses, and secondary losses. Finally, for rotors, stators, and ducts, the heat transfer to the working fluid within the region (red process) results in an increase in relative total temperature and entropy with a decrease in relative total pressure. The

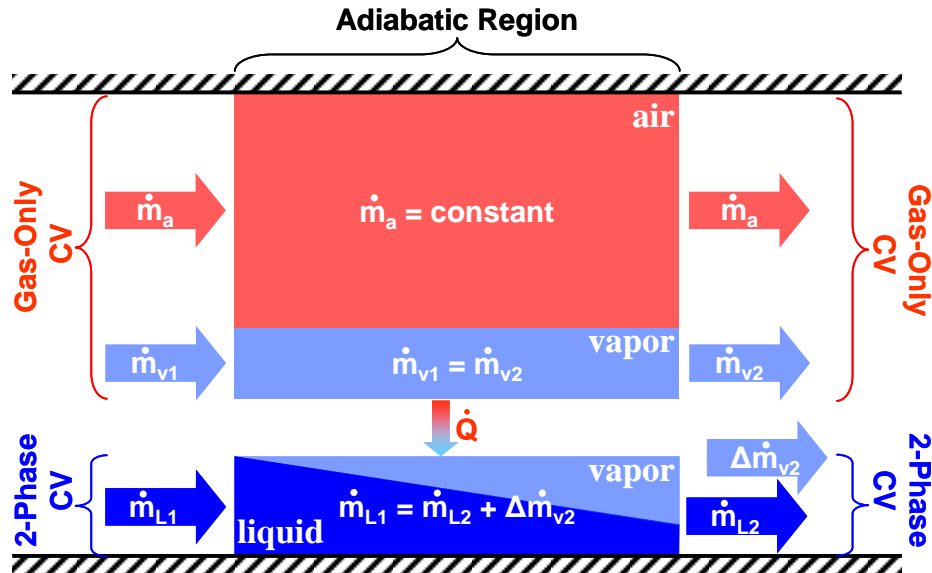


**Figure 4.61 Conceptual Picture for Defining the Two Constant Mass Flow Control Volumes Used for MLC/MPC Heat-Transfer Calculations**

heat transfer from the working fluid (blue process) results in a decrease in total temperature and entropy with an increase in relative total pressure. The flow field, therefore, behaves in a manner similar to Rayleigh Flow as heat is added or removed from the working fluid. Heat transfer from the working fluid is defined as a negative heat transfer, whereas heat transfer to the working fluid is a positive heat transfer.

The heat-transfer rate is calculated from the change in relative total temperature throughout the region applied to the appropriate constant mass flow control volume. Two constant mass flow control volumes are defined to account for all the working fluid moving through the region, and these control volumes are conceptually separated and shown in [Figure 4.61](#) for an evaporation process, though a condensation process could have just as easily been represented.

One is a gas-only mass flow control volume defined to contain the air mass flow and the water vapor mass flow entering the region. The other is a two-phase mass flow control volume accounting for the liquid water mass flow entering the region even though this liquid water may change phase in the region. [Eqn. 4-226](#) is used to calculate the heat transfer from the gas-only mass flow control volume to the two-phase mass flow control volume.

$$\dot{Q} = \dot{m}_A \bar{c}_{p,A} (T'_{t2} - T'_{t1}) + \dot{m}_V \bar{c}_{p,V} (T'_{t2} - T'_{t1}) \quad \text{Eqn. 4-226}$$

The mass flow function, ([Eqn. 4-225](#)), is used to calculate the flow field across the region in the plane relative to the blade row when the ratios of relative total pressure, total temperature, and cross-sectional geometry are provided. The relative total pressure ratio, relative total temperature ratio, and area ratio are now defined separately. Relative total pressure ratio developed in [Eqn.s 4-227 through 4-229](#) is obtained from radial work, heat transfer, and loss and deviation correlations modified from those of NACA-SP36 [\[4.107\]](#).

$$\left(\frac{P'_{t2}}{P'_{t1}}\right) = \left(\frac{P'_{t2}}{P'_{t1}}\right)^* \left(1 - \frac{\gamma_G M_1'^2 \dot{Q}}{2C_{p,G} T'_{t1} \dot{m}_G}\right) \quad \text{Eqn. 4-227}$$

where

$$\left(\frac{P'_{t2}}{P'_{t1}}\right)^* = \left(\frac{P'_{t2}}{P'_{t1}}\right)_{id} - \varpi' \left(1 - \left[\frac{1}{1 + \frac{\gamma_G - 1}{2} M_1'^2}\right]^{\frac{\gamma_G}{\gamma_G - 1}}\right) \quad \text{Eqn. 4-228}$$

where

$$\left(\frac{P'_{t2}}{P'_{t1}}\right)_{id} = \left\{1 + \frac{(\gamma_G - 1)}{2} \frac{U_2}{\sqrt{\gamma_G R_G T'_{t1}}} \left[1 - \left(\frac{r_1}{r_2}\right)^2\right]\right\}^{\frac{\gamma_G}{\gamma_G - 1}} \quad \text{Eqn. 4-229}$$

The relative total-temperature ratio with heat transfer is calculated using [Eqn.s 4-227](#) and [4-230](#).

$$\left(\frac{T'_{t2}}{T'_{t1}}\right) = 1 + \frac{(U_2^2 - U_1^2)}{2C_{p,G} T'_{t1}} + \frac{\dot{Q}}{C_{p,G} T'_{t1} \dot{m}_G} \quad \text{Eqn. 4-230}$$

The area ratio used in the MFF is defined in [Figure 4.59](#) such that the areas used are perpendicular to the relative inlet and exit velocities.

This tool was successfully used and compared to data for and analysis of the Pratt and Whitney FT-8 ground power turbine. It was also successfully applied to look at the operability of the Pratt & Whitney F135 low bypass fan and HPC. These results can be thoroughly examined in Hale, Klepper, Hurwitz [[4.104](#)].

#### REFERENCES:

**4.104** Hale, A., Klepper, J., Hurwitz, W., "A Numerical Capability to Analyze the Effects of Water Ingestion on Compression System Performance and Operability," GT2005-68480, ASME TURBO Expo, Reno-Tahoe, Nevada, June 2005.

**4.105** "Recommended Practices for the Assessment of the Effects of Atmospheric Water Ingestion on the Performance and Operability of Gas Turbine Engines," Propulsion and Energetics Panel Working Group 24, Advisory Group for Aerospace Research and Development (AGARD), NATO, 1995

**4.106** Hearsey, R.M. "Program HT0300 NASA 1994 Volume 2." The Boeing Company, 1994. Klepper, Jason, Hale, Alan, and Davis, Milt, "A Numerical Investigation of Steam Ingestion on Compression System Performance," ASME Paper #GT2004-54190, 2004 ASME TURBO Expo, June 2004.

**4.107** Lieblein, S. "Chapter VI: Experimental Flow in Two-Dimensional Cascades." *Aerodynamic Design of Axial-Flow Compressors*, NASA-SP-36, 1965, pp. 183-226.

**4.108** Smith, S. L. "1-D Meanline Code Technique to Calculate Stage-by-Stage Compressor Characteristics." M.S. Thesis, The University of Tennessee, Knoxville, TN, 1999.

**4.109** Willbanks, C. E. and Schulz, R. J. "Analytical Study of Icing Simulation for Turbine Engines in Altitude Test Cells." AEDC-TR-73-144 (AD-770069), November 1973.

**4.110** Klepper, Jason, Hale, Alan, and Davis, Milt, "A Numerical Investigation of Steam Ingestion on Compression System Performance," ASME Paper #GT2004-54190, 2004 ASME Turbo Expo, June 2004.

#### 4.11 INTEGRATION OF MLC & DYNTTECC, TECHNICAL APPROACH

The integration of the **MLC** ([Section 4.2](#)) and **DYNTTECC** ([Section 4.4](#)) is described in this section as reported by Tibboel [4.111]. The combination of these codes is because of long-recognized shortcomings of characteristics maps used in **DYNTTECC**. To circumvent those shortcomings, the **MLC** was incorporated as a subroutine of **DYNTTECC**. **DYNTTECC** previously called a series of subroutines to read the characteristic map file and interpolate for the desired mass flow. The user can now direct it to bypass the map and instead have the characteristics calculated at each time step in **MLC**.

The decision to allow operation with loss, deviation and MVDR specified stemmed from the previously existing mode of operating **DYNTTECC** with a map. In this mode, the total pressure and total temperature ratios, when provided by characteristics maps, depend only on rotor speed, inlet flow velocity, inlet total pressure and temperature, area and gamma. The goal of this work was to replace those maps, so the integration of the **MLC** imitated that interface as closely as possible.

Loss and deviation are not provided directly, so **MLC** calculates them using a correlation algorithm. The Hearsey [4.112] correlations are the best algorithm currently available in the code for specifying loss and deviation. The Hearsey correlations provide an estimate, so an add-loss and add-deviation map must be developed for each stage to provide more accurate results. To avoid having **DYNTTECC** specify a component exit condition, that map is extended to provide meanline velocity density ratio. A calibration process is used to create the map, including MVDR information.

The **MLC** subroutine pulls information for the correlation calculations from a separate input file. That input file also provides additional geometry information which is not already provided by **DYNTTECC**. Information that is passed from **DYNTTECC** includes constants ( $R$ ,  $\gamma$ ,  $g_c$ ); total pressure, total temperature and Mach number at the component inlet; mass flow; rotor speed; component inlet and exit areas; exit static pressure; and the stage inlet station.

#### REFERENCES:

**4.111** Tibboel, G. A., "Modification of a One-Dimensional Dynamic Compression System Model to Calculate Stage Characteristics Internally." M.S. Thesis, The University of Tennessee, Knoxville, TN, 2002.

**4.112** Hearsey, R.M. "Program HT0300 NASA 1994 Volume 2." The Boeing Company, 1994.

## 5 LESSONS LEARNED

Over the span of 40 years, turbine engine modeling and simulation technology for analysis of compression system operability issues has been in development here at AEDC. Over the years a set of lessons learned have been established that can provide guidance to the next application or development activity. These lessons fall into several categories: Application, Development, Programmatic, Transition and Awareness.

### **APPLICATION**

- One must understand the relevant physics of the problem to understand the level of fidelity one must have to simulate the issue at hand
  - Steady-state versus dynamic behavior
  - Things happen in a rotor revolution (2-3 millisec).
  - Compression systems will respond and stall to an event that lasts a minimum of 1 rotor revolution.
  - Dynamic pressure measurements indicate that the dynamic distortion intensity can be as much as twice as that observed in steady-state intensity.
- One must obtain enough geometry and/or experimental information to simulate the application of interest. Generally that information lies with the engine manufacturer
  - Annulus geometry
  - Blade geometry
  - Stage characteristics
- One must understand the compression system stall process to be able to model it within the numerical simulation.
  - Rotating stall initiation
  - Flow breakdown generally at the tip of the system
  - Poststall behavior even though it may not be specifically modeled
  - Time frame in which stall develops
  - Recovery from stall or surge and what can be done to initiate it
- One must understand the established distortion methodology (SAE ARP-1420)
  - Current established methodology combines the inlet distortion pattern intensities with an estimate of the engine sensitivity to broad (classical) distortion patterns. The effects of complex patterns on engine stability are thus estimated using engine sensitivities that may or may not represent accurate engine behavior.
  - Current analysis practices may use only the distortion pattern intensities and a general knowledge of past experience (“doghouse plot”) to make profound decisions about stability effects.

### **DEVELOPMENT**

- The Simulation must be formulated with an appropriate level of physics either from first principals or those effects not formulated must be modeled usually using experimental data as a guide
- Formulate the physical models within appropriate coordinate systems (e.g., circular compression systems need to be formulated in cylindrical coordinate systems)
  - The effects of blade blockage are more easily included in cylindrical coordinate systems.
  - Cylindrical coordinate systems allow for simpler grids.
- Formulate the mathematical algorithm solution technique that best fits the desired solution outcome.



**PROGRAMMATIC**

- Must have a good connection to manufacturers – they own the necessary geometry and much of the data for comparisons
- Must be relevant to current weapon system test and evaluation
- Must validate your simulation results such that test and evaluation organizations/personnel will value the potential contribution that the simulation can make
- Must have an appropriate people networking process in place to gain access to required information and obtain advocacy
- Must plan for funding shortages and continuances across government fiscal years.

**TRANSITION**

- One must recognize that ease-of-use is a primary concern when transitioning a numerical simulation to analysis engineers for application
  - Graphic User Interfaces (GUI's) are a must
  - Input and Output must be easily recognized and use standard nomenclature
  - If at all possible, programming technology necessary to execute the code should be minimized
- Transition to test and evaluation organizations will require training of T&E personnel and constant interaction to foster appropriate use of the simulation
- New users will find things that are broke or will break them on their own accord – fix them and thank them
- New Users will think of new ways to use your code – accommodate their suggestions and plan for incorporating their suggestions into code development as soon as feasible.

**AWARENESS**

- Be aware of what others are doing so that re-invention of the wheel does not occur.
  - Academia – compression system instability has been a topic of research for many universities including: MIT, Virginia Tech, Purdue, Penn State, and Georgia Tech
  - Government – Research in compressor performance and operability has been and is still a topic of interest at the Air Force Research Laboratory (AFRL) and NASA Glenn Research Center
  - Industry – Engine manufacturers are continuously investing in new analysis techniques to improve their product. Access to that information is generally not available through public means but only through a need to know basis.
- To be relevant one must strive to be connected to the outside world (i.e. beyond the borders of one's own organization) through interaction at appropriate technical conferences (e.g. ASME International Gas Turbine Institute Turbo Expo) and membership in technical committees associated with turbine engine performance and operability (e.g. SAE S-16 Turbine Engine Inlet Flow Distortion Committee).

## CHAPTER 6 TABLE OF CONTENTS

6	List of References .....	386
6.1	Chapter 2 References .....	386
6.2	Chapter 3 References .....	390
6.3	Chapter 4 References .....	405

### 6 LIST OF REFERENCES

The following list of references is compiled from the references in each chapter. Those in the chapters are hyperlinked (**denoted by red**) such that if a reader is reading the document electronically in the PDF version and comes across a reference, he can **click** the reference number and it will take him to the specific reference information. This allows the reader of the electronic version the ability to immediately know what the reference number refers to. If however, the reader is reading a paper version, the following list may be a more convenient way of determining the reference information. In addition, the reader, whether the document be electronic or paper, will discover that the same reference may appear many times within the document with different reference numbers. That is because it was determined that the references alluded to by the individual paper that make up the document should be left as they were referenced in the paper. As such, the list of references below contain the same numbering system as provided in the individual chapters but are not hyperlinked where they are called out in the document.

#### 6.1 CHAPTER 2 REFERENCES

2.1 Kimzey, W. F., "An Analysis of the Influence of Some External Disturbances on the Aerodynamic Stability of Turbine Engine Axial Flow Fans and Compressors", AEDC-TR-77-80, August, 1977.

2.2 Chamblee, C. E., M. W. Davis, Jr., and W. F. Kimzey, "A Multi-Stage Axial Flow Compressor Mathematical Modeling Technique with Applications to Two Current Turbofan Compression Systems", AIAA Paper # AIAA-80-0054, Presented at the AIAA 18th Aerospace Sciences Meeting, Pasadena, CA, April, 1980.

2.3 Davis, Milton W., Jr., "A Stage-by-Stage Compressor Modeling Technique for Single- and Dual-Spool Compression Systems", Unpublished Master's Thesis, University of Tennessee, Knoxville, Tennessee, August 1981.

2.4 Davis, M. W., Jr., "A Stage-by-Stage Compressor Modeling Technique for Single- and Dual-Spool Compression Systems", AEDC-TR-81-13, March 1982.

2.5 Davis, M. W., Jr., "A Stage-by-Stage Dual-Spool Compression System Modeling Technique", ASME Paper #82-GT-189, March 1982, Presented at the 1982 IGTI Conference, London, England.

2.6 Davis, M. W., Jr., "A Stage-by-Stage Post-Stall Compression System Modeling Technique: Methodology, Validation, and Application", Ph.D. Dissertation, Virginia Polytechnic Institute and State University, December 1986

- 2.7 Davis, M. W., Jr., "A Post-Stall Compression System Modeling Technique", AEDC-TR-86-34, February 1987.
- 2.8 Davis, M. W. , Jr. and W. F. O'Brien, "Stage-by-Stage Poststall Compression System Modeling Technique", Journal of Propulsion and Power, Vol. 7, Number 6, November-December 1991, pp. 997-1005.
- 2.9 Davis, M. W., Jr., "Parametric Investigation into the Combined Effects of Pressure and Temperature Distortion on Compression System Stability", AIAA Paper # AIAA-91-1895, Presented at the 27th Joint Propulsion Conference, Sacramento, CA, June 1991.
- 2.10 Hale, A. A. and M. W. Davis, Jr., "DYNAmic Turbine Engine Compressor Code: DYNTECC -- Theory and Capabilities", AIAA Paper # AIAA-92-3190, Presented at the 28th Joint Propulsion Conference and Exhibit, Nashville, TN, July 1992.
- 2.11 Gorrell, S. E. and M. W. Davis, Jr., "Application of a Dynamic Compression System Model to a Low Aspect Ratio Fan: Casing Treatment and Distortion", AIAA Paper # AIAA-93-1871, Presented at the 29th Joint Propulsion Conference and Exhibit, Monterey, CA, June 1993.
- 2.12 Hale, A. A., M. W. Davis, Jr., and K. R. Kneile, "Turbine Engine Analysis Compressor Code: TEACC -- Part I: Technical Approach and Steady Results", AIAA Paper # AIAA-94-0148, Presented at the 32nd Aerospace Sciences Meeting and Exhibit, Reno Nevada, January 1994.
- 2.13 Owen, A. K., and M. W. Davis, Jr., "Modeling the Dynamic Behavior of an Axial-Centrifugal Compression System", AIAA Paper # AIAA-94-2802, Presented at the 30th AIAA Joint Propulsion Conference and Exhibit, Indianapolis, IN. June 1994.
- 2.14 Davis, M. W., Jr. and T. A. Bapty, "Interactive User's Interface for a Dynamic Compression System Simulation," AIAA-95-0244, Presented at the 33rd Aerospace Sciences Meeting, Reno, NV. ,January 1995.
- 2.15 Shahrohi, K. A., "Application of a Modified Dynamic Compression System Model to a Low-Aspect Ratio Fan: Effects of Distortion," Unpublished Master's Thesis, Vanderbilt University, Nashville, Tennessee, May 1995.
- 2.16 Shahrohi, K. A., and M. W. Davis, Jr., "Application of a Modified Dynamic Compression System Model to a Low-Aspect Ratio Fan: Effects of Distortion," AIAA-95-0301, Presented at the 33rd Aerospace Science Meeting, Reno, NV, January 1995.
- 2.17 Davis, M. W., Jr., O'Brien, W. F., Owen, A. K., and W. T. Cousins., "Joint Dynamic Airbreathing Propulsion Simulations Partnership (JDAPS)," ASME Paper # 95-GT-279, Presented at the 40th ASME International Gas Turbine & Aeroengine Congress & Exposition, Houston, Texas, June 1995
- 2.18 Garrard, G. D., M. W. Davis, Jr., and A. A. Hale, "Recent Advances in Gas Turbine Engine Dynamic Models Developed Through JDAPS," ASME Paper # 95-GT-146, Presented at the 40th ASME International Gas Turbine & Aeroengine Congress & Exposition, Houston, Texas, June 1995.

- 2.19 Davis, M. W., Jr., A. A. Hale, K. A. Shahrokhi, and G. D. Garrard, "Euler Modeling Techniques for the Investigation of Unsteady Dynamic Compression System Behavior", Presented at the 85th Session of the Propulsion and Energetics Panel of AGARD, Derby, England, May 1995.
- 2.20 Garrard, G. D., "ATEC: The Aerodynamic Turbine Engine Code for the Analysis of Transient and Dynamic Turbine Engine System Operations," Ph.D. Dissertation, the University of Tennessee, Knoxville, August, 1995.
- 2.21 Chalk, J. C. "Adaptation of a Three-Dimensional Numerical Simulation to Represent Gas Turbine Engine Compression Systems." Master's Thesis, The University of Tennessee, Knoxville, TN, 1996.
- 2.22 Hale, A. A., "A Three-Dimensional Turbine Engine Analysis Compressor Code (TEACC) for Steady-State Inlet Distortion." Ph.D. Dissertation, Virginia Polytechnic Institute and State University, Blacksburg, VA, 1996.
- 2.23 Garrard, Doug, "ATEC, The Aerodynamic Turbine Engine Code for the Analysis of Transient and Dynamic Gas Turbine Engine System Operations, Part 2: Numerical Simulations", ASME Paper # 96-GT-194, June 1996.
- 2.24 Garrard, Doug, "ATEC, The Aerodynamic Turbine Engine Code for the Analysis of Transient and Dynamic Gas Turbine Engine System Operations, Part 1: Model Development", ASME Paper # 96-GT-193, June 1996.
- 2.25 Garrard, Doug, Davis, Milt, Jr., Hale, Alan, Chalk, Jacqueline, and Savelle, Stephen, "Analysis of Gas Turbine Engine Operability with the Aerodynamic Turbine Engine Code", ISABE 97-7034, Presented at the International Society for Air Breathing Engines Thirteenth International Symposium on Air Breathing Engines, Chattanooga, Tennessee, September 7-12, 1997.
- 2.26 Davis, M.W., et. al., "An Approach for the Development of an Aerodynamic-Structural Interaction Simulation for Aeropropulsion Systems", ASME-96-480, June 1996.
- 2.27 Garrard, D., Davis, M. W., Wehofer, S. and G. Cole, "A One-Dimensional, Time-Dependent Inlet/Engine Numerical Simulation for Aircraft Propulsion Systems," ASME-97-GT-333, June, 1997
- 2.28 Chalk, J. C. H., "Adaptation of a Three-Dimensional Numerical Simulation to Represent Gas Turbine Engine Compression Systems", AEDC TR-97-1, April 1997
- 2.29 Hale, A. A., and W. F. O'Brien, "A Three-Dimensional Turbine Engine Analysis Compressor Code (TEACC) for Steady-State Inlet Distortion," Journal of Turbomachinery, Vol. 120, July 1998, pp. 422-430.
- 2.30 Garrard, Doug, et. al. "A Parametric Starting Study of an Axial-Centrifugal Gas Turbine Engine Using a One-Dimensional Dynamic Engine Model and Comparisons to Experimental Results, Part 2: Simulation Calibration and Trade-off Study", ASME Paper # 98-GT-471, June 1998

- 2.31 Garrard, Doug, et. al. "A Parametric Starting Study of an Axial-Centrifugal Gas Turbine Engine Using a One-Dimensional Dynamic Engine Model and Comparisons to Experimental Results, Part 1: Model Development and Facility Description", ASME Paper # 98-GT-470, June 1998
- 2.32 Hale, Alan, Chalk, Jacqueline, Klepper, Jason, and Kneile, Karl, "Turbine Engine Analysis Compressor Code, Part II: Multi-stage Compressors and Inlet Distortion", AIAA-99-3214, July 1999.
- 2.33 Asbury, Sarah, Roberts, Brandon, and Hale, Alan, "A Graphical Technique for Compressor Analysis to Collocate Velocity Vectors and Mean Camber Lines", AIAA Paper # 2002-0311, January 2002.
- 2.34 Davis, Milt, Alan Hale, and Dave Beale, "An Argument for Enhancement of the Current Inlet Distortion Ground Test Practice for Aircraft Gas Turbine Engines", Journal of Turbomachinery, Vol. 124, Number 2, April 2002, pp. 235-241.
- 2.35 Davis, M. W., Jr., W. Baker, G. Power, and D. Beale, "A Proposal for Integration of Wind Tunnel and Engine Test Programs for the Evaluation of Airframe-Propulsion Compatibility Using Numerical Simulations", Journal of Engineering for Gas Turbines and Power, Vol. 124, Number 3, July 2002, pp. 447-458.
- 2.36 Klepper, Jason, Hale, Alan, and Davis, Milt, "A Numerical Investigation of Steam Ingestion on Compression System Performance," ASME Paper #GT2004-54190, 2004 ASME Turbo Expo, June 2004.
- 2.37 Hale, Alan, Klepper, Jason, and Hurwitz, Wayne, "A Numerical Capability to Analyze the Effects of Water Ingestion on Compression System Performance and Operability", ASME Paper # GT2005-68480, June 2005.
- 2.38 Davis, Milt and Peter Montgomery, "A Flight Simulation Vision for Aeropropulsion Altitude Ground Test Facilities", Journal of Engineering for Gas Turbines and Power, Vol. 127, January 2005, pp. 8-17.
- 2.39 Hale, Alan, Milt Davis, and Jim Sirbaugh, "A Numerical Simulation Capability for Analysis of Aircraft Inlet-Engine Compatibility", Journal of Engineering for Gas Turbines and Power, Vol. 128, July 2006, pp. 473-481.
- 2.40 Beale, D., Davis, M., and Sirbaugh, J., "Requirements and Advances in Simulating Aircraft Inlet Total-Pressure Distortion in Turbine Engine Ground Tests," ASME Paper No. GT2006-90038, ASME Turbo Expo 2110, Barcelona, Spain, May 8-11, 2006.
- 2.41 Davis, Milt, Beale, Dave, Boyer, Keith, and O'Dowd, Devin, "An Example for Integrated Gas Turbine Engine Testing and Analysis Using Modeling and Simulation", Presented at the 2006 ITEA Modeling and Simulation Conference, Las Cruces, NM, December 2006.
- 2.42 Davis, Milt (Tech Editor), "Performance Predictions and Simulation of Gas Turbine Engine Operation for Aircraft, Marine, Vehicular, and Power Generation" RTO-TR-AVT-036, February 2007.

2.43 Davis, Milt, and Hale, Alan, "A Parametric Study on the Effects of Inlet Swirl on Compression System Performance and Operability Using Numerical Simulations", GT2007-27033, Presented at the 2007 ASME International Gas Turbine Institute's Turbo Expo in Montreal, Canada, May 2007

2.44 Davis, Milt, Jr., Beale, Dave, and Sheoran, Yogi, "Integrated Test and Evaluation Techniques as Applied to an Inlet Swirl Investigation Using the F109 Gas Turbine Engine", GT2008-50074, Presented at the 2008 ASME International Gas Turbine Institute's Turbo Expo in Berlin, Germany, June 2008.

2.45 Davis, Milt, Jr., Hale, Alan, Vining, Charles, and Cousins, William, "Application of Numerical Analysis Tools for Airframe-Propulsion Integrated Test and Evaluation", GT2008-50194, Presented at the 2008 ASME International Gas Turbine Institute's Turbo Expo in Berlin, Germany, June 2008.

2.46 Davis, Milt, et.al., "Demonstration of an Integrated Test and Evaluation (IT&E) Process for Airframe-Propulsion Systems as Applied to a Current Weapon System Program", Presented at the 2010 AIAA Aerospace Sciences Meeting, January 2010.

2.47 Davis, Milt and Kidman, David, "Prediction and Analysis of Inlet Pressure and Temperature Distortion on Engine Operability from a Recent T-38 Flight Test Program", Presented at the 2010 ASME International Gas Turbine Institute Turbo Expo, June 2010.

## 6.2 CHAPTER 3 REFERENCES

3.1 Chamblee, C. E., M. W. Davis, Jr., and W. F. Kimzey, "A Multi-Stage Axial Flow Compressor Mathematical Modeling Technique with Applications to Two Current Turbofan Compression Systems", AIAA Paper # AIAA-80-0054, Presented at the AIAA 18th Aerospace Sciences Meeting, Pasadena, CA, April, 1980

3.2 Davis, Milton W., Jr., "A Stage-by-Stage Compressor Modeling Technique for Single-and Dual-Spool Compression Systems", Unpublished Master's Thesis -- University of Tennessee, Knoxville, Tennessee, August 1981.

3.3 Davis, M. W., Jr., "A Stage-by-Stage Dual-Spool Compression System Modeling Technique", ASME Paper #82-GT-189, March 1982, Presented at the 1982 IGTI Conference, London, England.

3.4 Davis, M. W. , Jr. and W. F. O'Brien, "Stage-by-Stage Poststall Compression System Modeling Technique", Journal of Propulsion and Power, Vol. 7, Number 6, November-December 1991, pp. 997-1005.

3.5 Davis, M. W., Jr., "A Stage-by-Stage Post-Stall Compression System Modeling Technique: Methodology, Validation, and Application", Ph.D. Dissertation, Virginia Polytechnic Institute and State University, December 1986

3.6 Greitzer, E. M., "Surge and Rotating Stall in Axial Flow Compressors- Part 11: Experimental Results and Comparison with Theory," *ASME Journal of Engineering for Power*, Vol. 98, April 1976, pp. 199-217.



- 3.7 Gamache, R. N., "Axial Compressor Reversed Flow Performance," Ph.D. Dissertation, Massachusetts Inst. of Technology, May 1985.
- 3.8 Eastland, A. H. J., "Investigation of Compressor Performance in Rotating Stall: I-Facility Design and Construction and Initial Steady State Measurements," MIT Gas Turbine and Plasma Dynamics Lab. Rept. 164, June 1982
- 3.9 O'Brien, W. F., "Dynamic Simulation of Compressor and Gas Turbine Performance", AGARD Lecture Series, LS-183, May 1992
- 3.10 Bloch, G. S., and W. F. O'Brien, "A Wide-Range Axial- Flow Compressor Stage Performance Model," 37th International Gas Turbine Conference, ASME, Cologne, Germany, June 1-4, 1992.
- 3.11 Gamache, R. N., "Axial Compressor Reversed Flow Performance." Ph.D. Dissertation, Massachusetts Inst. of Technology, May 1985.
- 3.12 Copenhaver, W. W., "Stage Effects on Stalling and Recovery of a High-speed 10-stage Axial-Flow Compressor," Ph.D. Dissertation, Iowa State University. October 1988.
- 3.13 Copenhaver, W. W., and T. H. Okiishi, "Rotating Stall Performance and Recoverability of a High-speed Ten-Stage Axial-Flow Compressor," AIAA Paper No. 89-2684, July 1989.
- 3.14 Copenhaver, W. W., and C. J. Worland, "Acquisition of Unsteady Pressure Measurements from a High Sped Multi-Stage Compressor." ASME Paper No. 88-GT-189, June 1988.
- 3.15 Hopf, W. R., and W. G. Steenken, "Stall Recovery Control Strategy Methodology and Results." AIAA Paper No. AIAA-85-1433, July 1985.
- 3.16 Bloch, G. S., and W. F. O'Brien. "A Wide-Range Axial- Flow Compressor Stage Performance Model, " 37th International Gas Turbine Conference, ASME, Cologne, Germany, June 1-4, 1992.
- 3.17 Lieblein, S., "Loss and Stall Analysis of Compressor Cascades," Trans. of the ASME, Journal of Basic Engineering. 1959. pp. 387-400.
- 3.18 Horlock J. H., *Aria1 Flow Compressors*, Robert E. Krega Publishing Company. 1973.
- 3.19 Dixon, S. L., *Fluid Mechanics, Thermodynamics of Turbomachinery* Pergammon Press, 1975.
- 3.20 Moses, H. L., and S. B. Thomason, "An Approximation for Fully Stalled Cascades." ASME Journal of Turbomachinery. 1986, pp. 188-189.
- 3.21 Turner, R. C., and D. W. Sparkes, "Complete Characteristics for a Single-Stage Axial-Flow Fan." Thermodynamics and Fluid Mechanics Convention, Proceedings of the Institution of Mechanical Engineers, Cambridge, England, 1964,
- 3.22 Koff, S. G., and E. M. Greitzer. "Axis-symmetrically Stalled Flow Performance for Multistage Axial Compressors," ASME Journal of Turbomachinery, 1986, pp. 216-223.

- 3.23 Carneal, J. P., "Experimental Investigation of Reversed Flow in a Compressor Cascade," M.S. Thesis, Virginia Polytechnic Institute and State University, Blacksburg, VA, 1990.
- 3.24 Yocum, A. M., III, "An Experimental and Numerical Investigation of the Performance of Compressor Cascades with Stalled Flow." Ph.D. Dissertation. Virginia Polytechnic Institute and State University, Blacksburg, VA. 1988.
- 3.25 Longley, J. P., and T. P. Hynes, "Stability of Flow Through Multistage Axial Compressors." ASME Journal of Turbomachinery, 1990, pp. 126-132.
- 3.26 Graham, R. W., and E. C. Guentert. "Compressor Stall and Blade Vibration," Chapter XI of Aerodynamic Design of Axial Flow Compressors, Johnson, I. A. and Bullock, R. O., NASA SP-36, 1965.
- 3.27 Sugiyama, Y., "Surge Transient Simulation in Turbo-Jet Engine,": Doctoral Dissertation, University of Cincinnati, May 1984.
- 3.28 Boyer, K. M., and W. F. O'Brien. "Model Predictions for Improved Recoverability of a Multistage Compressor," AIAA Paper 89-2687, July 1989.
- 3.29 O'Brien, W. F., "Dynamic Simulation of Compressor and Gas Turbine Performance", AGARD Lecture Series, LS-183, May 1992
- 3.30 Boyer, K. M., and O'Brien, W. F., "Model Predictions for Improve Recovery of a Multistage Axial-Flow Compressor, AIAA Paper # 89-2687, July 1989.
- 3.31 Davis, M. W. , Jr. and W. F. O'Brien, "Stage-by-Stage Poststall Compression System Modeling Technique", Journal of Propulsion and Power, Vol. 7, Number 6, November-December 1991, pp. 997-1005.
- 3.32 Davis, M. W., Jr., "A Stage-by-Stage Post-Stall Compression System Modeling Technique: Methodology, Validation, and Application", Ph.D. Dissertation, Virginia Polytechnic Institute and State University, December 1986
- 3.33 MacCallum, H. R. L., and Pilidis, P., "The Prediction of Surge Margins During Gas Turbine Transients," ASME Gas Turbine Conference, ASME Paper 85-GT-208, Houston, TX, March 1985.
- 3.34 Crawford, R. A., and Burwell, A. E., "Quantitative Evaluation of Transient Heat Transfer on Axial Flow Compressor Stability, "AIAA/SAE/ASME/ASEE 21st Joint Propulsion Conference, AIAA Paper 85-1352, Monterey, CA, July 1985
- 3.35 Davis, M. W. , Jr. and W. F. O'Brien, "Stage-by-Stage Post-stall Compression System Modeling Technique", Journal of Propulsion and Power, Vol. 7, Number 6, November-December 1991, pp. 997-1005.
- 3.36 Davis, M. W., Jr., "A Stage-by-Stage Post-Stall Compression System Modeling Technique: Methodology, Validation, and Application", Ph.D. Dissertation, Virginia Polytechnic Institute and State University, December 1986

- 3.37 Gorrell, S. E. and M. W. Davis, Jr., "Application of a Dynamic Compression System Model to a Low Aspect Ratio Fan: Casing Treatment and Distortion", AIAA Paper # AIAA-93-1871, Presented at the 29th Joint Propulsion Conference and Exhibit, Monterey, CA, June 1993.
- 3.38 Prince, Jr, D. C., D. C. Wisler, and D. E. Hilvers. "A Study of Casing Treatment Stall Margin Improvement Phenomena." ASME 75-GT-60.
- 3.39 Greitzer, E. M., J. P. Nikkanen, and D. E. Haddad. "A Fundamental Criterion for the Application of Rotor Casing Treatment." ASME Journal of Fluids Engineering, 101 (June 1979): 237-244.
- 3.40 Takata, H. and Y. Tsukuda. "Stall Margin Improvement by Casing Treatment - its Mechanism and Effectiveness." ASME 75-GT-13.
- 3.41 Fujita, H. and H. Takata. "A Study on Configurations of Casing Treatment for Axial Flow Compressors." Bulletin of JSME, 27 (August 1984):1675-1681.
- 3.42 Ostdiek, F. R., W. W. Copenhaver, and D. C. Rabe. "Compressor Performance Tests in the Compressor Research Facility." AGARD Conference on Unsteady Aerodynamic Phenomena in Turbomachines, Proceedings No. 468, Aug. 1989.
- 3.43 Hale, A. A. and M. W. Davis. "DYNAMIC Turbine Engine Compressor Code DYNTECC - Theory and Capabilities." Presented at the AIAA/ASME/SAE/ASEE Joint Propulsion Conference, AIAA-92-3190, July 1992.
- 3.44 Boyer, K. M. and W. F. O'Brien. "Model Predictions for Improved Recoverability of a Multistage Axial-Flow Compressor." Presented at the AIAA/ASME/SAE/ASEE Joint Propulsion Conference, AIAA-89-2687, July 1989.
- 3.45 Davis, M. W.. "Parametric Investigation into the Combined Effects of Pressure and Temperature Distortion on Compression System Stability." Presented at the AIAA/ASME/SAE/ASEE Joint Propulsion Conference, AIAA-91-1895, June 1991.
- 3.46 Davis, M. W. and W. F. O'Brien. "Stage-by-Stage Post-stall Compression System Modeling Technique." Journal of Propulsion and Power, 7 (November-December 1991): 997-1005.
- 3.47 Davis, M. W., Jr., "A Stage-by-Stage Post-Stall Compression System Modeling Technique: Methodology, Validation, and Application", Ph.D. Dissertation, Virginia Polytechnic Institute and State University, December 1986
- 3.48 Gorrell, S. E. and M. W. Davis, Jr., "Application of a Dynamic Compression System Model to a Low Aspect Ratio Fan: Casing Treatment and Distortion", AIAA Paper # AIAA-93-1871, Presented at the 29th Joint Propulsion Conference and Exhibit, Monterey, CA, June 1993.
- 3.49 Ostdiek, F. R., W. W. Copenhaver, and D. C. Rabe. "Compressor Performance Tests in the Compressor Research Facility." AGARD Conference on Unsteady Aerodynamic Phenomena in Turbomachines, Proceedings No. 468, Aug. 1989.

- 3.50 Hale, A. A. and M. W. Davis. "DYNamic Turbine Engine Compressor Code DYNTECC - Theory and Capabilities." Presented at the AIAA/ASME/SAE/ASEE Joint Propulsion Conference, AIAA-92-3190, July 1992.
- 3.51 McCoy, A. W., and Hooper, A. V., "Blade Adjustment in Axial-Flow Compressor Stages", Journal of the Aeronautical Sciences, Vol. 20, 1953, pp. 43-48.
- 3.52 Brown, L. E., "The Use of Experimental Interstage Data for Matching the Performance of Axial Compressor Stages Having Variable Setting Angle Blade Rows", ASME Paper No. 76-GT-42, New Orleans, March 1976.
- 3.53 Gamache, R. N., "Axial Compressor Reversed Flow Performance." Ph.D. Dissertation, Massachusetts Inst. of Technology, May 1985.
- 3.54 Koch, C. C., "Stalling Pressure Rise Capability of Axial Flow Compressor Stages", ASM Paper No. 81-GT-3, Presented at the International Gas Turbine Conference, Houston, Texas, March, 1981.
- 3.55 Davis, M. W., Jr., "A Stage-by-Stage Dual-Spool Compression System Modeling Technique", ASME Paper #82-GT-189, March 1982, Presented at the 1982 IGTI Conference, London, England.
- 3.56 Davis, Milton W., Jr., "A Stage-by-Stage Compressor Modeling Technique for Single-and Dual-Spool Compression Systems", Master's Thesis, University of Tennessee, Knoxville, Tennessee, August 1981.
- 3.57 Davis, M. W., Jr., "Parametric Investigation into the Combined Effects of Pressure and Temperature Distortion on Compression System Stability", AIAA Paper # AIAA-91-1895, Presented at the 27th Joint Propulsion Conference, Sacramento, CA, June 1991.
- 3.58 Reynolds, G. G., W. F. Vier, and T. P. Collins. "An Experimental Evaluation of Unsteady Flow Effects on an Axial Compressor - P3 Generator Program." AFAPL-TR-73-43, July 1973.
- 3.59 Kimzey, W. F. "An Analysis of the Influence of Some External Disturbances on the Aerodynamic Stability of Turbine Engine Axial Flow Fans and Compressors," Arnold Engineering Development Center-TR-77-80 (AD-A043543), Arnold Air Force Station, Tennessee, August 1977.
- 3.60 Goethert, B. H., "Research and Engineering Studies and Analysis of Fan Engine Stall, Dynamic Interaction with Other Subsystems and System Performance ," Air Force Aero Propulsion Laboratory TR-70-51, Wright-Patterson AFB, Ohio, July 1970.
- 3.61 Reynolds, G. G., Vier, W. F., and Collins, T. P., "An Experimental Evaluation of Unsteady Flow Effects on an Axial Compressor - P3 Generator Program," Air Force Aero Propulsion Laboratory - TR-73- 43, Wright-Patterson AFR, Ohio, July 1973.
- 3.62 Davis, M. W., Jr., "A Stage-by-Stage Dual-Spool Compression System Modeling Technique", ASME Paper #82-GT-189, March 1982, Presented at the 1982 IGTI Conference, London, England.

- 3.63 Davis, Milton W., Jr., "A Stage-by-Stage Compressor Modeling Technique for Single-and Dual-Spool Compression Systems", Master's Thesis, University of Tennessee, Knoxville, Tennessee, August 1981.
- 3.64 Davis, M. W., Jr., "Parametric Investigation into the Combined Effects of Pressure and Temperature Distortion on Compression System Stability", AIAA Paper # AIAA-91-1895, Presented at the 27th Joint Propulsion Conference, Sacramento, CA, June 1991.
- 3.65 Abdel-Fattah, A. M., "Response of a Turbofan Engine Compression System to Disturbed Inlet Conditions" Journal of Turbomachinery, Vol. 119, No. 4, October 1997.
- 3.66 Distortion Induced Engine Instability, AGARD LS-72-1974.
- 3.67 Owen, A. K., and M. W. Davis, Jr., "Modeling the Dynamic Behavior of an Axial-Centrifugal Compression System", AIAA Paper # AIAA-94-2802, Presented at the 30th AIAA Joint Propulsion Conference and Exhibit, Indianapolis, IN. June 1994.
- 3.68 Cousins, W. T., "Characteristics of Stall and Surge Behavior in Axi-Centrifugal Compressors", Ph.D Dissertation, Virginia Polytechnic and State University, December 1997.
- 3.69 Gamache, R. N. "Axial Compressor Reversed Flow Performance," Ph.D. Dissertation, Massachusetts Institute of Technology, May 1985.
- 3.70 Boyer, K. and W. F. O'Brien "Model Predictions for Improved Recoverability of a Multistage Axial-Flow Compressor," AIAA Paper 89-2689, Presented at the 25th Joint Propulsion Conference, Monterey, CA, July 1989.
- 3.71 Copenhaver, W. W. "Stage Effects on Stalling and Recovery of a High-Speed 10-Stage Axial-Flow Compressor," Ph.D. Dissertation, Iowa State University, Ames, IA, 1988.
- 3.72 Garrard, Doug, "ATEC, The Aerodynamic Turbine Engine Code for the Analysis of Transient and Dynamic Gas Turbine Engine System Operations, Part 1: Model Development", ASME Paper # 96-GT-193, June 1996.
- 3.73 Garrard, Doug, "ATEC, The Aerodynamic Turbine Engine Code for the Analysis of Transient and Dynamic Gas Turbine Engine System Operations, Part 2: Numerical Simulations", ASME Paper # 96-GT-194, June 1996.
- 3.74 Garrard, G. D., "ATEC: The Aerodynamic Turbine Engine Code for the Analysis of Transient and Dynamic Turbine Engine System Operations," Ph.D. Dissertation, the University of Tennessee, Knoxville, August, 1995.
- 3.75 SAE Aerospace Information Report, AIR-1419, "Inlet Total-Pressure Distortion Considerations for Gas Turbine Engines", May 1983.
- 3.76 SAE Aerospace Recommended Practice, ARP-1420, "Gas Turbine Engine Inlet Flow Distortion Guidelines", March
- 3.77 Smith, R. E., "Marrying Airframes and Engines in Ground Test Facilities – An Evolutionary Revolution," AIAA Paper No. 95-0950, 1st AIAA Aircraft Engineering, Technology, and Operations Congress, Los Angeles, CA, September 19- 21, 1995.

- 3.78 Davis, M. W., Jr., "Parametric Investigation into the Combined Effects of Pressure and Temperature Distortion on Compression System Stability", AIAA Paper # AIAA-91-1895, Presented at the 27th Joint Propulsion Conference, Sacramento, CA, June 1991.
- 3.79 Davis, M. W., Jr., W. Baker, G. Power, and D. Beale, "A Proposal for Integration of Wind Tunnel and Engine Test Programs for the Evaluation of Airframe-Propulsion Compatibility Using Numerical Simulations", Journal of Engineering for Gas Turbines and Power, Vol. 124, Number 3, July 2002, pp. 447-458.
- 3.80 Davis, Milt, Alan Hale, and Dave Beale, "An Argument for Enhancement of the Current Inlet Distortion Ground Test Practice for Aircraft Gas Turbine Engines", Journal of Turbomachinery, Vol. 124, Number 2, April 2002, pp. 235-241.
- 3.81 Davis, Milt and Kidman, David, "Prediction and Analysis of Inlet Pressure and Temperature Distortion on Engine Operability from a Recent T-38 Flight Test Program", Presented at the 2010 ASME International Gas Turbine Institute Turbo Expo, June 2010.
- 3.82 Wimer, R. & Hall, A., "Computer Modeling to Solve Problems with the T-38 Propulsion Modernization Program", Paper/Presentation Presented on October 25, 2007 at the NDIA 10<sup>th</sup> Annual System Engineering Conference.
- 3.83 Leyes, R. A., The History of North American Small Gas Turbine Aircraft Engines, Chapter 6, General Electric Small Aircraft Engine, "The J85 Turbojet Engine", AIAA Library of Flight Series, 1999, pp. 261-279
- 3.84 Hale, A. A. and M. W. Davis, Jr., "DYNamic Turbine Engine Compressor Code: DYNTECC -- Theory and Capabilities", AIAA Paper # AIAA-92-3190, Presented at the 28th Joint Propulsion Conference and Exhibit, Nashville, TN, July 1992.
- 3.85 Davis, M. W., Jr., "Parametric Investigation into the Combined Effects of Pressure and Temperature Distortion on Compression System Stability", AIAA Paper # AIAA-91-1895, Presented at the 27th Joint Propulsion Conference, Sacramento, CA, June 1991.
- 3.86 Shahroki, K. A., and M. W. Davis, Jr., "Application of a Modified Dynamic Compression System Model to a Low-Aspect Ratio Fan: Effects of Distortion," AIAA-95-0301, Presented at the 33rd Aerospace Science Meeting, Reno, NV, January 1995.
- 3.87 Milner, E. J., "Analytical Prediction of the Performance and Stability of a J85-13 Compressor with distorted Inlet Flow", NASA TM X-3515, May 1977.
- 3.88 Tesch, W. A., & Steenken, W. G., "Blade Row Dynamic Digital Compression Program – Volume I: J85 Clean Inlet Flow and Parallel Compressor Models", NASA CR-134978, March 1976.
- 3.89 Calogeras, J. E., Mehalic, C. M., & Burstadt, P. L., "Experimental Investigation of the Effect of Screen-Induced Total Pressure Distortion on Turbojet Stall Margin", NASA TM X-2239, March 1971.
- 3.90 Mehalic, C. M., & Lottig, R. A., "Stead-State Inlet Temperature Distortion Effects on the Stall Limits of a J85-GE-13 Turbojet Engine", NASA TM X-2990, February 1974.



- 3.91 Braithwaite, W. M., Graber, E.J., & Mehalic, C., M., "The effects of Inlet Temperature and Pressure Distortion on TurboJet Performance" NASA TM X-71431, November 1973.
- 3.92 SAE S-16 Committee, ARP 1420, Revision B,"Gas Turbine Inlet Flow Distortion Guidelines," Society of Automotive Engineers, February 2002.
- 3.93 SAE Aerospace Information Report AIR-1419, "Inlet Total-Pressure Distortion Considerations for Gas Turbine Engines," May 1983.
- 3.94 Hale, A. A., "A Three-Dimensional Turbine Engine Analysis Compressor Code (TEACC) for Steady-State Inlet Distortion." Ph.D Dissertation, Virginia Polytechnic Institute and State University, Blacksburg, VA, 1996.
- 3.95 Hale, A. A., and W. F. O'Brien, "A Three-Dimensional Turbine Engine Analysis Compressor Code (TEACC) for Steady-State Inlet Distortion," Journal of Turbomachinery, Vol. 120, July 1998, pp. 422-430.
- 3.96 Hale, Alan, Chalk, Jacqueline, Klepper, Jason, and Kneile, Karl, "Turbine Engine Analysis Compressor Code, Part II: Multi-stage Compressors and Inlet Distortion", AIAA-99-3214, July 1999.
- 3.97 Seyler, D. R. and Gestolow, J. P. "Single Stage Experimental Evaluation of High Mach Number Compressor Rotor Blading Part 2- Performance of Rotor 1B." NASA-CR-54582, September 1967.
- 3.98 Reid, L. and Moore, R. D. "Design and Overall Performance of Four Highly Loaded, High-Speed Inlet Stages for an Advanced High-Pressure-Ratio Core Compressor." NASA-TP-1337, 1978.
- 3.99 Lieblein, S. "Chapter VI: Experimental Flow in Two-Dimensional Cascades." *Aerodynamic Design of Axial-Flow Compressors*, NASA-SP-36, 1965, pp.183-226.
- 3.100 Robbins, W. H., Jackson, R. J. and Lieblein, S. "Chapter VII: Blade-Element Flow in Annular Cascades." *Aerodynamic Design of Axial-Flow Compressors*, NASA-SP-36, 1965, pp. 227-254.
- 3.101 SAE Aerospace Information Report AIR-1419, "Inlet Total-Pressure Distortion Considerations for Gas Turbine Engines," May 1983.
- 3.102 Davis, Milt, et.al., "Demonstration of an Integrated Test and Evaluation (IT&E) Process for Airframe-Propulsion Systems as Applied to a Current Weapon System Program", Presented at the 2010 AIAA Aerospace Sciences Meeting, January 2010.
- 3.103 Gorrell, S. E. and M. W. Davis, Jr., "Application of a Dynamic Compression System Model to a Low Aspect Ratio Fan: Casing Treatment and Distortion", AIAA Paper # AIAA-93-1871, Presented at the 29th Joint Propulsion Conference and Exhibit, Monterey, CA, June 1993.
- 3.104 Shahrooki, K. A., and M. W. Davis, Jr., "Application of a Modified Dynamic Compression System Model to a Low-Aspect Ratio Fan: Effects of Inlet Distortion," AIAA-95-0301, January 1995

- 3.105 Hah, C., et. al., "Effects of Inlet Distortion on the Flow Field in a Transonic Compressor Rotor", Transaction of the ASME, Journal of Turbomachinery, Vol 120, April 1998, pp. 233-246.
- 3.106 Chima, R. V., "A Three-Dimensional Unsteady CFD Model of Compressor Stability", ASME GT2006-90040, ASME Turbo Expo 2006, Barcelona, Spain, May 2006.
- 3.107 Davis, M. W., Jr., "Parametric Investigation into the Combined Effects of Pressure and Temperature Distortion on Compression System Stability", AIAA Paper # AIAA-91-1895, Presented at the 27th Joint Propulsion Conference, Sacramento, CA, June 1991.
- 3.108 Davis, Milt and Kidman, David, "Prediction and Analysis of Inlet Pressure and Temperature Distortion on Engine Operability from a Recent T-38 Flight Test Program", Presented at the 2010 ASME International Gas Turbine Institute Turbo Expo, June 2010.
- 3.109 Hale, A. A. and M. W. Davis, Jr., "DYNamic Turbine Engine Compressor Code: DYNTECC -- Theory and Capabilities", AIAA Paper # AIAA-92-3190, Presented at the 28th Joint Propulsion Conference and Exhibit, Nashville, TN, July 1992.
- 3.110 Davis, M. W., Jr., "Parametric Investigation into the Combined Effects of Pressure and Temperature Distortion on Compression System Stability", AIAA Paper # AIAA-91-1895, Presented at the 27th Joint Propulsion Conference, Sacramento, CA, June 1991.
- 3.111 Shahrooki, K. A., and M. W. Davis, Jr., "Application of a Modified Dynamic Compression System Model to a Low-Aspect Ratio Fan: Effects of Distortion," AIAA-95-0301, Presented at the 33rd Aerospace Science Meeting, Reno, NV, January 1995.
- 3.112 Milner, E. J., "Analytical Prediction of the Performance and Stability of a J85-13 Compressor with distorted Inlet Flow", NASA TM X-3515, May 1977.
- 3.113 Mehlic, C. M., & Lottig, R. A., "Stead-State Inlet Temperature Distortion Effects on the Stall Limits of a J85-GE-13 Turbojet Engine", NASA TM X-2990, February 1974.
- 3.114 Braithwaite, W. M., Graber, E.J., & Mehlic, C., M., "The effects of Inlet Temperature and Pressure Distortion on TurboJet Performance" NASA TM X-71431, November 1973.
- 3.115 Davis, M. W., Jr., "Parametric Investigation into the Combined Effects of Pressure and Temperature Distortion on Compression System Stability", AIAA Paper # AIAA-91-1895, Presented at the 27th Joint Propulsion Conference, Sacramento, CA, June 1991.
- 3.116 Davis, Milt and Kidman, David, "Prediction and Analysis of Inlet Pressure and Temperature Distortion on Engine Operability from a Recent T-38 Flight Test Program", Presented at the 2010 ASME International Gas Turbine Institute Turbo Expo, June 2010.
- 3.117 Braithwaite, W. M. and R. H. Soeder, "Combined Pressure and Temperature Distortion Effects on Internal Flow of a turbofan Engine." AIAA Paper No. AIAA-79-1309, Presented at the AIAA/SAE/ASME 15th Joint Propulsion Conference, Las Vegas, NV, June 1979.
- 3.118 Soeder, R. H., and G. A. Bobula, "Effects of Steady-State Temperature and Combined Distortion on Inlet Flow to a Turbofan Engine." NASA-TM79237, August 1979.

- 3.119 Soeder, R. H., and C. M. Mehalic, "Effect of Combined Pressure and Temperature Distortion Orientation on High-Bypass-Ratio Turbofan Engine Stability." NASA-TM-83771, October 1984.
- 3.120 Hale, A. A. and M. W. Davis, Jr., "DYNamic Turbine Engine Compressor Code: DYNTECC -- Theory and Capabilities", AIAA Paper # AIAA-92-3190, Presented at the 28th Joint Propulsion Conference and Exhibit, Nashville, TN, July 1992.
- 3.121 Davis, M. W., Jr., "Parametric Investigation into the Combined Effects of Pressure and Temperature Distortion on Compression System Stability", AIAA Paper # AIAA-91-1895, Presented at the 27th Joint Propulsion Conference, Sacramento, CA, June 1991.
- 3.122 Shahroghi, K. A., and M. W. Davis, Jr., "Application of a Modified Dynamic Compression System Model to a Low-Aspect Ratio Fan: Effects of Distortion," AIAA-95-0301, Presented at the 33rd Aerospace Science Meeting, Reno, NV, January 1995.
- 3.123 Eden, R. M., "The Northrop Grumman T-38 Talon: 40 Years Plus & Still Teaching Pilots to Fly", AIAA 2001-0313, 39<sup>th</sup> Aerospace Science Meeting & Exhibit, 8-11 January 2001, Reno, Nevada.
- 3.124 Briskin, T. A., Howell, P. N., & Ewing, A. C., "J85 Rejuvenation Through Technology Insertion", RTO EN-14, October 2000.
- 3.125 Wimer, R. & Hall, A., "Computer Modeling to Solve Problems with the T-38 Propulsion Modernization Program", Paper/Presentation Presented on October 25, 2007 at the NDIA 10<sup>th</sup> Annual System Engineering Conference.
- 3.126 Leyes, R. A., The History of North American Small Gas Turbine Aircraft Engines, Chapter 6, General Electric Small Aircraft Engine, "The J85 Turbojet Engine", AIAA Library of Flight Series, 1999, pp. 261-279
- 3.127 Hale, A. A. and M. W. Davis, Jr., "DYNamic Turbine Engine Compressor Code: DYNTECC -- Theory and Capabilities", AIAA Paper # AIAA-92-3190, Presented at the 28th Joint Propulsion Conference and Exhibit, Nashville, TN, July 1992.
- 3.128 Davis, M. W., Jr., "Parametric Investigation into the Combined Effects of Pressure and Temperature Distortion on Compression System Stability", AIAA Paper # AIAA-91-1895, Presented at the 27th Joint Propulsion Conference, Sacramento, CA, June 1991.
- 3.129 Shahroghi, K. A., and M. W. Davis, Jr., "Application of a Modified Dynamic Compression System Model to a Low-Aspect Ratio Fan: Effects of Distortion," AIAA-95-0301, Presented at the 33rd Aerospace Science Meeting, Reno, NV, January 1995.
- 3.130 Milner, E. J., "Analytical Prediction of the Performance and Stability of a J85-13 Compressor with distorted Inlet Flow", NASA TM X-3515, May 1977.
- 3.131 Tesch, W. A., & Steenken, W. G., "Blade Row Dynamic Digital Compression Program – Volume I: J85 Clean Inlet Flow and Parallel Compressor Models", NASA CR-134978, March 1976.

- 3.132 Calogeras, J. E., Mehalic, C. M., & burstadt, P. L., "Experimental Investigation of the Effect of Screen-Induced Total Pressure Distortion on Turbojet Stall Margin", NASA TM X-2239, March 1971.
- 3.133 Mehalic, C. M., & Lottig, R. A., "Stead-State Inlet Temperature Distortion Effects on the Stall Limits of a J85-GE-13 Turbojet Engine", NASA TM X-2990, February 1974.
- 3.134 Braithwaite, W. M., Graber, E.J., & Mehalic, C., M., "The effects of Inlet Temperature and Pressure Distortion on TurboJet Performance" NASA TM X-71431, November 1973.
- 3.135 SAE S-16 Committee, ARP 1420, Revision B,"Gas Turbine Inlet Flow Distortion Guidelines," Society of Automotive Engineers, February 2002.
- 3.136 SAE Aerospace Information Report AIR-1419, "Inlet Total-Pressure Distortion Considerations for Gas Turbine Engines," May 1983.
- 3.137 Society of Automotive Engineers, "A Current Assessment of the Inlet/Engine Temperature Distortion Problem," Aerospace Resource Document AIR 5867, 2009.
- 3.138 Hale, A. A., et.al., "An Investigation into the Effects of Highly Transient Flight Maneuvers on Heat and Mass Transfer on the T38 Air Force Trainer Inlet", ASME GT2010-YYYYY, To be Presented at the 2010 IGTI Conference, June 2010.
- 3.139 Davis, Milt, Hale, Alan, "A Parametric Study on the Effects of Inlet Swirl on Compression System Performance and Operability using Numerical Simulations," ASME Paper #GT2007-27033, 2008 ASME Turbo Expo, May 2007.
- 3.140 Davis, Milt, Beale, Dave, Sheoran, Yogi, "Integrated Test and Evaluation Techniques as Applied to an Inlet Swirl Investigation Using the F109 Gas Turbine Engine," ASME Paper #GT2008-50074, June 2008.
- 3.141 Boulding, B. and Sheoran, Y., "Inlet Flow Angularity Descriptors Proposed for Use with Gas Turbine Engines", SAE Paper # 2002-01-2919
- 3.142 Boyer, Keith, "An Improved Streamline Curvature Approach for Off-Design Analysis of Transonic Compression Systems", PhD Dissertation, Virginia Polytechnic and State University, Blacksburg, VA, April 2001.
- 3.143 Cumpsty, N. A., Compressor Aerodynamics, Longman Scientific & Technical, 1989, pp.47-48.
- 3.144 Hearsey, R.M., *Program HT0300, NASA 1994 Version*, The Boeing Company.
- 3.145 NASA SP-36, *Aerodynamic Design of Axial-Flow Compressors*, edited by Johnsen, I.A. and Bullock, R.O., 1965.
- 3.146 Seyler, D. R. and Gestolow, J. P. "Single Stage Experimental Evaluation of High Mach Number Compressor Rotor Blading Part 2- Performance of Rotor 1B." NASA-CR-54582, September 1967.

- 3.147 Smith, S. L., "1-D Meanline Code Technique to Calculate Stage-by-Stage Compressor Characteristics," M.S. Thesis, University of Tennessee, Knoxville, TN, 1999
- 3.148 Schmid, N. R., Leinhos, D. C., and Fottner, L., „Steady Performance Measurements of a Turbofan Engine with Inlet Distortions Containing Co-and Counterrotating Swirl from an Intake Diffuser for Hypersonic Flight:, Journal of Turbomachinery, Vol. 123, April 2001, pp. 379-385
- 3.149 SAE S-16 Committee, ARP 1420, Revision B,"Gas Turbine Inlet Flow Distortion Guidelines," Society of Automotive Engineers, February 2002.
- 3.150 SAE Aerospace Information Report AIR-1419, "Inlet Total-Pressure Distortion Considerations for Gas Turbine Engines," May 1983.
- 3.151 SAE S-16 Committee, ARD50026, "A current Assessment of Planer Waves," Society of Automotive Engineers, September 1995.
- 3.152 Society of Automotive Engineers, "A Current Assessment of the Inlet/Engine Temperature Distortion Problem," Aerospace Resource Document ARD50015, 1991.
- 3.153 Davis, M. W., Jr., et al. "A Proposal for Integration of Wind Tunnel and Engine Test Programs for the Evaluation of Airframe-Propulsion Compatibility Using Numerical Simulations." Journal of Engineering for Gas Turbines and Power, July 2002, pp. 447-458.
- 3.154 Hale, Alan, Milt Davis, and Jim Sirbaugh, "A Numerical Simulation Capability for Analysis of Aircraft Inlet-Engine Compatibility", Journal of Engineering for Gas Turbines and Power, Vol. 128, July 2006, pp. 473-481.
- 3.155 Garrard, G. D., Davis, M. W., Jr., Wehofer, S., and G. Cole, "A One-Dimensional, Time Dependent Inlet/Engine Numerical Simulation for Aircraft Propulsion Systems", ASME Paper # 97-GT-333, June 1997.
- 3.156 Batterton, P. G., and Gold, H., "Experimental Test Results of a Generalized-Parameter Fuel Control," NASA TN D-7198, March 1973.
- 3.157 Calogeras, J. E., "Experimental Investigation of Dynamic Distortion in a Mach 2.50 Inlet with 60 Percent Internal Contraction and its Effect on Turbojet Stall Margin," NASA TM X-1842, October 1969.
- 3.158 Choby, D. A., Burstadt, P. L., and Calogeras, J. E., "Unstart and Stall Interactions Between a Turbojet Engine and an Axisymmetric Inlet with 60-Percent Internal-Area Contraction," NASA TM X-2192, March 1971.
- 3.159 Cole, G. L., Neiner, G. H., and Crosby, M. J., "An Automatic Restart Control System for an Axisymmetric Mixed-Compression Inlet," NASA TN D-5590, December 1969.
- 3.160 Costakis, W. G., and Wenzel, L. M., "An Experimental Investigation of Compressor Stall using an On-Line Distortion Indicator and Signal Conditioner," NASA TM X-3182, April 1975.
- 3.161 Garrard, G. D., "ATEC: The Aerodynamic Turbine Engine Code for the Analysis of Transient and Dynamic Turbine Engine System Operations," Ph. D. Dissertation, The University of Tennessee, Knoxville, August, 1995.

- 3.162 Hager, R. D., "Analysis of Internal Flow of J85-13 Multistage Compressor," NASA TM X-3513, April 1977.
- 3.163 Moeckel, W. E., "Approximate Method for Predicting Form and Location of Detached Shock Waves Ahead of Plane or Axially Symmetric Bodies," NACA TN 1921, July 1949.
- 3.164 Quealy, A., Cole, G. L., and Blech, R. A., "Portable Programming on Parallel/Networked Computers Using the Application Portable Parallel Library (APPL)," NASA TM-106238, July 1993.
- 3.165 Varner, M. O., Martindale, W. R., Phares, W. J., Kneile, K. R., and Adams, J. C., Jr., "Large Perturbation Flow Field Analysis and Simulation for Supersonic Inlets," NASA CR 174676, September 1984.
- 3.166 Ziemianski, J. A., and Ball, C. L. "Propulsion Technology Challenges for Turn-of-the-Century Commercial Aircraft," NASA TM-106192, June 1993.
- 3.167 Davis, Milt, Hale, Alan, Vining, Charles, and Cousins, William, "Application of Numerical Analysis Tools for Airframe-Propulsion Integrated Test and Evaluation," ASME Paper #GT2008-50194, 2008 ASME Turbo Expo, June 2008.
- 3.168 Davis, Milt, Hale, Alan, Klepper, Jason, Dubreus, Terrance, and Cousins, William, "Demonstration of an Integrated Test and Evaluation (IT&E) Process for Airframe-Propulsion Systems as Applied to a Current Weapon System Program," AIAA Paper, 2010 Aerospace Science Conference, January 2010.
- 3.169 Suresh, A., Townsend, S.E., Cole, G.L., Slater, J.W., Chima, R. "Analysis of Compressor-Inlet Acoustic Interactions Using Coupled Component Codes" AIAA Paper 99-0749, 1999.
- 3.170 Numbers, K., and Hamed, A., 1997, "Development of a Coupled Inlet-Engine Dynamic Analysis Method," AIAA Paper No. 97-2880.
- 3.171 Numbers, K., and Hamed, A., "Conservative Coupling Technique for Dynamic Inlet-Engine Analysis", *Journal of Propulsion and Power*, Vol. 19, No. 3, May-June, 2003, pp. 444-455.
- 3.172 Davis, M. W., Jr. "Parametric Investigation into the Combined Effects of Pressure and Temperature Distortion on Compression System Stability," AIAA-91-1895, June 1991.
- 3.173 Hearsey, R. M. "HTO300 – A Computer Program for the Design and Analysis of Axial Turbomachinery," March 1970.
- 3.174 Yao, J., Gorrell, S., and Wadia, A., "Unsteady RANS Analysis of Distortion Transfer Through Two Military Fans", To Be Published in the *Journal of Turbomachinery* in 2007
- 3.175 Hale, A. A., and O'Brien, W. F. "A Three-Dimensional Turbine Engine Analysis Compressor Code (TEACC) for Steady-State Inlet Distortion," *Journal of Turbomachinery*, Vol. 120, July 1998, pp. 422-430.



- 3.176 Hale, Alan, et al. "Turbine Engine Analysis Compressor Code: TEACC – Part II: Multi-Stage Compressors and Inlet Distortion," AIAA-99-3214, June 1999.
- 3.177 Davis, Milt, Hale, Alan, and Beale, Dave. "An Argument for Enhancement of the Current Inlet Distortion Ground Test Practice for Aircraft Gas Turbine Engines," Journal of Turbomachinery, April 2002, pp. 235-241.
- 3.178 NASA SP-36, *Aerodynamic Design of Axial-Flow Compressors*, edited by Johnsen, I.A. and Bullock, R.O., 1965.
- 3.179 Buning, P.G., Jespersen, D.C., Pulliam, T.H., Chan, W.M., Slotnick, J.P., Krist, S.E., and Renze, K.J., OVERFLOW User's Manual- version 1.8, NASA Langley Research Center, February 1998.
- 3.180 Meilunas, R., "Overview of the Simulation, Test and Evaluation Process Network: STEPNET, AIAA-2007-6572, August 2007.
- 3.181 Pandya, M.J., Frink, N.T., and Noack, R.W.: "Progress Toward Overset-Grid Moving Body Capability for USM3D Unstructured Flow Solver", AIAA 2005-5118, June 2005.
- 3.182 Chima, Rod, "A Three-Dimensional Unsteady CFD Model of Compressor Stability," ASME Paper GT2006-90040.
- 3.183 Nazir, J., Couch, R., and M. Davis, "An Approach for the Development of an Aerodynamic-Structural Interaction Numerical Simulation for Aeropropulsion Systems" ASME Paper # 96-GT-480, June 1996.
- 3.184 Sharp, R., Anderson, S., Dube, E., Futral, S., Otero, I., "User's Manual for ALE3D," Lawrence Livermore National Laboratory, unpublished, 1995.
- 3.185 Hale, A. A. and M. W. Davis, Jr., "DYNamic Turbine Engine Compressor Code: DYNTECC -- Theory and Capabilities", AIAA Paper # AIAA-92-3190, Presented at the 28th Joint Propulsion Conference and Exhibit, Nashville, TN, July 1992.
- 3.186 AEDC Fact Sheet, Release 2007-092, AEDC Website, [www.arnold.af.mil](http://www.arnold.af.mil)
- 3.187 Aeropropulsion Systems Test Facility (ASTF) Fact Sheet, Release 2007-096, AEDC Website, [www.arnold.af.mil](http://www.arnold.af.mil)
- 3.188 Engine Test Facility Fact Sheet, Release 2007-086, AEDC Website, [www.arnold.af.mil](http://www.arnold.af.mil)
- 3.189 Garrard, D., Davis, M., Chalk, J., Savelle, S., "Analysis of Gas Turbine Engine Operability with the Aerodynamic Turbine Engine Code," ISABE97-7034, AIAA, September 1997.
- 3.190 Davis, M., "C-Plant Exhauster Study," Internal Sverdrup Technology, Inc. Memorandum, August 30, 1996.
- 3.191 Bates, L. B., "Development of a Dynamic Model and Simulation of 16T (Job 2347)," Internal Sverdrup Technology, Inc. Memorandum, September 9, 1995.

- 3.192 Propulsion Wind Tunnel Facility Fact Sheet, Release 2007-088, AEDC Website, [www.arnold.af.mil](http://www.arnold.af.mil)
- 3.193 Hale, A.A. and Davis, M. W., "DYNamic Turbine Engine Compressor Code DYNTECC – Theory and Capabilities", AIAA/SAE/ASME/ASEE 28th Joint Propulsion Conference, Nashville, TN, July 6-8, 1992, AIAA-92-3190.
- 3.194 Cunningham, D. H., Memo for Record, "Wind Tunnel Static Model Equations", February 6, 1984, Revised, May 3, 1984.
- 3.195 [http://www.news.navy.mil/view\\_single.asp?id=2114](http://www.news.navy.mil/view_single.asp?id=2114) U.S. Navy photo by Photographer's Mate Jessica Davis, July 27, 2002.
- 3.196 "Recommended Practices for the Assessment of the Effects of Atmospheric Water Ingestion on the Performance and Operability of Gas Turbine Engines," Propulsion and Energetics Panel Working Group 24, Advisory Group for Aerospace Research and Development (AGARD), NATO, 1995.
- 3.197 Klepper, Jason, Hale, Alan, and Davis, Milt, "A Numerical Investigation of Steam Ingestion on Compression System Performance," ASME Paper #GT2004-54190, 2004 ASME Turbo Expo, June 2004.
- 3.198 Willbanks, C.E. and Schulz, R.J. "Analytical Study of Icing Simulation for Turbine Engines in Altitude Test Cells." AEDC-TR-73-144 (AD-770069), November 1973.
- 3.199 Smith, S.L. "1-D Meanline Code Technique to Calculate Stage-by-Stage Compressor Characteristics." M.S. Thesis, The University of Tennessee, Knoxville, TN, 1999.
- 3.200 "Recommended Practices for the Assessment of the Effects of Atmospheric Water Ingestion on the Performance and Operability of Gas Turbine Engines," Propulsion and Energetics Panel Working Group 24, Advisory Group for Aerospace Research and Development, NATO, 1995.
- 3.201 Hale, Alan, Klepper, Jason, and Hurwitz, Wayne, "A Numerical Capability to Analyze the Effects of Water Ingestion on Compression System Performance and Operability," ASME Paper #GT2005-68480, 2005 ASME Turbo Expo, June 2005.
- 3.202 "Willbanks, C.E. and Schulz, R.J. "Analytical Study of Icing Simulation for Turbine Engines in Altitude Test Cells." AEDC-TR-73-144 (AD-770069), November 1973.
- 3.203 Smith, S.L. "1-D Meanline Code Technique to Calculate Stage-by-Stage Compressor Characteristics." M.S. Thesis, The University of Tennessee, Knoxville, TN, 1999.
- 3.204 Hale, Alan, Klepper, Jason, and Hurwitz, Wayne, "A Numerical Capability to Analyze the Effects of Water Ingestion on Compression System Performance and Operability," ASME Paper #GT2005-68480, 2005 ASME Turbo Expo, June 2005.
- 3.205 "Willbanks, C.E. and Schulz, R.J. "Analytical Study of Icing Simulation for Turbine Engines in Altitude Test Cells." AEDC-TR-73-144 (AD-770069), November 1973.

3.206 Smith, S.L. "1-D Meanline Code Technique to Calculate Stage-by-Stage Compressor Characteristics." M.S. Thesis, The University of Tennessee, Knoxville, TN, 1999.

3.207 Meacock, A. J., and White, A. J., "The Effect of Water Injection on Multi-Spool Gas Turbine Behavior", ASME Paper GT2004-53320, June 2004.

### 6.3 CHAPTER 4 REFERENCES

4.1 Cohen, H., Rogers, G. F. C., and H. I. H. Saravanamuttoo, Gas Turbine Theory, Longman, Third Edition, 1987.

4.2 Cumpsty, N. A, Compressor Aerodynamics, Longman Scientific and Technical, 1989

4.3 Hearsey, R. M., "HTO300 – A Computer Program for the Design and Analysis of Axial turbomachinery", 1970

4.4 NASA SP-36 Aerodynamic Design of Axial-Flow Compressors, edited by Johnsen, I. A. and R. O. Bullock, 1965

4.5 Boyer, K.M. and W. F. O'Brien, "An Improved Steamline Curvature Approach for Off-Design Analysis of Transonic Axial Compression Systems", Transaction of the ASME, Journal of Turbomachinery, July 2003, Vol. 125, pp 475-481.

4.6 Greitzer, E. M., "Surge and Rotating Stall in Axial Flow Compressors, Part I: Theoretical Compression System Model", ASME Journal of Engineering for Power, Vol. 98, April 1978, pp.190-198.

4.7 Greitzer, E. M., "Surge and Rotating Stall in Axial Flow Compressors, Part II: Experimental Results and Comparisons with Theory", ASME Journal of Engineering for Power, Vol. 98, April 1978, pp 199-217.

4.8 Hale, A. A. and M. W. Davis, Jr., "DYNamic Turbine Engine Compressor Code: DYNTECC -- Theory and Capabilities", AIAA Paper # AIAA-92-3190, July 1992.

4.9 Reynolds, G. G., and W. G. Steenken, "Dynamic Digital Blade Row Compression Component Stability Model: Model Validation and Analysis of Planar Pressure Pulse Generator and Two-Stage Fan Test Data", AFAPL-TR-76-76, August 1976.

4.10 Hosney, W. M., Bitter, S. J., and Steenken, W. G., "Turbofan Engine Non-recoverable Stall Computer Simulation Development and Validation", AIAA Paper # 85-1432, July 1985.

4.11 Ward, G. G., "Compressor Stability Assessment Program (Techniques for Constructing Mathematical Models of Compression Systems and Propulsion Systems)", Air Force Aero Propulsion Laboratory, TR-74-107, Vol. II, Wright-Patterson Air Force Base, OH, December 1974.

4.12 Davis, M. W., Jr., "A Stage-by-Stage Dual-Spool Compression System Modeling Technique", ASME Paper 82-GT-189, March 1982.

- 4.13 Hosney, W. M., and W. G. Steenken, "Aerodynamic Instability Performance of an Advanced High-Pressure-Ratio Compression Component", AIAA Paper # AIAA-86-1619, June 1986.
- 4.14 Mazzawy, R. S. "Multiple Segment Parallel Compressor Model for Circumferential Flow Distortion." Transactions of the ASME, Journal of Engineering for Power, April 1977, pp. 288-296.
- 4.15 Tesch, W. A., and Steenken, W. G., "Blade Row Dynamic Digital Compressor Program, Vol. 1, J85, Clean Inlet Flow and Parallel Compressor Models", NASA CR-134978, Lewis Research Center, Cleveland, OH, March 1976
- 4.16 Longley, J. P. and Greitzer, E. M. "Inlet Distortion Effects in Aircraft Propulsion System Integration." AGARD-LS-183. Advisory Group for Aerospace Research & Development Lecture Series, May 1992.
- 4.17 Shahrooki, K. A., and M. W. Davis, Jr., "Application of a Modified Dynamic Compression System Model to a Low-Aspect Ratio Fan: Effects of Inlet Distortion," AIAA-95-0301, January 1995
- 4.18 Davis, M., Jr., "Parametric Investigation into the Combined Effects of Pressure and Temperature Distortion on Compression System Stability", AIAA Paper # AIAA-91-1895, June 1991.
- 4.19 Cousins, William T., et. al., "Inlet Distortion Testing and Analysis of a High-Bypass Ratio Turbofan Engine" Presented at the 16<sup>th</sup> International Symposium on Air Breathing Engines" Paper # ISABE-2003-1110, August, 2003.
- 4.20 Hynes, T. P. and E. M. Greitzer, "A Method for Assessing Effects of Inlet Flow Distortion on Compressor Stability", Transaction of the ASME, Journal of Turbomachinery, Vol. 109, pp 371-379.
- 4.21 Davis, Milt, and Hale, Alan, "A Parametric Study on the Effects of Inlet Swirl on Compression System Performance and Operability Using Numerical Simulations", GT2007-27033, May 2007
- 4.22 Davis, Milt, Jr., Beale, Dave, and Sheoran, Yogi, "Integrated Test and Evaluation Techniques as Applied to an Inlet Swirl Investigation Using the F109 Gas Turbine Engine", GT2008-50074, June 2008.
- 4.23 Bouldin, B. and Sheoran, Y., "Impact of Complex Swirl Patterns on Compressor Performance and Operability Using Parallel Compressor Analysis", ISABE2007-1140, September 2007
- 4.24 Hale, A. A., and W. F. O'Brien, "A Three-Dimensional Turbine Engine Analysis Compressor Code (TEACC) for Steady-State Inlet Distortion, "Transaction of the ASME, Journal of Turbomachinery, Vol. 120, July 1998, pp. 422-430.
- 4.25 Chima, R. "A Three-Dimensional Unsteady CFD Model of Compressor Stability", ASME Paper GT2006-90040, May 2006.

- 4.26 Davis, Milt, Hale, Alan, and Beale, Dave. "An Argument for Enhancement of the Current Inlet Distortion Ground Test Practice for Aircraft Gas Turbine Engines," Transaction of the ASME, Journal of Turbomachinery, April 2002, pp. 235-241.
- 4.27 Hale, Alan, Milt Davis, and Jim Sirbaugh, "A Numerical Simulation Capability for Analysis of Aircraft Inlet-Engine Compatibility", Journal of Engineering for Gas Turbines and Power, Vol. 128, July 2006, pp. 473-481.
- 4.28 Yao, J., Gorrell, S. E., and Wadia, A. R., "High-Fidelity Numerical Analysis of Per-Rev-Type Inlet Distortion Transfer in Multistage Fans – Part I: Simulations with Selected Blade Rows", ASME Paper GT2008-50812, June 2008. – To Be Published in the Journal of Turbomachinery -- 2009
- 4.29 Yao, J., Gorrell, S. E., and Wadia, A. R., "High-Fidelity Numerical Analysis of Per-Rev-Type Inlet Distortion Transfer in Multistage Fans – Part II: Entire Component Simulation and Investigation" ASME Paper GT2008-50813, June 2008. -- To Be Published in the Journal of Turbomachinery -- 2009
- 4.30 Smith, S. L. "1-D Meanline Code Technique to Calculate Stage-by-Stage Compressor Characteristics." M.S. Thesis, The University of Tennessee, Knoxville, TN, 1999.
- 4.31 Hearsey, R.M. *Program HT0300, NASA 1994 Version*, The Boeing Company.
- 4.32 Hale, A., Klepper, J., Hurwitz, W., "A Numerical Capability to Analyze the Effects of Water Ingestion on Compression System Performance and Operability," GT2005-68480, ASME Turbo Expo, Reno-Tahoe, Nevada, June 2005.
- 4.33 Boyer, K. M., "An Improved Streamline Curvature Approach for Off-Design Analysis of Transonic Compression System," Ph. D. Dissertation, Virginia Polytechnic Institute and State University, Blacksburg, VA, April 2001.
- 4.34 Klepper, J., "Technique to Predict Stage-By-Stage, Pre-Stall Compressor Performance Characteristics Using a Streamline Curvature Code With Loss and Deviation Correlations," MS Thesis, University of Tennessee, Knoxville, TN, August 1998.
- 4.35 Al-Daini, A. J. "Loss and Deviation Model for a Compressor Blade Element." Int. J. Heat & Fluid Flow, March 1986.
- 4.36 Bloch, G. S., Copenhaver, W. W. and O'Brien, W. F., "A Shock Loss Model for Supersonic Compressor Cascades," *Transactions of the ASME, Journal of Turbomachinery*, Vol. 121, January 1999, pp. 28-35.
- 4.37 Boyer, K. M., "An Improved Streamline Curvature Approach for Off-Design Analysis of Transonic Compression System," Ph. D. Dissertation, Virginia Polytechnic Institute and State University, Blacksburg, VA, April 2001.
- 4.38 Carter, A. D. S. and Hughes, H. P. "A Theoretical Investigation into the Effects of Profile Shape on the Performance of Aerofoils in Cascades." British A.R.C,R&M No. 2384, 1946.

- 4.39 Emery J. C., Herrig, L. J., Erwin, J. R., and Felix, A. R. "Systematic Two-Dimensional Cascade Tests of NACA 65-Series Compressor Blades at Low Speeds." NACA Report No. 1368, 1958
- 4.40 Grewe, K. H. "Pressure Distribution Measurements on Two-Dimensional Cascades at High Subsonic Mach Numbers," Part 1. DFL report 57/6a, AFOSR TN 57-289, Institut für Strömungs-mechanik, Technische Hochschule, Braunschweig, Germany, March 1957.
- 4.41 Hearsey, R.M. "Program HT0300 NASA 1994 Volume 2." The Boeing Company, 1994. Horlock, J. H. *Axial Flow Compressors*. Butterworth Publications Limited, 1958.
- 4.42 Horlock, J. H. "Some Recent Research in Turbo-Machinery." *Proceedings of the Institute of Mechanical Engineers*, Volume 182, Part 1, No. 26, 1967-68, pp.571-586.
- 4.43 Jansen, W. and Moffat, W.C. "The Off-Design Analysis of Axial-Flow Compressors." *Transactions of the ASME, Journal of Engineering for Power*, October 1967, pp. 453-462.
- 4.44 Lieblein, S. "Chapter VI: Experimental Flow in Two-Dimensional Cascades." *Aerodynamic Design of Axial-Flow Compressors*, NASA-SP-36, 1965, pp. 183-226.
- 4.45 Miller, G. R., Lewis Jr., G. W. and Hartman, M. J. "Shock Losses in Transonic Compressor Blade Rows." *Transactions of the ASME, Journal of Engineering for Power*, July 1961, pp. 235-242.
- 4.46 Robins, W. H., Jackson, R. J. and Lieblein, S. "Chapter VII: Blade-Element Flow in Annular Cascades." *Aerodynamic Design of Axial-Flow Compressors*, NASA-SP-36, 1965, pp. 227-254.
- 4.47 Smith, L. H., Jr. "The Radial-Equilibrium Equation of Turbomachinery." *Transactions of the ASME, Journal of Engineering for Power*, January 1966.
- 4.48 Hale, A. A. and M. W. Davis, Jr., "DYNamic Turbine Engine Compressor Code: DYNTTECC -- Theory and Capabilities", AIAA Paper # AIAA-92-3190, Presented at the 28th Joint Propulsion Conference and Exhibit, Nashville, TN, July 1992.
- 4.49 Davis, M. W., Jr., "A Post-Stall Compression System Modeling Technique", AEDC-TR-86-34, February 1987.
- 4.50 Davis, M. W., Jr., "A Stage-by-Stage Post-Stall Compression System Modeling Technique: Methodology, Validation, and Application", Ph.D. Dissertation, Virginia Polytechnic Institute and State University, December 1986
- 4.51 Davis, M. W. , Jr. and W. F. O'Brien, "Stage-by-Stage Poststall Compression System Modeling Technique", *Journal of Propulsion and Power*, Vol. 7, Number 6, November-December 1991, pp. 997-1005.
- 4.52 Shahroki, K. A., "Application of a Modified Dynamic Compression System Model to a Low Aspect Ratio Fan: Effects of Inlet Distortion." Master's Thesis, Vanderbilt University, Nashville, TN, 1995.



- 4.53 Davis, M. W., Jr., "A Stage-by-Stage Post-Stall Compression System Modeling Technique: Methodology, Validation, and Application". Ph.D. Dissertation, Virginia Polytechnic Institute and State University, December 1986.
- 4.54 Herbert, M. V., "A Theoretical Analysis of Reaction Rate Controlled Systems - Part 1," Chapter 6 in Combustion Research and Reviews, 1957, Agardograph No. 15, Butterworths Scientific Publications, London, England, February, 1957.
- 4.55 Lefebvre, A. H., "Fuel Effects on Gas Turbine Combustion - Ignition, Stability, and Combustion Efficiency." Journal of Engineering for Gas Turbine and Power, Vol. 107, January, 1985, pp. 23-37.
- 4.56 Derr, W. S. and Mellor, A. M., "Recent Developments" in Design of Modern Turbine Combustors. Edited by A. M. Mellor, Academic Press, Harcourt Brace Jovanovich, New York, NY, © 1990.
- 4.57 Oates, G. C. Aerothermodynamics of Gas Turbine and Rocket Propulsion. AIAA Education Series, J. S. Przemieniecki, Series Editor-in-Chief, American Institute of Aeronautics and Astronautics, Inc., Washington, DC, USA, © 1988.
- 4.58 Davis, M. W., Jr., "A Stage-by-Stage Dual-Spool Compression System Modeling Technique", ASME Paper #82-GT-189, March 1982, Presented at the 1982 IGTI Conference, London, England.
- 4.59 Davis, Milton W., Jr., "A Stage-by-Stage Compressor Modeling Technique for Single-and Dual-Spool Compression Systems", Unpublished Master's Thesis, University of Tennessee, Knoxville, Tennessee, August 1981
- 4.60 Garrard, G. D., "ATEC: The Aerodynamic Turbine Engine Code for the Analysis of Transient and Dynamic Turbine Engine System Operations," Ph.D. Dissertation, the University of Tennessee, Knoxville, August, 1995.
- 4.61 Garrard, Doug, "ATEC, The Aerodynamic Turbine Engine Code for the Analysis of Transient and Dynamic Gas Turbine Engine System Operations, Part 1: Model Development", ASME Paper # 96-GT-193, June 1996.
- 4.62 Garrard, Doug, "ATEC, The Aerodynamic Turbine Engine Code for the Analysis of Transient and Dynamic Gas Turbine Engine System Operations, Part 2: Numerical Simulations", ASME Paper # 96-GT-194, June 1996.
- 4.63 Kneile, K. R., and Hale, A. A., "Appendix C: Numerical Solution to the Governing Equations," Appendix C in Garrard, G. D., "ATEC: The Aerodynamic Turbine Engine Code for the Analysis of Transient and Dynamic Turbine Engine System Operations," Ph. D. Dissertation, The University of Tennessee, Knoxville, August, 1995.
- 4.64 Hale, A. A. and Davis, M. W., "DYNamic Turbine Engine Compressor Code DYNTTECC - Theory and Capabilities," AIAA-92-3190, Presented at the AIAA/SAE/ASME/ASEE 28th Joint Propulsion Conference and Exhibit, Nashville, TN, July 6-8, 1992.

- 4.65 Davis, M. W., "A Stage-by-Stage Post-Stall Compressor System Modeling Technique: Methodology, Validation, and Application," Ph. D. Dissertation, Virginia Polytechnic Institute and State University, August, 1986.
- 4.66 Greitzer, E. M., "REVIEW-Axial Compressor Stall Phenomena," Transactions of the ASME, Journal of Fluids Engineering, Vol. 102, June, 1980, pp. 134 - 151.
- 4.67 Garrard, G. D., Davis, M. W., Jr., and Hale, A. A., "Recent Advances in Gas Turbine Engine Dynamic Models Developed Through JDAPS," 95-GT-146, Presented at the 40th ASME International Gas Turbine and Aeroengine Congress and Exposition, Houston, TX, June 1995.
- 4.68 Herbert, M. V., "A Theoretical Analysis of Reaction Rate Controlled Systems - Part 1," Chapter 6 in *Combustion Research and Reviews, 1957*, Agardograph No. 15, Butterworths Scientific Publications, London, England, February, 1957.
- 4.69 Lefebvre, A. H., "Fuel Effects on Gas Turbine Combustion - Ignition, Stability, and Combustion Efficiency," Journal of Engineering for Gas Turbines and Power, Vol. 107, January 1985, pp. 24 - 37.
- 4.70 Derr, W. S., and Mellor, A. M., "Recent Developments," in Design of Modern Turbine Combustors, edited by A. M. Mellor, Academic Press, Harcourt Brace Jovanovich, New York, NY, © 1990.
- 4.71 Oates, G. C., Aerothermodynamics of Gas Turbine and Rocket Propulsion, AIAA Education Series, J. S. Przemieniecki, Series Editor-in-Chief, American Institute of Aeronautics and Astronautics, Washington, D. C., © 1988, pp. 218-220.
- 4.72 Crawford, R. A., and Burwell, A. E., "Quantitative Evaluation of Transient Heat Transfer on Axial Flow Compressor Stability," AIAA 85-1352, Presented at the 21st AIAA/SAE/ASME/ASEE Joint Propulsion Conference, Monterey, CA, July 8-10, 1985.
- 4.73 MacCallum, N. R. L., and Pilidis, P., "The Prediction of Surge Margins During Gas Turbine Engine Transients," ASME 85-GT-208, Presented at the Gas Turbine Conference and Exhibit, Houston, TX, March 18-21, 1985.
- 4.74 Sissom, L. E., and Pitts, D. R., Elements of Transport Phenomena, McGraw-Hill, Inc, New York, NY, © 1972, pp. 118-121.
- 4.75 Varner, M. O., Martindale, W. J., Phares, W. J., Kneile, K. R., and Adams, J. C., Jr., "Large Perturbation Flow Field Analysis and Simulation for Supersonic Inlets," NASA CR-174676, September, 1994.
- 4.76 Hale, A. A. and M. W. Davis, Jr., "DYNamic Turbine Engine Compressor Code: DYNTECC -- Theory and Capabilities", AIAA Paper # AIAA-92-3190, Presented at the 28th Joint Propulsion Conference and Exhibit, Nashville, TN, July 1992.
- 4.77 Davis, M. W., Jr., "Parametric Investigation into the Combined Effects of Pressure and Temperature Distortion on Compression System Stability", AIAA Paper # AIAA-91-1895, Presented at the 27th Joint Propulsion Conference, Sacramento, CA, June 1991.

- 4.78 Kimzey, W. F., "An Analysis of the Influence of Some External Disturbances on the Aerodynamic Stability of Turbine Engine Axial Flow Fans and Compressors", AEDC-TR-77-80, August, 1977.
- 4.79 Shahrohi, K. A., "Application of a Modified Dynamic Compression System Model to a Low-Aspect Ratio Fan: Effects of Distortion," Unpublished Master's Thesis, Vanderbilt University, Nashville, Tennessee, May 1995.
- 4.80 Shahrohi, K. A., and M. W. Davis, Jr., "Application of a Modified Dynamic Compression System Model to a Low-Aspect Ratio Fan: Effects of Distortion," AIAA-95-0301, Presented at the 33rd Aerospace Science Meeting, Reno, NV, January 1995.
- 4.81 Goethert, B. H. and Reddy, K. C., "Unsteady Aerodynamics of Rotor Blades of a Compressor under Distorted Flow Conditions." AGARD paper presentation, Silver Springs, MD, September 1970.
- 4.82 Hale, A.A, O'Brien, W., "A Three-Dimensional Turbine Engine Analysis Compressor Code (TEACC) for Steady-State Inlet Distortion," Journal of Turbomachinery, Vol. 120, Number 3, July 1998, pp 422-430.
- 4.83 Longley, J. P. and Greitzer, E. M. "Inlet Distortion Effects in Aircraft Propulsion System Integration." AGARD-LS-183. Advisory Group for Aerospace Research & Development Lecture Series, May 1992.
- 4.84 Chima, R. V., "A Three-Dimensional Unsteady CFD Model of Compressor Stability", ASME Paper GT2006-90040.
- 4.85 Marble, F. E., "Three-Dimensional Flow in Turbomachines," in *High Speed Aerodynamics and Jet Propulsion, Vol X, Aerodynamics of Turbines and Compressors*, Hawthorne, W. R., ed. Princeton University Press, Princeton, NJ., pp.83-165.
- 4.86 Nazir, J., Couch, R., Davis, M., "An Approach for the Development of an Aerodynamic-Structural Interaction Numerical Simulation for Aeropropulsion Systems," ASME Paper 1996-GT-480, 1996.
- 4.87 Couch, R. G., Albright, E., Alexander, N., "JOY Computer Code," Lawrence Livermore National Laboratory, UCID-19688, 1983.
- 4.88 Hallquist, J. O., "Theoretical Manual for DYNA3D," Lawrence Livermore National Laboratory, UCID-19401, draft, 1982
- 4.89 Nichols, A. L. III, Westerberg, K. W., "Modification of a Thermal Transport Code to Include Chemistry with Thermally Controlled Kinetics," Numer. Heat Transfer, Part B, Vol 24, pp 489-509, 1993.
- 4.90 Shapiro, A. B., "TOPAZ3D - A Three-Dimensional Finite Element Heat Transfer Code," Lawrence Livermore National Laboratory, UCID-20484, 1985.
- 4.91 Sharp, R., Anderson, S., Dube, E., Futral, S., Otero, I., "User's Manual for ALE3D," Lawrence Livermore National Laboratory, unpublished, 1995.

- 4.92 Tipton, R., "CALE User's Manual," Lawrence Livermore National Laboratory, unpublished, 1990.
- 4.93 Tipton, R., Lawrence Livermore National Laboratory, unpublished, 1992. Whirley, R. G., Engemann, B. E., 1993, A Nonlinear, Explicit, "Three Dimensional Finite Element Code for Solid and Structural Mechanics - User Manual", Lawrence Livermore National Laboratory, UCRL-MA-107254 Rev 1.
- 4.94 Whirley, R. G., Engemann, B. E., 1993, A Nonlinear, Explicit, "Three Dimensional Finite Element Code for Solid and Structural Mechanics - User Manual", Lawrence Livermore National Laboratory, UCRL-MA-107254 Rev 1.
- 4.95 "OVERFLOW 2.1t User's Manual", August 2008. Sirbaugh, J, "Turbomachinery Mods to OVERFLOW," Internal AEDC memo report, 2006.
- 4.96 Chen, J.P., Briley, W.R., "A Parallel Flow Solver for Unsteady Multiple Blade Row Turbomachinery Simulations," ASME Paper 2001-GT-0348, June 2001.
- 4.97 Chen, J.P., Barter, J.W., "Comparison of Time-Accurate Calculations for the Unsteady Interaction in Turbomachinery Stage," AIAA 98-3292, July 1998.
- 4.98 Chen, J.P., Ghosh, A.R., Sreenivas K., and Whitfield, D.L., "Comparison of Computations Using Navier-Stokes Equations in Rotating and Fixed Coordinates for Flow Through Turbomachinery," AIAA-97-0878, 1997.
- 4.99 Chen, J.P., and Whitfield, D.L., "Navier-Stokes Calculations for The Unsteady Flowfield of Turbomachinery," AIAA-93-0676, Jan. 1993.
- 4.100 Erdos, J.I., Alzner, E., and McNally W., "Numerical Solution of Periodic Transonic Flow Through a Fan Stage," AIAA Journal 15 (11), pp 1559-1568, 1977.
- 4.101 Whitfield, D.L., Janus, J.M. and Simpson, L.B., "Implicit Finite Volume High Resolution Wave-Split Scheme for Solving the Unsteady Three- Dimensional Euler and Navier-Stokes Equations on Stationary or Dynamic Grids," MSSU-EIRS-ASE-88-2, 1988.
- 4.102 Zhu J. and Shih, T.-H., "CMOTT Turbulence Module for NPARC," NASA CR 204143, Aug. 1997.
- 4.103 Sirbaugh, J, "Turbomachinery Mods to OVERFLOW," Internal AEDC memo report, 2006.
- 4.104 Hale, A., Klepper, J., Hurwitz, W., "A Numerical Capability to Analyze the Effects of Water Ingestion on Compression System Performance and Operability," GT2005-68480, ASME TURBO Expo, Reno-Tahoe, Nevada, June 2005.
- 4.105 "Recommended Practices for the Assessment of the Effects of Atmospheric Water Ingestion on the Performance and Operability of Gas Turbine Engines," Propulsion and Energetics Panel Working Group 24, Advisory Group for Aerospace Research and Development (AGARD), NATO, 1995
- 4.106 Hearsey, R.M. "Program HT0300 NASA 1994 Volume 2." The Boeing Company, 1994. Klepper, Jason, Hale, Alan, and Davis, Milt, "A Numerical Investigation of Steam

Ingestion on Compression System Performance,” ASME Paper #GT2004-54190, 2004 ASME TURBO Expo, June 2004.

4.107 Lieblein, S. “Chapter VI: Experimental Flow in Two-Dimensional Cascades.” *Aerodynamic Design of Axial-Flow Compressors*, NASA-SP-36, 1965, pp. 183-226.

4.108 Smith, S. L. “1-D Meanline Code Technique to Calculate Stage-by-Stage Compressor Characteristics.” M.S. Thesis, The University of Tennessee, Knoxville, TN, 1999.

4.109 Willbanks, C. E. and Schulz, R. J. “Analytical Study of Icing Simulation for Turbine Engines in Altitude Test Cells.” AEDC-TR-73-144 (AD-770069), November 1973.

4.110 Klepper, Jason, Hale, Alan, and Davis, Milt, “A Numerical Investigation of Steam Ingestion on Compression System Performance,” ASME Paper #GT2004-54190, 2004 ASME Turbo Expo, June 2004.

4.111 Tibboel, G. A., “Modification of a One-Dimensional Dynamic Compression System Model to Calculate Stage Characteristics Internally.” M.S. Thesis, The University of Tennessee, Knoxville, TN, 2002.

4.112 Hearsey, R.M. “Program HT0300 NASA 1994 Volume 2.” The Boeing Company, 1994.

## APPENDIX A TABLE OF CONTENTS

APPENDIX A	Joint Dynamic Airbreathing Propulsion Simulations (JDAPS).....	414
A.1	Vision, Mission and Goals of JDAPS .....	415
A.2	JDAPS Organizational Structure .....	416
A.3	Development of Production Simulations.....	417
A.4	Research and Development Activities.....	420
A.5	References: .....	422

### APPENDIX A JOINT DYNAMIC AIRBREATHING PROPULSION SIMULATIONS (JDAPS)

Today's gas turbine engines are the most reliable aircraft power plants produced to-date. This reliability has been obtained through extensive testing prior to introduction into service. To aid in the analysis of engine performance and operability, turbine engine numerical simulations have been developed which provide insight into a physical phenomena that may not be understood by test data alone. Simulations can fill information gaps and extend the range of test results to areas not tested. In addition, once a simulation has been validated, it can become a numerical experiment to conduct "what-if" studies to determine possible solutions to performance or operability problems.

Turbine engine numerical simulations fall into three categories:

1. Steady State
2. Transient
3. Dynamic

Steady state models provide point performance. In general, they tend to be component level models with cycle matching. The NASA Engine Performance Program, **NEPP**, [A.1] is a good example of a steady state simulation. Transient models provide engine performance for low frequency changes such as power excursions. The Advanced Turbine Engine Simulation Technique, **ATEST**, [A.2] is another government developed model capable of both transient and steady state operation. Dynamic simulations provide insight into turbine engine dynamic behavior such as engine surge, rotating stall, engine starting and inlet distortion. Although dynamic models are tailored for dynamic events, they can and do simulate transient and steady state behavior as well.

Dynamic turbine engine simulations have branched into two directions: (1) component models, and (2) full simulations. Component models have mainly dealt with the compression system since it is the system which experiences the most violent types of dynamic instabilities and subsequently most damaging to engine operability. Compression system models range from one-dimensional lumped system models to stage-by-stage and row-by-row systems able to handle three-dimensional phenomena. A few simulations have been developed to investigate combustion instabilities but are limited in their analysis capability.

Full turbine engine simulations are developed to provide insight into the effects of dynamic events on the whole engine performance and operability. Full simulations allow for engine control interaction and thus control design and modification. Full engine simulations have ranged from component level models to stage-by-stage and row-by-row models.



To aid in the development of these dynamic simulations, a partnership has come into existence, known as JDAPS ([Figure A.1](#)). The Joint Dynamic Air-breathing Propulsion Simulations is a partnership of government, university and industry organizations for the purpose of developing and applying dynamic turbine engine/component numerical simulations to aid in the understanding of turbine engine dynamic behavior.

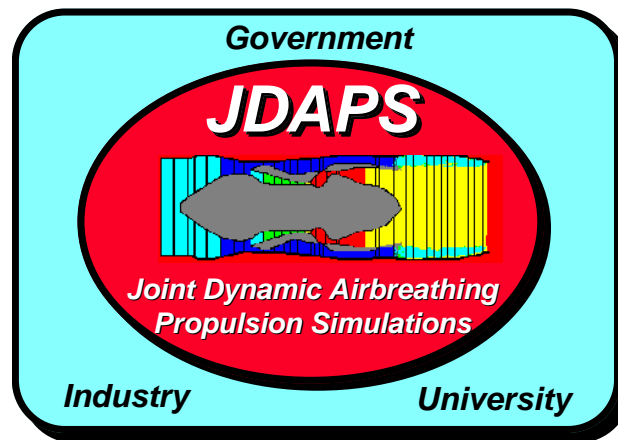


**Figure A.1 JDAPS Logo**

## **A.1 VISION, MISSION AND GOALS OF JDAPS**

### **Vision:**

The vision of **JDAPS** is to become a national focal point for the development and application of gas turbine engine system numerical simulations for dynamic/transient phenomena.

### **Mission:**

The mission of **JDAPS** is to provide and support the US gas turbine engine community with accurate, efficient and easily implemented numerical simulations of gas turbine engine systems and to coordinate with other national gas turbine engine simulation efforts.

### **Goals:**

The technical goals of **JDAPS** are:

- To develop, validate, and apply advanced analytical simulations for investigating gas turbine engine system dynamic performance and operability,
- To explore and understand dynamic engine phenomena using advanced numerical simulations, and
- To provide design guidance for improved engine performance and operability.
- The programmatic goals of **JDAPS** are:
  - To pool financial and technical resources to maximize the return on each partner's investment,
  - To minimize the duplication of effort through joint coordination of technical activities,

- To actively seek the advice and counsel of industry and academia to develop the most useful dynamic propulsion simulations, and
- To ensure adequate future resources for simulation development and application.
- To transition advanced simulations to the US propulsion community.

## **A.2 JDAPS ORGANIZATIONAL STRUCTURE**

**JDAPS** is a “grass-roots” organization. It was not decreed by some top level government agency to come into being. It arose from necessity because of limited funding in the downsizing of DOD and the gas turbine industry. Prior to the formalization of **JDAPS**, only AEDC, Wright Labs and Virginia Tech were working together on a joint effort to develop dynamic compression system models. However, as the models began to be applied and were successful, other government organizations (Army and NASA) decided to become involved in joint activities as well. For a while there existed a series of joint efforts which were tailored to the individual objectives of each joint effort. With each joint effort having some of the same partners, it became obvious that some form of organization structure was necessary to ensure proper coordination. Thus, the **JDAPS** partnership was formed.

Participation in **JDAPS** is a voluntary matter. **JDAPS** partners chose to participate on a variety of levels all the way from funding activities to occasional use of some of the dynamic simulations developed by the joint effort. All interested organizations are invited to participate at whatever level they choose.

### **Government Participants Included:**

- USAF Arnold Engineering Development Center (AEDC)
- USAF Academy
- USAF Wright Laboratory -- Compressor Research Facility (CRF)
- Army Vehicle Propulsion Directorate (AVPD)
- NASA Lewis Research Center (LeRC)

### **University Participants Included:**

- Virginia Polytechnic Institution and State University (Virginia Tech)
- Vanderbilt University
- Purdue University
- Tennessee Technological University (Tennessee Tech)

### **Industry Participants Included:**

- AlliedSignal
- Lycoming
- Allison Engine Company
- Boeing Commercial Airplane Group
- General Electric (Lynn Massachusetts)

Each organization brings something to the partnership. The government partners generally provide the majority of the financial resources for the development of the simulations but any

organization can participate in that activity. In fact, one industry partner, AlliedSignal provides funds to Virginia Tech for research which is beneficial to the overall **JDAPS** technical goals. The majority of the simulation development and much of the application is conducted by contractor personnel (currently Sverdrup Technology, Inc.) at AEDC. Simulation development is also carried out by personnel at NASA Lewis Research Facility and then incorporated into production codes by AEDC personnel. University participants provide the basic research capability that investigates new ideas and assesses if that technology can be transferred for application. In addition, university personnel can and do develop modules for production codes when their research becomes mature which is latter incorporated into production codes. Industry partners as well as the government partners become the end user and provide inputs for the development of new capabilities.

Two bi-annual meetings (one late summer and one in the winter) are conducted to review the technical progress of each activity. All participants are invited to attend this meeting. At the conclusion of this meeting, an executive council made up of the funding organizations and technical experts convene to review and prioritize each of the technical tasks.

### **A.3 DEVELOPMENT OF PRODUCTION SIMULATIONS**

To have a single organization responsible for maintaining the production codes, the **JDAPS** organization funnels all development and research activities through AEDC for incorporation into production simulations for use by all participants. Thus, the routine application of dynamic models are centered and focused at AEDC. Further development may occur at universities and is then integrated into the final dynamic production simulations at AEDC.

Because the compression systems of today's turbine engines experience dynamic behavior such as surge and rotating stall, it has been the focus of much of the effort expended by the **JDAPS** partners. New emphasis is now being applied to the combustion process because of interaction of the combustor with the compression system and because of combustion instabilities experienced in military turbine engines with augmentors. To effectively analyze the effects of dynamic behavior on system performance and operability, a full engine simulation with controls is required. A brief summary of the dynamic production simulations that are being developed by the **JDAPS** partners is presented below.

#### **COMPRESSION SYSTEM SIMULATIONS**

**DYNTECC (DYNamic Turbine Engine Compressor Code)**, is a one-dimensional, stage-by-stage axial compression system simulation which is able to analyze generic compression systems [A.3]. Illustrated in **Figure A.2** is a typical compression system along with its inlet and exit ducting representing portions of the inlet and combustor regions.

The system is represented by an overall control volume which models the forces, heat transfer, mass flow and work crossing the boundaries. In addition, the inlet and exit boundary conditions are specified either in a steady manner or they can be specified as a function of time. The overall control volume is broken into a set of elemental control volumes such as each compressor stage becomes an elemental control volume. The governing equations of mass, momentum and energy are solved across each elemental control volume. **DYNTTECC** uses a finite difference numerical technique to simultaneously solve the governing equations with turbomachinery source terms (mass flow bleed, blade force, and shaft work). The source terms are determined from a complete set of stage characteristics supplied by the user. **DYNTTECC** has the capability to analyze post-stall behavior as well as predict on the on-set of compression system instability. Stability limit analysis can be conducted for single-spool and dual-spool compression systems. The latest improvements to **DYNTTECC** which include crossflow treatment for the parallel compressor module are discussed in a paper by Shahroghi and Davis [A.4].

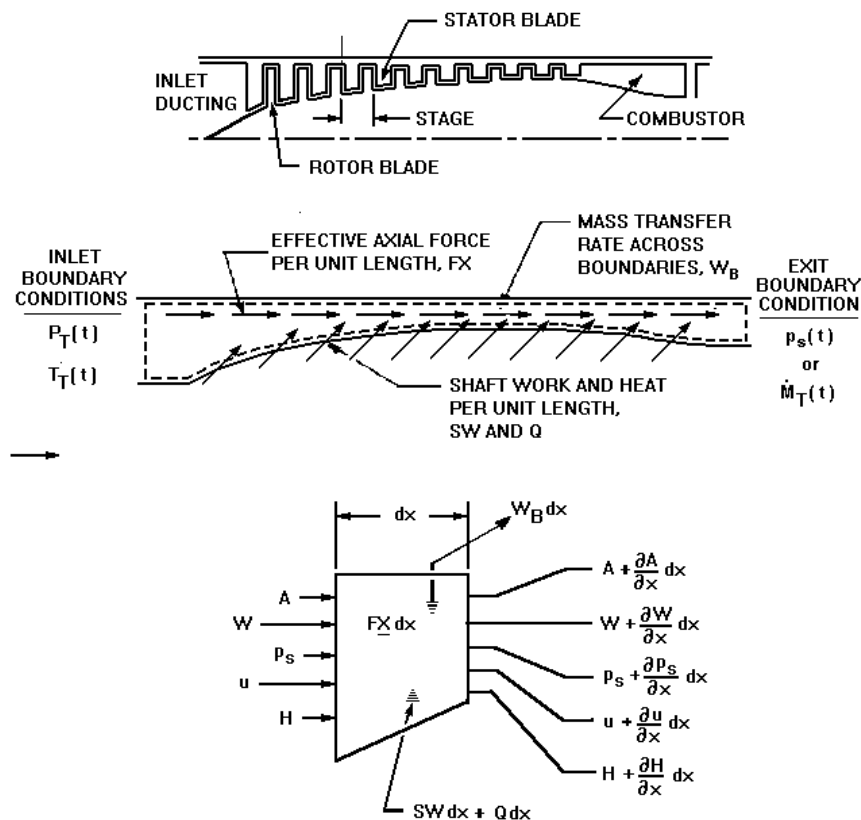


**Figure A.2 DYNTTECC General Modeling Technique**

In order to analyze complex dynamic distortion effects on compression systems, a new analytical technique is being developed. This technique goes beyond the current state-of-the-art within **DYNTTECC** which is based upon parallel compressor theory. An alternate approach is known as **TEACC** (Turbine Engine Analysis Compressor Code). **TEACC** allows for circumferential and radial control volumes to interact directly with each other via the three-dimensional Euler equations with body forces representing the forces associated with a blade row.

The overall technical approach for the development of **TEACC** is illustrated in **Figure A.3**. The code is developed using a three-dimensional Euler solver with turbomachinery source terms. These turbomachinery source terms (mass bleed, blade forces, and shaft work) are obtained from a streamline curvature code which is then coupled to the Euler solver. The streamline curvature code is applied separately across each blade row for many circumferential segments at discrete time intervals to update the turbomachinery source terms for high frequency response. Boundary conditions across each blade row for the streamline curvature code are obtained from the most current transient solution of **TEACC**.

Currently, **TEACC** has been operationally verified [A.5] for non-distorted steady operation. Future versions of **TEACC** will be able to address applications of complex dynamic distortion and their effects on compression system operability.

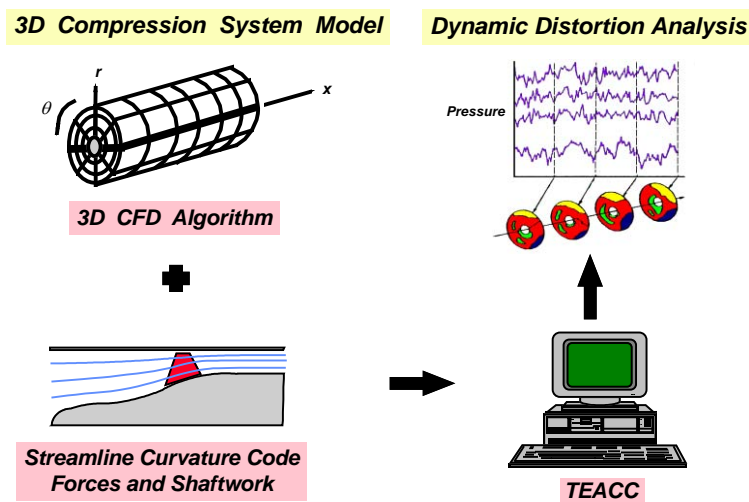
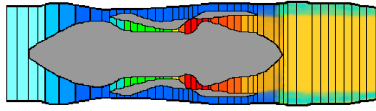


**Figure A.3 TEACC Overall Technical Approach**

## FULL TURBINE ENGINE SIMULATIONS

**DYNTTECC** has been extended to a full dynamic turbine engine model known as the **Aerodynamic Turbine Engine Code, ATEC** [A.6]. The technical approach is similar to that for **DYNTTECC** and is schematically represented in **Figure A.4**. Included in this development is the incorporation of a combustion modeling scheme, a turbine modeling scheme, the concept of mass flow choking points, augmentation operation, and exhaust nozzle flow. **ATEC** can be configured to use an explicit or an implicit integrator to numerically solve the differential equations. The advantage of using the implicit solver allows large time steps as compared to the explicit integrator. **ATEC** is not only a dynamic model but because of the implicit scheme it can compute transient events efficiently and thus can be used for transient behavior as well. When a dynamic event is sensed, the time step can be reduced in order to capture the event and switched over to the explicit solver for computational efficiency.

### Control Volume Definition



### Elemental Control Volume

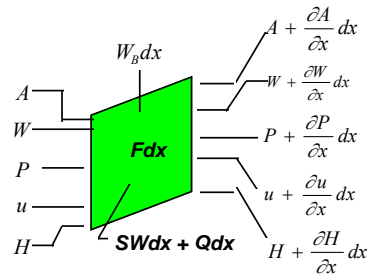


Figure A.4 ATEC Technical Approach

## A.4 RESEARCH AND DEVELOPMENT ACTIVITIES

Some research and development activities that enhance **JDAPS** production codes are centered in universities. Each university's activities are briefly described below:

### VIRGINIA TECH

**JDAPS** research at Virginia Tech (Virginia Polytechnic Institute and State University, VPI) is dedicated to the advancement of the technology of dynamic simulation for propulsion engines. Four areas of activity in the laboratories of the Center for Turbomachinery and Propulsion Research are discussed below.

#### Improved Stage Characteristic Prediction

The quality of **JDAPS** simulations are limited by the accuracy of the source terms in the modeling equations. In the initial **JDAPS** work [A.7], compressor performance characteristic curves were obtained from experiment, or estimated from experience. Virginia Tech research has provided the first wide-range stage characteristic prediction code. The **FULRANGE** code [A.8] predicts compressor stage performance for unstalled forward flow, stalled forward flow, and reversed flow using stage blade geometry and experimental correlations.

Recent work to improve **FULRANGE** has produced a two-dimensional model for rotating stall, **CRISPE**, which more accurately models in-stall characteristics. Current work will result in the application of a streamline curvature code for prediction of unstalled forward flow, performance. When combined and interfaced with **FULRANGE**, the improved methodology will provide a much improved wide-range compressor stage characteristic prediction method for use in **DYNTECC** and other dynamic system simulation codes.



## **Wide-Range Compression System Operation**

Virginia Tech research has produced a version of **DYNTECC** which allows for speed changes during a simulation event. An exit nozzle flow model for both choked and unchoked flow, which automatically senses the flow condition was added. It is now possible to run simulations over wide and varying speed ranges, down to zero speed. The modified model makes possible the investigation of the principles of the "extended starting theory", [A.9] an explanation for compressor stall and recovery behavior which draws from observed behavior during aerodynamic starting of multistage compressors.

## **Multi-Dimensional Compression System Modeling**

The current **JDAPS** production compression system model is one-dimensional. However, multi-dimensional models are required for complete simulation of the flow dynamics in engine components. Virginia Tech [A.10] has succeeded in creating a multi-dimensional compression system model. Surge with radial variations in single-passage and multi-duct flow have been successfully modeled, and work is progressing to adapt the model to multi-stage predictions of rotating stall.

## **Dynamic Combustion Modeling**

Investigation has just begun to add reacting flow equations to the multi-dimensional model, so that combustion system multistage dynamics can be predicted. An initial one-dimensional burner model has been successful in predicting flow with blowout and relight. The one-dimensional model was released to several **JDAPS** partners for use and has been incorporated into the dynamic turbine engine model, **ATEC**. The multi-dimensional combustor model adds an important new dimension to the **JDAPS** modeling capability.

## **VANDERBILT UNIVERSITY**

Vanderbilt's contribution to **JDAPS** is in the area of high speed computing capability and interactive graphical user interfaces (GUI) for the **JDAPS** simulations. The Computer Assisted Dynamic Data Monitoring and Analysis System or **CADDMAS** [A.11] is under development by Vanderbilt for the on-line processing of turbine engine data at AEDC. The CADDMAS system is capable of analyzing large amounts of dynamic stress sensors and visualizing the results on demand in real-time, during an actual engine test. The capabilities of the CADDMAS system vastly exceed the previous on-line analysis facilities at AEDC.

In the summer of 1993, Vanderbilt supported AEDC at the Compressor Research Facility in assessing the feasibility of bringing **DYNTECC** "on-line" during a typical test. The **DYNTECC** code was parallelized for circumferential distortion and run on a four processor "mini-CADDMAS" system. As part of the on-line modeling activity, Vanderbilt developed the software for generating an interactive user interface for **DYNTECC**. [A.12]

## **PURDUE UNIVERSITY**

A transient combustion computer code called TRACC (Transient Combustor Code) is to be developed by personnel at Purdue University which solves the quasi-one-dimensional, time-dependent Euler equations coupled with transport equations for the thermochemical variables of interest. A two-step chemical kinetics scheme involving a partial oxidation of the fuel to  $CO$  and  $H_2O$  followed by a  $CO$  oxidation step will be employed. The choice of finite rate chemistry

is motivated by the desire to simulate ignition and extinction events, while the choice of two-step chemistry is based on a tradeoff between simulating combustion efficiency degradation and computational efficiency. In the current formulation transport equations for the mass fractions of the fuel and carbon monoxide will be solved as well as an equation for the mixture fraction.

## **TENNESSEE TECH**

Tennessee Technological University is involved with **JDAPS** in the area of turbine engine augmentor combustion instabilities. A unified methodology [**A.13**] for carrying out both linear and nonlinear instability analysis for combustion instabilities associated with turbine engine augmentors will be developed. The method of modal analysis appears to be an appropriate basis for the development of such a methodology. Application of the process will result in a system of ordinary differential equations similar to those describing the behavior of a set of coupled mechanical oscillators. By its very nature, modal analysis represents the effects of combustion, damping devices and nonlinearity as changes in the augmentor take place.

## **A.5 REFERENCES:**

**A.1** Fishbach, L. H., "Computer Simulation of Engine Systems," AIAA Paper # 80-0051, January 1980.

**A.2** Chappell, M. A. and P. W. McLaughlin, "Approach to Modeling Continuous Turbine Engine Operation from Startup to Shutdown," **Journal of Propulsion and Power**, Vol. 9, June 1993, pp.466-471.

**A.3** Hale, A. A. and M. W. Davis, Jr., "DYNAMIC Turbine Engine Compressor Code: DYNTTECC -- Theory and Capabilities", AIAA-92-3190, 28th Joint Propulsion Conference and Exhibit, Nashville, TN, July 1992.

**A.4** Shahroghi, K. A., and M. W. Davis, Jr., "Application of a Modified Dynamic Compression System Model to a Low-Aspect Ratio Fan: Effects of Inlet Distortion," AIAA-95-0301, 33rd Aerospace Science Meeting, Reno, Nevada, January 1995.

**A.5** Hale, A. A., M. W. Davis, Jr., and K. R. Kneile, "Turbine Engine Analysis Compressor Code: TEACC -- Part I: Technical Approach and Steady Results", AIAA-94-0148, 32nd Aerospace Sciences Meeting and Exhibit, Reno Nevada, January 1994.

**A.6** Garrard, G. D., M. W. Davis, Jr., and A. A. Hale, "Recent Advances in Gas Turbine Engine Dynamic Models Developed Through **JDAPS**" ASME Paper to be given at the 40th ASME International Gas Turbine & Aeroengine Congress & Exposition, Houston, Texas, June 1995.

**A.7** Davis, M. W., Jr., and W. F. O'Brien, "Stage-by-Stage Poststall Compression System Modeling Technique," **Journal of Propulsion and Power**, December 1991, pp. 997-1005.

**A.8** Bloch, G. S. and W. F. O'Brien, "A Wide-Range Axial-Flow Compressor Stage Performance Model," ASME 92-GT-58, 37th International Gas Turbine Conference, ASME, Cologne, Germany, June 1992.

**A.9** O'Brien, W. F. and K. M. Boyer, "Stall and Recovery in Multistage Axial-Flow Compressors," **Proceedings of the AGARD 74th Specialists Meeting of the Propulsion and Energetics Panel, Luxembourg**, August 1989.

**A.10** Lindau, J. W. and W. F. O'Brien, "Solution Schemes for Stage-by-Stage Dynamic Compression System Modeling," AIAA-93-0154, 31st Aerospace Sciences Meeting, Reno, Nevada, January 1993.

**A.11** Tibbals, T. F., T. A. Bapty, and B. A. Abbott, "CADDMAS: A Real-Time Parallel System for Dynamic Data Analysis," ASME 94-GT-194, 39th International Gas Turbine Conference, ASME, The Hague, Netherlands, June 1994

**A.12** Davis, M. W., Jr. and T. A. Bapty, "Interactive User Interface for a Dynamic Compression System Simulation," AIAA-95-0244, 33rd Aerospace Sciences Meeting, Reno, Nevada, January 1995.

**A.13** Hyun-Gull, Y., J. Peddieson, and K. R. Purdy, "A General Formulation for Ramjet and Afterburner Combustion Instability Analysis," Developments in Theoretical and Applied Mechanics, Vol. XVII, 1994.

## TABLE OF CONTENTS

APPENDIX B	Flight Simulation Vision for Aeropropulsion Ground Test Facilities .....	424
B.1	The Plant Flight Simulation Vision.....	426
B.2	Technical Approach – Non-Distorted Inlet Flow .....	427
B.3	Non-Distorted Inlet Airflow Simulation Demo.....	431
B.4	Technical Approach –Distorted Inlet Flow .....	434
B.5	Putting the Pieces Together .....	436
B.6	References: .....	438

### APPENDIX B FLIGHT SIMULATION VISION FOR AEROPROPULSION GROUND TEST FACILITIES

The Arnold Engineering Development Center, AEDC, has within its assets, ground facility infrastructure for the testing of gas turbine engines at sea level and altitude conditions [B.1]. These facilities have been built-up over the last 50 years based upon a ground-testing philosophy and methodology that simulates engine conditions that would be present during steady state flight conditions. These methodologies have served the gas turbine propulsion community well as it has developed gas turbine engines for military and civilian transport aircraft. The major advantage of ground-testing is that systematic investigations can be conducted and repeated with certainty using current established methodologies. However, there are limitations that prohibit testing of certain types of transient phenomena and thus the engine's performance during flight maneuvers. These types of maneuvers have been relegated to flight-testing. Flying the aircraft with its propulsion system puts the gas turbine engine in the environment it is to operate within. However, because of limitations with instrumentation, measurements of engine performance are limited. Flight-testing can only provide the answer when the investigator knows exactly what to look for and how to obtain the information with the correct instrumentation. In addition to the performance measurement limitation, flight-testing can be expensive as compared to ground-testing and has a higher risk of loss of the aircraft as well as the pilot if something should go wrong. Thus, it has always been the wise course-of-action to conduct investigations and qualification of the propulsion system in ground-test facilities prior to any flight-testing and ultimate implementation within a fleet of aircraft.

To understand the limitations within the ground test methodology, a brief review of the current ground test practice is in order. As an aircraft flies through the atmosphere, whether it is subsonic or supersonic, the velocity and quality of the airflow must be presented to the compression system at conditions that will allow it to do its job (i.e. raise the pressure of the air to a higher level). Today's compression systems cannot accept supersonic flow at the engine face. In the case of high subsonic or supersonic flight, the engine inlet velocity must be slowed down to a point where the Mach number is on-the-order-of 0.5. In the case of low subsonic flow, the compression system will pull (suck) the airflow it requires. In both instances, the flight velocity and the atmospheric conditions (pressure and temperature) define the engine airflow conditions, which can be quantified by the specification of engine airflow, total pressure and total temperature ( $W$ ,  $P_T$ ,  $T_T$ ). By providing airflow to an engine at the pressure and temperature conditions that represent the flight condition, engine performance can be simulated as if the engine were actually flying at those conditions. To obtain engine thrust, the effect of the difference in engine nozzle exhaust pressure and atmospheric pressure can be accounted for by testing the engine in an environment such that the nozzle exhausts to a pressure associated

with the altitude condition of flight. When both of these conditions are met, a ground simulation of engine flight is obtained. This concept is illustrated in **Figure B.1**.

The air-side plant supplies the engine with the required airflow at the total pressure ( $P_T$ ) and temperature ( $T_T$ ) desired to simulate the flight condition (altitude and Mach number). The engine is situated in an isolated test cell that has a bellmouth attached to the engine inlet that is used to capture the airflow supplied by the plant as illustrated in **Figure B.2**.

The cell pressure is maintained by the exhaust plant that sets the altitude pressure and

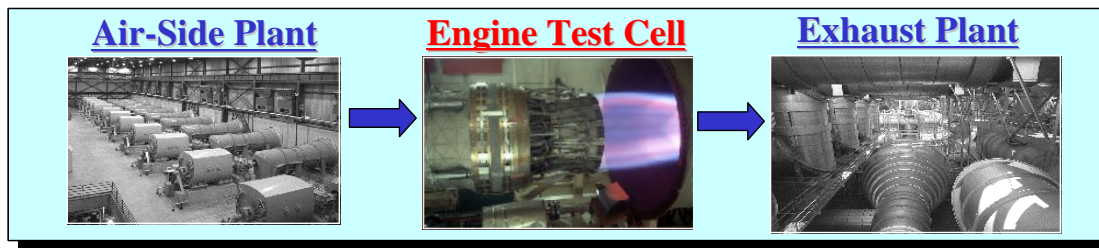


**Figure B.1 Typical Ground Test Facility/Engine Configuration**

exhausts the combustion products ultimately to atmosphere after they have been properly cleaned and cooled. These facilities were designed to operate the engine in a steady manner. The airside plant, as originally designed, did not have the capability to change the engine inlet temperature in a rapid manner. Some transient capability has been obtained with the original cell design (circa 1950) by small modifications such as removing airflow-measuring venturis and using atmospheric inbleed. However, these transient capabilities were very limited and did not produce true conditions as needed to simulate flight [B.2].

In a internal AEDC study, engine test cell requirements for the next 25 years have been established in order to support anticipated propulsion needs. To meet these future requirements, facility design modifications have been proposed and are currently being implemented as part of the Propulsion Consolidation and Streamlining (PCS) Program. A part of the study also addressed the need of changing conditions required for future transient testing. These requirements are driven by the anticipated mission profiles which can be categorized into three main areas.

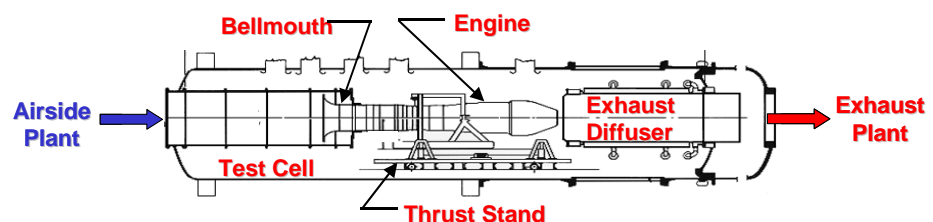


**Figure B.2 Typical Test Cell Configuration**

- **Zoom Climbs (altitude climbs at constant Mach number)**
- **Mach Dashes (accelerations and decelerations at constant altitude)**
- **Complex profiles (variations in both altitude and Mach number, such as wind-up-turns, spins, etc.)**

The required maximum rates of change of conditions for a typical test facility are:

- 1.75 psia/sec for inlet pressure
- -0.4 psia/sec for cell pressure,
- +15°F/sec or -10°F/sec for inlet temperature, depending upon the maneuver.

Airflow during these maneuvers will scale with the particular engine size being tested. In addition, flow varies with throttle setting and flight condition. The range considered in the study was 140 to 500 lbm/sec at sea level conditions.

Before the PCS program began, many of these mission profile rates were unattainable. As part of this program, new designs and concepts are being investigated via facility numerical modeling before implementation. Upon completion of this program it is expected that the facility will be able to achieve these desired transient rates. Better simulation of gas turbine engine operation will then be possible in a ground test facility. **Ref. B.2** discusses the changes implemented by the PCS program so far as well as those proposed for the future.

## B.1 THE PLANT FLIGHT SIMULATION VISION

During the last several years, AEDC has been in the process of modernizing and improving its plant facilities [B.3]. Many of these modifications have been investigated and made possible using a numerical plant model. The goal of the PCS program has been to improve the efficiency of the test facilities while increasing test capabilities. An additional capability that could be provided is the ability to “fly” the engine through flight maneuvers while in a ground-test facility. To do so requires simulation of an aircraft system to provide aerodynamic input to the propulsion system. This effort will support an ultimate capability for “flight-testing” an engine in an altitude test cell. Engine data along with aircraft maneuvers would be used to determine settings for the plant conditions, inlet distortion, and engine services to simulate transient flight conditions during ground-testing.

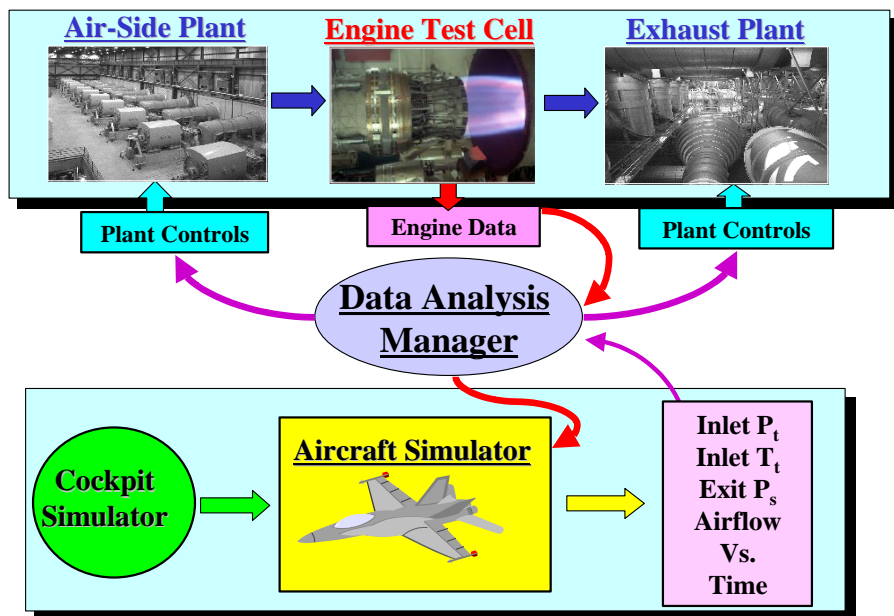


**Figure B.3 Non-Distorted Inlet Flow Plant Flight Simulation Vision**

Modeling and simulation capabilities will be acquired and/or developed for simulation of aircraft maneuvers and the environment presented to the propulsion device. The ultimate vision is to have a simulation of the aircraft providing input into the settings for the facility. In this way, the engine may be effectively “flight-tested” while in a ground test facility. This vision will be



presented in two phases. A pictorial of this vision in its simplest form, ***Non-Distorted Inlet Flow***, is presented in **Figure B.3**.

For non-distorted inlet airflow, an aircraft simulator is used to provide the plant set conditions for either steady or transient maneuvers. It is envisioned that a cockpit simulator is positioned in the control room for an operator to effectively provide inputs as if he were the pilot. The plant provides the conditions based on the aircraft simulator for the inlet pressure, temperature, airflow rate and altitude pressure. The actual engine is then “flown” at the conditions of the aircraft. The engine performance is fed back into the aircraft simulator to provide propulsion performance to the aircraft. Maneuvers such as zoom climbs and Mach dashes can be effectively simulated in this sort of test configuration.

More complex flight profiles such as wind-up turns and gas ingestion require simulation of complex inlet flow distortions. The vision must be modified for the inclusion of inlet flow distortion and will be discussed later in the paper.

## B.2 TECHNICAL APPROACH – NON-DISTORTED INLET FLOW

As ambitious as this vision appears, there is a very logical and inexpensive way to accomplish feasibility studies to see what is possible with the current and future modifications to AEDC's ground test facilities.

As a major part of the facility upgrade project, numerical models of the existing AEDC facilities are being developed. These models are being developed in a modular manner, which allows for proposed modifications to be easily incorporated into the simulation. Thus, where today's facilities may not support the Plant Flight Simulation Vision, modifications may be postulated and verified using the numerical simulation without the cost of implementing the idea via hardware. The Non-Distorted Inlet Airflow portion of the vision can thus be implemented via the numerical simulation as illustrated in **Figure B.4**.

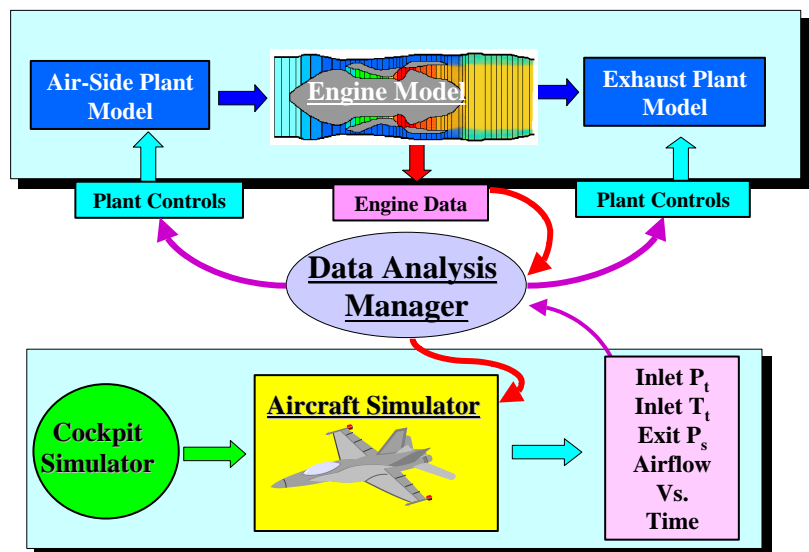


**Figure B.4 Numerical Simulation of the Non-Distorted Inlet Airflow Plant Simulation Vision**

To implement this simulation, it is necessary to characterize the major sub-simulations: the Facility Simulation, the Aircraft Simulator, the Cockpit Simulator, the Engine Model, and the Data Analysis Manager. The sub-simulations described in the next several paragraphs are typical simulations but may not necessarily be the ones used in any implementation of the vision.

## THE FACILITY SIMULATION

At the heart of the described system is the real-time mathematical model and simulation developed through the use of the MathWorks, Inc. Matlab/Simulink® software. Under this software, system models may be created through the use of block diagrams. Once the model is operating in the desired manner, optimized C code may be generated directly from these diagrams using the Real-Time Workshop® option of the Matlab/Simulink® software package.

The facility interfaces are modeled at the graphical user interface (GUI) level using a library of standard objects. Using the GUI, development of a real-time model becomes a one-step process that includes: code generation; compilation and dynamic download. This allows the model to be executed as a real-time task.

Figure B.5 shows the top level of the current facility configuration and its simulation in the Matlab/Simulink® software environment [B.3]. Each rectangular box, elliptical duct or control volume, and valve represents a masked subsystem of varying level of complexity. From this

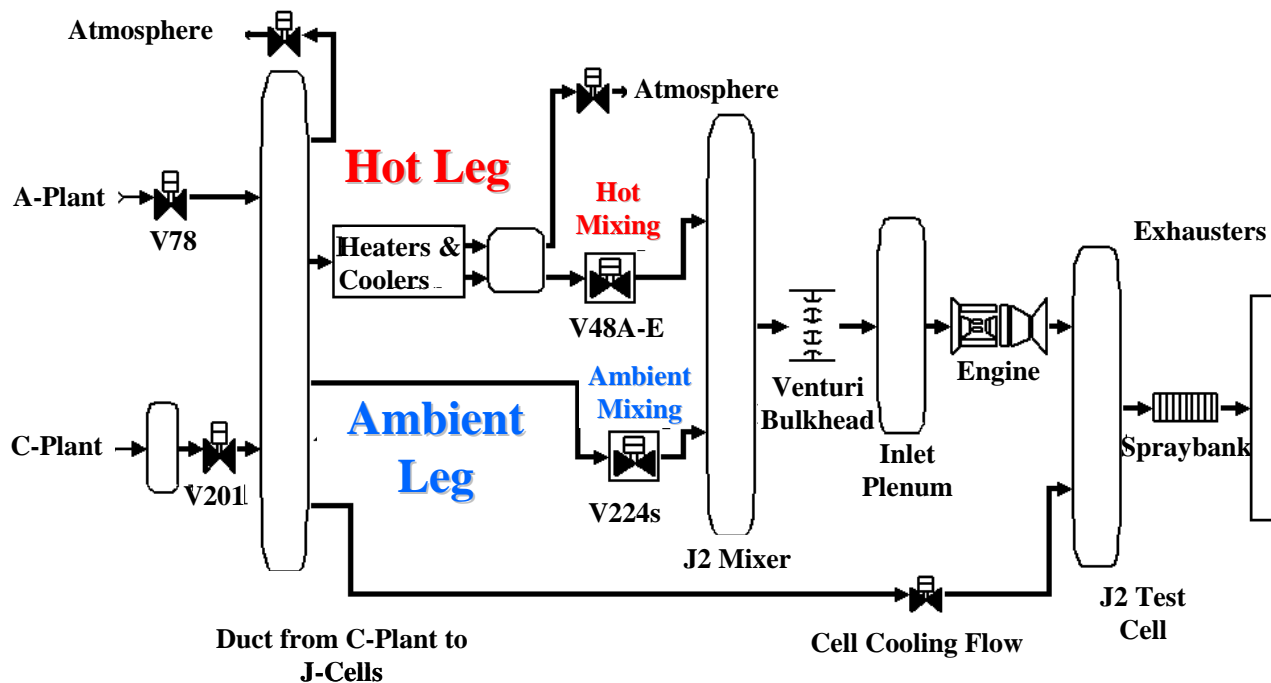


**Figure B.5 Diagram for the J-Turbine Engine Test Facility as it Currently Exists**

advantage point, however, the general layout of the system is clearly seen. Moving from left to right, the A-plant and/or C-plant passes air through its ducting and then through valves into the J1 or J2 test facilities. Upon leaving the test facilities, the exhaust gases pass through the exhaust ducting, valves, and finally into the exhausters.

A proposed modification is presented in **Figure B.6** that includes a cooling leg in order to provide rapid changes in inlet temperature. The temperature changes represent extremes that the current configuration may only be able to achieve by being on condition for a long period of time. In the future upgrade to the facility, air passing through turbo expanders for additional cooling can be mixed with ambient and hot air for greater temperature range capability. The major modifications are circled in Figure 6 for easy identification.

### THE AIRCRAFT SIMULATOR

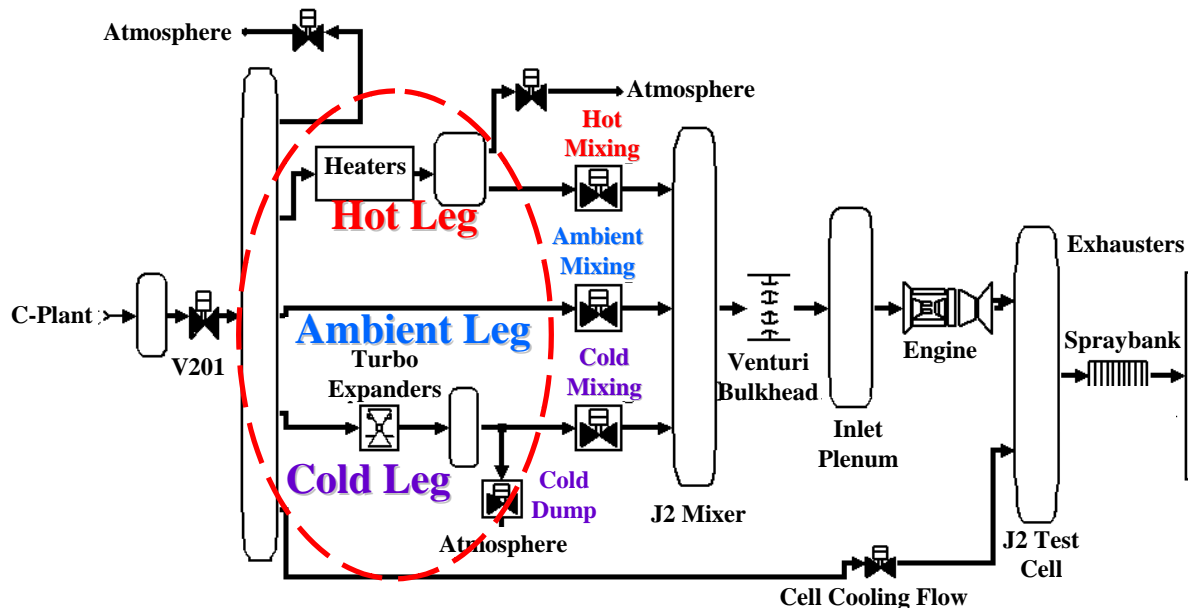


**Figure B.6 Proposed Future Modification to the J-Cells Facility to Allow Additional Cooling**

An aircraft simulator known as **GENESIS** [B.4,B.5] has been identified and is in use at AEDC. **GENESIS** is a simulation tool that can be used for the analysis of any time varying system. While **GENESIS** evolved over many years of aircraft applications, its use has become increasingly diversified. **GENESIS** comes with a large library of utility functions, which represent the common elements comprising any dynamic system. All dynamic utilities are self-initializing and possess the necessary logic to handle linear model generation. The **GENESIS** simulation provides the user with the capability to produce time responses, to generate linear models, and to debug the model of a nonlinear dynamic system. **GENESIS** is modular and a typical example of an aircraft simulator is illustrated in **Figure B.7**. **GENESIS** has been configured for the F-16 aircraft with an F110 turbofan engine **ATEST** simulation. It is proposed to use this aircraft simulation and the F110 engine as a demonstration of the concept.

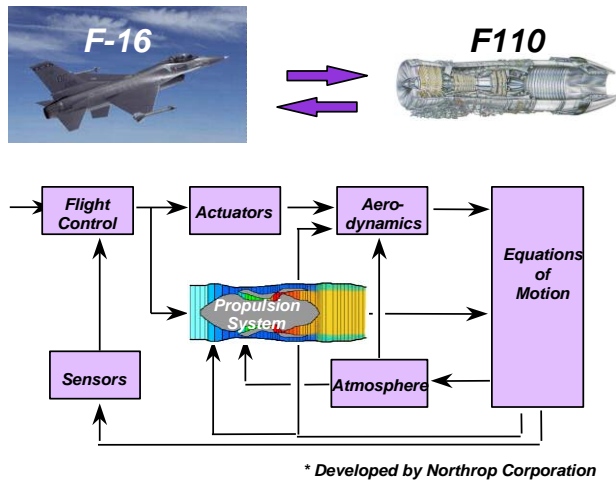


Figure B.7 The Aircraft Simulator, GENESIS

- Generic cockpit instrumentation,
- Visual system: photo realistic out-of-window view,
- Primary controls: control stick, pedals, throttle levers,



Figure B.8 AIRFOX's FlightLab Simulator

Any cycle code can be used. What has currently been implemented is the AEDC generated **ATEST**(AEDC Turbine Engine Simulation Technique) code [B.7]. To be complementary to the F-16 aircraft simulation with **GENESIS**, a simulation of the F110-GE-129 engine has been implemented within the facility simulation as well as **GENESIS**.

### THE COCKPIT SIMULATOR

The cockpit simulator can be obtained from commercial aircraft simulator companies. One such example is AIRFOX [B.6]. AIRFOX has developed a product known as FLIGHTLAB (illustrated in Figure B.8), which is a high performance, re-configurable desktop flight simulator that optimally fulfills the client's individual requirements, providing an expandable cost-effective solution.

Based on Matlab/Simulink® software tools, aircraft models can be created by block diagrams. An aircraft block library provides a selection of elements (e.g. engines, gear, wind, motivators, etc.) as well as ready-for-use aircraft models. Real-time simulation is implemented including:

Control panel: software configurable push buttons with LCD-display on button for secondary and user-defined controls.

**AIRFOX® FLIGHTLAB** provides real-time flight simulation with a generic aircraft cockpit and allows mathematical aircraft models to be modified using Matlab/Simulink® block diagrams.

### THE ENGINE MODEL

The engine model should be of the type that will provide engine performance. The most likely candidate for this sub-system is a cycle code or component-level code as illustrated in Figure B.9.

## THE DATA ANALYSIS MANAGER

As envisioned, this part of the approach is basically a data handler. This may be easily implemented with the Matlab/Simulink®

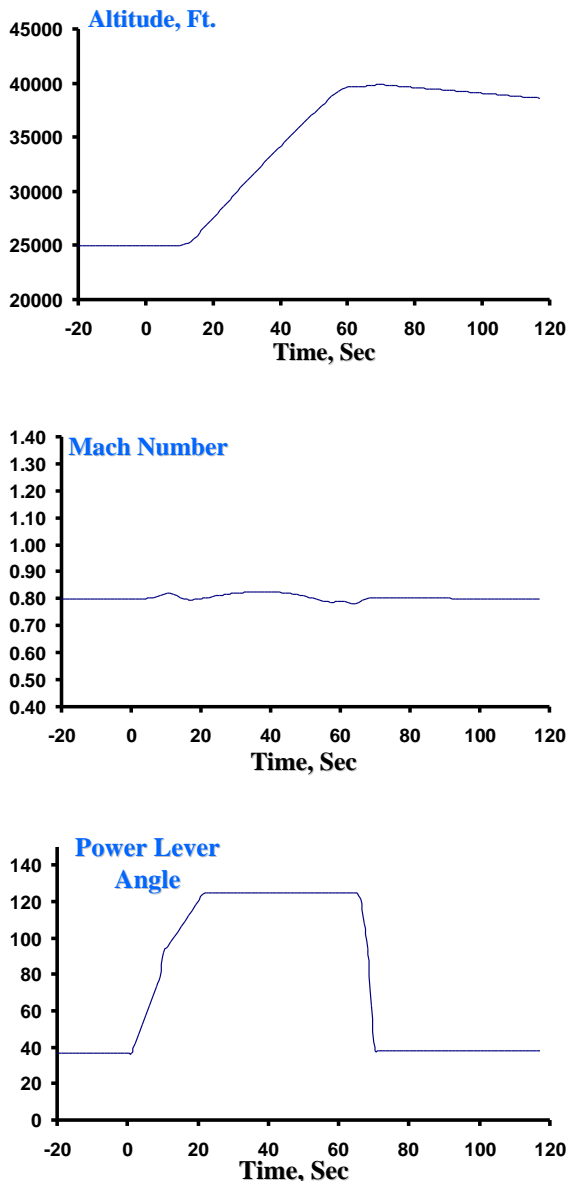


**Figure B.10 Altitude and Mach Number Conditions for Zoom-Climb from 25,000 to 40,000 ft at Mach Number of 0.8 – Conditions Obtained with GENESIS Flight Simulator**

was pulled back to establish a rapid climb rate. When the aircraft reached a climb angle of 30 degrees relative to the ground the stick was pushed forward to maintain a constant climb angle. At 38,000 ft. altitude the aircraft was rolled over 180 deg. using the ailerons. The stick was then

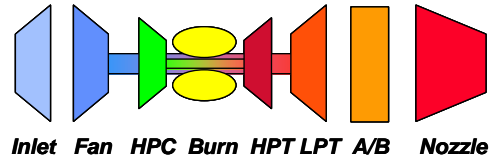
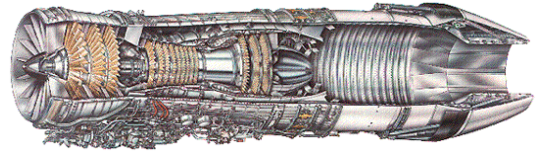


**Figure B.9 Component-Level Engine Model Representation**

environment, as part of the plant model, or it may be a separate routine that passes data to-and-from each of the other components. As we move on to the more complex vision, Distorted Inlet Airflow, the Manager may have to become more complex to be able to handle the information from databases.

### B.3 NON-DISTORTED INLET AIRFLOW SIMULATION DEMO

The initial portion of this vision allows for a simulation of aircraft maneuvers without distortion present. Aircraft altitude and speed changes can be accomplished by carefully simulating inlet and altitude conditions ( $P_T$ ,  $T_T$ , and  $P_0$ ), respectively. With simulations of certain AEDC turbine engine test facilities, a demonstration of the vision was accomplished and is presented within this section.

Two aircraft maneuvers have been chosen to be presented. The first is commonly known as a "Zoom-Climb". In this maneuver, the aircraft climbs in altitude with the goal of having the final Mach Number the same as the initial condition. A Zoom-Climb from an altitude of 25,000 ft to 40,000 ft. at a constant Mach Number of 0.8 was chosen and is presented in Figure B.10.

The climb was started with the aircraft flying at 25,000 ft. altitude Mach 0.8 level steady flight. Initially the aircraft was given a ramp to full throttle command and then the stick

pulled back to obtain a nearly level inverted flying condition at 40,000 ft. altitude. The aircraft was then rolled over another 180 deg. to an upright condition and the nose pushed down using the stick. Adjustments were then made to the stick and power level angle to establish a trim flying condition at 40,000ft. altitude Mach 0.8.

Note: The roll sequence was performed for 2 reasons:

- Pilots do not like to experience the large negative g's that would occur if the aircraft were pushed over in an upright attitude.
- Large negative angles of attack would be experienced by a non-rolled maneuver severely degrading inlet performance.

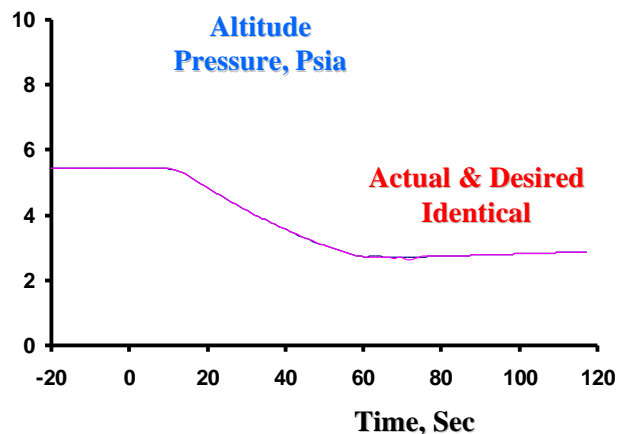
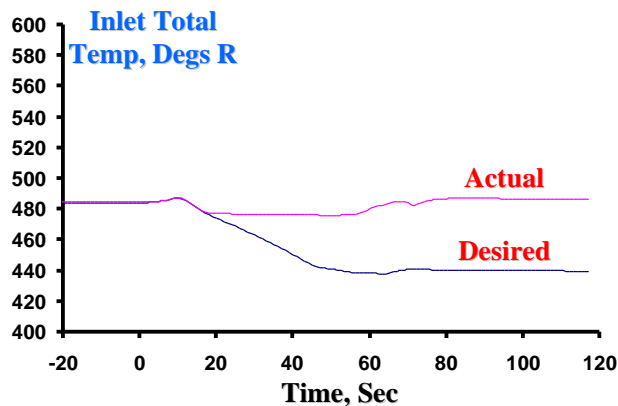
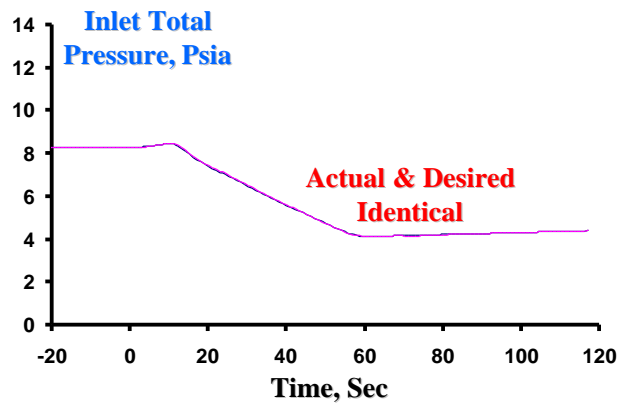


**Figure B.11 Facility Conditions for Zoom Climb from 25,000 to 40,000 ft Altitude with Current Facility Configuration**

Using engine inlet total pressure and temperature as well as altitude pressure from this maneuver, the ground facility model can be executed to determine if the aircraft maneuver can be simulated in the real facility. The maneuver was first executed in a model of the facility as it exists today [B.3]. Associated with this configuration is the ability to mix ambient air with the conditioned inlet air prior to the engine test cell plenum to obtain a better temperature simulation. Prior to this configuration, inlet temperature was controlled only by coolers and heat exchangers. The pertinent simulation parameters are presented in [Figure B.11](#).

As one can see, the inlet total pressure and the altitude pressure provided by the exhaust plant follow the desired conditions, identically. However, the inlet total temperature did not follow the desired conditions, mainly because there was no capacity with this configuration to cool the air to the conditions required.

In a proposed upgrade to the facility, cooled air along with ambient air will be able to be mixed with the conditioned air



[B.3]. Using a model of the proposed facility, the same “Zoom-Climb” was executed. Again inlet total pressure and altitude pressure followed the desired conditions. The inlet total temperature, was also able to follow the desired condition as illustrated in **Figure B.13**.

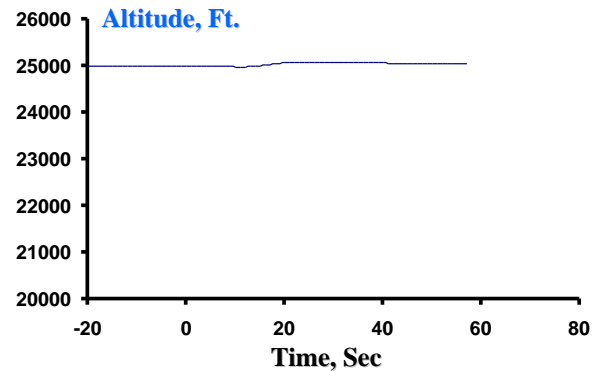
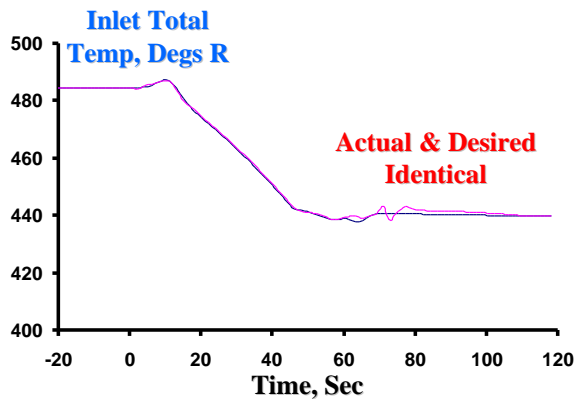
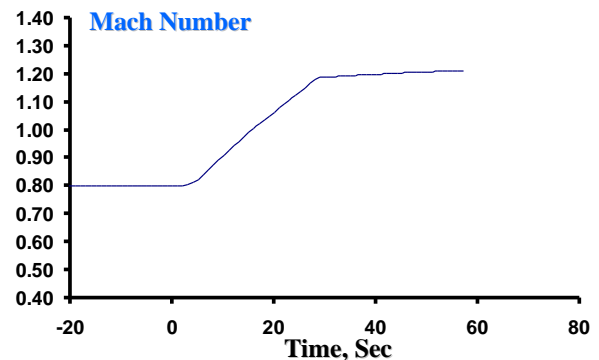


**Figure B.13 Inlet Temperature Conditions for Zoom-Climb Using the Future Facility Configuration**

The second maneuver is known as a Mach Dash. The Mach Dash was started with the aircraft flying at 25,000 ft. altitude Mach 0.8 level steady flight. Initially the aircraft was given a full throttle command, as illustrated in **Figure B.12**.



The stick was the pushed forward to keep the nose down and maintain a constant altitude. After a short period (5 sec.) it was necessary to pull the stick back to prevent the nose from rotating too far down and losing altitude. This position was held for another 5 seconds when it was necessary to rotate the nose back down to compensate for a decreased trim angle because of the increased speed. When the desired speed of Mach 1.2 was reached the power level was pulled back to maintain a constant velocity.

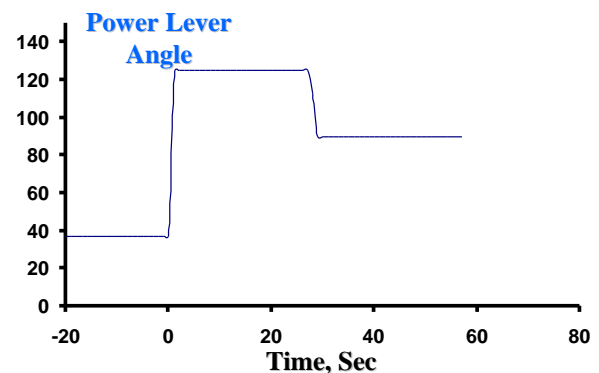


**Figure B.12 Altitude and Mach Number Conditions for Mach Dash from 0.8 to 1.2 at 25,000 ft Altitude – Conditions Obtained with GENESIS Flight Simulator**

Again, the ground facility model was executed to determine if the aircraft maneuver can be simulated in the facility. The maneuver was first executed in a model of the facility, as it exists today [B.3]. The pertinent simulation parameters are presented in **Figure B.14**. As one can see, the inlet total pressure and the altitude pressure provided by the exhaust plant follow the desired conditions, identically. The inlet temperature followed the desired path only after the facility had been held-on condition for approximately 15 minutes (Cold-Soaked) in order to allow

the facility metal to reach an equilibrium temperature close to that of the air. This negated any heat transfer to the air from the surroundings and allowed the transient to be accomplished with the prescribed temperature.

The facility model was executed again, this time with the proposed changes that would provide additional cooling to see if these changes would allow the transient to be performed without cold-soaking the facility. As illustrated in **Figure B.15**, the inlet temperature gets on-condition within a minute even when started near standard-day conditions

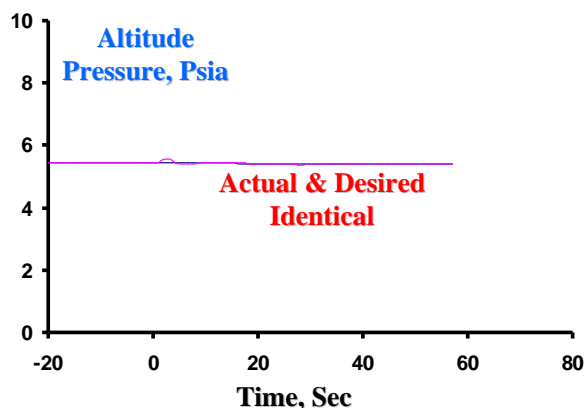
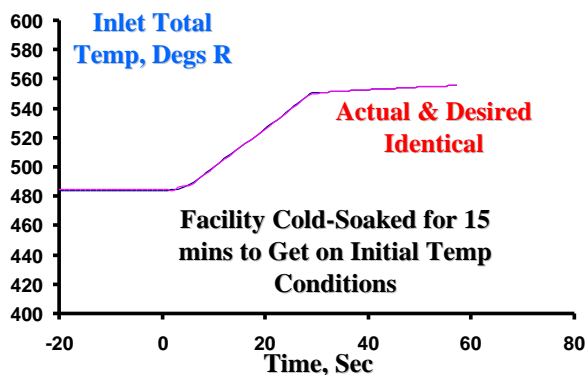
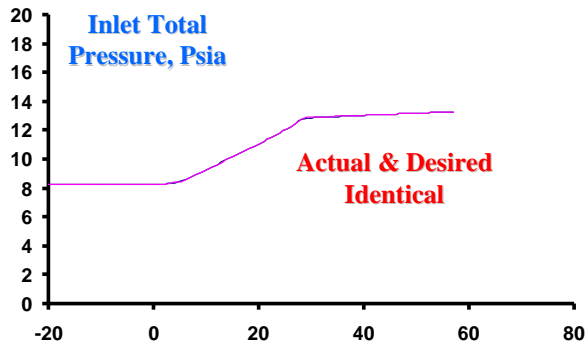


**Figure B.14 Facility Conditions for Mach Dash from 0.8 to 1.2 at 25,000 ft Altitude with Current Facility Configuration**

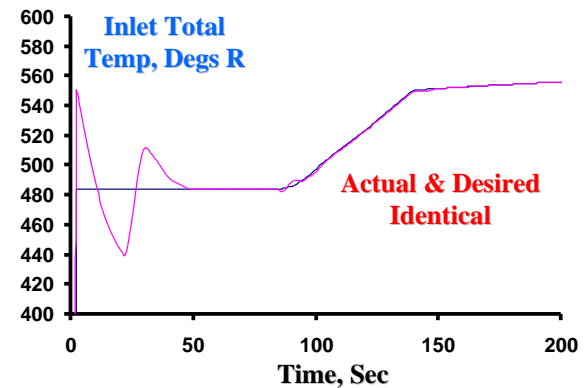


**Figure B.15 Inlet Temperature Conditions for Mach Dash Using the Future Facility Configuration**

#### B.4 TECHNICAL APPROACH – DISTORTED INLET FLOW

A second phase of this vision is to look at facility simulation capabilities with inlet distortion as would be produced during any rapid maneuver. In this phase, the plant system will now include a transient distortion generator as illustrated in **Figure B.16**.

Instead of the current method of producing distortion with screens, a device, yet to be designed, will be capable of changing the total conditions (both pressure and temperature) in a transient manner such that actual flight maneuvers could be simulated.

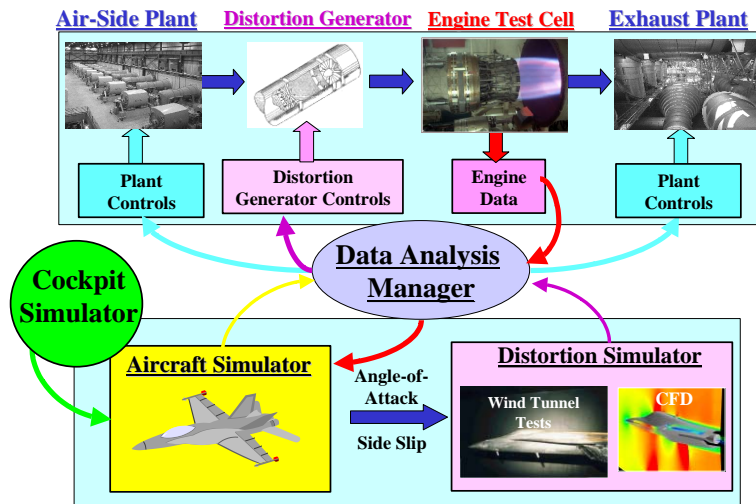


**Figure B.16 Distorted Inlet Flow Plant Flight Simulation Vision**

means to reduce cost of conducting the test portion of the T&E process.

The transient  $P_T$  distortion generator development approach includes the following steps: (1) simulation requirements definition, (2) concept identification, (3) concept selection, (4) concept development, and (5) prototype validation. The work has progressed into the concept development phase, which includes sub-scale tests of distortion generator elements.

The selected concept used an aerodynamic blockage method to effect distributions in total pressure. Shown in **Figure B.17**, the concept uses an array of porous blockage elements that open and close in patterns commensurate with the distortion pattern desired. The opening angle provides the means to vary the magnitude of the total pressure distortion. The generator may use square-shaped elements arranged on a Cartesian grid or trapezoidal-shaped elements on a polar grid (i.e. on rings of different radii). The concept development experiments adopted the polar arrangement.

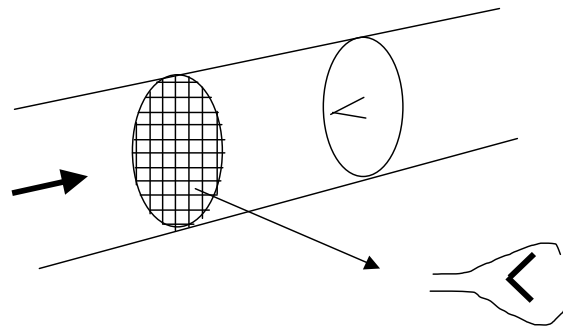


**Figure B.17 Transient Distortion Generator Concept – An Array of Blockage Elements Distributed Over**

In the future work, analysis of the results will be used to refine the definition of the distortion generator elements. The refinements will include element size, plan-form shape, porosity, and arrangement on the air supply duct cross section. The results will be used in the next phase of the development, assembly and testing of a sub-scale prototype distortion generator.

## THE DISTORTION SIMULATOR

For inlet flows that are distorted, the Aircraft Simulator not only provides information for plant inlet and exit conditions, but also supplies angle-of-attack and sideslip to a Distortion Simulator for determination of the inlet flow distortion present. The Distortion Simulator is envisioned to be a database of information correlated from both wind tunnel tests of the specific inlet and computational fluid dynamic calculations of that same inlet configuration. This information is fed into a Distortion Generator that will set a distortion pattern (includes both pressure and temperature distortion) that simulates what is expected in flight. The real engine test article feeds back its performance to the Aircraft Simulator and provides the propulsive power for the aircraft.

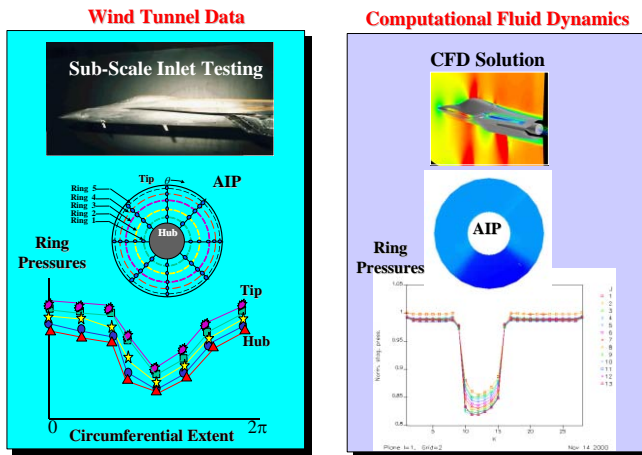


**Figure B.18 Inlet Data Obtained from Tests and CFD**

data and CFD solutions implemented in a database as illustrated in **Figure B.19**. Once the database is populated with AIP information, it can be used to drive the distortion generator to the desired conditions.

## B.5 PUTTING THE PIECES TOGETHER

Even though distorted Inflow capability of the Vision requires many hardware modifications to become reality, there are, as was the case with the Non-Distorted Inflow Phase, facility simulations which can provide an inexpensive way of determining the feasibility and approach of putting everything together. An overview of the whole Vision using numerical simulations is presented in **Figure B.20**.

The only simulation that has not been discussed is the 3D compressor simulation, **TEACC** (Turbine Engine Analysis Compressor Code). A complete description of the technology behind the development of **TEACC** is presented in **Ref. B.10**. **TEACC** will be used to modify compression system maps within the engine model when

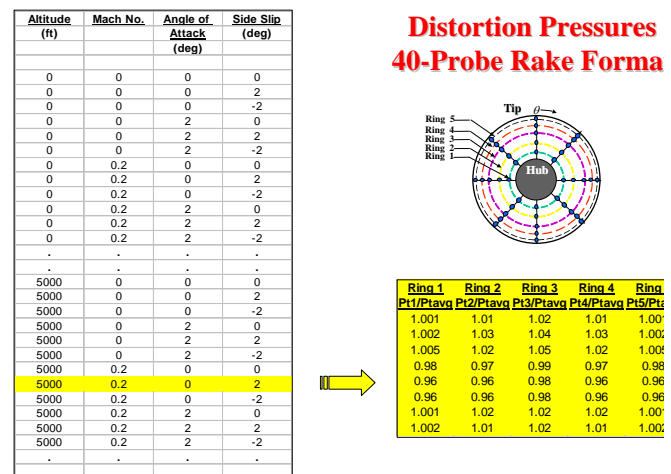


**Figure B.19 Distortion Simulator Database Concept**

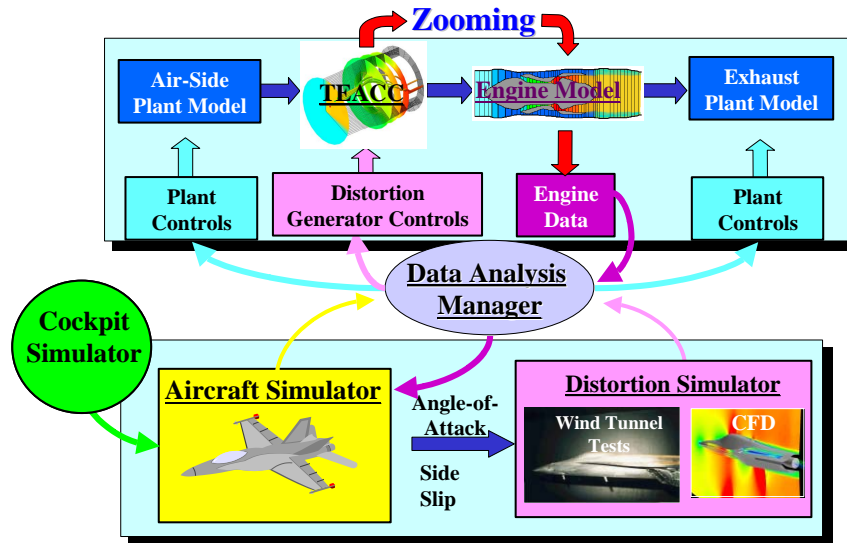


**Figure B.20 Plant Flight Simulation Vision – Distorted Inlet Flow – Numerical Simulation**

distortion is present. A zooming technique will be used as illustrated in **Figure B.20** to accomplish this task.

The initial activities deal with the implementation of **GENESIS** within the MATLAB environment for execution with the Plant Simulation. Plant Model passes the time-step to **GENESIS** for the next time of the Aircraft Simulation. Since **GENESIS** was developed as a FORTRAN “stand-alone” program, there are

integration issues. MATLAB is it’s own programming language, and as such, a FORTRAN program must be implemented as a “wrapped” executable. Major activities are thus the proper execution of **GENESIS** and its execution within the MATLAB environment.

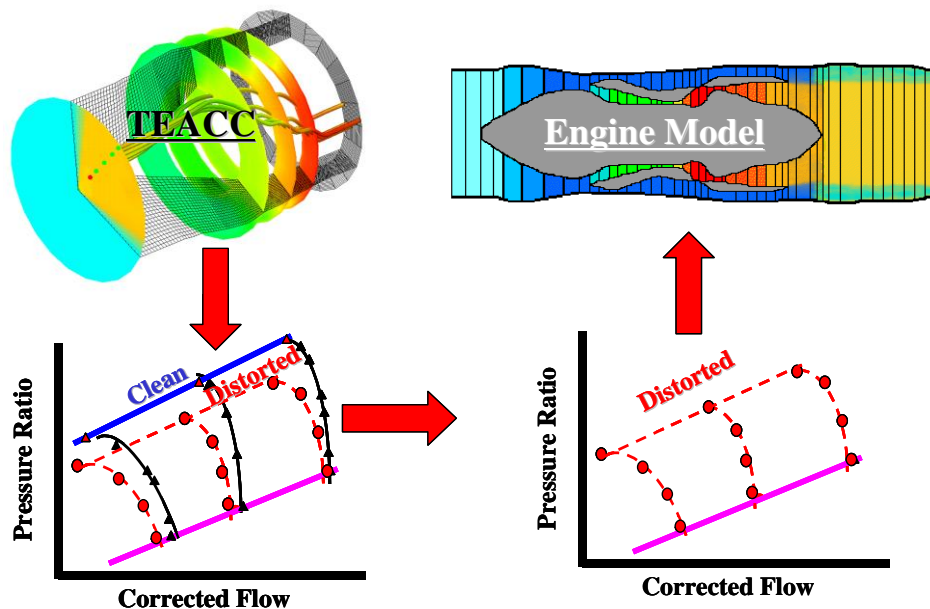


**Figure B.21 TEACC Zooming to Accomplish Modifications in Compression System Maps Due to Distortion**

The latter activities will be directed toward the development of the Distortion Simulator Database using an established aircraft, the F-16. This aircraft's inlet has been extensively tested in AEDC Wind Tunnels, but the data has not been saved from the 40-probe rakes. Much of the data has been reduced to a distortion index that does not quantify the AIP pressure distortion in the right form. Thus, CFD computations will be run to populate the Distortion Simulator for a typical maneuver.

## B.6 REFERENCES:

**B.1** "Aeropropulsion Systems Test Facility", AEDC Fact Sheet, AEDC Public Web Page -- <http://www.arnold.af.mil/aedc/factsheets/astf/ASTF.html>, April 1998.

**B.2** Montgomery, P. A., et.al., "Evolution of a Turbine Engine Test Facility to Meet the Test Needs of Future Aircraft". ASME International Gas Turbine Institute 2002 TurboExpo, Paper # TBD, June 2002.

**B.3** Montgomery, P. A., et. al., "A Real-Time Turbine Engine Facility Model and Simulation For Test Operations Modernization and Integration", ASME Paper # 2000-GT-0576, Presented at the ASME TurboExpo 2000 in Munich Germany, May 2000

**B.4** McKeehen., P. D., "**GENESIS** Simulation of a Modified Vista/F-16", AIAA Paper # 95-3381, Presented at Flight Simulation Technologies conference, Baltimore MD, August 1995.

**B.5** McKeehen, P. D., "Hypervelocity Vehicle Modeling and Simulation Using **GENESIS**", AIAA Paper # 99-4326, Presented at the AIAA Modeling and Simulation Technologies Conference and Exhibit, Portland, OR, August 1999.

**B.6** "AIRFOX **FLIGHTLAB**", AMST Systemtechnik Web Page, <http://www.amst.co.at/products/flitesim.htm>,

**B.7** Chappell, M. A., and McLaughlin, P. W., "Approach to Modeling Continuous Turbine Engine Operation from Startup to Shutdown," **Journal of Propulsion and Power**, Vol. 9, No. 3, May-June 1993, pp. 466 - 471.

**B.8** Davis, M. W., Jr, Hale, A. A., and D. Beale, "An Argument for Enhancement of the Current Inlet Distortion Ground Test Practice for Aircraft Turbine Engines", ASME Paper # 2001-GT-0507, Presented at the IGTI TurboExpo in New Orleans, LA, June 2001.

**B.9** Davis, M. W., Jr., et. al, "A Proposal for Integration of Wind Tunnel and Engine Test Programs for the Evaluation of Airframe-Propulsion Compatibility Using Numerical Simulations", ASME Paper # 99-GT-345, June 1999.

**B.10** Hale, A. A, and W. F. O'Brien, "A Three-Dimensional Turbine Engine Analysis Compressor Code (**TEACC**) for Steady-State Inlet Distortion", **Journal of Turbomachinery**, July 1998, pp.422-430



## APPENDIX C TABLE OF CONTENTS

APPENDIX C	Streamline Curvature Code (SLCC) HTSC Results .....	439
C.1	REPLICAS Calibration Procedure.....	439
C.2	Overall 1-D Maps.....	440
C.3	Transition of SLCC Solution to <b>TEACCSTALL</b> .....	445
C.4	Specific Data Analysis Tools.....	446

### APPENDIX C STREAMLINE CURVATURE CODE (SLCC) HTSC RESULTS

The streamline curvature code (**SLCC**), as described in [Section 4.3](#) was used to simulate the HTSC. The section will describe the calibration of the HTSC and the application of the **SLCC** to the HTSC at several flow points at 68.0% of the design speed line from WOD (wide-open discharge) to NS (near stall). These points were identified after reducing the data received from the Air Force Compressor Research Facility (CRF). The only data used in the **SLCC** calibration was clean inlet data since the **SLCC** solutions are axi-symmetric only. For the **SLCC** solutions, only points on the 68.0 % $N_{c,design}$  were included in the calibration with the stator 1 variable vanes set to -15.0 degrees, smooth casing treatment, HTSC rotor, and no screen. The following sections will describe the calibration procedures, comparison to data, and how the **SLCC** was used to develop characteristics for the higher fidelity **TEACCSTALL** code.

#### C.1 REPLICAS CALIBRATION PROCEDURE

As described in a previous section ([Section 3.2.3](#)), data rakes for total pressure and total temperature were located at the inlet of the compressor, at the inlet to each of the two stators, and at the exit of last stator. Data was at several radii and circumferential locations. For the purposes of the axi-symmetric **SLCC**, all of the circumferential content of the data was averaged while maintaining the radial content. The circumferentially averaged data was then used to do a radial calibration of the **SLCC** at the afore mentioned 6 data points of the 68.0 %  $N_{c,design}$ . A previously develop calibration method using the **REPLICAS** (Robust, Efficient Procedures and Logic for the Implementation of Computerized Analysis and Simulation) non-linear solver was used to calibrate the **SLCC** correlations to the HTSC application. This method allows for an input of the absolute total pressure and total temperature conditions (rotor), or absolute total pressure and circumferential velocity (stator) and letting **REPLICAS** adjust the correlations radially until the **SLCC** solution matches the radial distribution provided to **REPLICAS**.

The way the test data was used in the calibration is described in this section. For this particular application, the **SLCC** was calibrated to a radial distribution of data taken at the inlet to the stators and exit of the machine. [Figure C.1](#) shows a cartoon of the data locations by the blue "B", "D", and "F" circles. A circumferentially averaged radial distribution is known at these points. However, the calibration technique requires that we know totals and velocities at the exit of the bladed regions. Therefore, the data at location "B" (stator 1 inlet) was translated to the exit of rotor 1 (location "A") at constant percent-span. Data taken at location "D" (stator 2 inlet) was also translated to the exit of rotor 2 (location "C"). Data taken by the arc probes at the exit of the machine was also translated for location "F" to the exit of stator 2 (location "E"). With these translations, **REPLICAS** has enough information (radial distribution of total pressure and total temperature) to calibrate rotor 1 and rotor 2. Since no information is known about the flowfield across stator 1, it is left un-calibrated. Total pressure and total temperature is known at the exit of stator 2. However, to cross a stator, total pressure and circumferential velocity must be known at the exit of the stator. Since this is the last stator of the machine, the design intent

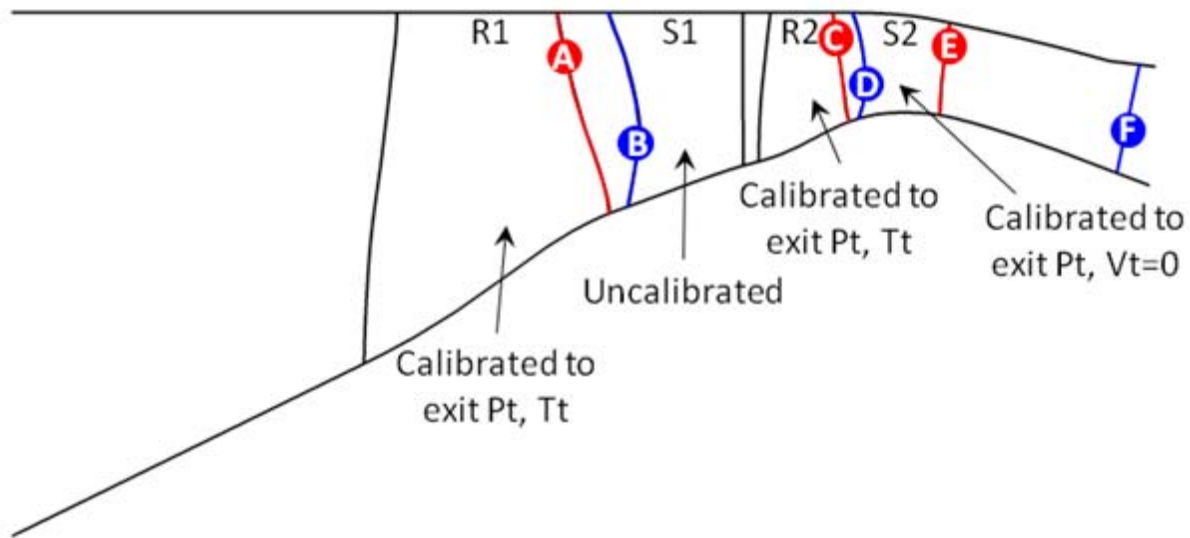


**Figure C.1 REPLICAS Calibration Procedure**

is most likely to take all of the circumferential velocity out of the flow; it was assumed for calibration purposes that the exit circumferential velocity of stator 2 was 0.

With **REPLICAS** dependents (totals and velocities) and independents (add loss and add deviation) configured, each of the 6 flow points was run through the calibration procedure to automatically calibrate the correlations to match the dependents. The results of this calibration procedure for each of the 6 flow points are provided in the next six sections.

## C.2 OVERALL 1-D MAPS

**Figure C.2** shows the overall characteristics of the **SLCC** compared to the CRF data for the six flow points calibrated. The six points are labeled:

WOD – Wide-Open Discharge

PE – Peak Efficiency

OL1 – Operating Line 1

OL2 – Operating Line 2

OL3 – Operating Line 2

NS – Near stall

The data is represented by black diamonds, while the **SLCC** results are shown in blue circles. The **SLCC** pressure ratios are consistently just slightly below the data. Since the radial distribution results of the **SLCC** match the data much closer (as shown in a later section), it can be assumed that the differences are in the 1-D averaging techniques. The maximum error occurs at the OL1 point with an **SLCC** error of -0.8%. Temperature ratio is generally closer than pressure ratio. The OL2 point is where the maximum error is -0.2%. The efficiency maximum

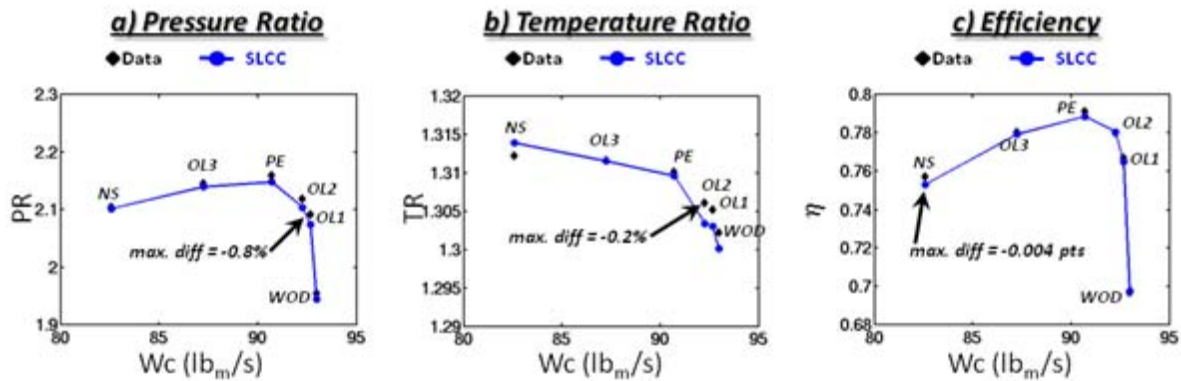


**Figure C.2 Overall 1-D Characteristics of the HTSC**

error -0.004 points at the NS point. In general the **SLCC** does a good job of matching the test data after calibration.

### WOD SOLUTION

The wide-open-discharge (WOD) point is the flow point farthest into choke on the 68.0%  $N_{c,design}$  speed line. The corrected flow at the point was 92.97 lb<sub>m</sub>/s. **Figure C.3** shows the radial distribution of totals at the same location that data was taken: stator 1 inlet, stator 2 inlet, and plane 23 (exit plane). The data is represented by symbols of 3 different colors for the three different circumferential rakes. There appears to be a spread of the totals circumferentially, so the average is what **SLCC** was calibrated to with **REPLICAS**. As can be seen by **Figure C.3**,

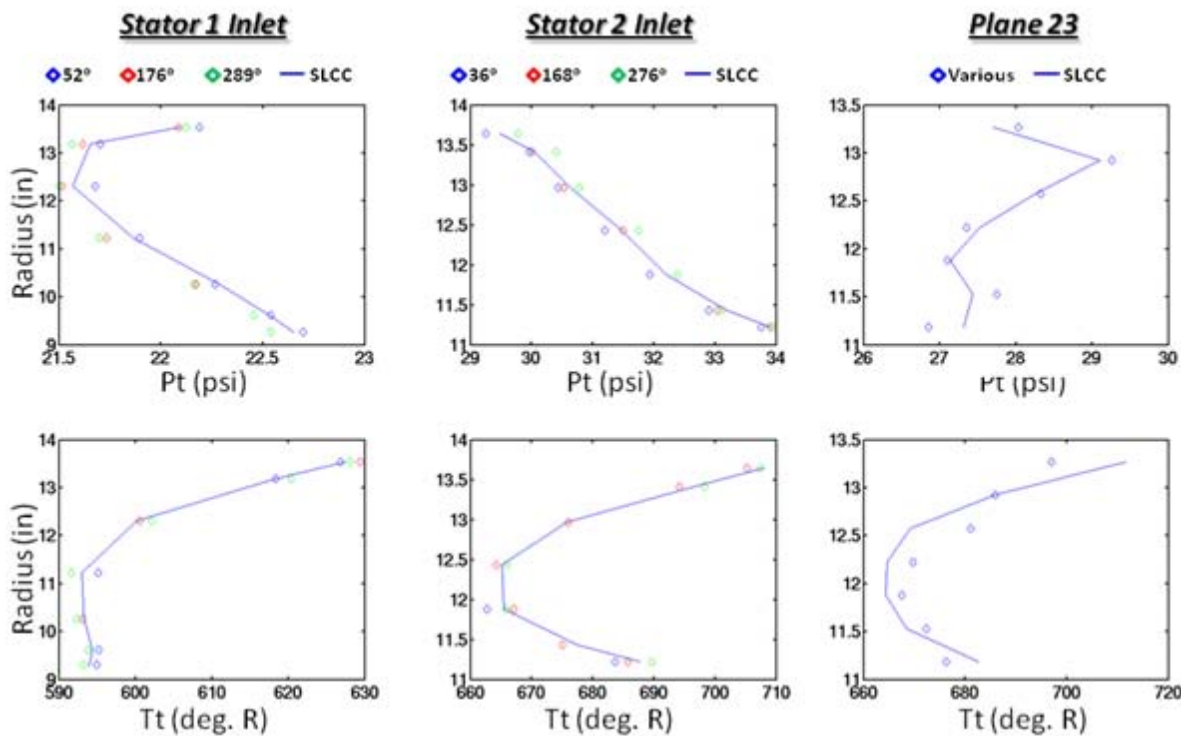


**Figure C.3 Radial Calibration – WOD  $W_c=92.97$  lb<sub>m</sub>/sec**

the **SLCC** solution follows the radial distribution of the data very well at the stator inlets. The total pressure at Plane 23 also closely matches the data for total pressure. However, there is some deviation in total temperature. Since temperature doesn't change across a stator in the **SLCC** (no heat transfer is modeled), it is only slightly changed from the inlet to stator 2 caused by a redistribution of the flow. In the data, there appears to be a fairly significant drop in total temperature across the stator. This can only be explained by heat transfer to the casing walls or error in the instrumentation, neither of which can the **SLCC** reproduce. Each of the six flow points shows this behavior.

### **OL1 SOLUTION**

The operating line 1 (OL1) point is the flow point with just slightly lower mass flow than the WOD on the 68.0%  $N_{c,design}$  speed line. The corrected flow at the point was 92.65 lb<sub>m</sub>/s. **Figure C.4** shows the radial distribution of totals at the same location that data was taken: stator 1 inlet, stator 2 inlet, and plane 23 (exit plane). The data is represented by symbols of 3 different colors for the three different circumferential rakes. There appears to be a spread of the totals circumferentially, so the average is what **SLCC** was calibrated to with **REPLICAS**. As can be seen by **Figure C.4**, the **SLCC** solution follows the radial distribution of the data very well at the stator inlets. The total pressure at Plane 23 also closely matches the data for total pressure. However, there is some deviation in total temperature as explained the WOD solution section.

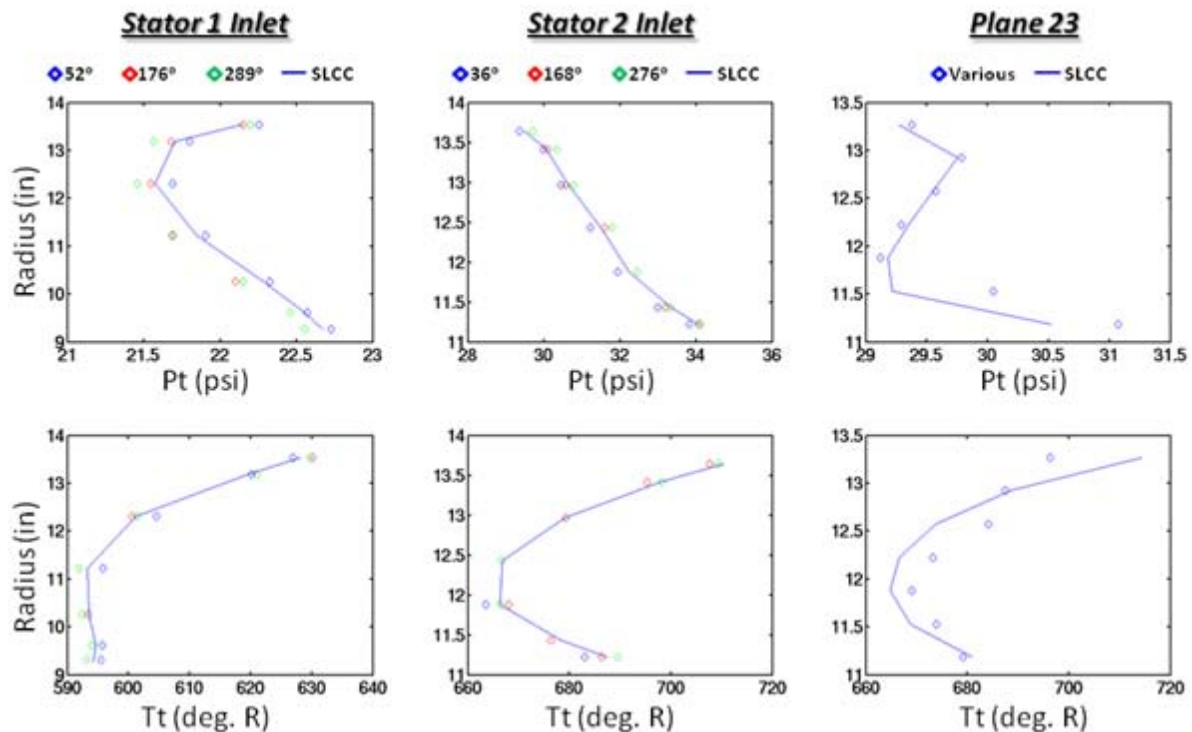


**Figure C.4 Radial Calibration – OL1  $W_c=92.65$  lb<sub>m</sub>/sec**

### **OL2 SOLUTION**

The operating line 2 (OL2) point is the next flow point in the on the 68.0%  $N_{c,design}$  speed line. The corrected flow at the point was 92.26 lb<sub>m</sub>/s. **Figure C.5** shows the radial distribution of

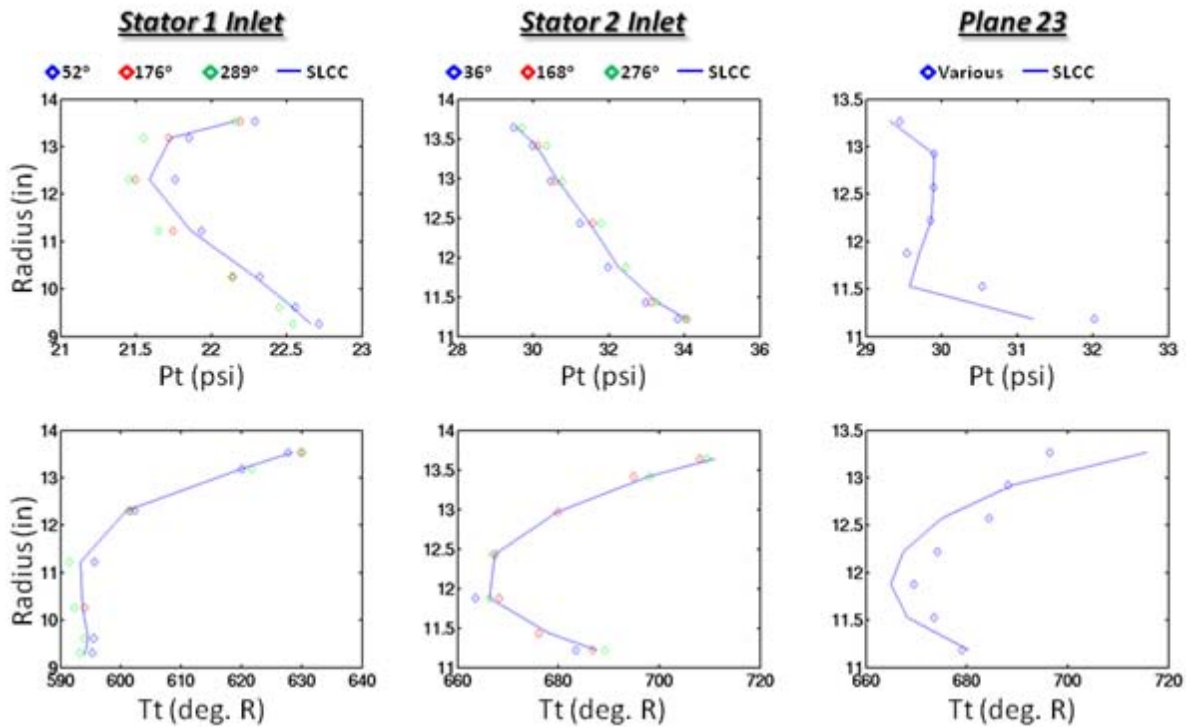


**Figure C.5 Radial Calibration – OL2  $W_c = 92.26 \text{ lb}_m/\text{sec}$**

totals at the same location that data was taken: stator 1 inlet, stator 2 inlet, and plane 23 (exit plane). The data is represented by symbols of 3 different colors for the three different circumferential rakes. There appears to be a spread of the totals circumferentially, so the average is what **SLCC** was calibrated to with **REPLICAS**. As can be seen by **Figure C.5**, the **SLCC** solution follows the radial distribution of the data very well at the stator inlets. The total pressure at Plane 23 also closely matches the data for total pressure. However, there is some deviation in total temperature as explained the WOD solution section.

### **OL3 SOLUTION**

The operating line 3 (OL3) point is the next flow point in the on the 68.0%  $N_{c, \text{design}}$  speed line. The corrected flow at the point was 87.23  $\text{lb}_m/\text{s}$ . **Figure C.6** shows the radial distribution of totals at the same location that data was taken: stator 1 inlet, stator 2 inlet, and plane 23 (exit plane). The data is represented by symbols of 3 different colors for the three different circumferential rakes. There appears to be a spread of the totals circumferentially, so the average is what **SLCC** was calibrated to with **REPLICAS**. As can be seen by **Figure C.6**, the **SLCC** solution follows the radial distribution of the data very well at the stator inlets. The total pressure at Plane 23 also closely matches the data for total pressure. However, there is some deviation in total temperature as explained the WOD solution section.

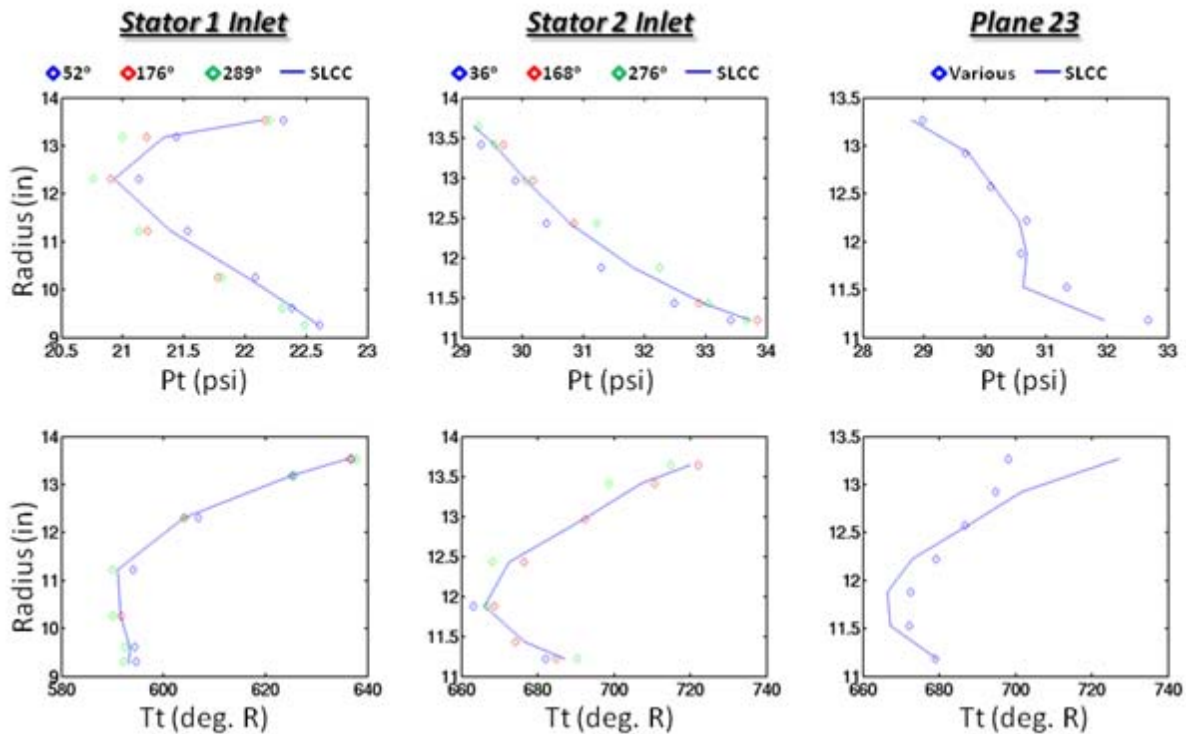


Figure C.6 Radial Calibration – OL3  $W_c = 87.23 \text{ lb}_m/\text{sec}$

## PE SOLUTION

The peak efficiency (PE) point is the flow point with the highest efficiency on the 68.0%  $N_{c, \text{design}}$  speed line. The corrected flow at the point was  $90.70 \text{ lb}_m/\text{s}$ . Figure C.7 shows the radial distribution of totals at the same location that data was taken: stator 1 inlet, stator 2 inlet, and plane 23 (exit plane). The data is represented by symbols of 3 different colors for the three different circumferential rakes. There appears to be a spread of the totals circumferentially, so the average is what **SLCC** was calibrated to with **REPLICAS**. As can be seen by Figure C.7, the **SLCC** solution follows the radial distribution of the data very well at the stator inlets. The total pressure at Plane 23 also closely matches the data for total pressure. However, there is some deviation in total temperature as explained the WOD solution section.



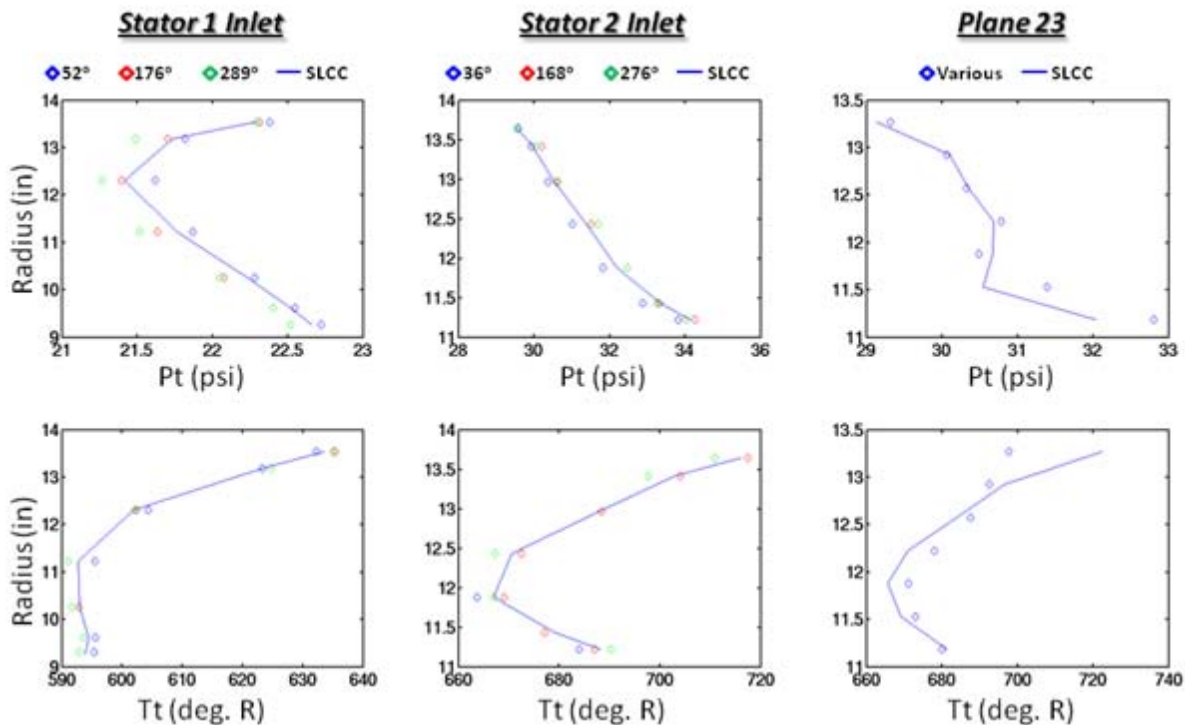


Figure C.7 Radial Calibration – PE  $W_c=90.70 \text{ lb}_m/\text{sec}$

### NS SOLUTION

The near-stall (NS) point is the last flow point in the on the 68.0%  $N_{c,\text{design}}$  speed line in this analysis. The corrected flow at the point was  $82.58 \text{ lb}_m/\text{s}$ . [Figure C.8](#) shows the radial distribution of totals at the same location that data was taken: stator 1 inlet, stator 2 inlet, and plane 23 (exit plane). The data is represented by symbols of 3 different colors for the three different circumferential rakes. There appears to be a spread of the totals circumferentially, so the average is what **SLCC** was calibrated to with **REPLICAS**. As can be seen by [Figure C.8](#), the **SLCC** solution follows the radial distribution of the data very well at the stator inlets. The total pressure at Plane 23 also closely matches the data for total pressure. However, there is some deviation in total temperature as explained the WOD solution section.

### C.3 TRANSITION OF SLCC SOLUTION TO TEACCSTALL

The **TEACCSTALL** code (described in detail in [Section 4.7](#)) can be used to model stall initiation in the presence of complex distortions. To drive the **TEACCSTALL** code, a radial distribution of characteristics at the machine inlet and exit, and between each bladed region is needed at multiple flow points. These can be provided by various methods. In the past, mixing plane CFD has provided the characteristics, but at this point in the HTSC effort, a 4 blade row HTSC CFD simulation is not available. So the quasi-3D, axi-symmetric **SLCC** solutions can be used to generate the characteristics that drive the higher fidelity (fully 3D) **TEACCSTALL** code to model stall initiation in the presence of complex distortions. A MATLAB<sup>®</sup> script was used to reduce the solutions of each of these flow points to a non-dimensional characteristic file for use in the **TEACCSTALL** code. The results of these simulations are provided in [Section 3.2.3](#).

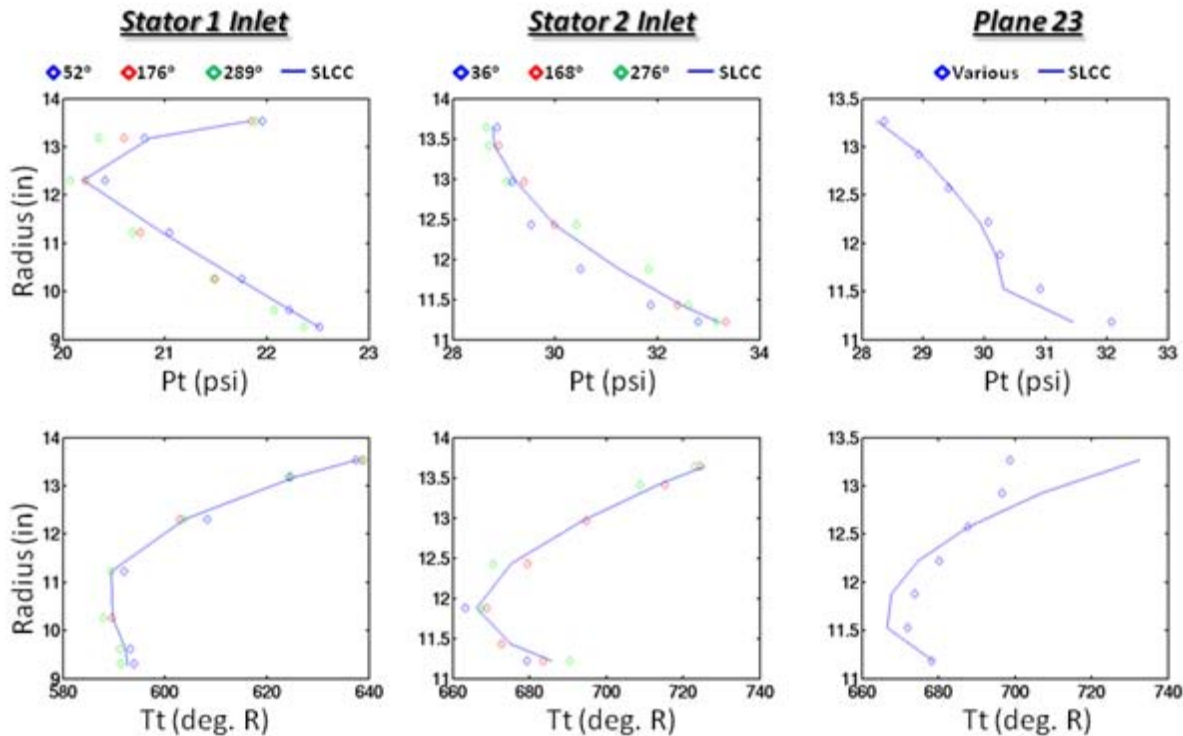


Figure C.8 Radial Calibration – NS  $W_c=82.58 \text{ lb}_m/\text{sec}$

## C.4 SPECIFIC DATA ANALYSIS TOOLS

### 1-D PLOTS

The 1-D plots of the **SLCC** comparison to Data were generated using MATLAB<sup>®</sup> scripts specifically created to read in “spreadsheet-like” data. The data points “spreadsheet” data was generated in the process of reducing the entire CRF generated data. The **SLCC** solution data from the 1-D summary in the **SLCC.01.out** was manually entered into “spreadsheet” files. Both of these files have similar content and were read in by the MATLAB<sup>®</sup> script. The 1-D averaged total pressure ratio, total temperature ratio, and efficiency were then plotted as a function of corrected mass flow. The resulting plots were exported to PNG (Portable Network Graphics) image files.

### 2-D RADIAL DISTRIBUTION PLOTS

The 2-D radial distribution of totals files were generated by a combination of FIELDVIEW<sup>®</sup> and MATLAB<sup>®</sup> scripts. The data points were written to a specifically formatted “spreadsheet-like” file at the time the data from the CRF was reduced and averaged. At the same time, a file with the X (axial), R (radial), and  $\theta$  (theta) locations was written out. Using the **SLCC.01.x** (geometry) and **SLCC.01.q** (solution) files were used in FIELDVIEW<sup>®</sup> to generate surface contours. From the surface contours and the locations specified in the X, R,  $\theta$  file, the point probe function in FIELDVIEW<sup>®</sup> was used to interpolate the **SLCC** solution to the exact same locations the data probes were in the flow field. The FIELDVIEW<sup>®</sup> results were output in a spreadsheet-like format. Both the data and the FIELDVIEW<sup>®</sup> generated output were read into a specifically configured MATLAB<sup>®</sup> script to plot the comparison of data and **SLCC** radial distributions of total

pressure and total temperature. The resulting plots were exported to PNG (Portable Network Graphics) image files.

### **STREAMLINE SOLUTIONS**

The streamline solutions were generated in FIELDVIEW® using the **SLCC.01.x** file generated from a converged solution of the **SLCC**. The figure is the grid of streamlines that is generated from the solution of the **SLCC**. The resulting figure was exported to JPG image files.

### **CONTOUR SOLUTIONS**

The contour plots were generated in FIELDVIEW® using the standard PLOT3D files, **SLCC.01.x** and **SLCC.01.q**, generated from a converged solution of the **SLCC**. The contours are smooth contours for Normalized Stagnation Pressure, Normalized Stagnation Temperature, and Mach Number plotted on a computational surface ( $K=1$ ). The resulting figure with the legend included was exported to JPG image files.

## APPENDIX D TABLE OF CONTENTS

APPENDIX – D	One-Dimensional Compressor Stage Characteristics .....	448
D.1	Unstalled Forward Flow .....	449
D.2	Stalled Forward Flow Modeling Technique .....	450
D.3	Reversed Flow Modeling Technique .....	452
D.4	Empirical Observations and Additions .....	453
D.4.1	Criteria Used For Stall Inception .....	453
D.4.2	Stalled-Flow Jet Exit Angle .....	454
D.4.3	Recovery Hysteresis .....	454
D.4.4	Reversed-Flow Pressure Prediction .....	455
D.5	Assembly into a Wide Range Prediction Model .....	455
D.5.1	Application to a Low-Speed Compressor .....	456
D.5.2	Application to a High-Speed Compressor .....	457
D.6	Stage Model Summary .....	461
D.7	Additional References .....	461

## APPENDIX D ONE-DIMENSIONAL COMPRESSOR STAGE CHARACTERISTICS

As has been seen in the previous examples, detailed stage-by-stage dynamic models require stage characteristics for the entire flow range spanning near design flows, stall, and reversed flow. The characteristics used were either taken from the modeled experiment, or estimated for ranges where the experimental values were not available. It is, of course, desirable to predict stage characteristics from design information for a complete simulation prior to an experiment. The following material summarizes results of an effort] to develop a stage characteristic prediction method.

### CITED EXAMPLE(S)

**D.1** O'Brien, W. F., "Dynamic Simulation of Compressor and Gas Turbine Performance", AGARD Lecture Series, LS-183, May 1992

**D.2** Bloch, G. S., and W. F. O'Brien, "A Wide-Range Axial- Flow Compressor Stage Performance Model," 37th International Gas Turbine Conference, ASME, Cologne, Germany, June 1-4, 1992.

**Note:** Sections from both cited references have been re-printed with permission of the authors.

### MODELING TECHNIQUE

The elementary axial-flow compressor stage mean-line analysis principles for forward, unstalled flow are well known. This type of analysis assumes incompressible, inviscid flow through a single stage and uses empirical correlations to estimate the pressure losses and flow deviation in each blade row. The classical correlations are given by Lieblein [D.9] and Carter [D.10], respectively for un-stalled operation.

## D.1 UNSTALLED FORWARD FLOW

A typical compressor stage and the flow angles associated with forward flow are shown in **Figure D.1**. Using the momentum equation for this geometry, the Euler turbine equation gives the stage temperature rise. For incompressible flow, the total pressure rise for the stage is related to the total temperature rise and the blade row pressure losses by

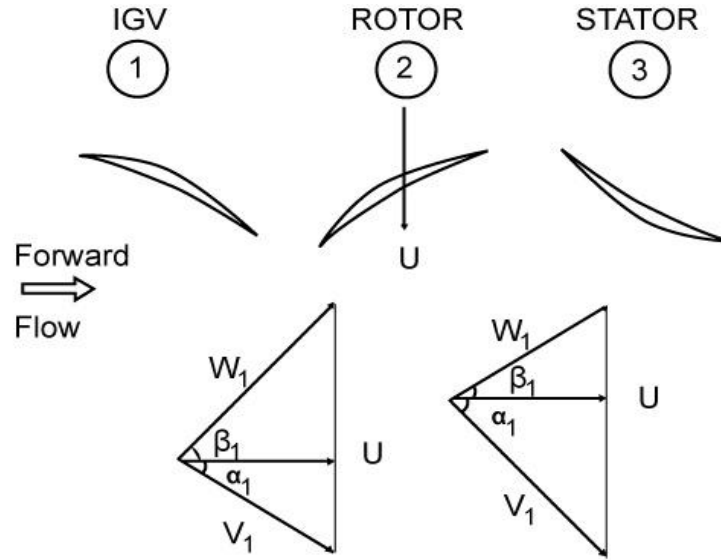


**Figure D.1 Mean Radius Section of a Compressor Stage in Forward Flow Operations**

$$\frac{\Delta T_o}{T_{o1}} = \frac{T_{o2} - T_{o1}}{T_{o1}} = \frac{U^2}{c_p T_{o1}} \left\{ 1 - \frac{V_{x1}}{U} \left( \frac{V_{x2}}{V_{x1}} \tan \beta_2 + \tan \alpha_1 \right) \right\} \quad \text{Eqn. D-1}$$

For incompressible flow, the total pressure losses are related to the cascade loss parameters by

$$P_{o2} - P_{o1} = \rho c_p \Delta T_o - (\Delta P_{oR} + \Delta P_{oS}) \quad \text{Eqn. D-2}$$

For incompressible flow, the stage efficiency is given by

$$\eta = 1 - \frac{\Delta P_{oR} + \Delta P_{oS}}{\rho c_p \Delta T_o} \quad \text{Eqn. D-3}$$

Since the angles in **Eqn. D-1** are flow angles and the pressure losses cannot be calculated directly, approximations for the deviation angle and loss coefficients must be made. To estimate the flow exit angle in the un-stalled, forward flow regime the model uses Carter's

correlation, which is for near design operation. Because the deviation does not change significantly until the blade stalls, this angle is assumed to be constant

$$\beta_2 - \beta_2' = \frac{m\theta}{\sqrt{\sigma}} \quad \text{Eqn. D-4}$$

where m is obtained from the reference.

The blade losses are calculated as the sum of profile, annular and secondary losses. The profile losses are given by Lieblein [D.9] and the annulus and secondary losses are given by Dixon [D.11] as follows.

$$\varpi_P = 2\sigma \frac{\cos^2 \beta_1}{\cos^3 \beta_2} \left( \frac{\theta^*}{c} \right)_2 \left\{ \frac{\frac{2H_2}{3H_2-1}}{\left[ 1 - \left( \frac{\theta^*}{c} \right)_2 \frac{\sigma H_2}{\cos \beta_2} \right]^3} \right\} \quad \text{Eqn. D-5}$$

$$\varpi_a = 0.02\sigma \left( \frac{c}{H} \right) \frac{\cos^2 \beta_1}{\cos^3 \beta_m} \quad \text{Eqn. D-6}$$

$$\varpi_s = \frac{0.072}{\sigma} \frac{\cos^2 \beta_1}{\cos^3 \beta_m} (\tan \beta_1 - \tan \beta_2)^2 \quad \text{Eqn. D-7}$$

where

$$\tan \beta_m = \frac{(\tan \beta_1 + \tan \beta_2)}{2} \quad \text{Eqn. D-8}$$

## D.2 STALLED FORWARD FLOW MODELING TECHNIQUE

For in-stall, forward flow operation, the flow is assumed to separate from the blade leading edge, as shown in Figure D.2. The approximation of Moses and Thomason [D.12] is used in the determination of the jet exit angle.

The jet velocity ratio is given by

$$\frac{V_2}{V_1} = \frac{-b \pm \sqrt{b^2 - 4ac}}{2a} \quad \text{Eqn. D-9}$$

where



$$a = 1 + \frac{0.15\sigma}{\cos \beta_1} \quad b = \frac{-2 \cos \beta_1 \cos \delta}{\cos \gamma} \quad c = \frac{2 \cos \beta_1 \cos \alpha}{\cos \gamma} - 1$$

To give meaningful results, only the positive result in **Eqn. D-9** is used. The fully mixed flow angle and loss coefficient are given by

$$\tan \beta_3 = \frac{V_2 \sin \beta_2}{V_1 \cos \beta_1} \quad \text{Eqn. D-10}$$

$$\varpi = \frac{P_{o1} - P_{o3}}{\rho V_1^2 / 2} \quad \text{Eqn. D-11}$$

$$\varpi = \left(1 + \frac{0.15\sigma}{\cos \beta_1}\right) \frac{V_2^2}{V_1^2} + 2 \cos \beta_1 \left(\cos \beta_1 - \frac{V_2}{V_1} \cos \beta_2\right) - \frac{\cos^2 \beta_1}{\cos^2 \beta_3} \quad \text{Eqn. D-12}$$

Because the profile losses for a stalled blade row are much larger than the annulus and secondary losses, the latter are ignored in this flow regime.

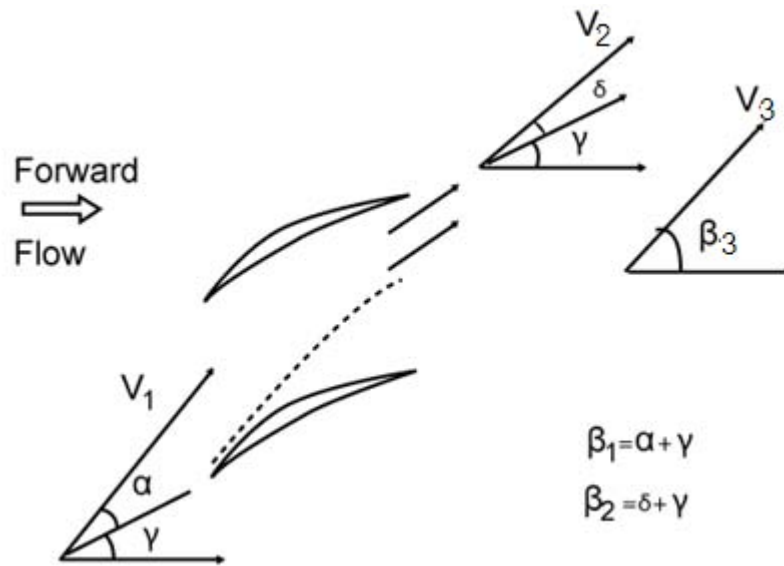


**Figure D.2 Compressor Cascade Geometry and Nomenclature for Stalled Operation**

### D.3 REVERSED FLOW MODELING TECHNIQUE

A typical compressor stage and the flow angles associated with reversed flow are shown in **Figure D.3**. The development of the basic stage performance equations is a direct extension of that presented previously with the subscripts changed to reflect the direction of flow.

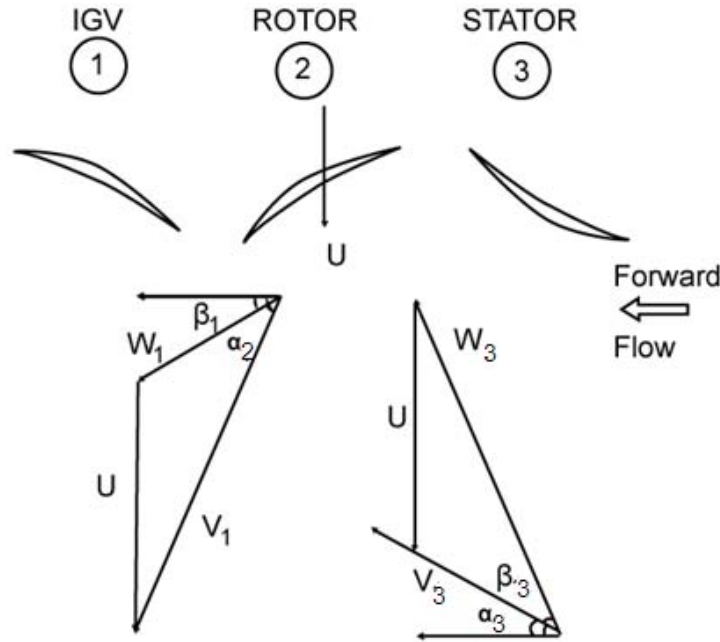


**Figure D.3 Mean Radius Section of a Compressor Stage in Reversed-Flow Operation**

Using the moment of momentum equation for this geometry, Euler's turbine equation gives the stage temperature rise.

$$\frac{\Delta T_o}{T_{o2}} = \frac{T_{o2} - T_{o1}}{T_{o2}} = \frac{-U^2}{c_p T_{o2}} \left\{ 1 - \frac{V_{x1}}{U} \left( \frac{V_{x2}}{V_{x1}} \tan \alpha_2 + \tan \beta_1 \right) \right\} \quad \text{Eqn. D-13}$$

It should be noted that the compressor does work on the fluid in the direction of flow, increasing its temperature in that direction. When the compressor is operating in reversed flow, the temperature at station 1 is greater than at station 2 and the result in **Eqn. D-13** is negative. The flow angle,  $\beta$ , is assumed to be the blade metal angle as suggested by Turner and Sparkes [D.13] and by Koff and Greitzer [D.14].

For incompressible flow in the reversed direction, the pressure losses are added in **Eqn. D-14** because they are positive in the direction of flow, which is from station 2 to station 1.

$$P_{o2} - P_{o1} = \rho c_p \Delta T_o + (\Delta P_{oR} + \Delta P_{oS}) \quad \text{Eqn. D-14}$$

In a cascade experiment to study reversed flow, Carneal [D.15] showed that losses in the reversed-flow region, when non-dimensionalized by wheel speed, collapse onto a single parabola as shown in **Figure D.4**.

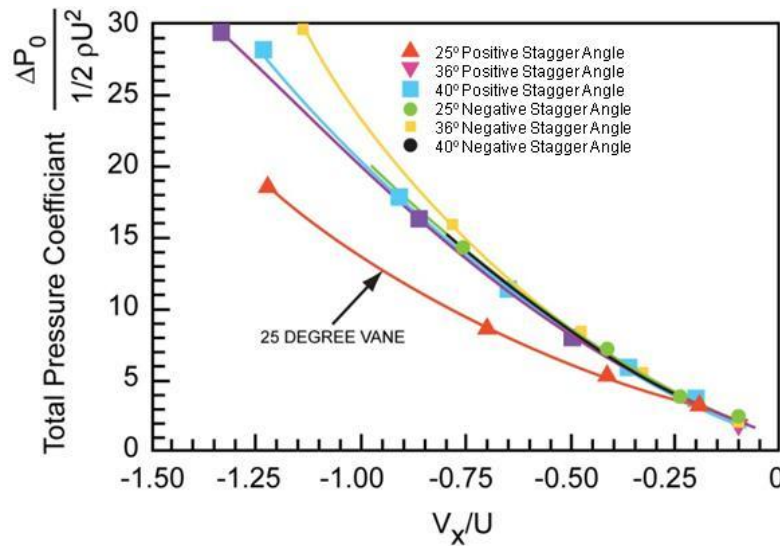


**Figure D.4 Corrected Pressure Losses in a Reversed-Flow Compressor Cascade**

losses as a function of mass flow, and this result is used in [Eqn. D-14](#) to calculate the stage pressure rise. Gamache [\[D.3\]](#) noted that the last stage stator in reversed flow functions in the same manner as the IGV during forward flow. The flow enters the blade row with a small angle of attack and is turned from the axial direction, accelerating the flow like a nozzle. Gamache measured a negligible pressure loss across this blade row in reversed-flow operation, so the model neglects the losses for the last stator of the compressor when operating in reversed flow. The stage efficiency ([Eqn D-3](#)) is not a meaningful number in reversed flow because the large pressure losses in the reversed flow and the use of correction factors discussed in a later section often make the result fall outside of the bounds of  $0 \leq \eta \leq 1$ .

## D.4 EMPIRICAL OBSERVATIONS AND ADDITIONS

Although the present model is based on fundamental fluid mechanics and experiments, some empirical additions have been necessary to achieve the desired agreement with measured characteristics. These additions were based on logical extensions of the published literature.

### D.4.1 Criteria Used For Stall Inception

Yocum [\[D.16\]](#) reported the angle of incidence at which flow separation would occur in a test cascade to be 8 degrees. Longley and Hines [\[D.17\]](#) reported that a stage operating as part of a multistage compressor can remain un-stalled at flows much lower than the isolated clean-flow stall point. It has been suggested that the pumping action of the downstream stages tends to prevent upstream flow separation. In an attempt to model this effect, the angle of incidence at which separation occurs is assumed to be the sum of the isolated stall incidence (8 degrees) and a correction for the location of the stage in a multistage environment, which leads to the following expression for stalling incidence.

$$i_{\text{stall}} = 8^\circ + a\Delta i$$

**Eqn. D-15**

While the data for reversed-flow losses were derived from cascade tests, it is possible to express the results in terms of wheel speed for a rotating cascade. Although the loss curve for one stagger angle diverges from the others at reversed flow coefficients less than -0.25, the region of typical compressor operation is  $V_x/UT - 0.25$ , even during a deep surge cycle. The implication of this result is that the reversed-flow losses are reasonably approximated as a function of mass flow only, independent of flow angle, solidity, blade shape, and other flow details. A parabola fit to the five coincident curves of Carneal's data is used to determine the blade row

Where 
$$a = \frac{\text{current stage \#}-1}{\text{total \#stages}-1} \quad \Delta i = i_{1\text{st stage stall}} - 8^\circ$$

The value used for the first stage stalling incidence was obtained from the first stage of the 3-stage compressor tested by Gamache [D.3], which stalled at 16 degree angle of incidence. If it is assumed that this result is generally applicable, the bounds on the incidence angle for separation are  $8 \leq i_{\text{stall}} \leq 16$  with  $8^\circ$  used for the last stage and  $16^\circ$  used for the first stage of a modeled compressor. This correlation was applied to all stages modeled and reported here. When a blade row stalls, the flow at the trailing edge consists of a high velocity jet near the pressure surface and a separated, recirculating region near the suction surface. It is expected that the wake will not have sufficient time to mix to a uniform condition before reaching the downstream blade row and that the recirculating region will be sufficient to initiate stall of the downstream row. For this reason, the model assumes that when the rotor stalls, the downstream stator stalls as well.

#### D.4.2 Stalled-Flow Jet Exit Angle

The reasoning used to determine the stalled flow jet exit angle is similar to that presented in the previous section. The approximation of Moses and Thomason [D.12] suggests that the flow leaves the trailing edge at approximately the stagger angle. The present author suggests that the pumping action of the downstream stages which delays the onset of stall in the upstream stages tends to reduce the extent of separation once stall occurs. The jet angle is assumed to be the sum of the trailing edge blade angle and a correction for the location of the stage in a multistage environment, which suggests the following correlation for the jet exit angle.

$$\beta_2 = \beta'_2 + a(\beta'_2 - \gamma) \quad \text{Eqn. D-16}$$

Where

$$a = \frac{\text{current stage \#}-1}{\text{total \#stages}-1}$$

The resulting bounds on the exit jet angle are  $\beta'_2 \leq \beta_2 \leq \gamma$  with the lower bound of  $\beta'_2$  used for the first stage and  $\gamma$  for the last stage.

#### D.4.3 Recovery Hysteresis

It is well-known that a compressor will not recover from stall until the mass flow is increased to a value greater than that which existed when stall was initiated, but the extent of the hysteresis that will be present is not well understood. The present model predicts the stage performance in the region where the characteristics are double valued, but does not attempt to calculate the extent of the hysteresis. To include this effect in the model, the stalled flow calculations are begun with an incidence of  $6^\circ$  before stall inception. This selected amount of hysteresis is considered reasonable based on experience of the author, but cannot be calculated by any present theory. Because the stalled calculations involve solving the quadratic in Eqn. D-9, solution is not possible for all incidence angles and not all of the predicted stage characteristics presented below show the full  $6^\circ$  of hysteresis.

#### D.4.4 Reversed-Flow Pressure Prediction

The flow field in a compressor operating in annulus reversed flow is not well understood, as there has been little research performed in this flow regime. The present model predicts reversed-flow performance with reference to the experiments of Carneal [D.15] and Eqn. D-12, with an empirical correction in the form of Eqn. D-15 to improve agreement with experiments.

$$P_{o2} - P_{o1} = a_1 \rho c_P \Delta T_o + a_2 (\Delta P_{oR} + \Delta P_{oS}) + a_3 \quad \text{Eqn. D-17}$$

Where  $a_1 = 0.31$ ;  $a_2 = 1.33$   $a_3 = 0.20$

By use of the performance of the first stage of the compressor tested by Gamache [D.3], the values for the coefficients in the above equation were obtained and were used in all predictions presented. It should be noted that at this time there is no theory to predict these coefficients.

#### D.5 ASSEMBLY INTO A WIDE RANGE PREDICTION MODEL

A full-range stage performance computer model (**FULRANGE**) was developed as an assembly of the methods discussed in the previous sections. To implement the model over the range of mass flow coefficients in the forward flow regime, the relative flow angle at the rotor inlet is varied from zero angle of attack to zero flow (relative flow angle is  $90^\circ$ ) in one degree increments and the appropriate flow calculation is applied. To generate the reversed-flow characteristics, the model increments the mass flow index,  $V/U$ , by a fixed (negative) amount and the reversed-flow calculations are performed. The information required by the model to predict stage performance is the rotor and stator mean-radius geometry, as summarized in Table D.1.

<b>Rotor Blade Leading Edge Angle</b>
<b>Rotor Blade Trailing Edge Angle</b>
<b>Rotor Blade Stagger Angle</b>
<b>Rotor Blade Mean Radius</b>
<b>Number of Rotor Blades</b>
<b>Rotor Blade chord</b>
<b>Rotor Blade Span</b>
<b>Rotor Blade Thickness/Chord Ratio</b>
<b>IGV or (upstream) Stator Exit Flow Angle</b>
<b>Stator Blade Leading Edge Angle</b>

**Table D.1 FULRANGE Model Input Parameters.**

### D.5.1 Application to a Low-Speed Compressor

To verify the accuracy of the **FULRANGE** technique, the model was used to predict the performance of the low-speed 3-stage rig [D.3]. This compressor had a constant flow path annulus with three non-repeating stages. For this machine, a stage was defined as a rotor and the downstream stator. The predicted and measured pressure characteristics for this machine are presented in Figure D.5. The predicted characteristics showed very good qualitative agreement in the forward flow region and excellent agreement in the reversed flow region. The prediction has the same curvature as the measured characteristic throughout the entire flow regime and has no unexplained discontinuities.

For all 3 stages of this machine, the **FULRANGE** model predicted the flow coefficient,  $V_x/U$ , within 0.01 of the measured value for transition to abrupt stall. It should be noted that this difference between predicted and measured transition represents an error of less than  $1^\circ$  angle of incidence to the rotor. The un-stalled pressure prediction was within 0.15 of the measured values for the first and third stages, but the second stage agreement was not as good. The un-stalled pressure prediction for the second stage was within 0.20 of the measured values. For flow coefficients greater than 0.10, approximately 90% of the in-stall data were within 0.10 of the predicted pressure characteristic.

The general shape of the predicted characteristic is the same for all stages, reaching a zero pressure rise at zero flow, while many compressors exhibit some positive pressure rise at zero flow. The mechanisms for this observed phenomenon are not well understood.

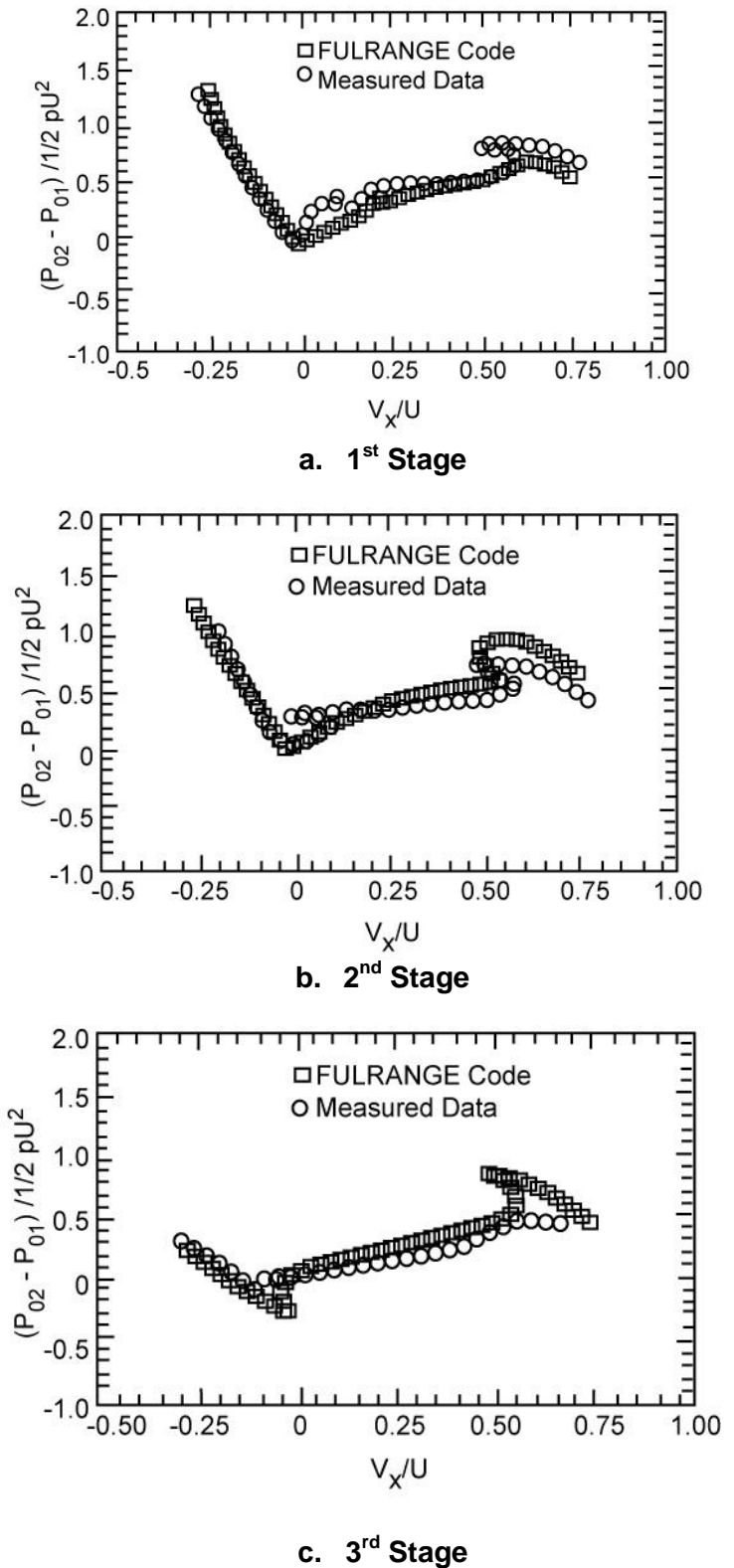


Figure D.5 Three Stage Test Compressor Pressure Characteristics



The first stage reversed-flow pressure prediction is coincident with the measured characteristic, as would be expected (this was the one stage used to develop the correlation coefficients). Application of the reversed-flow model to the second stage prediction yielded an essentially exact match to the characteristic. This supports the application of the results of Carneal [D.15], which indicated that both rotors and stators in reversed flow could be treated as nearly equal loss producers. For both of these stages, the slope of the characteristic is very steep. This is because the blade row losses in reversed flow are very large as shown in Figure D.4, and a large pressure is required at station 3 as shown in Figure D.5 to force air through the stage. The reversed-flow pressure prediction for the third stage is within 0.07 of the corresponding measured values. The more nearly horizontal characteristic for this stage is the result of the last stator in reverse flow operating in the same manner as the IGV in forward flow. Because there are small pressure losses in the last stator row (as compared to the first two stator rows), a smaller pressure at the stage exit will force flow backwards through this stage.

### D.5.2 Application to a High-Speed Compressor

The **FULRANGE** code was used to model the performance of the 10-stage, high-speed compressor tested by Copenhaver [D.4, D.5]. This compressor was the high pressure compressor for a modern high-performance gas turbine engine and was tested at five speeds ranging from 49.8% to 78.5% of design corrected speed to investigate stalling and recovery behavior. For this range of corrected speeds, the variable vane schedule was fixed so there was no change in stage geometry. The vanes open only at higher corrected speeds. Because the present model assumes incompressible flow across a single stage, the predicted stage characteristics are independent of wheel speed and the measured data are presented without distinction of the speed at which they were obtained. The flow, pressure, and temperature coefficients plotted in these figures are defined as follows.

$$\phi = \frac{\left[ \frac{m\sqrt{T_0}}{P_0 A} \right]}{0.5318} [\text{NC}] \quad \text{Eqn. D-18}$$

$$\psi^P = \left[ \text{PR}^{\frac{\gamma-1}{\gamma}} - 1 \right] [\text{NC}]^2 \quad \text{Eqn. D-19}$$

$$\psi^T = [\text{TR} - 1] [\text{NC}]^2 \quad \text{Eqn. D-20}$$

Before discussing the pressure and temperature characteristics, a comment regarding the flow coefficient predictions is in order. The model predicted the transition to stall within 2° angle of incidence to the rotor for all stages in the compressor. It is unknown whether this is the result of an underlying mechanism that is approximated but not yet understood, or whether this is a fortuitous coincidence.

### PRESSURE CHARACTERISTIC PREDICTIONS

The model consistently over-predicted the un-stalled pressure coefficients for the first three stages by a significant amount as shown in Figure D.6 and Figure D.7. The second stage characteristics are similar to those of the third stage and were omitted for brevity. The reasons for the significant disagreement in this area are not clearly understood at this time, but two theories are put forth. For the low corrected speeds at which this compressor was tested, the IGV and first two stator rows were fully closed (large stagger angles, as measured from an axial

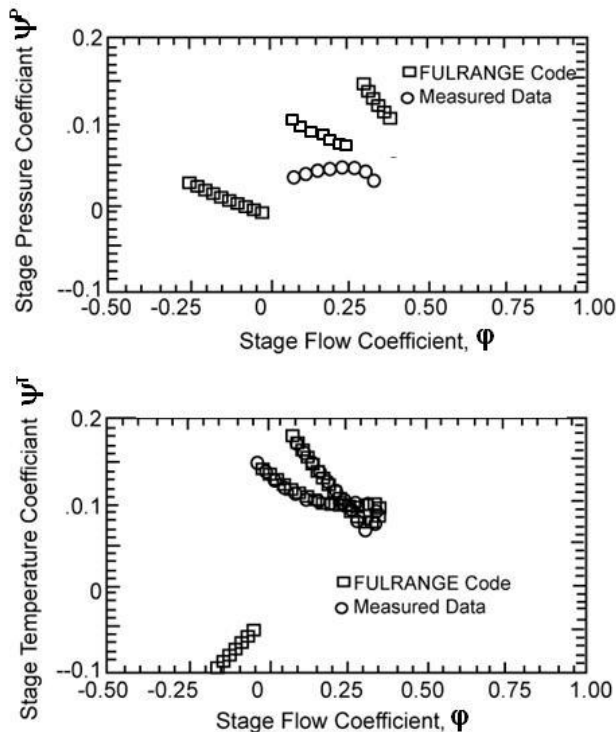


**Figure D.6 Ten-Stage Compressor First-Stage Characteristics**

characteristics for the second stage (not shown) and the third stage (Figure D.7), Copenhagen [D.4, D.5] concluded that choking existed in these stages. Because these stages appear choked at high flow coefficients, and because of the negatively sloped pressure characteristics for the entire operating region, Copenhagen concluded that they were operating in a high-flow manner under all conditions. Based on the flow angles calculated by the **FULRANGE** model, it is suggested that the stages were operating in-stall when the mass flow was low enough to eliminate the choking. The fact that there is good agreement between the predicted in-stall pressure rise and the measured performance for the second and third stages would tend to support this idea. The predicted and measured pressure performance of stages four through eight are very similar and the fifth stage characteristics shown in Figure D.8 as representative.

The un-stalled pressure predictions for these stages are nearly coincident with the actual data

reference). Under these conditions, the flow into the IGv is at a large angle of incidence and is turned significantly away from the axial direction. The large incidence is likely to cause separation from the IGv leading edge causing large pressure losses and a large flow deviation angle. This situation is far from design-point IGv operation and the current model is unable to approximate the performance accurately. It is believed that a similar flow separation may occur in the stator rows of stages two and three, as well. A second effect of the closed vanes is that the flow is accelerated significantly due to the reduction in apparent flow area. This area ratio is of sufficient magnitude to cause choking of the flow (even at moderately low mass

flow), a phenomenon which the present (incompressible) model is not capable of predicting.

Based on the nearly vertical pressure

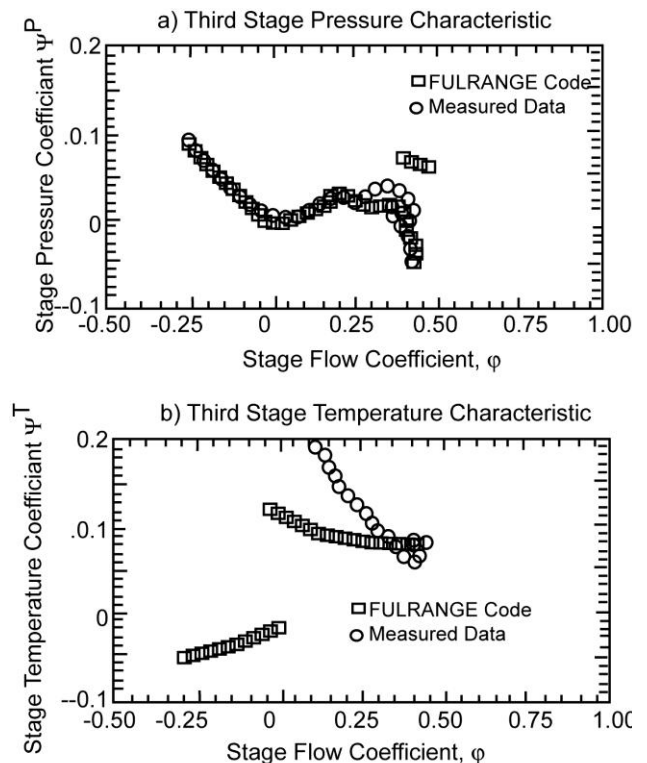


**Figure D.7 Ten-Stage Compressor Third-Stage Characteristics**

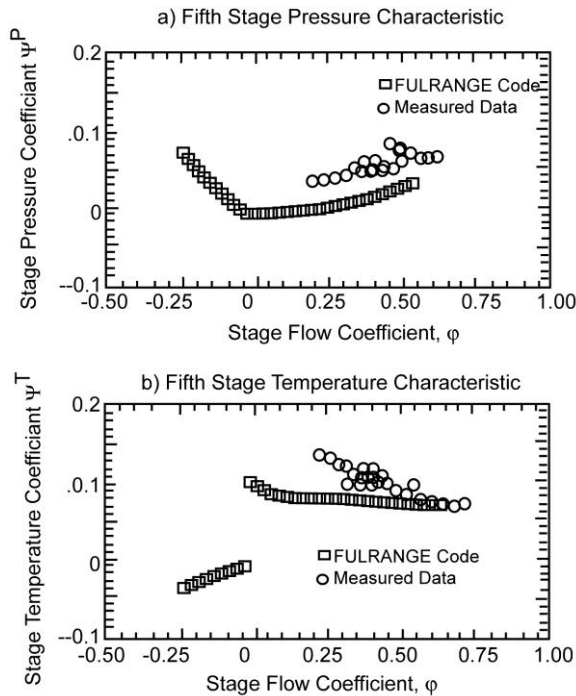


**Figure D.8 Ten-Stage Compressor Fifth-Stage Characteristics**

mass flows, the high velocity air at the stage entrance causes the pressure to drop and the stage performs like a turbine. When operated in-stall, the tenth stage was extracting work from the flow for all data points, with an apparent choking condition at a flow coefficient of 0.57. For these reasons, the predicted and measured performance was not close.

Before discussing the reversed-flow pressure characteristics, it should be noted that the instrumentation placed on this compressor resulted in a stage being defined as a stator followed by a downstream rotor. There are two implications of this stage definition for reversed-flow operation. The first implication is that there is no "last stage stator" for which the losses should be neglected, because the tenth stator is not part of a stage for which performance was measured; the tenth stage consists of stator 9 and rotor 10. The second implication is that the effect of the fully closed IGV and first two stators in reversed flow will only be seen in the first and second stages; stator 3 will control the flow angle into stage 2, stator 2 will control the flow angle into stage 1, and flow

points. The in-stall predictions have the same slope and curvature as the measured characteristics, but are significantly lower in magnitude. It is believed that the under-prediction is a result of the modeling assumption of axis-symmetry stalled flow. Continuing work is addressing methods for improved modeling of the circumferential variations which exist in in-stall flows. The qualitative agreement of the predicted and measured performance of the ninth stage is similar to that of the eighth and the tenth stages, and comparison is omitted for brevity.

Before discussing the operation of the tenth stage, it is instructive to look at the effect of density variation on stage performance. Under low speed conditions, the density increase across each stage is lower than the design value. The area reduction found in high speed, multi-stage compressors results in high axial velocities in the rear stages and can lead to choking. The un-stalled pressure prediction for the tenth stage agrees well with the measured data for flow coefficients less than 0.60 as shown in Figure D.9. At higher

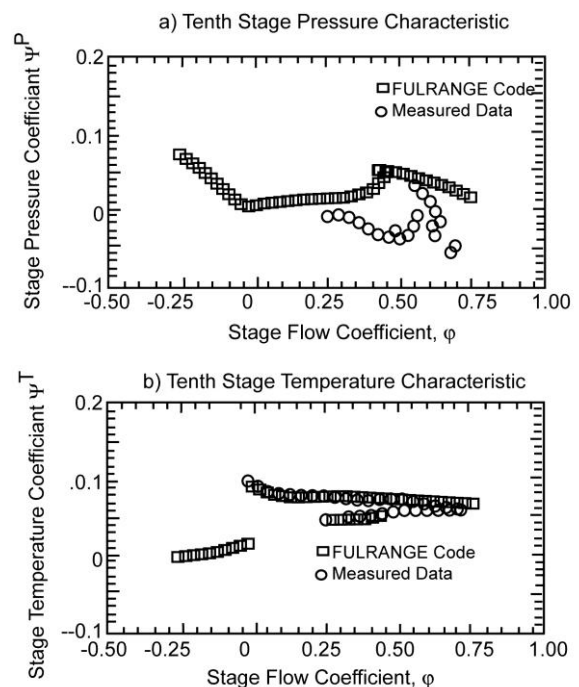


**Figure D.9 Ten-Stage Compressor Tenth-Stage Characteristics**

downstream of the IGV in reversed flow is outside of the compressor.

Because of the experimental difficulty of generating reversed flow in high-speed, high-pressure ratio compressors, no reversed-flow data were obtained. For the compressor, the quantitative predictions of the model are therefore unsupported. For similar stage geometry, Gamache [D.3] measured nearly identical performance in reversed flow. The last eight stages of the 10-stage compressor were geometrically similar, and the reversed-flow performance predictions for those stages are very similar. The model predicted a smaller (magnitude) slope of the reversed-flow pressure characteristic for the first two stages because the IGV and first two stators are closed to the flow path. This resulted in a larger relative flow angle into the first and second rotors and more work being done on the air in the reversed direction.

### **TEMPERATURE CHARACTERISTIC PREDICTIONS**

The un-stalled temperature predictions for the first three stages are higher than the measured characteristics, but show good qualitative agreement. It is believed that the errors in calculating the flow angles leaving the IGV and first two stators (which were fully closed to the flow path) resulted in the calculation of more flow turning than actually occurred. The predicted in-stall temperature rise for these stages is approximately correct at stall inception, but at lower mass flow the measured temperature rise increases much more than the present model predicts. This is believed to be the result of the significant viscous heating which occurs at low flow rates in high speed compressors. At this time, an interesting point can be made about the perceived inception of stall. In the un-stalled region, both the **FULRANGE** predictions and the measured temperature rise show a linear characteristic with negative slope. It is clear from the first and fifth stage data that the temperature characteristic experiences a discontinuous change in slope and curvature at the inception of stall (as defined by the slope of the pressure characteristic) and this is confirmed by the model. Since the change in slope of the measured temperature characteristic is much more pronounced than that of the pressure curve for these stages, it is suggested that temperature performance may be a better indicator of the onset of progressive stall. In reference to the performance of the second and third stages, the temperature characteristics would indicate that at flow coefficients less than 0.30 and 0.33, respectively, are operating in stall.

The un-stalled temperature prediction for the fourth through tenth stages showed excellent agreement with the measured performance. A large fraction of the predictions are almost coincident with the data in this region. The in-stall predictions for the fourth and fifth stages show the same trend of under-predicted temperature rise at low mass flow that was shown by the first three stages, but this trend is less pronounced for the fourth stage.

The in-stall temperature predictions for the sixth through tenth stages are of the same form as for the first five stages (negatively sloped with positive concavity), but the measured characteristics are positively sloped and linear. The measured data often show a steady-state drop in temperature with an increase in pressure, which violates the second law of thermodynamics, for a portion of the stalled characteristic. Copenhaver [D.5] suggested that the indicated drop in temperature was the result of significant recirculating flow within the rotating stall cells. As the flow moved backwards through each stage, work was done on it and its temperature increased.

For all stages, the reversed-flow temperature prediction is positively sloped and linear. The slope of the temperature characteristic is larger for the first two stages than for the last eight. This is because the IGV and first two stators are fully closed to the flow path, creating a larger relative flow angle to the rotor and resulting in higher turning. There are currently no reversed-flow data for this compressor, so comparisons cannot be made. Finally, all of the above



predictions must be viewed as the result of an axis-symmetric model. The model cannot presently account for two- and three-dimensional, non-uniform effects which may influence the flow field.

## D.6 STAGE MODEL SUMMARY

The model was applied to a 10-stage high-speed compressor and mixed results were shown. There were effects of compressibility apparent in the forward stages which could not be captured by the current model. The predicted pressure characteristics showed very good agreement with the un-stalled performance of the last five stages, although the tenth stage characteristics diverged at high mass flows. The in-stall prediction was positively sloped and similar for all stages, but the measured performance was dependent on the stage location; the measured slopes were positive for some stages and negative for others. The reversed-flow pressure characteristics are in good qualitative agreement with those of the low-speed compressor modeled, but no high-speed data exists in the open literature for this flow regime.

The un-stalled temperature predictions for the first three stages showed the correct trends, but were larger than the measured performance; for the last seven stages, the agreement was excellent in this flow regime. At low flow rates, the model under-predicted the temperature rise for the first five stages by a substantial amount; it is believed that this is the effect of significant viscous heating which is not captured by the present model. The in-stall performance of the last five stages indicated a significant amount of recirculating flow in the rotating stall cells which could not be predicted by the steady-state, mean-line stage model. As mentioned previously, the un-stalled temperature predictions for the ninth and tenth stages were very close to the measured values but the pressure characteristics did not show the same level of agreement. It is suggested that the stage losses, and hence the performance are a function of the environment in which the stage is operated as well as the aerodynamic design of the stage. The stage temperature characteristic is essentially linear in the un-stalled operating region, but has a discontinuous change in slope and curvature at the inception of progressive stall.

Because a stage can operate in-stall with a negatively sloped pressure characteristic, it is suggested that the temperature characteristic might be a better indicator of stall inception. When a stage stalls, it upsets the flow field downstream to a sufficient extent that it can drive the next downstream stage into stall, even if the downstream stage was operating away from the stall point. It is also possible that choking of a downstream stage can prevent upstream stages from operating at higher mass flows which might be attainable if the upstream stages were operated in isolation. For these reasons, it is suggested that there are certain points on the steady-state stage characteristics which cannot be reached in a multi-stage environment. This is complimentary to the conclusion that a stage operated in a multi-stage environment would operate un-stalled at flows significantly below the isolated clean-flow stall point, as reported by Longley and Hynes [D.17].

## D.7 ADDITIONAL REFERENCES

**D.3** Gamache, R. N., "Axial Compressor Reversed Flow Performance." Ph.D. Dissertation, Massachusetts Inst. of Technology, May 1985.

**D.4** Copenhaver, W. W., "Stage Effects on Stalling and Recovery of a High-speed 10-stage Axial-Flow Compressor," Ph.D. Dissertation, Iowa State University. October 1988.

- D.5** Copenhaver. W. W., and T. H. Okiishi, "Rotating Stall Performance and Recoverability of a High-speed Ten-Stage Axial-Flow Compressor," AIAA Paper No. 89-2684, July 1989.
- D.6** Copenhaver. W. W., and C. J. Worland, "Acquisition of Unsteady Pressure Measurements from a High Sped Multi-Stage Compressor." ASME Paper No. 88-GT-189, June 1988.
- D.7** Hopf, W. R.. and W. G. Steenken, "Stall Recovery Control Strategy Methodology and Results." AIAA Paper No. AIAA-85-1433, July 1985.
- D.8** Bloch, G. S., and W. F. O'Brien. "A Wide-Range Axial- Flow Compressor Stage Performance Model, " 37th International Gas Turbine Conference, ASME, Cologne, Germany, June 1-4, 1992.
- D.9** Lieblein. S., "Loss and Stall Analysis of Compressor Cascades," **Trans. of the ASME, Journal of Basic Engineering**. 1959. pp. 387-400.
- D.10** Horlock J. H., *Aria1 Flow Compressors*, Robert E. Krega Publishing Company. 1973.
- D.11** Dixon, S. L., *Fluid Mechanics*, **Thermodynamics of Turbomachinery** Pergammon Press, 1975.
- D.12** Moses, H. L., and S. B. Thomason, "An Approximation for Fully Stalled Cascades." **ASME Journal of Turbomachinery**. 1986, pp. 188-189.
- D.13** Turner, R. C., and D. W. Sparkes, "Complete Characteristics for a Single-Stage Axial-Flow Fan." Thermodynamics and Fluid Mechanics Convention, Proceedings of the Institution of Mechanical Engineers, Cambridge, England, 1964,
- D.14** Koff, S. G., and E. M. Greitzer. "Axis-symmetrically Stalled Flow Performance for Multistage Axial Compressors," **ASME Journal of Turbomachinery**, 1986, pp. 216-223.
- D.15** Carneal, J. P., "Experimental Investigation of Reversed Flow in a Compressor Cascade," M.S. Thesis, Virginia Polytechnic Institute and State University, Blacksburg, VA, 1990.
- D.16** Yocum. A. M., III, "An Experimental and Numerical Investigation of the Performance of Compressor Cascades with Stalled Flow." Ph.D. Dissertation. Virginia Polytechnic Institute and State University, Blacksburg, VA. 1988.
- D.17** Longley, J. P., and T. P. Hynes, "Stability of Flow Through Multistage Axial Compressors." **ASME Journal of Turbomachinery**, 1990, pp. 126-132.



## 7 NOMENCLATURE

The following list of symbols is not an inclusive set for all papers presented in this Technical Report. Since the papers were written over many years and by several different authors, the nomenclature would not necessarily be consistent. However, most engineers use common symbols for most definitions. The following symbols and their definition constitute the best available set of definitions across all papers. If the reader can't make out the specific definition used for the symbol of interest, he is encouraged to seek out the original reference and track down the symbol's intended meaning.

<b><u>Symbol</u></b>	<b><u>Definition</u></b>
a	Speed of Sound
a/c	Point of maximum camber as a fraction of chord
A	Area
B	Greitzer B Parameter
c	Chord
$c_p$	Specific heat at constant pressure
$C_l$	Lift coefficient
CFL	Courant, Fredricks, Lewy stability criteria
CALF	Combined Air Loading Factor
D	Diffusion factor
e	Specific energy
E	Total Energy
F	Force
FX	Axial Force
$H_{loss}$	Hub loss constant
H	Total Enthalpy
h	Enthalpy
i	Incidence
I	Rothalpy or Polar moment of inertia
IMP	Impulse function
k	Thermal conductivity or Reduced frequency
L	Length
m	Slope factor, meridional direction, mass
M or Mn	Mach number
MW	Molecular weight
MFF	Mass flow function

$n$	Reference minimum-loss-incidence-angle slope factor, index
$N$	Revolutions per second
$NR_{cor}$	Percent design corrected speed
$P$	Pressure
$PR$	Pressure ratio
$Q$	Heat transfer rate or Conservative variable
$r$	Radius
$r_c$	Radius of curvature
$R$	Gas constant for air
<b><math>R</math></b>	Universal gas constant
$s$	Entropy
$SW$	Shaft Work
$t/c$	Point of maximum thickness as a fraction of chord
$t$	Time
$T$	Temperature
$T_{loss}$	Tip loss constant
$TFF$	Turbine flow function
$TR$	Temperature ratio
$u$	Axial velocity
$U$	Wheel speed
$v$	Velocity in the y-direction, Cartesian coordinates
$V$	Absolute velocity or Volume
$w$	Flow Rate or Work or Velocity in Z-direction, Cartesian coordinates
$W$	Relative velocity or Width
$W_{cor}$	Corrected weight flow
$WDF$	Work done factor
$z$	Axial direction

**Greek****Definition**

$\alpha$	Absolute fluid angle
$\beta$	Relative fluid angle, blade metal angle
$\Delta$	Delta
$\delta$	Deviation
$\phi$	Streamline slope, stage flow coefficient, Equivalence Ratio

$\gamma$	Specific heat ratio or Stagger
$\lambda$	Blockage
$\rho$	Density
$\sigma$	solidity
$\theta$	Camber angle or Circumferential Direction
$\overline{\omega}$	Total pressure loss coefficient
$\omega$	Rotational Speed
$\Gamma$	Torque
$\phi$	Flow coefficient
$\Phi$	Source term in governing equations
$\Psi$ or $\psi$	Performance characteristic, Blade loading coefficient
$\eta$	Efficiency
$\Omega$	Rotational speed
$\tau$	Time Constant

<b><u>Subscript</u></b>	<b><u>Definition</u></b>
a	Axial component
act	Actual
B	Bleed
b	Blade
c	Critical or Corrected
cv	Control volume
cor	Corrected
choke	Choking condition
des	Design
g	gas
hub	Hub location
i	Incidence
id	Ideal
M	Mach number related
m	Meridional component, metal angle
max	Maximum
min	Minimum
new	new time

r	Radial direction component
ref	Reference condition
s	Speed or Static condition
ss	Stead state
shape	Shape factor
stall	Stalling condition
t	Total
th	Thickness factor
tip	Tip location
v	vapor
vloss	Viscous loss
z	Axial direction component
$\theta$	Circumferential (tangential) direction component

**Superscript****Definition**

'	relative to the blade row
b	solidity exponent
P	pressure
T	temperature
n	nth time
n-1	nth time minus 1
n+1	nth time plus 1